UNIVERSITÉ PARIS-SUD

ÉCOLE DOCTORALE : Sciences et Technologie de l'Information, des Télécommunications et des Systèmes

Institut d'Electronique Fondamentale

DISCIPLINE : Physique

THÈSE DE DOCTORAT

soutenance prévue le 24/06/2015

par

Karl David WEGNER

Förster Resonance Energy Transfer from Terbium Complexes to Quantum Dots for Multiplexed Homogeneous Immunoassays and Molecular Rulers / Transfert d'énergie par résonance de type Förster entre des complexes de terbium et des boîtes quantiques pour des immunodosages et des reglettes moléculaires multiplexés

Directeur de thèse :	Niko HILDEBRANDT	Professeur (IEF, Université Paris-Sud)
Composition du jury :		
Rapporteurs :	Wolfgang PARAK	Professeur (Université de Marburg)
	Martinus WERTS	Chargé de Recherche CNRS (Ecole normale supérieure de Rennes)
Examinateurs :	Fabienne MEROLA	Directrice de Recherche CNRS (Université de Paris-Sud)
	Antigoni ALEXANDROU	Directrice de Recherche CNRS (Ecole Polytechnique)
	Loïc CHARBONNIERE	Directeur de Recherche CNRS (LIMAA IPHC, Strasbourg)
	Peter REISS	Expert senior CEA (CEA Grenoble)

Acknowledgement

Foremost, I would like to express my sincere gratitude to my advisor / flatmate / friend Prof. Dr. Niko Hildebrandt for the continuous support of my PhD study and research, for his patience, motivation, enthusiasm, and immense knowledge. During the last four years, his trust in my abilities, the liberties in the laboratory, opportunities to attend to different conferences and his endless support, made me to the researcher, who I'm today and I'm very grateful for that.

I thank Prof. Dr. Wolfgang Parak and Dr. Martinus Werts for being the reviewers of my PhD thesis.

Special thanks goes to Dr. Daniel Geißler, who supported me since my diploma studies and also helped me in writing this thesis.

I would like to thank the former and actual members of the NanoBioPhotonics group for the nice working atmosphere and discussions.

Dr. Frank Morgner, Dr. Thomas Pons and all of my coauthors of my publications I would like to thank for the fruitful collaboration. Especially Dr. Igor Medintz I would like to thank for his support concerning my PhD thesis and beyond.

I gratefully wish to acknowledge Dr. Loïc Charbonniere, Dr. Peter Reiss, and the company Cezanne for the productive collaboration in the NanoFRET project and for memorable project meetings.

I would like to take the opportunity to thank all members of the family Hildebrandt / Chan Huot, who have let me be a part of their life during the last years. Thank you for the nice BBQs in the french summer, for the help with the french administration, and for the open ears not only for science problems.

In the end my greatest gratitude goes to my family for their love and support, believing in me, and all the advices that have brought me this far.

List of publications

Original publications

1. L. Mattsson, K. D. Wegner, N. Hildebrandt, and T. Soukka. Upconverting Nanoparticle to Quantum Dot FRET for Homogeneous Double-Nano Biosensors. *RSC Advances* **2015**, 5, 13270-13277.

2. S. Lindén, M. K. Singh, K. D. Wegner, M. Regairaz, F. Dautry, F. Treussart, and N. Hildebrandt. Terbium-Based Time-Gated Förster Resonance Energy Transfer Imaging for Evaluating Protein-Protein Interactions on Cell Membranes. *Dalton Transactions* **2015**, 44, 4994-5003.

3. B. Rogez, H. Yang, E. Le Moal, S. Leveque-Fort, E. Boer-Duchemin, F. Yao, Y. H. Lee, Y. ZhangY, K. D. Wegner, N. Hildebrandt, A. Mayne, and G. Dujardin. Fluorescence Lifetime and Blinking of Individual Semiconductor Nanocrystals on Graphene. *The Journal of Physical Chemistry C* **2014**, 118 (32), 18445-18452.

4. K. D. Wegner, F. Morgner, E. Oh, R. Goswami, K. Susumu, M. H. Stewart, I. L. Medintz, and N. Hildebrandt. Three-Dimensional Solution-Phase Förster Resonance Energy Transfer Analysis of Nanomolar Quantum Dot Bioconjugates with Subnanometer Resolution. *Chemistry of Materials* **2014**, 26 (14), 4299-4312.

5. K. D. Wegner, S. Lindén, Z. Jin, T. L. Jennings, R. el Khoulati, P. M. P. van Bergen en Henegouwen, and N. Hildebrandt. Nanobodies and Nanocrystals: Highly sensitive quantum dot-based homogeneous FRET-immunoassay for serum-based EGFR detection. *Small* **2014**, 10 (4), 734-740.

6. K. D. Wegner, Z. Jin, S. Lindén, T. L. Jennings, and N. Hildebrandt. Quantum-Dot-Based Förster Resonance Energy Transfer Immunoassay for Sensitive Clinical Diagnostics of Low-Volume Serum Samples. *ACS Nano* **2013**, 7 (8), 7411-7419.

7. K. Nchimi-Nono, K. D. Wegner, S. Lindén, A. Lecointre, L. Ehret-Sabatier, S. Shakir, N. Hildebrandt, and L. J. Charbonnière. Activated Phosphonated Trifunctional Chelates for Highly Sensitive Lanthanide-based FRET Immunoassays Applied to Total Prostate Specific Antigen Detection. *Organic & Biomolecular Chemistry* **2013**, 11, 6493-6501.

8. K. D. Wegner, P. T. Lanh, T. Jennings, E. Oh, V. Jain, S. M. Fairclough, J. M. Smith, E. Giovanelli, N. Lequeux, T. Pons, and N. Hildebrandt. Influence of Luminescence Quantum Yield, Surface Coating and Functionalization of Quantum Dots on the Sensitivity of Time-Resolved FRET Bioassays. *ACS Applied Materials & Interfaces* **2013**, 5, 2881-2892.

9. W. R. Algar, D. Wegner, A. L. Huston, J. B. Blanco-Canosa, M. H. Stewart, A. Armstrong, P. E. Dawson, N. Hildebrandt, and I. L. Medintz. Quantum Dots as Simultaneous Acceptors and Donors in Time-Gated Förster Resonance Energy Transfer Relays: Characterization and Biosensing. *Journal of the American Chemical Society* **2012** 134, 1876-1891.

10. D. Wegner, D. Geißler, S. Stufler, H.-G. Löhmannsröben, and N. Hildebrandt. Time-resolved and steady-state FRET spectroscopy on commercial biocompatible quantum dots. *Proceedings of SPIE 7909* **2011**, DOI: 10.1117/12.874760.

Reviews

1. K. D. Wegner and N. Hildebrandt. Quantum Dots: Bright and Versatile In vitro and In vivo Fluorescence Imaging Biosensors. *Chemical Society Reviews* **2015**, DOI: 10.1039/C4CS00532E.

2. N. Hildebrandt, K. D. Wegner, and W. R. Algar. Luminescent Terbium Complexes: Superior Förster Resonance Energy Transfer Donors for Flexible and Sensitive Multiplexed Biosensing. *Coordination Chemistry Reviews* **2014**, 273-274, 125-138.

3. D. Geißler, S. Lindén, K. Liermann, K. D. Wegner, L. J. Charbonnière, and N. Hildebrandt. Lanthanides and Quantum Dots as Förster Resonance Energy Transfer Agents for Diagnostics and Cellular Imaging. *Inorganic Chemistry* **2014**, 53, 1824-1838.

Oral presentations

1. K. D. Wegner, X. Qiu, and N. Hildebrandt. Nanoparticle-based homogenous FRET-immunoassays for sensitive multiplexed cancer diagnostics. *11th International Conference on Nanosciences & Nanotechnologies*, Thessaloniki, Greece, **2014**.

2. K. D. Wegner, X. Qiu, and N. Hildebrandt. Multiplexed quantum dot-based FRET immunoassays for sensitive cancer diagnostics. *Nanoscience with Nanocrystals (NaNaX) 6*, Bad Hofgastein, Austria, **2014**.

3. K. D. Wegner, S. Lindén, Z. Jin, and N. Hildebrandt. Bunte Quantenpunkte: Nanophotonik für Multiplexdiagnostik. *8. Deutsches BioSensor Symposium*, Wildau, Germany, **2013**.

4. K. D. Wegner, D. Geißler, H. G. Löhmannsröben, and N. Hildebrandt. Time-resolved and steady-state FRET spectroscopy on commercial biocompatible quantum dots. *SPIE Photonics West 2011 - Colloidal Quantum Dots / Nanocrystals for Biomedical Applications VI*; San Francisco, USA, **2011**.

5. K. D. Wegner, D. Geißler, H. G. Löhmannsröben, and N. Hildebrandt. Commercial quantum dots as FRET donors for nano-biotechnology.*3rd EuCheMS Chemistry Congress - European Association for Chemical and Molecular Sciences Chemistry Congress*, Nürnberg, Germany, **2010**.

Poster presentations

1. K. D. Wegner, X. Qiu, and N. Hildebrandt. Multicolor colloidal quantum dots for FRET-based multiplexed detection of cancer biomarkers. *30 years of colloidal quantum dots conference*, Paris, France, **2014**.

2. K. D. Wegner, X. Qiu, and N. Hildebrandt. Semiconductor quantum dots in homogeneous multiplexed FRET immunoassays. *E-MRS Spring meeting - European Materials Research Society Spring meeting*, Lille, France, **2014**.

3. K. D. Wegner, X. Qiu, S. Lindén, Z. Jin, and N. Hildebrandt. Terbium to Quantum Dot FRET for Multiplexed Cancer Diagnostics. *Lanthanide-Based Compounds: from Chemical Design to Applications*, Orléans, France, **2013**.

4. W. R. Algar, K. D. Wegner, A. L. Huston, J. B. Blanco-Canosa, M. H. Stewart, A. Armstrong, P. E. Dawson, N. Hildebrandt, and I. L. Medintz. Quantum Dots as Simultaneous Acceptors and Donors in Time-Gated Förster Resonance Energy Transfer Relays: Characterization and Biosensing. *Nanoscience with Nanocrystals (NaNaX) 5*, Fuengirola, Spain, **2012**.

5. W. R. Algar, K. D. Wegner, A. L. Huston, J. B. Blanco-Canosa, M. H. Stewart, A. Armstrong, P. E. Dawson, N. Hildebrandt, and I. L. Medintz. Quantum Dots as Simultaneous Acceptors and Donors in Time-Gated Förster Resonance Energy Transfer Relays: Characterization and Biosensing. *7th Workshop on Advanced Multiphoton and Fluorescence Lifetime Imaging Techniques*, Saarbrücken, Germany, **2012**.

6. K. D. Wegner, D. Geißler, H. G. Löhmannsröben, and N. Hildebrandt. Time-resolved and steady-state spectroscopy on commercial quantum dot-donor and dye-acceptor based FRET systems. *22. Lecture Conference of the GDCh-Division Photochemistry*, Erlangen, Germany, **2010**.

Contents

1 Introduction

Biological systems like the human body are of great complexity and can be compared with a clockwork. Like cogwheels in a clockwork many small reactions inside the biological system result in the overall reaction of the whole system, for example the increase of body temperature as reaction to an infection. Thereby most of the essential processes and reactions can be followed back to interactions, which take place on a nanometer length scale. The investigation of these interactions is of great importance for their understanding and to show their responsibility in the whole system. The obtained information are useful as they can improve medical treatment in case the clockwork got out of step. But the investigation of those processes sets also high demands on the sensitivity and precision of the analytical method used. Optical access in this nanometric distance range can be obtained by super-resolution microscopy, but sophisticated instrumentation and complex treatment of the obtained images is necessary and limit their applicability.
A simpler analytic method, which has shown to be very suitable for processes at the nanometric scale, is based on Förster resonance energy transfer (FRET). FRET is a non-radiative energy transfer from a donor to an acceptor based on Coulomb interaction. [1–3] Theoretical descriptions can be traced back to the mid 1940s when Theodor Förster derived the quantum mechanical description of this process used until today. [4] One cornerstone for the large popularity of FRET in nanometric measurements is the strong distance dependency for the transfer efficiency, also called FRET efficiency. The r^{-6} dependence allows sensitive measurements of distances, structural changes, and biomolecular processes in a distance range of ca. 1 nm to 20 nm. [1, 3, 5] The effective working distance for FRET measurements strongly depends on the chosen donor-acceptor pair and is characterized by their Förster distance, which is the donor-acceptor distance where the FRET efficiency equals 50 %. Common FRET pairs exhibit a Förster distance of around 3 to 6 nm, but the combination of lanthanide terbium complexes (LTCs) as FRET donors and quantum dots (QDs) as FRET acceptors enables exceptionally large Förster distances up to 11 nm. [6–8] LTCs possess exceptionally long photoluminescence (PL) decay times of several milliseconds compared to conventional luminophores, which have a PL decay time in the nanosecond range. [9,10] This long decay time and the well-structured PL emission bands of LTCs originate in their forbidden f-f transitions within the Tb^{3+} ion. Due to the forbidden character of these transitions the extinction coefficients of the Tb^{3+} ion is very low and the use of coordinating ligands to cage the ion is beneficial. The ligands serve as light

collection antennae and transfer their excitation energy to the Tb^{3+} ion. Additionally, the ligand shields the Tb^{3+} ion from environmentally induced quenching effects, for example, by water molecules, and provide the possibility to conjugate the LTC to biomolecules of interest. [11–13] The use of LTCs as FRET donors has shown to be advantageous as their long PL decay time can be used for time-gated measurements, which allow the distinction between the LTC signal and short-lived autofluorescence background, and thus result in an increased detection sensitivity for biological applications. [14, 15] Furthermore, the separated PL emission bands of LTCs allow a simple signal deconvolution of the LTC signal in the presence of several FRET acceptors, which is beneficial for multiplexed applications. [16–19]

QDs are semiconductor nanocrystals with unique photophysical properties. Their strong and broad absorption, bright and narrow-band PL emission with high quantum yields, and the strong photostability make them superior over conventional fluorophores. [20] A unique feature is their size-tunable emission bands, which is a result of the quantum confinement effect. Due to the smaller size of QDs compared to the calculated exciton Bohr radius (which can be assumed as hole-electron distance) the excitation of a QD leads to the creation of an exciton, which is confined in all three dimensions. As a result the continuous energy bands split into discrete levels. Thereby a decreasing size enhances this effect and results in a blue-shifted emission. [21, 22] Over the last decades the well-established synthesis strategies together with various methods to render QDs biocompatible and to enable the conjugation of biomolecules have resulted in a tremendous amount of QD-based applications. [23–28] In FRET-based applications QDs are most often used as donors and rarely as acceptors. Due to their broad absorbance band and high extinction coefficients, QDs provide excellent properties for the use as acceptors. But the same properties prevent a selective excitation of the FRET donor. Additionally, the similarity in lifetime to most conventional fluorophores used as FRET donors results in only a minor fraction of QDs in the ground state necessary for efficient FRET. [29–31] In contrast to conventional fluorophores, LTCs are well suited as donors for QDs because of their long PL decay time. The combination of the well-structured LTC PL emission bands and the size-tunable QD PL emission make this FRET pair an ideal choice for multiplexed applications. [6,7,30–32]

In vitro diagnostic can be used to indicate the onset of a disease and their progression. Therefore the concentration of specific biomarkers is measured in blood, plasma or serum samples of a patient. The most popular approach to target those biomarkers is the use of antibodies within immunoassays. Thereby the immunoassays can be divided into two measurement formats, namely heterogeneous and homogeneous assays. In contrast to the heterogeneous format, the homogeneous immunoassay avoids time-consuming separation and washing steps, which simplifies the execution and sets low demands on the measurement system. [33] FRET is a suitable analytical method for homogeneous immunoassays as the presence of the biomarker results in a close proximity of donor and acceptor conjugated to two individual detecting antibodies and thus enables FRET. [33, 34] Lanthanide

based FRET immunoassays are well established and have some advantages due to their long PL decay time, which enables highly sensitive detection of biomarker against a low background. [15, 35–39] The distance inside the immunoassays is given by the used antibodies, biomarkers, and luminophores, which act as signal generation system. The latter two cannot further be changed in their size, but the antibodies can be fragmented and would still be able to bind to the biomarker. One of the aims in this work was to investigate the influence of different antibody sizes on the sensitivity of the immunoassay for the detection of specific biomarkers. Therefore the full size IgG antibodies were fragmented into F(ab')$_2$ and F(ab) fragments and conjugated to either the donor or acceptor. The biomarkers used in this work were total prostate specific antigen (TPSA), carcinoembryonic antigen (CEA), neuron-specific enolase (NSE), and epidermal growth factor receptor (EGFR). TPSA comprises the sum of free PSA and PSA bound to proteins in the blood and an increase of the TPSA level can be concomitant with the presence of prostate cancer. The clinical cutoff value for TPSA is 4 ng/mL. NSE and CEA belong to a family of lung cancer biomarkers used for the differentiation between small cell lung cancer and non-small cell lung cancer. The clinical cutoff levels are 12.5 ng/mL and 5 ng/mL for NSE and CEA, respectively. These biomarkers also largely differ in their molecular weights, which are 32 kDa (TPSA), 95 kDa (NSE), and 180 kDa (CEA). Due to the strong distance dependency of FRET, the optimization of the donor-acceptor distance *via* differently sized antibodies conjugated either with donors or acceptors in order to find the best combination to provide the highest sensitivity was one goal of this work. Smaller than a F(ab) fragment are single domain antibodies, also called nanobodies. Nanobodies are single domain antigen binding fragments of heavy chain antibodies with a molecular weight of only 15 kDa and are used in many different antibody based applications. [40–43] In this work they will be used for the first time in a homogeneous immunoassay for the detection of a soluble form of EGFR based on LTC-to-QD FRET.

Next to the investigation of LTC-to-QD FRET in immunoassays this work also applied the system as molecular ruler. Distance measurements using the strong distance dependency of FRET date back to the initial publications of Stryer. [44, 45] Nowadays, FRET is used for the monitoring of inter- and intramolecular interactions, [46] protein folding, [47] or the movement of cellular transporters. [48] Common donor-acceptor pairs are based on organic dyes or fluorescent proteins, which are limited in their photophysical properties. The low photostability, similar decay times than the background, and a small stokes shift between absorbance and emission can make the measurements more difficult. Additionally, the small Förster distances limit the measurable distance and prevent the use in larger biological systems. The combination of LTC and QDs offers several advantages like a good photostability, long decay times and larger Förster distances. One focus of this work was the utilization of LTC-to-QD FRET for the characterization of the size and shape of QDs. These parameters are crucial as they are responsible for the behavior of QDs in biological applications. The structural analysis of QDs are mainly based on trans-

mission electron microscopy (TEM), dynamic light scattering (DLS) and size exclusion chromatography on HPLC. [49] All of these techniques have drawbacks like two dimensional view on QDs using TEM. Although DLS measurements provide information about the QD together with the surface coating, the shape cannot be resolved and additionally a hydration layer is included, which leads to an overestimation of the actual size. In HPLC based measurements the size is estimated in correlation to the retention time of a standard, which also does not allow any shape resolution and shows strong dependency on the standard. More sophisticated approaches are possible, but in order to investigate the QD size and shape in homogeneous measurements in a subnanomolar concentration range, under conditions that are similar to those later used in the actual application, FRET can be the method of choice. Time-resolved analysis of the LTC-to-QD FRET system allows the estimation of donor-acceptor distances using the mathematically fitted decay times and was already shown to be able to offer information about the size and shape of QDs. [6]

The thesis is divided into five chapters and completed by the appendix, which consists of the list of abbreviations, list of used bandpass filters, supplementary graphical information and tables, original publications with their supplementary information, and the bibliography. The first chapter provides the necessary background for FRET including FRET-based applications with the focus on immunoassays and as molecular ruler. The origin of the unique photophysical properties of the used LTCs and QDs will be explained together with their advantages in different applications. The following "Materials and Methods" chapter summarizes the used chemicals and contains the description of the applied analytical methods used for the characterization of the probes and the FRET assay measurements together with information about the evaluation of the obtained data. In two separated parts of the chapter "Results and Discussion" the results of the investigations using LTC-to-QD FRET in homogeneous immunoassays and as molecular ruler are presented. A summary of the obtained results and findings together with an outlook into future developments is given in the last chapter.
The thesis consists of two studies using LTC-to-QD FRET. In the first study the application of LTC-to-QD FRET in homogeneous serum-based immunometric assays is investigated. A detailed spectroscopic characterization of the used luminophores is performed before and after conjugation with different types of antibodies using stationary UV/Vis absorption spectroscopy and stationary and time-resolved luminescence spectroscopy in order to obtain the number of antibodies per luminophore and to verify any alteration of the photophysical properties due to the biomolecule conjugation. In the following, different combinations of conjugated full-size (IgG) antibodies and their fragments ($F(ab')_2$, F(ab)) for the detection of TPSA were investigated to optimize the immunoassay sensitivity using the Lumi4-Tb complex as FRET donor and eFluor 650 nanocrystal as FRET acceptor. The results presented in this first investigation, about how the fragmentation of antibodies influences the performance of the immunoassay for the detection of

TPSA, were already published in reference [50] and the article is attached in the full length together with supplementary information at the end of this work. Based on this investigation, the influence of differently sized biomarkers is investigated using TPSA, NSE, and CEA. Additionally, two other QDs (eFluor 605 nanocrystal, Qdot 705 ITK) were included as FRET acceptors and conjugated as well with IgG, F(ab')$_2$ and F(ab) antibodies for the detection of the different biomarkers. The immunoassay performance using different combinations of antibody sizes and QD colors are compared to results from already established commercial diagnostic kits targeting the same biomarkers and measured under the same conditions. Clinical (human) samples were measured for the biomarker TPSA to show the clinical applicability of the developed LTC-to-QD FRET immunoassay. Finally, duplex measurements of the biomarkers NSE and CEA prove the superior performance of LTC-to-QD FRET in multiplexing applications. The study is rounded up by an investigation of nanobodies conjugated either with Lumi4-Tb complex or to eFluor 650 nanocrystal for the detection of soluble EGFR. The presented results are the first demonstration of nanobody-based FRET immunoassays using LTC-to-QD energy transfer and were published in reference [51]. The article is attached in the full length together with supplementary information at the end of this work.

In the second study LTC-to-QD FRET was exploited as molecular ruler for the structural analysis of QDs. Prior to the presentation of the results the derivation of the distances from the measured multi-exponential decay curves including the necessary correction for LTCs not participating in FRET is explained, followed by the spectral characterization of the used FRET donors and FRET acceptors. In the first part of the study three different batches of biotinylated QDs with similar emission wavelengths are used in combination with Lumi4-Tb complexes bound to streptavidin. The strong biotin-streptavidin recognition enables efficient FRET and results in a donor-acceptor distance distribution depending on the batch of QDs, which was used to estimate the size, shape, and number of biotin bound on the surface. To avoid further alterations of the QD surface by the conjugation of biotin, a second approach for the establishment of a close proximity between LTC and QD was investigated, namely polyhistidine mediated self-assembly. Therefore the LTC was conjugated to a peptide and to a maltose binding protein, which both exhibit a hexahistidine tag that enables, depending on the QD coating, the coordination to the Zn-rich surface of QDs or to carboxylated surface ligands. A detailed time-resolved study of 11 QDs was performed with different sizes, shapes, and surface coatings in combination with the two LTC-donors, which also possessed different sizes, shapes, orientations, and binding conditions. The analysis of the multi-exponential decay curves of donor and acceptor allowed to obtain information about the size, shape, and biofunctionality of the investigated QD bioconjugates. The results were in agreement with other structural analysis methods, such as TEM or DLS, but with the advantage of a homogeneous measurement with three-dimensional resolution (not easily possible for TEM), without the inclusion of a hydration shell (drawback for DLS), and at low concentrations in the

same environment as used for the biological application. The results of both studies, using biotin-streptavidin recognition and polyhistidine mediated self-assembly, are already published in references [52] and [53], respectively. These articles are attached in the full length with their supplementary information at the end of the work.

2 | Background

2.1 Förster resonance energy transfer

2.1.1 Introduction

Many biosensing applications are based on the luminescence phenomenon for signal transduction. The successful targeting of an analyte is displayed by a change in luminescence intensity and/or lifetime. One opportunity for the manipulation of the luminescence properties in response to the analyte can be accomplished by non-radiative energy transfer. Such energy transfer involves a donor that transfers its energy to an acceptor. In contrast to non-radiative energy transfer, radiative energy transfer is based on the reabsorption of photons emitted from the donor and is observed at donor-acceptor distances larger than the wavelength. [2] There are several types of non-radiative transfers, which can be categorized by their effective working distance. For donor-acceptor distances shorter than ca. 2 nm electron exchange or electron transfer processes are predominant. Due to the requirement of overlapping orbitals they show an exponential decrease in transfer efficiency with increasing distance. Examples for long-range non-radiative interactions are nanosurface energy transfer (up to 40 nm), plasmon coupling (up to 80 nm), and singlet oxygen transfer (up to 100 nm). The most applied non-radiative energy transfers in biological sensing applications are Förster resonance energy transfer (FRET), bioluminescence resonance energy transfer (BRET) and chemiluminescence resonance energy transfer (CRET), which cover the distance range between ca. 1 nm to 20 nm. [8] Among these FRET is most favored in the fields of biology and biochemical applications. The working distance lies in a range that is important for many biological recognition processes and the strong distance dependency can be used for the measurements of distances within a biological system or for monitoring conformational changes of proteins. [5, 34, 44, 47, 48, 54–58]
This chapter provides the required theoretical background for a successful use of FRET in biological applications. For more theory and a larger overview regarding the formalism and applications the following references are recommended. [1–3, 58]

2.1.2 FRET theory

In the late 1940s the pieces of the puzzle for a theoretical description of the energy transfer leading to sensitized fluorescence of a second fluorophore were lying on the table. In experiments the phenomenon of sensitized fluorescence could be observed from the vapors of silver, cadmium, lead, zinc, and indium in the presence of mercury vapor. [59–61] First attempts for a theoretical description were done by Franck, Kallmann and London, in which the requirement of resonance between donor and acceptor and the correct distance dependence of the energy transfer was included but unrealistic sharp spectra were assumed. [61–63] Based on this work, in a "father and son project", J. Perrin and F. Perrin extended the theoretical framework by modeling the fluorophores as electrical dipoles oscillating in resonance and the assumption that the molecules can exist in different electronic states, generally divided in the ground state and excited state. [64] However, the predicted distance dependency was inversely proportional to the third power and thus overestimated. Although F. Perrin did a step in the right direction with the consideration of spectral broadening caused by the interaction of fluorophores within the solvent, the working distance range was still too large. [61]
In 1946 Theodor Förster was the first who could assemble the puzzle due to the inclusion of experimentally accessible parameters like spectra, quantum yields, and lifetimes. [65] Later on, he could verify his approach in a quantum mechanical description. [4] As a result, the predicted distance dependency was then inversely proportional to the sixth power, which fits the experimental data and is the reason why this energy transfer is also called Förster resonance energy transfer.

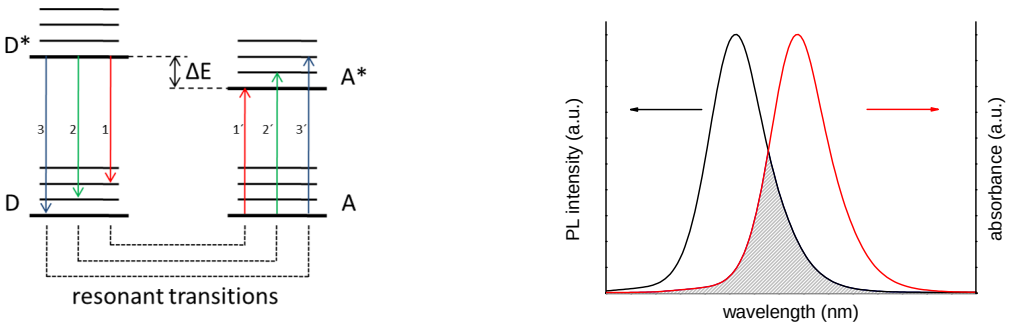

Figure 2.1: LEFT: The simplified Jablonski diagram illustrates the energy levels of a donor (D) and an acceptor (A) in the electronic ground state (D, A) and excited state (D*, A*). The numbers 1, 2, 3 refer to possible resonant transitions (reproduced with permission from ref. [2] Copyright Wiley-VCH Verlag GmbH & Co. KGaA). RIGHT: Spectral overlap (gray shaded area) of the donor PL emission (black curve) and the acceptor absorbance (red curve).

The following discussion of the FRET theory is mainly extracted from the references [2,3]. In a verbal definition, FRET is a non-radiative energy transfer from a donor to an acceptor in close proximity based on Coulomb interaction. A crucial requirement for the energy transfer is the fulfillment of the resonance condition. Therefore the donor-acceptor system has to "share" electronic transitions, which enable the excitation of the molecule from its ground state to the excited state (see Figure 2.1 left). In spectroscopic terms, this means that the photoluminescence (PL) emission spectrum of the donor has to overlap with the absorbance spectrum of the acceptor. The resulting spectral overlap is shown on the right side of Figure 2.1 as gray shaded area. Furthermore, the spectral overlap also defines the degree of the dipole-dipole interaction of donor and acceptor and thus the Coulomb interaction between both.
In general, the FRET process has to be considered as an additional deactivation pathway for an excited donor molecule. The associated rate constant for this process k_{FRET} is given by the equation 2.1:

$$k_{\mathrm{FRET}} = \frac{1}{\tau_{\mathrm{D}}} \left(\frac{R_0}{r} \right)^6 \tag{2.1}$$

τ_{D} is the PL decay time of the donor in absence of the acceptor, r the distance between donor and acceptor, and R_0 is the Förster distance.

The Förster distance in equation 2.1 is characteristic for a donor-acceptor pair and can be calculated using the quantum yield of the donor Φ_{D}, the refractive index of the medium n_{r}, the Avogadro constant N_{A}, the overlap integral $J(\lambda)$ and a factor κ^2, which represents the orientation of the dipole moments of donor and acceptor. The arrangement of the variables for the calculation of the Förster distance is shown in equation 2.2.

$$R_0^6 = \frac{9 \cdot (ln10) \cdot \Phi_{\mathrm{D}} \cdot \kappa^2}{128 \cdot \pi^5 \cdot n_{\mathrm{r}}^4 \cdot N_{\mathrm{A}}} \cdot J(\lambda) \tag{2.2}$$

Due to its strong influence on the Förster distance of a donor-acceptor pair, the overlap integral $J(\lambda)$ of equation 2.2 is a crucial variable. The calculation of this value relies on experimentally accessible data, namely the measurement of the donor emission and the acceptor absorbance (see equation 2.3).

$$J(\lambda) = \int F_{\mathrm{D}}(\lambda) \cdot \epsilon_{\mathrm{A}}(\lambda) \cdot \lambda^4 \cdot d\lambda \tag{2.3}$$

$F_{\mathrm{D}}(\lambda)$ is the area normalized emission spectrum of the donor and $\epsilon_{\mathrm{A}}(\lambda)$ extinction coefficient spectrum of the acceptor.

The before mentioned spectral overlap will not resemble the overlap integral and should only be used for a first approximation of the magnitude of the overlap integral and thus of the Förster distance. The reason is the λ^4 factor inside the equation 2.3, which always leads to a peak of the overlap integral at a longer wavelength than the intercept of donor emission and acceptor absorption in Figure 2.1 (right). [66]

The refractive index describes how light propagates through a medium and is normally larger than unity. Most FRET applications are performed in water-based solutions where the refractive index can range from 1.33 (water) to ca. 1.6. In presence of small biomolecules inside the solution like antibodies or proteins a value of 1.4 can be assumed and is also used in many different FRET-based applications.
The quantum yield (QY) is defined as the ratio of emitted photons over the number of absorbed photons by the fluorophore. A simple approach for the estimation of the QY is the relative measurement to a standard fluorophore. More sophisticated is the absolute measurement of the QY by using an integrating sphere or in conditions where all non-radiative deactivation pathways are suppressed. A high QY of the donor is advantageous for FRET, because it increases the probability for FRET due to the decreased number of other non-radiative deactivation pathways.
The orientation factor κ^2 in equation 2.2 describes the orientation of the dipole transition moments of donor and acceptor and can be calculated with the following equation:

$$\kappa^2 = (cos\alpha \; - \; 3 \; cos\beta \; cos\gamma)^2 \tag{2.4}$$

β and γ are the angles between the transition dipole moments of the donor emission and acceptor absorption and the donor-acceptor connection line, α is the angle arising by a direct coupling of the donor transition dipole moment and the acceptor transition dipole moment.

To support the understanding and spatial imagination of equation 2.4 the left scheme in Figure 2.2 serves as a graphical illustration for the interplay of the angles for the different dipole transition moments.

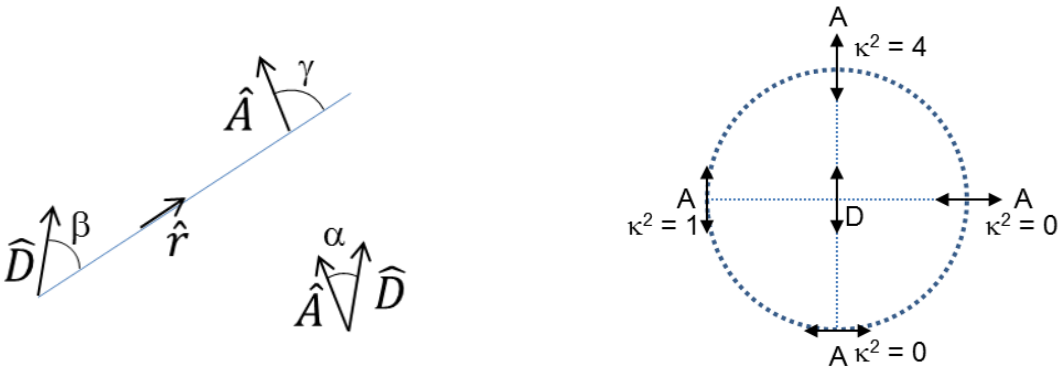

Figure 2.2: LEFT: The orientation of the dipole transition moments of donor emission $\hat{D}$ and acceptor absorption $\hat{A}$ is defined by their included angles β and γ with the donor-acceptor connection line $\hat{r}$, whereas α is the direct angle between $\hat{D}$ and $\hat{A}$ (reproduced with permission from ref. [66] Copyright Wiley-VCH Verlag GmbH & Co. KGaA). RIGHT: Different extreme orientations for the transition moments of donor (D) and acceptor (A) and the resulting value for the orientation factor κ^2 (reproduced with permission from ref. [2] Copyright Wiley-VCH Verlag GmbH & Co. KGaA).

Depending on the orientation of the transition dipole moments, the value for κ^2 ranges between 0 and 4. The corresponding orientations for the different values of κ^2 are shown in the right scheme of Figure 2.2. κ^2 can be measured using x-ray crystal structure or NMR structure analysis. However, those measurements are not applicable for most FRET applications. As a result the famous averaged value, $\kappa^2 = 2/3$, is used in many FRET-based applications. Thereby the background for this averaged value is that the donor and the acceptor fulfill the requirements for dynamic averaging. Dynamic averaging is based on the assumption that the donor and acceptor are able to rotate rapidly and independent from each other in all directions during the lifetime of the donor. This type of averaging is not applicable for all donor-acceptor systems. In cases, for which the free rotation is limited, due to the size of the fluorophore, intrinsic restricted rotation (as for fluorescent proteins), or the binding of the fluorophore to larger rigid host molecule (as for DNA), the isotropic assumption is no longer valid. Under these circumstances the donor-acceptor system is in a static averaging regime and for three dimensional orientational and spatial solution distributions κ^2 can take values between 0 and 2/3. [67] To summarize, it can be noted that a critical evaluation of the used donor-acceptor system concerning their appropriate averaging regime for κ^2 has to be done to avoid errors in the calculation of the Förster distance. A general assumption of $\kappa^2 = 2/3$ would result in a maximal error of 35 % for R_0, with one exception. If the real κ^2 is close to 0 a huge increase of the error is expected.

For the acquisition of quantitative information about the transfer efficiency, also called FRET efficiency (η_{FRET}) the FRET transfer rate and the decay time of the donor can be used like in the first part of equation 2.5. Under consideration of equation 2.1 the right side of equation 2.5 can be rearranged using the Förster distance and the distance between donor and acceptor r.

$$\eta_{\mathrm{FRET}} = \frac{k_{\mathrm{FRET}}}{\tau_{\mathrm{D}}^{-1} + k_{\mathrm{FRET}}} = \frac{R_0^6}{R_0^6 + r^6} \tag{2.5}$$

Consequently, changes in the distance between donor and acceptor influences the FRET efficiency. In a graphical illustration of equation 2.5 the strong distance dependency of the FRET efficiency is observable (see Figure 2.3). As the FRET sensitivity to distance changes is in the same range as many biological recognition systems or conformational processes, FRET is also used as a spectroscopic ruler. But the inverse proportion to the sixth power distance dependency also sets limits on the measurable distance range. As a result, reliable distance measurements using FRET can be performed in the range of ca. $0.5\,R_0$ to $2\,R_0$. Equation 2.5 also indicates that in case of $r = R_0$ the FRET efficiency equals 50 %. This characteristic parameter can be used to choose a donor-acceptor pair, which covers the distance range for the envisaged application.

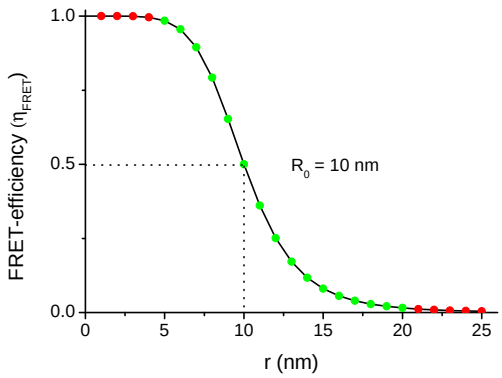

Figure 2.3: Calculated FRET efficiencies (η_{FRET}) for different distances of a donor-acceptor pair with a Förster distance of 10 nm. The green dots confine the range where accurate distance measurements using η_{FRET} are possible.

The FRET process has a direct impact on the photophysical properties of the donor and results in a decrease of its luminescence intensity (I), quantum yield (Φ), and lifetime (τ). This enables the calculation of the FRET efficiency using spectroscopic data of the donor (see equation 2.6).

$$\eta_{\mathrm{FRET}} = 1 - \frac{I_{\mathrm{DA}}}{I_{\mathrm{D}}} = 1 - \frac{\Phi_{\mathrm{DA}}}{\Phi_{\mathrm{D}}} = 1 - \frac{\tau_{\mathrm{DA}}}{\tau_{\mathrm{D}}} \tag{2.6}$$

DA and D describe the value in the presence of the acceptor and in the absence of the acceptor, respectively.

The calculation of the FRET efficiency together with the Förster distance enables the estimation of the donor-acceptor distance in equation 2.5, which allows to use FRET as molecular ruler.

2.2 FRET-based applications

Due to the biological important nanometer working distance and the high sensitivity for small distance changes, an innumerable amount of FRET-based applications were developed over the last decades. In many biological research fields like *in vitro* diagnostic, *in vitro* and *in vivo* imaging and also in super-resolution microscopy FRET measurements are a well established instrument of investigation. However, FRET is not restricted to pure research applications, it is also applied in clinical diagnostics and prognostic. An excellent recently published monograph dedicated only for FRET and FRET-based applications is highly recommended in order to obtain an overview. [58].
The spectrum of available and possible combinations of luminophores, which can be used as donors and/or acceptors in FRET measurements, is nearly infinite. Depending on the application each FRET pair combination provides advantages and disadvantages, and should be chosen carefully with respect to the application. Often used luminophores

are fluorescent proteins (FPs), organic dyes, lanthanide chelates, quantum dots (QDs), and noble metal nanoparticles (NPs). [57] FRET applications can be divided roughly in two categories, namely target sensing and structural analysis. Nearly every target of interest, like cancer markers, pathogen markers, microbes, cells, nucleic acids, toxins, drugs, can be sensed using FRET exploiting the wide field of recognition molecules, such as antibodies, aptamers, oligonucleotides (DNA, RNA), and peptides. [68, 69] Thereby most sensing techniques are based on the binding or cleavage of donor and acceptor in the presence of the target, which can be measured mainly by changes of the donor/acceptor emission intensity. The combination of FRET and microscopy techniques especially for single-particle or single-molecule tracking showed to be very advantageous as it allows highly resolved structural analysis of biomolecules, monitoring the folding of proteins, and provide an inside view in inter- and intra-cellular processes. The dynamics in distance changes can be measured by monitoring the alteration of donor/acceptor lifetimes and anisotropy. [47, 48, 70, 71]

Due to the tremendous amount of possible donor-acceptor combinations and their use in FRET applications, the following references provide a good overview about recent advances and established systems in this field. [57, 72–75]

Within this work, FRET was exploited for the detection of different cancer markers using homogeneous sandwich-immunoassays and as spectroscopic ruler to obtain information about the shape and size of nanoparticles. The next chapter provides a brief introduction to the different kinds of immunoassays with the focus on homogeneous immunoassays and a short introduction of the use of FRET as spectroscopic ruler. Additionally, the applied binding systems are described, which were used to enable a defined distance between donor and acceptor.

2.2.1 Immunoassays

The following discussion presents a summary extracted mainly from the reference [33], which is an excellent resource for detailed information about this topic. Immunoassays are used to detect an analyte or the corresponding antibody in blood or serum samples of a patient. Antibodies are produced by the immune system in an immunogenic reaction after contact with an analyte. The special properties of antibodies led to a widespread use of immunoassays in sensing applications and are based on i) a wide range of possible binding targets, for example natural and man-made chemicals, biomolecules, cells, and viruses; ii) a high specificity, as the recognition process is based on a key-lock principle; iii) a strong binding affinity. In general, two different measurement approaches can be distinguished, namely heterogeneous and homogeneous immunoassays. Heterogeneous assays differ from homogeneous assays due to the immobilization of the antibody or analyte on a solid surface and the existence of one or several separation steps. The separation step is used for the purification of the sample from unbound material and thus leads to an increase in selectivity and sensitivity. Both types of immunoassays can be performed in two different variants depending on the size and type of the analyte.

In case of a large analyte providing several epitopes for antibody binding the immunometric method is preferred. Immunometric-based measurements use two antibodies, which bind to different epitopes on the analyte. These antibodies can be divided into capture and detection antibodies in which the latter antibody comprises the necessary signal generation system for the measurement. In presence of an analyte both antibodies bind to the analyte in a sandwich-like format. Thereby the increase in the detection signal is proportional to the analyte concentration inside the sample.
The competitive immunoassay format is mainly used for the detection of small analytes, which can bind only to one antibody. This method requires the conjugation of the target analyte with a label, which is then also called a tracer. Inside the immunoassay the target analyte competes with the tracers for the binding to the antibodies. A crucial point in this format is the knowledge of the exact amounts of capture antibodies and tracers. Due to the competition of tracer and target analyte, the detected signal of the tracer is indirectly proportional to the concentration of the analyte in the sample. The graphical comparison of both methods is presented in Figure 2.4, in which also the signal dependency on the analyte concentration is presented.

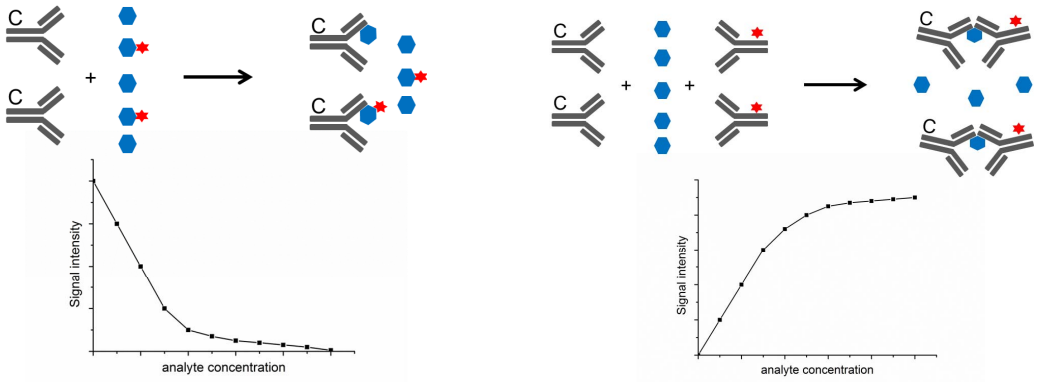

Figure 2.4: LEFT: Competitive immunoassay format in which the analytes (blue) compete with the tracers (analytes labeled with red star) for the binding to the capture antibodies (C). The graph below shows the signal intensity decreasing with increasing analyte concentration. RIGHT: Immunometric immunoassay format consists of the capture antibody (C) and detection antibody (with red star), which bind the analyte (blue) in a sandwich-like format. The increasing analyte concentration results in an increasing signal intensity.

Homogeneous assays

Although the heterogeneous assay format has a higher sensitivity compared to the homogeneous assay format, there are limitations that put the latter format in a favorite position. Due to the immobilization of capture antibodies or analytes on a solid surface, the analyte recognition process is limited by the diffusion rate of the analyte to the solid surface, which results in long incubation times. Furthermore, the separation step places special requirements on the measurement system and therefore requires sophisticated automation. These disadvantages reflect the benefits of the homogeneous assay format. Due to immunochemical reactions inside the whole reaction volume and the omitting of separation steps, homogeneous assays need only short incubation times and set low demands

on the measurement system. The crucial point in this format is the signal modulation in presence of the analyte. Due to the omitted separation steps, homogeneous immunoassays need labels that change their measurable properties in presence of the analyte and different assay formats compared to heterogeneous assays.

Homogeneous assay formats. One of the first performed homogeneous immunoassays was based on particle agglutination. Therefore human immunoglobulins were immobilized on sheep erythrocytes and the presence of anti-immunoglobulin antibodies, present in samples of rheumatoid arthritis patients, was monitored by the visible clumping of the erythrocytes. [76] Nowadays, the immunochemical induced aggregation is measured by the interference of the aggregates with light in terms of intensity changes (turbidimitry), scattering (nephelometry), or particle counting. [77,78] Common methods are also colorimeter measurements exploiting the color change of particles depending on their size, and dynamic light scattering (DLS). Although surface enhanced Raman scattering (SERS) can be used to monitor aggregation of particles in close proximity to the surfaces of gold and silver NPs, the application and sensitivity in homogeneous assays is limited. [79–81]
In lysis immunoassays the presence of the analyte induces the disruption of a liposome membrane, which leads to the release of detectable substances. The signal detection is based on a fluorescence enhancement effect triggered by the release of before quenched fluorophores. Due to the release of a large amount of detectable substances caused by a single analyte, the method is very sensitive but suffers from the lack of standardized probes and from cross-reactivity. [82]
An assay method that allows obtaining results within 30 s and easy execution is based on the change of the tumbling rate of nitroxide radicals measured by electron paramagnetic resonance (EPR) spectroscopy. The binding of the analyte inhibits or slows down the free rotation, which can be observed by a broadening of the spectra. The drawback of this spin immunoassay is the high equipment cost. [83]
The use of radioactive isotopes as labels in immunoassays is controversial. On the one hand these assays are very sensitive but on the other hand they are associated with a strong biohazard effect and the disposal of probes and samples is problematic. Radiolabels used in scintillation proximity assays release alpha and weak beta particles. The collision of the high energetic particles with scintillator molecules result in the emission of measurable photons. In the competitive format the radiolabel is conjugated to the analyte. After the binding to antibodies, immobilized on a latex sphere with dissolved fluorophores, the radiation will produce light pulses, which are detected by scintillation counting. [84]
The presence of an analyte in homogeneous assays can also be measured by monitoring the increase of a current, when electroactive labels like ferrocenes are used. Furthermore, in electrochemiluminescence immunoassays the presence of an analyte can enable an oxidation/reduction cycle on the anode resulting in the excitation of an organic fluorophore. [85, 86]

Enzymes as labels in homogeneous immunoassays play a critical role but as probes of biological origin they have to fulfill some requirements. First of all enzyme and substrate should not be present in the sample, the sample matrix should not affect their activity, and they have to be stable and retain activity under various conditions. Different methods are used to modulate the detection signals using enzymes. In enzyme-multiplied immunoassays techniques (EMITs) the binding of an antibody produces an inhibitory effect based on steric hindrance or conformation changes of the enzyme in order to prevent the digestion of the substrate. [87] For an enhanced substrate digestion in the presence of the analyte charge induced enzyme activation can be used. In this method antibodies labeled with enzymes and negatively charged antibodies bind on a multiepitope antigen and form a negatively charged complex. The Coulomb interaction between the negatively charged antigen complex and the polycationic substrate increase the affinity and thus the sensitivity. The drawback is the attraction of proteins inside the patient serum, which results in a nonlinear behavior of the calibration curve. [88] Promising methods, especially for homogeneous immunoassays, are enzyme channeling or enzyme effector immunoassays. The first method is based on the presence of two enzymes, in which the first enzyme catalyzes the formation of an intermediate substrate. If the second enzyme is in close proximity this intermediate substrate gets digested to a detectable product. The other method uses catalytic inert labels, like enzyme cofactors or enzyme fragments, that only in combination and in close proximity build up an active holoenzyme suitable to digest the actual substrate. [89, 90]

Luminescence oxygen channeling immunoassays are similar to the enzyme channeling approach. The requirement for this method is the close proximity of two beads. One bead consists of a incorporated photosensitizer, which produces singlet oxygen after radiation. The incorporated olefin in the second bead reacts with the singlet oxygen and creates an electronically excited product, which is luminescent. Due to a lifetime of ca. 4 µs, the singlet oxygen can travel ca. 300 nm in all directions, which enables the measurement over large distances. The limitation for this technique is the high reactivity of singlet oxygen with, for example, proteins, which demands low serum amounts inside the sample. [91]

One of the major players in the field of homogeneous immunoassays are measurement methods based on fluorescence. In fluorescence polarization immunoassays the restriction of the otherwise fast rotating fluorophore label is used to measure the binding of the analyte. The decrease of the rotation results in increased polarization of the emitter. Main target analytes are small molecules in a competitive format, because too large molecules do not allow fast reorientation. Consequently, there is only a minor difference in polarization making the identification of the presence of the analyte impossible. [92] Another variant for monitoring the temporal variation in fluorescence intensity is fluorescence correlation spectroscopy. The method enables the measurement of single molecules in 1 fL measurement volume. Bound and unbound antibodies can be distinguished by differences in their diffusion rate, which is greatly influenced when the analyte binds to the antibody.

An extension of this method is fluorescence cross-correlation spectroscopy, in which the detection of two fluorophores in close proximity is the evidence for the binding with the analyte. [93]

FRET-based immunoassays. The use of FRET in homogeneous immunoassays is characterized by a high sensitivity and selectivity. Different FRET pair combinations enable FRET from ca. 1 nm to 20 nm, which allows the detection of small and large analytes. Thereby the presence of the analyte is responsible to establish the close proximity of donor and acceptor at which FRET can occur. For an estimation of the analyte concentration the extent of donor quenching or, more sensitive, the extent of acceptor sensitization can be monitored.
In an immunometric format donor and acceptor are conjugated separately to monoclonal antibodies, which bind to different epitopes on the antigen. This provides the immunoassays with a high selectivity, because only the binding of both antibodies to their specific epitopes results in a positive FRET signal. In general, it is advantageous to conjugate several donors and acceptors to the antibodies to increase the probability that a few of them are in a distance for efficient FRET. Next to the direct labeling of the antibodies, another approach is the use of labeled oligonucleotides attached to the antibodies, which ensure, after binding of the analyte, a suitable distance of donor and acceptor for efficient FRET. This also increases the FRET assay sensitivity due to the stabilization of the intermolecular sandwich complex by the hybridization of the oligonucleotides. [69]
From the photophysical point of view the used luminophores in FRET immunoassays have to fulfill some requirements. First of all the excitation of the donor should cause a negligible excitation of the acceptor to ensure that only the binding event causes a sensitization of the acceptor. Spectrally separated emission spectra of donor and acceptor are advantageous in order to avoid spectral crosstalk, which would distort the signal detection. Furthermore, they have to be stable and their emission properties should not be influenced by the sample matrix.
Luminophores used within homogeneous FRET immunoassays ranging from organic fluorescent dyes, FPs, NPs, lanthanide chelates to upconversion nanoparticles (UCNPs). The advantage of UCNPs compared to all other mentioned fluorophores is the ability of an excitation in the infrared region (IR) and an emission in the visible region of the spectrum. The excitation in the infrared leads to negligible background from directly excited acceptors. The use of moderate energy light sources for the excitation of UCNPs is advantageous over multiphoton excitation, which also produces a low background of direct excited acceptors. But for multiphoton excitation an intense excitation source is necessary to enable the simultaneous absorption of low energy photons to excite the donor. [94]
In other resonance energy transfer approaches the use of external excitation sources is substituted by chemical activation or biochemical reaction. CRET uses, for example, isoluminol conjugated to an antigen, which can then sensitize fluorescein labeled antibodies after binding. The main drawback is the susceptibility of the chemiluminescent reaction

to differences in sample composition and is thus not suitable for clinical applications. [95] The advantage in BRET is that the used chromophores are sequestered and minimally affected by interfering substances.

Critical parameters in immunoassays. Among the critical parameters in immunoassays the most prominent are sensitivity and accuracy. Prior to an estimation of an unknown analyte concentration in a patient sample the dose-response curve, also called calibration curve, of the immunoassay needs to be measured. Therefore the changes of the detector signal in dependence of known analyte concentrations are measured and plotted as a function of the analyte concentration. An example for a calibration curve for an immunometric immunoassay is shown in Figure 2.5. The increasing analyte concentration results in an increase of the detection signal until all capture and detection antibodies are bound to analytes, which results in a leveling of the curve. In the first part of the curve, shown by the green dots, the calibration curve has a linear behavior and can be used to estimate the concentration in a patient sample. In this particular range the immunoassay performance needs to fulfill high standards in terms of sensitivity, selectivity, accuracy, and precision.

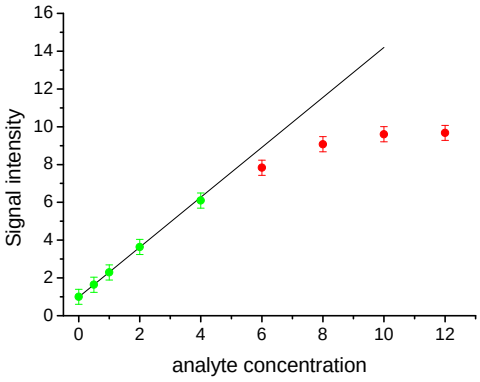

Figure 2.5: Calibration curve of a homogeneous immunoassay. The black line highlights the linear part of the curve in which the green dots represent the dynamic range for the measurement of unknown analyte concentrations. Due to saturation effects the signal intensity saturates at higher concentrations. This concentration range cannot be used for the estimation of the analyte (shown by the red dots).

Sensitivity is defined as the slope of the calibration curve. [96] But there is an ongoing debate about this definition and the possibility to compare different analytical methods based on the increase of the slope. [97, 98] The limit of detection (LOD) is the lowest concentration of an analyte that can be detected with reasonable certainty. [96] This certainty corresponds to the confidence level, which describes the probability of covering the expected value of an estimated parameter within an interval estimated for the parameter. [96] A quite popular approach for the determination of the LOD is to use the analytical sensitivity. Therefore the statistical deviation of the immunoassay in absence of the analyte is measured and added to the mean value using a specific factor, which corresponds to a defined confidence level. For example three times the standard deviation result in

a confidence level of ca. 99 %. This theoretical determined value is mostly far below the first concentration in a calibration curve, which raises the question of the reliability of this value. Only if the curve consists of calibrator concentrations in the similar range as the LOD, the value can be trusted. Using a linear expression to fit the calibration curve can also be misleading as the probability is given that the fitted curve is below the actual curve. To conclude, the analytical sensitivity is afflicted with uncertainties but may be useful for a first impression of the LOD of a new system. Ekins *et al.* proposed to consider the statistical error of the measurement and include this information in the calibration curve by calculation the quotient of the error in response divided by response curve slope. Due to the independence of the manner in which the calibration curve is plotted will allow to make a statement about the precision of two different analytical method. [97] Another more practical concept is the use of the functional sensitivity. [99] The crucial factor in this approach is the coefficient of variation (CV). The CV is used as an indicator for the repeatability of the analyte concentration estimation, which can be influenced by the used antibodies, instrumentation, and environmental circumstances. In order to estimate the LOD, the obtained CV values dependent on the analyte concentration are plotted as a so called precision profile (see Figure 2.6). Thereby the precision profile represent the statistical error in dose measurements. This can be used for intra-, interassay, inter-sample precision, and interlaboratory precision comparison. [100] Furthermore, it allows to compare different analytical methods. [97] The lowest concentration with a CV value smaller than a defined value is taken as LOD. In most commercial immunoassays this corresponds to a CV value lower than 20 %. Next to the LOD, the limit of quantification (LOQ) is another useful definition and similar to the functional sensitivity. LOQ describes the concentration range at which the analyte concentration can be accurately quantified, which equals three times the LOD. [101]

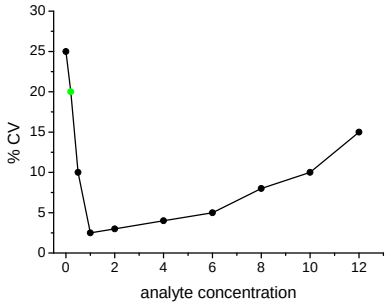

Figure 2.6: Precision profile for the estimation of the functional sensitivity. The green dot corresponds to the LOD of the assay if the defined CV value for the functional sensitivity is 20 %.

The accuracy of an immunoassay is very important and describes the relationship between averaged measured values and the true value. Sources of interference, which decrease the accuracy, are for example alteration of the antibody binding site conformation. The most prominent effects are low-dose hook and high-dose hook effect, which are directly visible in the calibration curve (see Figure 2.7).

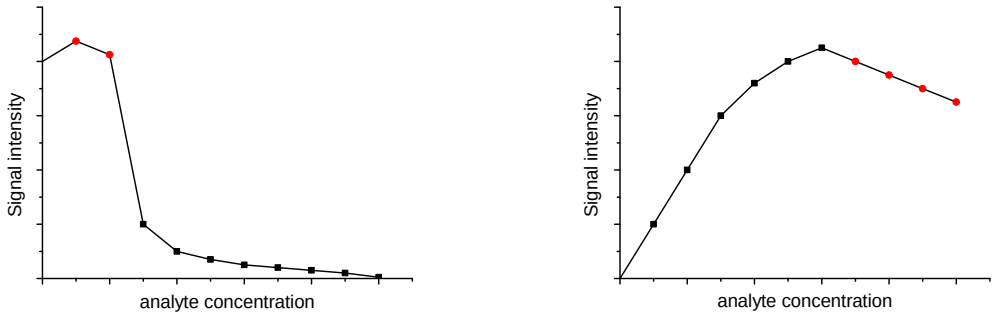

Figure 2.7: LEFT: Low-dose hook effect appears in competitive assays when the tracer has a high specific activity. RIGHT: High-dose hook effect is observed in immunometric assays in presence of an excess of analyte, which causes a saturation of the capture and detection antibodies. The effected concentrations are shown as red dots.

Low-dose effects appear in competitive assays as a consequence of a very high specific activity of the tracer and result in higher signals than in absence of the analyte. In immunometric assays the high-dose hook effect limits the working range of the immunoassay, because an excess of analyte saturates both the capture and the detection antibody. This leads to a decrease of the detection signal at high analyte concentrations. The high-dose hook effect is dependent on the used antibody concentration. In order to increase the working range at a given antibody concentration the sample can be diluted. Dilution is also useful to verify the accuracy of an assay. The sample should give the same results in different dilutions under consideration of the applied dilution factor. An important requirement in this measurement is that the antibodies exhibit the same affinity also in the diluted samples.

2.2.2 Spectroscopic ruler

The strong distance dependency of FRET can be used as a sensitive measurement tool to gain access to conformational changes of proteins, inter- and intramolecular distances of biomole-cules, and allows spatial as well as temporal analysis of proteins and DNA/RNA association in cells. Reaction mechanism, function, and activity of biomolecules are highly influenced by structural changes, which make the investigation of those changes important for the understanding of the biomolecule behavior. Biological structural changes are taking place in the (sub)millisecond time and nanometer length scale, which put the nanosecond time-scale FRET process in a favorite position. [48] The first publication, introducing FRET for the measurement of distances and thus as "spectroscopic ruler", was written by Stryer and Haugland in 1967. Within their work they also could verify the theoretical predicted r^{-6} distance dependency of Förster. [44] Measurable distances using FRET are far below the diffraction limit of light, which makes FRET the first applied optical super-resolution technique. FRET provides at least as good as, if not better size resolution than most of the super-resolution microscopy techniques. Another advantage is the independency of the instrumental system, which results in negligible interferences by instrumental noise and drift. [102] In order to calculate the distance from the Förster formalism (presented in chapter 2.1.2), the donor and optional the acceptor emission has to be measured using fluorescence spectrometers or fluorescence microscopy techniques. The obtained results are used for the calculation of the FRET efficiency, which is convertible to changes in donor-acceptor distance and/or orientation. Time-resolved measurements are preferable over steady-state measurement, because the latter one allows only to obtain a static, population-averaged FRET value. In contrast, time-resolved measurements are independent of the total donor-acceptor concentration and allow an insight view in the dynamics of conformational changes.

On the one hand, ensemble measurements of a large amount of donor-acceptor pairs provide useful information, but on the other hand, the results are an average over all measured distances. In order to obtain structural information of individual biomolecules single-molecule FRET (smFRET) can be used. The measurement of only a single donor-acceptor pair poses special requirements on the used fluorophores, like high brightness, high signal-to-noise ratio (SNR), good photostability, and low fluctuation rate. [46, 103] A common problem in all FRET measurements is the labeling ratio, which is normally not 100 %. The use of alternating-laser excitation (ALEX) in smFRET measurements allows to distinguish partially and complete labeled biomolecules. [104] The special feature of this method is the use of two laser sources in a confocal microscopy setup, which enable the switching between donor excitation and acceptor excitation. Next to the measurement of smFRET also the donor-acceptor stoichiometry is obtained, which helps to select only biomolecules where donor and acceptor are present. Other microscopy techniques capable for the measurement of smFRET are standard total-internal reflection illumination or nearfield scanning optical microscopy. [48] smFRET gave new insights in

protein folding, [47] RNA folding [105] and enabled the monitoring of cellular transporters. [48] Still an open project is the monitoring of correlated motion of multiple biomolecules using smFRET. First experiments with the use of three colors could be shown for the measurement of two independent distances within a single biomolecule. [70]
The distance range of FRET is limited to ca. 20 nm depending on the FRET pair used. For distance measurements beyond this range other techniques can be applied, which widen the range up to 70 nm. The most popular techniques exploiting noble nanoparticles for plasmonic nanoparticle-based surface energy transfer (NSET) or SERS. [102]

Biotin-streptavidin recognition

For an accurate measurement of the distance between a specific donor and acceptor, the binding of those should be selective and have a high binding affinity to ensure a stable complex during the time of observation. An established model system that exhibits both properties in a superior manner is the biotin-streptavidin recognition (see Figure 2.8).

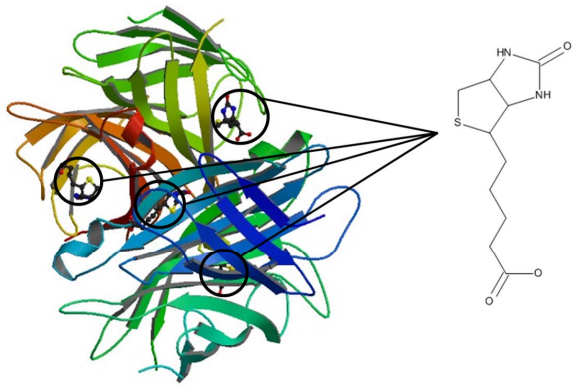

Figure 2.8: LEFT: Quaternary structure of a core streptavidin variant with coordinated biotin molecules in each subunit. (Image from the Research Collaboratory for Structural Bioinformatics (RCSB) Protein Data Bank (PDB) (www.rcsb.org) of PDB ID 1SWE [106]) RIGHT: Chemical structure of a biotin molecule.

Native streptavidin (sAv) is a tetrameric glycoprotein with a molecular mass of 66 kDa and each monomer consists of 159 amino acids. The protein was purified from the bacterium *Streptomyces avidinii* and has a high affinity for the coordination of biotin molecules, which are also known as vitamin H. The most applied sAv version in many biological applications is known as "core"-sAv. In comparison to its native form this modification of sAv only consists of 125-127 amino acids and no sugar residues, which results in some advantages over the native sAv. It shows a better water-solubility and simplified binding ability for biotinylated complexes. [107, 108] The superior property of this model system is the high binding constant of 10^{13} L/mol for the binding of biotin, which makes it one of the strongest non-covalent recognition processes in nature. [109,110] The binding of biotin by sAv is well investigated and is based on hydrogen bonding between the heteroatoms of biotin and residues of amino acids of the sAv. The binding is also supported by van

der Waals interactions between the biotin and tryptophane residues of the monomer or the close subunit. [109, 111] Due the ability of binding four biotin molecules, the possible existence of cooperative binding could not be solved clearly. [112, 113]
The application fields of the biotin-streptavidin recognition are very diverse and range from affinity chromatography over immunoassays to super-resolution microscopy. Especially interesting is also the low isoelectronic point and the lack of carbohydrates, which result in low non-specific binding in biological solutions. Another advantage is the small size of biotin, which allows the binding to biomolecules without strong interference of their intrinsic properties. [114, 115]
In some applications the possible binding of four biotin molecules can lead to a distortion of the measurement especially for single-molecule or single-particle tracking. The simplest way is the reduction of the tetrameric structure to a monomeric one, which enables the binding of only one biotin. The drawback of this approach is a reduction of the binding affinity. This effect was circumvented by a preparation method, in which the number of functional binding subunits can be controlled without decreasing binding affinity. [116, 117]

Metal-polyhistidine affinity

Another non-covalent binding system used in this work to obtain distinct donor-acceptor distances was based on metal chelation by histidine residues. In contrast to the specific binding of the biotin-streptavidin system, the polyhistidine chelation of divalent cations does not provide as high specificity but a binding constant of 0.1 nM to 100 nM, which is partially lower than for antibody-antigen recognition. The driving force for the binding is the strong metal-affinity between the polyhistidine residues and the metal ions, which is also exploited in protein purification using immobilized metal ion affinity chromatography (IMAC). [118] The resin in IMAC consists of immobilized metal ions like Ni, Cu, Co, Fe or Zn ions, which retain the histidine tagged protein of interest. In nanotechnology the growing utilization of nanoparticles, especially quantum dots, gained a strong interest in efficient bioconjugation methods with biomolecules. Covalent binding strategies using amino, carboxyl or maleimide functional groups and the before mentioned non-covalent biotin-streptavidin binding involve several steps of conjugation and purification including an uncertainty if the biomolecule is affected in its activity. Some quantum dots provide a Zn rich surface and most proteins exhibit the fused histidine tag from IMAC purification, which together enable a simple bioconjugation. Additionally, the binding of the very small histidine tag to proteins, peptides or nucleic acids is simple and does not alter their intrinsic properties. The bottleneck of this reaction is the accessibility of Zn ions on the nanoparticle surface. Too high density of long surface ligands in combination with large histidine tagged proteins result in a low binding probability. On the one hand, the histidine affinity is independent of the surface charge, but on the other hand, the amount of histidine residues strongly influences the binding affinity as well as equilibrium time

for the recognition process. Less than four histidine monomers result in a lower binding affinity and longer equilibrium time, whereas more than six monomers show no further improvement of both properties. Due to this reason the use of 6 histidine residues is used in most applications. In case of the non-covalent binding on solid surface providing divalent ions, the hexahistidine tags provide a polyvalency and cooperative interactions with the surface (see Figure 2.9). The binding valency of biomolecules can be controlled in a ratiometric approach. An advantage for FRET applications is a smaller distance between donor and acceptor caused by the small size of the hexahistidine in comparison to the biotin-streptavidin system. [118–121]

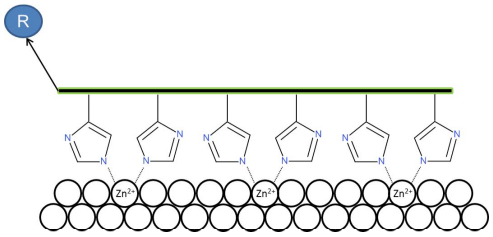

Figure 2.9: Hexahistidine binding to Zn ion rich surface. Different biomolecules presented by R can be attached to the polyhistidine complex .

2.3 Lanthanide complexes

2.3.1 Introduction

Lanthanides are one of the cornerstones of our modern technology. They are omnipresent and play a major role in the development of green energy sources, like for turbine generators in wind mills and in solar cells. They also can be found in a large variety of consumer products like computers, cell-phones, televisions, automotive catalytic converters, petroleum refining, light emitting diodes (LEDs) and in clinical applications. This versatile utilization of lanthanides is due to their unique electrical, optical and magnetic properties, which will be discussed in this chapter. [122–124]

The term lanthanides (Ln) covers a group of 15 elements, which belong to the third subgroup in the periodic system of elements. Ln together with the other members of the third subgroup, scandium ($_{21}$Sc) and yttrium ($_{39}$Y), are also called rare earth elements (REE). Although the name REE is misleading, as the most scarce REE thulium ($_{69}$Tm) can be found much more often in the earth crust than gold or platinum. [125] The discovery of the REE started with the mineral "Ytterbite" in 1787, which was found in a quarry near the village of Ytterby (Sweden). Johan Gadolin analyzed the mineral in 1794 and found an unknown oxide, which he named yttria. Further investigations were necessary to obtain the pure element yttrium. Between 1839 and 1843, it was Carl Gustav Mosander, who could separate two more oxides from yttria, namely erbium ($_{68}$Er) and terbium ($_{65}$Tb). The last discovered Ln was promethium ($_{59}$Pr) in 1938. The main reason for the long period of time for the discovery of the REE and in special the lanthanides, is their similarity in chemical behavior. [126]

This similarity can be explained by the electronic structure of the lanthanides. All 15 Ln from lanthanum ($_{57}$La) to lutetium ($_{71}$Lu) share the electron configuration of xenon, which is characterized by filled $5s$- and $5p$-orbitals. The valence electrons are placed in the $6s$-orbitals and in $4f$-orbitals, with the exception of the lanthanides La, cerium ($_{58}$Ce), gadolinium ($_{64}$Gd), and Lu, where also the $5d$-orbitals are partially involved. Consequently, the Ln differ mainly in the population of the $4f$-orbitals. This leads to the general electron configuration of $[\mathrm{Xe}]4f^i6s^2$, whereby i ranges from 0 for La to 14 for Lu. Due to the population of its inner $4f$-orbitals and to their placement as f-block elements between the s- and the d-block in the periodic system, Ln are also called inner transition elements. In general, the chemical and physical properties of an element will be influenced by the population of the outer orbitals. The special feature of Ln is the shielding of the inner $4f$-orbitals by the populated $5s$- and $5p$-orbitals, which leads to a reduced response to the environment and only small differences in chemical behavior. Due to the large size and diffuse localization of electrons in the f-orbitals, they provide an incomplete shielding of the outer electrons from the increasing nuclear charge. [127] The consequence is the so called lanthanide contraction, for which the ionic radius decreases with the population of the $4f$-orbitals and increasing nuclear charge. But the difference

is just 0.18 Å in the ionic radius from the first lanthanide La to the last lanthanide Lu. This small ionic-radius interval and the favored appearance for Ln as trivalent ions lead to an isomorphic replicability and to a collective occurrence. [124, 128]

2.3.2 Luminescence of lanthanides

In the following text the term lanthanides or Ln refers to the trivalent lanthanide ions. For the use in spectroscopy applications only Ln are suitable with unpaired electrons in the $4f$-orbitals, which is the case for the Ln from cerium (Ce^{3+}) $4f^1$ to ytterbium (Yb^{3+}) $4f^{13}$. [129] Prior to a detailed discussion about the spectral properties of lanthanides it is necessary to clarify important terms and theoretical aspects.
The term luminescence describes the emission of light from "cold matter". Incandescence on the other hand describes the emission of light from "hot matter", like from the sun or a tungsten light bulb. Luminescence is a general term (incl. the two phenomena fluorescence and phosphorescence), which describes the radiative deactivation of excited matter. The excitation of matter can be achieved through different processes, like the excitation by photons (PL), (bio) chemical reaction (chemoluminescence or bioluminescence), or by mechanical stress (triboluminescence). Dealing with lanthanides, photoluminescence plays the major role. [124] Apart from the type of excitation also the nature of the excited state is of importance, e.g., for the discrimination of fluorescence and phosphorescence. Fluorescence is defined as the emission of light from an excited singlet state. Due to the opposite spin of the electron in the excited state compared to the second electron in the ground state, the deactivation process is spin allowed and occurs fast within nanoseconds. In contrast to this the deactivation process in phosphorescence can last up to milliseconds or even seconds. Due to a process called intersystem crossing a transition of an electron from the excited singlet state to the excited triplet state is possible. The intersystem crossing process is characterized by a change of the spin orientation, which makes it to a formally forbidden transition according to one of the selection rules. [3] However, these rules are not strict and should be rather seen as the probability of a transition. There are three important ones, namely the spin selection rule, the symmetry selection rule, and the vibrational selection rule. The triplet-singlet transition responsible for phosphorescence will be enabled by spin-orbit coupling, which alleviate the spin selection rule. Due to the forbidden character of this transition the probability is quite low, which leads to long excited state lifetimes. The most important selection rule in the discussion of the emission of lanthanides is the symmetry selection rule also known as Laporte rule, which does not allow electron transitions in the same subshell. This means that $4f$-$4f$ transitions are forbidden, but these are the main transitions for lanthanides. This rule can be partially repealed by the coupling of vibrational states, which leads to the disruption of the spherical symmetry of the free ion once coupled to ligands. These before mentioned rules count mainly for electric dipole transitions. However, the scene changes taking into account the magnetic dipole transitions, which allow f-f transitions. [124]

For the understanding and interpretation of the electronic structure of lanthanides it is necessary to introduce the quantum numbers L, S, and J. These are used to describe the overall quantum state of the subshell. L stands for the total orbital quantum number, S is the total spin quantum number, and J the total spin-orbit angular momentum quantum number. For the description of the electronic levels of multiple-electron systems a specific notation will be used called spectroscopic terms. These terms can be calculated using the before introduced quantum numbers in the following definition: $^{2S+1}L_J$. The value for $2S+1$ describes the number of orientations of the spin quantum number and is also called multiplicity. The calculation of J depends on the strength of spin-orbit coupling of the individual states, which is mainly dependent on the atomic weight. For Ln the assumption can be made that there is only weak coupling of the individual states, which allows to use the Russel-Saunders coupling scheme for the calculation of J. [124, 130] Using the three Hund's rules it is possible to identify for each lanthanide the ground state arrangement of the electrons in an unfilled shell and assign it to a spectroscopic term. Figure 2.10 shows a small section of the electronic levels of the lanthanides, where the ground state terms and possible excited emissive spectroscopic terms are highlighted in blue and red, respectively.

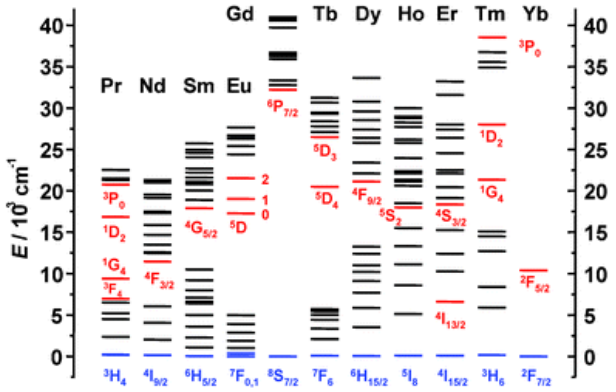

Figure 2.10: Overview of the main electronic levels involved in luminescence for different lanthanide ions. The ground state term of each lanthanide is highlighted in blue, whereas red spectroscopic terms refer to possible emissive excited states. (reprinted with permission from ref. [122] Copyright Royal Society of Chemistry 2005)

For the intrinsic emission property of lanthanides it is advantageous that the gap between the lowest lying excited state and the highest sublevel of its ground multiplet is large. This avoids deactivation by non-radiative processes, like vibrations of bound ligands. Analyzing the gaps of the lanthanides in Figure 2.10 europium (Eu^{3+}), Gd^{3+}, and Tb^{3+} seem to be the best ions in terms of their emission properties. However, Gd ions emit in the ultraviolet (UV) region, whereas Eu and Tb have their emission in the visible range and are thus highly suited for application in bioanalysis. The lanthanides neodymium (Nd), holmium (Ho), Er, and Yb are also interesting for biological applications or technical applications, as they have their emission in the near infrared region (NIR). [122] A general classification of the lanthanides as fluorescent or phosphorescent materials is not possible, as some ions show fluorescent behavior whereas others are phosphorescent and there are also ions which

exhibit both. [12,123] Moreover, the definition of phosphorescence is not absolutely clear. The IUPAC Gold Book defines phosphorescence as follows: "From a phenomenological point of view, the term has been used to describe long-lived luminescence. In mechanistic photochemistry, the term designates luminescence involving change in spin multiplicity, typically from triplet to singlet or *vice versa*. The luminescence from a quartet state to a doublet state is also phosphorescence." [101] Because several other states can be involved in Ln emission (e.g., Eu^{3+} and Tb^{3+} PL involves quintet-septet transitions) it is better to use the general term luminescence, when speaking about emission of the lanthanide ions. The used Ln in this work was Tb. In the following, a more focused view on the luminescence properties is given.

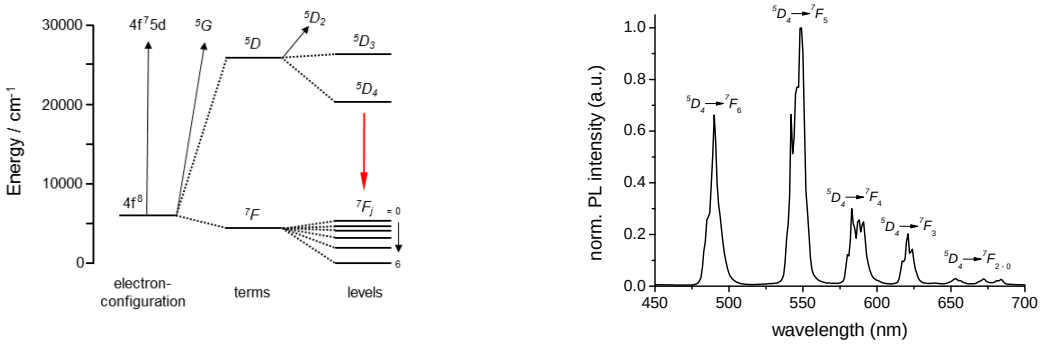

Figure 2.11: LEFT: Partial energy diagram describing the degeneration of the Tb energy levels from which finally luminescence can occur (red arrow). (reproduced from ref. [131]) RIGHT: Luminescence spectrum of a terbium complex showing the luminescence bands caused by the different $^5D_4 - ^7F_J$ transitions.

The trivalent Tb ion has the electronic configuration of [Xe]$4f^8$ and its energy levels are highly degenerated as for the other lanthanides. In Figure 2.11 (left) the part of the energy diagram is shown, which is important for the understanding of the luminescent properties. Due to interelectronic repulsion based on Coulomb interaction, the energy levels get divided into the spectroscopic terms with the ground state term $^7F_6$ and the lowest excited state $^5D_4$. [9, 122] Further degeneration of the spectroscopic terms *via* spin-orbit coupling leads to the different J-levels, which are important for the different emission transitions in the emission spectrum of the Tb ion depicted in Figure 2.11 (right). In the complex environment, where the Tb ion is coordinated with ligands, the energetic levels split into sublevels, due to the electric field of the ligands known as the Stark effect. The Stark splitting is not shown in the energy level diagram in Figure 2.11 (left), as it is a simplified depiction. However, it can be seen in the PL spectrum of Figure 2.11 (right), in which the different $^5D_4 - ^7F_J$ transition peaks show distinct sub-peaks (each $^5D_4 - ^7F_J$ transition can include $2J + 1$ sub-peaks).

The before mentioned shielding effect of the $5s$- and $5p$-orbitals, which is responsible for the lanthanide contraction, also avoids major effects caused by the environment on the luminescence spectrum. This is also the reason for the sharp and narrow emission transitions as the shielding only leads to splitting of the J-levels to an extent of ca. 100 cm^{-1} by an external field. [127]

2.3.3 Luminescent Tb complexes

The sharp and well-defined transitions of the Tb ion shown in Figure 2.11 (right) have very low intensities. The reason for this is based on the low extinction coefficients, which are for each transition smaller than $1\,M^{-1}cm^{-1}$. [132] The low extinction coefficients can be explained by the forbidden transitions of electrons within the $4f$-orbital subshell. Due to the Laporte rule a direct excitation of Tb ions has a very low probability. Another consequence of the formally forbidden transitions is that the lifetimes of the excited states can be up to several milliseconds. [9, 10] Nevertheless, the use of the Tb ions within luminescence applications can be enabled by the use of ligands, which act as sensitizer. In this process, called photosensitization or antenna effect, the ligand is excited and transfers the energy to the lanthanide cation. [133] In Figure 2.12 a simplified Jablonski diagram is shown, which describes the sensitization of the Tb ion by the ligand.

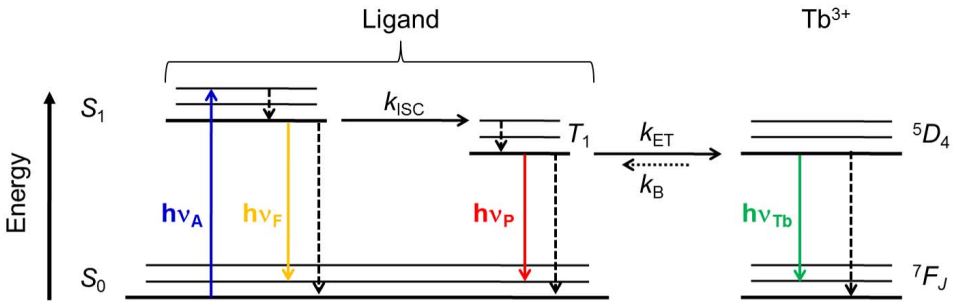

Figure 2.12: Sensitization of the Tb ion *via* ligands used as antenna. The absorption of photons by the ligand ($h\nu_A$) results in the promotion of the ligand from its ground state S_0 to its excited state S_1. Next to the emission of photons ($h\nu_F$) for the deexcitation of the ligand, the energy can be transferred *via* intersystem crossing k_{ISC} to the triplet state T_1. Similar energy levels for T_1 and the $^5D_4$ state of Tb, enable the energy transfer k_{ET} from the ligand to the Tb ion. If the energy difference between the T_1 and $^5D_4$ is to small the probability increases for unwanted back transfer k_B. The radiative deexcitation $h\nu_{Tb}$ from the $^5D_4$ to the different ^7F_J states causes the characteristic emission bands of Tb shown in Figure 2.11 (right). In all cases non-radiative deexcitaion is possible and shown as dashed black arrows.

The ligand should possess a strong absorbance and a high efficiency for intersystem crossing from the excited singlet to the triplet state. From this state the energy can be transferred to the Tb ion *via* transfer processes depending on the distance and type of transfer. [11,134,135] Transfer processes can be FRET, Dexter or charge transfer. Due to a larger energy transfer range and the possible dipole-dipole coupling of the excited triplet state of the ligand with $4f$-orbitals, FRET is more likely for Ln. Dominant charge transfer processes are mainly ligand to ligand charge transfer observable in solid state materials, and ligand to metal charge transfer (LMCT). LMCT is limited to the easily reducible lanthanide ions (samarium (Sm), Eu, and Yb) embedded in inorganic materials containing phosphors and play a minor role for the energy transfer to the Tb ion. However, the type of energy transfer from the ligand to the Tb ion is so far unclear as sensitization of the

lanthanide ion is very complex and involves numerous rate constants. [122, 124] Positive consequences from the sensitization by the ligand is a large effective Stokes shift between the absorption (250-400 nm) and emission (475-700 nm) of the Tb complex, which allows an easy spectral discrimination of the emission from the excitation light.
There are several requirements for the ligands, which can enhance the transfer rate and as such also the luminescence of Ln. First of all, the energy of the triplet state has to provide an efficient transfer to the lanthanide ion and on the other hand minimize the probability for back transfer. [127] This will also decrease the probability for photobleaching of the ligand. [10] Secondly, the ligand should provide an adequate coordination to form a kinetic and thermodynamic stable complex. For lanthanides the common coordination number is 8 to 9, where smaller coordination numbers will be balanced by solvent molecules. [127] These balancing can be problematic as the solvent molecules such as water can act as quencher and reduce the luminescence, due to an enhanced non-radiative deactivation process based on high energy vibration of the O-H bond. [136] The entropy driven complexation and the need for a saturated coordination sphere can be satisfied using polydentate ligands, whose synthesis is quite challenging. [122]
A key parameter for the characterization of luminescent materials is the photoluminescence QY (Φ) (see chapter 2.1.2). For lanthanide complexes the Φ describes the number of photons emitted by the lanthanide per number of photons absorbed by the ligand. Therefore the overall quantum yield is given by

$$\Phi_{\mathrm{Ln}}^{\mathrm{L}} = \eta_{\mathrm{ET}} \cdot \Phi_{\mathrm{Ln}}^{\mathrm{Ln}} \tag{2.7}$$

where $\Phi_{\mathrm{Ln}}^{\mathrm{L}}$ and $\Phi_{\mathrm{Ln}}^{\mathrm{Ln}}$ are the quantum yields resulting from indirect and direct excitation of the Ln ion, respectively. The variable η_{ET} describes the transfer efficiency from the ligand to the lanthanide ion. [122, 123] The intrinsic Φ of the directly excited lanthanide does not take into account the number of absorbed photons, but delivers information about the non-radiative processes, like back transfer to the ligand and luminescence quenching. The intrinsic Φ can be measured by the radiative lifetime of the lanthanide in absence of all non-radiative pathways. [124] In the case of Eu ions the intrinsic quantum yield can be measured using the corrected emission spectra or an integration sphere, which is not possible for Tb ions. The absence of of an isolated magnetic dipole transition prevent the simple estimation from the corrected emission spectra and the low absorbance does not allow to use the integration sphere. Furthermore, the prediction of the spectral intensities using the Judd-Ofelt theory is connected to larger uncertainties due to the proximity of the $4f^7\ 5d^1$ and $4f^8$ electronic configuration. [137,138] Due to those problems, a possible way to estimate the intrinsic quantum yield is the stepwise cooling of the sample until a minimum of non-radiative pathways is reached.
As water molecules increase the probability for non-radiative processes, it is important to evaluate the coordination of the ligand by measuring the number of water molecules in the first coordination sphere. This can be done by exchanging the solvent to its deuterated

analog, which do not lead to a deactivation of the excited state due to the lower vibrational energy of O-D bonds compared to O-H bonds. The number of water molecules can then be determined by measuring the observed lifetime in presence of water and deuterated water using a theoretical approach of Supkowski and Horrocks. [124]

2.3.4 Application of lanthanides

As stated in the beginning, lanthanides are an omnipresent material due to their special physical and chemical properties. Especially lanthanide containing phosphors are used in a broad variety of application fields, ranging from lighting and display devices, lasers, optical communication, night vision, security inks, counterfeiting tags, luminescent coating, probes for luminescent immunoassays, and bioconjugates for medical imaging and the photodynamic treatment of cancer. [139] Due to their wide luminescence range from the UV to NIR, lanthanides can be used as converter materials to transform UV and IR light into light with wavelengths in the visible (400 to 700 nm), which can be easily absorbed by photosensitive devices such as solar cells. Lanthanides gave always rise to new technologies. In this sense the invention of the Nd:YAG laser in 1964, with its main emission line at 1064 nm, had a large impact on science and is now one of the most wide spread lasers. Due to their favorable emission in the visible range, Tb and Eu are the most used lanthanides for lighting devices, where the purity of their emitted light (i.e. their narrow, line-shaped emissions spectra) makes them highly suitable for color reproduction in LEDs and displays. [124]

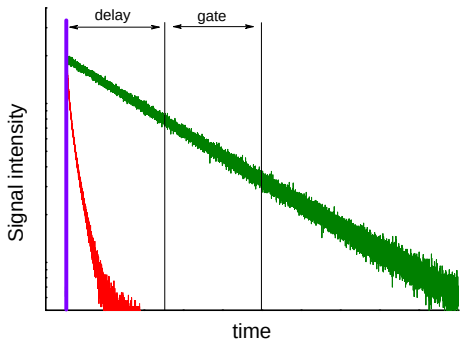

Figure 2.13: Time-gating measurements with lanthanide terbium complexes (LTCs). The excitation of the sample (purple line) results in the long lived decay of LTCs (green curve) and short lived autofluorescence signal from biological components inside the sample (red curve). During the delay, the time between excitation and actual measurement, the autofluorescence decays and allows a nearly background free detection of the signal in a certain gate. The gate width can be optimized to enhance the signal-to-noise ratio (SNR).

Apart from their technological impact, lanthanides are also beneficial in biological application. The main reason for this originates in their forbidden f-f transitions, which lead to long PL decay times in the micro to millisecond regime. Using time-resolved measurements and/or time-gating, short signal components from autofluorescence or light scattering of the biological sample can be easily distinguished, which greatly enhances

the signal-to-noise ratio and thus the sensitivity. The time-gated approach is shown in Figure 2.13. After pulsed excitation the detection of the signal will be started after the autofluorescence has decayed. By varying the temporal width of the detection window the SNR can be optimized.

The conjugation of lanthanide complexes to biomolecules will be established by covalently bound functional groups on the ligand. The most popular conjugation strategies are the use of Ln-complexes functionalized with NHS-esters or maleimide groups, which selectively bind to amino or thiol groups, respectively. The first reported use of Ln-complexes in biological applications was in the mid-1970s. Finnish researchers used Eu, Sm, Tb, and dysprosium (Dy) polyaminocarboxylates and beta-diketones as luminescent sensors in time-resolved luminescent immunoassays. [10]

The utilization of lanthanide complexes in microscopy has not been intensively investigated, mainly due to the lack of suitable microscopes that can excite the sample efficiently in the UV, and are able to image in time-gated mode on the long time scale of lanthanides. However, first applications of lanthanide complexes for steady-state or time-resolved imaging in cells and tissues could be shown. [140–145] Therefore they were conjugated to proteins, [146] peptides, [147] or antibodies. [148, 149] To compensate the low intensity of lanthanides complexes compared to well established dye stains, numerous lanthanide complexes can be enclosed in one nanoparticle, which strongly enhance the luminescence at one binding site. Furthermore, it is possible to bind a high amount of Ln complexes in a small area of the biomolecule without causing self-quenching effects. [150]

A lanthanide that has strongly influenced the field of magnetic resonant imaging (MRI) measurements is Gd. Due to the highest number of unpaired electrons in the $4f$-orbitals of lanthanides, Gd-complexes show a high degree of paramagnetism and thus have high relaxivity. [124] The combination of Gd with NIR emitting Ln in one particle can be used in multimodal applications, in which the shortcoming of one imaging technique is compensated by the combination with another one using the same imaging agent. In this case the combination of NIR imaging and MRI technique is advantageous. NIR enables a relatively deep penetration into the biological material with a high sensitivity, whereas MRI has a relatively low sensitivity, but enables a good spatial resolution and efficient tissue penetration. [151, 152]

The lanthanide complexes described above are so called downconversion materials, as they emit photons of lower energy compared to the excitation energy. In upconversion processes multiple photons are absorbed and lead to emission of a photon of higher energy. Due to the long lifetime of metastable excited states, lanthanides offer the possibility for sequential photon absorption, which make especially Tm, Nd, Dy, Ho, and Er highly suitable for the use in UCNPs. [122, 139, 153] UCNPs offer the advantage of the excitation in the NIR and emission in the visible range or even in the ultraviolet. This effect produces very low background signals and allows a deep penetration into biological material, which leads to their extensive use in bioanalysis [154] and bioimaging. [155]

2.3.5 Lanthanide complexes as FRET donors

The most often used lanthanide complexes as FRET donors comprise Tb or Eu ions and offer several advantages, which are mainly based on their exceptional photophysical properties. [12, 123, 156] Due to the use of lanthanide terbium complexes (LTCs) within this work, the following explanations are focused on LTCs as FRET donors.

Most conspicuous in comparison to other luminophores is their long lifetime in the millisecond range. As described in the previous chapter, the long lifetime enables time-gating measurements. Due to the much shorter lifetime of many acceptors, the emission of direct excited acceptors can be easily distinguished from the actual FRET sensitization. The long lifetime allows measurements with very low background. That is beneficial for the measurement of FRET sensitization of donor-acceptor pairs, which are separated by a large distance and thus exhibit a low FRET efficiency.

The circumstance that the donor lifetime is much longer than the intrinsic acceptor lifetime results in two major advantages. First of all it causes a similarity of the FRET-sensitized acceptor lifetime (τ_{AD}) and the lifetime of the donor in presence of the acceptor (τ_{DA}). This allows the substitution of τ_{DA} with τ_{AD} in equation 2.6 and enables the possibility to calculate the FRET efficiency from two individual energetic transitions (wavelengths). [2] The use of two individual channels in a ratiometric approach decreases the interference from the measurement system such as excitation energy fluctuations. To increase the FRET sensitization it is beneficial to populate several LTCs around a single acceptor. The acceptor can then be excited *via* FRET several times as long as excited LTCs are in close proximity. But this effect will not increase the FRET efficiency, it rather results to a decreased efficiency as several LTCs donors have to compete for one acceptor. [30]

Apart from the long lifetime the concentration of the emission in small bands leads to high area-normalized emission spectra for LTCs and result in large overlap integrals in combination with conventional FRET acceptors. [156–158] Furthermore, the well-defined emission bands are highly suitable for multiplexing applications. [16–19] Therefore acceptors are chosen with emission maxima between or beyond the emission bands of LTC, which result in a strong decreased probability for optical crosstalk.

All these advantages of LTCs in FRET-based applications are used for monitoring protein-protein interactions, orthogonal ligand-dependent protein-peptide binding events, high-through-put screening of potential drug candidates, and numerous *in vitro* bioassays. [75] Some of them are already included in commercially clinical diagnostics kits for the detection of different biomarkers. Such detection technologies are for example HTRF (CIS bio) [159], TRACE (Thermo Fisher Scientific) [160], LANCE (PerkinElmer) [161] or LanthaScreen (Life Technologies) [162].

2.4 Quantum dots

2.4.1 Introduction

Other key luminophores of this work were semiconductor nanocrystals (quantum dots, QDs). After the first theoretical descriptions and experiments in the 1980s, [163–166] the number of scientific and technological applications using QDs increased exponentially. The reason for their great utility in such diverse scientific fields as photovoltaics, optoelectronics, and biomedical applications is based on their unique photophysical properties. [167]

Although QDs are a quite "young" class of luminophores, over the last 15 years they have become an established label in the biological toolkit for luminescence based applications. This development was initiated in 1998 by the publication of two articles using QDs as a biological label in microscopy measurements for the first time. [168, 169] Because QDs are made of toxic heavy-metal ions, the increasing popularity in biological applications raised the question of their toxicity in biological systems. Different studies gave only controversial insights in their toxic behavior so that this question cannot be clearly answered.

The following chapter aims to give a brief overview of the preparation of QDs and the origin of their unique photophysical properties. Afterwards, examples of QD-based biological applications are presented together with a discussion about the advantages of using QDs inside FRET applications.

2.4.2 Preparation of QDs

In general, QDs can consist of atoms from the groups II-VI, III-V, or IV-VI of the periodic table of elements. The most utilized QDs in biological applications are cadmium (Cd)-based QDs due to well established synthetic routes and well-known conjugation strategies for the labeling of biomolecules.

For the use of QDs in biological applications there is a need to synthesize uniform and colloidal QDs with low polydispersity, which Murray *et al.* could establish in 1993 using a high temperature organometallic process. [170] The resulting QDs exhibit a crystal structure in which disturbances on the surface, called trap states, can enhance surface-related recombination, which is an unwanted non-radiative deactivation pathway of excited QDs. To circumvent this effect the core can be surrounded by a shell. Due to a larger band-gap in comparison to the core and the match in crystal structure, shells consisting of a few atomic layers of ZnS or CdS are ideally suited for the reduction of surface-related recombinations. [171, 172] The drawback of the approach from Murray *et al.* was the use of $Cd(CH_3)_2$ as precursor, which is a pyrophoric material and would not allow a simple large scale synthesis. A big step for the synthesis and later commercialization was the exchange of the precursor to CdO by Peng *et al.*. [173] The main parameters for the control of the shape and size of QDs are temperature, growth time, and the amount of precursors. [174]

Due to the synthesis in organic phase QDs are hydrophobic and need further processing to render them water-soluble in order to use them in biological applications. This can be achieved by the manipulation of the surface molecules of the QD. Popular strategies are a complete surface cap exchange, capping with amphiphilic surface ligands, [175] encapsulation in micelles or in silica shells. [25,27,176,177] The chosen surface molecules not only influences the photophysical parameters, they also contribute to the overall size of the QD, which is a critical parameter in biological applications. Next to the facile measurement of the inorganic core by transmission electron microscopy (TEM), the measurement of the hydrodynamic diameter is of importance for the later use as bioprobe. Especially in imaging applications in which the probe has to diffuse through the sample to reach the target, a small size is advantageous. [178] Furthermore, the large surface of QDs can cause numerous non-specific interactions with proteins in the biological media, which can influence the activity of the probe. [179] A surface ligand that provides a good solution for both issues is poly(ethylene glycol)-dihydrolipoic acid (PEG-DHLA). The inclusion of PEG inside the surface molecule structure has shown to be successfully decreasing non-specific binding and simultaneously increase the stability in biological media. [180] Using DHLA results in a small hydrodynamic diameter and additionally provides a good colloidal stability of the QD over a large pH range. [181, 182]

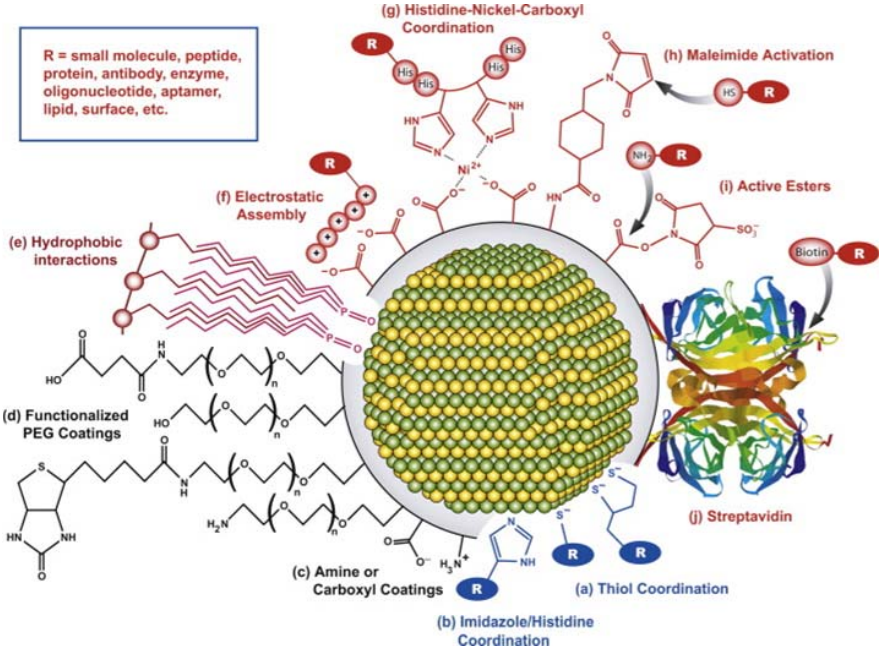

Figure 2.14: Overview about different strategies to render the QD water-soluble (a-e) and possible conjugation strategies (f-j) for the labeling of biomolecules (R).

The last step in the preparation of QDs is to provide functional groups to enable the binding to biomolecules. Numerous methods can be found in the literature and are applicable for nearly all kinds of biomolecules. [23, 24, 26, 27] The most popular strategies are the binding to amino groups using aniline-catalyzed hydrazine bond formation or to thiol groups *via* QDs functionalized with maleimide groups. [183] Due to the large surface, QDs allow a high number of functional groups on the surface, which enable the conjugation

of several biomolecules per QD. For the monitoring and tracking of single molecules one functional group per QD is preferred. In an attempt to provide monovalent QDs different approaches were investigated exploiting peptides, [184] oligonucleotides, [185] and the modified streptavidin-biotin recognition described in chapter 2.2.2. Figure 2.14 shows an overview about the different strategies for the preparation of a water-soluble QD and the possible chemical conjugation methods for the labeling of biomolecules.
The before presented multistep strategy for the preparation of a biocompatible functionalized QD can be reduced to nearly one step by direct synthesis of QDs in water. Advantages like the prevention of surface molecule manipulation, low cost production, and the use of green chemistry make this approach attractive. [186–188] Although the aqueous synthesized QDs have a lower QY than the organic synthesized ones, in a comparative study it could be shown that aqueous QDs can have a better biomolecule conjugation efficiency and stability in biological media. [189]
Next to classical synthesis approaches, QDs can also be produced within living organisms. Responsible for the growth of QDs in rats or in standard wild-type *Lumbricus rubellus* earthworms is an intrinsic heavy-metal detoxification process, which leads to the formation of Cd-based QDs after the intake of $CdCl_2$. [190, 191]

2.4.3 Photophysical properties

The unique photophysical properties of QDs are based on their quasi zero-sized-dimension and their semiconductor material. Semiconductors are defined as material, whose energetic states can be divided into a conduction band and a valence band with a separation by an energy bandgap of ca. 0.5 to 3.5 eV. [22] Depending on the size of the bandgap the excitation of an electron from the valence band to the conduction band can be enabled by using wavelengths with energies between the IR and the UV. In the condition of a promoted electron in the conduction band a positive hole is left in the valence band. The Coulomb interaction between the electron and the hole leads to the creation of a quasiparticle, which is called an exciton. Thereby the exciton Bohr radius describes the spatial distance between electron and hole within the exciton and can range from 1 to 100 nm. Due to the fact that the size of QDs is in the same range, the exciton is confined in all spatial directions, which results in a splitting of the continuous energy bands into discrete energy levels. [22] This phenomenon also known as quantum confinement effect is responsible for the unique photophysical properties of QDs and places them as an intermediate between bulk material and single molecules. Due to the quantum confinement, QDs consisting of the same material can emit at different wavelengths depending on their size (see Figure 2.15). A stronger confinement of excitons in smaller QDs results in a larger energy bandgap and thus in a blue shifted emission. The size dependent QD emission enables the possibility to cover the whole spectrum from UV to NIR. [21] Characteristic for the emission spectra is their Gaussian shape with a full width at half maximum (FWHM) of ca. 25 to 35 nm depending on the polydispersity of the QD batch.

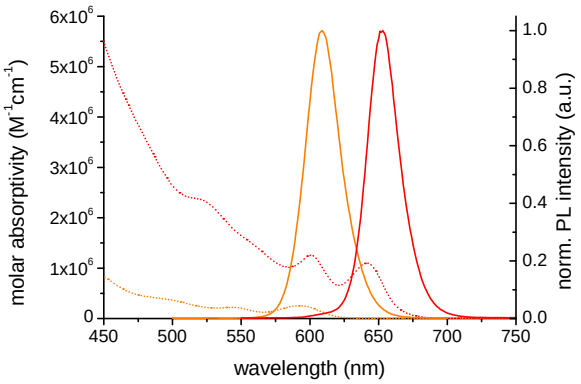

Figure 2.15: Absorbance (dashed) and emission spectra of two QDs that consist of the same material. The difference is there size as the QD with a emission peak at ca. 650 nm (red) is larger than the QD with the emission maximum at ca. 605 nm (orange).

Another unique property of QDs is their broadband absorbance spectrum, which is caused by an increased absorbance probability with increasing excitation energy. This enables the excitation of QDs at every wavelength below the emission band. [27, 192] Concerning their luminescence lifetime, QDs have a multi-exponential decay with lifetimes ranging from 10 to 100 ns. Due to their high QY in combination with high molar extinction coefficients, QDs exhibit an exceptional brightness. [193] Furthermore, they provide a large two-photon cross section up to 10^3 – 10^4 Goeppert-Mayer units, which is advantageous for multiphoton excitation. [194, 195] The before mentioned recombination of excitons on the surface of QDs in the trap states is also responsible for a phenomenon called intermittent fluorescence (blinking), visible only at the single QD level. [192]
In comparison to other common fluorophores like organic fluorescent dyes and fluorescent proteins, QDs have several advantages. FP's and fluorescent dyes exhibit a narrow excitation band, small Stokes shift, and broad emission spectra with a pronounced shoulder in the red, which limit the use in multiplex measurements. Due to the broad absorbance band, the multiplex capability is superior for QDs as several QDs can be excited using one excitation wavelength. Beneficial is also the Gaussian-shaped emission, which reduces the probability of optical crosstalk. [27] Additionally the SNR for FPs and organic dyes is strongly affected by their short lifetime (few nanoseconds) and tendency for photobleaching. QDs on the other hand have a high SNR based on their high brightness, strong photostability, and their longer lifetime, which allow time-gated measurements. [196–199] A detailed discussion of advantages and disadvantages of QDs in comparison to dyes can be found in the reference. [20]

2.4.4 QD-based applications

The unique photophysical properties of QDs result in a versatile utilization in different fields of biology. Especially their brightness and negligible photobleaching make them popular luminophores for *in vitro* and *in vivo* detection/imaging of biomolecules, cells, and

tissues. Apart from microscopy-related applications, they are also used for *in vitro* diagnostics where they enable ultrasensitive detection of biomolecules like nucleic acids, sugars, enzymes, antigens, and antibodies. Furthermore, their large surface is used as carrier for genes and drugs to monitor gene/drug delivery processes. [167] The tremendous amount of QD-based applications and techniques were reviewed and summarized in focused reviews specified after their use in biosensing, [27, 28, 200–202] *in vitro* imaging, [203–205] and *in vivo* imaging. [192, 206–209] Recommended reviews about the controversial topic of whether QDs are toxic or not can be found in the following references. [210–215]

As a passive label, QDs are mainly used within imaging applications. The bottleneck of QDs in cellular, tissue and whole animal imaging are mainly their large size, which prohibit an easy diffusion to the target. Different delivery strategies were developed, ranging from alteration of the QD-surface, using active ligand receptor mediated transportation, to mechanical delivery *via* electroporation or microinjection in order to enable the biological entry of QDs. Thereby the large surface is an ideal scaffold to decorate the QDs with different functions. Such manipulated QDs were successfully used for the detection of cancerous cells, [216] investigation of trafficking, and subcellular distribution of different biomarkers. [217] Due to the strong absorbance and scattering of biological tissue in the visible range, NIR-QDs are favored labels for *in vivo* imaging. [218] The large two-photon cross sections allow an efficient excitation of the QDs with two-photon excitation, which strongly enhance the SNR. Major applications of QDs for *in vivo* imaging are tracking of labeled stem cells, [219] neutrophils, [220] and viruses, [221] monitoring the efficiency of drug delivery, and treatment of cancer cells. [222–224] They have also been used for imaging-guided surgery of sentinel lymph nodes. [225, 226]

The full potential of QDs can be exploited when using them as an active label. Thereby the large surface is used to establish the biorecognition unit, which also causes a manipulation of the QD emission in presence of the target. Signal transduction caused by the change of the QD emission can be initiated by FRET. The utilization of QDs as donors in FRET-based applications is very beneficial due to their unique photophysical properties. First of all their size-tunable emission enables to tune the spectral overlap with the absorbance band of an acceptor in order to obtain the largest possible Förster distance. Furthermore, the broad absorbance band of QDs allows the excitation at a wavelength where the acceptor has a negligible absorbance, which increases the SNR due to less direct excitation of the acceptor. The excitation of several QDs with only one excitation wavelengths in combination with their narrow emission bands allows simple signal deconvolution in multiplexing applications. [8, 30]

In most applications QDs are used as FRET donors, although they are highly suitable FRET acceptors. The major limitation for using them as FRET acceptors is their broad absorbance band, which does not allow a selective excitation of the FRET donor. Additionally the similarity in lifetime to most conventional fluorophores results in the presence of only a small number of QDs in the ground state, which strongly limits the possibility

for FRET. On the other hand the broad absorbance band enables also very large overlap integrals as QDs can cover the whole emission spectrum of a FRET donor. [29–31]
The use of LTCs as FRET donors for QDs as FRET acceptors is very beneficial due to their exorbitant long lifetimes. After excitation, both LTCs and QDs are in the excited state, but after a few 100 nanoseconds the main fraction of QDs are in the ground state whereas most of the LTCs are still in the excited state. This allows an efficient FRET from the LTCs to QDs. Together with the time-gating measurement approach the signal of directly excited QDs can be suppressed and the FRET-sensitized QD emission can be selectively measured. Furthermore, the broad absorbance band with high extinction coefficients can cover most of the LTC emission bands resulting in very large Förster distances up to 11 nm. The size-tunability of QDs is advantageous for selecting emission peaks between the emission peaks of LTC. These properties make the use of LTC-to-QD FRET highly suitable for multiplexing application. [6, 7, 30–32]

3 | Materials and Methods

In this chapter the materials and methods will be described, which were used for the application of LTC-to-QD FRET in immunoassays and as spectroscopic ruler. More detailed information for the single applications can be found in the single chapters.

3.1 Used Chemicals

3.1.1 Buffer solutions

Table 3.1: Buffer ingredients

Name	**Purity**	**Vendor**
Albumin from bovine serum (BSA)	$\geq$ 98.0 %	*Sigma-Aldrich Chimie Sarl*
N,N-Dimethylformamide $HCON(CH_3)_2$	$\geq$ 99.8 %	*Sigma-Aldrich Chimie Sarl*
Hydrochloric acid (HCl)	–	*Sigma-Aldrich Chimie Sarl*
Newborn calf serum (NBCS)	–	*Cezanne / Thermo Fisher Scientific*
Phosphate buffered saline (1x PBS)	–	*Sigma-Aldrich Chimie Sarl*
Sodium bicarbonate ($NaHCO_3$)	$\geq$ 99.5 – 100.5 %	*Sigma-Aldrich Chimie Sarl*
Sodium hydroxide (NaOH)	–	*Sigma-Aldrich Chimie Sarl*
Sodium tetraborate decahydrate ($Na_2B_4O_7 \cdot 10\,H_2O$)	$\geq$ 99.5 %	*Sigma-Aldrich Chimie Sarl*
Trizma® hydrochloride ($NH_2C(CH_2OH)_3 \cdot HCl$)	$\geq$ 99.0 %	*Sigma-Aldrich Chimie Sarl*

3.2 Analytical methods

3.2.1 Characterization of the probes

Absorbance spectra of the conjugated samples were performed against air as reference in small-volume quartz cuvettes on a standard UV/Vis-spectrometer (Lambda 35, Perkin Elmer, USA) or using the SPECTROstar^{NANO} (BMG-Labtech, Germany) in combination with an LVis-microplate. The absorbance spectra were corrected for buffer absorbance. Stationary as well as time-resolved photoluminescence emission spectra of the samples were performed in small-volume quartz cuvettes on a FluoTime 300 "Easy Tau" (Pico Quant, Germany) fluorescence spectrometer. In order to obtain the PL decay curves of LTC-conjugates a xenon flash lamp with a repetition rate of 100 Hz at 350 nm was used. For the measurements of the QD PL decay curves a picosecond pulsed diode laser EPL-405 (Edinburgh Instruments, UK) with a center wavelength (405 ±7) nm was used as excitation source.

3.2.2 Time-resolved FRET assays

All FRET immunoassays and the biotin-streptavidin self-assembly measurements were performed on two fluorescence plate readers. The first plate reader was a modified KRYPTOR compact PLUS (Cezanne/Thermo Fisher Scientific, France) using 500 detection bins of 2 µs integration time. The system has an integrated pulsed nitrogen laser with an excitation wavelength of 337.1 nm and a repetition rate of 20 Hz. The second fluorescence plate reader is a prototype from Edinburgh Instruments (UK) developed during a joined project and referred in this work as EI plate reader. The system allows time-resolved FRET assay measurements using 4000 detection bins of 2 µs integration time. The excitation source was a pulsed nitrogen laser VSL 337 ND (Spectra Physics, USA) with an excitation wavelength of 337.1 nm and a repetition rate of 20 Hz.
The QD-histidine self-assembly measurements were performed on a modified KRYPTOR Immunoreader (Cezanne/Thermo Fisher Scientific, France) using 4000 detection-bins of 2 µs integration time. This plate reader has also an integrated pulsed nitrogen laser with an excitation wavelength of 337.1 nm and a repetition rate of 20 Hz.

Dichroic mirrors and bandpass filter

The instrumental construction for all used plate readers is shown in Figure 3.1. After sample excitation, a dichroic mirror is used to separate the emission signals from the sample into two individual detection channels. This separation allows the simultaneous measurement of the FRET acceptor signals (acceptor channel, ChA) and the FRET donor signals (donor channel, ChD) using two photomultiplier tubes (PMTs). A further selection of the emission wavelengths inside the channels is obtained by the use of bandpass filters, which are optimized for the emission detection of the LTC-conjugate or for the different QD-conjugates. A list of the used bandpass filter inside this work is shown in Table 6.1 in the Appendix 6.2.

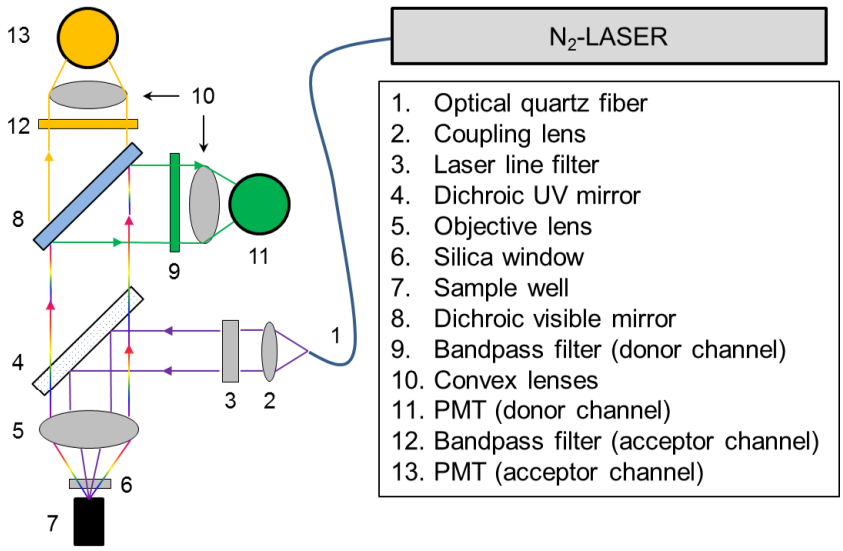

Figure 3.1: Simplified schematic instrumental setup of the used fluorescence plate readers.

3.3 Data evaluation

For data treatment and graphical illustration of the results, spectra, and PL decay curves Origin Pro 8.1 SR3 (OriginLab Corporation, Northhampton, MA, USA) and Microsoft Excel 2010 (Microsoft Corporation, Redmond, WA, USA) were used. The decay time analysis was performed using FluoFit Pro version 4.4.1.0 (PicoQuant, Germany) and FAST software version 3.1 (Edinburgh Instruments, UK).

Ratiometric evaluation of time-resolved FRET assays

The simultaneous measurement of the FRET donor and FRET acceptor signals in two independent channels allows the use of a ratiometric evaluation approach, which enable the correction of fluctuations of signal intensity caused by variations in the excitation source and differences in assay volume or concentrations. The calculation of this intensity ratio R_{I} is shown in equation 3.1

$$R_{\mathrm{I}} = \frac{I_{\mathrm{A}}}{I_{\mathrm{D}}} \tag{3.1}$$

I_{A} and I_{D} are the integrated intensities of an acceptor and donor PL decay curve, respectively, in a defined time-gate (measurement window).

The defined gate of the time-gated measurement used for the FRET immunoassays and biotin-streptavidin assays was 0.1 ms to 0.9 ms (see Figure 2.13 for further information about time-gated measurements). Two different time gates were used for the QD-hexahistidine self-assembly measurements. The integration window of the PL decay curves intensities using ITK-QDs assembly was from 0.05 ms to 0.5 ms. For the measurements using DHLA-QDs assembly the PL decay curves were integrated from 0.2 ms to 2 ms.

4 | Results and Discussion

4.1 Immunoassay

The first part of this thesis was concerned about the application of LTC-to-QD FRET inside homogeneous immunoassays. Due to the utilization of a capture and a detection antibody to target the biomarker, respectively the antigen, the immunometric format sets perfect requirements for the use of FRET as signal transduction method. By the conjugation of the capture antibody with the donor and the detection antibody with the acceptor, the binding of both to the antigen leads to a close proximity of donor and acceptor and enables FRET. Consequently, the immunometric approach in combination with FRET provides a high selectivity and specificity for the applied immunoassay.
Yet, the use of FRET sets also limitations in terms of the sensitivity for the immunoassay based on the strong distance dependency. Inside the immunometric immunoassay two full sized (IgG) antibodies detect the antigen and establish a certain distance depending on the size of the antigen. The molecular weight of a single IgG antibody is around 150 kDa with a dimension of 14.5 x 8.5 x 4 nm. [227] Assuming a biomarker size of ca. 2 nm, the maximum elongation distance between donor and acceptor in the sandwich format is around 22 nm. Additionally the utilization of QDs as luminophore with an approximate diameter of 15 nm results in possible donor-acceptor distances from ca. 15 to 30 nm. At these distances conventional FRET pairs using QD and dyes have very low FRET efficiencies and thus a very low FRET sensitization, which result in decreased sensitivity of the immunoassay. [3] These circumstances put the LTC-to-QD FRET approach in a favorite position as this combination can cover the large distances due to an effective energy transfer range up to ca. 20 nm.
The influence of the distance dependency on the performance of the LTC-QD FRET pair in the immunoassays were investigated using three differently sized biomarkers. These biomarkers or antigens exhibit sizes of 32 kDa for TPSA, 95 kDa for NSE, and 180 kDa for CEA. It is expected that with larger antigen size the donor-acceptor distance changes and results in differences depending on the used biomarker. However, this distance also depends on the position of the antibody binding epitopes on the antigen.
Next to the size of the biomarker also the influence of differently sized antibodies was investigated. Figure 4.1 shows a typical IgG antibody. The IgG antibody can be divided into two major regions, the Fc-domain and the antigen binding domain (AG-domain). As

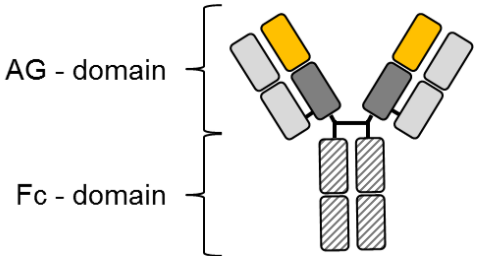

Figure 4.1: Schematic illustration of an IgG antibody. Gray stripped shows the Fc-domain connected *via* the hinge region with the antigen binding domain (AG-domain), which consists of light chains (light gray) and the heavy chains (dark gray + orange) with the actual antigen binding fragment (orange).

the name indicates the AG-domain is responsible for the binding of the antigen and consists of light chains (light gray) and heavy chains (dark gray + orange part), whereof the orange part is the actual antigen binding fragment. The hinge region which connects the Fc-domain and the AG-domain consists of thiol bonds. Under mild reduction conditions the thiol bonds in this area can be reduced and result in the splitting of the domains. The resulting AG-domain fragment is termed F(ab')$_2$ due to the presence of two antigen binding fragments. With enhanced reduction activity the F(ab')$_2$ can be divided into two single F(ab) fragments, which are still able to bind the target antigen. The here explained manipulation of an IgG antibody can be obtained using commercial kits and resultant fragments are schematically presented in Figure 4.2 (a) and (b).

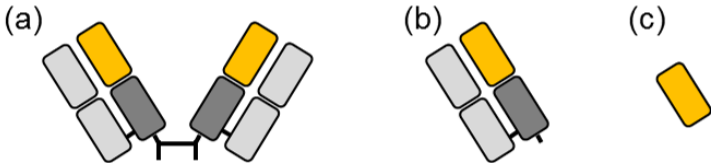

Figure 4.2: Schematic illustration of the obtained fragments under increasing reduction condition from an IgG antibody: (a) F(ab')$_2$ fragment and (b) F(ab) fragment, (c) shows a single domain antibody (nanobody or V_HH).

This fragmentation allows the application of differently sized antibodies ranging from 150 kDa for IgG, 100 kDa for F(ab')$_2$, to 50 kDa for F(ab) and enables the investigation of the influence on the performance for the immunoassay. The single domain antibodies (nanobodies, V_HH) shown in Figure 4.2 (c) represent a specialty as they have a size of only 15 kDa. This type of antibodies are the smallest antibodies that are still able to bind the antigen in a sufficient manner.
The differently sized antigens and the large variety of antibody sizes allow a detailed examination of the implementation of LTC-to-QD FRET in homogeneous immunometric immunoassays. The variation of distances between donor and acceptor offer the possibility to optimize the conditions for each targeted antigen to yield a high immunoassay sensitivity.

Prior to the utilization of the differently sized antibodies in an actual immunoassay the photophysical properties were investigated for the donor and acceptor before and after conjugation. Afterwards the different combinations of LTC labeled IgG, F(ab')$_2$, F(ab) donor-ABs with IgG, F(ab')$_2$, F(ab) acceptor-ABs conjugated to eQD650 was investigated in terms of the immunoassay sensitivity for the detection of TPSA. Based on these experiments promising antibody combinations were chosen for the detection of NSE and CEA using additionally a second QD color. The immunoassays were characterized by the measurements of the long-term stability, using real human samples (TPSA), and in comparison to commercial diagnostic kits. Finally, a duplexed measurement for the simultaneous detection of NSE and CEA using two QD colors in one sample was performed. The investigation was complemented by the detection of soluble EGFR using the nanobodies.

4.1.1 Materials and Methods

Table 4.1: Prepared buffer solutions

	buffer	**concentration**
buffer 1	PBS (pH 7.4)	137 mM NaCl, 2.7 mM KCl, 10 mM PO_4^{3-}
buffer 2	Sodium bicarbonate (pH 9.0)	100 mM
buffer 3	Sodium tetraborate (pH 8.3)	100 mM
buffer 4	Trizma® hydrochloride (pH 7.4)	100 mM
buffer 5	Sodium tetraborate (pH 8.5)	10 mM
buffer 6	Sodium tetraborate (pH 8.5) with $\omega_{BSA} = 0.5\,\%$	10 mM
buffer 7	Trizma® hydrochloride (pH 7.4) with $\omega_{BSA} = 0.5\,\%$	10 mM

Antibodies and antigens

The application of LTC-to-QD FRET in homogeneous time-resolved FRET immunoassays was conducted in close collaboration with the company Cezanne/Thermo Fisher Scientific. They provided lyophilized biomarker calibrator solutions and monoclonal antibodies for the first three biomarkers listed in Table 4.2. After an internal protocol the lyophilized samples were dissolved with ultrapure water and further diluted with newborn calf serum to provide specific concentrations for the measurements of the calibration curves. The Utrecht University (Utrecht, Netherlands) provided nanobodies (V_HH) for the detection of the epidermal growth factor receptor (EGFR). For the measurement of the calibration curve a soluble form of EGFR was used that was bought from R&D Systems Europe Ltd. (Lille, France). All biomarkers were measured in an immunometric format, using two monoclonal antibodies per biomarker. These two antibodies bind to different non-overlapping epitopes on the biomarker and differ in their binding affinity. The antibody

with the higher binding affinity was labeled with the FRET donor and the other lower binding antibody conjugated to the FRET acceptor, which results in the terms donor-antibody (donor-AB) and acceptor-antibody (acceptor-AB) shown in Table 4.2.

Table 4.2: Overview about the used biomarkers and their abbreviations as well as the used monoclonal antibodies conjugated with the FRET donor (donor-AB) or to the FRET acceptor (acceptor-AB).

biomarker	**abbreviation**	**donor-AB**	**acceptor-AB**
total prostate specific antigen	TPSA	PSR 222	PSS 233
neuron-specific enolase	NSE	E15	E20
carcinoembryonic antigen	CEA	GFR44	G15
epidermal growth factor receptor	EGFR	EgA1	EgB4

The monoclonal antibodies for the detection of TPSA, NSE, and CEA were used as full size antibodies (IgG) but also in a fragmented form, termed as F(ab')$_2$ and F(ab). The fragmentation was performed using the Pierce Mouse IgG1 F(ab) and F(ab')$_2$ preparation kit from Life technologies (Carlsbad, CA, USA). Successful preparation of F(ab')$_2$ and F(ab) antibodies was verified using SDS-PAGE.

FRET donor

The FRET donor within this work was a lanthanide terbium complex provided from the company Lumiphore Inc. (Richmond, CA, USA) with the brand name Lumi4-Tb. This LTC exhibit a NHS ester functionality for the conjugation to amino groups on the biomolecule of interest. The chemical structure of the Lumi4-Tb complex is shown in Figure 4.3.

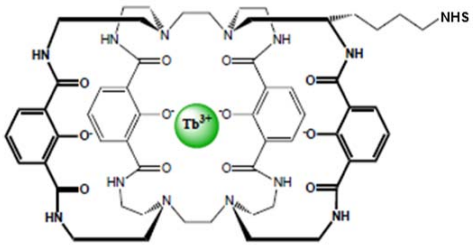

Figure 4.3: Chemical structure of the Lumi4-Tb complex provide by Lumiphore Inc. (Richmone, CA, USA).

FRET acceptors

FRET acceptors used within the FRET immunoassays were commercially available biocompatible QDs with three different emission maxima. A list of the used QDs, their abbreviation and functional groups on the surface is presented in Table 4.3. The first

two QDs were kindly provided by the company eBioscience (San Diego, CA, USA) as sulfhydryl reactive - eFluor 605/650 nanocrystal conjugation kit, whereas iQD705 was purchased from Invitrogen/Life Technologies (Carlsbad, CA, USA).

Table 4.3: Overview about the used quantum dots with their abbreviations and functional groups on the surface.

quantum dot	**abbreviation**	**functional groups**
eFluor 605 nanocrystal	eQD605	maleimide
eFluor 650 nanocrystal	eQD605	maleimide
Qdot 705 ITK	iQD705	amino (PEG)

Conjugation strategy

LTC - antibody conjugation For the conjugation of the LTCs to the donor-ABs the provided lyophilized Lumi4-Tb-NHS was dissolved in anhydrous *N,N*-dimethylformamide to a final concentration of 8 mM. After the antibody solution was washed four times with buffer 2 using a 30 kDa molecular weight cut-off (MWCO) Amicon Ultra-0.5 centrifugal filter (Merck Millipore, Darmstadt, Germany) and a benchtop centrifuge at 14.000 g (Eppendorf centrifuge 5424R, Hamburg, Germany), the dissolved LTC-solution was mixed with the antibody solution and incubated at room temperature for 2 h rotating at 30 rpm using an Intelli-Mixer RM-2M (ELMI). For the purification of free LTCs from donor-AB-LTC conjugates, the solution was washed four to six times with buffer 4 using a 3 kDa MWCO Amicon Ultra-4 centrifugal filter (for V_HH antibodies), 10 kDa or 30 kDa MWCO Amicon Ultra-4 centrifugal filter (for the donor-AB fragments F(ab')$_2$ and F(ab) of TPSA, NSE, and CEA), and 50 kDa MWCO Amicon Ultra-4 centrifugal filter (for the full-sized donor-AB of TPSA, NSE, and CEA) in a benchtop centrifuge at 4000 g (HERAEUS Megafuge 40R, Thermo Scientific, Waltham, MA, USA). The estimation of the final LTC concentration was obtained by absorbance measurements at 340 nm using a molar absorptivity of 26.000 $M^{-1}cm^{-1}$ as provided by the manufacturer. For the calculation of the conjugation ratio the absorbance at 280 nm was measured and used for a linear combination of the respective values of LTCs and antibodies within the LTC-antibody conjugates.

QD - antibody conjugation The conjugation using the sulfhydryl-reactive eFluor 605/650 conjugation kits was performed after an optimized manufacturer protocol, in which the incubation time was elongated from 2 h to 6 h. The acceptor-AB solution was prepared in molar excess compared to the QD concentration using buffer 1. For the purification of unbound antibodies, the QD-antibody solution was washed three to six times with buffer 3 using a 100 kDa MWCO Amicon Ultra-4 centrifugal filter (Merck Millipore, Darmstadt, Germany) in a benchtop centrifuge at 1000 g (HERAEUS Megafuge 40R, Thermo Scientific, Waltham, MA, USA). Resulting QD concentrations were determined by absorbance measurements using the molar absorptivities provided by the manufacturer, which are $1.1 \cdot 10^6\ M^{-1}cm^{-1}$ at 641 nm for eQD650 and $2.5 \cdot 10^5\ M^{-1}cm^{-1}$ at 594 nm

for eQD605. For the determination of the antibody concentrations of IgG, F(ab')$_2$, and F(ab) following molar absorptivities were used at a 280 nm: 210.000 $M^{-1}cm^{-1}$ (IgG), 140.000 $M^{-1}cm^{-1}$ (F(ab')$_2$) and 70.000 $M^{-1}cm^{-1}$ (F(ab)). With the linear combination of the respective absorbance values of QDs and antibodies within the QD-antibody conjugates the labeling ratio was determined.

The above described conjugation protocol was used for the full-size as well as for the fragmented antibodies responsible for the detection of TPSA, NSE, and CEA. However, for the V_HH antibodies an extra step was introduced in order to provide accessible thiol-groups for the conjugation. Therefore protected sulfhydryl groups (N-Succinimidyl S-Acetylthioacetate) were introduced to the acceptor-AB of EGFR (see Table 4.2) at five times molar excess using the SATA kit (Life technologies, Carlsbad, CA, USA). After deacylation of the sulfhydryl groups according to the manufacturer protocol, the antibody solution was used for the conjugation to eQD650 using the sulfhydryl-reactive eFluor 650 conjugation kit and purified by washing three to six times with buffer 3 using a 100 kDa MWCO Amicon Ultra-4 centrifugal filter (Merck Millipore, Darmstadt, Germany) in a benchtop centrifuge at 1000 g (HERAEUS Megafuge 40R, Thermo Scientific, Waltham, MA, USA). After quantification of the eQD650 concentration using the molar absorptivity of $1.1 \cdot 10^6$ $M^{-1}cm^{-1}$ at 641 nm and the antibody concentration of V_HH at 280 nm with the molar absorptivity of 35.800 $M^{-1}cm^{-1}$, the labeling ratio of the QD-antibody mixture was determined by the before mentioned linear combination approach.

The conjugation of iQD705 was different in comparison to the before mentioned QD conjugations. In a first step the thiol-groups of in buffer 1 dissolved F(ab')$_2$ antibodies were reduced using tris(2-carboxyethyl)phosphine hydrochloride (TCEP, Sigma-Aldrich Chimie Sarl, France) for 30 min while rotating at 30 rpm (Intelli-Mixer RM-2M, ELMI). In the same time a tip of a spatula of N-ϵ-maleimidocaproyl-oxysulfosuccinimide ester (Sulfo-EMCS, Life Technologies, Carlsbad, CA, USA) was added to iQD705 solution in buffer 1. After careful mixing the solution was also incubated for 30 min rotating at 30 rpm (Intelli-Mixer RM-2M, ELMI). For the purification of the access of TCEP as well as Sulfo-EMCS two with buffer 1 equilibrated 7 k MWCO Zeba spin desalting columns (Life Technologies, Carlsbad, CA, USA) for each solution were used in an Eppendorf centrifuge 5424R (Hamburg, Germany) at 1500 g. The purified antibody and QD solutions were mixed and incubated at room temperature rotating at 30 rpm (Intelli-Mixer RM-2M, ELMI). After an incubation time of 5 h the QD-antibody mixture was purified by washing three to six times with buffer 3 using a 100 kDa MWCO Amicon-4 centrifugal filter (Merck Millipore, Darmstadt, Germany) in a benchtop centrifuge at 1000 g (HERAEUS Megafuge 40R, Thermo Scientific, Waltham, MA, USA). The QD concentration was quantified using the molar absorptivity of $8.3 \cdot 10^6$ $M^{-1}cm^{-1}$ at 405 nm, whereas for the F(ab')$_2$ antibody concentration determination a molar absorptivity of 140.000 $M^{-1}cm^{-1}$ at 280 nm was used. The labeling ratio was determined as described before.

Execution of the FRET immunoassays

The homogeneous FRET immunoassays were performed on the EI plate reader and KRYPTOR compact PLUS using low-binding black 96-well microtiter plates with an optimal working volume of 150 µL. 50 µL of each LTC-antibody and QD-antibody conjugate solutions dissolved in buffer 7 were mixed at constant concentrations to yield 100 µL assay solution. Followed by the addition of 50 µL NBCS with increasing biomarker concentration and for the detection of soluble EGFR also using buffer 6 as diluent. Thereby each biomarker concentration was prepared three times and the immunoassay in absence of the biomarker were prepared ten times. The immunoassays were incubated for different time intervals at 37 °C and measured afterwards in triplicate on the before mentioned plate readers.
The duplexed measurements of the biomarkers NSE and CEA were performed on the same plate readers using the same type of well plate. The donor and acceptor antibody conjugates for the detection of both biomarkers were dissolved in buffer 7 and premixed, before 50 µL of donor-antibody conjugates and 50 µL of acceptor-antibody conjugates were mixed at constant concentrations to yield 100 µL assay solution. Serum samples with increasing concentrations of both biomarkers were prepared in 50 µL and mixed to the 100 µL assay solution. Each biomarker concentration was prepared three times. For the measurement of the donor and acceptor antibody conjugates in absence of the biomarker 50 µL of pure NBCS was used and prepared 10 times. The mixed solutions were incubated at 37 °C and measured after different incubation times. Thereby the measurement was performed using two different bandpass filters inside the QD detection channel (ChA), the bandpass filter 607/8 nm and 660/13 nm for the detection of the sensitization of eQD605 and eQD650, respectively. Control measurements were performed in absence of one biomarker and signal detection using both bandpass filters in order to investigate the biological crosstalk (binding affinity of antibodies to the other biomarker) and the optical crosstalk (signal bleed through other detection channel).

Calculation of the limit of detection using the analytical sensitivity approach
The calculated PL intensity ratios for the different concentrations of biomarker in the immunoassay were plotted as a function of the biomarker concentration. The resulting curve is the dose-response curve or better known as calibration curve. For the calculation of the limit of detection two approaches can be used and are explained in chapter 2.2.1 in the paragraph “Critical parameters in immunoassays”. In this work the performance of the individual immunoassays were quantified using the LOD based on the analytical sensitivity approach and calculated using equation 4.1.

$$\mathrm{LOD} = \frac{3 \cdot \sigma(0)}{\mathrm{m}} \tag{4.1}$$

$\sigma(0)$ *is the standard deviation of the immunoassay in absence of the biomarker and m is the slope of the linear part of the calibration curve.*

4.1.2 Characterization of FRET donors and FRET acceptors

The photophysical properties of the LTC and QD conjugates were carefully characterized by measuring the absorbance and emission spectra as well as the PL decay curves and were compared to the properties of the starting material. Special attention was given to the estimation of the labeling ratio, which is important for the later utilization of the probes in the immunoassay.

FRET donor

The FRET donor used in this work was the Lumi4-Tb complex from Lumiphore Inc. (Richmond, CA, USA). The complex was kindly provided by the company as Lumi4-Tb-NHS ester, which enables the conjugation to amine groups on the antibody. In this chapter the complete photophyscial characterization of the Lumi4-Tb complex conjugated to IgG, F(ab')$_2$, and F(ab) donor-ABs for the detection of TPSA will be discussed. The absorbance spectra, PL emission spectra, PL decay curves as well as information about the labeling ratio and decay times of all used FRET donor conjugates within the FRET immunoassays can be found in the Appendix 6.3.1. In the following text the simplified term LTC will be used instead of Lumi4-Tb complex.

Absorbance spectra After the successful conjugation and purification of the LTC-antibody conjugates the concentration of the LTC and the antibody was determined by the measurement of the absorbance spectrum. The black curve in Figure 4.4 shows the typical absorbance spectrum of the LTC-NHS ester. Important to note is that this is not the absorption of the Tb^{3+}, but the absorbance of the ligand. The absorbance maximum at 340 nm with an extinction coefficient of 26.000 $M^{-1}cm^{-1}$ is typical for this LTC.

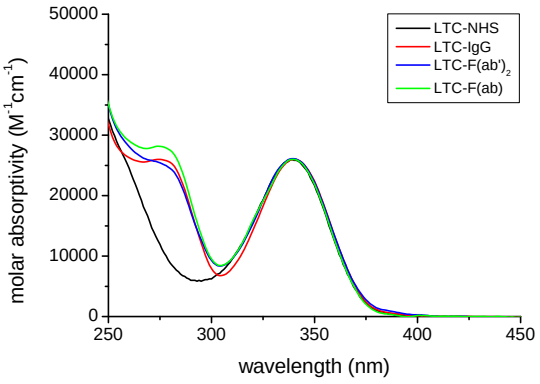

Figure 4.4: Absorbance spectra of unmodified LTC-NHS (black curve) in comparison to the differently sized TPSA donor-ABs conjugated with LTC.

After the conjugation of LTCs to different sized donor-ABs for the detection of TPSA, namely IgG, F(ab')$_2$, and Fab, an increase in the absorption at 280 nm can be observed and is caused by the presence of the antibodies. The conjugation of the LTCs to the

antibody has a negligible influence on the absorbance band of the LTC-ligand, which can be seen in Figure 4.4. In conclusion the photophysical properties of LTCs are not affected by the labeling to the antibody.
A linear combination approach enables the estimation of the respective LTC and antibody concentrations of the LTC-antibody conjugate, which can be used to calculate the labeling ratio of the conjugate. The results for the LTC-conjugates shown in Figure 4.4 are summarized in Table 4.4. The decreasing labeling ratio from IgG to F(ab) can be explained by the smaller size of fragmented antibodies. A direct relation can be seen in the comparison of the values for LTC-F(ab')$_2$ with 9.3 to LTC-F(ab) with a decreased labeling ratio of 3.9, because the F(ab')$_2$ antibody consist of two F(ab).

Table 4.4: Overview of LTC and antibody concentrations of the purified LTC-antibody conjugates shown in Figure 4.4 together with their calculated labeling ratio.

LTC-antibody	**LTC [µM]**	**AB [µM]**	**LTC/AB**
LTC-IgG	41	3.2	12.8
LTC-F(ab')$_2$	14	1.5	9.3
LTC-F(ab)	22	5.6	3.9

PL emission spectra As described in chapter 2.3.3 the excited LTC-ligands serve as antennae and sensitize the central Tb^{3+} *via* energy transfer, which results in LTC-typical $^5D_4 - ^7F_J$ transitions shown in the PL emission spectrum in Figure 4.5. The first four transitions at 495 nm, 545 nm, 585 nm, and 625 nm are strong, whereas the transitions in the range of 650 nm to 700 nm are much less pronounced.
The nearly identical emission spectra of the LTC-NHS and the different LTC-antibody conjugates are expected as there were no changes in the comparison of the absorbance spectra observed. Only minor differences inside the fine splitting of the individual emission bands are visible, which arises from small changes within the complex geometry caused by the labeling to the antibodies. [131]

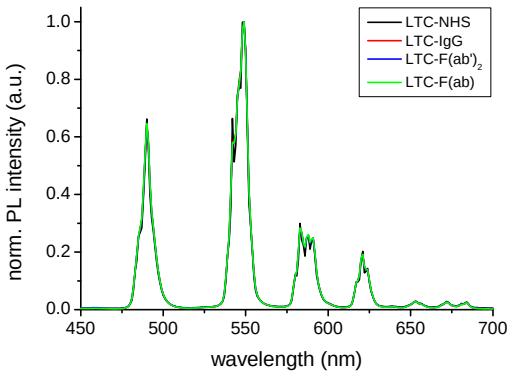

Figure 4.5: Comparison of the emission spectra before conjugation (LTC-NHS) and after conjugation to the differently sized donor-ABs for the detection of TPSA.

PL decay curves Due to the forbidden character of the $4f$-$4f$ transitions, the decay time of LTCs is in the millisecond range. As described before, the long lifetime is very beneficial in combination with time-gated measurements in order to perform sensitive FRET immunoassays with a high signal-to-noise ratio (see chapter 2.3.4).
Figure 4.6 shows the measured PL decay curves for LTC-NHS and the LTC-antibody conjugates. For a better comparison the PL decay curves were normalized to unity at 0.01 ms. Like the absorbance spectra and PL emission spectra, the shape of the PL decay curves of all LTC-antibody conjugates are similar and show a minor multi-exponential behavior. Due to the known dependency of PL decay times on the used diluent, the PL decay curves were measured in buffer 7 and in the same buffer containing 30 % newborn calf serum. To obtain the decay times, the PL decay curves were fitted using a bi-exponential fitting function based on equation 4.2.

$$I(t) = \sum A_i \cdot e^{-t/\tau_i} \tag{4.2}$$

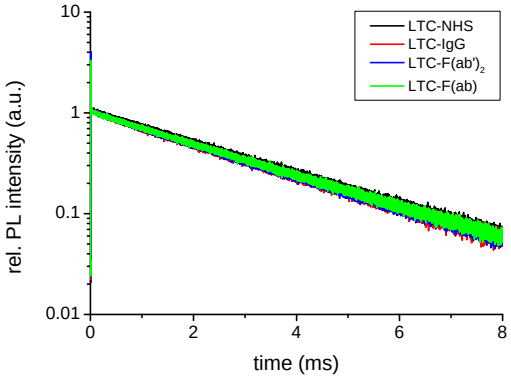

Figure 4.6: Comparison of the PL decay curves before conjugation (LTC-NHS) and after the conjugation to the different sized donor-ABs for the detection of TPSA.

The results for the different decay times τ_i together with their amplitudes A_i for LTC-NHS and the three LTC-antibody conjugates are shown in Table 4.5 and 4.6. Due to the bi-exponential behavior the average intensity-weighted, $\langle\tau\rangle_{\mathrm{Int}}$, and average amplitude-weighted, $\langle\tau\rangle_{\mathrm{Amp}}$, decay times were calculated according to the equation 4.3 and equation 4.4, and are included in the overview. [2, 3]

$$\langle\tau\rangle_{\mathrm{Int}} = \frac{\sum A_i \tau_i^2}{\sum A_i \tau_i} \tag{4.3}$$

$$\langle\tau\rangle_{\mathrm{Amp}} = \frac{\sum A_i \tau_i}{\sum A_i} \tag{4.4}$$

The comparison of averaged decay times for LTC-NHS and LTC-antibodies in Table 4.5 and 4.6 reveal that the conjugation results in a negligible change of the decay times. But as expected the change of the diluent from pure buffer to buffer containing 30 %

serum causes a strong decrease in the averaged decay time from 2.8 ms to ca. 2.3 ms. In order to calculate the Förster distance after equation 2.2, the quantum yield Φ_D has to be calculated. Thereby the intrinsic QY, Φ_{Ln}^{Ln} of equation 2.7, is used instead of the overall QY. As described in chapter 2.3.3 the intrinsic QY can be determined in absence of all non-radiative pathways. Therefore the PL decay time of the LTC is measured in a deuterated solution in order to prevent luminescence quenching by water. Under these conditions Φ_{ref} in equation 4.5 can be assumed as one and the measured decay time τ_{ref} equals the intrinsic decay time τ_0 of the Tb.

$$\Phi_{Tb} = \Phi_{ref}\frac{\langle\tau\rangle_{Amp}}{\tau_{ref}} \approx \frac{\langle\tau\rangle_{Amp}}{\tau_0} \tag{4.5}$$

The measured τ_0 under these condition for the used LTC is 3.45 ms and was applied in equation 4.5 for the calculation of the Φ_{Tb} in Table 4.5 and 4.6. [32] Due to the later utilization of the Φ_{Tb} for the calculation of the Förster distance, the QY was calculated using the averaged amplitude-weighted decay time of the LTC-conjugates. The reason for the use of $\langle\tau\rangle_{Amp}$ instead of $\langle\tau\rangle_{Int}$ is based on the dynamic quenching in FRET, which result in a dependency of the detected signal on the excited-state population rather than the integrated intensity. [228, 229]

Table 4.5: Overview of the fitted single decay times, calculated average decay times and QYs for LTC-NHS and LTC-antibody conjugates measured in buffer 7.

LTC-antibody	τ_i / **ms**	A_i	$\langle\tau\rangle_{Int}$ / **ms**	$\langle\tau\rangle_{Amp}$ / ms	Φ_{Tb}
LTC-NHS	1.7	303	2.8	2.8	0.81
	2.9	2012			
LTC-IgG	1.1	276	2.8	2.6	0.75
	2.8	2144			
LTC-F(ab')$_2$	0.9	241	2.8	2.7	0.78
	2.8	2584			
LTC-F(ab)	1.3	201	2.8	2.8	0.81
	2.9	2317			

Table 4.6: Overview of the fitted single decay times, the calculated average decay times and the QYs of the LTC-antibody conjugates measured in presence of 30 % newborn calf serum.

LTC-antibody	τ_i / **ms**	A_i	$\langle\tau\rangle_{Int}$ / **ms**	$\langle\tau\rangle_{Amp}$ / ms	Φ_{Tb}
LTC-IgG	0.6	399	2.3	2.2	0.64
	2.3	4146			
LTC-F(ab')$_2$	0.5	168	2.4	2.3	0.65
	2.4	2249			
LTC-F(ab)	0.4	67	2.3	2.3	0.66
	2.3	2186			

FRET acceptor

FRET acceptors used in the time-resolved FRET immunoassays were commercially biocompatible QDs, namely eQD605, eQD650, and iQD705. Thereby the numbers 605, 650, and 705 denoting the emission maxima of those QDs. eQD605 and eQD650 were kindly provided from the company eBioscience as a part of the sulfhydryl-reactive conjugation kit, whereas iQD705 was purchased from Invitrogen and exhibit amino functional groups on the surface. The first two QDs consist of a CdSe/ZnS core-shell structure, whereas iQD705 is a CdSeTe/ZnS QD.
The following chapter aims to exemplarily discuss the photophysical characteristics of the QDs conjugated with differently sized acceptor-ABs for the detection of TPSA. Absorbance spectra, PL emission spectra, PL decay curves as well as concentrations, labeling ratios and decay times of all other QD-antibody conjugates used can be found in the Appendix 6.3.1.

Absorbance spectra Figure 4.7 shows the absorbance spectra of the QDs conjugated with F(ab')$_2$ acceptor-ABs. The absorbance spectra are representative for semiconductor materials, which are characterized by a broad absorbance band with more or less defined exciton peaks. The progression of the absorbance curve depends on the bandgap of the QD and starts at energies larger than the bandgap with a continuous increased absorbance towards shorter wavelengths. Characteristic for the QDs in comparison with other common luminophores are their very high extinction coefficients over the whole absorbance band.
For the calculation of the QD concentrations within the antibody-QD conjugates the

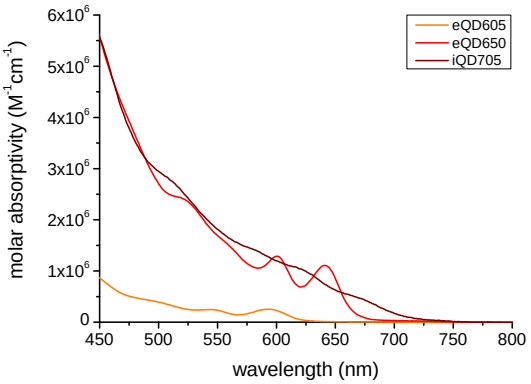

Figure 4.7: Absorbance spectra of eQD605, eQD650, and iQD705 conjugated with F(ab')$_2$ acceptor-ABs for the detection of TPSA measured in buffer 3.

extinction coefficients provided by the suppliers were used, which are $2.5 \cdot 10^5\,\mathrm{M^{-1}cm^{-1}}$ at 594 nm for eQD605, $1.1 \cdot 10^6\,\mathrm{M^{-1}cm^{-1}}$ at 641 nm for eQD650 and for iQD705 the extinction coefficient is $8.3 \cdot 10^6\,\mathrm{M^{-1}cm^{-1}}$ at 405 nm. Using a linear combination approach the respective antibody concentrations were calculated from the absorbance values at 280 nm. Due to the high background of QD absorption at 280 nm the estimation of the antibody concentration was afflicted with larger uncertainties than for the LTC-antibody conjugates.

The determined concentrations of the QDs and antibodies as well as the resulting labeling ratio for the antibody-QD conjugates are summarized in Table 4.7. The internal comparison of the values for the conjugation of IgG, F(ab')$_2$, or F(ab) acceptor-ABs to eQD605 reveal an increase in the labeling ratio, which is mainly attributed to the smaller size of the fragmented antibodies. The use of eQD650 instead of eQD605 enables the binding of more fragmented antibodies. The comparison of the labeling ratio of the different QDs conjugated with F(ab')$_2$ acceptor-ABs shows an increase from 4.7 (eQD605) to 14.3 (iQD705). This increase is attributed to the different sizes of the QD and thus the accessible surface for conjugation. An idea of these differences can be obtained by the comparison of their hydrodynamic diameter without any further functionalization, which is 11.2 nm for eQD605, 17 nm for eQD650, and 20.5 nm for the iQD705. The estimation of the hydrodynamic radius for the eBioscience QDs were done using dynamic light scattering using the intensity profile distribution, whereas the iQD705 was measured by size exclusion chromatography on HPLC. Large changes in the QD absorbance spectra due to the conjugation with antibodies are not expected as the contribution of the antibodies start below 300 nm.

Table 4.7: Overview of QD and antibody concentrations and their resulting labeling ratio.

antibody	**QD**	**AB [µM]**	**QD [µM]**	**AB/QD**
IgG	eQD605	1.1	0.4	2.8
F(ab')$_2$	eQD605	1.4	0.3	4.7
F(ab)	eQD605	1.9	0.2	9.5
IgG	eQD650	0.6	0.2	3.0
F(ab')$_2$	eQD650	3.1	0.3	10.3
F(ab)	eQD650	3.9	0.2	19.5
F(ab')$_2$	iQD705	4.3	0.3	14.3

PL emission spectra The emission spectra in Figure 4.8 were measured with the same QD-antibody conjugates for which the absorbance spectra were shown in Figure 4.7. The emission bands cover the wavelength range from 600 nm to 750 nm and exhibit the QD typical symmetric Gaussian shape. Although the eQD605 and eQD650 consist of the same core/shell material, the larger size of the latter QD lead to a red-shifted emission caused by the quantum confinement effect. The narrow emission bands are characterized by full-width-at-half-maximum of around 27 nm for eQD605 and eQD650, whereas the iQD705 posses a FWHM of ca. 60 nm. Combining the high luminescence quantum yields of 0.64 (eQD605), 0.68 (eQD650), and 0.5 (iQD705) together with their exceptional large extinction coefficients result in high brightness values.

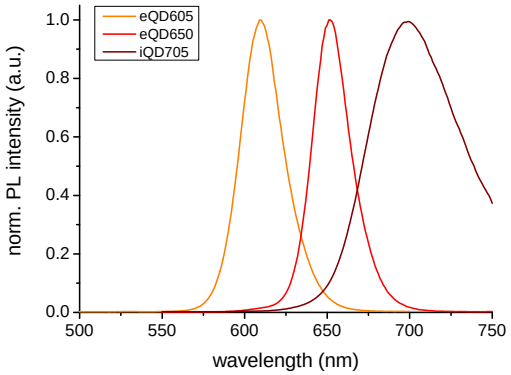

Figure 4.8: Emission spectra of eQD605, eQD650, and iQD705 conjugated with F(ab')$_2$ acceptor-ABs for the detection of TPSA measured in buffer 3.

PL decay curves The PL decay times of QDs are in the range of 10 ns to 100 ns and are significantly shorter in comparison to the long decay times of the LTC-conjugates. A representative PL decay curve is shown in Figure 4.9 for the eQD650 conjugated with F(ab')$_2$ acceptor-ABs for the detection of TPSA. The multi-exponential decay is caused by different emissive transitions within the QD as well as an inhomogeneous distribution of differently sized QDs inside the batch.

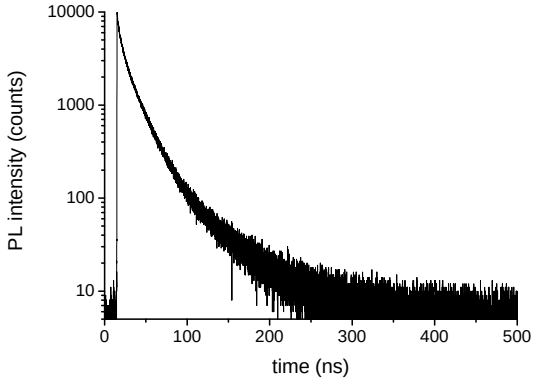

Figure 4.9: PL decay curve of eQD650 conjugated to F(ab')$_2$ acceptor-ABs for the detection of TPSA measured in buffer 3.

Conventional fluorophores like organic dyes and fluorescent proteins exhibit a decay time of 1 ns to 4 ns. The longer average decay time of QDs of 10 ns to 100 ns can be explained by their high dielectric constants. QDs exhibit a large dipole moment. The interaction of the background vacuum field with this dipole moment induces spontaneous emission. Due the high dielectric constant the vacuum field of the outside medium get reduced and the decay rate slows down. This leads to a dependency of the decay rate on the dielectric constant of QDs, which is dependent on the used QD material and size of the QD. [230] For the decay time analysis of the PL decay curves three exponents have to be used in equation 4.2, because of the multi-exponential behavior. For a better comparison $\langle\tau\rangle_{\mathrm{Int}}$ as well as $\langle\tau\rangle_{\mathrm{Amp}}$ were calculated according to equation 4.3 and 4.4, respectively. A summary of the averaged decay times for the unmodified eQD650 and eQD650 conjugated with

either IgG, F(ab')$_2$, or F(ab) acceptor-ABs for the detection of TPSA or NSE is shown in Table 4.8. Depending on the conjugated acceptor-AB the averaged values show small differences. The conjugation of fragmented TPSA acceptor-ABs result in a decreased $\langle\tau\rangle_{\mathrm{Amp}}$ from 10.7 ns to 8.8 ns. In case of the conjugation of fragmented NSE acceptor-ABs to eQD650 the $\langle\tau\rangle_{\mathrm{Amp}}$ increases from 10.7 ns to 16.1 ns compared to unmodified eQD650. An increase in the decay time reflects a decreased portion of non-radiative recombination inside the PL, which is a further proof how the conjugation of proteins can effect QD PL properties.

Table 4.8: Summary of the calculated intensity ($\langle\tau\rangle_{\mathrm{Int}}$) and amplitude ($\langle\tau\rangle_{\mathrm{Amp}}$) weighted averaged decay times of an unmodified eQD650 and eQD650 conjugated with either IgG, F(ab')$_2$, or F(ab) acceptor-ABs for the detection of TPSA or NSE.

	TPSA		NSE	
antibody-QD	$\langle\tau\rangle_{\mathrm{Amp}}$ / **ns**	$\langle\tau\rangle_{\mathrm{Int}}$ / ns	$\langle\tau\rangle_{\mathrm{Amp}}$ / **ns**	$\langle\tau\rangle_{\mathrm{Int}}$ / ns
bare-eQD650	10.7	22.5	10.7	22.5
IgG-eQD650	14.4	23.1	10.8	20.1
F(ab')$_2$-eQD650	10.9	21.7	13.7	23.2
F(ab)-eQD650	8.8	19.4	16.1	24.9

FRET properties of donor-acceptor pairs

The major requirement for FRET is a spectral overlap between the absorbance spectrum of the acceptor with the PL emission spectrum of the donor. The used QDs inside the immunoassay measurements show an exceptional large spectral overlap with LTC, which can be seen in Figure 4.10 left. In the left of Figure 4.10 the donor LTC PL emission is shown as gray contour together with the characteristic broad absorbance bands of the utilized QDs, which in case of eQD650 and iQD705 cover the whole emission spectrum of the LTC.

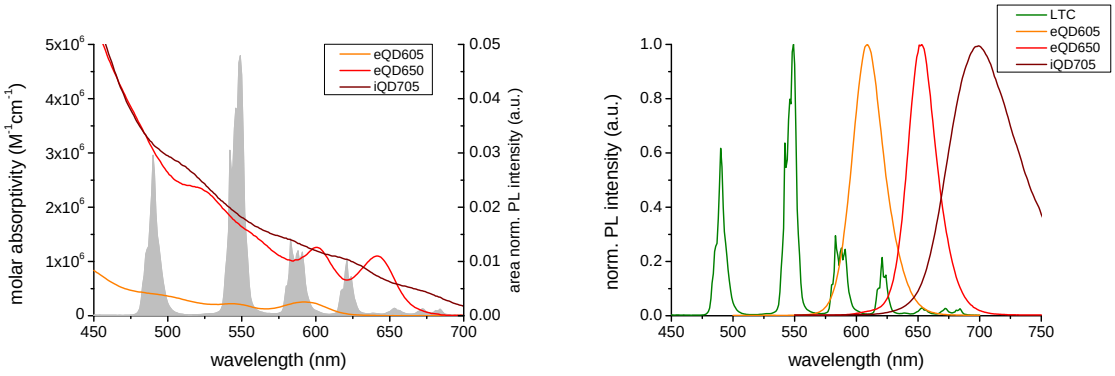

Figure 4.10: LEFT: Spectral overlap between the PL emission spectra of LTC (gray contour) and the extinction coefficient spectra of eQD605, eQD650 and iQD705. RIGHT: Normalized PL emission spectrum of LTC, eQD605, eQD650, and iQD705.

With the use of the area normalized PL emission spectrum of the donor and the extinction coefficient spectra of the different acceptors the overlap integral $J(\lambda)$ was calculated according to equation 2.3. The results are shown in Table 4.9. As discussed in chapter 2.1.2 the Förster distance R_0 can be calculated with the use of $J(\lambda)$ and equation 2.2. Therefore the refractive index was defined as 1.4 and the assumption of a dynamic system was made, which results in $\kappa^2 = 2/3$. Due to the presence of 30 % of serum inside the immunoassay measurements, the donor QYs in Table 4.6 were used for the calculation of the Förster distances. The resulting values of R_0 for the different donor-acceptor pairs are shown in Table 4.9.

Table 4.9: Summary of the calculated overlap integrals $J(\lambda)$ and the resulting Förster distance R_0 for eQD605, eQD650, iQD705 conjugated to F(ab')$_2$ for the detection of TPSA.

LTC-	$J(\lambda)/\ \frac{nm^4}{M \cdot cm}$	R_0 **/ nm**
eQD605	$1.96 \cdot 10^{16}$	7.6
eQD650	$1.59 \cdot 10^{17}$	10.8
iQD705	$1.67 \cdot 10^{17}$	10.9

In general, the Förster distances of the LTC-QD FRET pairs are much larger compared to other FRET pairs. The main reason for the exceptional R_0 values is the broad absorbance band of QDs with extremely high extinction coefficients, which result in large overlap integrals.

As discussed in the photophysical characterization of the FRET donor as well as FRET acceptors, the amount and type of conjugated antibodies has a minor influence on neither the extinction coefficient spectra of the QDs and the PL emission spectra of the LTC. The fluctuations of the calculated values in Table 4.9 is in the range of $\pm$ 2 %.

The choice of the used QDs for the immunoassay measurements was not only based on their expected large R_0 values, but rather on their emission maxima. Figure 4.10 (right) shows the LTC PL emission spectrum together with PL emission spectra of the different QDs. The emission maxima of the QDs are in between (eQD605, eQD650) and beyond (iQD705) the emission bands of LTC. This allows a simple signal deconvolution of the measured donor signals from sensitized acceptor signals and *vice versa*. Another advantage are the small Gaussian shaped emission spectra, which also enable the use of more than two QDs simultaneously as the optical crosstalk between them is expected to be small. These properties make LTC-QD FRET pairs highly suitable for multiplexing measurements and enable the simultaneous measurement of several biomarkers.

4.1.3 Influence of the fragmentation

In a first attempt of the application of LTC-to-QD FRET in immunoassays the influence of the antibody size on the immunoassay sensitivity was investigated.[1] Therefore different combinations of LTC conjugated to IgG, F(ab')$_2$, and F(ab) donor-ABs and IgG, F(ab')$_2$, and F(ab) acceptor-ABs conjugated to eQD650 were chosen with the aim to create different distances for the donor-acceptor pair in presence of the biomarker TPSA. As shown in chapter 4.1.2 the variation from IgG to F(ab) antibodies also results in different labeling ratios for LTC per antibody (AB) and AB per QD (see Figure 4.11).

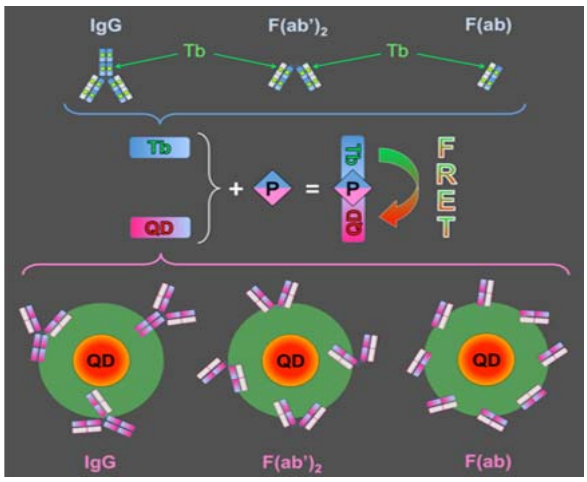

Figure 4.11: Schematic drawing presenting the different labeling ratios depending on the antibody size for LTC (top) and QDs (bottom).

Promising for a high FRET sensitization of an acceptor is the surrounding with a large number of donors, as discussed in chapter 2.3.5. For a first approximation which combination of LTC-AB and AB-QD can result in a good FRET sensitization, it is worth to look at the LTC per QD ratio for the different combinations. Table 4.10 takes into account the calculated LTC-AB and AB-QD ratios after conjugation presented in Tables 4.4 and 4.7 for the calculation of the theoretical possible LTC per QD ratio for the different sandwich immunoassays. These numbers are of pure theoretical nature as they presume a complete labeling and neglect factors like steric hindrance or the divalency of the IgG and F(ab')$_2$ antibodies, which influences the binding.

Table 4.10: LTC-AB / AB-QD ratios for the different sandwich immunoassays. LTC per QD ratios highlighted in bold were used for FRET immunoassays for the detection of TPSA.

LTC-AB	**QD-IgG**	**QD-F(ab')$_2$**	**QD-F(ab)**
LTC-IgG	**31**	**56**	**210**
LTC-F(ab')$_2$	23	**40**	150
LTC-F(ab)	9.4	17	**62**

[1] Work was published in: *ACS Nano*, **2013**, 7 (8), 7411-7419

Based on the assumption that a high LTC per QD ratio results in a efficient FRET sensitization, the combinations using F(ab)-QDs with the different sized LTC-ABs are favorable. The high numbers of 210 for LTC-IgG / QD-F(ab) to 62 for LTC-F(ab) / QD-F(ab) are also a result of the different sizes of the used FRET donor and acceptors. Due to the small size of the LTCs, the labeling ratio of LTC per AB is highest for LTC-IgG conjugate. This results in the highest LTC per QD ratio for all AB-QD combinations. On account of the large size of the IgG antibody (ca. 10 nm) and the distribution of the labeled LTCs, it is not ensured that all LTCs are in a suitable distance to the acceptor in presence of the antigen. The high ratios for F(ab)-QDs are attributed to the large number of F(ab) antibodies on the surface. A comparison of IgG antibodies and QDs reveals that they are similar in size, which results in an increase of the labeling ratio with decreasing size of the antibody. The similar size of IgG and QDs causes also problems in their purification. In contrast to fragmented antibodies that allow due to their smaller size an efficient purification using conventional spin-columns. On the other hand the large amount of F(ab)s on the QD surface can result in steric hindrance for the binding of antigens and thus cause a lower sensitivity.
Several different combinations were chosen for the time-resolved homogeneous FRET immuno-assay measurements (see bold highlighted LTC per QD ratios in Table 4.10). All FRET assays contained 50 µl of each LTC-AB and AB-QD conjugate at constant concentration, to which 50 µl of serum with increasing concentrations of TPSA was added. After careful mixing the solutions were incubated at 37 °C up to 90 min and measured afterwards on the different fluorescence plate readers.

PL decay curves The presence of the antigen results in the formation of a sandwich complex of LTC-AB/TPSA/AB-QD wherein the sandwich complex donor and acceptor are in close enough proximity to enable FRET. The FRET process causes changes in the photophysical properties of the donor, which can be monitored using stationary and time-resolved emission measurements. In this work the consequences of FRET on donor and acceptor were measured with time-resolved spectroscopy, which allows the use of the time-gating approach for the suppression of background signals from the biological components and the direct excitation of the acceptor. Representative PL decay curves for the LTC-IgG and F(ab')$_2$-eQD650 combination for increasing TPSA concentrations (6 nM, 12 nM, and 24 nM) are shown in Figure 4.12.
Due to the constant concentration of LTC-AB and AB-QD, the changes in the PL decay curves are caused by the presence of the antigen TPSA. With increasing antigen concentration the PL decay curves in the QD detection channel shows higher PL intensities as well as new decay time components, which originate from FRET sensitization (see Figure 4.12 left). The black curve in the absence of antigens is a mixture of directly excited QDs and spectral crosstalk of LTC in the QD detection channel. Concomitant to the FRET sensitization, the PL decay curves measured in the LTC detection channel in Figure 4.12 (right) show a decrease of the intensities with increasing antigen concentration due to

FRET quenching. This observation is a clear evidence for FRET from LTC to QD in presence of the antigen.

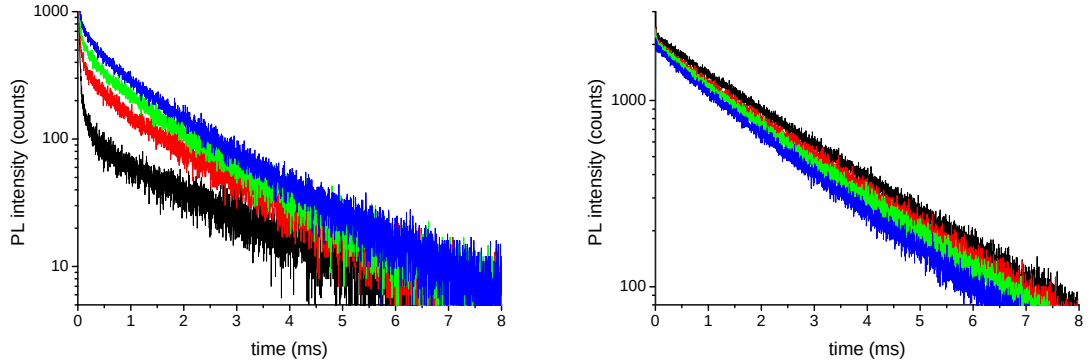

Figure 4.12: LEFT: PL decay curves measured in the QD detection channel with increasing concentrations of TPSA (black, no TPSA; red, 6 nM; green, 12 nM; blue, 24 nM). The used bandpass filter for the QD detection was (660 ± 13) nm. RIGHT: PL decay curves measured in the LTC detection channel with increasing concentrations of TPSA (black, no TPSA; red, 6 nM; green, 12 nM; blue, 24 nM). The used bandpass filter for the LTC detection was (494 ± 20) nm.

All investigated combinations show the similar behavior in FRET sensitization and quenching and the corresponding decay curves are shown in the Appendix 6.3.3. But there are differences in the extent of the FRET quenching. In contrast to all combinations using F(ab')$_2$-QDs where a similar quenching behavior can be observed, the combination of LTC-IgG and IgG-QD results in a small quenching effect. This can mainly be attributed to the long distance between donor and acceptor, which results in a larger amount of unquenched donors. The PL decay curves of the LTC detection channel for the combinations using F(ab)-QDs are shown in Figure 4.13.

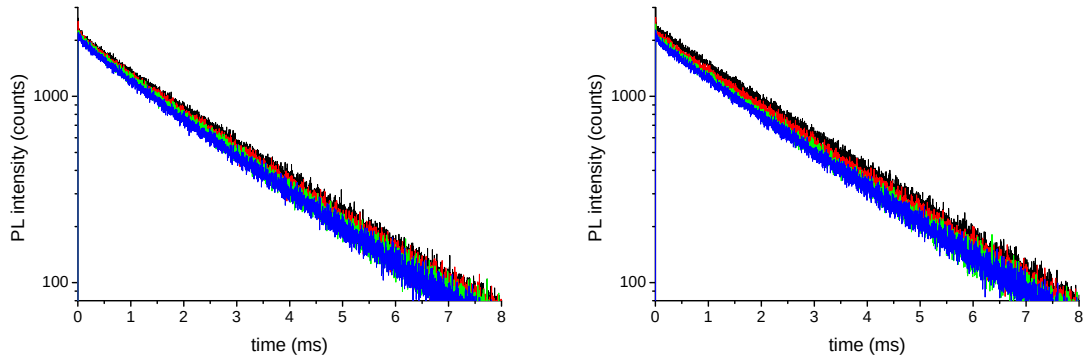

Figure 4.13: LEFT: PL decay curves measured in the LTC detection channel for LTC-IgG/TPSA/F(ab)-QD with increasing concentrations of TPSA (black, no TPSA; red, 6 nM; green, 12 nM; blue, 24 nM).RIGHT: PL decay curves measured in the LTC detection channel for LTC-F(ab)/TPSA/F(ab)-QD with increasing concentrations of TPSA (black, no TPSA; red, 6 nM; green, 12 nM; blue, 24 nM). The used bandpass filter for the LTC detection was (494 ± 20) nm in both cases.

The lower quenching rate for these combinations can be the result of the high labeling ratio of the F(ab)-QD, which causes steric hindrance for the binding of the antigen and

thus the LTC-AB. Furthermore, the fragmentation of the antibody also reduces its binding affinity. Consequently there are more unbound LTC-AB in the sample causing a high background of unquenched LTC-AB. Due to the large background of unquenched donor, the FRET quenching is much harder to observe and makes the measurement of the acceptor sensitization so valuable. The lower background in the QD detection channel allows to observe FRET sensitization even for small FRET intensities or low FRET efficiencies.

Time-gated FRET immunoassay For the quantification of the performance of the different LTC-AB and AB-QD combinations, calibration curves were measured using 18 serum samples with increasing concentration of TPSA antigen from 0.6 nM to 36 nM. The intensities from the simultaneously measured PL decay curves in the QD detection channel as well as in the LTC detection channel were integrated from 0.1 ms to 0.9 ms and the intensity ratios were calculated according to the equation 3.1. The resulting calibration curves for the different combinations are shown in Figure 4.14.

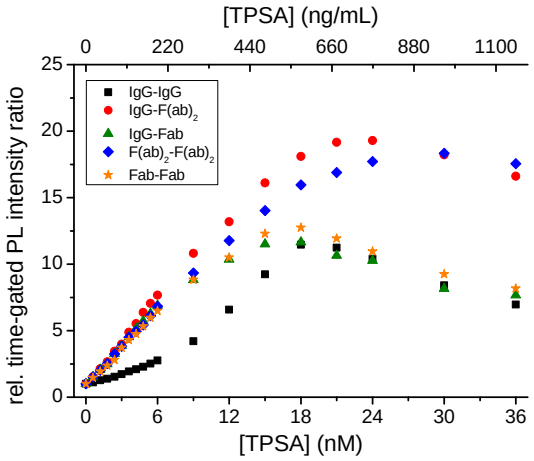

Figure 4.14: Relative time-gated PL intensity ratios as a function of the TPSA antigen concentration for the different LTC-AB and AB-QD combinations.

In general, with increasing antigen concentration the intensity ratios increase until 15 nM to 25 nM where the leveling of the calibration curve indicates the saturation of the LTC-AB and AB-QD conjugates. The saturation effect also limits the dynamic range, which is the concentration between the LOD and the saturation concentration. For the measured systems the dynamic range spans approximately 2 to 3 orders of magnitude. At higher concentration the decreasing of the signal is caused by the high-dose hook effect, which is based on the formation of individual LTC-AB/TPSA and TPSA/AB-QD conjugates. The KRYPTOR compact PLUS clinical plate reader exhibits a dilution procedure for the compensation of this effect, but this requires the use of the automatic pipette arm.
The comparison of the calibration curve curvatures reveals a strong difference for the LTC-IgG/TPSA/IgG-QD FRET pair. The sigmoidal behavior is mainly attributed to free IgG-AB caused by the insufficient purification of free IgG-AB from IgG-QD conjugate. As mentioned before, the similarity in size makes the purification complicated and

results in the competition with the LTC-IgG for antigen binding. The result of the competition is a smaller increase of the calibration curve compared to other combinations.
By using the analytical sensitivity approach the limit of detection was calculated. Therefore the slope of the linear part of the calibration curve and the standard deviation of the immunoassay in absence of the antigen were used in equation 4.1. Table 4.11 shows the summary of the calculated LODs for the different systems.

Table 4.11: Limit of detection (LOD) calculated using the analytical sensitivity.All values have an error of approximately 20 %.

LTC-AB	**QD-AB**	**LOD (nM)**	**LOD (ng/ml)**	**LOD (fmol)**
LTC-IgG	IgG-eQD650	0.27	8.4	13.0
LTC-IgG	F(ab')$_2$-eQD650	0.06	1.8	2.8
LTC-IgG	F(ab)-eQD650	0.05	1.6	2.5
LTC-F(ab')$_2$	F(ab')$_2$-eQD650	0.08	2.6	4.1
LTC-F(ab)	F(ab)-eQD650	0.05	1.6	2.5

The calculated LODs are given for 50 µl serum samples, which means that the LODs are three times lower in the complete 150 µl measurement volume. Despite the LTC-IgG/TPSA/IgG-QD combination, the obtained LODs are below the clinical cutoff level for TPSA (4 ng/ml). Comparing the LODs of the IgG-QD to the QDs conjugated with fragmented antibodies reveals a strong decrease and thus a higher sensitivity using the same LTC-IgG conjugate as FRET donor. A comparison of F(ab')$_2$-QD and F(ab)-QD shows only a minor difference from 1.8 ng/ml to 1.6 ng/ml. The utilization of the fragmented antibodies labeled with LTC in combination with fragmented QD-antibody conjugates has no further advantages as the LODs are quite similar compared to the use of LTC-IgG. It can be concluded that the LTC labeled in the Fc-domain of the antibody have no major participation in the sensitization of the acceptor *via* FRET.
From Table 4.11 it can be concluded that the combination of LTC-IgG either with F(ab')$_2$-QD or F(ab)-QD can strongly enhance the sensitivity in comparison to the conventional approach of using two IgG antibodies. Although not all LTCs of the LTC-IgG conjugate participate in FRET, the non-fragmented antibody provide an unchanged affinity and stability in comparison to the fragmented counterparts. In contrast to the utilization of fragmented antibodies conjugating to the QD surface has some advantages. Primarily the increased labeling ratio enables the binding of a higher number of donor-AB antigen conjugates, which results in a high number of donors surrounding a single acceptor. A clear advantage of the F(ab')$_2$-QD or F(ab)-QD could not be made as the results are quite similar. From the theoretical point of view the high number of donors around the acceptor for the F(ab)-QD is potentially compensated by the smaller affinity, high labeling ratio and thus sterical hindrance, or the non-oriented labeling strategy.
The results presented in this chapter were published in *ACS Nano*, **2013**, 7 (8), 7411-7419. The original publication in the full length is attached in the Appendix 6.3.3.

4.1.4 Detection of TPSA / NSE / CEA using two QD colors

The first promising experiences and results using differently sized antibodies for the optimization of the immunoassay performance were applied for the detection of the biomarkers NSE and CEA in order to verify the prior obtained results and to show the flexibility of the LTC-to-QD FRET system for the choice of the biomarker. Due to the increasing biomarker size from TPSA (32 kDa) over NSE (95 kDa) to CEA (180 kDa), the immunoassay could benefit from the small size of fragmented antibodies and thus result in an enhanced sensitivity. In conclusion of the presented results in chapter 4.1.3 the utilization of LTCs conjugated to fragmented antibodies show no significant advantage over LTC-IgG conjugates. Therefore the LTCs were conjugated to the full-sized donor-ABs shown in Table 4.2 for the detection of the different biomarkers. Next to the before used eQD650 another QD was included as FRET acceptor in the investigation, which exhibits an emission maximum at 605 nm and is denoted as eQD605. Due to a smaller overlap integral with the LTC-donor, the Förster distance is with 7.7 nm smaller than for eQD650 with 10.8 nm. The QDs were conjugated with IgG, F(ab')$_2$, and F(ab) acceptor-ABs for the detection of TPSA, NSE, and CEA.
The differently sized antigens and antibodies together with two QD colors offer a rich variety of combinations in order to investigate the influences of distances on the FRET immunoassay. Additionally the included second QD is a first step towards multiplexing application and can also verify the flexibility of the LTC-to-QD FRET in homogeneous immunoassays using differently emitting QDs. The increasing antigen size is expected to result in increased FRET sensitization in combination with fragmented antibodies and especially for the eQD605 conjugates, as the smaller Förster distance results in lower sensitization compared to eQD650 conjugates for similar donor-acceptor distances.
The concentrations and labeling ratios of LTC-antibody conjugates used within this measurements are shown in the Appendix 6.3.2. Each QD type was either conjugated with IgG, F(ab')$_2$, or F(ab) acceptor-ABs for the detection of TPSA, NSE, and CEA and the resulting labeling ratios are presented for TPSA in Table 4.7 and for NSE as well as CEA in the Appendix 6.3.2.

Evaluation of the performance based on the LOD

For a evaluation of the performance using LTC-IgG in combination with IgG-QD, F(ab')$_2$-QD, or F(ab)-QD for the detection of TPSA, NSE, and CEA the calibration curves were measured using 18 serum samples with increasing concentrations of the individual biomarker. These measurements were done for acceptor-ABs conjugated to eQD605 and to eQD650. After an incubation time up to 180 min at 37 °C the immunoassays were measured on fluorescence plate readers. The obtained PL decay curves were evaluated using the time-gated approach. Thereby the detection window, in which the PL decay intensities were integrated, ranged from 0.1 ms to 0.9 ms and were further treated using equation 3.1 in order to obtain the intensity ratios. The relative intensity ratios were

plotted as a function of the antigen concentration and led to the calibration curve of the used donor-acceptor combination. The calibration curves for the detection of NSE using different sized acceptor-ABs conjugated to either eQD605 or eQD650 are shown in Figure 4.15.

All used combinations presented in Figure 4.15 show, independent of the used QD, an increase in the intensity ratios with increasing antigen concentration. Due to the constant concentration of LTC-AB and AB-QD, the increase is attributed to FRET sensitization caused by the presence of the antigen. Depending on the QD used the saturation effect appears between 1-2 nM for eQD605 and 2-3 nM for eQD650. The decreased dynamic range using the same QD concentrations is caused by the lower antibody per QD labeling ratio for eQD605. As shown in Table 4.7 the labeling ratios for eQD605 are smaller than for eQD650, which is attributed to the smaller size and thus smaller surface of the eQD605.

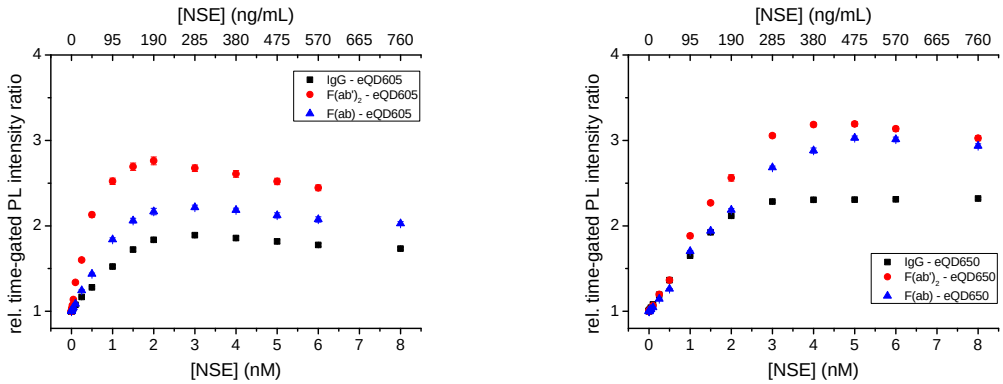

Figure 4.15: LEFT: Relative time-gated PL intensity ratios as a function of the NSE antigen concentration for the combinations of LTC-IgG and differently sized acceptor-ABs conjugated to eQD605. RIGHT: Relative time-gated PL intensity ratios as a function of the NSE antigen concentration for the combinations of LTC-IgG and differently sized acceptor-ABs conjugated to eQD650.

A further proof of an earlier saturation of AB-eQD605 conjugates can be seen in the appearance of the high-dose hook effect, which is not observed for AB-eQD650 conjugates. Despite the difference in the saturation the AB-QD conjugates also differ in the extent of the FRET sensitization, which can be seen by the higher intensity ratios of ca. 3.2 using the F(ab')$_2$-eQD650 conjugate in comparison to 2.8 using the F(ab')$_2$-eQD605 conjugate. The calibration curves measured with eQD605 and eQD650 conjugated with the differently sized acceptor-ABs for the detection of TPSA and CEA show a similar behavior and are presented in the Appendix 6.3.2.

For further quantification the slopes of the different calibration curves and the standard deviations of the immunoassays in absence of the acceptor were used in equation 4.1 to obtain the limit of detection according to the analytical sensitivity approach. The resulting LODs for the detection of NSE are shown in bars in Figure 4.16. Thereby the LODs calculated for the utilization of eQD605-conjugates are highlighted in orange and for eQD650-conjugates in red.

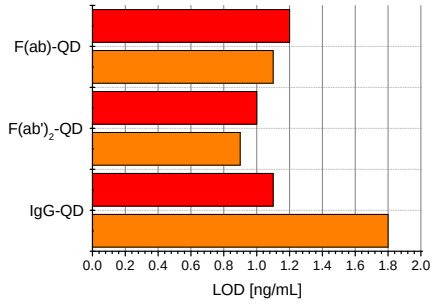

Figure 4.16: Limit of detections (LODs) estimated according to the analytical sensitivity approach for the detection of NSE using LTC-IgG and differently sized acceptor-ABs conjugated to either eQD605 (orange bars) or eQD650 (red bars). All values have an error of approximately 20 %.

The variation of the acceptor-AB size from IgG to F(ab) conjugated to eQD650 for the detection of NSE show no significant advantages for the utilization of fragmented antibodies as the LOD remains at around 1.1 ng/mL. For the AB-eQD605 conjugates the use of fragmented antibodies is beneficial as the LOD decreases from 1.8 ng/mL for the IgG-eQD605 to 0.9 ng/mL for F(ab')$_2$-eQD605.
The calculated LODs for the detection of TPSA and CEA are shown in Figure 4.17 using the same color coding as in Figure 4.16.

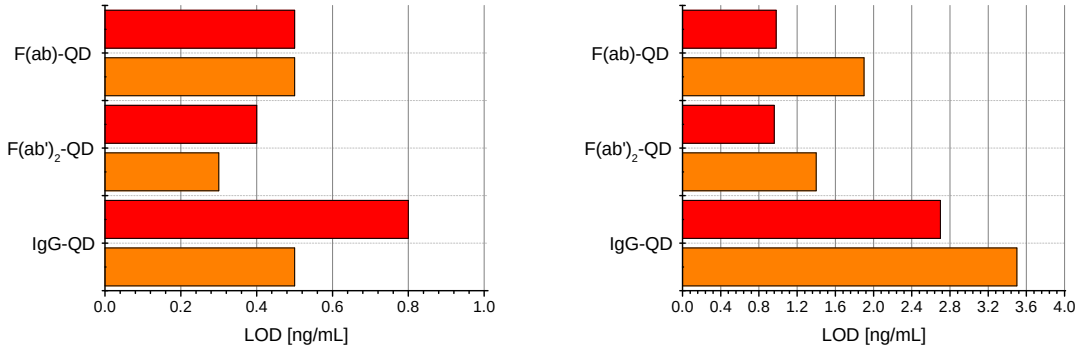

Figure 4.17: LEFT: Limit of detections (LOD) estimated according to the analytical sensitivity approach for the detection of TPSA using LTC-IgG and differently sized acceptor-ABs conjugated to either eQD605 (orange bars) or eQD650 (red bars). RIGHT: LODs estimated after the analytical sensitivity approach for the detection of CEA using LTC-IgG and differently sized acceptor-ABs conjugated to either eQD605 (orange bars) or eQD650 (red bars). All values have an error of approximately 20 %.

The presented LODs in Figure 4.17 left for the detection of TPSA using AB-eQD650 conjugates show an improvement to the LODs presented in chapter 4.1.3. Main reasons for the improvement are an optimization of the purification of the probes and of the measurement setup of the used fluorescence plate reader. The conjugation of fragmented antibodies result in a slightly decreased LOD in combination with eQD650, whereas the AB-eQD605 conjugates present similar LODs independent of the antibody type used.

This could be attributed to the small size of the biomarker TPSA, which enables a suitable distance of donor and acceptor for efficient FRET for all LTC-AB/TPSA/AB-QD combinations. In comparison to the largest antigen CEA used in this investigation, the use of fragmented antibodies result in a strong decrease of the LOD. For both eQD605 and eQD650 antibody conjugates the use of fragmented antibodies decreases the LOD by more than half. The slightly higher values for the use of AB-eQD605 conjugates originates mainly from the smaller Förster distance compared to the eQD650, as the large antigen may introduce a longer distance between donor and acceptor. The comparison of all obtained LODs using the fragmented antibodies for the detection of the different biomarker shows a small advantage for the F(ab')$_2$-QD conjugate. Next to the smaller size than IgG antibodies, F(ab')$_2$ antibodies exhibit a divalent antigen binding possibility, which is an advantage compared to the F(ab) antibodies with only one binding opportunity.

Distance analysis Next to the utilization of FRET as an efficient signal transduction system for molecular binding events, it offers also the opportunity to estimate the distance between the donor and acceptor. After the calculation of the Förster distance from the spectral data of the donor and acceptor, the FRET efficiency has to be estimated in order to calculate the distance with the use of equation 2.5. Using the fitted PL decay times of the PL decay curves measured in presence of increasing concentration of antigen allows the calculation of the FRET efficiency according to equation 2.6. A detailed description for the evaluation of the distance between donor and acceptor using lanthanides as FRET donor and QD as acceptors is given in chapter 4.2.2.
To gain information on how far the utilization of fragmented antibodies in combination with differently sized antigen and two different QDs influences the distance between donor and acceptor and thus the FRET sensitization, a distance analysis was performed. The results for the distances using the different biomarkers and differently sized acceptor-ABs for QD conjugation are shown in Figure 4.18.

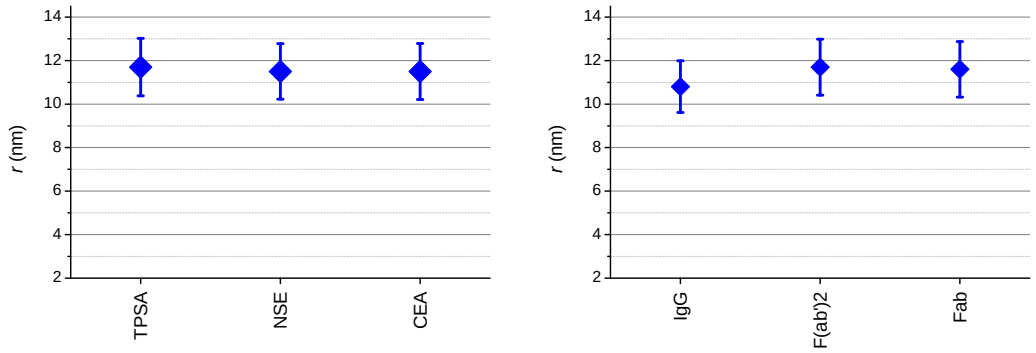

Figure 4.18: LEFT: Calculated donor-acceptor distances (r) for TPSA, NSE, and CEA using LTC-IgG and F(ab)-eQD650 conjugates. RIGHT: Calculated donor-acceptor distances (r) for combinations of LTC-IgG and IgG-eQD650, F(ab')$_2$-eQD650, F(ab)-eQD650 conjugates for the detection of TPSA.

The distances for the different biomarkers in Figure 4.18 (left) show no differences, although their sizes increase significantly. The average distance using LTC-IgG and F(ab)-eQD650 conjugates as measurement tool for each biomarker remains at around 12 nm. A possible explanation for this unchanged distance could be given by the epitope binding sites of the biomarker. The antibodies were provided by the company Cezanne and are usually used in commercial diagnostic kits for the same biomarker. The signal transduction method of these kits is also based on FRET and the antibodies are chosen to reveal a suitable donor-acceptor distance after binding to the biomarker. This basically means that although the size of antigen increases the distance between the antibody binding epitopes remains nearly the same, which is the reason for the unchanged donor-acceptor distance using different biomarkers. But the distance similarity of the fragmented antibodies compared to the full-sized antibody in Figure 4.18 (right) is unexpected as the actual size of the antibody decreases. A major role inside the donor-acceptor distance plays the orientation of the antibody. In case of the Y-shaped IgG antibodies the probability is high that they rather lay on the QD surface than to stand upright. This laying on the QD surface would result in a similar distance of the IgG antibody to the fragmented antibodies.
A large difference in the donor-acceptor distance can be observed for the utilization of eQD605 and eQD650 within the immunoassay shown in Figure 4.19.

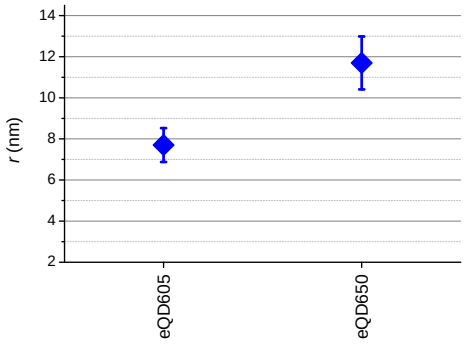

Figure 4.19: Calculated donor-acceptor distances (r) for the detection of TPSA using LTC-IgG in combination with F(ab)-eQD605 or F(ab)-eQD650 conjugates.

The increase of the donor-acceptor distance from ca. 8 nm for F(ab)-eQD605 to ca. 12 nm F(ab)-eQD650 in combination with LTC-IgG is attributed to the different size of the used QDs.
In conclusion, the fragmented antibodies do not result in a shorter donor-acceptor distance but rather lead to higher labeling ratio an enable the binding of more biomarker per QD. The larger amount of LTC per QD concomitantly result in higher FRET sensitization and thus an higher sensitivity. Due to the slight advantage of the combination using LTC-IgG as FRET donor and F(ab')$_2$-QD as FRET acceptor, further investigations were made with this combination.

Long-term storage of the probe A crucial issue in clinical applications is the long-term storage capability of the probes. Most research experiments were made with fresh conjugated and purified probes and their stability and performance are not investigated in long-term experiments. Especially biocompatible QDs conjugated with proteins are vulnerable in terms of their colloidal stability. This is also one of the reasons why QD-conjugates are not used in commercial clinical diagnostic kits.
Due to this reason the calibration curves of the most promising combination (LTC-IgG as FRET donor and F(ab')$_2$-QD as FRET acceptor) for the detection of TPSA, NSE, and CEA were measured after several months and compared to the initial calibration curves directly after conjugation of the probe (see Figure 4.20, NSE measurement is shown in the Appendix 6.3.2)

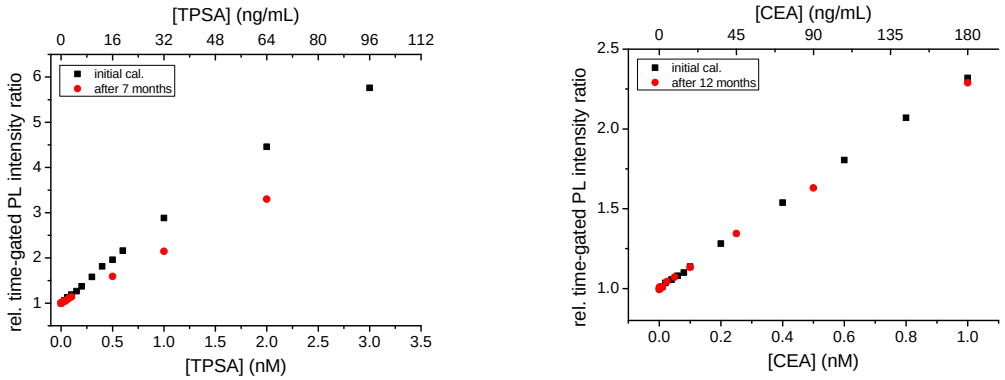

Figure 4.20: LEFT: Comparison of the relative time-gated PL intensity ratios as a function of the TPSA antigen concentration for the combination of LTC-IgG and F(ab')$_2$-eQD650 directly after conjugation and measured after 7 months. RIGHT: Comparison of the relative time-gated PL intensity ratios as a function of the CEA antigen concentration for the combination of LTC-IgG and F(ab')$_2$-eQD650 direct after conjugation and measured after 12 months.

The calibration curve measured after 7 months for TPSA in Figure 4.20 (left) shows decreased intensity ratios compared to the initial measurement. This could be caused by small aggregates observed in the probe that lead to a decrease in the QD-concentration. However, the calculated limit of detection decreased from 0.4 ng/ml (initial calibration curve) to 0.3 ng/ml (after 7 months). The major reason for the decreased LOD is the lower standard deviation of the immunoassay in absence of the biomarker. Larger aggregates that precipitated over several months could have contributed to the higher standard deviation in the first measurements. In normal clinical practice for each patients sample a new calibration curve is measured, which takes into account the decrease of intensity over time.
Exceptionally stable was the F(ab')$_2$-eQD650 conjugate for the detection of CEA. After one year there are no differences in the calibration curves shown in Figure 4.20 (right) and also no changes of the LOD. The long-term stability of these conjugates are promising for future application in clinical diagnostic kits.

Real sample measurements For the estimation of an unknown biomarker concentration in a patient sample the measurement of a calibration curve is the first step. This investigation would be incomplete without the measurement of real patient samples for the biomarker TPSA in human sera purchased from the company biomnis (Lyon, France). Three different concentrations were investigated LTC-IgG as FRET donor and F(ab')$_2$-eQD650 conjugate as FRET acceptor. The real samples were treated like the self-prepared serum samples and 50 µl were added to 100 µl LTC-AB and AB-QD mixture. Each concentration was prepared three times and measured in triplicate. The obtained intensity ratio was used to estimate the concentration using the simultaneous measured calibration curve. The results are listed in Table 4.12 together with the concentrations provided by the supplier.

Table 4.12: Concentration estimated from the calibration curve measured with LTC-IgG as FRET donor and F(ab')$_2$-eQD650 conjugate as FRET acceptor and the provided concentration by the supplier for three different real patient serum samples containing different concentrations of the biomarker TPSA. All values have an error of approximately 20 %.

	TPSA [nM]	**TPSA [ng/ml]**	**Reference [ng/ml]**	**deviation (%)**
Real sample 1	0.2	5.4	4.5	20
Real sample 2	-0.02	-0.56	0.55	202
Real sample 3	0.05	1.7	1.8	10

The second real sample in Table 4.12 has a TPSA concentration in the range of the estimated LOD for this FRET pair combination, which could explain the large deviation from the reference TPSA concentration. Real sample 1 and 3 exhibit higher biomarker concentrations and the deviation is below 20 %, which is a good result for use of LTC-to-QD FRET inside the homogeneous immunoassay for the detection of TPSA. These first results of real samples using an unoptimized immunoassay are quite promising and further optimization of the assay could improve the quantification.

Comparison to commercial kits As mentioned in the beginning the used antibodies for the detection of TPSA, NSE, and CEA in an immunometric homogeneous immunoassay are already utilized in commercial diagnostic kits for these biomarkers. The signal transduction is also based on FRET, but from a europium-complex to, depending on the biomarker, different organic dyes. In order to compare the performance of the used LTC-to-QD FRET with varied antibody sizes to the commercial kits, the LOD of the commercial kits for the different bimomarker was evaluated using the same biomarker concentrations and after the manual provided with the kit. The resulting LODs are listed in Table 4.13 and 4.14 for the use of eQD605 and eQD650 AB-conjugates, respectively. For a better comparison the LODs are calculated on the whole 150 µl reaction volume.
In comparison to the commercial kits the obtained LODs are higher for the investigated

Table 4.13: Limit of detection (LOD) obtained using the commercial kit in comparison to the LODs of the different combinations of LTC-IgG with IgG-eQD605, F(ab')$_2$-eQD605, and F(ab)-eQD605 conjugates. All values have an error of approximately 20 %.

	LOD (Kit)	**LOD IgG**	**LOD F(ab')$_2$**	**LOD F(ab)**
		[ng/ml]		
TPSA	0.02	0.18	0.09	0.15
NSE	0.09	0.61	0.30	0.37
CEA	0.1	1.18	0.46	0.64

Table 4.14: Limit of detection (LOD) obtained using the commercial kit in comparison to the LODs of the different combinations of LTC-IgG with IgG-eQD650, F(ab')$_2$-eQD650, F(ab)-eQD650 conjugates. All values have an error of approximately 20 %.

	LOD (Kit)	**LOD IgG**	**LOD F(ab')$_2$**	**LOD F(ab)**
		[ng/ml]		
TPSA	0.02	0.27	0.12	0.15
NSE	0.09	0.35	0.33	0.40
CEA	0.1	0.91	0.32	0.33

LTC-to-QD FRET pair combinations, but in a similar range. A further optimization of the immunoassay procedure and using automated pipetting could improve the obtained values. On the other hand the measured LODs are very low and allow the quantification of biomarkers far below their clinical cutoff values, which are 4 ng/ml for TPSA, 12.5 ng/ml for NSE, and 5 ng/ml for CEA. Heterogeneous immunoassays like commercial ELISA-based diagnostic kits show comparable detection limits as obtained for the FRET-based commercial kits for all investigated antigens.

Simultaneous measurement of NSE and CEA biomarkers

Although the obtained LODs using LTC-donors and QD-acceptors are higher than for the commercial diagnostic kits, there is one advantage offered only by this FRET pair combination and that is the multiplexing capability. One trend in diagnostics is the simultaneous measurement of several biomarkers in one sample. The advantages are less time-consuming preparation of the different analysis methods, and reduction of material and patients sample. The europium complex used as donor in combination with organic dyes as acceptors in the commercial diagnostic kits for the measurement of TPSA, NSE, and CEA cannot provide such application. The main limitation is that the donor only provides one intense emission band in the visible spectrum and as such allows a spectral overlap only with one optimized dye as acceptor. LTCs provide several intense emission bands, which are suitable for the utilization of several acceptors. The combination of LTC in a multiplexed assay using five different emitting dyes for the detection of different lung cancer markers was demonstrated by Geißler *et al.* [19] The major obstacle in the use of dyes as acceptors are their pronounced emission shoulder in the red. This causes

interferences for the simultaneous measurement of several dyes, as their emission bleeds through into other measurement channels. This can lead to an increase in signal intensity in a measurement channel, where actually no biomarker is present. To correct for this pollution a mathematical correction of the obtained data has to be made.
The big advantage of using QDs as acceptors is their narrow symmetric Gaussian shape emission spectra. In Figure 4.10 (right) it can be seen that the emission spectra of the QDs are less affected by the other QD emission bands. With a careful selection of the detection wavelength for the different QDs a minor spectral crosstalk inside the measurement channel can be obtained. Together with the structured emission of the LTC-donor the signal deconvolution should be simpler compared to the used LTC-to-dye FRET multiplexing approach.
As proof of principle, the simultaneous detection of the biomarkers NSE and CEA was chosen. The measurement system consisted of LTC-IgG and F(ab')$_2$-eQD605 or F(ab')$_2$-eQD650 conjugates for the detection of either NSE or CEA.

Optical and biological crosstalk Prior to the simultaneous measurement of both biomarkers, the measurement system has to be checked for biological and optical crosstalk. Biological crosstalk originates from the binding of NSE detection antibodies to the CEA antigen or the binding of the NSE antigen to CEA detection antibodies. This crosstalk can interfere with the concentration estimation and lead to overestimated antigen concentrations.
To test the used system for biological crosstalk, immunoassays were performed with NSE detection antibodies and increasing concentrations of CEA and the same for the CEA targeting system. The results are exemplarily discussed for the combination of LTC-IgG and F(ab')$_2$-eQD605 (NSE-AB) for the detection of NSE and LTC-IgG and F(ab')$_2$-eQD650 (CEA-AB) for the detection of CEA, the control measurements with exchanged QDs are shown in the Appendix 6.3.2. For the detection of the QD sensitization in presence of the respective antigen two different bandpass filters were used. The KRYPTOR compact PLUS is equipped with a filter wheel, which allows a fast changing of the acceptor bandpass filters. Figure 4.21 shows the calibration curves obtained using the bandpass filters for the detection of NSE (left) and for the detection of CEA (right).
The Figure 4.21 left shows positive and negative controls measured in the NSE detection channel in order to estimate the influence of either the CEA antigen (CEA AG) or the presence of a second pair of antibodies in the solution. The increase of the intensity ratios in presence of NSE-AB and increasing concentrations of NSE antigen (NSE AG) represents the classical measurement of the antigen in a singleplex format. In contrast to the increase in presence of NSE, the addition of CEA AG to NSE-ABs causes no change in the intensity ratios. This is an evidence for a negligible biological crosstalk and the presence of increasing CEA AG concentrations will not cause the binding of NSE-ABs in an immunometric format and thus no FRET sensitization is observed. In presence of NSE-AB and CEA-AB the addition of NSE antigen results in a lower increase of the

intensity ratios compared to the singleplex format in absence of CEA AB. This effect is mainly attributed to a two-times higher LTC concentration, which results in twice as much intensities inside the donor channel compared to the singleplex format. Consequently by using the ratiometric approach the increasing in the intensity ratio is cut in half compared to the singleplex measurement. Similar to the addition of CEA antigen to NSE-AB, the presence of CEA-AB causes no significant increase in the intensity ratio. It is important to note that these measurements were performed in the eQD605 detection channel and that a sensitization of eQD650 due to the presence of CEA-AB and CEA antigen cannot be measured inside this detection channel.

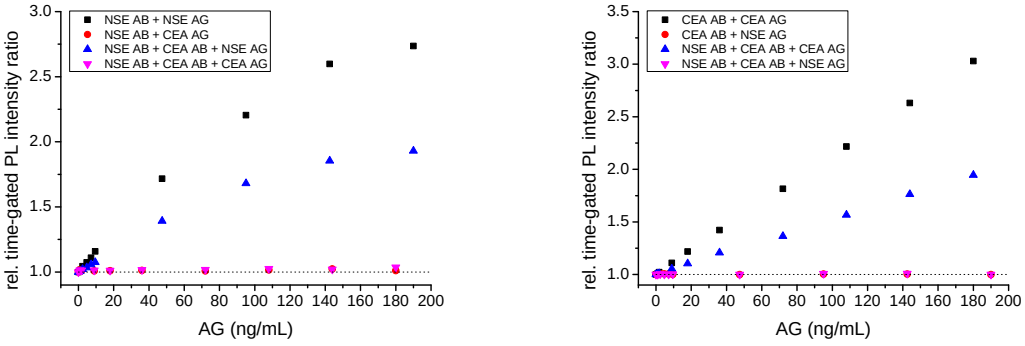

Figure 4.21: LEFT: Relative time-gated PL intensity ratios measured in the QD detection channel for eQD605 for the evaluation of the biological crosstalk of CEA detection antibodies (CEA AB) and the CEA antigen (CEA AG) within the NSE detection using the bandpass filter (607±8) nm. RIGHT: Relative time-gated PL intensity ratios measured in the QD detection channel for eQD650 for the evaluation of the biological crosstalk of NSE detection antibodies (NSE AB) and the NSE antigen (NSE AG) within the CEA detection using the bandpass filter (660 ± 13) nm.

The control measurements for the influence of the detection of CEA in presence of NSE-AB and NSE antigen shown on the right in Figure 4.21 are similar to the discussed results for NSE and show no biological crosstalk effects. Analogous, those measurements were performed using the bandpass filter for the detection of eQD650 and thus the FRET sensitization due to the binding of NSE-AB with increasing concentration of NSE is not detected.

This behavior of the monoclonal antibodies in the control measurements show their high specificity for the binding to the target antigen, which is very important for an independent measurement of several biomarkers in a multiplexed format. Apart form the biological crosstalk the optical crosstalk was investigated. Therefore the time-gated PL intensity ratios were measured in the QD detection channels for eQD605 and eQD650 with increasing concentrations of either NSE or CEA. The resulting relative intensity ratios are shown in Figure 4.22.

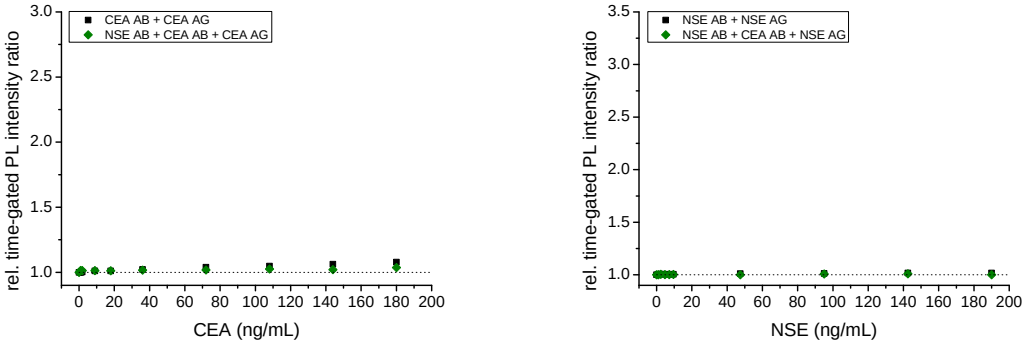

Figure 4.22: LEFT: Relative time-gated PL intensity ratios measured in the QD detection channel for eQD605 with increasing CEA antigen (CEA AG) concentration in presence of CEA detection antibodies (CEA-AB) or NSE detection antibodies (NSE-AB) + CEA-AB using the bandpass filter (607 ± 8) nm. RIGHT: Relative time-gated PL intensity ratios measured in the QD detection channel for eQD650 with increasing NSE antigen (NSE AG) concentration in presence of NSE detection antibodies (NSE-AB) or CEA detection antibodies (CEA-AB) + NSE-AB using the bandpass filter (660 ± 13) nm.

Optical crosstalk describes the bleed through of eQD650 emission in the QD detection channel, in which the sensitization of eQD605 is supposed to be measured and *vice versa*. The pollution, also called bleed through, into other measurement channels results in overestimated biomarker concentrations. In order to estimate the optical crosstalk immunoassays were performed, in which increasing amounts of CEA antigen were added to solutions of CEA-AB or CEA-AB + NSE-AB and the time-gated PL intensity ratio was monitored in the QD-detection channel for the measurement of NSE (see Figure 4.22 left). The constant relative intensity ratios close to unity are an evidence for negligible optical crosstalk of eQD650 with increasing sensitization. The same results were obtained monitoring the QD detection channel of eQD650 with increasing emission of sensitized eQD605 due to the FRET in presence of NSE antigen.

Duplexed measurements The control measurements reveal negligible influence of biological or optical crosstalk, which enables the independent concentration estimation of the two biomarkers in a duplexed immunometric measurement format. The measurement scheme was similar to the singleplex format. The donor-AB solutions for the detection of NSE and CEA were premixed together as well as the acceptor-AB solutions. For each measurement 50 µL of mixed donor-AB and acceptor-AB solution were added into the wells of the 96-well microtiter plate. The antigen solutions were prepared using newborn calf serum as diluent and contained increasing concentrations of both biomarkers. To the 100 µL of mixed donor-AB and acceptor-AB solution 50 µL of the serum-based antigen mixture was added and carefully mixed. The samples were incubated at 37 °C for up to 180 min and measured on the fluorescence plate readers, using a bandpass filter of (607 ± 8) nm for the detection of eQD605 and a bandpass filter of (660 ± 13) nm for the detection of eQD650. The resultant PL decay curves were treated after the time-gated ratiometric approach presented earlier for the singleplex immunoassays. The obtained relative intensity ratios are shown in Figure 4.23.

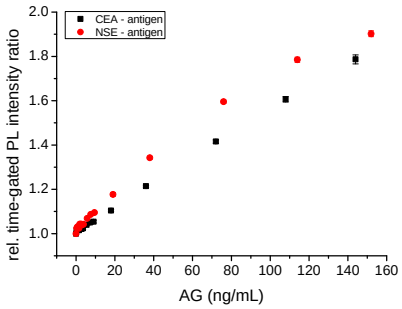

Figure 4.23: Relative time-gated PL intensity ratios measured for the detection of NSE and CEA in a duplexed immunoassay format. The increasing intensity ratios in presence of CEA antigen were measured using F(ab')$_2$-eQD650 and the bandpass filter (660 ± 13) nm and of NSE using F(ab')$_2$-eQD605 and the bandpass filter (607 ± 8) nm.

Important for the interpretation of the intensity ratios in Figure 4.23 is that they were measured using two different bandpass filters. The increase of the intensity ratio with increasing antigen concentration show the successful recognition by the corresponding antibody pair. Due to the lower antigen concentration the saturation of the calibration curves is not visible. The duplexed immunoassay was performed with either using F(ab')$_2$-eQD605 for the detection of NSE and F(ab')$_2$-eQD650 for CEA and the other way around using F(ab')$_2$-eQD650 for NSE and F(ab')$_2$-eQD605 for CEA. The measured control experiments as well as the duplexed calibration curve can be found in the Appendix 6.3.2. For a performance comparison of the duplexed immunoassay to single immunoassays the calibration curves were used to estimate the LODs according to the analytical sensitivity approach. The resultant LODs for both systems in comparison to the LODs obtained in single immunoassay measurements are shown in Table 4.15 and 4.16.

Table 4.15: Comparison of the limit of detection (LOD) calculated using the analytical sensitivity for the single and duplex immunoassay format using F(ab')$_2$-eQD650 for NSE and F(ab')$_2$-eQD605 for CEA detection. All values have an error of approximately 20 %.

Antigen	**AB-Donor**	**AB-Acceptor**	**Single LOD [ng/ml]**	**Duplex LOD [ng/ml]**
CEA	LTC-IgG	F(ab')$_2$-eQD605	1.4	3.7
NSE	LTC-IgG	F(ab')$_2$-eQD650	1.0	1.1

Table 4.16: Comparison of the limit of detection (LOD) calculated using the analytical sensitivity for the single and duplex immunoassay format using F(ab')$_2$-eQD605 for NSE and F(ab')$_2$-eQD650 for CEA detection. All values have an error of approximately 20 %.

Antigen	**AB-Donor**	**AB-Acceptor**	**Single LOD [ng/ml]**	**Duplex LOD [ng/ml]**
CEA	LTC-IgG	F(ab')$_2$-eQD650	1.1	1.6
NSE	LTC-IgG	F(ab')$_2$-eQD605	0.9	1.3

The duplexed measurement using F(ab')$_2$-eQD605 for the detection of CEA results in an increase of the LOD from 1.4 ng/mL in the singleplex format to 3.7 ng/mL in the duplexed format, whereas the LOD for the detection of NSE is in both formats around 1 ng/mL (see Table 4.15). This could be caused by the lower FRET sensitization of the eQD605 in presence of CEA antigen. In comparison to the twice as high donor signal the calculated intensity ratio get more affected resulting in a less steep increase of the calibration curve. The performance for the detection of CEA in the duplexed format can be improved exchanging the QDs for the detection of the antigens (see Table 4.16). In this combination using F(ab')$_2$-eQD605 for NSE detection and F(ab')$_2$-eQD650 for CEA, the obtained LODs are quite similar in both formats. In general, the LODs are far below the clinical cutoff levels of the respective antigens and make the duplexed format a promising approach for the detection of two biomarkers from a single sample. Thereby the system is very flexible and each combination of antigen can be measured using the respective antibodies.

Outlook to triplex measurement The structured emission bands of the LTCs exhibit several gaps and the duplexed approach can be extended to up to five suitable acceptors. As a short outlook a third QD, iQD705, was conjugated with F(ab')$_2$ acceptor-ABs for the detection of TPSA. The emission maximum is in the range of 705 nm and thus beyond the emission bands of the LTC. The performance for the detection of TPSA was compared to the already implemented eQD605 and eQD650 and the resulting calibration curves are shown in Figure 4.24.

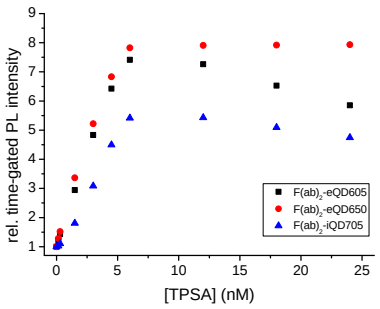

Figure 4.24: Comparison of the relative time-gated PL intensity ratios using combinations of LTC-IgG with F(ab')$_2$-eQD605, F(ab')$_2$-eQD650, or F(ab')$_2$-iQD705 with increasing TPSA concentration.

In Figure 4.24 the sensitization of F(ab')$_2$-iQD705 is not as strong as for the antibody conjugates using eQD605 and eQD650. The lower sensitization results also in a higher LOD compared to afore mentioned QDs (see Table 4.17).
Although the iQD705 has a similar Förster distance as eQD650 and exhibits the highest labeling ratio of F(ab')$_2$ antibodies per QD, the obtained LOD is with 0.9 ng/ml nearly twice as high as for eQD605 or eQD650 (see Table 4.17). The main reason for the lower sensitivity is attributed to the large size of the QD caused mainly by the thick PEG coat-

Table 4.17: Comparison of the limit of detection (LODs) calculated using the analytical sensitivity approach for the detection of TPSA using combinations from LTC-IgG with F(ab')$_2$-eQD605, F(ab')$_2$-eQD650, or F(ab')$_2$-iQD705. All values have an error of approximately 20 %.

AB-Acceptor	QD	**LOD [ng/ml]**
F(ab')$_2$	eQD605	0.3
F(ab')$_2$	eQD650	0.4
F(ab')$_2$	iQD705	0.9

ing to render the QD water-soluble and biocompatible. As the Förster distance counts from the center of the QD the thick coating prevents a close proximity of the donor compared to eQD650. The larger distance results in a lower FRET efficiency and thus lower sensitization in presence of the antigen.

However, the measurable calibration curve with an LOD much below the clinical cutoff level using a QD from a different company and also different surface coating reveals the flexibility in terms of the used LTC-to-QD FRET approach for homogeneous immunoassays. A future step is the implementation of the third QD inside a triplex immunoassays for the simultaneous detection of TPSA, NSE and CEA.

4.1.5 Nanobodies for EGFR detection

Our collaboration partner from the Utrecht University kindly provided single domain antigen binding fragments of heavy chain antibodies, which are also called nanobodies or V_HH. This term is attributed to their small size of only 15 kDa and 4 x 2.5 x 3 nm dimension, which is much smaller than the F(ab) fragments with 50 kDa used in the before presented investigations. The nanobodies were used inside a homogeneous immunometric immunoassay for the detection of soluble EGFR.[2] Although the nanobodies are very small the used EGFR is a dimer with total size of 190 kDa. For the realization of the sandwich immunoassays two nanobodies were provided, which bind to non-overlapping epitopes on the ectodomain I and III of EGFR. The distance between the epitopes on the EGFR is about 4 nm. Counting the size of 4 nm for each nanobody plus the radius of the used QD of 7 nm results in a maximum distance of ca. 19 nm. Due to the large Förster distance of 10.8 nm and the established and optimized conjugation protocol, eQD650 was used as FRET acceptor in combination with LTC as FRET donor.
Due to the small size of the nanobodies the labeling ratio of LTC per V_HH was only 1.4. In contrast the conjugation of V_HH to eQD650 was exceptional high with 30 V_HH per QD. The purification of free V_HH from the V_HH-eQD650 conjugate was very simple and efficient due to the large size differences. However, the non-oriented labeling strategy could lead to a certain percentage of inactive V_HH on the QD-surface.
The same immunoassay preparation protocol was used like for the afore mentioned immunoassays. A volume of 50 µL of each LTC-V_HH and V_HH-QD conjugates were mixed together, which gave 100 µL solution with a constant donor and acceptor concentration. Then 50 µL antigen solution with different concentrations of EGFR, prepared in NBCS or buffer 7, were added and after careful mixing incubated at 37 °C. The immunoassays were measured on both fluorescence plate readers.

The pre-FRET incident

The measured PL decay curve of the immunoassay in absence of EGFR show a different behavior as expected from the mathematical addition of the single measurement of LTC-V_HH and V_HH-QD conjugates. Figure 4.25 shows the measured and calculated PL decay curves.
In Figure 4.25 the gray PL decay curve is the calculated addition of the short-lived decay curve of pure V_HH-QD (magenta) and the long-lived decay curve of LTC-V_HH (orange). The black PL decay curve is the actual curve when both conjugates are present in the same solution. The appearance of a new decay time components with increased intensity (shown by the gray arrow) indicates a FRET sensitization also in absence of EGFR, termed pre-FRET. Reasons for this behavior could be a possible intrinsic hydrophobicity of the used V_HH-conjugates. The partial aggregation and dimerization of the nanobodies could result

[2] Work was published in: *Small*, **2013**, 734-740

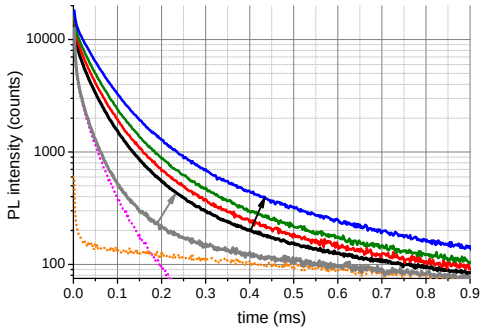

Figure 4.25: PL decay curves of the mathematical addition of the pure QD decay curve (magenta) and the pure LTC decay curve (orange) shown as gray PL decay curve and in presence of increasing concentrations of EGFR (black, 0 nM; red, 0.6 nM; green, 1.5 nM; blue, 6 nM). The gray and black arrows indicate FRET sensitization due to non-specific binding and EGFR binding, respectively. The used bandpass filter for the QD detection was (660 ± 13) nm

in a FRET sensitization, due to the close proximity of donor and acceptor. Experiments using increased amounts of free V_HH or Tween 20, to reduce the hydrophobicity, could not reduce the pre-FRET effect. Another theory is non-specific binding with BSA used in the assay to avoid non-specific binding of the antibodies to the walls of the microtiter plate and to human serum albumin within the serum samples. Measurement of the PL decay curves of the immunoassay without and different concentrations of BSA caused differences in the amount of the pre-FRET signal and thus supported the theory of non-specific binding by BSA. However, to assure stable assay condition the BSA was kept at 0.5 % for further investigations.
Despite the pre-FRET incident the increase of EGFR concentration revealed an increasing FRET sensitization shown by the black arrow in Figure 4.25. Furthermore, a longer decay time component appears in the decay curve attributed mainly to the larger distance between donor and acceptor caused by EGFR. The increased distance caused by the EGFR detection leading to a longer decay time in comparison to the non-specific binding of BSA is shown schematically in Figure 4.26.

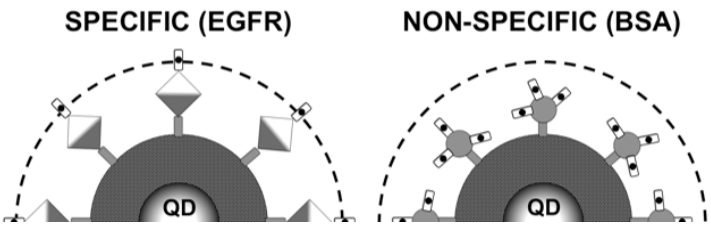

Figure 4.26: Schematic drawing for the specific EGFR detection (left) and non-specific binding of the V_HH antibodies with BSA (right).

That shows that apart from the non-specific binding with BSA the immunoassay is still able to detect EGFR in an efficient manner. In comparison to the measured PL decay curves for FRET sensitization using fragmented antibodies the new decay time is shorter and yields a higher FRET efficiency, due to small-sized V_HH.

Time-gated analysis

The performance of the immunoassay was assessed by the measurement of 18 EGFR samples with increasing concentrations ranging from 0.2 nM to 30 nM. The obtained time-gated PL intensity ratios measured in the QD and LTC detection channels are shown in Figure 4.27 left and right, respectively.

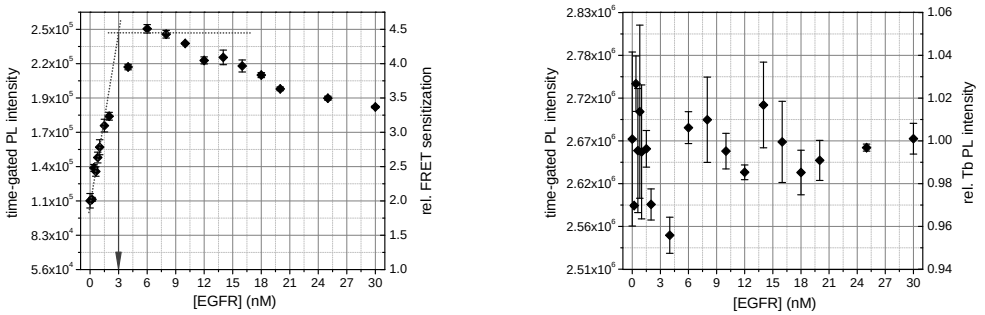

Figure 4.27: LEFT: Time-gated PL intensities in the QD detection channel as a function of the EGFR concentration. RIGHT: Time-gated PL intensities in the LTC detection channel as a function of the EGFR concentration.

In Figure 4.27 left the time-gated PL intensity ratios increases until they level off at a EGFR concentration of ca. 3 nM. This saturation concentration is three to five times lower than expected from the initially used LTC-V_HH and V_HH-QD conjugate concentrations of 8 nM and 15 nM, respectively. This could be a consequence of the non-specific binding to BSA as the involved V_HH-conjugates cannot take part in the detection of EGFR.
The time-gated PL intensity ratios in the LTC detection channel fluctuate at around $\pm$ 6 % without any significant tendency for enhanced quenching in the presence of increased EGFR concentration (see Figure 4.27 right). Due to a large fraction of LTC-V_HH conjugates that do not take part in FRET together with the low FRET efficiency, the small fraction of FRET-quenched LTC conjugates is masked by the high background of unquenched LTC conjugates. In comparison the low signal background in the QD detection channel in Figure 4.27 (left) enables the observation of the small signal changes due to FRET sensitization. It also shows the high-dose hook effect for concentrations larger than 9 nM.
Due to the encountered problems with non-specific binding to BSA the calibration curves were measured using buffer or serum as diluent for the preparation of the EGFR concentrations. The measured relative time-gated PL intensity ratios are shown in Figure 4.28.
A clear difference can be observed in the time-gated PL intensities and thus the level of FRET sensitization using buffer or serum as diluent for EGFR (see Figure 4.28). The much smaller increase in the intensity ratios for serum samples can be attributed to an increased amount of non-specific binding with proteins inside the serum. This also influences the estimated LODs where buffer as diluent yields a LOD of 0.12 nM (23 ng/mL) and serum a higher LOD of 0.18 nM (34 ng/mL).

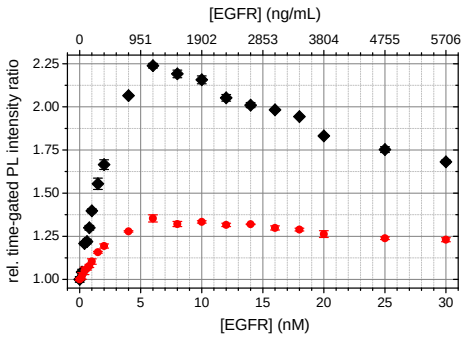

Figure 4.28: Calibration curves for the detection of EGFR using buffer (black) or serum (red) as diluent.

However, this was the first demonstration of homogeneous immunometric immunoassays for the detection of EGFR using V_HH-antibodies and LTC-to-QD FRET and the calculated LODs are below the clinical cut-off level of 45 ng/mL. The investigation presented here is already published in *Small*, **2013**, 734-740 and is attached in full length in the Appendix 6.3.4.

4.2 Spectroscopic ruler

As already mentioned before, FRET cannot only be used as a signal transduction system for the detection of an analyte, it also offers the possibility to estimate the distance between donor and acceptor. Several studies have shown the application of FRET as nanoscopic ruler for monitoring conformational changes of proteins and for the measurement of intramolecular distances within a biomolecule. The application of FRET for the structural analysis of nanoparticles, especially quantum dots, is relatively new. Thereby the size and shape of QDs are important parameters due to their great influence on their behavior in biological applications. A detailed structural analysis of size and shape can be used to predict the behavior inside cells, retention time for *in vivo* imaging, and partially the degree of their toxicity.

A common strategy for the size determination is TEM, which allows the measurement of the QD core size. The drawback of TEM is that allows only a two dimensional view on the QDs. Furthermore, the sample preparation results in dried QDs on a copper grid, which is a different environment than in the actual biosensing application. As an alternative DLS can be used, which enables the measurement of the entire QD including the organic coating. The estimated size counts for the assumption of a spherical QD and differences in shapes cannot be directly resolved. Additionally, the overall size is overestimated due to the inclusion of the hydration shell. Another measurement method is size-exclusion chromatography on HPLC. The size will be estimated by the retention time relative to a standard curve of proteins.

In conclusion, there is a demand for a structural analysis method working under physiological conditions, with three-dimensional size estimation, resolving the shape, and at low working concentration. These requirements can be fulfilled by LTC-to-QD FRET as spectroscopic ruler. The distance analysis is based on time-resolved measurements and the calculation of decay times from the obtained PL decay curves. Thereby the average decay time allows a statement about the overall size in a spherical assumption of the QD and the single decay time components can be used to estimate the shape of the QD. The advantage of the LTC-QD FRET pair is their large difference in the excited-state decay times between LTC and QD, which allows the measurement of the FRET decay time in the LTC detection channel and QD detection channel. Additionally, the observed large Förster distances allow the measurement of QDs with a thick coating.

At first some fundamental basics of time-resolved decay time analysis are recalled together with the special treatment of the measured PL decay curves within LTC-to-QD FRET measurements. Afterwards the used FRET donor and acceptor are characterized in terms of their photophysical properties before the results of LTC-to-QD FRET as spectroscopic ruler based on biotin-streptavidin recognition will be presented for the structural analysis of three biotinylated QDs. The size and shape analysis of 11 QDs, in which the close proximity of donor and acceptor is established *via* polyhistidine mediated self-assembly will complete the study.

4.2.1 Materials and Methods

Table 4.18: Prepared buffer solutions

	buffer	**concentration**
buffer 8	Sodium tetraborate (pH 8.5) with $\omega_{BSA} = 0.1\,\%$	10 mM

Biotin-streptavidin system

The FRET donor in the biotin-streptavidin assays was a commercially available streptavidin-labeled LTC Lumi4-Tb provided by the company Lumiphore Inc. (Richmond, CA, USA) with the brand name Lumi4-Tb-Strep. The labeling ratio was 4.4 LTCs per streptavidin. In the following part the used term for this conjugate is Tb-sAv.
The biotinylated QDs used as FRET acceptors are used without any further treatment and are listed in Table 4.19. The last two QDs in Table 4.19 were self-synthesized QDs kindly provided from our collaboration partner at the Ecole supérieure de physique et de chimie industrielles de la ville de Paris (ESPCI).

Table 4.19: Overview about the biotinylated QDs used as FRET acceptors with their used abbreviations inside this work and their source.

Quantum dot	**abbreviation**	**source**
Qdot 605 biotin conjugate	Biot-iQD605	Invitrogen/Life Technologies (Carlsbad, CA, USA)
eFluor 605 biotinylated NC	Biot-eQD605	eBioscience (San Diego, CA, USA)
p(DT-SB)605(A)	Biot-TPQD605 A	ESPCI-CNRS-UPMC (Paris, France)
p(DT-SB)605(B)	Biot-TPQD605 B	ESPCI-CNRS-UPMC (Paris, France)

QD-hexahistidin system

The used FRET donors in the QD-hexahistidin self-assembly measurements were provided by our collaboration partner (U.S. Naval Research Laboratory, Washington D.C., USA) and consist of a Lumi4-Tb complex (Lumiphore Inc. Richmond, CA, USA), which was conjugated either to a hexahistidine peptide with the sequence $H_2N \cdot SGAAAGLS \cdot (His)_6$ or to maltose binding proteins. Inside this work the abbreviation for these complexes are Tb-PEP and Tb-MBP, respectively.
The five used Qdot ITK carboxyl quantum dots were purchased from Invitrogen/Life Technologies (Carlsbad, CA, USA), whereas the DHLA capped QDs were self-synthesized

and kindly provided by our collaboration partner (U.S. Naval Research Laboratory, Washington D.C., USA). In Table 4.20 all used QDs within the measurements are listed together with their used abbreviations inside this work.

Table 4.20: Overview about the QDs used as FRET acceptors in the QD-hexahistidin self-assembly measurements with their used abbreviations inside this work.

Quantum dot	**abbreviation**
Qdot ITK 525 carboxyl	ITK-QD525
Qdot ITK 565 carboxyl	ITK-QD565
Qdot ITK 605 carboxyl	ITK-QD605
Qdot ITK 655 carboxyl	ITK-QD655
Qdot ITK 705 carboxyl	ITK-QD705
	DHLA-QD573
	DHLA-QD578
	DHLA-QD590
	DHLA-QD615

Further Analytical methods

Dynamic light scattering and transmission electron microscopy measurements for the structural characterization of the QDs used in the biotin-streptavidin and QD-hexahistidine self-assembly measurements were carried out by the collaboration partners or were provided by the supplier. Specific information of the instrumental setup and experimental conditions can be found in the attached original publications in the appendix 6.4.1 and 6.4.2.

Execution of the self-assembly assays

The biotin-streptavidin assays were performed in a low-binding black 96-well microtiter plate with an optimal working volume of 150 µL. Tb-sAv concentration was kept constant at 0.2 nM, whereas the Biot-QD concentration was varied from 0.02 nM to 0.6 nM. Each Biot-QD concentration was prepared three times and the Tb-sAv only sample (zero QD concentration) 10 times. Control measurements using the same Biot-QD concentrations but without Tb-sAv were prepared in the same way. The pipetting scheme was divided into three steps. At first 50 µL buffer 8 was added into the well plate followed by 50 µL of Tb-sAv and finally 50 µL Biot-QD solution. Tb-sAv and the different Biot-QD concentrations were prepared using buffer 8. After an incubation time of 90 min at 37 °C the samples were measured in triplicate using both the EI plate reader and the KRYPTOR compact plus.

The QD-hexahistidine self-assembly measurements were performed at the Fraunhofer Institute for Applied Polymer Research (Potsdam, Germany) and the data for further analy-

sis was kindly provided by Dr. Frank Morgner. In brief the measurements were performed on a modified KRYPTOR Immunoreader using a black 300-well microtiter plate with an optimal working volume of 150 µL. The concentration of the different used QDs were varied from 0.2 nM to 10 nM depending on the LTC-QD conjugate, whereas the LTC concentration was constant for Tb-PEP and Tb-MBP (between ca. 5 nM to 10 nM depending as well on the LTC-QD-bioconjugate). The incubation time was 60 min.

4.2.2 FRET-based decay time analysis

For the following discussion it is essential to recall basic concepts and equations for the understanding of decay curves and their treatment in order to obtain the correct decay times of the system. Provided information and equations inside the next chapter "Fundamental basics" are taken mainly from the following reference [3]

Fundamental basics

In general, the emission properties of a fluorophore can be characterized by its emission spectrum, quantum yield and decay time. The most sensitive parameter is the decay time and its analysis allows to retrieve information about the condition of the fluorophore in a given environment, which is not possible using the stationary emission spectrum or the quantum yield.
The requirement for fluorescence is the excitation of a molecule from the ground state to its excited state, schematically presented in the simplified Jablonski diagram for the resonance transitions in Figure 2.1. After the promotion the deexcitation back the ground state can be enabled under the emission of photons with the rate constant k_{rad} or due to non-radiative pathways described by the general rate constant k_{nr}. The average time of the molecule in the excited state prior to returning to its ground state is defined as decay time or lifetime of the molecule and depends on the before mentioned rate constants as shown in equation 4.6.

$$\tau = \frac{1}{k_{\mathrm{rad}} + k_{\mathrm{nr}}} \tag{4.6}$$

After the excitation of the sample a certain amount of molecules are in the excited state and can be described by the population n_0. The deexcitation of this population follow the rate $k_{\mathrm{rad}}+k_{\mathrm{nr}}$ and can be described by the following equation 4.7 in which $n(t)$ is the population at time t following excitation.

$$\frac{dn(t)}{dt} = (k_{\mathrm{rad}} + k_{\mathrm{nr}}) \cdot n(t) \tag{4.7}$$

Fluorescence is a random process characterized by a spontaneous emission of photons in a given period of time, which results in an exponential decay of the excited state population according to $n(t) = n_0 \cdot exp(-t/\tau)$. The access to the excited state population

$n(t)$ is given by its proportionality to the measurable fluorescence intensity. Consequently, the population $n(t)$ can be substituted by the time-dependent fluorescence intensity $I(t)$. The integration of equation 4.7 using the intensity results in the general expression for a single exponential decay (see equation 4.8).

$$I(t) = I_0 \cdot exp(-t/\tau) \tag{4.8}$$

I_0 is the intensity at time 0, τ the decay time defined in equation 4.6.

One has to keep in my mind that the fluorophores emit randomly throughout the decay of the ensemble of fluorophores resulting in an averaged value for the obtained decay time. The expression in equation 4.8 is valid for a fluorophore with a single decay time. In presence of a second fluorophore with a different decay time the situation is more complex and results in a time distribution of emitted photons, which create a more complex intensity decay. The different contributions can be taken into account by the introduction of pre-exponential factors α_i, which describe the fraction and thus the amount of fluorophores with a specific decay time. In order to recover the different α_i and their corresponding decay time from the intensity curve, the expression in equation 4.8 has to be modified and the resulting multi-exponential model is shown in equation 4.9.

$$I(t) = \sum_i \alpha_i \cdot exp(-t/\tau_i) \tag{4.9}$$

$\sum_i \alpha_i$ is normalized to unity.

The reason for a multi-exponential decay is not restricted to the mixture of two different molecules with different decay times, also a single fluorophore can decay in a complex manner. This can be caused by different environments of the fluorophore in the same sample, or also due to energy transfer processes. A common problem in decay time analysis is the compensation of the pre-exponential factor for the decay time and *vice versa* in order to achieve the best mathematical fit to the measured decay curve. The mathematical correlation of both factors results in similar decay fits of the same decay curve using different values for α_i and τ_i.

LTC-based FRET spectroscopic ruler

A requirement for the calculation of the donor-acceptor distance according to equation 2.5 is the calculation of the Förster distance and the FRET efficiency. For the determination of the Förster distance the equation 2.2 can be used, whereas the FRET efficiency is accessible by using the PL decay times of the donor in presence and in absence of the acceptor according to equation 2.6. The used FRET donor (LTC) and the FRET acceptor (QDs) in this study exhibit a multi-exponential decay, which demand the use of equation 4.9 for the decay time analysis. Resultant single decay times and their corresponding pre-exponential factors, also called amplitudes or fractions, can be used to calculate an

average decay time of the donor in the absence and in the presence of the acceptor or of the FRET-sensitized acceptor. Thereby the averaging has to be amplitude-weighted due to the dynamic FRET process. [228, 229] These averaged decay times can then be used in 2.6 for the calculation of the FRET efficiency and thus to estimate the donor-acceptor distance.
The long decay time of LTCs is advantageous for the time-gating approach and for the independent evaluation of the FRET decay time in the donor and acceptor channel, but it also results in one drawback for the decay time analysis. Due to the presence of unquenched LTCs, the measured PL decay curve in both measurement channels contains signals from the unquenched donor. In order to estimate the pure FRET decay time for the calculation of the donor-acceptor distance the measured PL decay times need to be corrected for the free LTC. The description of the decay time correction is mainly taken from reference [8].

Decay time correction for free LTC The following description is a general approach for the correction of the influence of free LTC in the PL decay curves of LTC-to-QD FRET systems. In general, the decay curve of LTCs bound to a biomolecule can be fitted using two exponents, with a short τ_{D1} and a dominant long decay time τ_{D2}. QDs exhibit a multi-exponential decay curve and at least three exponents have to be used for an acceptable fit. Due to the utilization of a least squares analysis method the quality of the fit is judged by the parameter chi-square, which is minimized by optimizing the parameter values (decay time and fraction). A chi-square around one and a random distribution of the residuals, between the measured and calculated decay curve, around zero characterize a good fit. The assumption of the decay time correction is that the presence of unquenched LTC results in a fixed decay time but, depending on the amount of free LTC, different fractions. Due to the crosstalk of LTC emission also in the QD detection channel, PL decay curves measured in both the donor as well as the acceptor channel have to be corrected for the contribution of unquenched donor.
In case of FRET the donor decay curves can be fitted using triple-exponential decay functions, whereas the FRET sensitized acceptor decay curve requires a quadruple exponential fit. To increase the quality of the decay time fitting the fit range has to be carefully chosen. Disturbances of directly excited QDs and autofluorescence in the first microseconds can be avoided by introducing a delay of the fit starting point of around 10 µs to 50 µs after the excitation pulse. Additionally, in the acceptor channel the signal intensity after a certain time range contains mainly the contribution of the LTC crosstalk and should not be taken into account for fitting. The mainly used fit approach for such long decay times with a delay in the start point is the tail fit, which basically means that the fit starts at a different time t_0 for donor and acceptor decay channel after the excitation pulse. This delayed start of the fit shows no large influences on the fitted decay time but the single amplitudes A_{i-FIT} need to be corrected from t_0 to the actual start at 0 to yield the correct amplitudes A_i of the complete decay function according to equation 4.10.

$$I = A_{\mathrm{i-FIT}} \cdot exp\left(-\frac{t-t_0}{\tau}\right) = A_i \cdot exp\left(-\frac{t}{\tau}\right) \rightarrow A_i = A_{i-FIT} \cdot exp\left(\frac{t_0}{\tau}\right) \tag{4.10}$$

The correction of the amplitudes is necessary as they are used for the estimation of the average amplitude decay time in order to make a statement about the average donor-acceptor distance and thus about the overall size of the QD. Additionally, the corrected amplitudes contain information about the amount of an estimated donor-acceptor distance from the single decay time on the overall size of the QD and thus deliver important information about its shape.
The FRET quenched PL decay curves measured in the donor channel can then be fitted with three exponents, yielding three amplitudes ($\alpha_{\mathrm{DA}*1}, \alpha_{\mathrm{DA}*2}$, and $\alpha_{\mathrm{DA}*0}$) and three decay times ($\tau_{\mathrm{DA1}}, \tau_{\mathrm{DA2}}$, and τ_{DA0}). From which τ_{DA0} is fixed to the intrinsic long decay time τ_{D2} of the LTC-complex. In order to estimate the average FRET decay time only τ_{DA1} and τ_{DA2} are used as the third component represents the unquenched donor. The exclusion of the third fraction demands a redefinition of the first two fractions according to equation 4.11 and 4.12

$$\alpha_{\mathrm{DA1}} = \frac{\alpha_{\mathrm{DA}*1}}{\alpha_{\mathrm{DA}*1} + \alpha_{\mathrm{DA}*2}} \tag{4.11}$$

$$\alpha_{\mathrm{DA2}} = \frac{\alpha_{\mathrm{DA}*2}}{\alpha_{\mathrm{DA}*1} + \alpha_{\mathrm{DA}*2}} \tag{4.12}$$

The extraction of the dominant long decay time of unquenched donor is simple by introducing one dedicated exponent in the decay fit function. Due to similar decay times of the short component τ_{D1} in comparison to the FRET decay time, introducing of an extra exponent will not resolve such similar decay times. Therefore a correction factor z_D has to be used, which is shown in equation 4.13. The obtained fraction for the long decay time τ_{DA0} in the FRET case is set in relation to the fraction in absence of the acceptor τ_{D2} in order to calculate the relative amount of donor taking part in FRET and concomitantly the amount of free donor in presence of the FRET pair. The multiplication with the fraction in absence of the acceptor of the short component α_{D1} yields the fraction of unquenched donor molecules with a short decay time.

$$z_D = \alpha_{\mathrm{D1}}\left(\frac{\alpha_{\mathrm{DA}*0}}{\alpha_{\mathrm{D2}}}\right) \tag{4.13}$$

In order to calculate the average FRET quenched decay time under consideration of the redefined α_{DA1} and α_{DA2} fractions ($\alpha_{\mathrm{DA1}} + \alpha_{\mathrm{DA2}} = 1$) and the correction factor z_D for the short component of unquenched donor equation 4.14 can be used.

$$\langle \tau_{\mathrm{DA}} \rangle = \frac{\alpha_{\mathrm{DA1}}\tau_{\mathrm{DA1}} + \alpha_{\mathrm{DA2}}\tau_{\mathrm{DA2}} - z_D(\alpha_{\mathrm{DA1}} + \alpha_{\mathrm{DA2}})\tau_{\mathrm{D1}}}{\alpha_{\mathrm{DA1}} + \alpha_{\mathrm{DA2}} - z_D(\alpha_{\mathrm{DA1}} + \alpha_{\mathrm{DA2}})} = \frac{\alpha_{\mathrm{DA1}}\tau_{\mathrm{DA1}} + \alpha_{\mathrm{DA2}}\tau_{\mathrm{DA2}} - z_D\tau_{\mathrm{D1}}}{1 - z_D} \tag{4.14}$$

The donor crosstalk inside the QD detection channel must also be corrected in order to yield the pure FRET sensitized decay time. Thereby the obtained decay curves in the acceptor channel are fitted using four exponents. The resultant fractions are $\alpha_{\mathrm{AD}*1}$, $\alpha_{\mathrm{AD}*2}$, $\alpha_{\mathrm{AD}*3}$, and $\alpha_{\mathrm{AD}*0}$ with decay times $\tau_{\mathrm{AD}*1}$, $\tau_{\mathrm{AD}*2}$, $\tau_{\mathrm{AD}*3}$, and $\tau_{\mathrm{AD}*0}$, from which the last one is fixed to the long decay time of the intrinsic donor τ_{D2}. Similar as in the donor channel the short component of the donor in absence of the acceptor has to be corrected using the correction factor z_A according to equation 4.15.

$$z_A = \alpha_{\mathrm{D1}} \left(\frac{\alpha_{\mathrm{AD}*0}}{\alpha_{\mathrm{D2}}} \right) \tag{4.15}$$

For the calculation of the average FRET sensitized decay time only the first three components are used as the fourth component is the free and unquenched donor. Thereby the fractions α_{ADi} must be corrected by the FRET rate $k_{\mathrm{FRETi}} = \tau_{\mathrm{ADi}}^{-1} - \langle \tau_{\mathrm{D}} \rangle^{-1}$. This correction considers the FRET efficiency dependent excitation of the acceptors in different donor-acceptor distances using equation 4.16.

$$\alpha_{\mathrm{ADi}} = \frac{(\alpha_{\mathrm{AD}*\mathrm{i}}/k_{\mathrm{FRETi}})}{(\alpha_{\mathrm{AD}*1}/k_{\mathrm{FRET1}}) + (\alpha_{\mathrm{AD}*2}/k_{\mathrm{FRET2}}) + (\alpha_{\mathrm{AD}*3}/k_{\mathrm{FRET3}})} \tag{4.16}$$

The corrected averaged FRET sensitized decay time can then be calculated after equation 4.17.

$$\langle \tau_{\mathrm{AD}} \rangle = \frac{\alpha_{\mathrm{AD1}}\tau_{\mathrm{AD1}} + \alpha_{\mathrm{AD2}}\tau_{\mathrm{AD2}} + \alpha_{\mathrm{AD3}}\tau_{\mathrm{AD3}} - z_A\tau_{\mathrm{D1}}}{1 - z_A} \tag{4.17}$$

Using this corrections to consider unquenched LTC contribution in the donor as well as acceptor channel allows the calculation of the pure FRET quenched and FRET sensitized decay times and thus the determination of donor-acceptor distances.

4.2.3 Characterization of FRET donors and FRET acceptors

FRET donors

Similar to the investigation in FRET immunoassays, the used FRET donor was the Lumi4-Tb complex from Lumiphore Inc. (Richmond, CA, USA). The absorbance and PL emission spectrum for the Lumi4-Tb complex conjugated to streptavidin is shown in Figure 4.29 together with the PL decay curve.

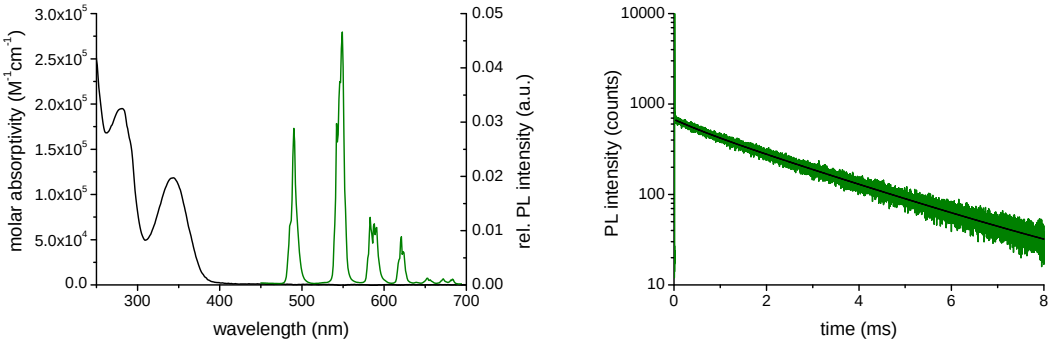

Figure 4.29: LEFT: Absorbance and PL emission spectrum for Lumi4-Tb-streptavidin. RIGHT: PL decay curve of Lumi4-Tb-streptavidin.

The representative spectra in Figure 4.29 resemble the typical photophysical properties of the Lumi4-Tb complex, which is only negligible influenced by the conjugation to a sAv. Important to note is that the absorbance spectrum in Figure 4.29 (left) is a linear combination of the absorbance spectrum of the Lumi4-Tb complex with maximum at 340 nm and a molar absorptivity of 26.000 $M^{-1}cm^{-1}$ and the absorbance spectrum of the sAv with a maximum around 280 nm.

For the investigation of LTC-to-QD FRET using the biotin-streptavidin recognition for structural analysis, the Lumi4-Tb complex was conjugated to streptavidin (Tb-sAv). The conjugated complex was kindly provided by the company Lumiphore Inc. and was used without any further treatment. The labeling ratio, averaged amplitude-weighted decay time, and the quantum yield are listed in Table 4.21.

The investigation of LTC-to-QD FRET based on the polyhistidine mediated self-assembly was performed using two different biomolecules. The first one was a peptide with a molecular weight of 1.5 kDa and peptide sequence of $GSGAAAGLS(HIS)_6$ with an NHS-ester for the conjugation of Lumi4-Tb-NHS, further denoted as Tb-PEP. The second LTC-donor was a maltose binding protein (Tb-MBP) with a molecular weight of ca. 44 kDa containing a hexahistidine in its sequence and labeled as well using Lumi4-Tb-NHS. The labeling ratios, averaged amplitude-weighted decay times and the quantum yields for both LTC-donors are listed in Table 4.21.

Table 4.21: Overview of the averaged amplitude decay times, quantum yields, and labeling ratios of LTC conjugated to different biomolecule of interest (BOI) used as FRET donors inside the structural analysis measurements based on biotin-streptavidin recognition or polyhistidine mediated self-assembly.

	$\langle\tau\rangle_{\mathrm{Amp}}$ / ms	Φ_{Tb}	LTC / BOI
Tb-sAv	2.3 ± 0.1	0.65	4.2
Tb-PEP	2.75 ± 0.05	0.80	1.0
Tb-MBP	2.35 ± 0.35	0.68	1.3

FRET acceptors

Biotin-streptavidin model system Three different types of QDs were used as FRET acceptors for the structural analysis based on the biotin-streptavidin recognition. Thereby two batches are commercial QDs from the companies Invitrogen by LifeTechnologies Corp. (USA) and eBioscience, Inc. (USA), denoted as Biot-iQD605 and Biot-eQD605, respectively. These QDs have an amphiphilic polymer / lipid coating, whereas the third batch has a poly(dithiol-co-sulfobetaine) polymeric ligands on the surface and was kindly provided from our collaboration partner from (Dr. Thomas Pons, ESPCI, Paris, France), further denoted as Biot-TPQD605. All QD batches were conjugated with biotin on the QD surface (Biot-QDs) in order to be used in the biotin-streptavidin recognition. Thereby Biot-TPQD605 was provided as two batches with different amount of biotin used in the conjugation and with the expectation to yield different amounts of biotin on the surface. These batches are further denoted as Biot-TPQD605 A and Biot-TPQD605 B.
The measured absorbance and PL emission spectra for the different QDs are shown in Figure 4.30 (left) and the measured PL decay curves in Figure 4.30 right. During the characterization the two batches of Biot-TPQD605 show similar behavior and only one batch is illustrated.

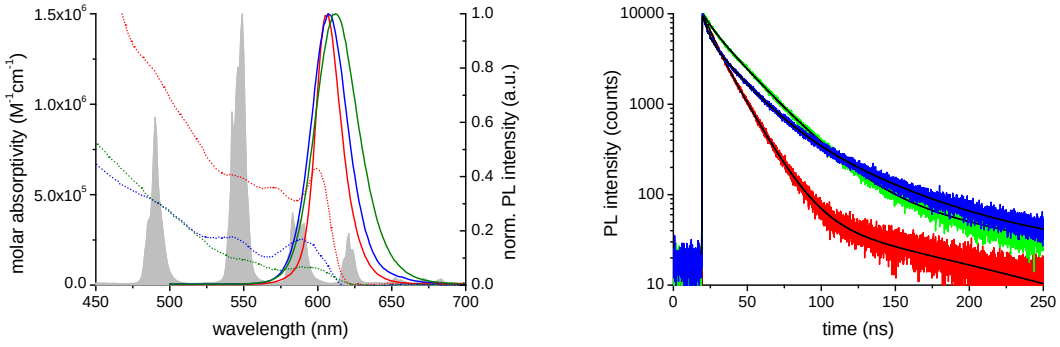

Figure 4.30: LEFT: Absorbance spectra (dotted) and normalized PL emission spectra of the used FRET acceptors Biot-iQD605 (red), Biot-eQD605 (blue), and Biot-TPQD605 (green) and the PL emission spectrum of Tb-sAv as gray surface in the background to show the spectral overlap of the donor with the different acceptors. RIGHT: Multi-exponential decay curves of Biot-iQD605 (red), Biot-eQD605 (blue), and Biot-TPQD605 (green).

The dotted curves in Figure 4.30 (left) are the measured absorbance spectra of the Biot-QDs and show the typical broad absorbance band with several pronounced exciton peaks between 525 nm to 625 nm. In comparison to the PL emission spectrum of Tb-sAv (gray surface in the background) all Biot-QDs display a large spectral overlap with the most intense emission peaks of the donor. Together with the high QD extinction coefficients this results in large Förster distances of up to 9.1 nm for the combination of Tb-sAv / Biot-iQD605 (see Table 4.22).
The included PL emission spectra of the Biot-QD batches in Figure 4.30 (left) present the characteristic symmetrical Gaussian shape with a maximum at around 605 nm. The broadening of the FWHM from Biot-iQD605 (20 nm) to Biot-TPQD605 (34 nm) is attributed the different synthesis strategies and coatings of the QDs (see Table 4.22 for comparison). All measured PL decay curves of the QDs presented in Figure 4.30 (right) exhibit a multi-exponential behavior and the PL decay times were fitted using three components. The resultant averaged intensity-weighted decay times are shown in Table 4.22 together with their quantum yields, which were measured against fluorescein and rhodamine as standards. The decay time of only 17 ns and the high QY of 0.73 together with the twice as high extinction coefficients make Biot-iQD605 to the best performing QD, which also results in the largest Förster distance. Due to the ligand exchange strategy for the preparation of water-soluble Biot-TPQD605, the QD is more compact but also presents a very low QY of only 0.07. However, the calculated Förster distance of 7.4 nm is comparable to the Biot-eQD605 with 7.8 nm. Table 4.22 presents the summary of the discussed parameters.

Table 4.22: Summary of the main paramter of the Biot-QDs in terms of their source, the full-width-at-half-maxima (FWHM) of the emission peak, quantum yield (Φ), the average intensity weighted decay time ($\langle\tau\rangle_{\mathrm{Int}}$), and the calculated Förster distance (R_0).

	source	**FWHM (nm)**	Φ	$\langle\tau\rangle_{\mathrm{Int}}$ **/ ns**	R_0 **(nm)**
Biot-iQD605	Invitrogen	20	0.73	17	9.1
Biot-eQD605	eBioscience	29	0.65	29	7.8
Biot-TPQD605 A	ESPCI	34	0.07	31	7.4
Biot-TPQD605 B	ESPCI	34	0.07	31	7.4

QD - hexahistidine self-assembly For the spectroscopic ruler measurements using the polyhistidine mediated self-assembly two different batches of QDs were used. One batch of six QDs were self-synthesized by our collaboration partner (Dr. Igor Medintz, NRL, Washington, DC, USA) and exhibit a dihydrolipoic acid (DHLA) coating and are in the following discussion denoted as DHLA-QDs. The second batch were five different emitting QDs coated with carboxyl functionalized polymers purchased from Invitrogen LifeTechnologies (USA). The abbreviation of these QDs is ITK-QDs. Figure 4.31 shows the absorbance spectra (left) and PL emission spectra (right) of the ITK-QDs.

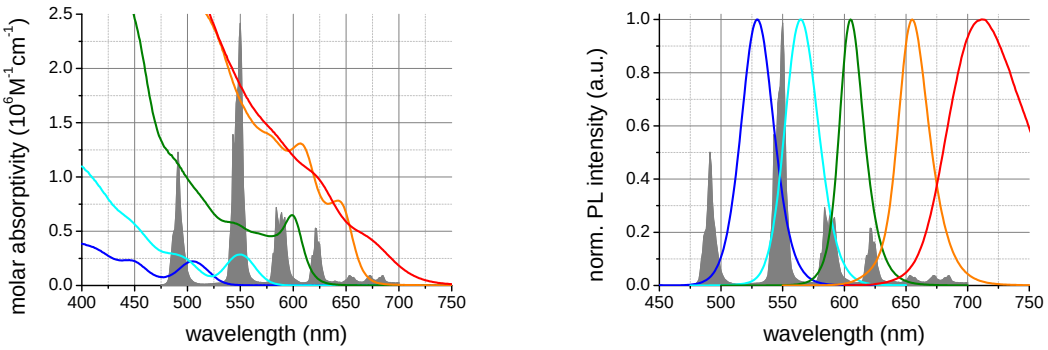

Figure 4.31: Absorbance spectra (left) and the normalized PL emission spectra (right) of ITK-QD525 (blue), ITK-QD565 (cyan), ITK-QD605 (green), ITK-QD655 (orange), and ITK-QD705 (red) shown together with the LTC PL emission spectra (gray).

The absorbance and normalized PL emission spectra show the characteristic behavior of QDs. Very high extinction coefficients and large spectral overlaps with the LTC emission bands result in large Förster distances, which are given in Table 4.23. The emission maxima are indicated by the numbering of the ITK-QDs and lay between or beyond the PL emission bands of the LTC-donor, which enables facile signal deconvolution. Table 4.23 summarizes the major properties of the ITK-QDs.

Table 4.23: Overview of the core/shell materials, extinction coefficients (ϵ), quantum yields (Φ), and the calculated Förster distances (R_0) for the different ITK-QDs.

	core / shell	ϵ **[M^{-1}cm^{-1}]**	Φ	R_0 **(nm)**
ITK-QD525	CdSe/ZnS	$3.6 \cdot 10^5$ (405 nm)	0.52	5.4
ITK-QD565	CdSe/ZnS	$1.1 \cdot 10^6$ (405 nm)	0.75	7.4
ITK-QD605	CdSe/ZnS	$2.8 \cdot 10^6$ (405 nm)	0.7	9.1
ITK-QD655	CdSe/ZnS	$2.4 \cdot 10^6$ (405 nm)	0.64	11
ITK-QD705	CdSeTe/ZnS	$8.3 \cdot 10^6$ (405 nm)	0.5	11.1

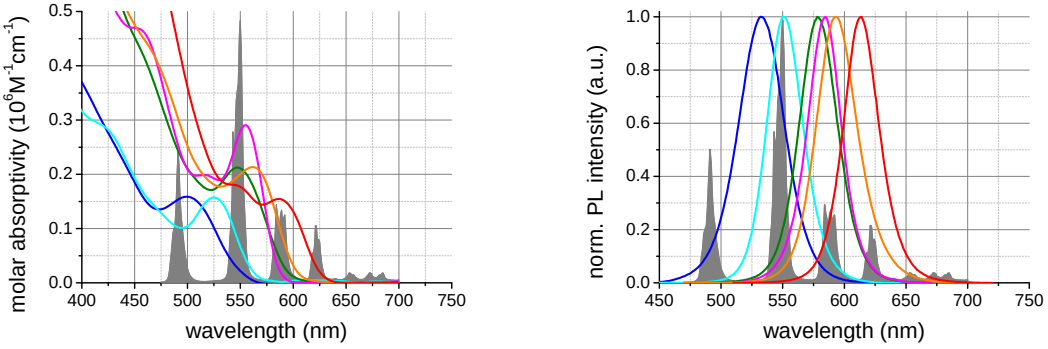

Figure 4.32: Absorbance spectra (left) and the normalized PL emission spectra (right) of DHLA-QD530 (blue), DHLA-QD537 (cyan), DHLA-QD573 (green), DHLA-QD578 (magenta), DHLA-QD590 (orange), and DHLA-QD615 (red) shown together with the LTC PL emission spectra (gray).

Figure 4.32 shows the absorbance spectra (left) and the normalized PL emission spectra (right) for DHLA-QDs.
The photophysical behavior has similar characteristics as the ITK-QDs with the difference that the emission bands are not so nicely distributed across the LTC emission spectrum. As it could be also seen on the numbering of the DHLA-QDs, which indicates the emission maxima, the QDs can be divided into three groups of similar emission maxima. Due to the smaller spectral overlap and lower extinction coefficients the DHLA-QDs exhibit smaller Förster distances (shown in Table 4.24).

Table 4.24: Overview of the core/shell materials, quantum yields (Φ), and the calculated Förster distances (R_0) for the different DHLA-QDs.

	core / shell	Φ	R_0 **(nm)**
DHLA-QD530	CdSe/ZnS	0.23	5.5
DHLA-QD537	CdSe/ZnS	0.20	6.1
DHLA-QD573	CdSe-CdZnS/ZnS	0.08	7.1
DHLA-QD578	CdSe/ZnS	0.14	7.5
DHLA-QD590	CdSeTe/ZnS	0.10	7.4
DHLA-QD615	CdSe CdS-CdZnS/ZnS	0.24	7.3

Figure 4.33 shows the PL decay curves measured for the ITK-QDs (left) and DHLA-QDs (right). All decay curves have a multi-exponential decay with components in the one to several hundred nanoseconds range.

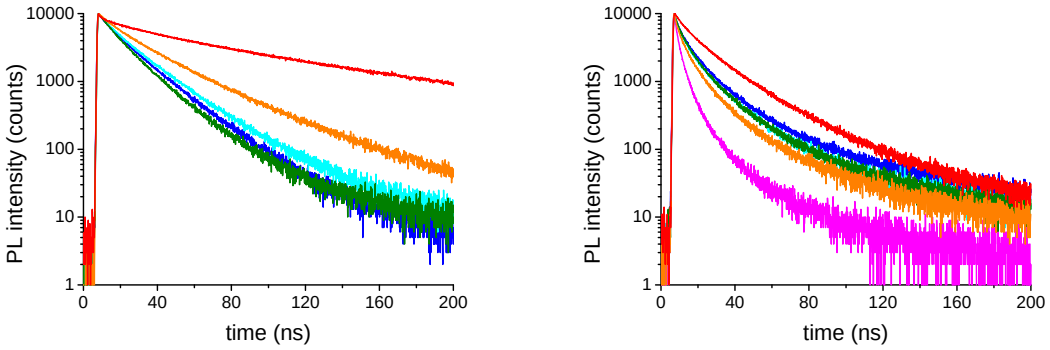

Figure 4.33: PL decay curves of ITK-QDs (left) with ITK-QD525 (blue), ITK-QD565 (cyan), ITK-QD605 (green), ITK-QD655 (orange), and ITK-QD705 (red) and of the DHLA-QDs with DHLA-QD530 (blue), DHLA-QD537 (cyan), DHLA-QD573 (green), DHLA-QD578 (magenta), DHLA-QD590 (orange), and DHLA-QD615 (red).

4.2.4 Biotin-streptavidin system

In the first structural analysis of QDs the biotin-streptavidin recognition was used to bring the LTC-donor in close proximity to the QD-acceptor in order to establish efficient FRET. Therefore the Lumi4-Tb complex conjugated to streptavidin was used as FRET donor and further denoted as Tb-sAv in the following discussion. Three different batches of biotinylated QDs were investigated to obtain information about their size and shape.[3] A schematic figure of the investigated system is shown in Figure 4.34, where the cross shape of sAv presents the four binding sites for biotin. In a first study using the same

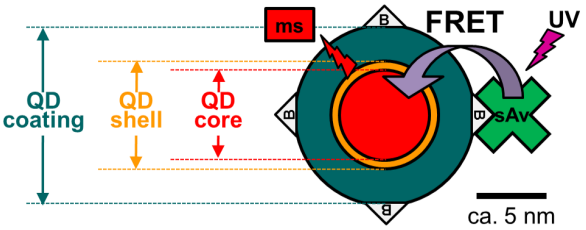

Figure 4.34: Time-resolved LTC-to-QD FRET bioassay using LTC-labeled streptavidin (Tb-sAv) and biotinylated (B) QDs for biological recognition.

biotin-streptavidin recognition for multiplexed size and shape investigation of different sized QDs based on LTC-to-QD FRET, the feasibility of the spectroscopic ruler approach was shown. [6] However, in this analysis the contribution of the unquenched LTC-donor signal on the evaluated decay times and the corresponding pre-exponential factors were not taken into account. Nevertheless, the study showed that the random labeling of LTC-complexes on the sAv molecule and the different shapes of used QDs resulted in a donor-acceptor distance distribution, which could be measured by FRET.
The investigated QDs in this study exhibit different sizes and shapes and similar absorption and emission wavelengths. This allows a better comparison of the direct influence of the different structural properties on the FRET distance analysis. The FRET experiments were executed at a constant Tb-sAv concentration of 0.2 nM with varied concentrations of biotinylated QDs (Biot-QDs) from 0.02 nM to 0.6 nM. After the addition of Tb-sAv and Biot-QD dissolved in buffer 8 the samples were incubated at 37 °C for 90 min before the measurement on the different fluorescence plate readers. Although the donor-acceptor distance distribution is concentration independent, the measurement using different acceptor concentrations is advantageous. Primarily it provides a set of independent PL decay curves, which increases the statistical characterization of the evaluated distances. [6] Secondly several information can be obtained like the number of biotin molecules on the QD surface and the LOD for the biotin-streptavidin recognition.

[3] Work was published in: *ACS Applied Materials and Interfaces*, **2013**, 5, 2881-2892

Time-gated FRET analysis

The obtained PL decay curves for the different Tb-sAV / Biot-QD combinations with increasing QD concentration were treated with the similar time-gated approach shown already in the FRET immunoassay measurements. Therefore the PL decay curve intensities measured in the LTC and QD detection channel were integrated from 0.1 ms to 0.9 ms. The resulting time-gated PL intensities in the channels were plotted as a function of the Biot-QD concentration and the obtained values for the combination of Tb-sAv / Biot-TPQD605 B are shown in Figure 4.35 for the QD detection channel (left) and the LTC detection channel (right).

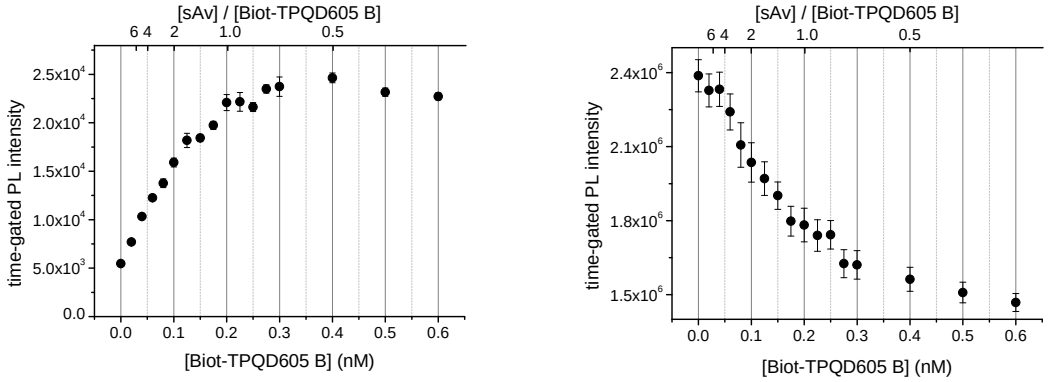

Figure 4.35: PL time-gated intensities as a function of Biot-TPQD605 B measured in the QD detection channel (left) and in the LTC detection channel (right).

The PL time-gated intensities in Figure 4.35 (left) obtained in the QD detection channel show a significant increase caused by FRET sensitization in presence of very small Biot-QD concentrations. Concomitant to the strong FRET sensitization of the Biot-QD acceptor, the Tb-sAv PL time-gated intensities measured in the LTC detection channel show a strong quenching. These strong changes provide further evidence for the exceptional high binding affinity of the biotin-streptavidin recognition, which results in efficient FRET also at Biot-QD concentrations lower then 100 pM. With increasing Biot-QD concentration a saturation effect is observed resulting in no further increase of the time-gated PL intensities, due to the constant Tb-sAv concentration. In the presented combination the saturation is at a sAv to Biot-QD ratio of ca. 1, which corresponds to a Biot-TPQD605 B concentration of 0.2 nM.

This saturation concentration can be also used for the estimation of the number of biotin molecules bound on the QD surface. Therefore the time-gated PL intensity ratios were calculated and the tangents of the linearly increasing and the saturation parts of the FRET assay curves used. The intercept of the tangents defines the approximate biot/QD ratio. Figure 4.36 show the time-gated PL intensity ratios of two batches of QDs as a function of their concentration together with the tangents used for the calculation of biot/QD ratio.

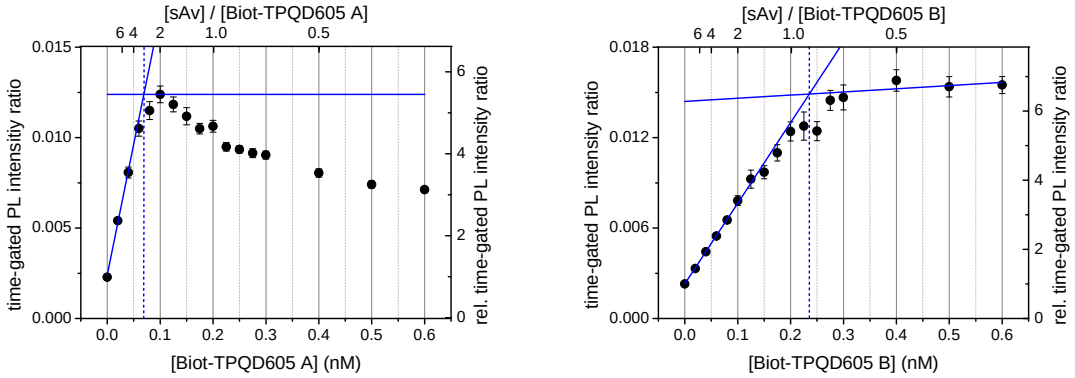

Figure 4.36: Time-gated PL intensity ratio as function of increasing Biot-TPQD605 A (left) or Biot-TPQD605 B (right) concentration together with the tangents used for the calculation of the individual biotin per QD conjugation ratio.

The results of the presented QDs in Figure 4.36 show a significant difference in the intercept of the tangents and thus also in their biot/QD ratio. Both QDs are Biot-TPQD605 but conjugated with different initial amounts of biotin. That shows nicely the possibility to distinguish different ratios and allows an estimation of the biotin number. Due to the large surface of QDs it is expected that more than one biotin is bound on the surface, which results in an intercept smaller than 1 sAv per QD (sAv/QD ratio is shown as top x-axis in Figure 4.36). That is the case for Biot-TPQD605 A resulting a biotin number of 3 to 4 per QD. The decrease of the PL intensity ratios after the saturation is mainly caused by coaggregation of multivalent sAv and Biot-QDs. In contrast, for Biot-TPQD605 B the intercept is at sAv/QD ratio smaller than 1. In this case it has to be assumed that only 1 biotin is bound on the surface of the QD. However, the sAv/QD axis is not linear and a precise determination of the biotin number becomes complicated. The approximate error is in the range of 30 % and thus in an acceptable range compared to other measurement methods.

Similar to the dose-response curves measured for the FRET immunoassays, the time-gated PL intensity ratios in Figure 4.36 can be used as calibration curves to calculate the LOD of the systems after the analytical sensitivity approach using equation 4.1. As comparison system a lanthanide europium complex conjugated to sAv as FRET donor for the organic dye APC conjugated with biotin (as acceptor) was chosen. This FRET pair is also used in the commercial homogeneous FRET immunoassays in the diagnostic kits of the BRAHMS-KRYPTOR immunoassays. The LOD for that system is (24 ± 12) pM. [7] The calculated LODs for the different used QD batches are shown in Table 4.25.

The LOD inside this system is mainly depending on the number of biotins on the surface, QY of the QD and the FRET efficiency. For all of them counts that with an increase in that values the LOD decreases. The first three QD batches have the similar biotin number on their surface, which is 3 to 4. But as it could be seen in the FRET acceptor characterization the QY of the commercial QDs is with 0.73 (Biot-iQD605) and 0.65 (Biot-eQD605) by far higher than the QY of 0.07 for the self-synthesized Biot-TPQD605. The influence of the biot/QD ratio on the LOD can be seen in the internal comparison

Table 4.25: Calculated limit of detection (LOD) for the combination of Tb-sAv with Biot-iQD605, Biot-eQD605, Biot-TPQD605 A and Biot-TPQD605 B based on the analytical sensitivity approach. All values have an error of approximately 20 %.

	LOD [pM]
Biot-iQD605	0.063
Biot-eQD605	0.094
Biot-TPQD605 A	0.73
Biot-TPQD605 B	2.0

of Biot-TPQD605 A and B. The much smaller number of only 1 in comparison to 3 to 4 biotin per QD for Biot-TPQD605 A results in an increase of the LOD from 0.73 pM to 2.0 pM. However, in comparison to the LODs of the commercial systems the use of Biot-TPQD605 B as FRET acceptor in combination with Tb-sAv as FRET donor leads to 12 fold lower LOD and in the case of Biot-iQD605 even to a 384-fold decrease.
Time-gated PL intensities and time-gated PL intensity ratios for the systems not shown in this chapter and can be found in the Appendix 6.4.1.

Size and shape analysis

One could expect for the different QD batches a similarity in size and shape due to the shared emission maximum at around 605 nm, but TEM images show different shapes for each batch (see Figure 4.37).

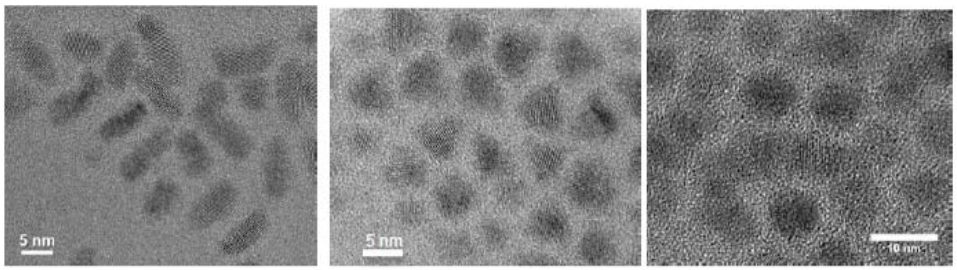

Figure 4.37: High resolution TEM images for Biot-iQD605, Biot-eQD605, and Biot-TPQD605.

From the images in Figure 4.37 it can be seen that Biot-iQD605 has a very elongated shape, which is different to Biot-eQD605 and Biot-TPQD605. These QDs are more spherical, but also elongated, tetrahedral, and star-shaped QDs are visible. Although in TEM mainly the dense inorganic core/shell structure can be imaged, it is assumed that the polymer coating follows more or less the given shape of the core. Consequently, the donor-acceptor distance distribution caused by the different shapes should be measurable using LTC-to-QD FRET and decay time analysis.
For each Tb-sAv / Biot-QD combination the PL decay curves in the QD detection channel and LTC detection channel for selected QD concentration were measured.

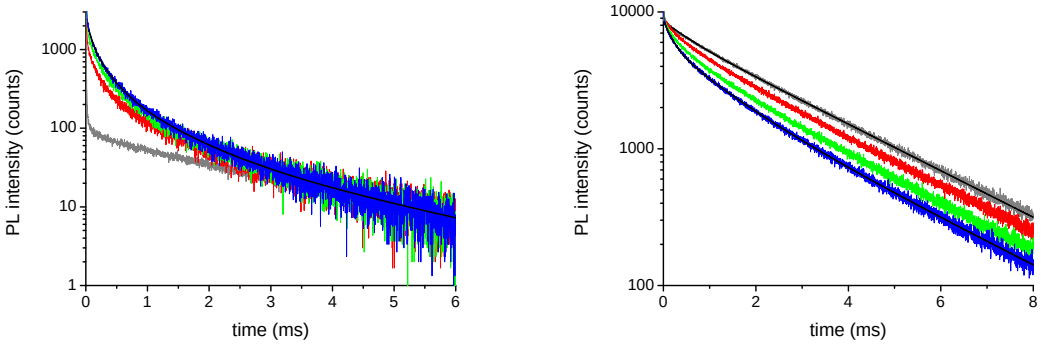

Figure 4.38: PL decay curves of Tb-sAv with increasing concentrations of Biot-TPQD605 B measured in the QD detection channel (left) and in the LTC detection channel (right). Gray pure Tb-sAv, red, 0.06 nM QD; green, 0.1 nM QD; blue, 0.15 nM QD.

Figure 4.38 shows the typical obtained PL decay curves of Tb-sAv in the presence of increasing concentrations of Biot-QD. In this example Biot-TPQD605 B was added. The PL decay curves show a strong quenching measured in the LTC detection channel and a strong FRET sensitization of Biot-TPQD605 B in the QD detection channel with increasing QD concentration. This behavior is expected as the Förster distances of the used Tb-sAv / Biot-QD systems range from 9.1 nm to 7.4 nm and the maximum donor-acceptor distance introduced by the biotin-streptavidin recognition is 5 nm, which corresponds to the size of the streptavidin.
A first hint for structural difference can be seen in a comparison of the PL decay curves measured in the LTC detection channel. Figure 4.39 show the decay curves measured in both channels using different concentrations of Biot-iQD605.

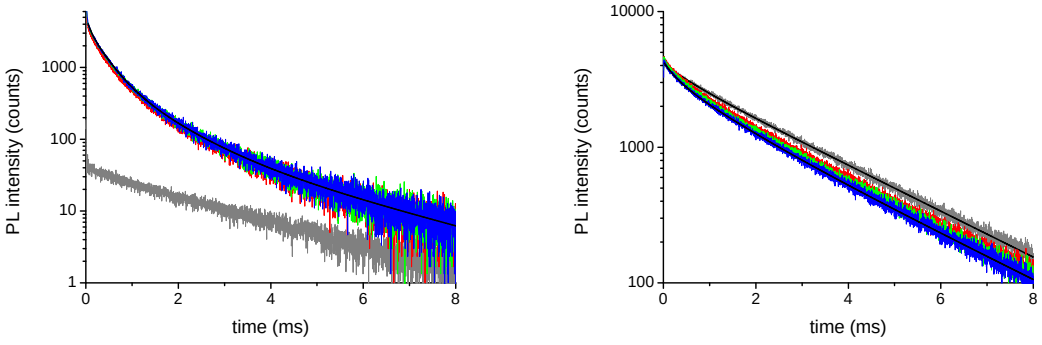

Figure 4.39: PL decay curves of Tb-sAv with increasing concentrations of Biot-iQD605 measured in the QD detection channel (left) and in the LTC detection channel (right). Gray pure Tb-sAv, red, 0.06 nM QD; green, 0.1 nM QD; blue, 0.15 nM QD.

The donor quenching is less pronounced using Biot-iQD605, see Figure 4.39 (right). The difference in donor quenching is mainly attributed to the difference in the thickness of the coating. Both commercial QDs, Biot-iQD605 and Biot-eQD605 (curves shown in the Appendix 6.4.1), show a strong colloidal stability on the cost of a thicker coating. In contrast to that the FRET sensitization is stronger for commercial QDs, if the decay curves are compared in Figure 4.38 (left) and Figure 4.39 (left). The FRET efficiency

might be more efficient for the Biot-TPQD605 resulting to a stronger donor quenching, but the low QY of only 7 % lead to a smaller sensitization output.
For more quantitative discussion about the differences in size and shape of the used QD batches a detailed decay time analysis was performed using the measured PL decay curves. Thereby the donor and acceptor decay curves were fitted under the consideration of the influence of unquenched Tb-sAv inside the sample using the crosstalk approach presented in chapter 4.2.2. In order to calculate the required FRET efficiency for the donor-acceptor distance calculation the average amplitude-weighted decay time of the donor in absence of the acceptor was calculated and is presented in Table 4.26 together with Förster distances for each Tb-sAv / Biot-QD system.

Table 4.26: Average amplitude-weighted decay time of Tb-sAv in absence of the acceptor and Förster distances for each each Tb-sAv / Biot-QD system.

	Biot-iQD605	**Biot-eQD605**	**Biot-TPQD605 B**
R_0 (nm)	9.1 ± 0.4	7.8 ± 0.3	7.4 ± 0.3
$\langle \tau_D \rangle$ (µs)	2310 ± 120	2280 ± 120	2270 ± 120

The multi-exponential PL decay curves measured in the QD detection channel and in the LTC detection channel were fitted according to the procedure describes in chapter 4.2.2 and the obtained decay times were used to calculate the FRET efficiencies. Table 4.27 summarizes the obtained results. Using the Förster distances of Table 4.26 and the calculated FRET efficiencies enabled the calculation of the donor-acceptor distances according to a equation 2.5 in chapter 2.1.2. The resultant donor-acceptor distances with the corresponding fraction of the decay time are summarized in Table 4.28.
Comparing the average as well as the single decay times in Table 4.27 reveal a strong similarity of those values independent of the used detection channel. This is an evidence for the efficient energy transfer based on FRET from the LTC-donor to the QD-acceptor. Only in the PL decay curves measured in the QD detection channel (acceptor channel) a third decay component was found. The decay time of only 30 µs to 60 µs is very short compared to the next larger decay time of around 200 µs and cannot be resolved in the LTC detection channel (donor channel). The large background caused by unquenched Tb-sAv covers the short component in the evaluation of the decay times in the donor channel. A direct comparison of the decay time values obtained from the acceptor channel and donor channel reveals slightly larger values for the latter one. This overestimation is also caused by the strong fraction of long-lived LTC-emission in the donor channel. Due to the significant influence of the long-lived decay components in the donor channel, the estimated decay times from the acceptor channel have liability as they are less disturbed by unquenched long-lived Tb-sAv components.
The average decay time can be used for the estimation of the average donor-acceptor distance, which describes the overall size of the QD. In contrast to TEM where only the inorganic core can be measured, these distance values count for the core plus the

Table 4.27: Decay times and calculated FRET efficiencies for the different QD batches. All values have an error of approximately 10 %.

		Biot-iQD605	**Biot-eQD605**	**Biot-TPQD605 B**
			average	
D	$\langle\tau_{DA}\rangle$ (µs)	790	890	610
	$\langle\eta_{FRET-DA}\rangle$	0.66	0.61	0.73
A	$\langle\tau_{AD}\rangle$ (µs)	630	840	540
	$\langle\eta_{FRET-AD}\rangle$	0.73	0.63	0.76
			first	
D	τ_{DA1} (µs)	270	240	200
	$\eta_{FRET-DA1}$	0.88	0.89	0.91
A	τ_{AD1} (µs)	320	300	230
	$\eta_{FRET-AD1}$	0.86	0.87	0.90
			second	
D	τ_{DA2} (µs)	1110	1110	1030
	$\eta_{FRET-DA2}$	0.52	0.51	0.54
A	τ_{AD2} (µs)	870	1010	740
	$\eta_{FRET-AD2}$	0.63	0.56	0.67
			third	
A	τ_{AD0} (µs)	60	60	30
	$\eta_{FRET-AD0}$	0.97	0.97	0.97

Table 4.28: Calculated donor-acceptor distances and the fraction of the corresponding decay time. All values have an error of approximately 15 %.

		Biot-iQD605	**Biot-eQD605**	**Biot-TPQD605 B**
			average	
D	r_{DA} (nm)	8.1	7.2	6.3
A	r_{AD} (nm)	7.7	7.1	6.1
			first	
D	α_{DA1}	0.40	0.29	0.52
	r_{DA1} (nm)	6.5	5.5	5.0
A	α_{AD1}	0.40	0.20	0.32
	r_{AD1} (nm)	6.7	5.7	5.1
			second	
D	α_{DA2}	0.60	0.71	0.48
	r_{DA2} (nm)	9.0	7.7	7.2
A	α_{AD2}	0.58	0.77	0.62
	r_{AD2} (nm)	8.4	7.5	6.6
			third	
A	α_{AD0}	0.02	0.03	0.05
	r_{AD0} (nm)	5.0	4.3	4.1

organic coating without the drawback of the inclusion of hydration shell like for DLS measurements. The average distance decreases from Biot-iQD605 to Biot-TPQD605 B from ca. 8 nm to ca. 6 nm, see Table 4.28. As could be already qualitatively obtained by the comparison of the donor quenching, the decrease in size is mainly attributed to the thinner coating to render the QD biocompatible. Assuming a spherical shape of the QD batches the diameter obtained from the FRET measurements are 16 ± 3 nm for Biot-iQD605, 14 ± 2 nm for Biot-eQD605, and 12 ± 2 nm for Biot-TPQD605 B.
However, the difference in shape, shown in the TEM images (Figure 4.37), should be visible in the obtained single decay time components and the contribution to the overall shape quantified by their pre-exponential factor (fraction). It is expected that spherical QDs show a single FRET decay time component with a high fraction, whereas elongated QDs exhibit two major FRET decay times with almost equal fraction caused by donor-acceptor distances for the minimum and maximum of the ellipsoid axes. The resultant average donor-acceptor distances with the corresponding fraction within the PL decay curve and thus contribution to the overall size are presented in Table 4.28. The investigated QD batches show two major donor-acceptor distances and a minor short distance. This is in agreement with results from the TEM images as they are rather elongated and not spherical in shape. The amount of the third fraction is in comparison to the first and second with only maximal 6 % on the whole decay curve quite negligible, but important for a better evaluation of the PL decay curves. In the prior study of Morgner *et al.* it was shown that in case of an elongation of the QD the ratio of short to long distance decay time fraction increases. [6] This is due to the higher amount of FRET pairs on the short axis in comparison to the long axis of the ellipsoid shaped QD. As shown in the TEM image the Biot-eQD605 is a mixture of quasispherical and tetrahedral QDs, which is in agreement with the FRET results. The fraction of the donor-acceptor distance with 20 % at 5.7 nm is small compared to the long donor-acceptor distance of 7.5 nm with a fraction of 77 %, which represent the rather uniform shape of this QD. In comparison the short distance for Biot-TPQD605 B present a higher fraction of 32 % at 5.1 nm, which is caused by the more elongated shape of this QD. As already be seen in the TEM image the Biot-iQD605 show a pronounced elongation, which results in the highest fraction of 40 % for the short distance at 6.7 nm.
The obtained results show the feasibility to use LTC-to-QD FRET for the structural analysis of size and shape of QDs. A combination with common structural analysis methods like TEM, HPLC, or DLS would allow a detailed picture of the used QD material and can help to complete and/or verify the information of the measurement methods. This investigation was published in *ACS Applied Materials and Interfaces*, **2013**, 5, 2881-2892 and is attached in the full lengths in the Appendix 6.4.1.

4.2.5 QD - hexahistidine self-assembly

The limitation of the before presented study using LTC-to-QD FRET for the structural analysis of QD materials was the dependency on the establishment of a biotin-streptavidin recognition to enable efficient FRET. This system requires the conjugation of biotin molecules on the QD surface and the investigation has shown that the FRET efficiency is closely related to the biotin number bound on the surface. Furthermore, the used streptavidin was labeled with up to four LTC-complexes, which result in different donor-acceptor distances even if only one Tb-sAv was bound to the Biot-QD. Consequently, the estimated distances are thus an average value and would not allow a precise shape determination.
To increase the flexibility of LTC-to-QD FRET as a tool for the analysis of the size and shape of different QDs, the binding of the LTC-donor should not involve further alteration of the biocompatible QD. Due to this reason an alternative binding approach was investigated based on the polyhistidine mediated self-assembly to divalent cations. Several studies have shown the successful hexahistidine binding to the Zn-rich surface of QDs. In this investigation both, a peptide and a protein, were conjugated with the Lumi4-Tb complex and the binding to the QD was provided by the included hexahistidine (His_6) tag. The self-assembly of His_6 can be disturbed by a high density of very long molecules on the surface, which prevent the attachment on the Zn-surface. The influence of the surface coating was also considered during the investigation by the use of two batches of QDs with different surface coatings. One batch of QDs exhibit short DHLA surface ligands (DHLA-QDs), whereas the other batch posses long carboxylated polymers on the surface (ITK-QDs). The schematic drawing in Figure 4.40 shows the polyhistidine-carboxyl interactions to the polymers of the investigated ITK-QDs and *via* polyhistidine-Zn coordination to the Zn-rich QD surface of the DHLA-QDs together with the resulting different Tb to QD distances.

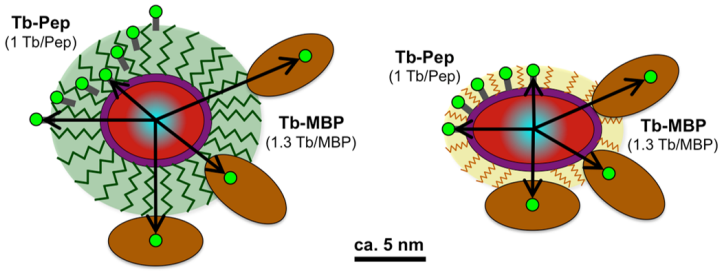

Figure 4.40: Bioconjugation of Tb conjugated to peptides (Tb-PEP) and maltose binding proteins (Tb-MBP) *via* hexahistidine self-assembly to the organic coating (green) of ITK-QD (left) and to the Zn-rich surface of DHLA-QDs (right) enabled by the short surface ligands (yellow/orange).

In total 11 QDs with different sizes, shapes and surface coatings in combination with two different types of LTC-donor molecules (peptide and protein) were investigated using time-resolved LTC-to-QD FRET. The structural analysis was completed by the comparison to the results obtained from TEM, DLS, and HPLC measurements. FRET assay measurements of all combinations, TEM, HPLC, and DLS measurements were performed by the collaboration partner and the data kindly provided for further treatment.[4]

ITK-QDs

The first investigated batch of QDs were commercial ITK-QDs from Invitrogen with a carboxyl functionalized polymer coating. Due to the dense and long surface molecules the His_6 tag is most probably not able to coordinate on the QD surface. But the carboxyl groups can mimic nitrilotriacetic acid (NTA). NTA is known to bind divalent cations like Ni^{2+} or Zn^{2+}, which enables the binding of His_6 modified molecules. [118] In this study the successful binding of the His_6 modified LTC-donor was obtained without the addition of divalent cations. The utilized LTC-donors have a strong difference in their size and dimension. Tb-PEP has a length of 1.2 nm and a linear shape, which result in a defined donor-acceptor distance independent of the binding position. In contrast, Tb-MBP has a dimension of 3.0 x 4.0 x 6.5 nm with different possible binding positions for LTC. This results in donor-acceptor distance distributions depending on the His_6 coordination to the QD and the position of the LTC itself, with a proximal largest distance of 6.5 nm. The binding can also be influenced by the negatively charged carboxyl groups on the QD surface due to electrostatic interaction with the protein.

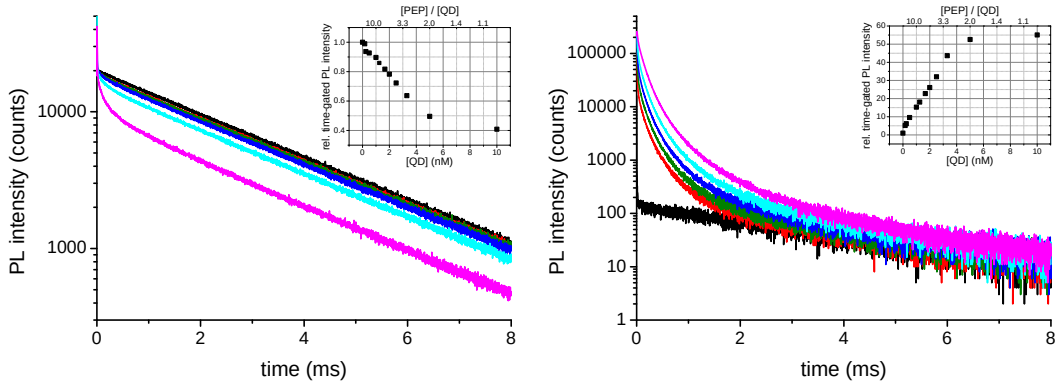

Figure 4.41: Representative PL decay curves measured in the donor channel (left) and in the acceptor channel (right) for a constant Tb-PEP concentration and increasing concentrations of ITK-QD705 (black, 0 nM; red, 0.25 nM; green, 0.5 nM; blue, 1.0 nM; cyan, 2.0 nM; and magenta, 5.0 nM). The insets show the corresponding time-gated intensities of the PL decay curves using an integration window of 0.2 ms to 2 ms.

Time-resolved PL decay curves were measured with varied ITK-QD concentrations ranging from 0.2 nM to 10 nM in the presence of a constant concentration of Tb-PEP (ca. 10 nM)

[4]Work was published in: *Chemistry of Materials*, **2014**, 26, 4299-4312

or Tb-MBP (ca. 5.5 nM). The measurement of different LTC / ITK-QD ratios allows to obtain more statistical data and improves the precision, which is not possible with the measurement of a single concentration. Representative PL decay curves measured in the donor channel and acceptor channel for Tb-PEP / ITK-QD705 and Tb-MBP / ITK-QD705 are shown in Figure 4.41 and 4.42, respectively.

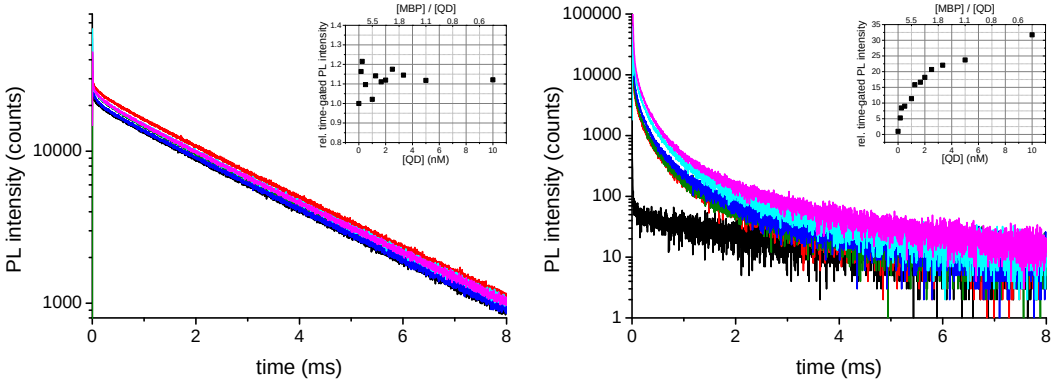

Figure 4.42: Representative PL decay curves measured in the donor channel (left) and in the acceptor channel (right) for a constant Tb-MBP concentration and increasing concentrations of ITK-QD705 (black, 0 nM; red, 0.25 nM; green, 0.5 nM; blue, 1.0 nM; cyan, 2.0 nM; and magenta, 5.0 nM). The insets show the corresponding time-gated intensities of the PL decay curves using an integration window of 0.2 ms to 2 ms.

The comparison of the PL decay curves with increasing ITK-QD concentration measured in the donor channel using Tb-PEP (Figure 4.41 (left)) or Tb-MBP (Figure 4.42 (left)) as donor reveal a stronger quenching for the Tb-PEP / ITK-QD705 system, which becomes more obvious in the time-gated donor intensities shown as insets in the Figures. Due to a large contribution of LTC, which is not taking part in FRET, the time-gated donor intensities reveal a fluctuation of around 10 % rather than a significant quenching for the measurement using Tb-MBP as donor. However, a strong QD sensitization for the utilization of both donors is observed and shown in Figure 4.41 (right) and Figure 4.42 (right) for Tb-PEP and Tb-MBP, respectively. Once again the covered FRET quenching due to the high background of unquenched Tb-MBP in the donor channel is clearly visible in the acceptor channel as FRET sensitization of the QD. The comparison of the time-gated intensities obtained for the donor channel and acceptor channel show in case of Tb-PEP a 2.5 fold quenching and 50 fold sensitization and for Tb-MBP only a 30 fold sensitization as no quenching effect can be observed. Due to the lower background, the acceptor channel is more sensitive to small intensity changes resulting in the measurement of strong sensitization. The measured time-resolved PL decay curves for all ITK-QDs using either Tb-PEP or Tb-MBP as donor posses the same behavior and are shown in the Supporting Information of the attached publication in the Appendix 6.4.2.
These multi-exponential decay curves measured in the donor and acceptor channel were treated after the procedure described in chapter 4.2.2 in order to obtain the single decay times and thus the single donor-acceptor distances together with their corresponding

corrected fractions. The obtained results for all ITK-QDs are graphically summarized in the Figure 4.43.

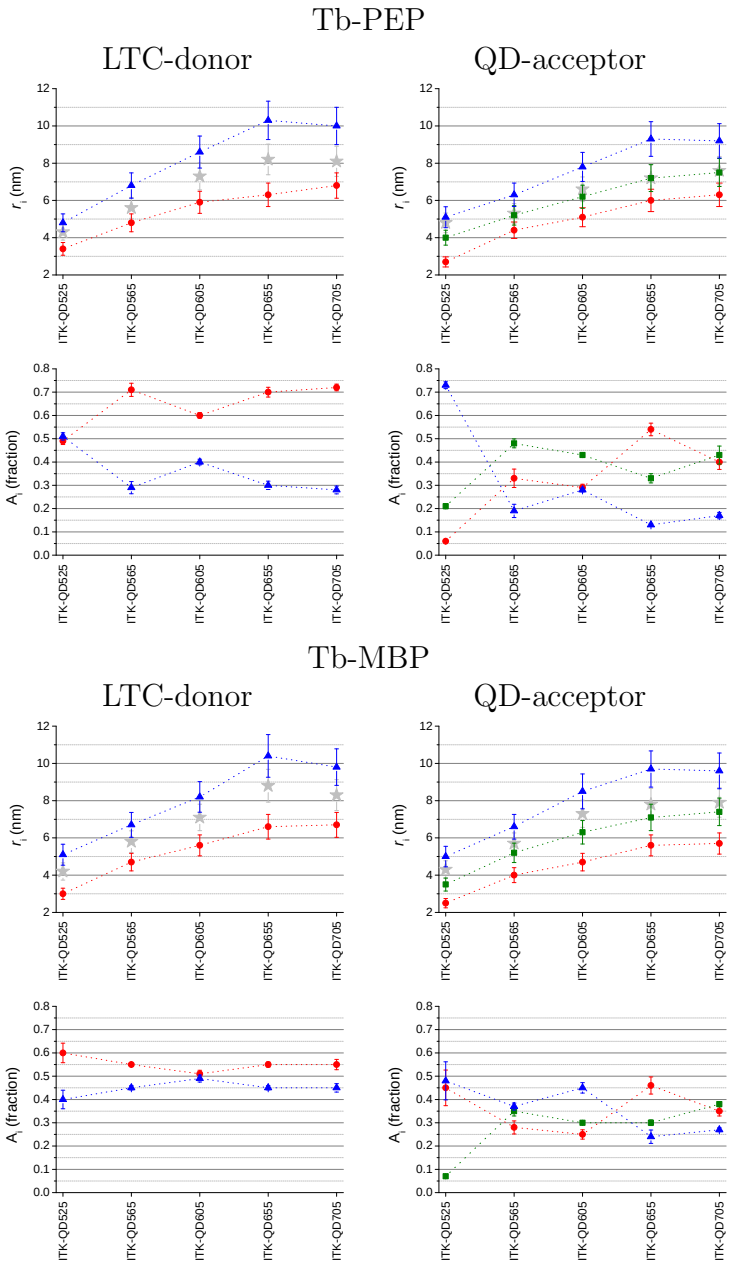

Figure 4.43: Overview of the donor-acceptor distances (top) and their corresponding fractions (bottom) for the five different ITK-QDs using Tb-PEP or Tb-MBP as FRET donor.. Average distance $\langle r \rangle$ in gray and single distances / fractions in red (r_1, A_1), green (r_2, A_2), and blue (r_3, A_3).

Decay times are concentration independent and thus all PL decay curves measured with different LTC / ITK-QD ratios were used to obtain statistically reliable donor-acceptor distances. As seen by the small error bars in Figure 4.43 the deviations of the single fits result in only small deviations from the average values. The averaged distances calculated from the averaged amplitude-weighted decay times of the Tb-PEP / ITK-QD and Tb-MBP / ITK-QD systems are shown in Table 4.29 together with provided sizes based on TEM and HPLC data from the supplier and measured sizes using TEM and DLS from our collaboration partner.

Table 4.29: Overview of the sizes (in nm) of ITK-QDs determined using TEM, HPLC, DLS, and the averaged distances obtained from the donor channel $\langle r_D \rangle$ and acceptor channel $\langle r_A \rangle$ using the two FRET based approaches with Tb-PEP or Tb-MBP as donor. [a] data provided by Invitrogen. [b] error ±15 %

					Tb-PEP[b]		Tb-MBP[b]	
	TEM	**TEM**[a]	**HPLC**[a]	**DLS**	$\langle r_D \rangle$	$\langle r_A \rangle$	$\langle r_D \rangle$	$\langle r_A \rangle$
ITK-QD525	2.0 ± 0.2	1.5 to 2.0	6.0	9.4 ± 1.7	4.3	4.8	4.2	4.3
ITK-QD565	2.6 ± 0.3	2.3	7.0	10.3 ± 0.5	5.6	5.3	5.8	5.7
ITK-QD605	5.0 ± 0.7 2.2 ± 0.3	4.7 2.0	8.0	13.3 ± 0.6	7.3	6.6	7.1	7.3
ITK-QD655	6.4 ± 0.7 2.9 ± 0.3	6.0 3.0	9.0	14.8 ± 0.6	8.2	7.2	8.8	7.8
ITK-QD705	5.5 ± 0.8 3.2 ± 0.4	6.0 3.0	9.3	13.5 ± 0.6	8.1	7.6	8.3	7.9

The average distance in Figure 4.43 (top) indicate a significant increase of the overall size from ITK-QD525 to ITK-QD705 independent of the used FRET donor. Furthermore, the sizes of ITK-QD655 and ITK-QD705 are similar, which can be also seen in the size determination using TEM, HPLC and DLS shown in Table 4.29. The direct comparison of the donor-acceptor distances estimated from the FRET quenched decay times (donor channel) and from FRET sensitized decay times (acceptor channel) reveal slightly larger distances using the first one. A reason for the larger distance is the high background of long-lived LTC in the donor channel. Although a correction of unquenched LTC contribution was performed the influence inside the donor channel cannot be fully suppressed, which results in higher reliability of the values obtained in the acceptor channel. As shown in Table 4.29 the calculated average sizes using the FRET spectroscopic ruler approach are smaller than the sizes obtained with HPLC and DLS, due to the omitting of weight standard and the exclusion of the hydration shell. But the distances are larger then the size obtained by TEM measurements, which is attributed to the consideration of the organic coating in the FRET approach. This shows the higher precision of size estimation for a biocompatible QD using LTC-to-QD FRET as measurement tool.

Next to the size estimation using the averaged decay times, the single decay times and their corresponding fraction can be used to gain information of the shape of the QD. Thereby

the single decay times represent a single donor-acceptor distance of the investigated QD and the fraction shows the relative amount of FRET pairs in this specific distance. In case of only a single distance a spherical shape is expected, whereas for two shorter distances with a large fraction compared to an included long distance with smaller fraction an ellipsoidal shape is assumed. In order to verify the shape estimated by the single distances of the LTC-to-QD FRET systems the TEM images of the used ITK-QDs are shown in Figure 4.44

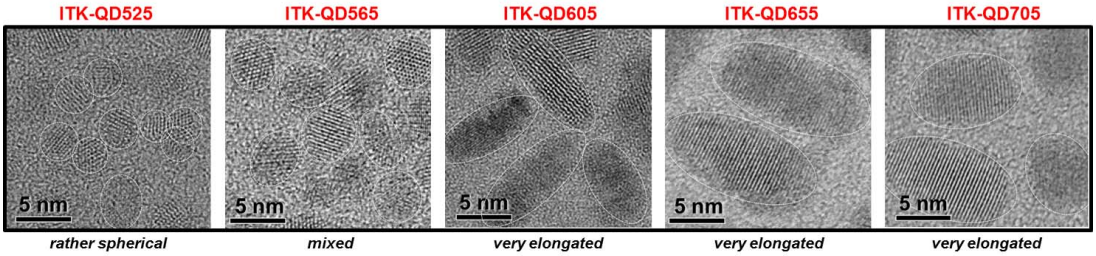

Figure 4.44: Transmission electron microscopy (TEM) images of the different ITK-QDs with highlighted shapes by a gray line.

The direct comparison of the single distances obtained for the Tb-PEP / ITK-QD and Tb-MBP / ITK-QD system show the same trend for both systems with slightly larger values for the latter one. But a large difference can be seen in the corrected fractions of those distances (see Figure 4.43). The fractions for the Tb-PEP / ITK-QD system show more variation depending on the used ITK-QD, whereas the fractions of the Tb-MBP / ITK-QD system are more or less similar independent of the investigated ITK-QD. This effect is mainly based on the narrower distance distribution of the Tb-PEP donor as it has a defined length and only a single labeling position for LTC. In contrast to Tb-MBP where the several labeling positions for LTC within the MBP protein are available, which lead to a much larger donor-acceptor distance distribution. This advantage of the Tb-PEP system will be used for the further discussion of the different ITK-QD shapes.
The TEM images in Figure 4.44 reveal an increased elongation with increased size of the ITK-QDs. The PL decay curves measured in the donor channel can be evaluated using a two exponential fit function, which results in two distinguishable single donor-acceptor distances (see Figure 4.43 “LTC-donor”). Despite of ITK-QD525, the distribution of the fractions with nearly ca. 70 % for the short distance (red) and only ca. 30 % for the long distance (blue) points to an elongated shape of the ITK-QDs and is in agreement with the shape seen in the TEM images. The obtained fractions of the fitted decay times in the acceptor channel further show an increasing of the elongation with an increasing size of the QD, because of the increasing fraction for the short distance and decreasing fraction of the long distance. Additionally the low background in the acceptor channel allows to resolve another component (green) enabling a more three-dimensional view on the QDs (see Figure 4.43 “QD-acceptor”).
A different behavior is observed for ITK-QD525 in terms of fraction distribution and thus distribution of donor-acceptor pairs on this QD. The similar fractions of ca. 50 %

in the donor channel and the very pronounced fraction of 75 % for the long distance in the acceptor channel speaking for rather spherical shape, which is confirmed by the TEM image. This first study shows not only the differentiation of spherical and elongated shape of QDs using FRET for structural analysis but also the possibility to estimate the degree of elongation.

DHLA-QDs

The six different self synthesized DHLA-QDs exhibit emission bands that are not distributed over the whole LTC emission spectrum as shown for the five ITK-QDs (see chapter 4.2.3 Figure 4.32). This indicates smaller differences in their sizes based on the quantum-confinement effect and leads to a challenging size and shape estimation using LTC-to-QD FRET. Apart from their similar sizes they also differ in the used coating material. ITK-QDs were coated with a long polymer where instead the DHLA coating of the DHLA-QDs is quite short. For a relative quantification of the length of the coating material the distance of the QD measured with TEM can be subtracted from distance measured by DLS. The result is in good approximation with thickness of the coating, although for the DLS measurement the hydration shell will be included in the calculation leading to an overestimation of the values. However, the estimated length for DHLA is 3.3 ± 0.8 nm and for the polymer of ITK-QDs roughly 7.0 ± 1.1 nm. These short DHLA ligands allow a direct coordination of the His_6 tag of the Tb-PEP and Tb-MBP on the Zn-rich QD surface. Next to the stronger binding of the LTC-donors the binding to the direct QD surface instead of the binding to the ligands (for the ITK-QDs) should allow a much more precise size and shape evaluation, which is necessary due to the expected small differences for this batch of QDs.

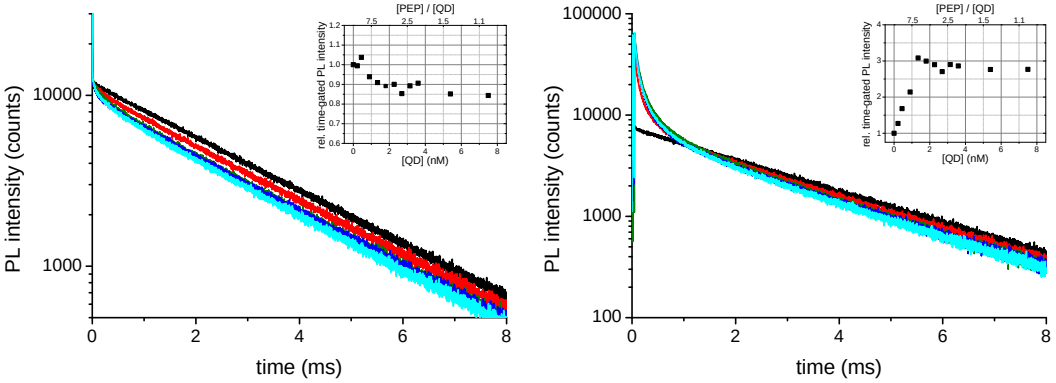

Figure 4.45: Representative PL decay curves measured in the donor channel (left) and in the acceptor channel (right) for a constant Tb-PEP concentration and increasing concentrations of DHLA-QD578 (black, 0 nM; red, 0.9 nM; green, 1.8 nM; blue, 2.7 nM; and cyan, 5.4 nM). The insets show the corresponding time-gated intensities of the PL decay curves using an integration window of 0.05 ms to 0.5 ms.

The FRET assay measurements using the different DHLA-QDs and either Tb-PEP or Tb-MBP as donor were performed similarly to the experiments using ITK-QDs. Time-

resolved PL decay curves were measured with varied DHLA-QD concentrations ranging from 0.3 nM to 11 nM in the presence of a constant concentration of Tb-PEP (ca. 7.5 nM) or Tb-MBP (ca. 11 nM). Representative PL decay curves measured in the donor channel and acceptor channel for Tb-PEP / DHLA-QD578 and Tb-MBP / DHLA-QD578 are shown in Figure 4.45 and 4.46, respectively.

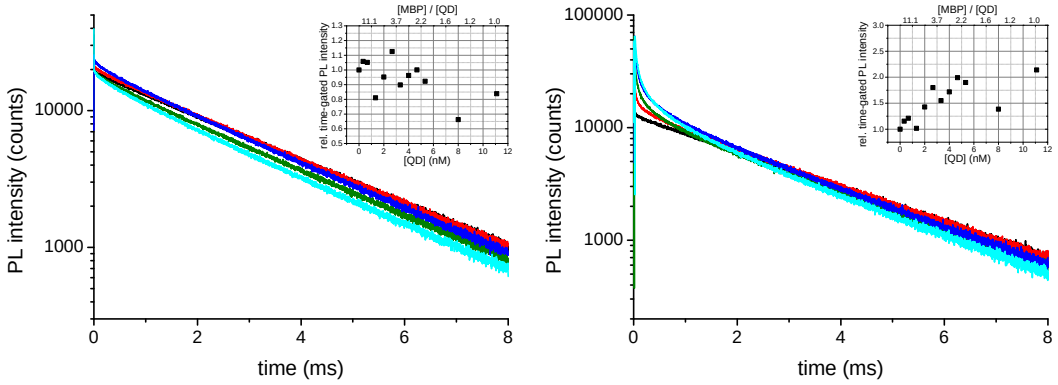

Figure 4.46: Representative PL decay curves measured in the donor channel (left) and in the acceptor channel (right) for a constant Tb-MBP concentration and increasing concentrations of DHLA-QD578 (black, 0 nM; red, 0.9 nM; green, 1.8 nM; blue, 2.7 nM; and cyan, 5.4 nM). The insets show the corresponding time-gated intensities of the PL decay curves using an integration window of 0.05 ms to 0.5 ms.

The measured PL decay curves show a similar behavior to those measured using ITK-QDs. With increasing QD concentration the Tb-PEP / DHLA-QD system shows a pronounced quen-ching of the LTC-donor (left) and a strong sensitization of the QD (right) presented in Figure 4.45. The strong UV excitation of the sample with a wavelength of 337 nm and high molar absorptivity of QDs at this wavelength lead to a strong direct excitation of QDs and thus very high PL intensities. This results in a saturation of the used detection PMTs visible mainly in the acceptor channel (Figure 4.45 and 4.46 right). However, the FRET sensitized PL curves are much more intense and show a significant longer decay. Using an appropriate delay for the fit procedure allows to suppress this saturation effect. For a better comparison of quenching and sensitization effects measured in the donor and acceptor channel in the presence of increasing concentrations of DHLA-QD578, the time-gated intensities were calculated from 0.05 ms to 0.5 ms of each PL decay curve. The shorter integration window compared to ITK-QDs is attributed to the shorter FRET sensitized PL decay curve. The insets in the Figure 4.45 and 4.46 show that the quenching effect for Tb-PEP is smaller than for the ITK-QDs but still significant compared the Tb-MBP / DHLA-QD system where only a fluctuation of the donor signals can be obtained. Due to the lower background in the acceptor channels a significant increase with increasing QD concentration of the time-gated intensities can be observed, with a maximum of 3 fold using the Tb-PEP donor. However, the significantly shorter FRET sensitized PL decay curves compared to those measured using ITK-QDs with the same LTC-donors indicate shorter donor-acceptor distances attributed to the thinner DHLA coating.

The multi-exponential decay curves measured in the donor and acceptor channel for all DHLA-QDs using either Tb-PEP or Tb-MBP as FRET donor were treated after the procedure described in chapter 4.2.2. The obtained single decay times with the corresponding corrected fractions were used to calculate the amplitude-averaged decay time for FRET quenching (donor channel) and FRET sensitization (acceptor channel) using Tb-PEP or Tb-MBP as donor and thus enable the calculation of the average donor-acceptor distances for the different DHLA-QDs. The resultant average distances are summarized in Table 4.30 together with sizes calculated from TEM or DLS measurements.

Table 4.30: Overview of the sizes (in nm) of DHLA-QDs determined using TEM, DLS, and averaged distances obtained from the donor channel $\langle r_D \rangle$ and acceptor channel $\langle r_A \rangle$ using the two FRET based approaches with Tb-PEP or Tb-MBP as donor. [a] error ±15 %

			Tb-PEP[a]		Tb-MBP[a]	
	TEM	**DLS**	$\langle r_D \rangle$	$\langle r_A \rangle$	$\langle r_D \rangle$	$\langle r_A \rangle$
DHLA-QD530	2.4 ± 0.4 1.2 ± 0.2	5.9 ± 1.0	3.7	4.1	4.9	5.0
DHLA-QD537	2.4 ± 0.3	5.6 ± 1.0	4.3	4.2	5.2	5.3
DHLA-QD573	2.7 ± 0.3	5.4 ± 1.0	6.1	5.0	6.8	6.6
DHLA-QD578	2.4 ± 0.3	5.9 ± 1.0	6.1	5.4	7.1	6.7
DHLA-QD590	4.0 ± 0.3 2.1 ± 0.3	6.3 ± 1.0	5.0	4.7	6.4	6.4
DHLA-QD615	4.0 ± 0.4	6.3 ± 1.0	6.1	5.2	7.0	6.8

Due to the larger LTC background, the average distances estimated in the donor channel are larger than compared to the values obtained from the acceptor channel as already explained for the ITK-QDs. More interesting is the comparison of the distances obtained with Tb-PEP / DHLA-QD system to Tb-MBP / DHLA-QD systems, which reveals differences of 1 nm to 1.5 nm (see Table 4.30). These LTC-donor depending differences are not so pronounced in the ITK-QD measurements as it can be seen in Table 4.29. This effect is based on two circumstances the short DHLA coating and the distribution of LTC labeled to different position within the MBP. In the case of DHLA-QDs the shorter length of the surface ligands allows efficient FRET to far distant LTC labeled to MBP, which are out of the FRET range when using the thicker coated ITK-QDs. The inclusion of larger distant donor-acceptor pairs results in a shift to longer average distances. In comparison, sizes estimated from TEM and DLS measurements show that, despite of DHLA-QD573 and DHLA-QD578, the calculated average sizes of DHLA-QDs using the FRET approach are larger than the TEM values and smaller than from DLS measurements, which is expected as explained before for the ITK-QDs.

To support and verify the conclusions of the shape analysis the TEM images of the investigated DHLA-QDs are shown in Figure 4.47.

Based on the TEM images and the position of the emission bands the DHLA-QDs can be divided into three groups, namely DHLA-QD530 and DHLA-QD537, DHLA-QD573

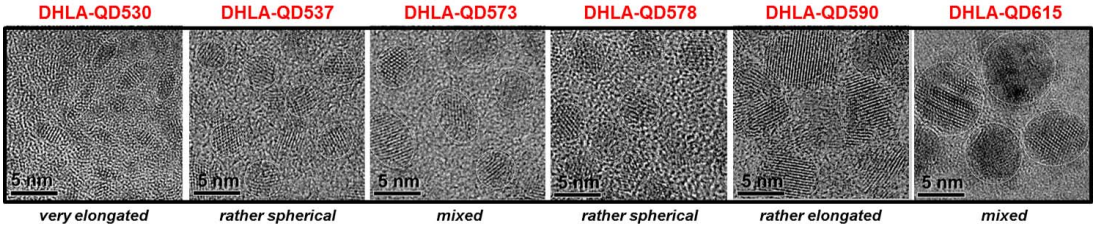

Figure 4.47: Transmission electron microscopy (TEM) images of the different DHLA-QDs.

and DHLA-QD578, and DHLA-QD590 and DHLA-QD615. Each group is similar in their average size but quite different in their shape. The fitted single decay times from the multi-exponential decay curves were used to calculate single donor-acceptor distances, which are shown with the corresponding fractions of the decay time in Figure 4.48 for each DHLA-QD evaluated from the donor and acceptor channel.

Similar to the results for the ITK-QDs the use of Tb-PEP as donor enables more precise shape information, due to the defined donor-acceptor distance. The comparison of the average distance reveals a smaller size for the first pair (DHLA-QD530 and DHLA-QD537), whereas the other QDs are relatively similar in their size and no further general trend can be observed. The utilization of Tb-MBP as donor shows the same trends in the average size but a closer look to the corresponding fractions reveals similar values for measured QDs. Due to a dominant fraction of 60 % to 70 % for the long distance, it can be assumed that most of LTCs are in large distance to the QD.

Like for the ITK-QDs further estimation of the shape will be discussed with data provided for the measurements of the Tb-PEP / DHLA-QD system. Starting with the first pair that shows an increase in the overall size from DHLA-QD530 to DHLA-QD537 but no differences in their fractions measured in the donor channel (see Figure 4.48) But the fractions obtained from the decay times observed in the acceptor channel allow a better differentiation. The smaller fraction for the long distance (blue) with ca. 30 % in comparison to the shorter distance (green) with ca. 45 % points to rather elongated shape for DHLA-QD530. In contrast the PL decay curves measured for DHLA-QD537 allow to use only a two exponential function for a good fit. This results in only two distances in the acceptor channel with a fraction for both of around 50 %, which strongly suggested a spherical shape with a mixture of sizes between 3.8 nm to 4.8 nm.

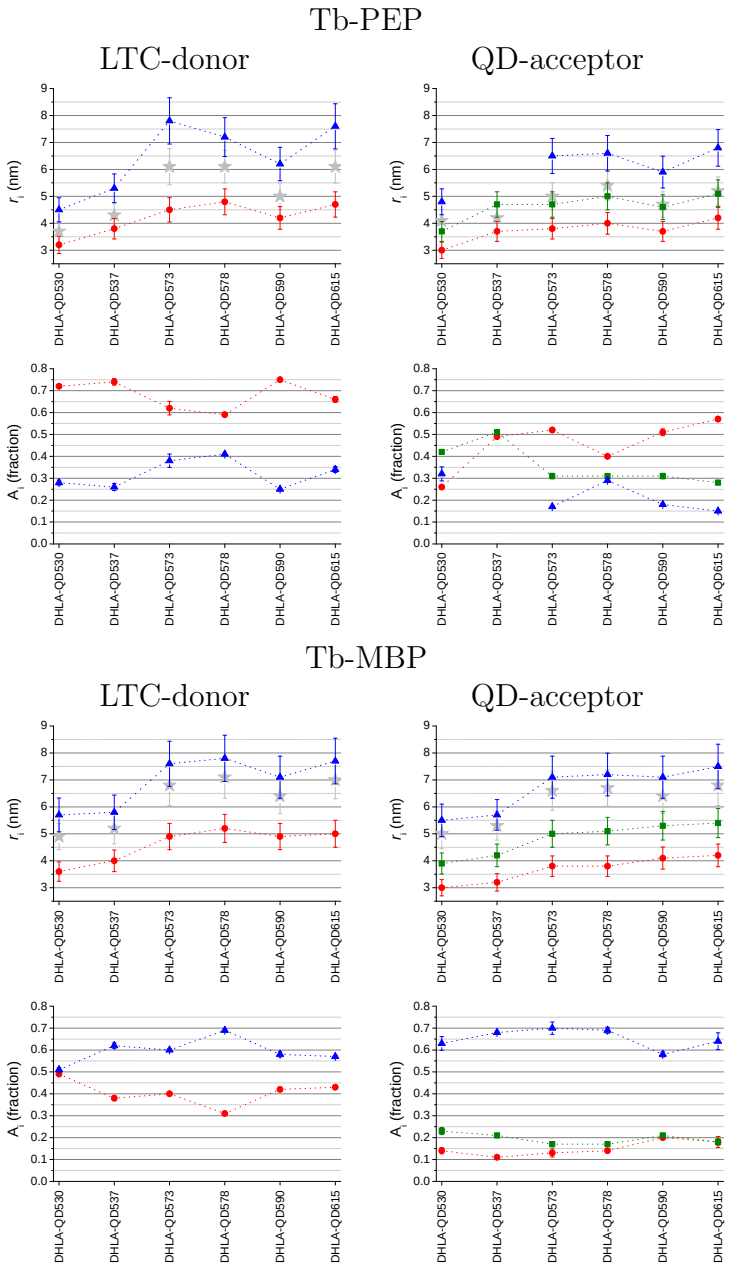

Figure 4.48: Overview of the donor-acceptor distances (top) and their corresponding fractions (bottom) for the six different DHLA-QDs using Tb-PEP or Tb-MBP as FRET donor. Average distance $\langle r \rangle$ in gray and single distances / fractions in red (r_1, A_1), green (r_2, A_2), and blue (r_3, A_3).

Also for the second pair, DHLA-QD573 and DHLA-QD578, the donor fits show similar fractions and a similar average donor-acceptor distance. Once again the lower background in the acceptor channel is advantageous as clear difference in distribution of the fractions can be seen. The DHLA-QD573 shows a pronounced short distance with a fraction of 50% and minor fraction of 20% leading to the conclusion of an elongated shape. In contrast to DHLA-QD578 where the fractions are quite similar but still the longest distance has the smallest fraction. This could be interpreted as less elongated but rather a mixed spherical shape for DHLA-QD578, which could also be seen in the TEM images.

The last pair DHLA-QD590 and DHLA-QD615 is hard to distinguish either using the results obtained in the donor channel or in the acceptor channel. They are very similar

in size and shape with a slightly larger size of DHLA-QD615. The distribution of the fractions points towards elongated shape for both QDs.
The investigated DHLA-QDs are challenging in terms of the structural analysis due to the similar shape and size. Additionally, the low QY result in less QD sensitization measured in the acceptor channel, which makes decay time fitting more sophisticated than for the ITK-QDs. Nevertheless, the LTC-to-QD FRET spectroscopic ruler approach could show a nice differentiation of the QDs of the first and second pair and enabled to obtain precise size and shape information of this QD batch.
This investigation was published in *Chemistry of Materials*, **2014**, 26, 4299-4312 and is attached in the full lengths in the Appendix 6.4.2.

5 | Summary and Outlook

5.1 Summary

This work presents the application of lanthanide terbium complexes (LTCs) and quantum dots (QDs) as donor-acceptor pair for Förster resonance energy transfer (FRET) in two distinct research fields. The long PL decay times of LTCs together with their well-structured PL emission bands in combination with the broad absorbance bands and size-tunable, narrow emission bands of QDs offer exceptional advantages compared to other FRET pairs, like an increased signal-to-noise ratio and a strong multiplexing capability. These advantages were exploited for the application in homogeneous immunometric assays for the detection of several biomarkers and as molecular ruler for the structural analysis of biocompatible QDs. Important theoretical background for FRET, LTCs, and QDs were also described in this work, including a brief overview about their advantages in different biological applications.

In the first experimental part of this work the strong distance dependency of FRET was exploited for the optimization of the performance of homogeneous immunoassays to detect the biomarkers total prostate specific antigen (TPSA), neuron-specific enolase (NSE), carcinoembryonic antigen (CEA), and epidermal growth factor receptor (EGFR). Therefore differently sized antibodies were prepared using a commercial fragmentation kit for the production of the fragments F(ab')$_2$ and F(ab) from an IgG antibody. The prepared antibodies differ largely in their size as the IgG antibody has a molecular weight of 150 kDa, F(ab')$_2$ a molecular weight of 100 kDa, and F(ab) a molecular weight of 50 kDa, and all of them were able to bind to the biomarker. After the successful preparation of the differently sized antibodies they were conjugated with LTCs or to different QDs and carefully characterized using stationary absorption spectroscopy and stationary as well as time-resolved luminescence spectroscopy. The characterization was used to verify any alteration caused by the conjugation of the luminophore with the antibody and to estimate the conjugation ratio.

The conjugation of LTCs to the differently sized antibodies resulted in no alteration of the absorbance spectra, as the main absorbance peak at 340 nm stayed unchanged for all conjugates. Due to an increased absorption at 280 nm, the successful conjugation was verified as it is the typical absorbance wavelength of proteins. Using a linear combination approach allowed to calculate the labeling ratio of LTCs to antibodies from the absorbance measurement. Thereby the labeling ratio decreased from the IgG antibody to

the F(ab) fragment, which was attributed to the smaller size of the antibody fragment. The measured PL spectrum of LTC-conjugates showed the typical four intense emission bands at 495 nm, 545 nm, 585 nm, and 625 nm, and only minor differences in the fine splitting of the individual bands after antibody conjugation. Depending on the presence of serum in the buffer solution the bi-exponential fit of the PL decay curves enabled the calculation of amplitude averaged decay times between 2.2 ms and 2.8 ms. The quantum yields calculated from the averaged decay times ranging between 64 % and 81 % and are used for the calculation of the Förster distance. Similar to the LTC-antibody conjugates, the QD-antibody conjugates showed also no alteration in their absorbance spectra due to the conjugation. The typical broad band absorbance spectra with high extinction coefficients were observed and a linear combination approach was used to calculate the labeling ratios. Due to the high background of QD absorption at 280 nm the estimation of the antibody concentration was afflicted with larger uncertainties than for the LTC-antibody conjugates. However, some general trends were observed. First of all with decreasing antibody size the antibody per QD ratio was increased, which is attributed to the smaller size of the fragments compared to the large IgG antibody. An intercomparison of the $F(ab')_2$ fragment on three different QDs revealed an increase of the labeling ratio from eQD605 to iQD705 caused by the larger size and thus larger surface of the latter QD. The measured PL emission spectra of the three QDs used within the immunoassay measurements (eQD605, eQD650, and iQD705) showed the typical size-dependent behavior and narrow Gaussian shape emission covering the range from 605 nm to 705 nm. All QDs showed a multi-exponential PL decay curve with decay times between 10 ns to 100 ns and only minor changes depending on the conjugated antibody. In general, the conjugation of the differently sized antibodies had less influence on the important parameters necessary for the calculation of the Förster distance, namely the donor emission spectrum, donor luminescence quantum yield, and acceptor absorbance spectra. The used FRET pairs with LTC as donor and eQD605, eQD650, and iQD705 as acceptors result in calculated Förster distances of 7.6 nm, 10.8 nm, and 10.9 nm, respectively.

In general LTC-to-QD FRET enabled the measurement of all biomarkers with subnanomolar detection limits in 50 µL serum samples inside homogeneous immunometric assays measured on two different fluorescence plate readers. Using differently sized antibodies conjugated with LTCs or to QDs revealed that the decrease of the acceptor antibody size is beneficial for the sensitivity of the immunoassay. The limit of detection (LOD), which was used to compare the performance of the different combinations, was decreased by nearly the half comparing full size antibodies to fragmented antibodies conjugated to the QD surface. However, the difference in sensitivity between $F(ab')_2$ and F(ab) antibodies was negligible for all investigated biomarkers. In contrast, the decrease of the donor antibody size did not result in a further increased sensitivity. These results were transferable as shown by the use of two differently emitting QDs as FRET acceptors. The first assumption that a decreased size of the antibodies due to the fragmentation results

in a shorter donor-acceptor distance and thus an higher FRET sensitization could not be approved. Calculated average donor-acceptor distances from PL decay curves revealed a similar distance for the use of IgG, F(ab')$_2$ or F(ab) antibodies conjugated on the QD surface in combination with a full size antibody labeled with LTCs. A clear difference in donor-acceptor distance was observed when the same antibody was conjugated to either eQD605 or eQD650, which was attributed to the larger size of the eQD650 itself. Interesting was also the comparison of the average donor-acceptor distance for the different biomarkers. Although they are very different in size (TPSA with a molecular weight of 32 kDa to CEA with a molecular weight of 180 kDa) there was no distance difference observed in the average donor-acceptor distance. This can be explained by the origin of the antibodies used. They are from commercial diagnostics kits and optimized for FRET measurements. During this optimization antibodies were chosen, which bind to different epitopes on the biomarker with similar distances to each other to enable efficient FRET independent of the actual size of the biomarker. One crucial point for the use of antibody conjugates in commercial applications is their long-term stability. In common diagnostic kits the warrant long-term stability is around 4 weeks, depending on the used biomarker and their corresponding antibodies. To prove the long-term stability of the QD-antibody conjugates the LOD measurement was repeated after a few month up to one year after preparation. It could be shown that the performance of the probes were similar to the day when they were conjugated and thus revealed an exceptional long-term stability in solution storing at 4 °C. To prove the developed LTC-QD FRET system for the application in clinical measurements of biomarker concentrations, the TPSA concentrations in human serum samples were investigated. The results gave a good agreement with the reference values as they were within an error range of ±20 %. However, in comparison to already commercial diagnostic kits for the measurement of the same biomarkers based on a europium complex as donor and different organic dyes as acceptor, the used LTC-to-QD FRET system showed lower sensitivity. A further optimization of the used antibody concentrations, incubation time, and instrument settings could result in at least as good as, if not better LODs than those of the commercial kits. Nevertheless, the sensitivity for all biomarkers was below the cutoff level and in a clinical relevant concentration range. Although the sensitivity of the commercial system was higher, it has the drawback that the system cannot be used in multiplexed applications. The successful application of the simultaneous detection of NSE and CEA was shown for the use of LTC as FRET donor and eQD605 and eQD650 as FRET acceptors. The major problem of multiplexed measurements is the spectral crosstalk caused by broad acceptor emission bands, which result in the need of a post treatment to correct those values. Due to the narrow Gaussian shaped emission spectra of the QDs no crosstalk correction was necessary and the obtained data were directly usable to calculate the calibration curves. The comparison between the detection of the biomarker in a single format and in the duplexed format revealed only a minor increase of the LOD and showed also clinically relevant subnanomolar

detection limits.
An exceptional LTC-to-QD FRET immunoassay was the detection of EGFR using nanobodies. The very small size of the nanobodies resulted in high labeling ratios on QDs and only a small ratio for the LTC labeling. Although the presence of proteins resulted in a FRET signal in the absence of the antigen, the increase of the FRET signal in presence of EGFR was more pronounced and could be used for the measurement of a calibration curve and thus for an estimation of the LOD. The system showed further a sensitivity to the presence of serum, which increased the LOD in comparison to a serum free diluent. However, the estimated LODs where below the clinical cutoff level for both diluents and presents the first application of nanobodies for the detection of an antigen using LTC-to-QD FRET.
In conclusion the presented study examined the utilization of LTC-to-QD FRET in time-gated homogeneous immunoassays using differently sized antibodies for the detection of several biomarkers. All biomarkers were measured at clinically relevant concentrations in small volume serum samples. The decreasing antibody size showed to be beneficial for the performance of the immunoassay and sample preparation. Highlights of the study were the measurement of real patient samples and the first duplexed application of LTC-to-QD FRET for the simultaneous detection of two biomarkers in one sample.

The second experimental part investigated the application of LTC-to-QD FRET for the structural analysis of biocompatible QDs. As size and shape have a great influence on the behavior of QDs in biological applications, it is important to investigate those parameters. The investigated FRET pair offers several advantages over classical characterization methods like TEM, DLS, or HPLC measurements and especially as it enables a detailed shape analysis. Due to the large size difference between small LTCs and large QDs, several LTCs were arranged around one QD, which resulted in a donor-acceptor distance distribution with different FRET efficiencies. A detailed decay time analysis of the multi-exponentional PL decay curves of LTC and QDs allowed to retrieve single decay times. Thereby the long decay times of LTCs are several magnitudes longer than the intrinsic decay time of QDs, which allows to obtain the FRET decay time, necessary for distance estimation, from the PL decay curves of either FRET donor or the FRET acceptor. The corresponding FRET efficiencies were calculated using those FRET decay times and enabled the estimation of the donor-acceptor distances according to the Förster formalism. The similarity of the FRET decay times was the proof for successful FRET between the LTC and QD. Prior to the use of the retrieved decay times for distance calculation, the data was corrected for unquenched LTC signals in both channels. To establish the LTCs in close proximity to the QD two different strategies were used, namely biotin-streptavidin recognition and polyhistidine mediated self-assembly. Each probe was carefully characterized using stationary absorption spectroscopy and stationary as well as time-resolved luminescence spectroscopy.
As donor in the two binding systems the LTC Lumi4-Tb complex was used and conju-

gated to streptavidin (Tb-sAv), a peptide (Tb-PEP), and to the maltose binding protein (Tb-MBP). The two latter donor complexes exhibited a hexahistidine (His_6) tag for the chelation to divalent cations like Zn. Similar to the LTC-antibody conjugates the absorbance and emission spectra as well as the PL decay curves were hardly affected by the binding to the different biomolecules. The appearance of an absorbance band at 280 nm proved the successful binding to the biomolecules. The typical characteristics of LTCs with an absorbance band at 340 nm together with narrow and well separated emission bands between 490 nm to 650 nm could be observed for all donor complexes. Thereby the average amplitude decay times are between 2.3 ms and 2.75 ms with quantum yields ranging from 65 % to 80 %. In total, three different batches of QDs were used during the investigations. The first batch were biotinylated QDs to enable the biotin-streptavidin recognition. For the polyhistidine mediated self-assembly two different batches of QDs were used, which differ mainly in their surface coating. One batch exhibits dihydrolipoic acid as surface ligands, whereas the second batch possessed long carboxylated polymers on the surface. All QDs showed the characteristical broad absorbance band with high extinction coefficients, narrow Gaussian shape PL emission bands with quantum yields ranging from 7 % to 75 %, and multi-exponential PL decay curves with decay times between 10 ns to 100 ns. The calculated Förster distances range from 5.4 nm to 11.1 nm, depending on the spectral overlap between LTC and QD.

In the first application of LTC-to-QD FRET the biotin-streptavidin recognition was applied using Tb-sAv and three different biotinylated QDs (Biot-QDs), which all exhibit a similar emission maximum but different surface coatings. Two of them were from commercial sources with an amphiphilic polymer/lipid coating (Biot-iQD605 and Biot-eQD605), whereas the third one was self-synthesized and rendered water-soluble *via* ligand exchange reaction (Biot-TPQD605). The FRET assays were executed using a constant concentration of Tb-sAv and increasing concentrations of the individual Biot-QD. The resulting PL decay curves of LTC and Biot-QD were measured in the so called donor (LTC) and acceptor (Biot-QD) channel on a fluorescence plate reader. The PL decay curves measured in the donor channel showed strong quenching of the LTC decay curve intensities and concomitant the measured PL decay curve intensities in the acceptor channel increased due to the strong FRET sensitization of the Biot-QD, which was observed for all measured LTC-QD FRET pairs. These decay curves were used for a detailed decay time analysis. The averaged FRET decay time was used for an estimation of the overall QD size with the assumption of a spherical shape. It was shown that the size is decreasing from Biot-iQD605 to Biot-TPQD605, which is attributed mainly to their different coatings. The ligand exchange reaction yields a QD with a thinner coating than the amphiphilic encapsulation approach of the commercial QDs. Due to the thinner coating and thus smaller donor-acceptor distance for Biot-TPQD605 the LTC quenching was more pronounced than for the other Biot-QDs. More detailed shape information were obtained from the single decay times and their fractions, which are very useful to make a state-

ment about the QD dimension. Thereby the information from the acceptor channel were more detailed as the smaller background of LTC allowed the evaluation of three distances (three-dimensions), whereas in the donor channel only two distances could be retrieved. The fraction of the single decay times are important as they contain the information about the amount of donor-acceptor pairs in this particular distance. In general, the QD batches showed two major donor-acceptor distances, which pointed towards an elongated shape. Important for the degree of elongation was the proportion of the fractions of the two major distances. An increasing amount of FRET pairs with short distance compared to the fraction with longer donor-acceptor distance indicates a more elongated shape. In case of the Biot-eQD605 there was only a small fraction for the short distance and a large fraction for the long distance, arising from a rather mixed shape. The largest fraction for the short distance was obtained for Biot-iQD605 as these are the most elongated QDs in the study, which was confirmed by TEM measurements. Next to the shape analysis the measurement of increasing Biot-QD concentrations in the presence of a constant concentration of Tb-sAv was used for the evaluation of the obtained PL decay curves using the time-gated approach. The obtained intensity ratios were plotted as a function of the QD concentration. Due to the FRET sensitization of the QDs the intensity ratios for all Biot-QDs were increasing until all biotins on the QD surface were saturated. This saturation point was used for the estimation of the number of biotin on the QD surface. During the preparation of the Biot-TPQD605 two different initial biotin concentrations were used, resulting in two batches (denoted with A and B) with an unknown biotin number. Using the LTC-to-QD FRET system the number of biotin was estimated for batch A to ca. 1 and for batch B to ca. 3 to 4 biotins on the QD surface. Similar values of 3 to 4 biotins per QD were also found for the other Biot-QDs and enabled, next to the size and shape information, insights into the bioconjugation performance.

The precision of the biotin-streptavidin system for dimensional analysis was limited by the labeling ratio of four LTCs per Tb-sAv conjugate. Consequently, the binding of one Tb-sAv to a Biot-QD already provide different donor-acceptor distances depending on the position of the LTCs within the streptavidin molecule. Additionally, the presence of biotin on the QD surface was necessary to establish the close proximity between donor and acceptor. Due to these reasons another binding strategy was investigated based on the polyhistidine mediated self-assembly of biomolecules on the QD surface, which did not involve any further alteration of the QD surface. The binding and the application for size and shape analysis was performed on two different batches of QDs, which differed mainly in their surface coating. One batch of six QDs exhibited dihydrolipoic acid as surface ligands (DHLA-QDs), which is a short ligand known to enable the binding of hexahistidine (His_6) tagged molecules. The other batch consisted of five commercial ITK-QDs with long carboxylated polymers on the surface. The donors exhibiting a His_6 tag were Tb-PEP and Tb-MBP. All QDs were measured with both donors at a constant donor concentration and increasing QD concentrations on a fluorescence plate reader. The ob-

tained multi-exponential decay curves measured in the donor and acceptor channel were used for an extensive decay time analysis to obtain the average decay times (information about the average size) and single decay times (information about the three-dimensional shape).

First of all, FRET was observed for all QDs using either Tb-MBP or Tb-PEP as donor. But in a direct comparison of the used donor revealed large differences for the applicability in the structural analysis of the investigated QDs. These differences were attributed to the dimension of the used donor. Tb-PEP had a defined length of 1.2 nm with the His_6 tag on one end and the LTC on the other. In contrast to Tb-MBP that had a dimension of 3.0 x 4.0 x 6.5 nm and offers several labeling positions for LTCs. Although the labeling ratio for both donors was around one LTC per biomolecule the different available positions in Tb-MBP resulted in larger donor-acceptor distance distributions than for Tb-PEP. Due to that reason the average distances estimated using Tb-MBP were larger compared to the utilization of Tb-PEP and furthermore in shape analysis the fractions of the different donor-acceptor pairs showed no significant differences and thus could not be used for a clear statement about the shape. Consequently, the Tb-PEP donor with well defined length and small donor-acceptor distance distribution allowed to estimate more precise information about the QD dimension.

The investigation of the five different ITK-QDs using Tb-PEP as donor revealed an increasing average size from ITK-QD525 to ITK-QD705. Thereby the estimated size is larger than from the TEM measurements (neglecting the organic coating) and smaller than estimated by DLS measurements (inclusion of the hydration shell). These results showed the higher precision of the FRET approach compared to the other methods. The analysis of the single decay times showed a pronounced elongation with increasing size as the fraction of the long distance decreases and the fraction of the short distance increases. One exception is the ITK-QD525, which only shows one dominant fraction for the long distance and minor fractions for the short distance, arising from its spherical shape. The obtained results for the different shapes were in agreement with TEM images.

As the DHLA-QDs were quite similar in size, shown by their close emission maxima in the PL emission spectra, the analysis was more complicated and the different QDs difficult to distinguish. Additionally, the low QY resulted in less QD sensitization, which made the decay time evaluation more sophisticated in comparison to the ITK-QDs. However, the increasing overall size of the different DHLA-QDs could be measured and were in agreement with the expected values compared with the TEM and DLS data. Furthermore, the differentiation of DHLA-QDs with similar emission but different shapes were also possible and in agreement with the TEM images.

The LTC-to-QD FRET approach for the structural analysis of biocompatible QDs was successfully presented using: i) different binding strategies; ii) QDs with different size, shape, and coatings; iii) LTCs conjugated to different biomolecules also with different sizes, shapes, and binding conditions. Big advantages of this approach are that it is ho-

mogeneous, fast, using very low concentrations at physiological conditions, and mostly has a subnanometer resolution. Although this method allows more precise information about the size and shape of QDs, in conditions in which they are also later applied, standard measurements such as TEM, DLS and HPLC are still important to verify the obtained results.

5.2 Outlook

The application of LTC-to-QD FRET in homogeneous immunoassays and as molecular ruler demonstrate the versatility of this FRET pair. Advantages like large Förster distances, time-gated measurements, strong multiplexing capability, and large surfaces of QDs for binding of different kinds of biomolecules in combination with the unique photophysical properties of the individual luminophores, make the application of this FRET pair interesting as probe for *in vitro* and *in vivo* measurements and thus enable to gain insights into the complex mechanism of biological systems.

Concerning the application of this FRET pair in immunoassays, the presented use of a third QD color for the detection of TPSA will give access to the simultaneous measurement of three different biomarkers using one LTC as donor and three QDs as acceptors. It is expected that the small PL emission bands of QDs strongly reduce the probability for optical crosstalk, which was the main drawback of organic dyes in LTC-based multiplex applications. The substitution of organic dyes as acceptors in the already presented multiplexed application for the simultaneous measurement of five different markers for the differentiation of non-small cell lung cancer and small cell lung cancer using five differently colored QDs without the use of a crosstalk matrix and higher sensitivity would be a big step towards a commercial application of QDs for *in vitro* diagnostics. As it was shown in this work the system is generic for different biomarkers and can be applied for the detection of all biomarkers for which two targeting antibodies exist.

The precise characterization of the size and shape of biocompatible QDs using LTC-to-QD FRET presents a valuable alternative to already established structural analysis techniques. Especially the measurement at low concentration and under physiological conditions with three dimensional shape resolution distinguish this approach from others. Thereby this method is not limited to QDs, any nanoparticle suitable acting as acceptor for the LTC-donor can be characterized and make the molecular ruler approach very versatile. Apart from the structural analysis of nanoparticles, the experience in distance distributions within the LTC-QD system can be used in future applications of the distance analysis in *in vitro* and *in vivo*. Therefore the large Förster distances will allow measurements of distances in large biological systems. Furthermore, the multiplexing opportunity of the system can be used to study complex distance changes using different acceptors, which enable the measurement of several distances from a single sample. The advancement of this structural analysis technique by the introduction of mathematical models for a more precise evaluation of the donor-acceptor distance distribution would be beneficial in order to increase the sensitivity to the different shapes of QDs.

6 | Appendix

6.1 Abbreviations

acceptor-AB - acceptor-antibody
AB - antibody
AG-domain - antigen binding domain
ALEX - alternating-laser excitation
BOI - biomolecule of interest
BRET - bioluminescence resonance energy transfer
BSA - Albumin from bovine serum
CEA - carcinoembryonic antigen
ChA - acceptor channel
ChD - donor channel
CRET - chemiluminescence resonance energy transfer
CV - coefficient of variation
DHLA - dihydrolipoic acid
DLS - dynamic light scattering
DNA - deoxyribonucleic acid
donor-AB - donor-antibody
EGFR - epidermal growth factor receptor
EMIT - enzyme-multiplied immunoassays technique
EPR - electron paramagnetic resonance
FP - fluorescent protein
FRET - Förster resonance energy transfer
FWHM - full-width-at-half-maximum
His_6 - hexahistidine
HPLC - high performance liquid chromatography
IMAC - immobilized metal ion affinity chromatography
IR - infrared region
LED - light emitting diode
LMCT - ligand to metal charge transfer
Ln - lanthanides
LOD - limit of detection
LOQ - limit of quantification
LTC - lanthanide terbium complex
MRI - magnetic resonant imaging
MWCO - molecular weight cut-off
NBCS - newborn calf serum
NIR - near infrared region
NMR - nuclear magnetic resonance
NP - nanoparticle

NSE - neuron-specific enolase
NSET - nanoparticle-based surface energy transfer
NTA - nitrilotriacetic acid
PEG - poly(ethylene glycol)
PL - photoluminescence
PMT - photomultiplier tube
QD - quantum dot
QY - quantum yield
RNA - ribonucleic acid
REE - rare earth elements
ref. - reference
sAv - streptavidin
SERS - surface enhanced Raman scattering
smFRET - single-molecule FRET
SNR - signal-to-noise ratio
TEM - transmission electron microscopy
TPSA - total prostate specific antigen
UNCP - upconversion nanoparticle
UV - ultraviolet
Vis - visible

6.2 Used bandpass filter

Table 6.1: List of the different luminophores and their corresponding bandpass filter. The abbreviation AB is used as a general term for antibody conjugate.

Luminophore	**bandpass filter**
Tb-AB	Semrock-494/20
Tb-sAV	
Tb-PEP	Semrock-497/16
Tb-MBP	
ITK-QD525	Semrock 525/15
ITK-QD565	Semrock 567/15
DHLA-QD573	
DHLA-QD578	
Biot-iQD605	Semrock 605/15
Biot-eQD605	
Biot-pQD605A	
Biot-pQD605B	
QITK-QD605	
DHLA-QD590	
DHLA-QD615	
eQD605-AB	Delta 607/8
ITK-QD655	Semrock 655/15
eQD650-AB	Semrock 660/13
ITK-QD705	Semrock 740/13
iQD705-AB	Semrock 716/40

6.3 Immunoassay

6.3.1 Characterization

FRET donor conjugates

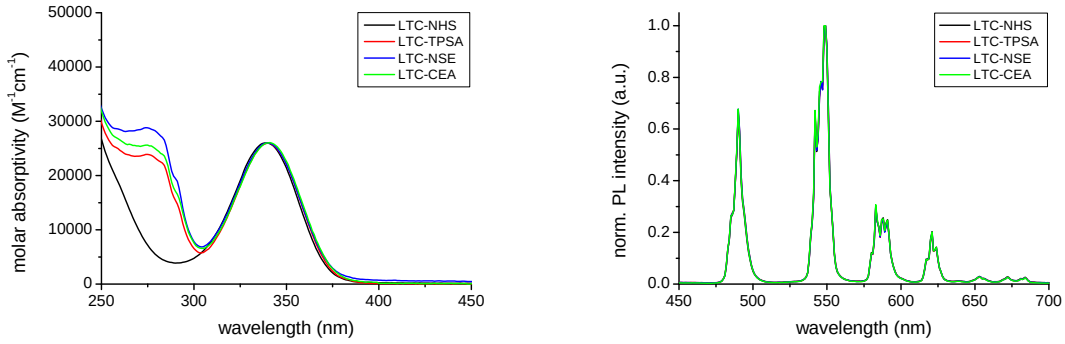

Figure 6.1: LEFT: Absorbance spectra of unmodified LTC-NHS (black curve) in comparison to IgG donor-ABs conjugated with LTC for the detection of TPSA, NSE, and CEA. RIGHT: Comparison of the PL emission spectra before conjugation (LTC-NHS) and after conjugation to IgG donor-ABs for the detection of TPSA, NSE, and CEA.

Table 6.2: Overview of the LTC and antibody concentrations of the purified LTC-antibody conjugates shown in Figure 6.1 together with their calculated labeling ratio.

LTC-antibody	antigen	LTC [µM]	AB [µM]	LTC/AB
LTC-IgG	TPSA	36.3	3.0	12
LTC-IgG	NSE	19.6	1.8	11
LTC-IgG	CEA	27.4	2.2	12

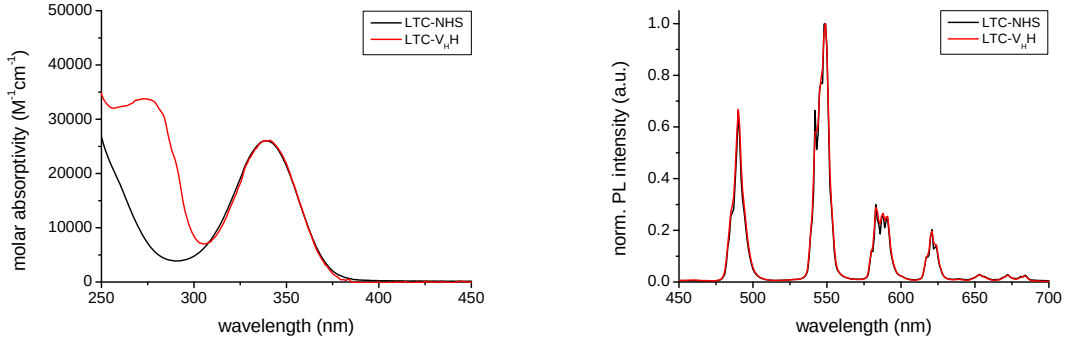

Figure 6.2: Absorbance spectra (left) and PL emission spectra (right) of unmodified LTC-NHS (black curve) in comparison to LTC-V_HH conjugate for the detection of EGFR.

Table 6.3: Concentration of the LTC and V_HH of the probe together with the calculated labeling ratio for the detection of EGFR.

LTC-antibody	**antigen**	**LTC [µM]**	**AB [µM]**	**LTC/AB**
LTC-V_HH	EGFR	3.6	2.5	1.4

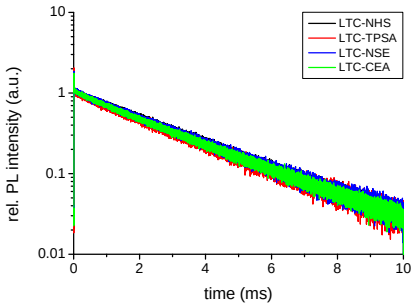

Figure 6.3: Comparison of the PL decay curves before conjugation (LTC-NHS) and after conjugation to IgG donor-ABs for the detection of TPSA, NSE, and CEA.

Table 6.4: Overview about the fitted single decay times, calculated average decay times and QYs for LTC-NHS and LTC-antibody conjugates measured in buffer 8.

LTC-antibody	**antigen**	τ_i / **ms**	A_i	$\langle\tau\rangle_{\text{Int}}$ / **ms**	$\langle\tau\rangle_{\text{Amp}}$ / ms	Φ_{LTC}
LTC-NHS		1.7	303	2.8	2.8	0.81
		2.9	2012			
LTC-IgG	TPSA	1.4	250	2.8	2.6	0.76
		3.0	733			
LTC-IgG	NSE	1.5	213	2.8	2.7	0.78
		3.0	879			
LTC-IgG	CEA	1.1	258	2.8	2.6	0.76
		2.9	1485			

Table 6.5: Overview of the fitted single decay times, the calculated average decay times and the QYs of the LTC-antibody conjugates measured in presence of 30 % newborn calf serum.

LTC-antibody	**antigen**	τ_i / **ms**	A_i	$\langle\tau\rangle_{\text{Int}}$ / **ms**	$\langle\tau\rangle_{\text{Amp}}$ / ms	Φ_{LTC}
LTC-IgG	TPSA	0.8	1318	2.3	2.2	0.65
		2.3	15838			
LTC-IgG	NSE	0.6	1095	2.2	2.1	0.60
		2.3	8828			
LTC-IgG	CEA	0.5	989	2.2	2.1	0.61
		2.3	8067			

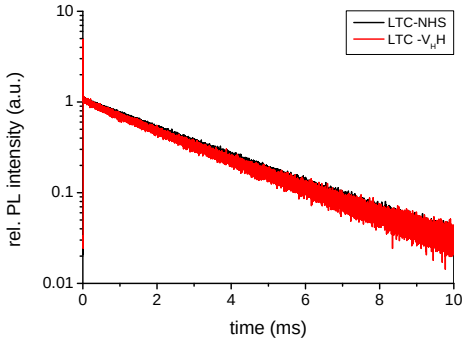

Figure 6.4: Comparison of the PL decay curves before conjugation (LTC-NHS) and after conjugation to V_HH for the detection of EGFR.

Table 6.6: Overview of the fitted single decay times, calculated average decay times and QYs for LTC-NHS and LTC-antibody conjugates measured in buffer 8 and for LTC-V_HH in presence of 30 % newborn calf serum.

LTC-antibody	**antigen**	τ_i / **ms**	A_i	$\langle\tau\rangle_{Int}$ / **ms**	$\langle\tau\rangle_{Amp}$ / ms	Φ_{LTC}
LTC-NHS		1.7	303	2.8	2.8	0.81
		2.9	2012			
LTC-V_HH	EGFR	1.7	326	2.8	2.7	0.78
		3.1	782			
LTC-V_HH	EGFR	1.4	3489	2.1	2.0	0.59
		2.2	10729			

FRET acceptor conjugates

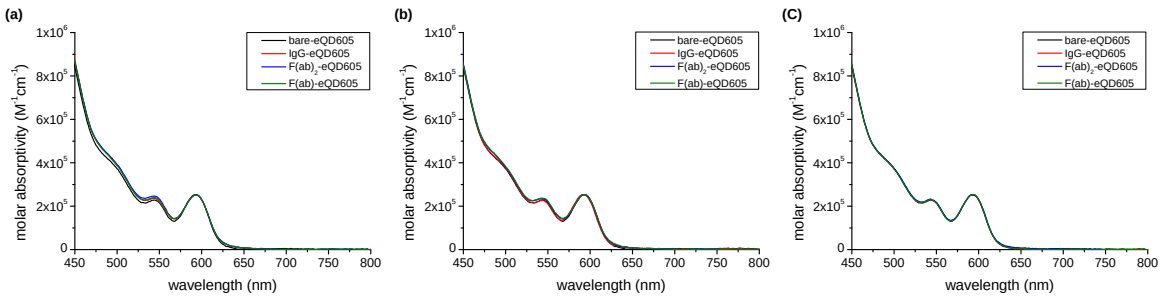

Figure 6.5: Absorbance spectra of unmodified eQD605 (bare-eQD605) in comparison to IgG-eQD605 (red), F(ab')$_2$-eQD605 (blue), F(ab)-eQD605 (green) conjugates for the detection of TPSA (a), NSE (b), and CEA (c).

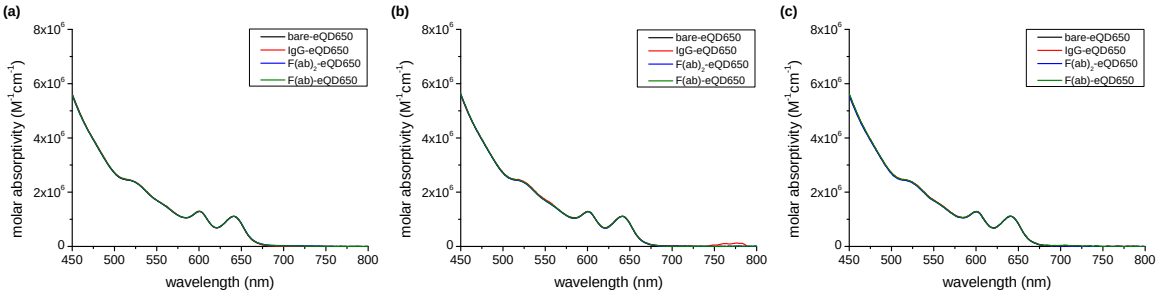

Figure 6.6: Absorbance spectra of unmodified eQD650 (bare-eQD650) in comparison to IgG-eQD650 (red), F(ab')$_2$-eQD650 (blue), F(ab)-eQD650 (green) conjugates for the detection of TPSA (a), NSE (b), and CEA (c).

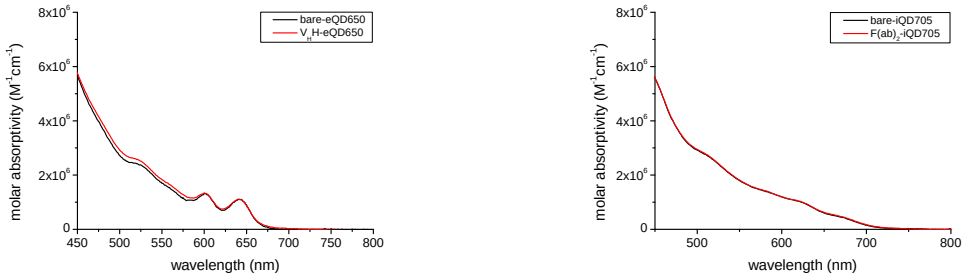

Figure 6.7: Absorbance spectra of unmodified eQD650 (bare-eQD650) and iQD705 (bare-iQD705) in comparison to V_HH-eQD650 for the detection of EGFR (left) and F(ab')$_2$-iQD705 for the detection of TPSA (right).

Table 6.7: Overview about QD and antibody concentrations and their resulting labeling ratio for the different antibody-QD conjugates for the detection of TPSA used as probes in chapter 4.1.3.

antibody	**QD**	**AB [µM]**	**QD [µM]**	**AB/QD**
IgG	eQD650	0.9	0.4	2.3
F(ab')$_2$	eQD650	1.1	0.3	3.7
F(ab)	eQD650	4.6	0.3	15.3

Table 6.8: Overview of QD and antibody concentrations and their resulting labeling ratios for the different antibody-QD conjugates for the detection of NSE used as probes in chapter 4.1.4.

antibody	QD	AB [µM]	QD [µM]	AB/QD
IgG	eQD605	1.5	0.5	3.0
$F(ab')_2$	eQD605	2.7	0.5	5.4
F(ab)	eQD605	2.1	0.3	7.0
IgG	eQD650	1.7	0.2	8.5
$F(ab')_2$	eQD650	4.0	0.3	13.3
F(ab)	eQD650	7.5	0.3	25.0

Table 6.9: Overview about QD and antibody concentrations and their resulting labeling ratios for the different antibody-QD conjugates for the detection of CEA used as probes in chapter 4.1.4.

antibody	QD	AB [µM]	QD [µM]	AB/QD
IgG	eQD605	0.8	0.3	2.7
$F(ab')_2$	eQD605	2.1	0.3	7.0
F(ab)	eQD605	2.4	0.3	8.0
IgG	eQD650	0.8	0.3	2.7
$F(ab')_2$	eQD650	2.8	0.3	9.3
F(ab)	eQD650	5.3	0.3	17.7

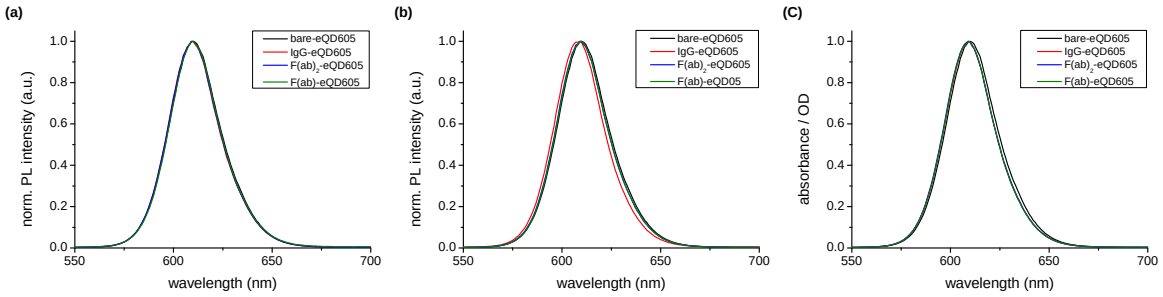

Figure 6.8: Normalized PL emission spectra of unmodified eQD605 (bare-eQD605) in comparison to IgG-eQD605 (red), $F(ab')_2$-eQD605 (blue), F(ab)-eQD605 (green) conjugates for the detection of TPSA (a), NSE (b), and CEA (c).

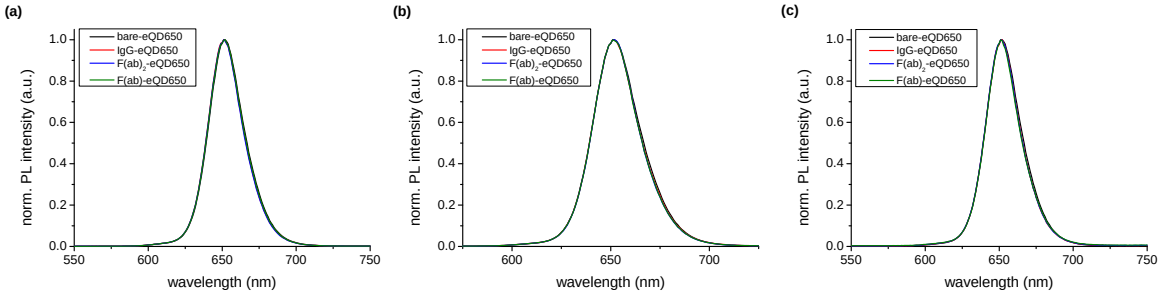

Figure 6.9: Normalized PL emission spectra of unmodified eQD650 (bare-eQD650) in comparison to IgG-eQD650 (red), F(ab')$_2$-eQD650 (blue), F(ab)-eQD650 (green) conjugates for the detection of TPSA in chapter 4.1.3 (a) and for TPSA (b) and CEA (c) detection in chapter 4.1.4.

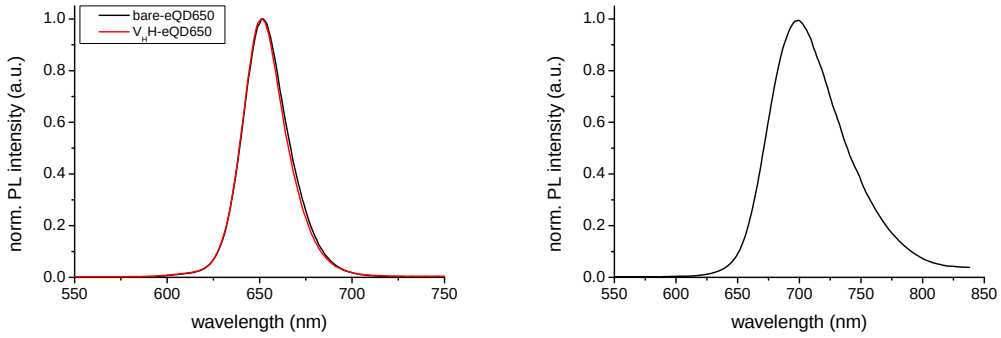

Figure 6.10: Normalized PL emission spectra of unmodified eQD650 (bare-eQD650) in comparison to V_HH-eQD650 for the detection of EGFR (left) and F(ab')$_2$-iQD705 PL emission spectrum for the detection of TPSA (right).

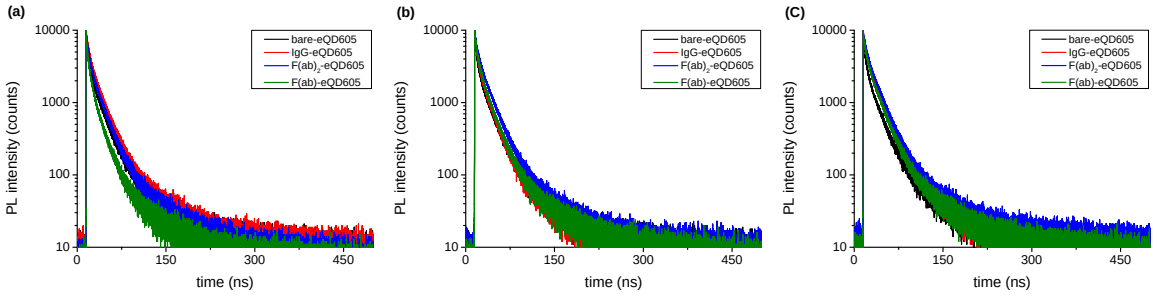

Figure 6.11: PL decay curves of unmodified eQD605 (bare-eQD605) in comparison to IgG-eQD605 (red), F(ab')$_2$-eQD605 (blue), F(ab)-eQD605 (green) conjugates for the detection of TPSA (a), NSE (b), and CEA (c).

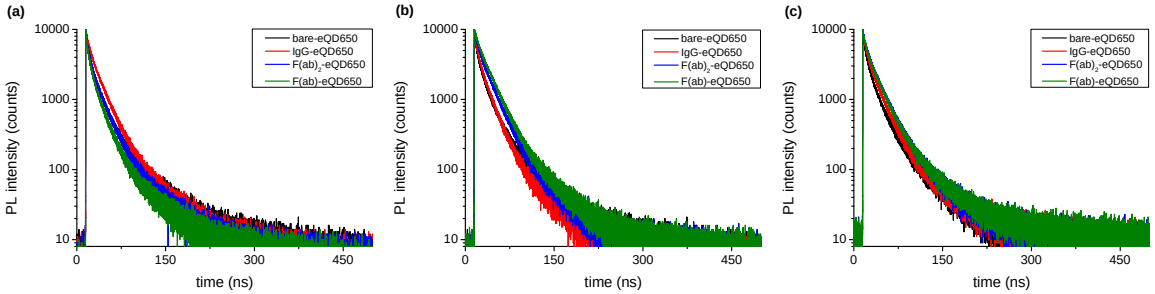

Figure 6.12: PL decay curves of unmodified eQD650 (bare-eQD650) in comparison to IgG-eQD650 (red), F(ab')$_2$-eQD650 (blue), F(ab)-eQD650 (green) conjugates for the detection of TPSA (a), NSE (b), and CEA (c).

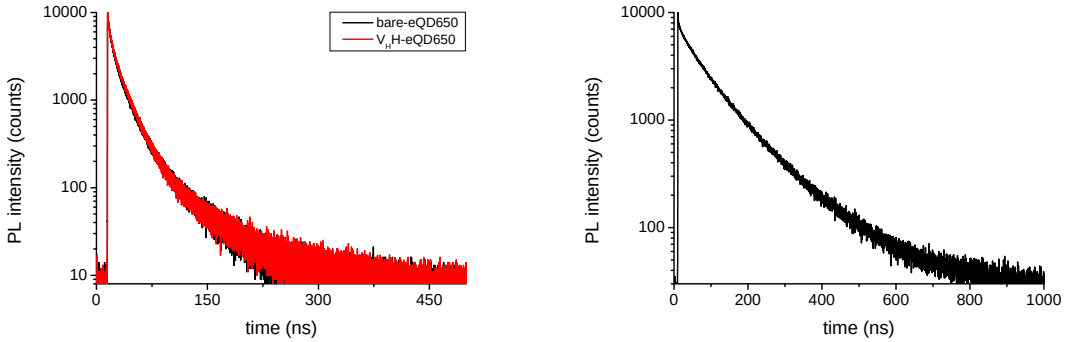

Figure 6.13: PL decay curves of unmodified eQD650 (bare-eQD650) in comparison to V_HH-eQD650 for the detection of EGFR (left) and F(ab')$_2$-iQD705 PL decay curve for the detection of TPSA (right).

Table 6.10: Summary of the calculated intensity ($\langle\tau\rangle_{\mathrm{Int}}$) and amplitude ($\langle\tau\rangle_{\mathrm{Amp}}$) weighted averaged decay times of an unmodified eQD650 and eQD650 conjugated with either IgG, F(ab')$_2$, or F(ab) acceptor-Abs for the detection of CEA.

antibody-QD	$\langle\tau\rangle_{\mathrm{Amp}}$ **/ ns**	$\langle\tau\rangle_{\mathrm{Int}}$ / ns
bare-eQD650	10.7	22.5
IgG-eQD650	12.7	23.2
F(ab')$_2$-eQD650	15.2	25.1
F(ab)-eQD650	14.9	25.0

Table 6.11: Summary of the calculated intensity ($\langle\tau\rangle_{\mathrm{Int}}$) and amplitude ($\langle\tau\rangle_{\mathrm{Amp}}$) weighted averaged decay times of an unmodified eQD605 and eQD605 conjugated with either IgG, F(ab')$_2$, or F(ab) acceptor-Abs for the detection of TPSA or NSE.

	TPSA		NSE	
antibody-QD	$\langle\tau\rangle_{\mathrm{Amp}}$ **/ ns**	$\langle\tau\rangle_{\mathrm{Int}}$ / ns	$\langle\tau\rangle_{\mathrm{Amp}}$ **/ ns**	$\langle\tau\rangle_{\mathrm{Int}}$ / ns
bare-eQD605	8.6	21.1	8.6	21.1
IgG-eQD605	11.5	21.6	9.0	20.0
F(ab')$_2$-eQD605	9.7	20.0	12.0	21.7
F(ab)-eQD605	6.5	16.4	9.8	20.0

Table 6.12: Summary of the calculated intensity ($\langle\tau\rangle_{\mathrm{Int}}$) and amplitude ($\langle\tau\rangle_{\mathrm{Amp}}$) weighted averaged decay times of an unmodified eQD605 and eQD605 conjugated with either IgG, F(ab')$_2$, or F(ab) acceptor-Abs for the detection of CEA.

antibody-QD	$\langle\tau\rangle_{\mathrm{Amp}}$ **/ ns**	$\langle\tau\rangle_{\mathrm{Int}}$ / ns
bare-eQD605	8.6	21.1
IgG-eQD605	12.3	22.3
F(ab')$_2$-eQD605	13.2	22.8
F(ab)-eQD605	11.3	21.7

Table 6.13: Summary of the calculated intensity ($\langle\tau\rangle_{\mathrm{Int}}$) and amplitude ($\langle\tau\rangle_{\mathrm{Amp}}$) weighted averaged decay times of an unmodified eQD650 and eQD650 conjugated with V_HH for the detection of EGFR.

antibody-QD	$\langle\tau\rangle_{\mathrm{Amp}}$ **/ ns**	$\langle\tau\rangle_{\mathrm{Int}}$ / ns
bare-eQD650	10.7	22.5
V_HH-eQD650	11.5	22.7

Table 6.14: Summary of the calculated intensity ($\langle\tau\rangle_{\mathrm{Int}}$) and amplitude ($\langle\tau\rangle_{\mathrm{Amp}}$) weighted averaged decay times of iQD705 conjugated with F(ab')$_2$ acceptor-Abs for the detection of TPSA.

antibody-QD	$\langle\tau\rangle_{\mathrm{Amp}}$ **/ ns**	$\langle\tau\rangle_{\mathrm{Int}}$ / ns
F(ab')$_2$-iQD705	65.5	104.1

6.3.2 Detection of TPSA / NSE / CEA using two QD colors

Calibration curves

TPSA

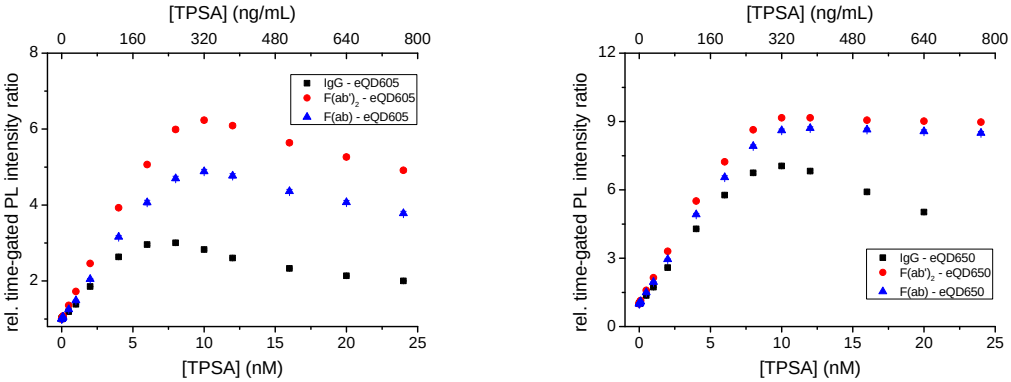

Figure 6.14: LEFT: Relative time-gated PL intensity ratios as a function of the TPSA antigen concentration for the combinations of LTC-IgG and differently sized acceptor-ABs conjugated to eQD605. RIGHT: Relative time-gated PL intensity ratios as a function of the TPSA antigen concentration for the combinations of LTC-IgG and differently sized acceptor-ABs conjugated to eQD650.

CEA

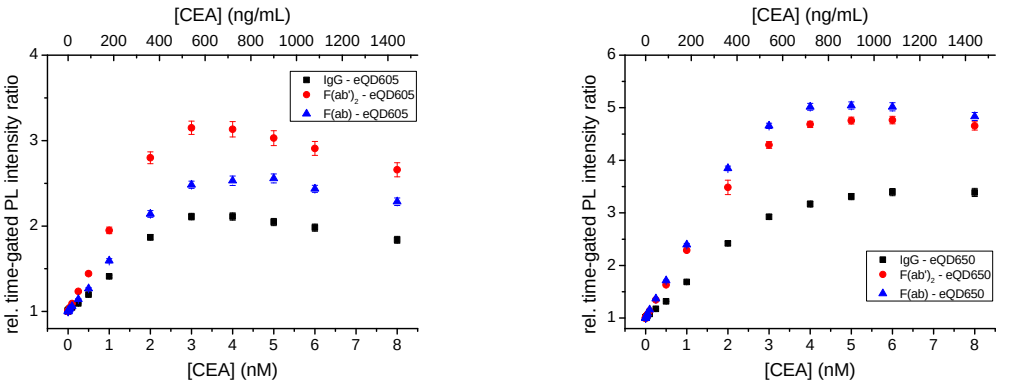

Figure 6.15: LEFT: Relative time-gated PL intensity ratios as a function of the CEA antigen concentration for the combinations of LTC-IgG and differently sized acceptor-ABs conjugated to eQD605. RIGHT: Relative time-gated PL intensity ratios as a function of the CEA antigen concentration for the combinations of LTC-IgG and differently sized acceptor-ABs conjugated to eQD650.

Long-term measurement NSE

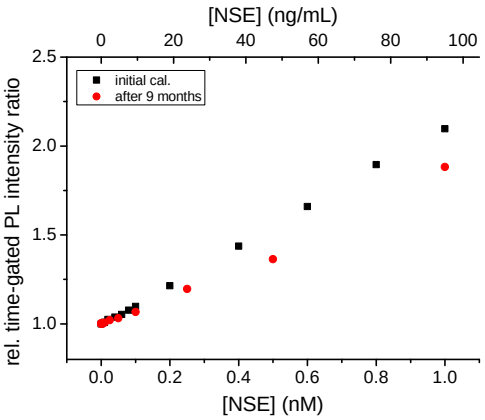

Figure 6.16: Comparison of the relative time-gated PL intensity ratios as a function of the NSE antigen concentration for the combinations of LTC-IgG and and F(ab')$_2$-eQD650 direct after conjugation and measured after 9 months.

Duplex measurement using F(ab')$_2$-eQD650 for the detection of NSE and F(ab')$_2$-eQD605 for the detection of CEA

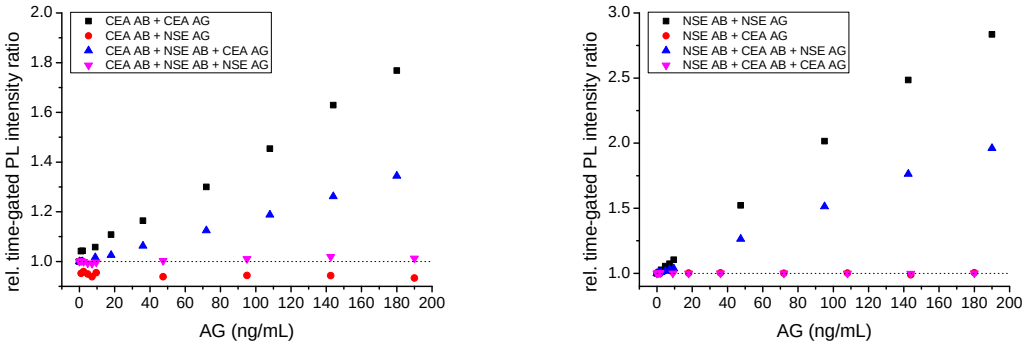

Figure 6.17: LEFT: Relative time-gated PL intensity ratios measured in the QD detection channel for eQD605 for the evaluation of the biological crosstalk of NSE detection antibodies (NSE-AB) and the NSE antigen (NSE AG) within the CEA detection using the bandpass filter (607 ± 8) nm. RIGHT: Relative time-gated PL intensity ratios measured in the QD detection channel for eQD650 for the evaluation of the biological crosstalk of CEA detection antibodies (CEA-AB) and the CEA antigen (CEA AG) within the NSE detection using the bandpass filter (660 ± 13) nm.

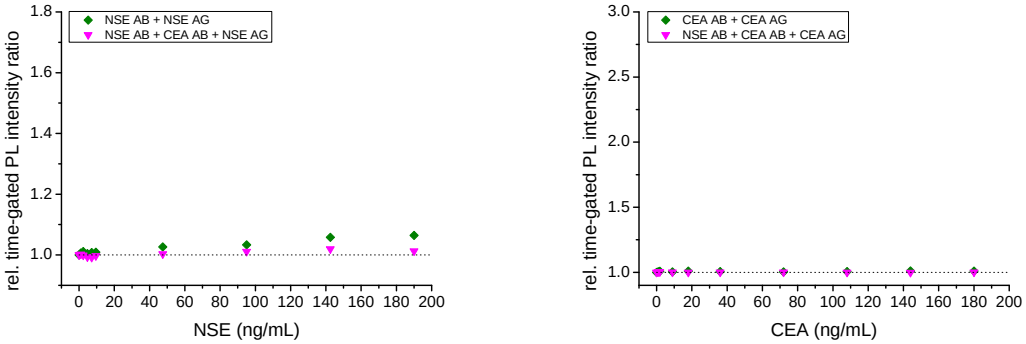

Figure 6.18: LEFT: Relative time-gated PL intensity ratios measured in the QD detection channel for eQD605 with increasing NSE antigen (NSE AG) concentration in presence of NSE detection antibodies (NSE-AB) or CEA detection antibodies (CEA-AB) + NSE-AB using the bandpass filter (607 ± 8) nm. RIGHT: Relative time-gated PL intensity ratios measured in the QD detection channel for eQD650 with increasing CEA antigen (CEA AG) concentration in presence of CEA detection antibodies (CEA-AB) or NSE detection antibodies (NSE-AB) + CEA-AB using the bandpass filter (660 ± 13) nm.

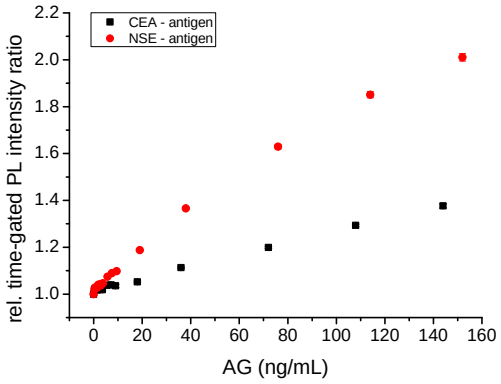

Figure 6.19: Relative time-gated PL intensity ratios measured for the detection of NSE and CEA in a duplexed immunoassay format. The increasing intensity ratios in presence of NSE antigen was measured using F(ab')$_2$-eQD650 and the bandpass filter (660 ± 13) nm and of CEA using F(ab')$_2$-eQD605 and the bandpass filter (607 ± 8) nm.

6.3.3 Influence of the fragmentation

Original publication:

Quantum-Dot-Based Förster Resonance Energy Transfer Immunoassay for Sensitive Clinical Diagnostics of Low-Volume Serum Samples.

K. D. Wegner, Z. Jin, S. Lindén, T. L. Jennings, and N. Hildebrandt.
ACS Nano **2013**, 7 (8), 7411-7419.

Quantum-Dot-Based Förster Resonance Energy Transfer Immunoassay for Sensitive Clinical Diagnostics of Low-Volume Serum Samples

K. David Wegner,[†] Zongwen Jin,[†] Stina Lindén,[†] Travis L. Jennings,[‡] and Niko Hildebrandt[†,*]

[†]Institut d'Electronique Fondamentale, Université Paris-Sud, 91405 Orsay Cedex, France and [‡]eBioscience, Inc., 10255 Science Center Drive, San Diego, California 92121, United States

ABSTRACT A myriad of quantum dot (QD) biosensor examples have emerged from the literature over the past decade, but despite their photophysical advantages, QDs have yet to find acceptance as standard fluorescent reagents in clinical diagnostics. Lack of reproducible, stable, and robust immunoassays using easily prepared QD-antibody conjugates has historically plagued this field, preventing researchers from advancing the deeper issues concerning assay sensitivity and clinically relevant detection limits on low-volume serum samples. Here we demonstrate a ratiometric multiplexable FRET immunoassay using Tb donors and QD acceptors, which overcomes all the aforementioned limitations toward application in clinical diagnostics. We demonstrate the determination of prostate specific antigen (PSA) in 50 μL serum samples with subnanomolar (1.6 ng/mL) detection limits using time-gated detection and two different QD colors. This concentration is well below the clinical cutoff value of PSA, which demonstrates the possibility of direct integration into real-life *in vitro* diagnostics. The application of IgG, F(ab')$_2$, and F(ab) antibodies makes our homogeneous immunoassay highly flexible and ready-to-use for the sensitive and specific homogeneous detection of many different biomarkers.

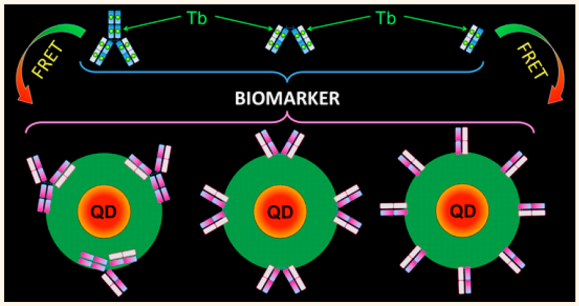

KEYWORDS: FRET · quantum dot · terbium · multiplexing · immunoassay · PSA · diagnostics

Next generation molecular diagnostics platforms are focusing on emerging technologies capable of providing rapid assays with enhanced sensitivity and efficient multiplexing performance for biomarker detection.[1] A major driving force is the desire to realize the goals of personalized medicine and point-of-care testing under clinically relevant conditions, especially for biomarkers found in blood, serum, or plasma.[2] Nanobiophotonics, which couples the speed and sensitivity of luminescence with the ultrasmall dimensions of nanoparticles,[3] and in particular colloidal quantum dots (QDs), is in a competitive position to meet the challenging requirements of multiplexed *in vitro* diagnostics (IVD). Although QDs offer distinct advantages in photostability with high brightness and color tunability if used in appropriate solvents,[4−14] they have yet to gain acceptance into standard clinical practice as reporter tags, due largely to either physical or chemical stability issues or insufficient sensitivity in biological media such as serum or plasma.[15] A highly specific QD bioconjugate capable of preserving its advantageous optical properties within such indispensable clinical sample matrices would be of immense utility toward meeting IVD criteria.

Tb-to-QD Förster resonance energy transfer (FRET) has proven itself to be an efficient tool for spectro-temporal multiplexing, offering several unique advantages over organic dye-based FRET systems for biomolecular sensing.[16−21] For specific and sensitive biomarker detection in homogeneous sandwich assays, antibodies remain the biomolecule of choice. However, the combination of QDs with antibodies has yet to be established within this context. Such developments have been hindered by insufficient labeling chemistries and the large donor−acceptor distances, which result from

* Address correspondence to niko.hildebrandt@u-psud.fr.

Received for review June 26, 2013 and accepted August 2, 2013.

Published online August 02, 2013
10.1021/nn403253y

the thick surface coatings of commercial QDs. Still, these commercial polymer/lipid-based coatings are indispensable for maintaining bright and stable QDs in clinical media such as serum or plasma. Although it has been shown that QDs can be used in FRET-based immunoassays,[22−31] these assays were heterogeneous, competitive, and/or nonratiometric, and, most importantly, measured in buffer systems instead of in serum. Serum validation is essential if QD-based immunoassays are to be accepted for IVD use, and so we found it helpful to list the traits for what may be considered the "ideal" immunoassay:

(1) *homogeneous* (no washing and separation steps)
(2) *serum-based* (human serum samples)
(3) *sensitive* (clinically relevant detection limits)
(4) *specific* (use of at least two primary antibodies for target binding)
(5) *fast* (liquid phase binding kinetics and quick measurement)
(6) *small* (small sample volumes below 100 μL)
(7) *reproducible* (ratiometric measurement in order to correct for medium interferences)
(8) *robust* (stable performance independent of individual user or environment)
(9) *flexible* (universal format for many biomarkers, facile conjugate production/purification)
(10) *multiplexed* (simultaneous measurement of several biomarkers)
(11) *stable* (long-term stability and shelf life).

In the QD-based biosensor presented here, we demonstrate that, by thoughtful design changes, we were able to develop such an ideal immunoassay attaining clinically relevant limits of detection (1.6 ng/mL) on prostate specific antigen (PSA) in 50 μL serum samples using commercial reagents and instrumentation.

RESULTS AND DISCUSSION

Flexible Antibody Conjugation and Purification. To date, FRET sandwich immunoassays using commercially available, stable, and biocompatible polymer/lipid embedded QDs (*e.g.*, Life Technologies or eBioscience) have not been realized. This is due to the limited distance range for QD−dye FRET pairs and the large donor−acceptor distance within such a sandwich complex. The complex in this scenario is composed of a QD with a thick surface coating (*ca.* 15 nm diameter), a first antibody (AB, *ca.* 150 kDa corresponding to a length of approximately 10 nm for the Y-shaped IgG), a biomarker (different sizes, *e.g.*, 34 kDa or *ca.* 2 nm for PSA), and finally a second AB with the reporter tag. The total distance between the QD and reporter fluorophore may be between ~15 and 30 nm, which is well beyond the measurable distance range of 5−10 nm for traditional FRET pairs. We solve the dilemma of these physical limitations with a two-pronged approach: (1) increasing the effective measurable energy transfer range to ~20 nm by time-gated Tb-to-QD FRET and (2) decreasing AB sizes from full IgG (*ca.* 150 kDa) to reduced F(ab′)$_2$ (*ca.* 100 kDa) and further to F(ab) (*ca.* 50 kDa) fragments of two different monoclonal primary antibodies against PSA to bring the Tb closer to the central QD. These two design modifications combine to make a system that is more compact in separation distance and more efficient in energy transfer, thereby enabling the potential for a homogeneous QD-based FRET immunoassay. The fulfillment of this compact design relies heavily upon the successful formation of different AB fragments and optimizing conjugation chemistry for bioconjugate assembly.

TABLE 1. Tb Donor/QD Acceptor Ratios for the Different Sandwich Immunoassays[a]

Tb-AB\QD-AB	QD-IgG	QD-F(ab′)$_2$	QD-F(ab)
Tb-IgG	31	56	210
Tb-F(ab′)$_2$	23	40	150
Tb-F(ab)	9.4	17	62

[a] Calculated ratios of Tb/QD in a theoretical sandwich immunoassay based on the measured Tb/AB and AB/QD ratios after conjugation to the different formats. Calculations are based on a linear model of combination, disregarding divalency of IgG or F(ab′)$_2$ and the effects of steric hindrance. The calculated values are meant purely as a guide for the eye to show the complex with the highest potential ratio of Tb/QD, which would in turn be the most sensitive (lowest detection limit) immunoassay.

The relatively small Tb complexes (NHS-activated Lumi4-Tb [Tb] delivered in lyophilized form for long-term storage, Lumiphore, Inc.)[32] were conjugated in a straightforward manner *via* coupling of NHS-activated Tb to available primary amines of the ABs.[33] AB coupling to the QD nanocrystals was accomplished using sulfhydryl-reactive conjugation chemistry as described in detail elsewhere[34] (eFluor 650NC [QD650] conjugation kits, eBioscience, Inc.). Labeling ratios of the Tb and QD conjugates were determined by UV/vis absorption spectroscopy as 13 Tb/IgG, 9.4 Tb/F(ab′)$_2$, 3.9 Tb/F(ab), 2.4 IgG/QD650, 4.3 F(ab′)$_2$/QD650, and 16 F(ab)/QD650 (with a determination error of ±30%). This shows that the Tb/AB labeling ratio decreases and AB/QD labeling increases with decreasing AB size, as expected from the size comparison of the different components (cf. Scheme 1). Based on these measured ratios, Table 1 calculates the theoretical number of Tb per QD for the different combinations. Clearly, the scenario combining the QD-F(ab) conjugate with the Tb-IgG sensitizer would be expected to yield the highest Tb/QD ratio and thus the highest proportion of Tb-to-QD FRET because the large difference in excited-state lifetimes (2.3 ms for Tb and few tens of nanoseconds for QD) allows the excitation of one QD by multiple Tb in a serial manner assuming there is enough excitation energy for multiple Tb (which is reasonable for the pulsed laser excitation).[35] This higher overall brightness of the FRET system (more QD emission intensity per QD due to FRET sensitization by multiple Tb) is also expected to lead to a higher sensitivity of the immunoassay.[20] Apart from a

possible higher FRET efficiency, the smaller ABs for QD conjugation have another important advantage, namely, an easier (QD-AB) conjugate purification (which is much more problematic for QD/IgG conjugates which are similar in size) by convenient spin column separation. One problem of high labeling ratios might be steric hindrance. The conjugation of *ca.* 16 F(ab) fragments in a random orientation on the QD surface might lead to inaccessibility of some F(ab)s to Tb-ABs *via* PSA binding, especially when the ABs are the relatively large IgGs. As would be expected from the Tb/QD ratio (Table 1), larger ABs for QDs combined with smaller ABs for Tb were disadvantageous (*e.g.*, QD-IgG and Tb-F(ab) lead to few large ABs on the QD and a low labeling ratio of Tb on small ABs; this results in the disadvantageous situation of large donor–acceptor distances and only few donor–acceptor pairs) and are therefore not treated further within this study.

In order to demonstrate the multiplexability of our FRET assay by using different QD colors, we also labeled IgG antibodies to QD605 (eFluor 605NC, eBioscience) with an approximate labeling ratio of 0.5 ± 0.3 IgG/QD605. The lower the labeling ratio, the higher the probability to have a significant amount of unconjugated QDs (assuming a Poisson distribution of labeling), which cannot participate in FRET. However, due to the very long excited-state lifetimes of Tb, incomplete labeling is not problematic for FRET-based assays.[21] Unconjugated QDs provide a short-lived luminescence signal, which is not specific for binding to a biomarker and which contributes only very few background signals that are largely suppressed due to time-gated detection in the millisecond range. FRET-sensitized QD emission can only be caused by binding with Tb-ABs *via* PSA and is therefore specific for PSA. This luminescence is long-lived (due to sensitization by long-lived Tb) and can therefore be efficiently distinguished from the short-lived luminescence of unlabeled QDs.

Optical Characterization of the FRET Assays. The photophysical properties (Figure 1) of Tb and QD were not influenced by AB conjugation. The broad overlap of the Tb emission and the QD absorption (Figure 1) combined with the large QD molar absorptivity values (especially for QD650) leads to very long Förster distances (donor–acceptor distance of 50% FRET efficiency), calculated as $R_0 = 0.02108\ (\kappa^2 \Phi_{Tb} n^{-4} J)^{1/6}$ nm, with the FRET orientation factor $\kappa^2 = 2/3$, the Tb-centered luminescence quantum yield $\Phi_{Tb} = 0.67 \pm 0.5$, the refractive index $n = 1.35$, and the overlap integral $J = \int F_{Tb} \varepsilon_{QD} \lambda^4 d\lambda$ (from 450 to 700 nm with the area-normalized Tb emission spectrum F_{Tb} and the QD molar absorptivity spectra ε_{QD}; cf. Figure 1). These values were $R_0 = 10.7 \pm 0.5$ nm and $R_0 = 7.7 \pm 0.3$ nm for the Tb-QD650 and Tb-QD605 FRET pairs, respectively. Taking into account that FRET is measurable between *ca.* 0.5 and 2 times R_0, these large Förster distances increase the FRET range to distances of up to approximately 20 nm. Such Tb-to-QD FRET systems follow quite well the classical r^{-6} distance-dependent FRET model and have been studied extensively before.[17,18,20,21,35–40]

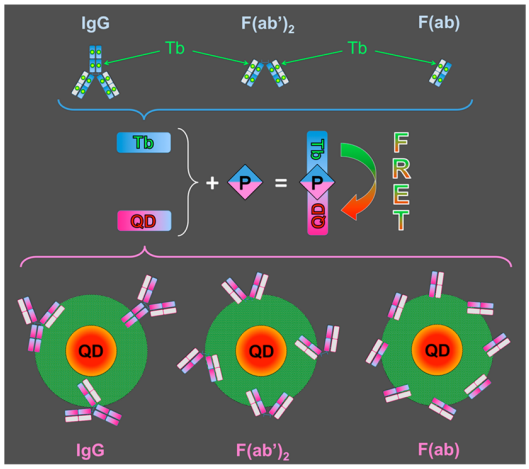

Scheme 1. Principle of the QD-based homogeneous FRET immunoassay. Tb-antibody conjugates (top) and QD-antibody conjugates (bottom) contain each a different primary antibody (which are further reduced to $F(ab')_2$ and F(ab) fragments) against PSA. All possible combinations of the six different conjugates were used to specifically recognize PSA (P) in FRET sandwich immunoassays (center).

All FRET assays contained 50 μL of each AB conjugate (Tb and QD) at constant concentrations to which 50 μL of serum with increasing concentrations of PSA was added. For the QD650, all possible AB configurations from Scheme 1 were used. For QD605 (which served to demonstrate the capability of multiplexing), only the IgG conjugates were applied. The Tb donor to QD acceptor distance (r_{DA}) is expected to be quite large due to two different antibodies, the PSA antigen and the thick QD coating. As mentioned above, the system using two IgGs could easily lead to r_{DA} values of ~15 to 30 nm. In fact, an exact r_{DA} estimation is extremely difficult because many distance-determining factors need to be taken into account: (1) the application of IgGs and smaller $F(ab')_2$ and F(ab) fragments, (2) a random orientation and distribution of the acceptor ABs on the QDs (as depicted in Scheme 1), (3) a random distribution of several Tb over the donor ABs, and (4) the various possible orientations and distances of the Tb-ABs to the QD due to the flexibility of the "(Tb-AB)-PSA-(QD-AB)" binding and sterical hindrance problems for highly labeled systems. Assuming a diameter of 14 nm for the QD650,[40] and a Tb-AB on the surface of the QD (due to the binding flexibility mentioned above), the minimum r_{DA} value would be approximately 7 nm. The maximum distance would be caused by an elongated "(Tb-IgG)-PSA(QD-IgG)" system with Tb and QD on opposite ends. This scenario would lead to a maximum r_{DA} value of *ca.* 29 nm (10 nm IgG + 2 nm PSA + 10 nm IgG + 7 nm QD radius). Using the

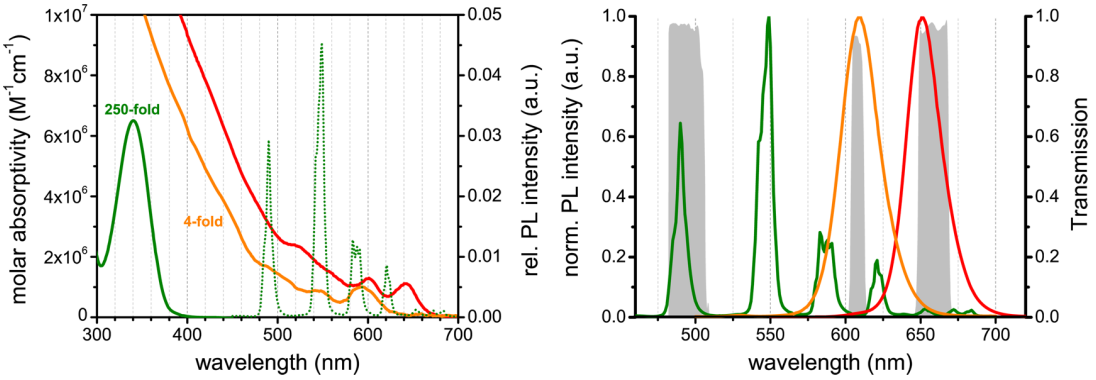

Figure 1. Optical properties of the FRET assay components. Left: Molar absorptivity spectra of Tb (green, multiplied by 250), QD605 (orange, multiplied by 4), and QD650 (red). For the calculation of the overlap integrals between Tb donor emission and QD acceptor absorption, the area-normalized Tb emission spectrum (green dotted) is also shown. Right: Photoluminescence (PL) intensity spectra of Tb (green), QD605 (orange), and QD650 (red) antibody conjugates normalized to unity at their respective maxima. The gray spectra in the background define the transmission of the optical band-pass filters within the Tb (494 ± 20 nm), QD605 (607 ± 8 nm), and QD650 (660 ± 13 nm) detection channels. Tb-centered, QD605, and QD650 PL quantum yields are 0.67 ± 0.5, 0.70 ± 0.07, and 0.55 ± 0.07, respectively.

Förster distance of $R_0 = 10.7$ nm and the FRET efficiency (η_{FRET}) calculated by

$$\eta_{FRET} = \frac{{R_0}^6}{{R_0}^6 + {r_{DA}}^6} = 1 - \frac{\tau_{DA}}{\tau_D} \quad (1)$$

with the photoluminescence (PL) decay times of pure Tb-AB (τ_D = 2.3 ms) and of the FRET pair (τ_{DA}) leads to FRET efficiencies of η_{FRET}(max) = 0.92 and η_{FRET}(min) = 0.0025 and FRET decay times of τ_{DA}(min) = 0.17 ms and τ_{DA}(max) = 2.3 ms. As all donor−acceptor distances between 7 and 29 nm are possible, one would expect PL decay curves with a decay time distribution ranging from *ca.* 0.17 ms (maximum FRET) to *ca.* 2.3 ms (minimum FRET or emission from unquenched Tb).

Pulsed excitation with 337 nm (in the absorption maximum of Tb; cf. Figure 1) leads to excited-state Tb and QD and PL decay curves as those shown in Figure 2 for the F(ab′)$_2$ conjugates of Tb and QD650 (the PL decay curves for the other systems are shown in the Supporting Information). The PL decay curves of PSA-containing assays (6, 12, and 24 nM shown as representative curves) acquired in the QD detection channel show higher PL intensities (sensitization) and new decay time components, originating from FRET sensitization, compared to the PL decay curve of the assay containing no PSA (black curve). In agreement with the QD sensitization, the Tb detection channel shows a concomitant FRET quenching in intensity and decay time. Although the single PL decay time components cannot be determined from these decay curves, both the QD-sensitized and the Tb-quenched decay curves reveal new decay components in the expected range from *ca.* 0.17 to 2.3 ms. Thus, the PL decay curves give clear evidence of FRET from Tb (FRET-quenched) to QD (FRET-sensitized) upon PSA recognition by the antibody conjugates (formation of "(Tb-AB)-PSA-(QD-AB)" sandwich complexes).

Another interesting aspect can be found in the comparison of the PL decay curves of the different FRET systems in the Tb detection channel. Within the QD-F(ab′)$_2$-containing systems (Figure 2 and Figure S2), the FRET quenching (new shorter decay components) becomes much more obvious than for the systems containing QD-IgG or QD-F(ab) (Figures S1, S3, S4, and S5), for which only a slight intensity increase can be detected. For the IgG systems, we attribute this behavior to many Tb-QD pairs at very long distances leading to a large majority of unquenched Tb. In the case of the F(ab) systems, the large labeling ratio and the small F(ab) fragments on the QD might lead to steric hindrance, preventing the formation of "(Tb-IgG)-PSA-(QD-F(ab))" sandwich complexes and leading to a large amount of unbound Tb-IgG, which leads to an excess of unquenched Tb. Reduced affinity of the F(ab) fragments compared to the full IgGs could be another reason for the reduced PL quenching.

Homogeneous FRET Immunoassays for PSA. The homogeneous FRET immunoassays were measured on a KRYPTOR compact plus (Cezanne/Thermo Fisher Scientific) clinical fluorescence plate reader, which simultaneously detects the time-gated PL intensities (integration of the PL intensities within the time window from 0.1 to 0.9 ms after pulsed excitation) in the Tb donor and the QD acceptor channels (cf. filter transmission spectra in Figure 1 for wavelength ranges of these two channels). This time-gating allows very efficient suppression of the short-lived sample autofluorescence and of the very strong fluorescence from directly excited QDs. The time-gated intensities in the QD acceptor channel I_{QD}(0.1−0.9 ms) and the Tb donor channel I_{Tb}(0.1−0.9 ms) are used to calculate the FRET ratio F_R (FRET sensitization divided by FRET quenching):

$$F_R = \frac{I_{QD}(0.1 - 0.9\ \text{ms})}{I_{Tb}(0.1 - 0.9\ \text{ms})} \quad (2)$$

F_R is used for the determination of the biomarker concentration and leads to very low coefficients of variation

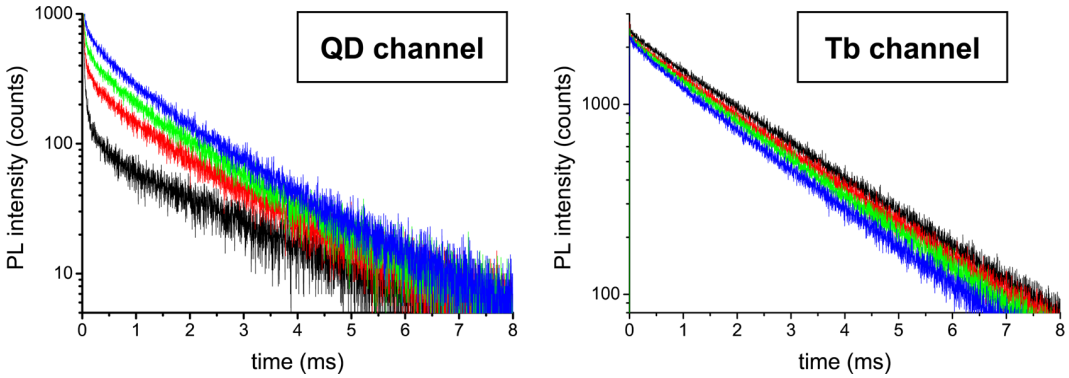

Figure 2. PL decay curves of the "(Tb-F(ab′)$_2$)-PSA-(QD650-F(ab′)$_2$)" FRET immunoassays. The addition of 50 μL serum containing increasing PSA concentrations (black, no PSA; red, 6 nM; green, 12 nM; blue, 24 nM) to a 100 μL solution of Tb- and QD-antibody conjugates with constant concentrations leads to an increasing FRET sensitization of the QDs (PL measured in the QD650 detection channel: 660 ± 13 nm, left) and an increasing FRET quenching of the Tb (PL measured in the Tb detection channel: 494 ± 20 nm, right). Left: Black QD curve containing no PSA is composed of a short QD component (in the microsecond range) from direct QD excitation and a long Tb component (in the millisecond range) from spectral cross-talk of Tb in the QD detection channel. A new FRET decay time component (in the tens to hundreds of microseconds range) with increasing intensity (from red to blue) becomes clearly visible once Tb and QD are brought in close proximity due to the antibody−PSA binding. Right: Black Tb curve without PSA contains only long-lived Tb emission (no QD PL cross-talk in this channel), which is FRET-quenched (decreased PL decay time) due to antibody−PSA binding. PL decay curves for all other antibody combinations shown in Scheme 1 can be found in the Supporting Information.

(CV) because the ratiometric measurement intrinsically corrects for medium interferences. Within the assays, 50 μL of serum was mixed with 100 μL of AB conjugate solution (50 μL of Tb and QD conjugate each at a constant concentration). Apart from PSA-free serum, 18 serum samples with PSA concentrations ranging from 0.6 to 36 nM were measured. Each measurement takes 5 s per sample. Figure 3 shows the assay calibration curves achieved with these different concentrations. All assay curves show a strong increase of F_R with increasing PSA concentrations until *ca.* 10−20 nM PSA, which is the concentration range, where the ABs (QD and/or Tb conjugates) become saturated by PSA biomarkers and higher PSA concentrations do not provide additional FRET. It should be noted that the concentrations of Tb and QD are constant for all samples, which means that the increase of the time-gated FRET ratio is caused by FRET sensitization of QDs by Tb (the increase of F_R cannot be caused by nonspecific signals, *e.g.*, due to an increasing QD or Tb concentration). For most samples, the so-called "hook-effect" becomes apparent at even higher concentrations, where an excess of PSA leads to a stronger formation of individual "(Tb-AB)-PSA" and "(QD-AB)-PSA" complexes (compared to the "(Tb-AB)-PSA-(QD-AB)" FRET complexes), and thus a decreasing F_R is observed.[41] In order to distinguish the F_R values of the increasing slope (concentrations before the hook-effect) from the decreasing slope (concentrations after the hook-effect), the automated KRYPTOR plate reader system performs a kinetic measurement. This means that the system measures F_R directly after the addition of the serum sample to the AB conjugate solutions and then every few minutes in order to evaluate the increase of F_R over time. Using the calibration curve for the specific assay (in our case PSA), the system knows the highest value for the dynamic range (saturation of F_R in the curves in Figure 3) and can automatically dilute the sample in case the sample concentration is too high. Although we have not used the automated pipetting, this feature is a standard tool on the KRYPTOR compact clinical plate reader. Apart from avoiding problems with the hook-effect, the automated and calibrated dilution (using kinetic measurements) allows for a much larger dynamic range because also highly concentrated samples can be analyzed.

The QD-IgG assay curve differs from the others in that the curvature is rather of sigmoidal shape. This is consistent with our previous observation that an efficient separation of free IgG from the QD-IgG conjugates after labeling is difficult due to the similar sizes of QD and IgG. The shape of the red assay curve in Figure 3 is most probably caused by a small amount of free IgG antibodies, which are still present in the QD-IgG conjugate solution. These free ABs will participate in binding but not in energy transfer, and thus the initial increase of F_R is less steep compared to the QD conjugates with the smaller AB fragments, for which separation is much easier using spin column purification. The assumption of free ABs in the QD-IgG conjugate solution is further supported by the QD605 assay curve (Figure 3 right), for which a lower labeling ratio of *ca.* 0.5 AB/QD605 was used. In this configuration, there are free QDs (and no free ABs) in the QD605 conjugate solution, which is unproblematic for time-gated FRET detection (free acceptor fluorophores do not contribute to the FRET signal).[21] The increase of F_R with increasing PSA concentration shows a similar shape to the QD650 conjugates of fragmented ABs. However, it should be noted that the increase is less steep because the lower labeling ratio leads to less

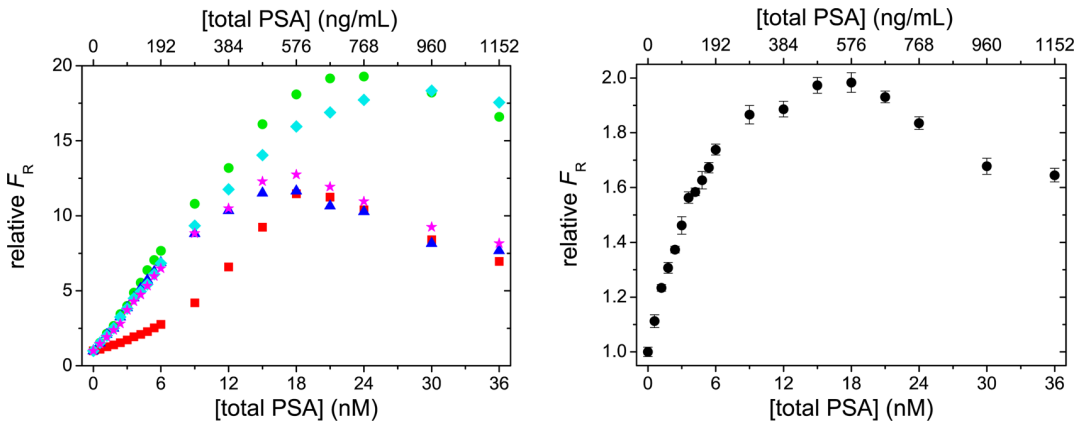

Figure 3. Tb-to-QD time-gated homogeneous FRET PSA immunoassays. Left (QD650): Relative time-gated (0.1−0.9 ms) PL intensity ratios (F_R normalized to unity at [total PSA] = 0) as a function of total PSA concentration. The selected antibody pairs were IgG + IgG (red squares), IgG + F(ab′)$_2$ (green dots), IgG + F(ab) (blue triangles), F(ab′)$_2$ + F(ab′)$_2$ (cyan rhombi), and F(ab) + F(ab) (magenta stars) for Tb and QD650, respectively. Increasing PSA concentrations led to a strong increase of F_R for all antibody combinations with a linear detection range spanning *ca.* 3 orders of magnitude for the F(ab′)$_2$ systems. For intercomparison, all curves were measured under the same experimental conditions. Right (QD605): Relative F_R values of the "(Tb-IgG)-PSA-(QD-IgG)" pair show a similar behavior to the QD650-based FRET systems and demonstrate the feasibility of a QD-based multiplexed homogeneous immunoassay. Limits of detection (LODs) for the assays can be found in Table 2.

TABLE 2. Limits of Detection (LODs), Dynamic Range, and Maximum Coefficients of Variation (CV_{max}) for the Different Homogeneous FRET Immunoassays[a]

Tb conjugate	QD conjugate	LOD (nM)	saturation (nM)	LOD (ng/mL)	LOD (fmol)	CV_{max} (%)
Tb-IgG	QD650-IgG	0.27	18	8.4	13.0	1.9
Tb-IgG	QD650-F(ab′)$_2$	0.06	21	1.8	2.8	1.8
Tb-IgG	QD650-F(ab)	0.05	15	1.6	2.5	0.7
Tb-F(ab′)$_2$	QD650-F(ab′)$_2$	0.08	21	2.6	4.1	2.6
Tb-F(ab)	QD650-F(ab)	0.05	15	1.6	2.5	0.6
Tb-IgG	QD605-IgG	0.25	15	7.9	12.0	1.3

[a] LODs of PSA are given for the 50 μL serum samples (LODs in the complete 150 μL measurement volume are 3 times lower). Saturation concentrations (the concentrations for which the PL intensity ratios in Figure 3 do not further increase) determine the dynamic range (which lies between the LOD and the saturation value). LODs were determined using the calibration curve concentration corresponding to the average F_R value plus 3 times its standard deviation of 30 serum samples containing no PSA (zero biomarker samples). The fmol LOD values were determined for a volume of 50 μL. The maximum coefficients of variation (CV_{max}) are given for the 30 serum samples containing no PSA. CVs for all samples containing PSA were below that maximum value. All values have an error of approximately 20%.

FRET signal per AB. We also note that carefully optimized ultracentrifugation or gel filtration chromatography might lead to better purification results of the QD-IgG conjugates. However, we wanted to demonstrate improved separation of small AB fragments using similar conditions for all QD-AB conjugates, in particular, by using convenient spin column purification, which can be performed using a standard laboratory benchtop centrifuge.

The limits of detection (LODs; cf. Table 2) of all homogeneous FRET assays are in the subnanomolar (few ng/mL) PSA range, and the dynamic range spans approximately 2 to 3 orders of magnitude. As expected from Table 1, the LODs are favorable for the AB-fragment-containing QD conjugates. The difference of ABs for the Tb conjugates is negligible, which we attribute to the relatively large distances in our sandwich immunoassay (Tb donors labeled to the Fc region of the IgG are too far away from the QD acceptor to participate in efficient FRET). Although the difference in LOD from QD650-IgG to QD650-F(ab′)$_2$ and QD650-F(ab) is quite significant (0.27 nM compared to 0.06 and 0.05 nM), there is only a minor difference between QD-F(ab′)$_2$ and QD-F(ab). As already mentioned above, there might be two main reasons for this. First, a high labeling ratio might lead to steric hindrance for Tb-AB binding *via* PSA. Second, F(ab) contains only one binding site (whereas IgG and F(ab′)$_2$ contain two), and the random orientation as well as the reduced affinity might lead to lower binding efficiencies per AB. In other words, the advantages of the small F(ab)s (compared to F(ab′)$_2$) are compensated by their disadvantages. Thus, both F(ab′)$_2$ and F(ab) are very well-suited for our Tb-to-QD FRET immunoassays.

Another remarkable aspect concerns the very low coefficients of variation for the QD-F(ab)-containing FRET systems. This important advantage is most probably caused by the higher labeling ratio of the small F(ab) fragments per QD, which leads to a lower background signal of directly excited QDs per "(Tb-AB)-PSA-(QD-AB)" binding (more FRET pairs per QD because multiple Tb can excite one QD in a serial manner due to

the large difference in excited-state lifetimes as explained above). Therefore, the fluorescence reader system can be used at a higher detector sensitivity without detector saturation. The best immunoassay system combining maximum sensitivity (minimum LOD), minimum antibody modification (no IgG reduction for the Tb conjugates), and maximum separation efficiency is therefore the "(Tb-IgG)+(QD-F(ab))" system.

CONCLUSIONS

In this study, we examine the application of Tb-to-QD FRET in a time-gated homogeneous immunoassay for PSA. We note that Chen *et al.* reported an initial demonstration where they used FRET from self-made Tb complexes to QD-doped microparticles for a homogeneous detection of α-fetoprotein.[31] However, in this preliminary study, the authors only presented a superficial photophysical analysis of the FRET processes and performed the assays in buffer. In contrast, we present (1) a full photophysical study of all pertinent FRET components and processes; (2) the use of two stable and biocompatible QDs with different colors; (3) a full characterization of assays using three types of antibodies (IgG, $F(ab')_2$, and F(ab)); and (4) high sensitivity in serum samples, which is the medium of relevance for diagnostic applications with minimal sample preparation.

We find that the PL decays of both Tb- and QD-antibody conjugates with and without PSA give clear evidence of PSA-binding-induced FRET from Tb to QD. The FRET ratio F_R can be used to sensitively and accurately determine biomarker concentrations at clinically relevant concentrations in small-volume serum samples. In the case of the PSA assay presented here, the LOD of 1.6 ng/mL (Table 2) is well below the commonly used serum PSA cutoff value of 4 ng/mL and even below the 2 ng/mL cutoff value proposed for higher-sensitivity PSA diagnosis.[42] Apart from PSA, the homogeneous Tb-to-QD FRET immunoassay is suitable for any other biomarker for which two specific IgG antibodies exist. Our flexible bioconjugation strategy offers facile assembly and purification of the Tb- and QD-AB conjugates, where the highest sensitivity assay (lowest LOD) resulted from F(ab)-based QD conjugates, due to higher Tb/QD pairs at closer donor−acceptor distances. To our knowledge, this is the first QD-based immunoassay to combine successfully all 11 attributes of an ideal homogeneous assay (as enumerated in the introduction) for real-life clinical diagnostics. Although our detection limits are very low and in a clinically relevant concentration range, it should be noted that commercial assays (*e.g.*, the standard KRYPTOR total PSA kit) still provide lower LODs. Nevertheless, these assays are fully optimized commercial immunoassay kits, and they use conventional fluorophores as FRET acceptors, which limit their multiplexing capability. Therefore, such assays do not exist as multiplexed kits. Our demonstration of replacing such standard fluorophores with QDs for homogeneous FRET immunoassays in combination with our recent work on highly increased sensitivity and multiplexing using up to five different biomarkers[18,19] strongly suggests that further development and optimization of Tb-to-QD FRET immunoassays will soon generate multiplexed diagnostic kits with even lower LODs for fast, flexible, and efficient early disease detection.

MATERIALS AND METHODS

Antibodies. The anti-PSA IgGs "PSR222" and "PSS233" were provided by Cezanne/Thermo Fisher Scientific. F(ab) and $F(ab')_2$ fragments of IgGs were generated using Pierce Mouse IgG1 F(ab) and $F(ab')_2$ preparation kit (Thermo Fisher Scientific). Fragmentation was verified using SDS-PAGE.

QD-Antibody Conjugates. eFluor650/605 nanocrystal conjugation kit−sulfhydryl reactive (provided by eBioscience in lyophilized form) was used for all QD conjugations. Details of the conjugation chemistry are described in ref 34. Antibody solutions (in concentration access compared to the QD solutions) were prepared in 1× PBS and conjugated to QDs according to the manufacturer's instructions. Unbound proteins were separated by washing 3−6 times in 100 kDa molecular weight cutoff (MWCO) spin columns (Millipore) with 100 mM sodium tetraborate buffer (pH 8.3) as the wash buffer. QD concentrations were determined by absorbance measurements using molar absorptivities of $1.1 \times 10^6\ M^{-1}\ cm^{-1}$ (at 641 nm) for QD650 and of $2.5 \times 10^5\ M^{-1}\ cm^{-1}$ (at 594 nm) for QD605 as provided by the manufacturer. Antibodies were quantified by absorbance measurements at 280 nm using molar absorptivities of 210 000, 140 000, and 70 000 $M^{-1}\ cm^{-1}$ for IgG, $F(ab')_2$, and F(ab), respectively. The labeling ratios were determined by linear combination of the respective absorbance values of QDs and antibodies within the QD-antibody conjugates.

Tb-Antibody Conjugates. Lumi4-Tb-NHS (provided by Lumiphore in lyophilized form) was dissolved to 8 mM in anhydrous DMF and mixed (in concentration excess to the antibody solutions) with the antibody samples in 100 mM carbonate buffer at pH 9.0. The mixtures were incubated while rotating at 25 rpm (Intelli-Mixer, ELMI) for 2 h at room temperature. For Tb-antibody conjugate purification, the samples were washed 4−6 times with 100 mM Tris-Cl pH 7.2 using 10 kDa MWCO spin columns (Millipore) for both $F(ab')_2$ and F(ab), and 50 kDa MWCO spin columns for IgG. Tb concentrations were determined by absorbance measurements at 340 nm using a molar absorptivity of 26 000 $M^{-1}\ cm^{-1}$ as provided by the manufacturer. Antibodies were quantified by absorbance measurements at 280 nm. The labeling ratios were determined by linear combination of the respective absorbance values of Tb and antibodies within the Tb-antibody conjugates.

Optical Characterization. Absorption spectra (Lambda 35 UV/vis System, PerkinElmer) and emission spectra (FluoTime 300, PicoQuant) were recorded in tris(hydroxymethyl)aminomethane (Tris-Cl, Sigma Aldrich) buffer with a pH of 7.4 and sodium tetraborate buffer with a pH of 8.5 (Sigma Aldrich) for Tb and QD samples, respectively. PL quantum yields and Förster distances were determined as described elsewhere.[40] PL decay curves were acquired directly from the FRET immunoassay samples (*vide infra*) on an EI fluorescence plate reader (Edinburgh Instruments) using 4000 detection bins of 2 μs integration time and nitrogen laser (VSL 337 ND, Spectra Physics) excitation (337.1 nm, 20 Hz). Optical transmission filter band-pass wavelengths were 494 ± 20 nm (Semrock) for the Tb detection channel, 660 ± 13 nm (Semrock) for the QD650 detection channel, and 607 ± 8 nm (Delta) for the QD605 detection channel.

Homogeneous FRET Immunoassays. The Tb- and QD-antibody conjugates were each dissolved in 50 μL Tris-Cl buffer containing 0.5% bovine serum albumin (BSA, Sigma-Aldrich). The concentrations (of the ABs; for the Tb and QD concentrations, see labeling ratios in the article) were approximately 6.9 nM for the Tb-IgG, 11.4 nM for the Tb-F(ab')$_2$, 16.2 nM for the Tb-F(ab), 12.6 nM for the QD650-IgG, 11.7 nM for the QD650-F(ab')$_2$, 23.1 nM for the QD650-F(ab), and 2.1 nM for the QD605-IgG. Then, 50 μL serum samples (added to the 100 μL solutions containing both the Tb and QD conjugates) were prepared from a stock solution of normal human serum containing 69.7 μg/mL PSA by dilution with purified newborn calf serum (both provided by Cezanne/Thermo Fisher Scientific) to yield the desired PSA concentrations. Serum without PSA was pure newborn calf serum. Time-gated (0.1−0.9 ms) PL intensity measurements were acquired on a KRYPTOR compact plus fluorescence plate reader (Cezanne/Thermo Fisher Scientific) using 500 detection bins of 2 μs integration time and nitrogen laser excitation (337.1 nm, 20 Hz, 100 pulses). Optical transmission filter band-pass wavelengths were 494 $\pm$ 20 nm (Semrock) for the Tb detection channel, 660 $\pm$ 13 nm (Semrock) for the QD650 detection channel, and 607 $\pm$ 10 nm (Delta) for the QD605 detection channel. All FRET assays were measured in black 96-well microtiter plates with an optimal working volume of 150 μL. Each sample containing PSA serum samples was prepared three times, and the samples without PSA were prepared 10 times. All samples were measured in triplicate. After sample preparation, the microtiter plates were incubated for 120 min at 37 °C before measurements on the KRYPTOR and EI fluorescence plate readers.

Conflict of Interest: The authors declare no competing financial interest.

Acknowledgment. The authors thank Lumiphore, Inc. for the gift of Lumi4-Tb-NHS reagent, and the European Commission (FP7 project NANOGNOSTICS), the European Innovative Medicines Initiative IMI (project OncoTrack), the Investissements d'Avenir Program France (project NanoCTC), and the Agence National de la Recherche France (project NanoFRET) for financial support.

Supporting Information Available: PL decay curves of the following FRET immunoassays: (1) the "(Tb-IgG)-PSA-(QD650-IgG)", (2) "(Tb-IgG)-PSA-(QD650-F(ab')$_2$)", (3) "(Tb-IgG)-PSA-(QD650-F(ab))", (4) "(Tb-F(ab))-PSA-(QD650-F(ab))", and (5) "(Tb-IgG)-PSA-(QD605-IgG)". This material is available free of charge *via* the Internet at http://pubs.acs.org.

REFERENCES AND NOTES

1. Select Biosciences Market Report: *Mutiplexed Diagnostics 2010*, May 2010, Sudbury, UK.
2. Jain, K. K. Applications of Nanobiotechnology in Clinical Diagnostics. *Clin. Chem.* **2007**, *53*, 2002–2009.
3. Hötzer, B.; Medintz, I. L.; Hildebrandt, N. Fluorescence in Nanobiotechnology: Sophisticated Fluorophores for Novel Applications. *Small* **2012**, *8*, 2297–2326.
4. Algar, W. R.; Susumu, K.; Delehanty, J. B.; Medintz, I. L. Semiconductor Quantum Dots in Bioanalysis: Crossing the Valley of Death. *Anal. Chem.* **2011**, *83*, 8826–8837.
5. Gill, R.; Zayats, M.; Willner, I. Semiconductor Quantum Dots for Bioanalysis. *Angew. Chem., Int. Ed.* **2008**, *47*, 7602–7625.
6. Kuang, H.; Zhao, Y.; Ma, W.; Xu, L.; Wang, L.; Xu, C. Recent Developments in Analytical Applications of Quantum Dots. *TrAC, Trends Anal. Chem.* **2011**, *30*, 1620–1636.
7. Medintz, I. L.; Uyeda, H. T.; Goldman, E. R.; Mattoussi, H. Quantum Dot Bioconjugates for Imaging, Labelling and Sensing. *Nat. Mater.* **2005**, *4*, 435–446.
8. Rosenthal, S. J.; Chang, J. C.; Kovtun, O.; McBride, J. R.; Tomlinson, I. D. Biocompatible Quantum Dots for Biological Applications. *Chem. Biol.* **2011**, *18*, 10–24.
9. Alivisatos, A. P. Semiconductor Clusters, Nanocrystals, and Quantum Dots. *Science* **1996**, *271*, 933–937.
10. Alivisatos, P. The Use of Nanocrystals in Biological Detection. *Nat. Biotechnol.* **2004**, *22*, 47–52.
11. Chan, W. C. W.; Nie, S. M. Quantum Dot Bioconjugates for Ultrasensitive Nonisotopic Detection. *Science* **1998**, *281*, 2016–2018.
12. Han, M. Y.; Gao, X. H.; Su, J. Z.; Nie, S. Quantum-Dot-Tagged Microbeads for Multiplexed Optical Coding of Biomolecules. *Nat. Biotechnol.* **2001**, *19*, 631–635.
13. Resch-Genger, U.; Grabolle, M.; Cavaliere-Jaricot, S.; Nitschke, R.; Nann, T. Quantum Dots *versus* Organic Dyes as Fluorescent Labels. *Nat. Methods* **2008**, *5*, 763–775.
14. Jin, Z.; Hildebrandt, N. Semiconductor Quantum Dots for *In Vitro* Diagnostics and Cellular Imaging. *Trends Biotechnol.* **2012**, *30*, 394–403.
15. Hildebrandt, N. Biofunctional Quantum Dots: Controlled Conjugation for Multiplexed Biosensors. *ACS Nano* **2011**, *5*, 5286–5290.
16. Algar, W. R.; Malanoski, A. P.; Susumu, K.; Stewart, M. H.; Hildebrandt, N.; Medintz, I. L. Multiplexed Tracking of Protease Activity Using a Single Color of Quantum Dot Vector and a Time-Gated Förster Resonance Energy Transfer Relay. *Anal. Chem.* **2012**, *84*, 10136–10146.
17. Algar, W. R.; Wegner, D.; Huston, A. L.; Blanco-Canosa, J. B.; Stewart, M. H.; Armstrong, A.; Dawson, P. E.; Hildebrandt, N.; Medintz, I. L. Quantum Dots as Simultaneous Acceptors and Donors in Time-Gated Förster Resonance Energy Transfer Relays: Characterization and Biosensing. *J. Am. Chem. Soc.* **2012**, *134*, 1876–1891.
18. Geißler, D.; Charbonnière, L. J.; Ziessel, R. F.; Butlin, N. G.; Löhmannsröben, H.-G.; Hildebrandt, N. Quantum Dot Biosensors for Ultrasensitive Multiplexed Diagnostics. *Angew. Chem., Int. Ed.* **2010**, *49*, 1396–1401.
19. Geißler, D.; Stufler, S.; Löhmannsröben, H.-G.; Hildebrandt, N. Six-Color Time-Resolved Förster Resonance Energy Transfer for Ultrasensitive Multiplexed Biosensing. *J. Am. Chem. Soc.* **2013**, *135*, 1102–1109.
20. Charbonnière, L. J.; Hildebrandt, N. Lanthanide Complexes and Quantum Dots: A Bright Wedding for Resonance Energy Transfer. *Eur. J. Inorg. Chem.* **2008**, 3241–3251.
21. Geißler, D.; Hildebrandt, N. Lanthanide Complexes in FRET Applications. *Curr. Inorg. Chem.* **2011**, *1*, 17–35.
22. Esteve-Turrillas, F. A.; Abad-Fuentes, A. Applications of Quantum Dots as Probes in Immunosensing of Small-Sized Analytes. *Biosens. Bioelectron.* **2013**, *41*, 12–29.
23. Ge, S.; Ge, L.; Yan, M.; Song, X.; Yu, J.; Liu, S. A Disposable Immunosensor Device for Point-of-Care Test of Tumor Marker Based on Copper-Mediated Amplification. *Biosens. Bioelectron.* **2013**, *43*, 425–31.
24. Härmä, H.; Soukka, T.; Shavel, A.; Gaponik, N.; Weller, H. Luminescent Energy Transfer between Cadmium Telluride Nanoparticle and Lanthanide(III) Chelate in Competitive Bioaffinity Assays of Biotin and Estradiol. *Anal. Chim. Acta* **2007**, *604*, 177–183.
25. Kattke, M. D.; Gao, E. J.; Sapsford, K. E.; Stephenson, L. D.; Kumar, A. FRET-Based Quantum Dot Immunoassay for Rapid and Sensitive Detection of *Aspergillus amstelodami*. *Sensors (Basel, Switzerland)* **2011**, *11*, 6396–6410.
26. Long, F.; Gu, C.; Gu, A. Z.; Shi, H. Quantum Dot/Carrier-Protein/Haptens Conjugate as a Detection Nanobioprobe for FRET-Based Immunoassay of Small Analytes with All-Fiber Microfluidic Biosensing Platform. *Anal. Chem.* **2012**, *84*, 3646–3653.
27. Qian, J.; Wang, C.; Pan, X.; Liu, S. A High-Throughput Homogeneous Immunoassay Based on Förster Resonance Energy Transfer between Quantum Dots and Gold Nanoparticles. *Anal. Chim. Acta* **2013**, *763*, 43–49.
28. Wei, O. D.; Lee, M.; Yu, X.; Lee, E. K.; Seong, G. H.; Choo, J.; Cho, Y. W. Development of an Open Sandwich Fluoroimmunoassay Based on Fluorescence Resonance Energy Transfer. *Anal. Biochem.* **2006**, *358*, 31–37.
29. Zeng, Q. H.; Zhang, Y. L.; Liu, X. M.; Tu, L. P.; Kong, X. G.; Zhang, H. Multiple Homogeneous Immunoassays Based on a Quantum Dots−Gold Nanorods FRET Nanoplatform. *Chem. Commun.* **2012**, *48*, 1781–1783.
30. Zhang, C. L.; Gao, D.; Zhou, G. H.; Chen, L.; Zhang, X. A.; Cui, Z. Q.; He, Z. K. Label-Free Homogeneous Immunosensor Based on FRET for the Detection of Virus Antibody in Serum. *Chem.—Asian. J.* **2012**, *7*, 1764–1767.
31. Chen, M. J.; Wu, Y. S.; Lin, G. F.; Hou, J. Y.; Li, M.; Liu, T. C. Quantum-Dot-Based Homogeneous Time-Resolved

Fluoroimmunoassay of α-Fetoprotein. *Anal. Chim. Acta* **2012**, *741*, 100–105.
32. Xu, J.; Corneillie, T. M.; Moore, E. G.; Law, G.-L.; Butlin, N. G.; Raymond, K. N. Octadentate Cages of Tb(III) 2-Hydroxyisophthalamides: A New Standard for Luminescent Lanthanide Labels. *J. Am. Chem. Soc.* **2011**, *133*, 19900–19910.
33. Hermanson, G. T. *Bioconjugate Techniques*, 2nd ed.; Academic Press: San Diego, CA, 2008.
34. Jennings, T. L.; Becker-Catania, S. G.; Triulzi, R. C.; Tao, G.; Scott, B.; Sapsford, K. E.; Spindel, S.; Oh, E.; Jain, V.; Delehanty, J. B.; *et al.* Reactive Semiconductor Nanocrystals for Chemoselective Biolabeling and Multiplexed Analysis. *ACS Nano* **2011**, *5*, 5579–5593.
35. Algar, W. R.; Kim, H.; Medintz, I. L.; Hildebrandt, N. Emerging Non-traditional Förster Resonance Energy Transfer Configurations with Semiconductor Quantum Dots: Investigations and Applications. *Coord. Chem. Rev.* **2013**http://dx.doi.org/10.1016/j.ccr.2013.07.015.
36. Charbonniere, L. J.; Hildebrandt, N.; Ziessel, R. F.; Löhmannsröben, H.-G. Lanthanides to Quantum Dots Resonance Energy Transfer in Time-Resolved Fluoro-immunoassays and Luminescence Microscopy. *J. Am. Chem. Soc.* **2006**, *128*, 12800–12809.
37. Hildebrandt, N.; Charbonniere, L. J.; Beck, M.; Ziessel, R. F.; Löhmannsröben, H.-G. Quantum Dots as Efficient Energy Acceptors in a Time-Resolved Fluoroimmunoassay. *Angew. Chem., Int. Ed.* **2005**, *44*, 7612–7615.
38. Hildebrandt, N.; Charbonniere, L. J.; Löhmannsröben, H.-G. Time-Resolved Analysis of a Highly Sensitive Förster Resonance Energy Transfer Immunoassay Using Terbium Complexes as Donors and Quantum Dots as Acceptors. *J. Biomed. Biotechnol.* **2007**No. 79169.
39. Morgner, F.; Geißler, D.; Stufler, S.; Butlin, N. G.; Löhmannsröben, H.-G.; Hildebrandt, N. A Quantum-Dot-Based Molecular Ruler for Multiplexed Optical Analysis. *Angew. Chem., Int. Ed.* **2010**, *49*, 7570–7574.
40. Wegner, K. D.; Lanh, P. T.; Jennings, T.; Oh, E.; Vaibhav, J.; Fairclough, S. M.; Smith, J. M.; Giovanelli, E.; Lequeux, N.; Pons, T.; *et al.* Influence of Luminescence Quantum Yield, Surface Coating, and Functionalization of Quantum Dots on the Sensitivity of Time-Resolved FRET Bioassays. *ACS Appl. Mater. Interfaces* **2013**, *5*, 2881–2892.
41. Wild, D. *The Immunoassay Handbook*, 4th ed.; Elsevier: Amsterdam, 2013.
42. Greene, K. L.; Albertsen, P. C.; Babaian, R. J.; Carter, H. B.; Gann, P. H.; Han, M.; Kuban, D. A.; Sartor, A. O.; Stanford, J. L.; Zietman, A.; *et al.* Prostate Specific Antigen Best Practice Statement: 2009 Update. *J. Urol.* **2013**, *189*, S2–S11.

Quantum Dot-Based Förster Resonance Energy Transfer Immunoassay for Sensitive Clinical Diagnostics of Low-Volume Serum Samples

K. David Wegner[1], Zongwen Jin[1], Stina Lindén[1], Travis L. Jennings[2], and Niko Hildebrandt[1*]

[1] Institut d'Electronique Fondamentale, Université Paris-Sud, 91405 Orsay Cedex, France

[2] eBioscience, Inc., 10255 Science Center Drive, San Diego, California 92121, USA

Corresponding author: niko.hildebrandt@u-psud.fr

SUPPORTING INFORMATION

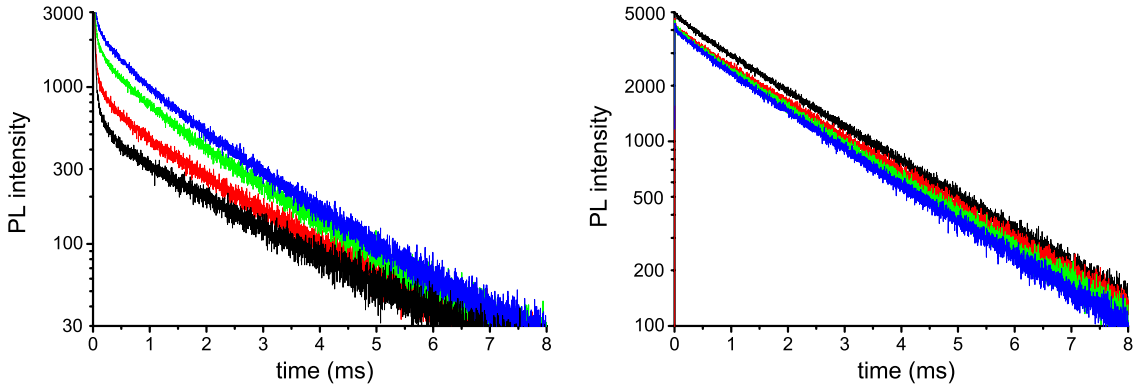

Figure S1: PL decay curves of the (Tb-IgG)-PSA-(QD650-IgG) FRET immunoassays

The addition of 50 µL serum containing increasing PSA concentrations (black: no PSA; red: 6 nM; green: 12 nM; blue: 24 nM) to a 100 µL solution of Tb and QD antibody conjugates with constant concentrations leads to an increasing FRET sensitization of the QDs (**left:** PL measured in the QD650 detection channel) and an increasing FRET quenching of the Tb (**right:** PL measured in the Tb detection channel). The black QD curve containing no PSA (left) is composed of a short QD component (in the µs range) and a long Tb component (in the ms range) from spectral crosstalk of Tb in the QD detection channel. A new FRET decay time component (in the tens to hundreds of µs range) with increasing intensity (from red to blue) becomes clearly visible once Tb and QD are brought in close proximity due to the antibody-PSA binding. The black Tb curve containing no PSA (right) contains only long-lived Tb emission (no QD PL crosstalk in this channel), which is FRET-quenched (decreased PL intensity) due to antibody-PSA binding.

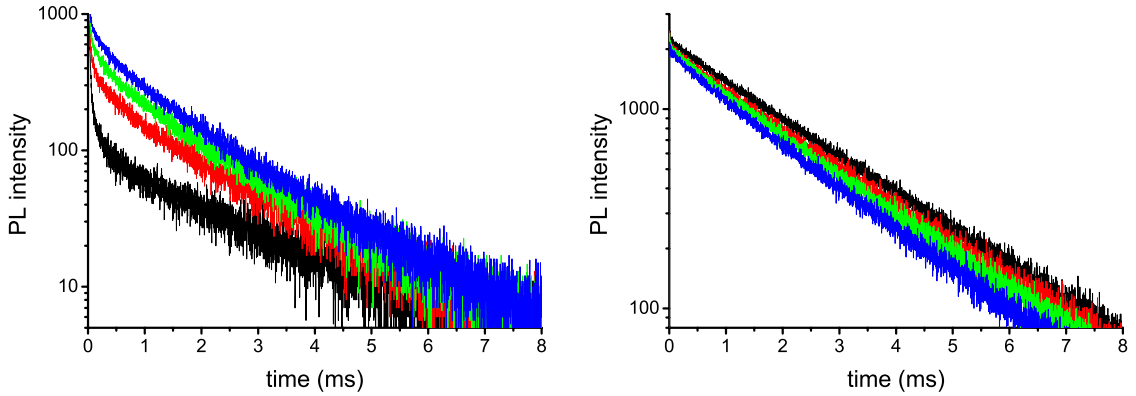

Figure S2: PL decay curves of the (Tb-IgG)-PSA-(QD650-F(ab')$_2$) FRET immunoassays

The addition of 50 µL serum containing increasing PSA concentrations (black: no PSA; red: 6 nM; green: 12 nM; blue: 24 nM) to a 100 µL solution of Tb and QD antibody conjugates with constant concentrations leads to an increasing FRET sensitization of the QDs (**left:** PL measured in the QD650 detection channel) and an increasing FRET quenching of the Tb (**right:** PL measured in the Tb detection channel). The black QD curve containing no PSA (left) is composed of a short QD component (in the µs range) and a long Tb component (in the ms range) from spectral crosstalk of Tb in the QD detection channel. A new FRET decay time component (in the tens to hundreds of µs range) with increasing intensity (from red to blue) becomes clearly visible once Tb and QD are brought in close proximity due to the antibody-PSA binding. The black Tb curve containing no PSA (right) contains only long-lived Tb emission (no QD PL crosstalk in this channel), which is FRET-quenched (decreased PL decay time) due to antibody-PSA binding.

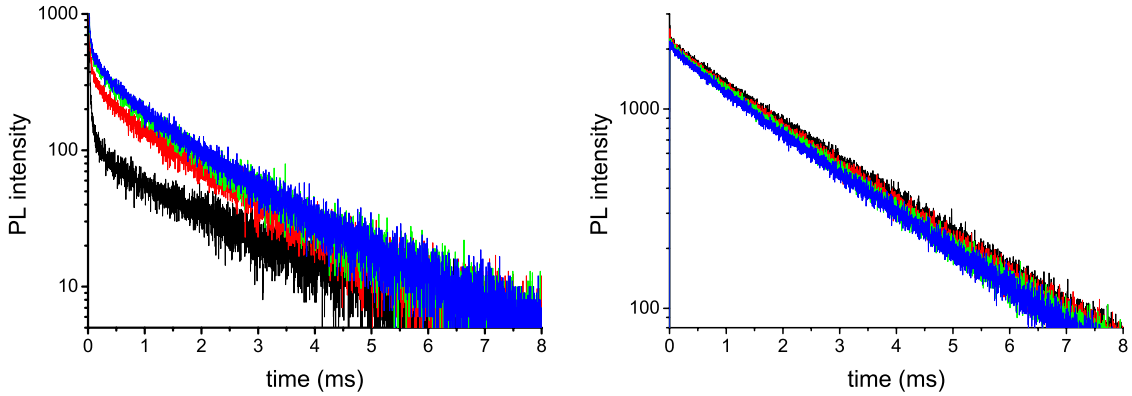

Figure S3: PL decay curves of the (Tb-IgG)-PSA-(QD650-F(ab)) FRET immunoassays

The addition of 50 µL serum containing increasing PSA concentrations (black: no PSA; red: 6 nM; green: 12 nM; blue: 24 nM) to a 100 µL solution of Tb and QD antibody conjugates with constant concentrations leads to an increasing FRET sensitization of the QDs (**left:** PL measured in the QD650 detection channel) and an increasing FRET quenching of the Tb (**right:** PL measured in the Tb detection channel). The black QD curve containing no PSA (left) is composed of a short QD component (in the µs range) and a long Tb component (in the ms range) from spectral crosstalk of Tb in the QD detection channel. A new FRET decay time component (in the tens to hundreds of µs range) with increasing intensity (from red to blue) becomes clearly visible once Tb and QD are brought in close proximity due to the antibody-PSA binding. The black Tb curve containing no PSA (right) contains only long-lived Tb emission (no QD PL crosstalk in this channel), which is FRET-quenched (decreased PL decay time) due to antibody-PSA binding.

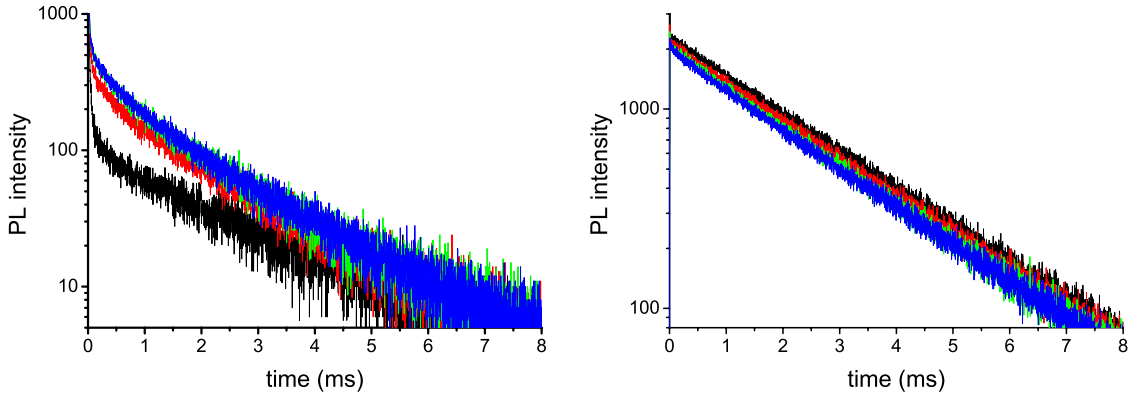

Figure S4: PL decay curves of the (Tb-F(ab))-PSA-(QD650-F(ab)) FRET immunoassays

The addition of 50 µL serum containing increasing PSA concentrations (black: no PSA; red: 6 nM; green: 12 nM; blue: 24 nM) to a 100 µL solution of Tb and QD antibody conjugates with constant concentrations leads to an increasing FRET sensitization of the QDs (**left:** PL measured in the QD650 detection channel) and an increasing FRET quenching of the Tb (**right:** PL measured in the Tb detection channel). The black QD curve containing no PSA (left) is composed of a short QD component (in the µs range) and a long Tb component (in the ms range) from spectral crosstalk of Tb in the QD detection channel. A new FRET decay time component (in the tens to hundreds of µs range) with increasing intensity (from red to blue) becomes clearly visible once Tb and QD are brought in close proximity due to the antibody-PSA binding. The black Tb curve containing no PSA (right) contains only long-lived Tb emission (no QD PL crosstalk in this channel), which is FRET-quenched (decreased PL intensity) due to antibody-PSA binding.

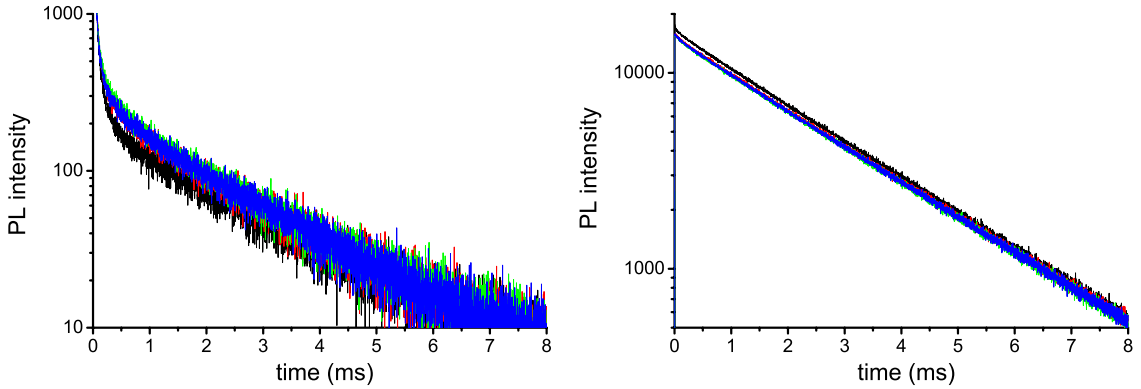

Figure S5: PL decay curves of the (Tb-IgG)-PSA-(QD605-IgG) FRET immunoassays

The addition of 50 µL serum containing increasing PSA concentrations (black: no PSA; red: 6 nM; green: 12 nM; blue: 24 nM) to a 100 µL solution of Tb and QD antibody conjugates with constant concentrations leads to an increasing FRET sensitization of the QDs (**left:** PL measured in the QD605 detection channel) and an increasing FRET quenching of the Tb (**right:** PL measured in the Tb detection channel). The black QD curve containing no PSA (left) is composed of a short QD component (in the µs range) and a long Tb component (in the ms range) from spectral crosstalk of Tb in the QD detection channel. A new FRET decay time component (in the ms range) with increasing intensity (from red to blue) becomes clearly visible once Tb and QD are brought in close proximity due to the antibody-PSA binding. The black Tb curve containing no PSA (right) contains only long-lived Tb emission (no QD PL crosstalk in this channel), which is FRET-quenched (decreased PL intensity) due to antibody-PSA binding.

6.3.4 Nanobodies for EGFR detection

Original publication:

Nanobodies and Nanocrystals: Highly Sensitive Quantum Dot-based Homogeneous FRET Immunoassay for Serum-based EGFR Detection.

K. D. Wegner, S. Lindén, Z. Jin, T. L. Jennings, R. el Khoulati, P. M. P. van Bergen en Henegouwen, and N. Hildebrandt.

Small **2014**, 10 (4), 734-740.

Nanobodies and Nanocrystals: Highly Sensitive Quantum Dot-Based Homogeneous FRET Immunoassay for Serum-Based EGFR Detection

*K. David Wegner, Stina Lindén, Zongwen Jin, Travis L. Jennings, Rachid el Khoulati, Paul M. P. van Bergen en Henegouwen, and Niko Hildebrandt**

Semiconductor quantum dot nanocrystals (QDs) for optical biosensing applications often contain thick polyethylene glycol (PEG)-based coatings in order to retain the advantageous QD properties in biological media such as blood, serum or plasma. On the other hand, the application of QDs in Förster resonance energy transfer (FRET) immunoassays, one of the most sensitive and most common fluorescence-based techniques for non-competitive homogeneous biomarker diagnostics, is limited by such thick coatings due to the increased donor-acceptor distance. In particular, the combination with large IgG antibodies usually leads to distances well beyond the common FRET range of approximately 1 to 10 nm. Herein, time-gated detection of Tb-to-QD FRET for background suppression and an increased FRET range is combined with single domain antibodies (or nanobodies) for a reduced distance in order to realize highly sensitive QD-based FRET immunoassays. The "(nano)^2" immunoassay (combination of nanocrystals and nanobodies) is performed on a commercial clinical fluorescence plate reader and provides sub-nanomolar (few ng/mL) detection limits of soluble epidermal growth factor receptor (EGFR) in 50 µL buffer or serum samples. Apart from the first demonstration of using nanobodies for FRET-based immunoassays, the extremely low and clinically relevant detection limits of EGFR demonstrate the direct applicability of the (nano)$^{2-}$ assay to fast and sensitive biomarker detection in clinical diagnostics.

1. Introduction

Semiconductor quantum dots (QDs) continue to be of large interest for spectrally and temporally multiplexed biosensing because they provide high photostability, bright fluorescence, size-tunable absorption and emission wavelengths and a large surface area for attaching several biomolecules of the same or different kind.[1–5] Functional bioconjugation of QDs in particular, preserving both the QD photophysical properties and the binding properties of the biomolecule, has been widely investigated.[6–8]

Antibodies are among the most applied tools for biomolecular detection and targeted therapy, and are therefore one of the most important biomolecules for QD-bioconjugation. However, the large size of full IgG antibodies (ca. 150 kDa molecular weight and 14.5 × 8.5 × 4 nm dimension)[9] and the different possible antibody attachment groups for bioconjugation[10] are disadvantageous for labeling many antibodies in a controlled manner to a QD. To overcome this problem single domain antibodies (also called "nanobodies" or V_HH) have been proposed for QD conjugation.[11–14]

K. D. Wegner, S. Lindén, Dr. Z. Jin, Prof. N. Hildebrandt
NanoBioPhotonics
Institut d'Electronique Fondamentale
Université Paris-Sud, 91405 Orsay Cedex, France
E-mail: niko.hildebrandt@u-psud.fr
Dr. T. L. Jennings
eBioscience, Inc., 10255 Science Center Drive
San Diego, California, 92121, USA
R. el Khoulati, Dr. P. M. P. van Bergen en Henegouwen
Cell Biology, Department of Biology, Science Faculty
Utrecht University, Utrecht, The Netherlands

DOI: 10.1002/smll.201302383

NANO MICRO small

V_HH are single domain antigen binding fragments of heavy chain antibodies (ca. 15 kDa and 4 × 2.5 × 3 nm)[15] that were first discovered in Camelus dromedarius.[16] To date, they are established functional biomolecules that can be easily selected, produced, and manipulated using standard molecular biology techniques. V_HHs can be found in many antibody-based applications including the detection of different targets such as toxins, haptens, bacteria, viruses, and cellular biomarkers.[12,15,17–20]

Despite the many advantages of nanobodies, they have never been applied in non-competitive homogeneous immunoassays, which do not require any washing or separation steps (simple mix-and-measure method) and are therefore highly important for rapid and sensitive biosensing.[21] Förster resonance energy transfer (FRET) is one of the most sensitive and most common fluorescence-based techniques for such homogeneous immunoassays.[21] As FRET is strongly distance dependent, the use of the small V_HHs for FRET sandwich immunoassays appears to be very advantageous. Nabiev et al. have recently developed compact QD-V_HH conjugates, which could be successfully used in flow cytometry and fluorescence immunostaining and were also proposed as promising probes for FRET-based biosensing.[12]

Here we show for the first time that such QD-V_HH conjugates can indeed be efficiently applied for homogeneous FRET-based biosensing. We selected a challenging sandwich immunoassay, in which two V_HH bind non-competitively to different epitopes of the ectodomain of the epidermal growth factor receptor (EGFR) in order to detect soluble EGFR in serum samples. This is of high interest for the prognosis and diagnosis of cancer.[22–24] The assay is not only challenging in the sense of high sensitivity (ng/mL limits of detection, LODs) and the measurement in serum (required for clinical diagnostics). As we use commercial QDs with a thick polyethylene glycol (PEG)-based coating (ca. 7 nm QD radius),[25] two V_HH (ca. 4 nm length per V_HH, vide supra) and a large EGFR dimer (ca. 190 kDa; V_HHs specific against domain I and III at ca. 4 nm distance) the overall distance for FRET is expected to be larger than 10 nm (7 nm + 4 nm + 4 nm + 4 nm = 19 nm in the case of maximum elongation), which is beyond the distance range of conventional FRET pairs.[26] We therefore used time-gated detection of FRET from Tb-complexes to QDs, which allows Förster distances (donor-acceptor distance for which FRET is 50% efficient) of up to 11 nm.[27] Our assay, which we have coined "(nano)^2", is performed on a clinical fluorescence plate reader and provides sub-nanomolar (few ng/mL) LODs of soluble EGFR in 50 µL buffer or serum samples. Our results demonstrate the suitability of QD-V_HH-based FRET for sensitive biosensing in challenging environments (serum) and the direct application to homogeneous serum-based biomarker detection in clinical diagnostics.

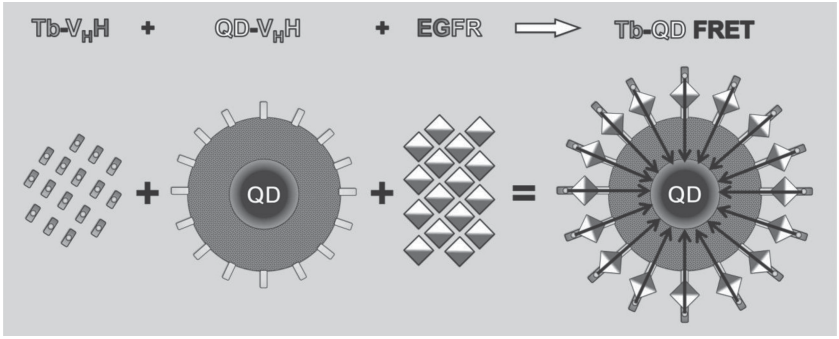

Scheme 1. Principle of the homogeneous (nano)^2-immunoassay. The combination of Tb-labeled V_HH and V_HH-labeled QDs allows the formation of Tb-V_HH-EGFR-QD-V_HH sandwich complexes, which results in FRET from several Tb to the central QD. Time-gated detection of FRET-sensitized QD photoluminescence is used for a sensitive quantification of soluble EGFR in serum. Random labeling and orientation of the V_HH is not taken into account in the Scheme.

2. Results and Discussion

The principle of the (nano)^2-immunoassay is shown in **Scheme 1**. 50 µL of each Tb-V_HH and QD-V_HH conjugate solutions are mixed at constant concentrations to yield 100 µL of assay solution. Two different anti-EGFR V_HH, which bind to two different non-overlapping epitopes on the ectodomain of EGFR, are used for Tb and QD. Commercial Tb-complexes (Lumi4®-Tb-NHS, Lumiphore, Inc.) and QDs (eFluor 650NC antibody conjugation kit, eBioscience) were used for bioconjugation. The broad spectral overlap of Tb-emission and QD-absorbance (**Figure 1**) leads to a large Förster distance calculated as $R_0 = 0.02108\ (\kappa^2\ \Phi_{Tb}\ n^{-4}\ J)^{1/6}$ nm = 11.0 ± 0.5 nm, with the FRET orientation factor κ^2 = 2/3, the Tb-centered luminescence quantum yield $\Phi_{Tb} = 0.67 \pm 0.5$, the refractive index $n = 1.35$ and the spectral overlap integral $J = \int F_{Tb}\ \varepsilon_{QD}\ \lambda^4\ d\lambda$ (from 450 to 700 nm). This very large

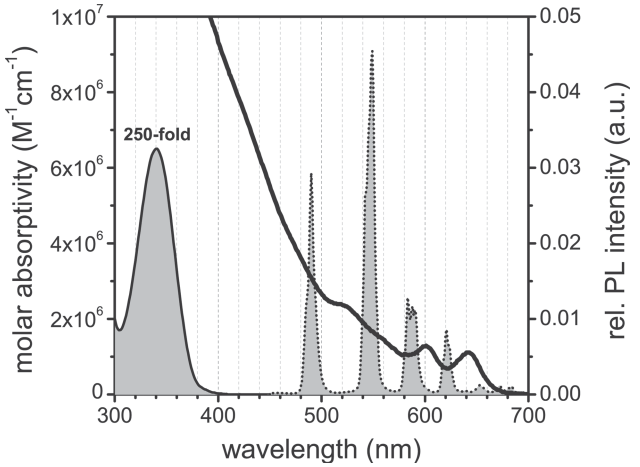

Figure 1. Molar absorptivity spectra of the Tb donor (ε_{Tb}, black curve with gray background, multiplied by 250) and QD acceptor (ε_{QD}, black curve). For the calculation of the overlap integral *J* between Tb-donor emission and QD-acceptor absorption, the area normalized Tb photoluminescence (PL) spectrum (F_{Tb}, black dotted curve with gray background) is also shown.

R_0 value allows for long-distance FRET beyond the common limit of ca. 10 nm, a necessary requirement for our large QD-based sandwich immunoassay system.

As a result of the small V_HH size, the labeling ratio of Tb per nanobody is relatively low (ca. 1.5 Tb/V_HH) and the labeling ratio of nanobody per QD is relatively high (ca. 30 V_HH/QD). This conjugation feature has two main advantages: 1) the free V_HH can be easily separated from the large QDs by using convenient spin-column purification; and 2) many V_HH will be available on the QD surface for EGFR-binding. After addition of EGFR-containing buffer or serum samples (50 µL) to the assay solution, the specific recognition of EGFR by the two different V_HH leads to the formation of FRET sandwich immunocomplexes consisting of one QD and several Tb (Scheme 1, right). With so many Tb-donors surrounding, this configuration leads to an increased probability of FRET sensitization and therefore a higher FRET-sensitized photoluminescence (PL) intensity per QD.[28]

Within the detection setup, pulsed UV light (337 nm) is applied and excites both the Tb-donors and the QD-acceptors (see Figure 1). Both fluorophores begin the process in an electronically excited state. However, the QD's PL decay is ~100 000× faster than for the Tb emitters (PL lifetimes of ~20 ns vs ~2 ms). By simply delaying the collection window by 0.1 ms (~5000 × the QD PL lifetimes), all QDs have decayed to the ground state and no further observed QD-emission may originate from direct excitation. At the same time, more than 95 % Tb are still in their excited state after 0.1 ms (considering an exponential decay and a PL lifetime of ~2 ms) and efficient FRET can occur from the associated Tb donors to the QD as ground-state acceptor. Time-gated (nearly background fluorescence-free) PL of the QD-acceptor and the Tb-donor are simultaneously detected in two detection channels using transmission filters for wavelength separation (see **Figure 2**).

Measuring the QD-acceptor PL decays (**Figure 3**) and the time-gated PL intensities (integration in a time-window from 0.1 to 0.9 ms, **Figure 4**) shows significant FRET sensitization with increasing EGFR concentration. The QD-acceptor decay curves reveal some interesting aspects about the (nano)^2-immunoassay, which are related to the use of V_HH. The mixture of Tb-V_HH and QD-V_HH (assay solution without any EGFR) already shows significant FRET. This becomes clear by comparing the thick black curve (50 µL Tb-V_HH + 50 µL QD-V_HH + 50 µL buffer, no EGFR) with the thick gray curve (mathematical sum of [50 µL Tb-V_HH + 100 µL buffer] and [50 µL QD-V_HH + 100 µL buffer], no EGFR) in Figure 3a. The gray curve contains only the pure QD component (dotted curve with a short decay time) and the pure Tb component (dotted curve with a long decay time). The black curve has a much stronger intensity (FRET-sensitization) and contains a new decay time component, which is significantly longer than the pure QD and shorter than the pure Tb component (strong evidence for FRET from Tb to QD). Although camelid V_HHs are known to have a higher solubility than human V_H fragments,[29] our first assumption was that hydrophobic interaction or V_HH dimerization[30] could lead to a partial V_HH aggregation and Tb-to-QD FRET when both Tb-V_HH and QD-V_HH are present in the same sample. However, addition of excess of free V_HH (in order decrease the fraction of Tb-V_HH+QD-V_HH in close distance within such aggregates) and the addition of Tween-20 (in order to decrease hydrophobic interactions) did not lead to any significant changes (see Supporting Information). Another possibility of such "pre-FRET" is related to non-specific binding caused by the 0.5 % BSA in all samples. In fact, control experiments without BSA and different amounts of BSA revealed a significant influence of BSA on the "pre-FRET" signal (see Supporting Information). We assume that BSA-induced non-specific binding can bring a small fraction of Tb-V_HH and QD-V_HH in close proximity, which leads to this "pre-FRET" effect even without EGFR. As the (nano)^2-immunoassay aims at biomarker detection in serum samples we retained the 0.5 % of BSA (ca. 76 µM), which saturates non-specific binding (e.g. to the walls of the microplate wells and to human serum albumin in the serum samples) and assures stable assay conditions.

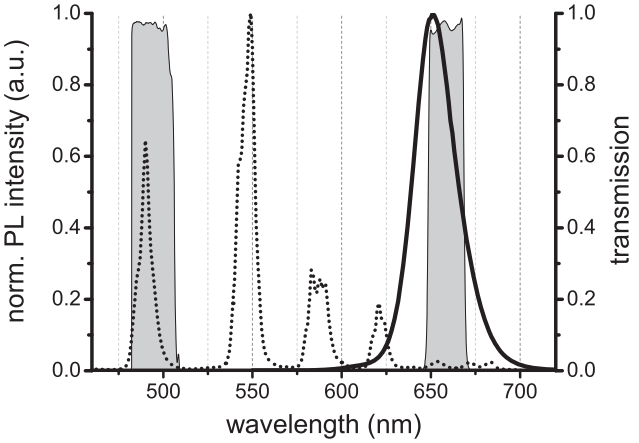

Figure 2. PL intensity spectra of Tb-V_HH (black dotted) and QD-V_HH (black) conjugates normalized to unity at their respective maxima. The gray spectra in the background define the transmission of the optical bandpass filters within the Tb (494 ± 20 nm) and QD (660 ± 13 nm) detection channels.

Despite this "pre-FRET" in the mixture without EGFR, the addition of EGFR leads to further FRET sensitization (thin black curves in Figure 3a) showing another new decay time component. This decay time is longer than the component from the non-specific binding-induced "pre-FRET" as indicated in Figure 3b. Taking into account the smaller size of BSA (ca. 66 kDa vs. ca. 190 kDa for EGFR) and the fact that non-specific binding between V_HH and BSA can occur over the complete surface of the BSA (compared to the specific binding of the V_HH to two defined epitopes of EGFR), the longer decay time for specific EGFR binding is most probably caused by a larger distance (see **Scheme 2**). A larger distance r leads to a lower FRET efficiency η_{FRET}, which results in a longer decay time τ_{DA} $[R_0^6/(R_0^6 + r^6) = \eta_{FRET} = 1 - \tau_{DA}/\tau_D]$. It should be noted that the BSA concentration is ca. 7600 times higher than the V_HH concentrations (76 µM vs. 10 nM), which should lead to a low probability of QD-V_HH and Tb-V_HH binding. However, taking into account that the largest part of BSA will bind to the walls of the microplate

NANO MICRO small

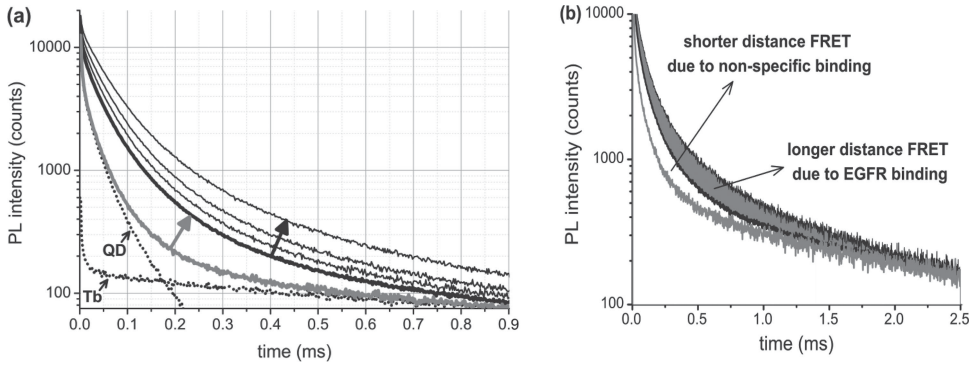

Figure 3. (a) QD detection channel PL decay curves of: gray = mathematical sum of (50 µL Tb-V_HH + 100 µL buffer, dotted Tb curve) + (50 µL QD-V_HH + 100 µL buffer, dotted QD curve); black from bottom to top = (50 µL of 0 nM, 0.6 nM, 1.5 nM or 6 nM EGFR) + (50 µL Tb-V_HH) + (50 µL QD-V_HH). The gray and black arrows indicate FRET sensitization due to non-specific binding ("pre-FRET") and EGFR binding, respectively. (b) Non-specific binding via BSA causes a faster decay (illustrated by the white area) compared to specific binding via EGFR (gray area) due to shorter Tb-QD distances for non-specific binding (see Scheme 2).

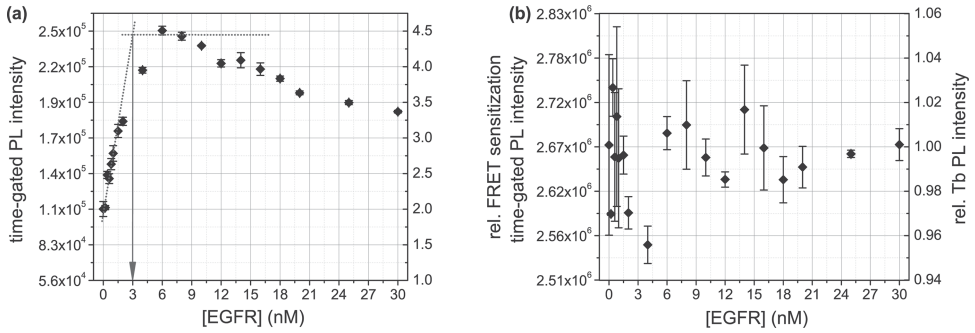

Figure 4. Time-gated PL intensity (integration from 0.1 to 0.9 ms) in the QD detection channel (a) and in the Tb detection channel (b) as a function of EGFR concentration. The QD PL shows FRET sensitization until binding saturation (indicated by the gray arrow) followed by a PL intensity decrease (hook effect). Tb-quenching is not detectable (maximum changes ±6% without specific direction) due to a large fraction of Tb-V_HH, which do not participate in FRET, and a relatively low FRET efficiency.

wells and that the "pre-FRET" sensitization is ca. 4.5-times smaller than FRET sensitization due to EGFR binding (Figure 4a), a small fraction of Tb and QD might still be brought into proximity as suggested in Scheme 2.

Although a detailed time-resolved study would be necessary to find the exact decay times of the FRET components, the FRET sensitization due to Tb-V_HH-EGFR-QD-V_HH binding displays significantly shorter decay time components (more efficient FRET) compared to sandwich assays realized with full IgG antibodies or F(ab')$_2$ and F(ab) fragments, as we have demonstrated for prostate specific antigen immunoassays using the same Tb-to-QD FRET system.[31] This more efficient FRET for the V_HH-based system demonstrates that the shorter nanobodies can indeed realize shorter distances within FRET immunoassays.

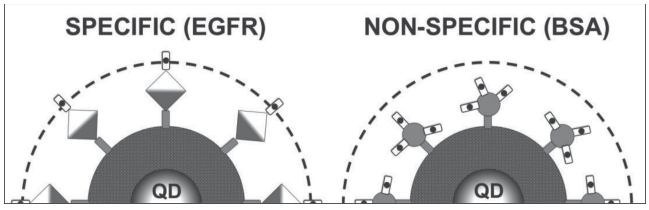

Scheme 2. Tb-donors (small black dots) to QD-acceptor distance comparison for specific (via EGFR, left) and non-specific (via BSA, right) binding, indicating a shorter Tb-to-QD distance for non-specific binding. Randomly oriented binding and multiple QDs per BSA (due to non-specific binding) are omitted for clarity.

Another interesting aspect can be found in the time-gated QD PL intensities (Figure 4). The FRET sensitization increases linearly with EGFR concentration until it levels off at a concentration of approximately 3 nM of EGFR (in the 50 µL sample), which corresponds to ca. 1 nM (1/3 of 150 µL) in the total assay volume. The V_HH concentration is ca. 2.7 nM (1/3 of 8 nM V_HH in the 50 µL Tb-V_HH solution) and 5 nM (1/3 of 15 nM V_HH in the 50 µL QD-V_HH solution) for Tb and QD, respectively. Thus, the concentration of binding saturation is approximately 3 or 5 times lower than the V_HH concentrations. The V_HH concentration for the QDs was chosen higher than for Tb because there are ca. 30 V_HH on one QD and not all of them will be available for EGFR binding due to random orientation. Moreover, with this high labeling ratio (leading to a QD concentration of ca. 0.17 nM in the assay) it can be assumed that the large majority of QDs will take part in FRET at the saturation concentration of ca.

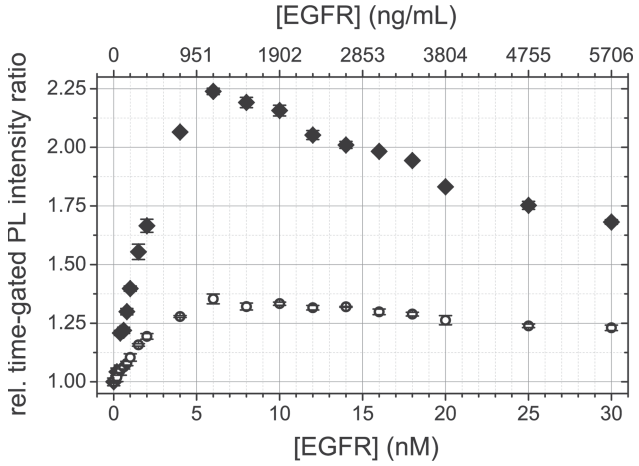

Figure 5. Calibration curves of the (nano)^2-immunoassays using 50 µL buffer (rhombi) or serum (circles) samples. The time-gated (0.1–0.9 ms) PL intensity ratios (normalized to unity for EGFR-free samples) increase with increasing EGFR concentration until the Tb-V_HH-EGFR-QD-V_HH binding is saturated and no further FRET sensitization occurs. Both curves were acquired using the same experimental conditions. The LODs (within the 50 µL samples) are 0.12 nM (23 ng/mL or 6 fmol) and 0.18 nM (34 ng/mL or 9 fmol) for buffer and serum samples, respectively.

1 nM EGFR. On the other hand there is a large fraction (ca. 2/3) of the 2.7 nM Tb-V_HH, which do not take part in binding, possibly due to non-functional V_HH and non-specific binding. Taking into account a relatively low FRET efficiency (due to the large donor-acceptor distance) per Tb-donor on the one hand and a high fraction of Tb-V_HH per QD (see Scheme 1) on the other hand, this situation leads to minimal FRET-quenching of the Tb PL intensity (Figure 4b) but significant FRET sensitization of time-gated QD PL (Figure 4a). In fact this is one of the big advantages of measuring FRET sensitization (small increasing signal against low background) instead of FRET quenching (small decreasing signal against high background). Apart from this behavior (Figure 4) the assay is also showing the so-called hook effect, for which the FRET sensitization decreases after binding saturation because higher EGFR concentrations lead to the formation of single Tb-V_HH-EGFR or QD-V_HH-EGFR complexes and therefore less donor-acceptor pairs.

In order to evaluate the diagnostic performance of the (nano)^2-immunoassay we determined the limits of detection (LODs) for soluble EGFR in buffer and serum. We therefore performed simultaneous time-gated (0.1–0.9 ms) detection of the Tb-donor and the QD-acceptor PL intensities on a KRYPTOR compact plus clinical fluorescence plate reader using 18 different EGFR concentrations ranging from 0.2 to 30 nM. The FRET ratio (time-gated PL from the QD-channel and the Tb-channel) was used for the acquisition of assay calibration curves in serum or buffer (**Figure 5**). Although the buffer-based measurements show a stronger FRET ratio increase compared to the serum measurements, both lead to typical immunoassay calibration curves with an increasing signal as a function of biomarker concentration followed by a decreasing FRET ratio after binding saturation (hook effect). The LODs were determined by using the corresponding concentration of the average FRET ratio plus three times its standard deviation (30 measurements) for the EGFR-free samples. Both buffer and serum measurements resulted in sub-nanomolar LODs (0.12 nM or 23 ng/mL EGFR for buffer and 0.18 nM or 34 ng/mL EGFR for serum) within the 50 µL samples (LODs within the total 150 µL measuring volume are three times lower). These LODs are below the recommended cut-off level of 45 ng/mL and well in the concentration range for revealing relevant clinical information.[23,24]

3. Conclusion

In conclusion we have demonstrated for the first time a homogeneous V_HH-based FRET immunoassay, which uses Tb-to-QD energy transfer. The (nano)^2-immunoassay requires relatively short incubation times (ca. 1h), does not need any washing and separation steps (simple mix-and-measure procedure), is measured quickly (5 s per sample) and ratiometrically (low coefficients of variation), and time-gated detection (void of autofluorescence background and directly excited QDs) allows sub-nanomolar detection limits of EGFR (in both buffer or serum), which is in a relevant clinical range of EGFR serum levels for cancer diagnostics. This proof-of-principle for very sensitive V_HH-based FRET biosensing in combination with the fast, easy and inexpensive production of ultra-small V_HH antibodies (compared to monoclonal IgG antibodies), the possibility of oriented V_HH conjugation, and the unrivaled optical properties of QDs for sensitive and multiplexed biomarker detection will make our (nano)^2-immunoassay a valuable tool for future in vitro diagnostics and other FRET-based biosensing applications in imaging and spectroscopy.

4. Experimental Section

Nanobodies binding to EGFR (EgA1 and EgB4)[32] were produced as described elsewhere.[20] In brief, single bacterial clones were picked, grown in 2xTY containing 100 g/ml ampicillin and 0.1% (w/v) glucose and nanobody-expression was induced by the addition of IPTG. After four hours of induction, bacteria were harvested by centrifugation (2000 rpm, 15 min) and the pellet was frozen overnight at −20 °C. Cells were thawed, re-suspended in PBS and the nanobodies were purified form the periplasmic fraction by IMAC using TALON beads. The nanobodies show high affinity binding after fluorophore conjugation.[19]

eFluor 650 Nanocrystal Conjugation Kit – Sulfhydryl Reactive (provided by eBioscience in lyophilized form) was used for QD conjugation. Prior to conjugation, protected sulfhydryl groups (N-Succinimidyl S-Acetylthioacetate) were introduced to V_HH (EgB4) at 5× molar excess using SATA kit (Thermo Fisher Scientific). The sulfhydryl groups were deprotected by diacylation according to the manufacurer's protocol. Sulfhydryl-activated V_HH solutions (in concentration excess compared to the QD solutions) were prepared in 1 × PBS and conjugated to QDs according to manufacturer's instructions. Unbound V_HH were separated by washing 3–6 times in 100 kDa molecular weight cutoff (MWCO) spin-columns (Millipore) using 100 mM sodium-tetraborate (pH

8.3) as the wash buffer. QD concentrations were determined by absorbance measurements using a molar absorptivity of 1.1×10^6 $M^{-1}cm^{-1}$ (at 641 nm) for QD650. V_HH were quantified by absorbance measurements at 280 nm using a molar absorptivity of 35 800 M^{-1} cm^{-1}. The labeling ratios were determined by linear combination of the respective absorbance values of QDs and V_HH within the QD-V_HH conjugates.

Lumi4-Tb-NHS[33] (provided by Lumiphore in lyophilized form) was dissolved to 8 mM in anhydrous DMF and mixed (in concentration excess to the V_HH) with the V_HH (EgA1) solutions in 100 mM carbonate buffer at pH 9.0. The mixtures were incubated rotating at 25 rpm (Intelli-Mixer, ELMI) for two hours at room temperature. For Tb-V_HH conjugate purification the samples were washed 4–6 times with 3 kDa MWCO spin-columns (Millipore) using 100 mM TRIS/Cl (pH 7.2) as the wash buffer. Tb concentrations were determined by absorbance measurements at 340 nm using a molar absorptivity of 26 000 $M^{-1}cm^{-1}$ as provided by the manufacturer. The labeling ratios were determined by linear combination of the respective absorbance values of Tb and V_HH within the Tb-V_HH conjugates.

The Tb- and QD-V_HH conjugates were each dissolved in 50 µL 10 mM TRIS/Cl-buffer (pH 7.4) containing 0.5 % bovine serum albumin (BSA, Sigma-Aldrich). The concentrations in these 50 µL solutions were approximately 8 nM V_HH (12 nM Tb using the labeling ratio of 1.5 Tb/V_HH) for the Tb-V_HH and 15 nM V_HH (0.5 nM QD using the labeling ratio of 30 V_HH/QD) for the QD-V_HH. 50 µL buffer or serum samples containing soluble EGFR were prepared from a stock solution of 100 µg/mL EGFR in sterile PBS (R&D Systems) by dilution with 10 mM TRIS/Cl-buffer (pH 7.4) containing 0.5 % BSA or purified new born calf serum (provided by Cezanne/Thermo Fisher Scientific) to yield the desired EGFR concentrations. These EGFR samples with different concentrations were added to the 100 µL assay solutions containing both the Tb-V_HH and QD-V_HH conjugates. Time-resolved and time-gated PL intensity measurements (Figures 3 and 4) were acquired on a KRYPTOR compact plus fluorescence plate reader (Cezanne/Thermo Fisher Scientific) using 475 detection bins of 2 µs integration time and nitrogen laser excitation. Optical transmission filter bandpass wavelengths were (494 ± 20) nm (Semrock) for the Tb detection channel and (660 ± 13) nm (Semrock) for the QD detection channel. Longer time-resolved PL intensity measurements (Figure 3b) were acquired on an EI fluorescence plate reader (Edinburgh Instruments) using 4000 detection bins of 2 µs integration time and nitrogen laser (VSL 337 ND, Spectra Physics) excitation (337.1 nm, 20 Hz). All FRET assays were measured in black 96-well microtiter plates with an optimal working volume of 150 µL. Each sample containing EGFR was prepared three times and the EGFR-free samples were prepared ten times. All samples were measured in triplicates. After sample preparation the microtiter plates were incubated for 60 min at 37 °C before measurements.

Absorption spectra (Lambda 35 UV–vis System, PerkinElmer) and emission spectra (FluoTime 300, PicoQuant) were recorded in TRIS/Cl (Sigma Aldrich) with a pH of 7.4 and sodium-tetraborate with a pH of 8.5 (Sigma Aldrich) for Tb and QD samples, respectively. PL quantum yields and Förster distances were acquired as described elsewhere.[25] PL decay curves were acquired directly from the FRET immunoassay samples on the KRYPTOR and EI fluorescence plate readers.

Supporting Information

Supporting Information is available from the Wiley Online Library or from the author.

Acknowledgement

We thank Lumiphore, Inc. for the gift of Lumi4®-Tb-NHS reagent and the European Commission (FP7 project NANOGNOSTICS), the European Innovative Medicines Initiative IMI (project OncoTrack), the Investissements d'Avenir Program France (project NanoCTC), the Agence National de la Recherche France (project NanoFRET), and Stichting STOPhersentumoren.nl for financial support.

[1] S. J. Rosenthal, J. C. Chang, O. Kovtun, J. R. McBride, I. D. Tomlinson, *Chem. Biol.* **2011**, *18*, 10–24.
[2] H. Kuang, Y. Zhao, W. Ma, L. Xu, L. Wang, C. Xu, *Trac – Trend. Anal. Chem.* **2011**, *30*, 1620–1636.
[3] B. Hötzer, I. L. Medintz, N. Hildebrandt, *Small* **2012**, *8*, 2297–2326.
[4] Z. Jin, N. Hildebrandt, *Trends Biotechnol.* **2012**, *30*, 394–403.
[5] E. Petryayeva, W. R. Algar, I. L. Medintz, *Appl. Spectrosc.* **2013**, *67*, 215–252.
[6] W. R. Algar, D. E. Prasuhn, M. H. Stewart, T. L. Jennings, J. B. Blanco-Canosa, P. E. Dawson, I. L. Medintz, *Bioconjugate Chem.* **2011**, *22*, 825–858.
[7] N. Erathodiyil, J. Y. Ying, *Accounts Chem. Res.* **2011**, *44*, 925–935.
[8] S. Jiang, K. Y. Win, S. Liu, C. P. Teng, Y. Zheng, M.-Y. Han, *Nanoscale* **2013**, *5*, 3127–3148.
[9] A. G. Amit, R. A. Mariuzza, S. E. V. Phillips, R. J. Poljak, *Science* **1986**, *233*, 747–753.
[10] G. T. Hermanson, *Bioconjugate Techniques*, 2nd ed., Academic Press, San Diego **2008**.
[11] K. Boeneman Gemmill, J. R. Deschamps, J. B. Delehanty, K. Susumu, M. H. Stewart, R. H. Glaven, G. P. Anderson, E. R. Goldman, A. L. Huston, I. L. Medintz, *Bioconjugate Chem.* **2013**, *24*, 269–281.
[12] A. Sukhanova, K. Even-Desrumeaux, A. Kisserli, T. Tabary, B. Reveil, J. M. Millot, P. Chames, D. Baty, M. Artemyev, V. Oleinikov, M. Pluot, J. H. M. Cohen, I. Nabiev, *Nanomed. Nanotechnol.* **2012**, *8*, 516–525.
[13] M. B. Zaman, T. N. Baral, Z. J. Jakubek, J. B. Zhang, X. H. Wu, E. Lai, D. Whitfield, K. Yu, *J. Nanosci. Nanotechnol.* **2011**, *11*, 3757–3763.
[14] S. T. Low-Nam, K. A. Lidke, P. J. Cutler, R. C. Roovers, P. M. P. van Bergen en Henegouwen, B. S. Wilson, D. S. Lidke, *Nat. Struct. Mol. Biol.* **2011**, *18*, 1244–1249.
[15] A. de Marco, *Microb. Cell Fact.* **2011**, *10*, 44.
[16] C. Hamers-Casterman, T. Atarhouch, S. Muyldermans, G. Robinson, C. Hamers, E. B. Songa, N. Bendahman, R. Hamers, *Nature* **1993**, *363*, 446–448.
[17] G. P. Anderson, R. D. Bernstein, M. D. Swain, D. Zabetakis, E. R. Goldman, *Anal. Chem.* **2010**, *82*, 7202–7207.
[18] J. Wesolowski, V. Alzogaray, J. Reyelt, M. Unger, K. Juarez, M. Urrutia, A. Cauerhff, W. Danquah, B. Rissiek, F. Scheuplein, N. Schwarz, S. Adriouch, O. Boyer, M. Seman, A. Licea, D. V. Serreze, F. A. Goldbaum, F. Haag, F. Koch-Nolte, *Med. Microbiol. Immunol.* **2009**, *198*, 157–174.

[19] S. Oliveira, G. A. M. S. van Dongen, M. Stigter-van Walsum, R. C. Roovers, J. C. Stam, W. Mali, P. J. van Diest, P. M. P. van Bergen en Henegouwen, *Mol. Imag.* **2012**, *11*, 33–46.
[20] R. C. Roovers, T. Laeremans, L. Huang, S. De Taeye, A. J. Verkleij, H. Revets, H. J. de Haard, P. M. P. van Bergen en Henegouwen, *Cancer Immunol. Immunol.* **2007**, *56*, 303–317.
[21] D. Wild, *The Immunoassay Handbook*, 4th ed., Elsevier, Amsterdam **2013**.
[22] A. A. Ghazani, S. McDermott, M. Pectasides, M. Sebas, M. Mino-Kenudson, H. Lee, R. Weissleder, C. M. Castro, *Nanomed. Nanotechnol.* **2013**, DOI: 10.1016/j.nano.2013.03.011.
[23] K. S. Asgeirsson, A. Agrawal, C. Allen, A. Hitch, I. O. Ellis, C. Chapman, K. L. Cheung, J. F. R. Robertson, *Breast Cancer Res.* **2007**, *9*(6), R75.
[24] V. Müller, I. Witzel, K. Pantel, S. Krenkel, H. J. Lück, R. Neumann, T. Keller, I. Dittmer, F. Jänicke, C. Thomssen, *Anticancer Res.* **2006**, *26*, 1479–1487.
[25] K. D. Wegner, P. T. Lanh, T. Jennings, E. Oh, V. Jain, S. M. Fairclough, J. M. Smith, E. Giovanelli, N. Lequeux, T. Pons, N. Hildebrandt, *ACS Appl. Mater. Interfaces* **2013**, *5*, 2881–2892.
[26] J.R. Lakowicz, *Principles of Fluorescence Spectroscopy*, 3rd ed., Springer, New York **2006**.
[27] D. Geißler, L. J. Charbonnière, R. F. Ziessel, N. G. Butlin, H.-G. Löhmannsröben, N. Hildebrandt, *Angew. Chem. Int. Ed.* **2010**, *49*, 1396–1401.
[28] L. J. Charbonnière, N. Hildebrandt, *Eur. J. Inorg. Chem.* **2008**, 3241–3251.
[29] S. Muyldermans, *Annu. Rev. Biochem.* **2013**, *82*, 17.1–17.23.
[30] G. J. Sonneson, J. R. Horn, *Biochemistry* **2009**, *48*, 6693–6695.
[31] K. D. Wegner, Z. Jin, S. Lindén, T. L. Jennings, N. Hildebrandt, *ACS Nano* **2013**, *7*, 7411–7419.
[32] E. G. Hofman, M. O. Ruonala, A. N. Bader, D. van den Heuvel, J. Voortman, R. C. Roovers, A. J. Verkleij, H. C. Gerritsen, P. M. P. van Bergen en Henegouwen, *J. Cell Sci.* **2008**, *121*, 2519–2528.
[33] J. Xu, T. M. Corneillie, E. G. Moore, G.-L. Law, N. G. Butlin, K. N. Raymond, *J.Am. Chem. Soc.* **2011**, *133*, 19900–19910.

Received: August 4, 2013
Published online: October 2, 2013

NANO MICRO
small

Supporting Information

for *Small*, DOI: 10.1002/smll.201302383

Nanobodies and Nanocrystals: Highly Sensitive Quantum Dot-Based Homogeneous FRET Immunoassay for Serum-Based EGFR Detection

*K. David Wegner, Stina Lindén, Zongwen Jin, Travis L. Jennings, Rachid el Khoulati, Paul M. P. van Bergen en Henegouwen, and Niko Hildebrandt**

Nanobodies and Nanocrystals: Highly sensitive quantum dot-based homogeneous FRET-immunoassay for serum-based EGFR detection

K. David Wegner, Stina Linden, Zongwen Jin, Travis L. Jennings, Rachid el Khoulati, Paul M.P. van Bergen en Henegouwen, and Niko Hildebrandt**

Supporting Information

Evaluation of possible V_HH aggregation

Excess of free V_HH (20 nM) was added to the assay mixtures without EGFR (Tb-V_HH and QD-V_HH containing 2.7 nM and 5 nM of V_HH, respectively) in order to evaluate if the "pre-FRET" (FRET in the assay mixture containing no EGFR) is caused by hydrophobic interactions or V_HH dimerization leading to the formation of V_HH aggregates. Addition of an excess of free V_HH should lead to less Tb-V_HH/QD-V_HH in close proximity within such aggregates and therefore reduced FRET. However, the addiditon of neither EgA1 (VHH within Tb-V_HH) nor EgB4 (V_HH within QD-V_HH) leads to any significant change in the pre-FRET curve (Supporting Figure 1). All samples were measured after 10, 20, 30, 60, 90 and 120 min. without significant differences in the decay curves. Therefore only the curves after 60 min. are shown in Supporting Figure 1.

Another control experiment in order to evaluate the influence of hydrophobic interactions was the addition of 0.1% Tween-20 to the assay mixture (to reduce hydrophobic interactions). However, the addition of Tween-20 had no significant influence compared to the mixture without Tween-20 (it rather slightly increases the intensity of the curve) as shown in the comparison of Supporting Figure 2b (no Tween-20) and 2d (0.1 % Tween-20).

Evaluation of BSA-induced non-specific binding

For these control experiments the Tb-V_HH and QD-V_HH samples were prepared in TRIS/Cl buffer (pH 7.4) containing no BSA. For the Tb-V_HH/QD-V_HH mixtures 50 µL of each sample were mixed with 50 µL of TRIS/Cl buffer containing different amounts of BSA in order to give a final BSA concentration (in the complete assay volume) of 0 %, 0.5 % or 5 %. All samples were measured after 10, 20, 30, 60, 90 and 120 min. without significant differences in the decay curves. Therefore only the curves after 60 min. are shown in Supporting Figure 2. Comparison of Supporting Figure 2a, b and c shows a significant increase of "pre-FRET" (black curve compared to red curve for each graph) with increasing BSA concentration. Moreover the signals of the samples containing no BSA (Supporting Figure 2a) are much lower compared to the other samples, which is caused by non-specific binding of Tb-V_HH and QD-V_HH to the well walls, showing the necessity of BSA in the assays. It should be noted that the "pre-FRET" only becomes very obvious for 5 % BSA (Supporting Figure 2c), whereas the 0.5 % BSA curve (Supporting Figure 2b) shows only weak pre-FRET. This is in contrast to the assays presented in the manuscript, for which a significant "pre-FRET" is already visible for 0.5 % BSA (Figure 3a). This effect

is most probably caused by the different Tb-V_HH and QD-V_HH stock solutions, which already contain 0.5 % BSA in the assay case (manuscript Figure 3a), whereas they are BSA-free (BSA is only added with the buffer) in the control experiments (Supporting Figure 2). Thus within the assays non-specific binding of Tb-V_HH and QD-V_HH is already established in the stock solutions and the "pre-FRET" sensitization is faster for the mixture than for the control assays, where higher amounts of BSA are necessary to show significant "pre-FRET" within the same time range.

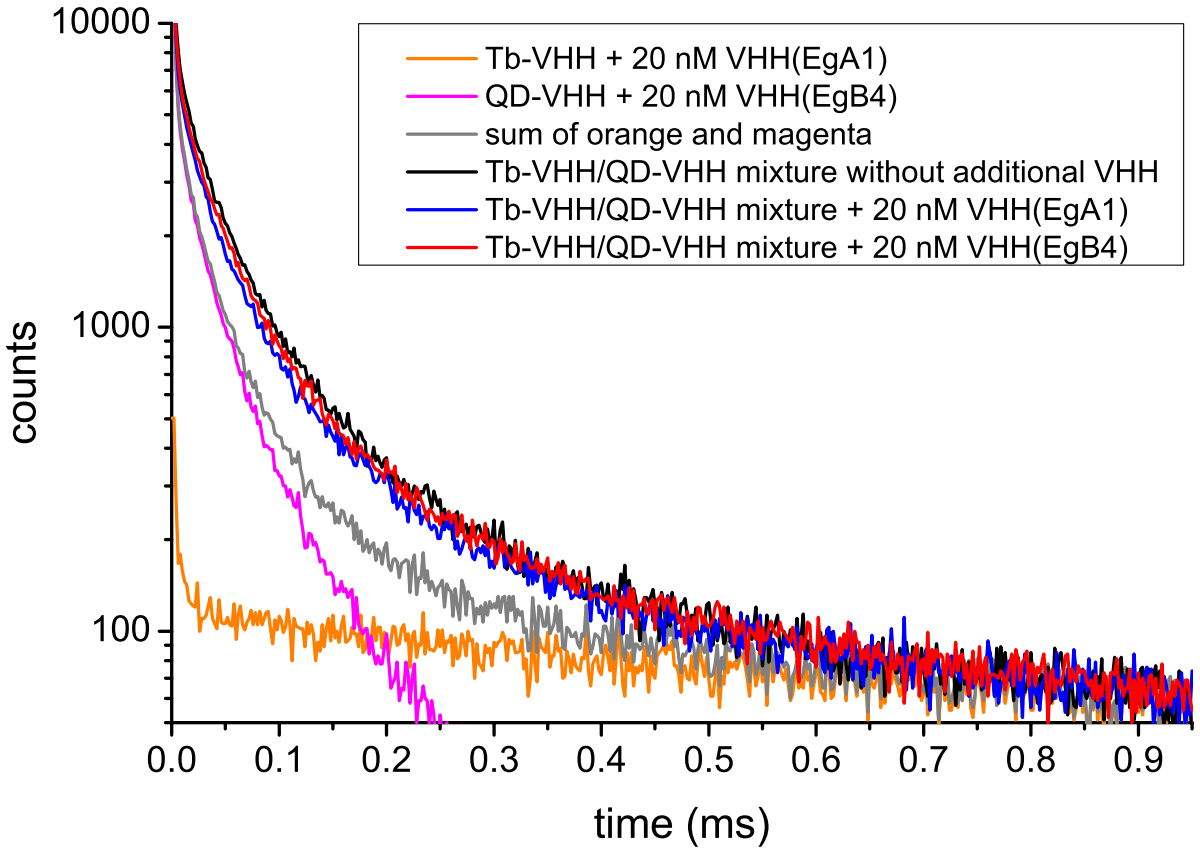

Supporting Figure 1: Addition of an excess of free V_HH (blue and red) does not lead to a significant reduction of "pre-FRET" without free V_HH (black).

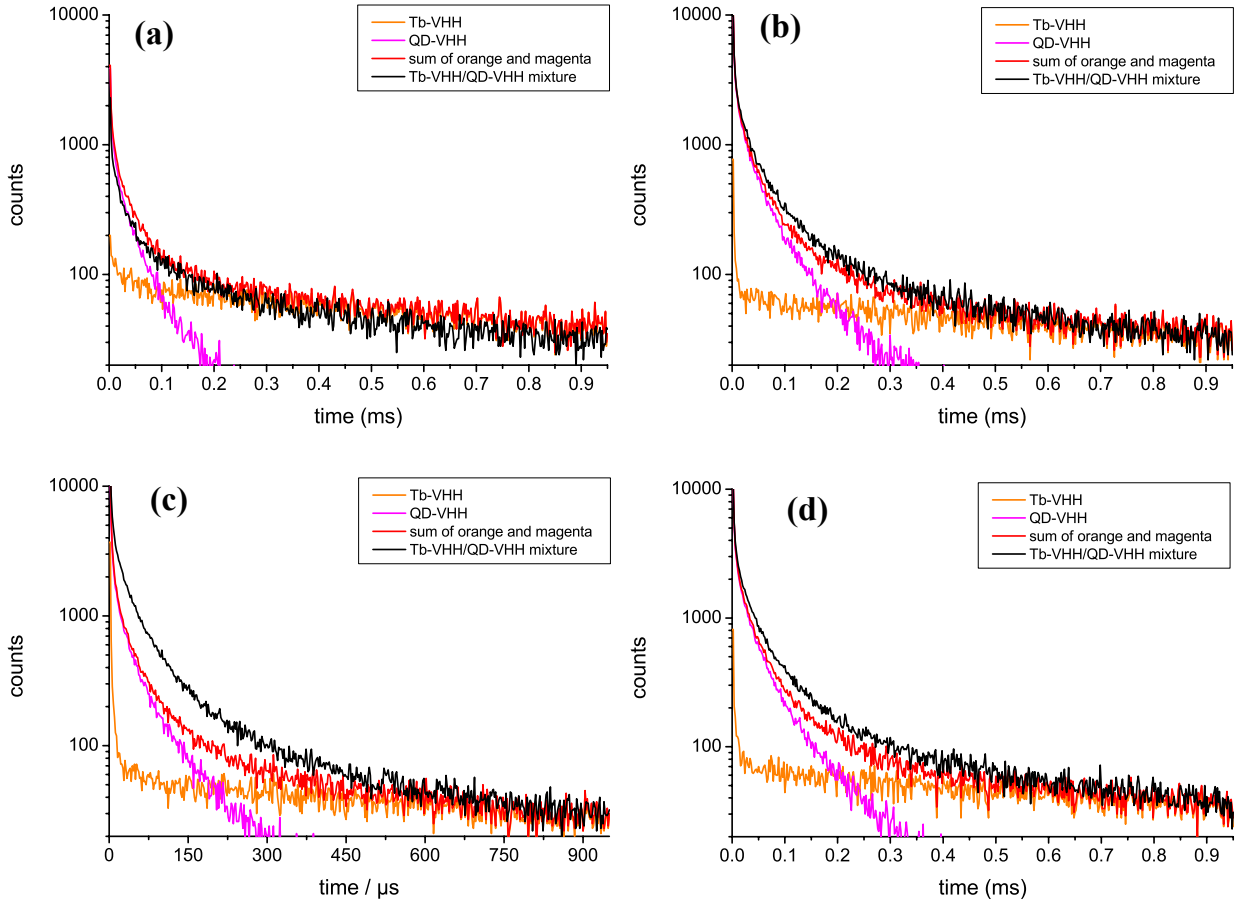

Supporting Figure 2: Pure Tb-VHH (orange), pure QD-VHH (magenta), the mathematical sum of both (red) and the mixture of both (black) at equal concentrations for all curves. The different samples contain 0% BSA (a), 0.5% BSA (b), 5% BSA (c) and 0.5% BSA + 0.1% Tween-20 (d). The difference between the black and the red curve increases from 0 to 0.5 to 5% BSA, which confirms that the pre-FRET signal is caused by BSA-induced non-specific binding. Addition of Tween-20 does not have any significant influence on the decay curves.

6.4 Spectroscopic ruler

6.4.1 Biotin-streptavidin system

Original publication:

Influence of Luminescence Quantum Yield, Surface Coating and Functionalization of Quantum Dots on the Sensitivity of Time-Resolved FRET Bioassays.

K. D. Wegner, P. T. Lanh, T. Jennings, E. Oh, V. Jain, S. M. Fairclough, J. M. Smith, E. Giovanelli, N. Lequeux, T. Pons, and N. Hildebrandt.

ACS Applied Materials & Interfaces **2013**, 5, 2881-2892.

ACS APPLIED MATERIALS & INTERFACES

Forum Article

www.acsami.org

Influence of Luminescence Quantum Yield, Surface Coating, and Functionalization of Quantum Dots on the Sensitivity of Time-Resolved FRET Bioassays

K. David Wegner,[†] Phung Thi Lanh,[†] Travis Jennings,[‡] Eunkeu Oh,[§,⊥] Vaibhav Jain,[§] Simon M. Fairclough,[#] Jason M. Smith,[#] Emerson Giovanelli,[∥] Nicolas Lequeux,[∥] Thomas Pons,[∥] and Niko Hildebrandt[†,*]

[†]Institut d'Electronique Fondamentale, Université Paris-Sud, 91405 Orsay Cedex, France

[‡]eBioscience, Inc., 10255 Science Center Drive San Diego, California 92121, United States

[§]Optical Sciences Division, Code 5600, U.S. Naval Research Laboratory, Washington, D.C. 20375, United States

[⊥]Sotera Defense Solutions, Annapolis Junction, Maryland 20701, United States

[#]Department of Materials, University of Oxford, Oxford, Oxfordshire, OX1 3PH, United Kingdom

[∥]Laboratoire de Physique et d'Etude des Matériaux, ESPCI-CNRS-UPMC UMR8213, 75005 Paris, France

Supporting Information

ABSTRACT: In clinical diagnostics, homogeneous time-resolved (TR) FRET immunoassays are used for fast and highly sensitive detection of biomarkers in serum samples. The most common immunoassay format is based on europium chelate or cryptate donors and allophycocyanin acceptors. Replacing europium donors with terbium complexes and the acceptors with QDs offers large photophysical advantages for multiplexed diagnostics, because the Tb-complex can be used as FRET donor for QD acceptors of different colors. Water-soluble and biocompatible QDs are commercially available or can be synthesized in the laboratory using many available recipes from the literature. Apart from the semiconductor material composition, an important aspect of choosing the right QD for TR-FRET assays is the thickness of the QD coating, which will influence the photophysical properties and long-term stability as well as the donor−acceptor distance and FRET efficiency. Here we present a detailed time-resolved spectroscopic study of three different QDs with an emission maximum around 605 nm for their application as FRET acceptors (using a common Tb donor) in TR-bioassays: (i) Invitrogen/Life Technologies Qdot605, (ii) eBioscience eFluorNC605 and iii) ter-polymer stabilized CdSe/CdS/ZnS QDs synthesized in our laboratories. All FRET systems are very stable and possess large Förster distances (7.4−9.1 nm), high FRET efficiencies (0.63−0.80) and low detection limits (0.06−2.0 pM) within the FRET-bioassays. Shapes, sizes and the biotin/QD ratio of the biocompatible QDs could be determined directly in the solution phase bioassays at subnanomolar concentrations. Both commercial amphiphilic polymer/lipid encapsulated QDs and self-made ligand-exchanged QDs provide extremely low detection limits for highly sensitive TR-FRET bioassays.

KEYWORDS: *FRET, quantum dot, biosensor, diagnostics, terbium, multiplexing, spectroscopy, immunoassay, biotin, streptavidin*

INTRODUCTION

Semiconductor nanocrystals or quantum dots (QDs) are important fluorophores for optical biosensing applications because they combine spectrally broad absorption with high molar absorptivity and spectrally narrow emission with high brightness.[1−4] Three-dimensional quantum confinement allows tuning of absorption and emission wavelengths over a large range of the UV−vis−NIR spectral region by changing QD sizes and/or materials.[1,5] Despite the photophysical advantages of QDs, their applications in biosensing remain most often limited to research studies. The adoption of QDs within clinical diagnostic kits is still limited although several commercial suppliers of biocompatible QDs exist.[6] QDs with superior photoluminescence (PL) properties are usually synthesized in organic solvents and thus they require exchange of surface ligands or coating with water-soluble shells (e.g., polymers or lipids) in order to be used in aqueous solutions.[7,8] Such steps can cause significant alterations in brightness, stability and/or size of the QDs. Moreover, the relatively large surfaces of QDs give rise to multiple interactions with the biological environment, which can cause further changes in the physical and chemical properties of QDs. It is therefore very important to investigate various different QDs for each application. A detailed steady-state and time-resolved spectroscopic analysis

Special Issue: Forum on Biomedical Applications of Colloidal Photoluminescent Quantum Dots

Received: December 11, 2012
Accepted: February 27, 2013
Published: March 15, 2013

   dx.doi.org/10.1021/am3030728 | *ACS Appl. Mater. Interfaces* 2013, 5, 2881−2892

Scheme 1. Time-Resolved Tb-to-QD FRET Bioassay Using Tb-Labeled Streptavidin (sAv) and Biotinylated (B) QDs for Biological Recognition[a]

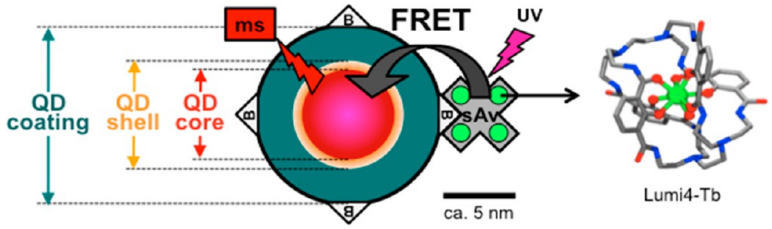

[a]Once the binding is established, the close proximity between the Tb-complexes (Lumi4-Tb) and the QD enables efficient FRET. Three different biotinylated QDs with emission maxima at ca. 605 nm were investigated: Commercial Qdot605 (Invitrogen/Life Technologies), eFluorNC605 (eBioscience), and self-made CdSe/CdS/ZnS core/shell/shell QDs. The cross shape of sAv represents the four binding sites for biotin. The four Lumi4-Tb are bound to free lysine groups of sAv and are therefore randomly distributed over the sAv. This distribution as well as the non-spherical shapes of the QDs (cf. Figure 3) lead to a Lumi4-Tb to QD-center distance distribution. Out of this distribution, we could identify three main distances that were further averaged to one average Tb-to-QD distance (cf. Table 2). Biotin and Lumi4-Tb (adapted from ref 22, copyright 2011 American Chemical Society) not to scale.

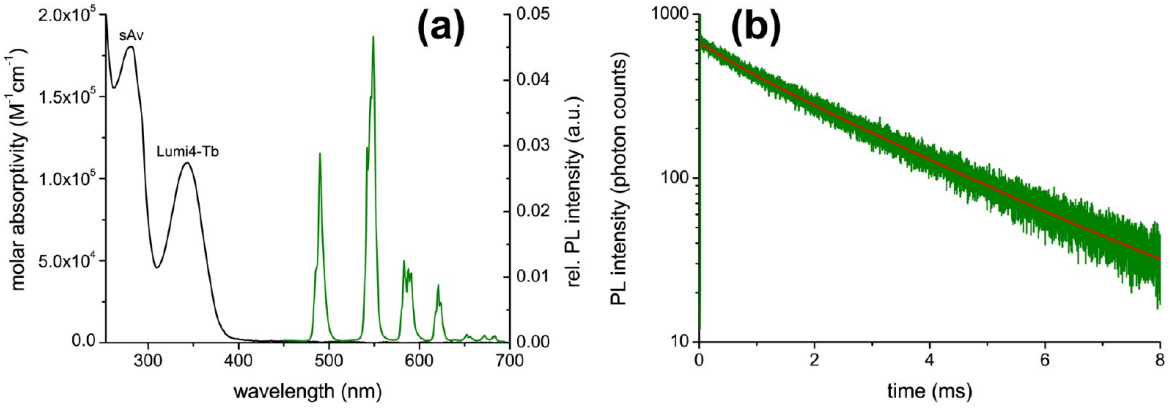

Figure 1. (a) Absorbance (black) and emission (green) spectra λ_{ex} = (350 ± 1) nm of the Lumi4-Tb-sAv donor. (b) Luminescence decay curve (green) and respective fit (red) of Lumi4-Tb-sAv leading to an amplitude-weighted average lifetime of $\langle\tau\rangle$ = 2290 μs λ_{ex} = (350 ± 1) nm, λ_{em} = (490 ± 1) nm.

using all fluorescent and biological components necessary for a sensitive bioassay can reveal much important information for bringing the QD-based biosensor a significant step closer to its integration into the "real world" of diagnostics.

Typical bioassays used in such diagnostic applications are FRET (Förster resonance energy transfer) immunoassays, for which two primary antibodies against different epitopes on the same biomarker are conjugated with a FRET donor and acceptor, respectively. FRET immunoassays are homogeneous (no washing or separation steps required), inherently ratiometric (ratio of FRET-sensitized acceptor and FRET-quenched donor fluorescence can be measured) and very sensitive (fluorescence detection), which make them especially interesting for quick and facile diagnostic tests, detecting low concentrations of biomarkers (e.g., in point-of-care diagnostics).[9] Luminescent lanthanide complexes provide another important contribution to FRET immunoassays. The long luminescence lifetimes of lanthanides offer the possibility of time-gated or time-resolved detection, which leads to a significant autofluorescence background suppression and therefore the realization of lower detection limits.[10−13] These assays are frequently used in "real world" diagnostics and are commercially available under brand names such as HTRF (homogeneous time-resolved fluorescence), TRACE (time-resolved amplified cryptate emission) or LANCE (lanthanide chelate excitation).[14−16]

In prior work we have demonstrated the benefits of combining lanthanide donors with quantum dot acceptors for different multiplexed FRET bioassay formats.[17−21] Here we present a spectroscopic investigation of one of the main materials and interfaces used within these assays, the QDs. Taking advantage of biotin-streptavidin (biot-sAv) recognition, we established a comparative study of time-resolved FRET between a commercial luminescent terbium complex (Lumi4-Tb, Lumiphore, Inc., USA) labeled to sAv and three different biotinylated CdSe-based QDs emitting around 605 nm (Scheme 1). Two batches of QDs with amphiphilic polymer/lipid coatings from commercial sources (Qdot605 from Invitrogen by LifeTechnologies Corp., USA and eFluorNC605 by eBioscience, Inc., USA), and one batch of QDs coated with poly(dithiol-co-sulfobetaine) polymeric ligands (pDTSB), synthesized in our laboratories, were compared. All tested systems showed efficient FRET, high stability in biological buffers and femto- to picomolar limits of detection (LODs). Simultaneous time-resolved (TR) luminescence detection of donor and acceptor emission allowed us to analyze the FRET processes from the energy-providing (donor) and the energy-receiving (acceptor) side. Thus we were able to measure precisely FRET efficiencies, QD sizes and shapes, and

quantification of biotin per QD ratios as well as their influence on LODs using subnanomolar concentrations and low-volume (150 μL) samples.

EXPERIMENTAL SECTION

Materials. The terbium complex conjugated to streptavidin (Lumi4-Tb-sAv) was produced and provided by Lumiphore (Richmond, USA). The CdSe/ZnS core/shell-based biotinylated QD Qdot605 was purchased from Invitrogen (Qdot605 biotin conjugate, Life Technologies, Carlsbad, USA). The CdSe/ZnS core/shell-based biotinylated QD eFluorNC605 was produced and provided by eBioscience (San Diego, USA). The CdSe/CdS/ZnS core/shell/shell-based biotinylated QDs p(DT-SB)605(A) and p(DT-SB)605(B) were synthesized using standard synthetic procedures in non-coordinating high-boiling-point solvents,[23,24] and cap exchanged with p(DT-SB) as well as biotinylation following previously described procedures.[25] Unconjugated biotins were purified using ultrafiltration and size exclusion chromatography.[25] For all measurements (unless mentioned differently) sodium-tetraborate with a pH of 8.5 was used as buffer. In case of the FRET-assay measurements bovine serum albumin (BSA, Sigma-Aldrich, Lyon, France) was added to the buffer. All chemicals were used as received. Water was purified by Purelab Option-Q (ELGA Labwater Veolia water STI, Antony, France).

Analytical Methods. Structural characterization of the Qdot605 was carried out using a JEOL 2100-FS analytical high-resolution transmission electron microscope (HR-TEM) with a 200 kV accelerating voltage. Samples for TEM were prepared by spreading a drop of the QD dispersion onto the ultrathin carbon film on holey carbon support film on Au grid (300 mesh, Ted Pella, Inc.) and letting it dry. TEM images of the eFluorNC605 were taken using a JEOL 2010 running at 200 kV. A solution diluted in chloroform was dropcast on Cu grid with ultrathin carbon support and left overnight to dry. TEM images of the homemade biotinylated p(DT-SB) QDs were acquired on a JEOL 2010F microscope operated at 200 kV. Photoluminescence quantum yields of the QDs were measured using fluorescein in basic ethanol (97%) and rhodamine 6G in ethanol (95%) as standards.[26] Absorbance measurements were performed on a SPECTROstar^{Nano} (BMG-Labtech, Germany) in combination with the LVis-microplate. The Lumi4-Tb/sAv labeling ratio was determined by the absorbance spectrum (Figure 1a) using molar absorptivities of ε(343 nm) = 26 000 M^{-1} cm^{-1} and ε(280 nm) = 2600 M^{-1} cm^{-1} for Lumi4-Tb and ε(280 nm) = 168 000 M^{-1} cm^{-1} for the tetrameric protein sAv (24 tryptophans (n_{Trp}), 24 tyrosines (n_{Tyr}), and no disulfide bonds (n_{dsb}) using the following equation:[27] $\varepsilon(280\text{ nm}) = (5500n_{Trp} + 1490n_{Tyr} + 125n_{dsb})$ M^{-1} cm^{-1}.

PL spectra and decay curves for the characterization of the samples were measured on the fluorescence spectrometer FluoTime 300 "Easy Tau" (PicoQuant, Germany). For the PL decay curve of Lumi4Tb-sAv a xenon flash lamp with a repetition rate of 100 Hz at 350 nm was used. In case of the QDs a picosecond pulsed diode laser EPL-405 (Edinburgh Instruments, UK) with a center wavelength of (405 ± 7) nm and repetition rate of 2 MHz was used. The PL decay curves were fitted with FluoFit Pro version 4.4.1.0. (PicoQuant, Germany). For the measurement of the PL decay curves of the Tb to QD FRET an EI fluorescence plate reader (Edinburgh Instruments, UK) with 4000 detection bins of 2 μs integration time was used. A nitrogen laser VSL 337 ND (Spectra Physics, USA) was used for excitation (337.1 nm, 20 Hz, 600 flashes). (494 ± 20) nm and (660 ± 13) nm bandpass filters were used for donor and acceptor, respectively. The data were fitted with FAST software version 3.1 (Edinburgh Instruments, UK). Time-gated intensity measurements for the FRET-assays were obtained with a modified KRYPTOR fluorescence plate reader (Cezanne/Thermo Fisher Scientific, France) using 500 detection bins of 2 μs integration time. An integrated nitrogen laser was used for excitation (337.1 nm, 20 Hz, 100 flashes). The same bandpass filters as within the EI plate reader were used. Time-gated PL intensities (100 to 900 μs) were acquired simultaneously for donor and acceptor. All FRET assays were measured in black 96-well microtiter plates with an optimal working volume of 150 μL. Lumi4Tb-sAv concentration was kept constant at 0.2 nM in all FRET-assay measurements. QD concentrations were varied from 0.02 nM to 0.6 nM. Each QD concentration was prepared three times. The pure Lumi4-Tb-sAv sample (zero QD concentration) was prepared ten times. All samples were measured in triplicates. In control measurements the different QD concentrations were measured without the presence of Lumi4Tb-sAv. After preparation the samples were incubated for 90 min at 37 °C before the measurements in the EI and KRYPTOR fluorescence plate readers. OriginPro 8.1 SR3 (OriginLab Corporation) and Microsoft Excel (Microsoft Corporation) were used for graphs and calculations.

PL Decay Time Analysis. The decay time analysis in the donor and acceptor channel was performed as follows for every FRET system. Due to the large difference in the excited-state lifetimes of Tb and QD (ca. 5 orders of magnitude, vide infra) the decay times caused by FRET are the same for Tb (decay time of the donor in presence of the acceptor τ_{DA}) and QD (decay time of the acceptor in the presence of the donor $\tau_{AD} = \tau_{DA}$).[18] All decay curves were fitted using a multiexponential PL intensity decay function

$$I = \sum A_i \exp(-t/\tau_i) = A \sum \alpha_i \exp(-t/\tau_i) \quad (1)$$

where A is the total amplitude and α_i are the amplitude fractions ($\Sigma\alpha_i = 1$). All PL lifetime averaging for the dynamic FRET quenching process was performed using amplitude weighted average lifetimes[28,29]

$$\langle\tau\rangle = \sum \alpha_i \tau_i \quad (2)$$

First the decay curve of the pure Lumi4-Tb-sAv donor (e.g., gray curve in Figure 4c for the eFluorNC605 FRET system) was fitted using a double-exponential decay function, which led to the amplitude fractions α_{D1} and α_{D2}, the PL decay times τ_{D1} and τ_{D2} (with $\tau_{D2} > \tau_{D1}$) and the average PL decay time of the pure donor (in the absence of the acceptor) $\langle\tau_D\rangle$. The FRET-quenched decay curves in the donor detection channel were fitted using a triple-exponential decay function, leading to the amplitude fractions α_{DA*1}, α_{DA*2}, and α_{DA*3} and the PL decay times τ_{DA1}, τ_{DA2}, and τ_{DA3}, for which the third decay time component was fixed to $\tau_{DA3} = \tau_{D2}$ in order to take into account the emission of unquenched donors. For the calculation of the average donor decay time in the presence of the acceptor $\langle\tau_{DA}\rangle$, only the first two amplitudes and decay times were used (as the third component represents unquenched donors). Therefore, the amplitude fractions must be redefined for these two decay times τ_{DA1} and τ_{DA2}

$$\alpha_{DA1} = \frac{\alpha_{DA*1}}{\alpha_{DA*1} + \alpha_{DA*2}} \text{ and } \alpha_{DA2} = \frac{\alpha_{DA*2}}{\alpha_{DA*1} + \alpha_{DA*2}} \quad (3)$$

As the unquenched donor possesses two decay time components (τ_{D1} and τ_{D2}), $\langle\tau_{DA}\rangle$ must be corrected for the shorter time component (τ_{D1}). As this shorter decay time of the "pure" donor falls within the time-range of the FRET-quenched decay times, the use of an additional exponential for the fit procedure leads to inconsistent fit results. We therefore applied a correction factor z_D (the fraction of unquenched donors in the short time components), which is determined by comparing the amplitude fractions of τ_{D2} and τ_{DA3} ($\tau_{DA3} = \tau_{D2}$) multiplied by the amplitude fraction α_{D1}

$$z_D = \alpha_{D1}(\alpha_{DA*3}/\alpha_{D2}) \quad (4)$$

The average FRET-quenched decay time is then

$$\langle\tau_{DA}\rangle = \frac{\alpha_{DA1}\tau_{DA1} + \alpha_{DA2}\tau_{DA2} - z_D\tau_{D1}}{1 - z_D} \quad (5)$$

and the average FRET-efficiency is

$$\langle\eta_{FRET}\rangle = 1 - \frac{\langle\tau_{DA}\rangle}{\langle\tau_D\rangle} \quad (6)$$

The FRET-sensitized decay curves in the acceptor detection channel were fitted using a quadruple-exponential decay function, leading to the amplitude fractions α_{AD*0}, α_{AD*1}, α_{AD*2}, and α_{AD*3} and the PL decay times τ_{AD0}, τ_{AD1}, τ_{AD2} and τ_{AD3}, for which the fourth decay time component was fixed to $\tau_{AD3} = \tau_{D2}$ in order to take into account the

emission of unquenched donors, which is much less intense compared to the donor channel but still present due to spectral crosstalk of the Tb emission in the QD acceptor detection channel. The correction factor z_A (the fraction of unquenched donors in the short time components) is almost negligible but is still taken into account for a correct treatment

$$z_A = \alpha_{D1}(\alpha_{AD*3}/\alpha_{D2}) \quad (7)$$

To calculate the average FRET decay time $\langle\tau_{AD}\rangle$ only the amplitudes and lifetimes with $i = 0-2$ are taken into account ($i = 3$ represents the unquenched donor emission). Moreover, the amplitudes α_{AD*i} must be corrected by the FRET rates $k_i = 1/\tau_{ADi} - 1/<\tau_D>$, to take into account the dependence of the excitation of the acceptors (and therefore the amplitude fractions) on the different FRET efficiencies for the different distances (corresponding to the decay times τ_{ADi}). The corrected amplitude fractions are (for $i = 0-2$)

$$\alpha_{ADi} = \frac{\alpha_{AD*i}/k_i}{\sum \alpha_{AD*i}/k_i} \quad (8)$$

The average FRET decay time is then calculated by:

$$\langle\tau_{AD}\rangle = \frac{\alpha_{AD0}\tau_{AD0} + \alpha_{AD1}\tau_{AD1} + \alpha_{AD2}\tau_{AD2} - z_A\tau_{D1}}{1 - z_A} \quad (9)$$

and the average FRET-efficiency is

$$\langle\eta_{FRET}\rangle = 1 - \frac{\langle\tau_{AD}\rangle}{\langle\tau_D\rangle} \quad (10)$$

For each FRET decay time, the donor–acceptor distance r_x can be calculated by

$$r_x = R_0\left(\frac{\tau_x}{\langle\tau_D\rangle - \tau_x}\right)^{1/6} \quad (11)$$

where τ_x represents the different lifetimes τ_{DAi}, τ_{ADi}, $\langle\tau_{DA}\rangle$, or $\langle\tau_{AD}\rangle$. The fractions of FRET-pairs found at the different distances corresponding to τ_{DAi} and τ_{ADi} are given by the amplitude fractions of these decay times.

RESULTS AND DISCUSSION

Spectroscopic Analysis of FRET Donor and Acceptors.

To establish a profound basis for this comparative FRET study using one Tb-complex as donor and different QDs (Qdot605, eFluorNC605, and p(DT-SB)605) as acceptors, we performed a spectral and time-resolved analysis of the separated FRET components. The donor within all FRET-pairs (Table 1) was the supramolecular Tb-complex Lumi4-Tb labeled to streptavidin (sAv). Lumi4-Tb consists of a chelating ligand coordinating a Tb^{3+} ion in its center. The ligand shows a strong absorption band with a maximum molar absorptivity of ca. 26 000 M^{-1} cm^{-1} at 340 nm, which shifts to ca. 343 nm when labeled to sAv. The absorbance spectrum (Figure 1a) shows a linear combination of sAv (maximum at 280 nm) and Lumi4-Tb (maximum at 343 nm) absorption, resulting in a labeling ratio of ca. 4.2 Lumi4-Tb/sAv. After ligand absorption the energy is transferred to the central Tb^{3+} ion, which then shows the typical Tb-emission lines with major peaks around 490, 545, 585, and 620 nm (and some peaks with minor intensities between 645 and 690 nm). Figure 1a shows the intensity-normalized (area under the emission spectrum from 450 to 690 nm normalized to unity) emission spectrum of Lumi4-Tb. This emission has an almost monoexponential long-lifetime luminescence decay behavior (Figure 1b) with a minor decay time of 630 μs (4% and 14% of the overall intensity and amplitude, respectively) and a major decay time of 2560 μs (96% and 86% of the overall intensity and amplitude,

Table 1. Properties of the Tb Donor and the QD Acceptors Used within the FRET Study

	material	size (nm)[e]	source	biomolecule	Φ^g	R_0 (nm)[h]
Lumi4-Tb	supramolecular Tb-complex[a]	ca. 1.0	Lumiphore	streptavidin, ca. 4.2 Lumi4-Tb/sAv	0.67	donor for all acceptors
Qdot605	CdSe/ZnS core/shell QD coated with polymer/PEG layer[b]	core/shell: 4.0 × 9.4 complete QD: 16	Invitrogen/Life Technologies	biotin, ca. 3–4 biot/QD	0.73	9.1
eFluorNC605	CdSe/ZnS core/shell QD coated with PEG-lipid layer[c]	core/shell: 6.0 complete QD: 14	eBioscience	biotin, ca. 3–4 biot/QD	0.65	7.8
p(DT-SB)605(A)	CdSe/CdS/ZnS core/shell/shell QD coated with ter-polymer layer[d]	core/shell/shell: 6–7 complete QD: 12	ESPCI[f]	biotin, ca. 3–4 biot/QD	0.07	7.4
p(DT-SB)605(B)	CdSe/CdS/ZnS core/shell/shell QD coated with ter-polymer layer[d]	core/shell/shell: 6–7 complete QD: 12	ESPCI[f]	biotin, ca. 1 biot/QD	0.07	7.4

[a]www.lumiphore.com. [b]www.invitrogen.com. [c]www.ebioscience.com. [d]Reference 25. [e]core/shell: diameters or minimum/maximum length of ellipsoid axes as measured by TEM; complete QDs incl. coating: diameters as determined by our FRET donor–acceptor distances study; hydrodynamic diameter values provided by suppliers: 16 nm for Qdot605 (size exclusion chromatography on HPLC), 20–26 nm for eFluorNC605 (DLS) and 16–18 nm for p(DT-SB)605 (DLS). [f]cf. addresses of the authors. [g]Measured in borate buffer against fluorescein and rhodamine as standards for the QDs. Measured by $\Phi = <\tau>/\tau_{int}$ for Lumi4-Tb, with τ_{int} = 3450 μs the intrinsic lifetime of Lumi4-Tb.[17] [h]Förster distances as calculated within this study (cf. Supporting Information).

dx.doi.org/10.1021/am3030728 | ACS Appl. Mater. Interfaces 2013, 5, 2881–2892

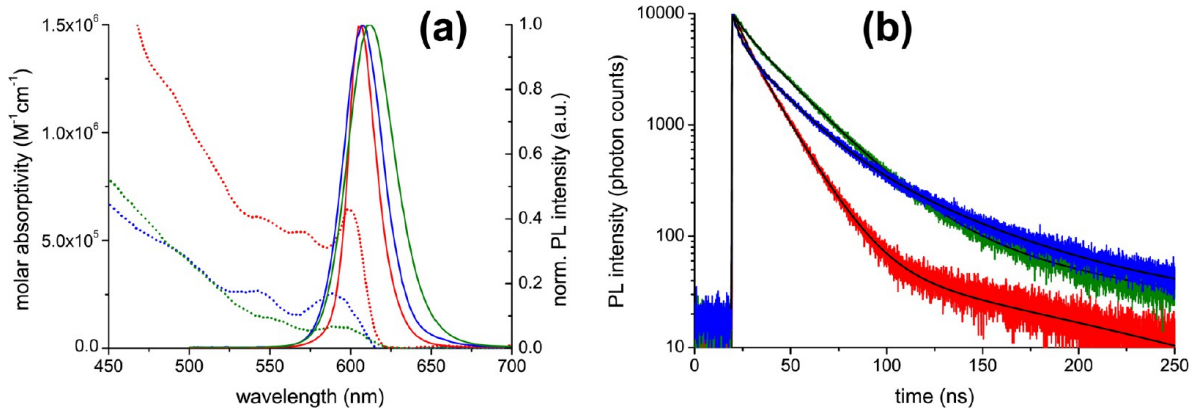

Figure 2. (a) Absorption (dotted lines) and PL emission spectra (λ_{ex} = (410 ± 0.5) nm; intensity-normalized to unity at PL maxima) of the different biotinylated QDs used as FRET acceptors. (b) PL decay curves (λ_{ex} = (405 ± 7) nm, λ_{em} in the intensity maxima) of the different biotinylated QDs and their respective multiexponential fit curves with average PL lifetimes of 17 ns (red), 29 ns (blue), and 31 ns (green). Red = Qdot605, blue = eFluorNC605, green = p(DT-SB)605.

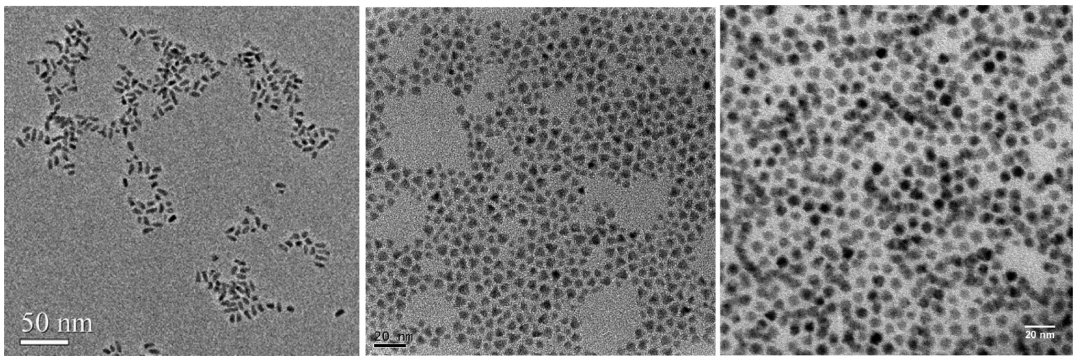

Figure 3. TEM images (showing only the core/shell structure of the QDs) of Qdot605 (left), eFluorNC605 (center), and p(DT-SB)605 (right). High-resolution images can be found in the Supporting Information, Figure S1.

respectively). The average lifetime is $\langle\tau\rangle$ = (2290 ± 100) μs. This is the amplitude-weighted average lifetime (cf. eq 2), which must be used for the donor within the dynamic FRET quenching process.[28] The long excited-state lifetime is crucial for FRET to QDs, because energy can only be transferred to the QDs after these have decayed back to their ground states following their very efficient direct excitation at the UV excitation wavelength of Lumi4-Tb. In our case the difference in lifetimes is ca. 5 orders of magnitude (ca. 2.3 ms for Lumi4-Tb and ca. 25 ns for the QDs, see Figures 1b and 2b).

The acceptors for our FRET study were different surface functionalized and biotinylated water-soluble QDs (Table 1). The p(DT-SB)605 QDs were synthesized with different amounts of biotins on the surface in order to evaluate the influence of the biotin surface coverage for biosensing applications. Apart from the Qdot605, for which a biot/QD ratio of "typically 5 to 7" is given by the supplier, all biot/QD ratios were unknown. The values in Table 1 were found within our FRET experiments (vide infra). The biot/Qdot605 ratio is 3 to 4 in our case. As a fresh sample of biot-Qdot605 was used we do not expect any loss of biotin over time. We rather assume a batch-to-batch variation as already indicated by the explanation "typically 5−7 Biotin molecules/Qdot conjugate" within the product description of LifeTechnologies. To compare the different QD performance in FRET bioassays, we chose similar absorption and emission wavelengths. As shown in Figure 2a all QDs show the characteristic broad absorption spectra with several pronounced exciton peaks between 525 and 625 nm. The absorption spectra have large molar absorptivity values and are nicely overlapping with the most intense emission peaks of Lumi4-Tb (Figure 1a), which leads to long Förster distances R_0 (the donor−acceptor distance for which FRET is 50% efficient) between 7.4 and 9.1 nm (Table 1). As the absorbance of the Qdot605 is significantly larger than for the other two QDs, it also possesses the highest R_0 in combination with Lumi4-Tb as donor. All PL spectra are very symmetrical and have a maximum intensity around 605 nm with full-width at half-maximum values of 20 nm (Qdot605), 29 nm (eFluorNC605) and 34 nm (p(DT-SB)605). The PL decay curves (Figure 2b) are multi-exponential with intensity-weighted average lifetimes of 17 ns (Qdot605), 29 ns (eFluorNC605) and 31 ns (p(DT-SB)605). Qdot605 and eFluorNC605 are very bright with PL quantum yields of 73 and 65%, respectively. p(DT-SB)605 (7%) provide significantly lower values, as expected from ligand-exchanged QDs, which are more compact but display a reduced quantum yield compared to encapsulated QDs.[30,31]

TEM images of the semiconductor parts (polymer coatings not visible) of the different QDs (Figure 3) show that the QDot605 QDs are very elongated, whereas the eFluorNC605 and p(DT-SB)605 are much closer to spherical shape, although some elongation as well as tetrahedral and star-shaped QDs are visible. The difference in shape is quite interesting because it should also become visible in the FRET data due to the

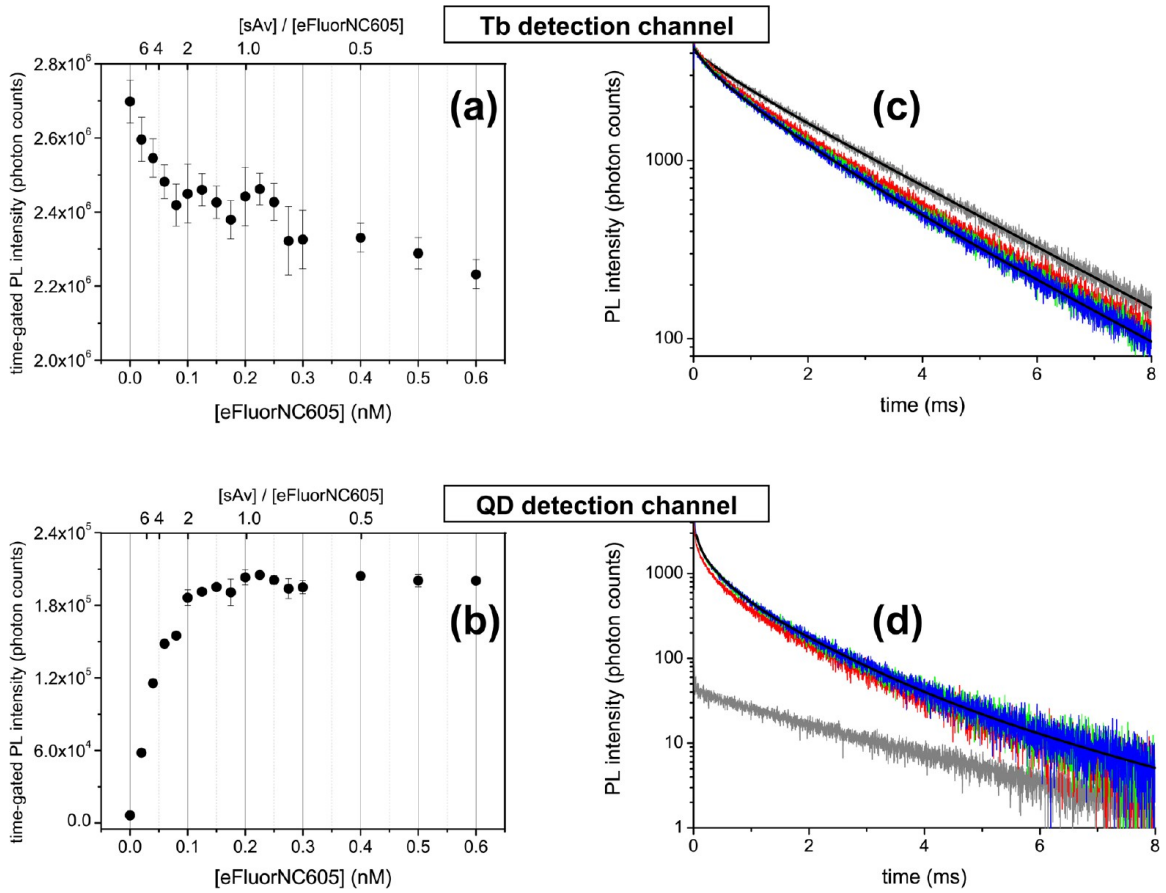

Figure 4. Time-gated (100−900 μs) PL intensity (as a function of eFluorNC605 concentration) of (a) the Lumi4-Tb donor and (b) the eFluorNC605 acceptor showing efficient FRET donor quenching and acceptor sensitization, which increases until a sAv/eFluorNC605 concentration ratio of approximately one. The PL decay curves of the (c) donor and (d) acceptor show a strongly multiexponential decay behavior caused by FRET from Lumi4-Tb to eFluorNC605 situated at different distances from the QD. Only some representative decay and fit curves are presented. Gray: pure Lumi4-Tb-sAv (The pure Lumi4-Tb luminescence is also visible in the QD detection channel due to spectral crosstalk. This leads to a nonzero time-gated intensity at zero QD concentration in graph b. Such spectral crosstalk can be corrected for multiplexed measurements,[33] but is not necessary for the ratiometric measurement approach we chose for our single donor−acceptor pair experiments); red, 0.06 nM QD; green, 0.1 nM QD; blue, 0.15 nM QD; black, fit curves (for clarity, only a few representative fit curves are shown here).

strongly distance dependent FRET process and the random distribution of Lumi4-Tb-sAv all over the QD surfaces. In prior work we had already demonstrated TR-FRET as a multiplexed molecular ruler for the size and shape analysis of five different types of QDs.[32] The shape analysis of the QDs used within this study by FRET will be further discussed in detail below.

TR-FRET Analysis. Within all FRET experiments the Lumi4-Tb-sAv donor concentration was kept constant at 0.2 nM while the biot-QD concentrations were increased. First, time-gated intensities (100 − 900 μs) were measured simultaneously for the donor and the acceptor on the KRYPTOR fluorescence plate reader system. Afterward complete PL decay curves (from 0 to 8 ms) of the donor and the acceptor were acquired on the EI fluorescence plate reader for selected concentrations in order to perform a time-resolved FRET analysis. The time-gated PL intensity and decay time curves are shown in Figure 4 and 5 for the FRET system Lumi4-Tb-sAv-biot-eFluorNC605 and Lumi4-Tb-sAv-biot-p(DT-SB)605(B). The curves for the other two FRET systems (Lumi4-Tb-sAv-biot-Qdot605 and Lumi4-Tb-sAv-biot-p(DT-SB)605(A)) can be found in the Supporting Information (Figures S2 and S3). For all FRET systems small concentrations of biotinylated QD acceptors (<100 pM) already lead to a significant Lumi4-Tb donor quenching and a very strong QD acceptor sensitization. After a sAv/QD ratio of one is reached (at ca. 0.2 nM QD concentration) these FRET quenching and sensitization processes are saturated because further addition of QDs will not lead to additional FRET-pairs (the concentration of Lumi4-Tb-sAv is constant). Because of several biotins per QD saturation starts already before the complete saturation (flat curve) at Lumi4-Tb-sAv/QD = 1. The number of biotin molecules per QD and the stoichiometry of the FRET systems are discussed in an own section (vide infra). Tb donor quenching is most efficient for p(DT-SB)605, followed by eFluorNC605 and Qdot605. This indicates that the average donor−acceptor distance increases from p(DT-SB)605 to Qdot605 or, in other words, that the QD surface coating thickness increases from p(DT-SB)605 to Qdot605. On the acceptor side Qdot605 and eFluorNC605 show much stronger sensitization than p(DT-SB)605, which can be explained by the differences in PL quantum yields (Table 1).

Time-resolved spectroscopic measurements of lanthanide to QD FRET systems have the large advantage, that the FRET analysis can be performed for both the donor and the acceptor

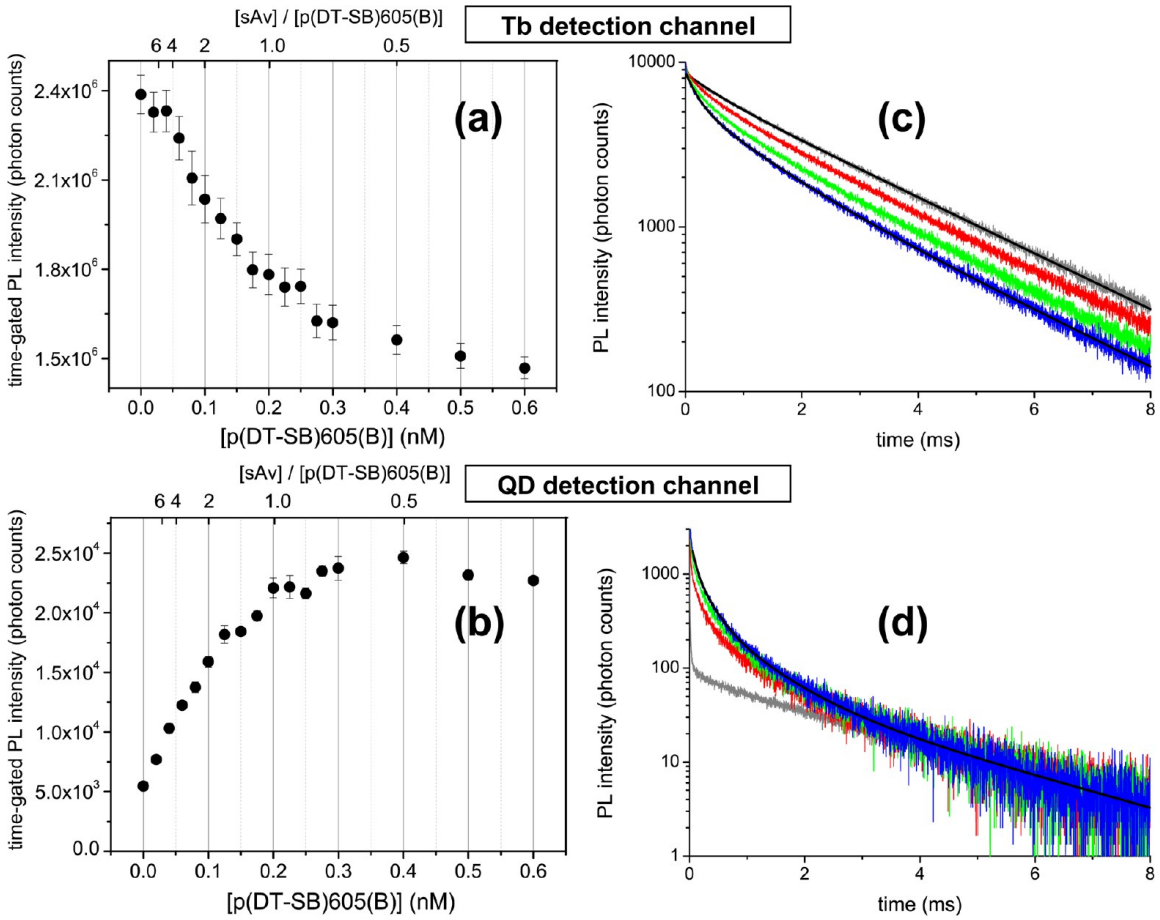

Figure 5. Time-gated (100−900 μs) PL intensity (as a function of p(DT-SB)605(B) concentration) of (a) the Lumi4-Tb donor and (b) the p(DT-SB)605(B) acceptor showing efficient FRET donor quenching and acceptor sensitization, which increases until a sAv/p(DT-SB)605(B) concentration ratio of approximately one. The PL decay curves of the (c) donor and (d) acceptor show a strongly multiexponential decay behavior caused by FRET from Lumi4-Tb to p(DT-SB)605 situated at different distances from the QD. Only some representative decay and fit curves are presented. Gray, pure Lumi4-Tb-sAv (for explanation of Lumi4-Tb emission in the QD detection channel, see caption of Figure 4); red, 0.06 nM QD; green, 0.1 nM QD; blue, 0.15 nM QD; black, fit curves (for clarity only few representative fit curves are shown here).

emission because the FRET-quenched PL decay times can be found in both the FRET-quenched donor and the FRET-sensitized acceptor curves ($\tau_{DA} = \tau_{AD}$ due to the large difference in excited state lifetimes of the Tb-donor and the QD-acceptor).[18] If the same FRET decay times are found for the donor and the acceptor, this will be a strong evidence for energy transfer. Other quenching mechanisms of the donor could lead to different decay behaviors of donor and acceptor. Probably the most important advantage of the time-resolved acceptor analysis is the fact that there is only FRET-sensitized PL because emission from direct QD excitation decays already after some hundreds of nanoseconds and the emission of unquenched donors (which appears as strong background signal in the donor detection channel) does not appear in the acceptor PL. This means that the QD acceptor detection channel is a pure FRET channel. It only requires taking into account spectral crosstalk effects of Tb-donor emission that can still pass through the bandpass filters of the acceptor channel. In the case of the multiexponential decays caused by the Lumi4-Tb to QD distance distribution in our FRET systems an analysis with a small unquenched Tb background PL in the acceptor channel (ca. 20% of the total emission intensity for the Lumi4-Tb-sAv-biot-Qdot605 system) is much more reliable than an analysis with a large unquenched Tb background PL in the donor channel (ca. 80% of the total emission intensity for the same FRET system).

Our PL decay time analysis had two main goals. First, we were interested in the average FRET decay time, which gives access to an average donor−acceptor distance and therefore the average size of the complete QD (including the size of the organic coating around the inorganic QD core/shell system). Second, a determination of different PL decay times and their correlation with the corresponding amplitudes within the exponential decay function could give access to the shape of the different QDs. Within a simplified model we would expect that the very elongated Qdot605 would show at least two average FRET decay times with almost equal amplitude fractions, caused by the two donor−acceptor distances for the minimum and maximum ellipsoid axes of the elongated QD. The other two QDs are more spherical and should therefore show one major FRET decay time (high amplitude fraction) and possibly one minor decay time (due to the fact that they are not perfectly spherical and a minor fraction of a second average donor−acceptor distance should still exist). In particular, we would expect that the ratio of short to long distance decay time amplitude fraction increases with elongation of the QDs (due

dx.doi.org/10.1021/am3030728 | ACS Appl. Mater. Interfaces 2013, 5, 2881−2892

Table 2. Decay Times, FRET Efficiencies, Donor (D)−Acceptor (A) Pair Distances. and Fractions

		Qdot605	eFluorNC605	p(DT-SB)605(A)	p(DT-SB)605(B)
R_0 (nm)		9.1 ± 0.4	7.8 ± 0.3	7.4 ± 0.3	7.4 ± 0.3
$\langle\tau_D\rangle$ (μs)		2310 ± 120	2280 ± 120	2290 ± 120	2270 ± 120
Decay Times (μs) and FRET Efficiencies[a]					
		average			
D	$\langle\tau_{DA}\rangle$	790	890	550	610
	$\langle\eta_{FRET\text{-}DA}\rangle$	0.66	0.61	0.76	0.73
A	$\langle\tau_{AD}\rangle$	630	840	460	540
	$\langle\eta_{FRET\text{-}AD}\rangle$	0.73	0.63	0.80	0.76
		first			
D	τ_{DA1}	270	240	170	200
	$\eta_{FRET\text{-}DA1}$	0.88	0.89	0.93	0.91
A	τ_{AD1}	320	300	160	230
	$\eta_{FRET\text{-}AD1}$	0.86	0.87	0.93	0.90
		second			
D	τ_{DA2}	1110	1110	960	1030
	$\eta_{FRET\text{-}DA2}$	0.52	0.51	0.58	0.54
A	τ_{AD2}	870	1010	600	740
	$\eta_{FRET\text{-}AD2}$	0.63	0.56	0.74	0.67
		third			
A	τ_{AD0}	60	60	30	60
	$\eta_{FRET\text{-}AD0}$	0.97	0.97	0.99	0.97
Donor−Acceptor Distances (in nm) and Fractions[b]					
		average			
D	r_{DA}	8.1	7.2	6.1	6.3
A	r_{AD}	7.7	7.1	5.9	6.1
		first			
D	α_{DA1}	0.40	0.29	0.51	0.52
	r_{DA1}	6.5	5.5	4.9	5.0
A	α_{AD1}	0.40	0.20	0.27	0.32
	r_{AD1}	6.7	5.7	4.8	5.1
		second			
D	α_{DA2}	0.60	0.71	0.49	0.48
	r_{DA2}	9.0	7.7	7.0	7.2
A	α_{AD2}	0.58	0.77	0.69	0.62
	r_{AD2}	8.4	7.5	6.2	6.6
		third			
A	α_{AD0}	0.02	0.03	0.04	0.05
	r_{AD0}	5.0	4.3	3.6	4.1

[a]Errors ± 10%. [b]Errors ± 15%.

to two short axes and one long axis of an elongated ellipsoid), as we have demonstrated before for FRET from Tb donors to QDs with different shapes.[32]

The results of the time-resolved FRET analysis (using eqs 1−11) within both the donor and the acceptor detection channel are summarized in Table 2 (the complete data can be found in the Supporting Information). The data show an excellent match between the results obtained from the donor and the acceptor channel, which gives strong evidence that the energy was efficiently transferred from the donor to the acceptors. Using the QD acceptor decay curves allows for the resolution of an additional decay time (distance) with low emission intensity. This is not possible in the donor channel because of the strong background signal of unquenched Tb-donor emission. Although this "pure" Tb-background was corrected for both channels (cf. eqs 4 and 7) the correction in the donor channel (ca. 80% of the total emission intensity) has much more influence than in the acceptor channel (ca. 20% of the total emission intensity). The strong fraction of long-lived Tb-emission in the donor channel leads to a slight overestimation of the average FRET decay time and distance compared to the acceptor data. Moreover, as amplitude and decay time are correlated (one can compensate for the other) in the mathematical fit procedure,[26] it is more difficult to correctly resolve the donor channel components because the signal to background ratio is lower than in the acceptor channel. Nevertheless, the results from both channels are quite similar, which demonstrates the efficiency of our correction procedures.

Taking advantage of the strong distance dependence of FRET, interesting information about distances and the fractions of donor−acceptor pairs at these distances can be extracted from the data. First of all the average donor−acceptor distance is the longest for Qdot605 and decreases by ca. 1 nm for the eFluorNC605 and an additional 1 nm for the p(DT-SB)605, which clearly shows that the QD coating (separation distance between the photoactive QD core and the biotin molecules on the QD surface) is the largest for Qdot605. As a first

approximation the average donor−acceptor distance can be used as the average radius of the QDs (assuming spherical shape), leading to diameters of ca. (16 ± 3) nm, (14 ± 2) nm, and (12 ± 2) nm for the Qdot605, eFluorNC605, and p(DT-SB)605, respectively. These donor−acceptor distance-based results do not suffer from deviations in size determination because of hydration or elongation of the nanoparticles, which is often the case for dynamic light scattering or size exclusion chromatography.

A closer look at the single distances calculated from the multiexponential fit reveals additional information about the shape of the different QDs. Although the donor and acceptor channel data provide similar information, the acceptor channel should be less error-prone because of the higher signal to background ratio, as already mentioned above. As expected the p(DT-SB)605(A) and p(DT-SB)605(B) show the same results concerning distances and fractions of donor−acceptor pairs at the different distances and they are therefore treated together as p(DT-SB)605 in the following considerations. For the time-resolved FRET analysis these two dots serve rather as another independent control of our fit procedures. Because of the relatively large (no point dipoles) and more or less elongated QDs as well as the random labeling of Lumi4-Tb over the sAv protein all of our investigated FRET systems displayed a donor−acceptor distance distribution. The aim of our time-resolved study was to extract reliable and reproducible information from all the PL decay curves with as few fit parameters as possible. Therefore a triple-exponential fit was applied to the donor PL decays, whereas a quadruple-exponential fit was used for the acceptor PL decays (cf. Experimental Section for details). The determined PL decay times (and distances) can be interpreted as average decay times (and distances) within the overall distribution. All different FRET systems show two main average donor−acceptor distances and one minor average short distance, which can only be resolved within the acceptor channel. The appearance of two main distances shows that none of the QDs is a spherical particle, for which only one major distance component would exist. The different α values in Table 2 represent the fractions of donor−acceptor pairs at the three resolved distances. The amount of donor−acceptor pairs at the shortest distance is almost negligible (below 6% for all FRET systems). However, it is important to include the corresponding decay time in the fits in order to improve the fit result and the resolution of the main two FRET distances. As already mentioned above the fraction of donor−acceptor pairs at the short major distance should increase with elongation of the particle and this is exactly the case for our results. The eFluorNC605 are a mixture of quasi-spherical and tetrahedral QDs (cf. Figure 3 center) with relatively uniform sizes. This is reflected in the relatively small fraction of the short main component (ca. 20% at a 5.7 nm distance). The p(DT-SB)605 are a bit more elongated (Figure 3 right), which results in a relative increase of the short main FRET component (ca. 30% at a 5 nm distance). For the strongly elongated Qdot605 (Figure 3 left) the short main component further increases up to ca. 40% at a 6.7 nm distance. Although it is difficult to determine the exact shape of the nanoparticles with our three main average decay times and their amplitude fractions, these three distances provide very useful information about the QD sizes and shapes under conditions for which they were intended for (a solution phase bioassay at subnanomolar concentrations in our case) instead of "unnatural" conditions such as the analysis on a TEM grid. We believe that our FRET technique is extremely useful to provide this "natural" information, which can be used profitably in combination with the data obtained from TEM, DLS, HPLC or other analytical techniques to complete and/or verify the shape and size information about the QD materials.

Analysis of Unquenched Tb Luminescence and the Number of Biotins per QD. Another interesting aspect of our FRET systems is the remaining unquenched Tb luminescence even at concentrations, for which the QDs are in excess (see the Supporting Information for the complete data). A priori, one would assume that all Lumi4-Tb are quenched (at least partially) once every Lumi4-Tb-sAv has bound to a QD. However, all decay time fits show a significant fraction of unquenched Lumi4-Tb even at QD excess. These fractions are given by the amplitude (α_{DA*3}) of the long unquenched decay time component (τ_{DA3}) divided by the amplitude ($\alpha_{D2} = 0.86$) of this same decay time component for the decay curves of Lumi4-Tb-sAv without biot-QD ($\tau_{D2} = \tau_{DA3}$). This leads to unquenched Lumi4-Tb fractions of 64% for the Qdot605 FRET system, 58% for the eFluorNC605 FRET system, 51% for the p(DT-SB)(A) FRET system and 26% for the p(DT-SB)(B) FRET system. One must take into account that this is not the fraction of unquenched Lumi4-Tb-sAv but of unquenched Lumi4-Tb. Due to the random labeling ratio of 4.2 Lumi4-Tb per sAv some of the Lumi4-Tb complexes are too far away from the QD to be engaged in FRET. This situation is fulfilled for (i) Lumi4-Tb, which is situated on the far end (from the organic QD coating surface) of the sAv (regarding the simplified picture of Scheme 1 this will be approximately 50%), and (ii) Lumi4-Tb-sAv bound to QD coating surface spaces, which are far away from the QD center (because of the nonspherical shape of the QDs, there are closer and further center-to-surface distances). The latter point also explains why the fraction of unquenched Lumi4-Tb is largest for the Qdot605 FRET system (largest and most elongated QD) and decreases for the eFluorNC605 and the p(DT-SB)(A) FRET systems (smaller and less elongated). Another possibility could be a fraction of unreactive (e.g., denatured) Lumi4-Tb-sAv. However, regarding the smallest fraction of unquenched Lumi4-Tb (26%) for the p(DT-SB)(B) FRET system (for which the two long-distance arguments mentioned above are still valid, although less pronounced, see discussion below) and the fact that we used the same Lumi4-Tb-sAv for all FRET systems, the fraction of nonreactive Lumi4-Tb-sAv is rather small (significantly lower than 26%). The large difference in unquenched Lumi4-Tb-sAv for the two similar p(DT-SB)605(A) and (B) systems (only the number of biotins per QD are different) suggests that the higher overall quenching efficiency within the p(DT-SB)605(B) FRET system is caused by the lower number of biotins per QD (see Table 1). The intensity fraction ($\tau_{DA*3}\alpha_{DA*3}$) of the long unquenched Tb luminescence decay component as a function of QD/sAv ratio (see the Supporting Information, Figure S5) shows a linear quenching behavior with increasing amounts of QD, caused by the excess of Lumi4-Tb-sAv. The linear decrease of "pure" Tb emission intensity levels off at QD/sAv ratios below 0.5 and stays at a constant level after 0.5 QD/sAv for Qdot605, eFluorNC605, and p(DT-SB)605(A). This shows that for these QDs several sAv can bind to the QD surface (several biotins per QD) and there is no difference in Tb quenching between several sAv per QD or a single sAv per QD, as long as each sAv is bound to a biotin on a QD surface. The binding situation is different for the p(DT-SB)605(B) FRET system (with ca. 1

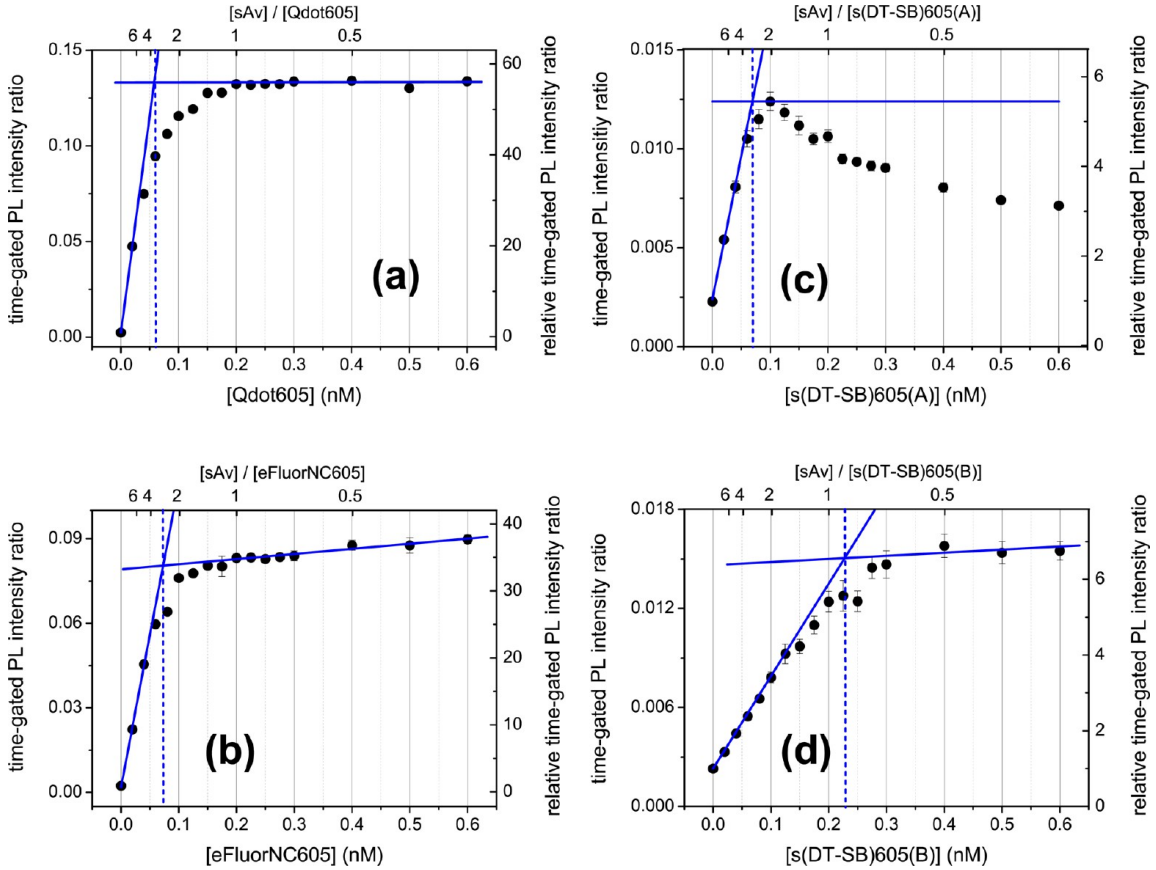

Figure 6. FRET-bioassay calibration curves. Time-gated (100−900 μs) intensity ratios of the FRET systems using Lumi4-Tb as a donor and (a) Qdot605, (b) eFluorNC605, (c) p(DT-SB)605(A), and (d) p(DT-SB)605(B) as acceptors as a function of QD concentration. The Lumi4-Tb-sAv concentration is constant at 0.2 nM within all assays. The intersection point of the blue lines (representing the linear increasing and the saturation parts of the assay curves) is used to determine the biotin molecules on the QD surface (equal to the sAv/QD ratio at that point). Most error bars are smaller than the data points.

biot/QD), for which the attachment of several sAv to one QD is not possible. For p(DT-SB)605(B) it seems that Tb quenching continues even after a 1/1 ratio of QD/sAv. We assume that in this FRET system, the binding of more than one QD per sAv (sAv has four binding sites for biotin) is the preferred system once QD and sAv are in a similar concentration range. This would explain the higher overall quenching efficiency (less unquenched Lumi4-Tb) as there are 4.2 Lumi4-Tb per sAv and the availability of more than one QD for one Lumi4-Tb-sAv leads to the quenching of more Lumi4-Tb per sAv. Figure 6d shows that a complete saturation of FRET-sensitization is reached around 0.5 sAv/p(DT-SB)605-(B), which suggests a formation of a maximum of two p(DT-SB)605(B) per Lumi4-Tb-sAv. For the other three FRET systems FRET-sensitization of QDs is saturated at a concentration of ca. one Lumi4-Tb-sAv per QD and a further addition of biot-QD does not lead to the creation of new FRET pairs (no more free Lumi4-Tb-sAv available). The tangents of the linearly increasing and the saturation parts of the FRET-assay curves were used to calculate the biot/QD ratios, which were 3 to 4 for Qdot605, eFluorNC605 and p(DT-SB)605(A) and ca. 1 for p(DT-SB)605(B). As the sAv/QD axis is not linear a precise determination of the biotin number becomes more difficult the higher the sAv/QD ratio. Nevertheless, we believe that our FRET-based results provide relatively precise results for the biotin labeling ratio (±30%) and thus we conclude that the biot/QD ratio for the Qdot605 is lower than "typically" suggested (5−7 biot/QD) by LifeTechnologies. For p(DT-SB)605(A) the PL intensity ratio curve decreased after saturation, which we attributed to coaggregation of multivalent sAv and biot-QDs, leading to less efficient binding of the Lumi4-Tb-sAv to the biotins on the QD surface when these QDs are in excess. The number of biomolecules per QDs is an important value for many biosensing applications. Our TR-FRET method provides very precise values for the biot/QD ratio measured under physiological conditions at subnanomolar concentrations.

TR-FRET Assays. Our study is based on homogeneous assays, which do not require any separation and washing steps because the FRET signal can be efficiently distinguished from the emission signals of all other components. Therefore, the assay format is very well suited for fast and easily applicable diagnostic tests such as point-of-care diagnostics. A general drawback of point-of-care assays is the lack of sensitivity and thus one of our major goals was the determination of detection limits for our TR-FRET bioassays using the different QD types. The KRYPTOR fluorescence plate reader, a clinical diagnostic plate reader that is commonly used for immunoassays in hospitals and clinical laboratories, is an ideal instrument for comparing sensitivities toward a clinical application. As biotin-streptavidin does not provide an ideal comparison to antibody−antigen immunoassay systems, we used the Eu-TBP/APC

FRET pair (which is used in the commercial BRAHMS-KRYPTOR immunoassays) in the same biotin-streptavidin configuration for comparison. This Eu-TBP-sAv-biot-APC FRET system has an LOD of (24 ± 12) pM.[20] We took advantage of the inherent ratiometric behavior of FRET and used the ratio of the time-gated PL intensities of the QD acceptors (e.g., graphs b in Figures 4 and 5) and the Tb-donor (e.g., graphs a in Figures 4 and 5) in order to achieve a very accurate and highly sensitive quantitative analysis. The time-gated PL ratios as a function of QD concentration for all Tb-to-QD FRET bioassays are presented in Figure 6.

For all four assays the addition of small biot-QD concentrations to Lumi4-Tb-sAv leads to a strong increase of the time-gated PL intensity ratio. This increase is linear until a concentration for which all biotins on the QD surface are bound to one sAv. Higher concentrations lead to a decrease in Lumi4-Tb-sAv per QD and the slope levels off. The limits of detection (LODs) for all assays were calculated as the concentration value for the PL intensity ratio of the sample containing no QDs (zero concentration) plus three times the standard deviation (of 30 measurements). The LOD is dependent on the amount of biotin per QD (more biotin results in a steeper slope), the FRET efficiency and the quantum yield of the QD (the higher these values the steeper the increasing slope of the PL intensity ratio curve). Moreover, the signal-to-noise ratio and reproducibility for the zero concentration sample is important but similar for all FRET systems (as these samples all contain only Lumi4-Tb-sAv). As the biot/QD ratios are not significantly different for the first three QDs the higher quantum yields of Qdot605 and eFluorNC605 are the main aspect that lead to favorable LODs, 0.063 pM and 0.094 pM, respectively, compared to 0.73 pM for p(DT-SB)605(A). The lower biot/QD ratio of p(DT-SB)605(B) leads to an additional increase of the LOD to 2.0 pM. Although these values cannot be transferred as one-to-one to an immunoassay LOD, they are 381-fold, 225-fold, 33-fold and 12-fold lower than the 24 pM LOD for the Eu-TBP/APC "gold standard" FRET system measured in the same biot-sAv configuration. We conclude that all QD systems (commercial and academic) provide very low (pico to subpicomolar) LODs, which means that they are all suitable for highly sensitive biosensing.

CONCLUSIONS

In this TR-FRET study, we have shown that different types of biocompatible QDs (encapsulated and ligand exchanged) can be used for highly sensitive biosensing with low pM to sub-pM detection limits. Our simultaneous TR-FRET analysis of the Lumi4-Tb donor and the QD acceptors allowed us to perform a very precise characterization of the QD materials in terms of shape, size and bioconjugation ratio. We found Qdot605 to be the largest and most elongated QDs with the thickest organic coating around the semiconductor material. Although this thick shell provides the QDs with high stability and brightness, they have the significant drawback of increasing the donor−acceptor distance, which decreases the FRET efficiency. From this point of view the self-synthesized QDs (p(DT-SB)605) show the highest FRET efficiency and thinnest coating. Time-resolved and time-gated analysis also gives close insights into the bioconjugation performance (how many biotins are attached to the QD surface). We could determine biot/QD ratios of ca. 3 to 4 for Qdot605, eFluorNC605 and p(DT-SB)605(A) and ca. 1 for p(DT-SB)605(B). In conclusion we have demonstrated the suitability of all studied QDs for highly sensitive clinical FRET-bioassays. We have performed a very precise and detailed analysis of biocompatible QDs with TR-FRET from Tb-based donor complexes. On the contrary to most of the other analytical technologies (e.g., dynamic light scattering, HPLC and TEM) our FRET method can analyze the biocompatible QDs under physiological conditions at sub-nanomolar concentrations and is therefore highly suited (ideally in combination with the other techniques) to give a more accurate picture of the QD properties at concentrations and conditions in which they are usually applied within fluorescence sensing applications.

ASSOCIATED CONTENT

Supporting Information

(1) Determination of the Förster distances; (2) high-resolution TEM images of Qdot605, eFluorNC605 and p(DT-SB)605; (3) time-gated PL intensities and decays of Lumi4-Tb-sAv-biotQdot605 and of Lumi4-Tb-sAv-biot-p(DT-SB)605(A); (4) control experiments using Lumi4-Tb-sAv and QDs without any biotin on the surface; (5) intensity fraction as a function of p(DT-SB)605(B)/sAv ratio; (6) complete TR-analysis data of the Lumi4-Tb-sAv-biot-Qdot605 FRET system, the Lumi4-Tb-sAv-biot-eFluorNC605 FRET system, the Lumi4-Tb-sAv-biot-p(DT-SB)605(A) FRET system, and the Lumi4-Tb-sAv-biot-p(DT-SB)605(B) FRET system. This material is available free of charge via the Internet at http://pubs.acs.org.

AUTHOR INFORMATION

Corresponding Author

*E-mail: niko.hildebrandt@u-psud.fr.

Notes

The authors declare no competing financial interest.

ACKNOWLEDGMENTS

The authors thank the Ministère de l'enseignement supérieure et de la recherche France (Investissement d'avenir project NanoCTC) and the European Commission (FP7 project NANOGNOSTICS) for financial support.

REFERENCES

(1) Algar, W. R.; Susumu, K.; Delehanty, J. B.; Medintz, I. L. *Anal. Chem.* **2011**, *83*, 8826.
(2) Gill, R.; Zayats, M.; Willner, I. *Angew. Chem., Int. Ed.* **2008**, *47*, 7602.
(3) Jin, Z.; Hildebrandt, N. *Trends Biotechnol.* **2012**, *30*, 394.
(4) Rosenthal, S. J.; Chang, J. C.; Kovtun, O.; McBride, J. R.; Tomlinson, I. D. *Chem. Biol.* **2011**, *18*, 10.
(5) Reiss, P.; Protiere, M.; Li, L. *Small* **2009**, *5*, 154.
(6) Hildebrandt, N. *ACS Nano* **2011**, *5*, 5286.
(7) Hezinger, A. F. E.; Tessmar, J.; Goepferich, A. *Eur. J. Pharm. Biopharm.* **2008**, *68*, 138.
(8) Medintz, I. L.; Uyeda, H. T.; Goldman, E. R.; Mattoussi, H. *Nat. Mater.* **2005**, *4*, 435.
(9) Wild, D. *The Immunoassay Handbook*, 2nd ed.; Elsevier: Amsterdam, 2005.
(10) Bünzli, J.-C. G. *Chem. Rev.* **2010**, *110*, 2729.
(11) Eliseeva, S. V.; Bünzli, J.-C. G. *Chem. Soc. Rev.* **2010**, *39*, 189.
(12) Hemmilä, I.; Mukkala, V. M. *Crit. Rev. Clin. Lab. Sci.* **2001**, *38*, 441.
(13) Selvin, P. R. *Annu. Rev. Biopharm. Biomed.* **2002**, *31*, 275.
(14) Mathis, G. *Clin. Chem.* **1993**, *39*, 1953.
(15) Mathis, G. *J. Biomol. Screen.* **1999**, *4*, 309.
(16) Hemmilä, I. *J. Biomol. Screen.* **1999**, *4*, 303.

(17) Algar, W. R.; Wegner, D.; Huston, A. L.; Blanco-Canosa, J. B.; Stewart, M. H.; Armstrong, A.; Dawson, P. E.; Hildebrandt, N.; Medintz, I. L. *J. Am. Chem. Soc.* **2012**, *134*, 1876.
(18) Charbonnière, L. J.; Hildebrandt, N. *Eur. J. Inorg. Chem.* **2008**, 3241.
(19) Charbonnière, L. J.; Hildebrandt, N.; Ziessel, R. F.; Löhmannsröben, H.-G. *J. Am. Chem. Soc.* **2006**, *128*, 12800.
(20) Geißler, D.; Charbonnière, L. J.; Ziessel, R. F.; Butlin, N. G.; Löhmannsröben, H.-G.; Hildebrandt, N. *Angew. Chem., Int. Ed.* **2010**, *49*, 1396.
(21) Hildebrandt, N.; Charbonnière, L. J.; Beck, M.; Ziessel, R. F.; Löhmannsröben, H. -G. *Angew. Chem., Int. Ed.* **2005**, *44*, 7612.
(22) Xu, J.; Corneillie, T. M.; Moore, E. G.; Law, G.-L.; Butlin, N. G.; Raymond, K. N. *J. Am. Chem. Soc.* **2011**, *133*, 19900.
(23) Li, J. J.; Wang, Y. A.; Guo, W. Z.; Keay, J. C.; Mishima, T. D.; Johnson, M. B.; Peng, X. G. *J. Am. Chem. Soc.* **2003**, *125*, 12567.
(24) Yu, W. W.; Peng, X. G. *Angew. Chem., Int. Ed.* **2002**, *41*, 2368.
(25) Giovanelli, E.; Muro, E.; Sitbon, G.; Hanafi, M.; Pons, T.; Dubertret, B.; Lequeux, N. *Langmuir* **2012**, *28*, 15177.
(26) Lakowicz, J. R. *Principles of Fluorescence Spectroscopy*, 2nd ed.; Kluwer Academic/Plenum: New York, 1999.
(27) Pace, C. N.; Vajdos, F.; Fee, L.; Grimsley, G.; Gray, T. *Protein Sci.* **1995**, *4*, 2411.
(28) Wu, P. G.; Brand, L. *Anal. Biochem.* **1994**, *218*, 1.
(29) Sillen, A.; Engelborghs, Y. *Photochem. Photobiol.* **1998**, *67*, 475.
(30) Liu, W.; Howarth, M.; Greytak, A. B.; Zheng, Y.; Nocera, D. G.; Ting, A. Y.; Bawendi, M. G. *J. Am. Chem. Soc.* **2008**, *130*, 1274.
(31) Uyeda, H. T.; Medintz, I. L.; Jaiswal, J. K.; Simon, S. M.; Mattoussi, H. *J. Am. Chem. Soc.* **2005**, *127*, 3870.
(32) Morgner, F.; Geißler, D.; Stufler, S.; Butlin, N. G.; Löhmannsröben, H.-G.; Hildebrandt, N. *Angew. Chem., Int. Ed.* **2010**, *49*, 7570.
(33) Geißler, D.; Stufler, S.; Löhmannsröben, H.-G.; Hildebrandt, N. *J. Am. Chem. Soc.* **2013**, *135*, 1102.

Influence of luminescence quantum yield, surface coating and functionalization of quantum dots on the sensitivity of time-resolved FRET bioassays

K. David Wegner[1], Phung Thi Lanh[1], Travis Jennings[2], Eunkeu Oh[3,4], Vaibhav Jain[3], Simon M. Fairclough[5], Jason M. Smith[5], Emerson Giovanelli[6], Nicolas Lequeux[6], Thomas Pons[6] and Niko Hildebrandt[1*]

Supporting Information

Determination of the Förster distances

The Förster distances R_0 mentioned in Table 1 were calculated using the following equation:

$$R_0 = 0.02108 \left(\kappa^2 \Phi_D n^{-4} J\right)^{1/6} \text{ nm}$$

where κ^2 is the FRET orientation factor, which was assumed to be 2/3 for random orientation during the FRET time (as verified by the unpolarized emission of Tb and QDs) caused by a large flexibility within the FRET system (e.g. biot-Sav binding, Lumi4-Tb-lysin binding, the sAv flexibility and the Lumi4-Tb flexibility). Φ_D is the Tb-centered luminescence quantum yield (Table 1), n is the index of refraction of the buffer solution (n = 1.4) and J is the spectral overlap integral in $M^{-1}cm^{-1}nm^4$.

$$J = \int \bar{I}_D(\lambda)\ \varepsilon_A(\lambda)\ \lambda^4\, d\lambda$$

is dependent on the acceptor molar absorptivity spectrum ε_A (Figure 2a) and the donor emission spectrum $\bar{I}_D$ normalized to unity (Figure 1a) and was calculated between 450 and 700 nm for each donor-acceptor pair.

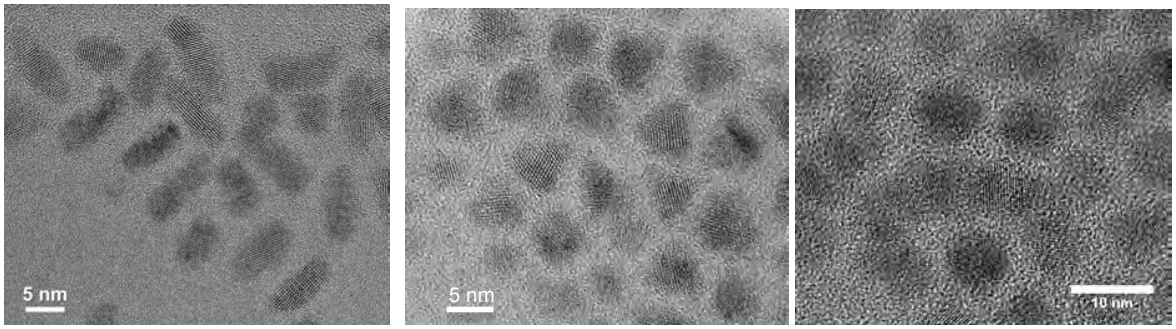

Figure S1: High resolution TEM images (showing only the core/shell structure of the QDs) of Qdot605 (left), eFluorNC605 (center) and p(DT-SB)605 (right).

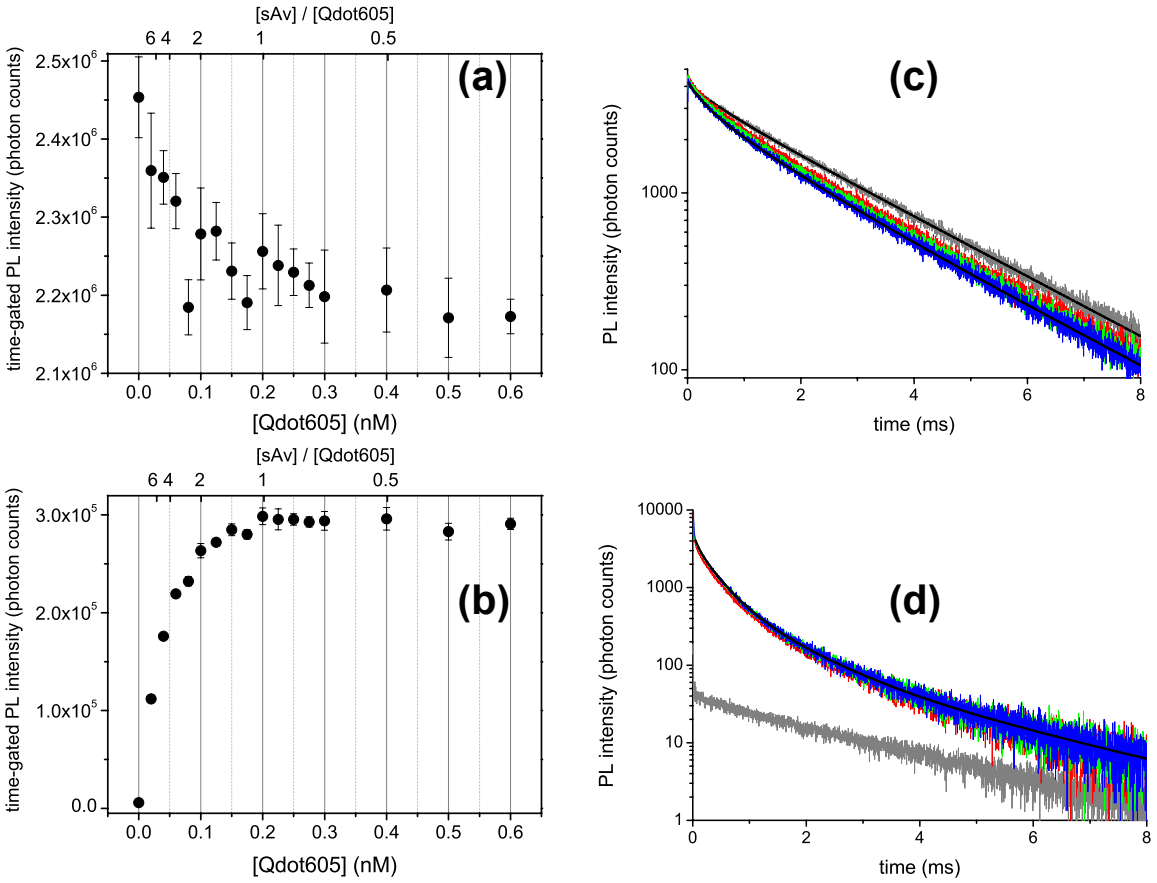

Figure S2: Time-gated (100 – 900 µs) PL intensity (as a function of Qdot605 concentration) of the Lumi4-Tb donor (a) and the Qdot605 acceptor (b) showing efficient FRET donor quenching and acceptor sensitization, which increases until a sAv/Qdot605 concentration ratio of approximately one. The PL decay curves of the donor (c) and the acceptor (d) show a strongly multi-exponential decay behavior caused by FRET from Lumi4-Tb to Qdot605 situated at different distances from the QD. Only some representative decay and fit curves are presented. Grey: pure Lumi4-Tb-sAv; red: 0.06 nM QD; green: 0.1 nM QD; blue: 0.15 nM QD; black: fit curves (for clarity only few representative fit curves are shown here).

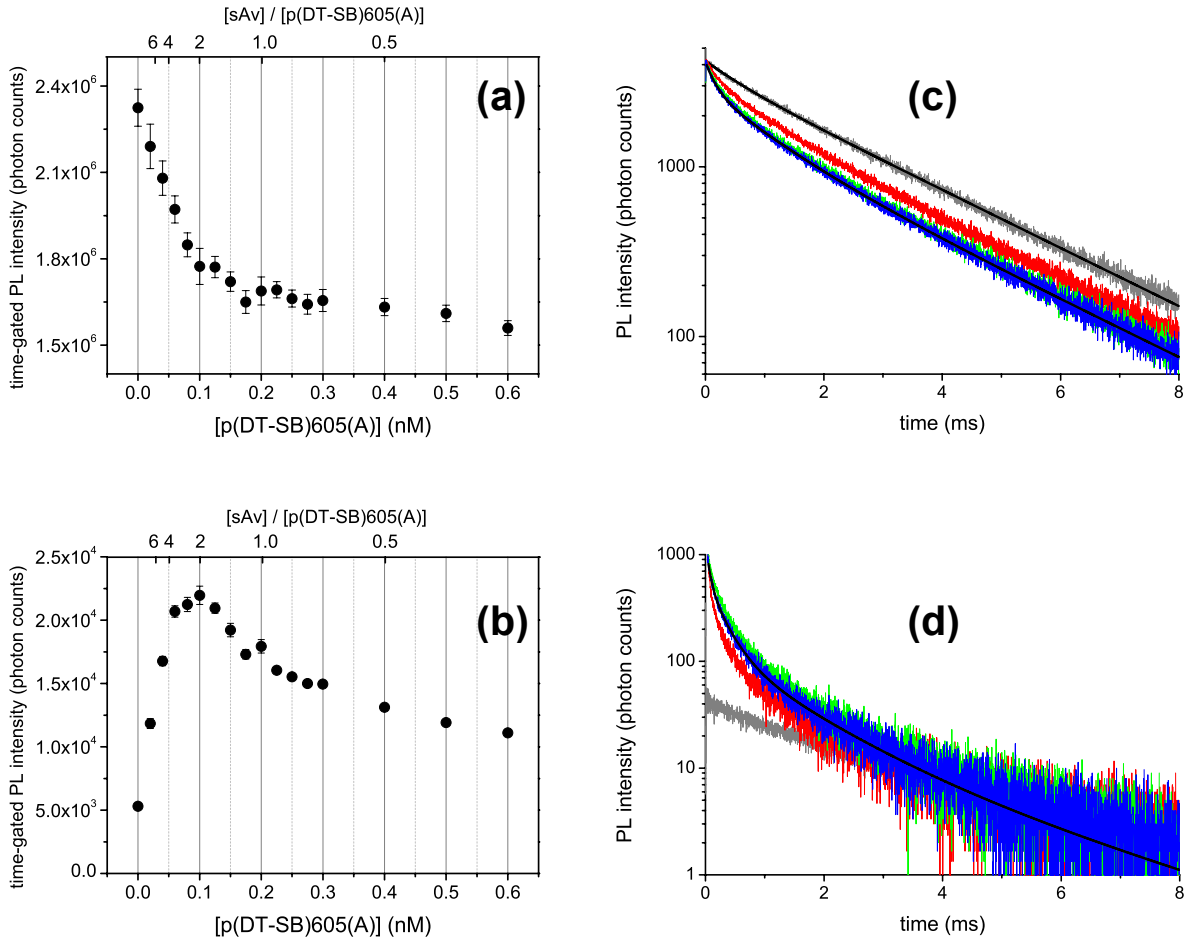

Figure S3: Time-gated (100 – 900 µs) PL intensity (as a function of p(DT-SB)605(A) concentration) of the Lumi4-Tb donor (a) and the p(DT-SB)605(A) acceptor (b) showing efficient FRET donor quenching and acceptor senitization, which increases until a sAv/p(DT-SB)605(A) concentration ratio of approximately one. The PL decay curves of the donor (c) and the acceptor (d) show a strongly multi-exponential decay behavior caused by FRET from Lumi4-Tb to p(DT-SB)605(A) situated at different distances from the QD. Only some representative decay and fit curves are presented. Grey: pure Lumi4-Tb-sAv; red: 0.06 nM QD; green: 0.1 nM QD; blue: 0.2 nM QD; black: fit curves (for clarity only few representative fit curves are shown here).

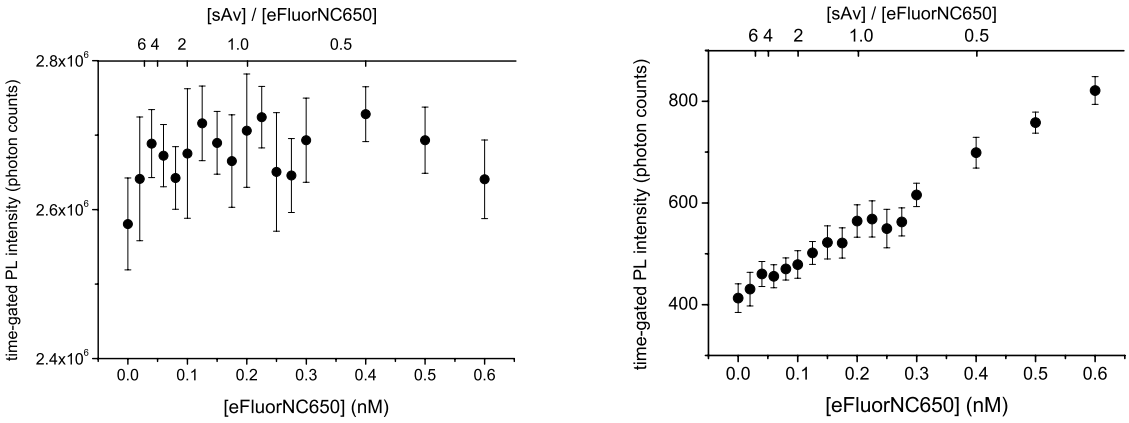

Figure S4: Control experiments using Lumi4-Tb-sAv and QDs (in this case eFluorNC650) without any biotin on the surface. Time-gated (100 – 900 µ s) PL intensity (as a function of eFluorNC650 concentration) of Lumi4-Tb (left) and eFluorNC650 (right). The donor intensities are in the same range as e.g. in Figure 4a within the manuscript. However they are constant and not quenched with increasing QD concentration because there is no binding between Lumi4-Tb-sAv and eFluoreNC650 (=no FRET). The time-gated eFluorNC650 PL intensities show a slight linear increase with QD concentration. However, this is due to very low intensities (below 1000 photon counts compared to an intensity range of ca. 60000 to 230000 photon counts for the FRET case in Figure 4b in the manuscript) of remaining (even after 100 µs of time-gating) QD PL resulting from direct excitation.

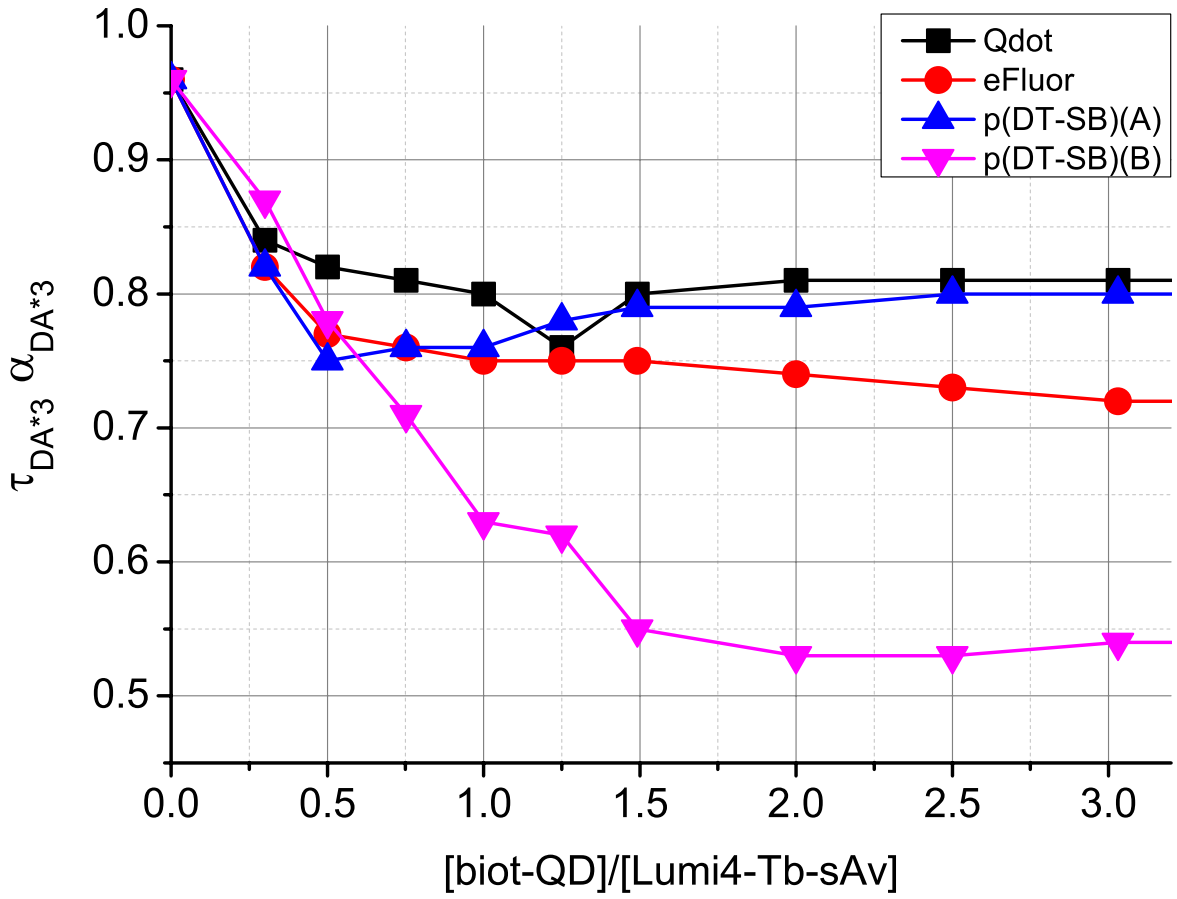

Figure S5: The intensity fraction (τ_{DA*3} α_{DA*3}) of the long unquenched Tb luminescence decay component τ_{DA*3} as a function of QD/sAv ratio.

Complete data from the TR-analysis of the Lumi4-Tb-sAv-biot-Qdot605 FRET system (all values are average values from three replicate measurements)

Donor Channel R_0(nm) 9.1

Channel 10-3999 fixed decay background

D or DA	Qdot [nM]	τ_1	A_1	α_{DA*1}	α_{DA1}	τ_2	A_2	α_{DA*2}	α_{DA2}	$\langle\tau_{DA}\rangle$	fixed τ_3	A_3	α_{DA*3}	$\langle\tau_D\rangle$	z(D)	$\langle\tau_{DA}\rangle$ corr	η_{FRET}	averaging	Qdot [nM]	sAv/QD	sAv/Biot
D	0.00					644	583	0.14			2582	3610	0.86	2312					0.00	inf.	inf.
DA	0.06	264	680	0.16	0.39	1081	1055	0.24	0.61	761	2580	2630	0.60	1857	0.10	773	0.67		0.06	3.3	0.83
DA	0.10	265	724	0.17	0.40	1094	1106	0.26	0.60	766	2580	2438	0.57	1802	0.09	778	0.66		0.10	2.0	0.50
DA	0.15	267	769	0.18	0.40	1105	1130	0.27	0.60	766	2580	2338	0.55	1767	0.09	778	0.66		0.15	1.3	0.33
DA	0.20	272	748	0.18	0.40	1106	1119	0.27	0.60	772	2580	2302	0.55	1770	0.09	784	0.66		0.20	1.0	0.25
DA	0.25	269	777	0.17	0.34	1111	1529	0.33	0.66	827	2580	2322	0.50	1707	0.08	843	0.64		0.25	0.8	0.20
DA	0.30	267	762	0.19	0.41	1114	1092	0.27	0.59	766	2580	2242	0.55	1759	0.09	778	0.66		0.30	0.7	0.17
DA	0.40	250	722	0.17	0.39	1084	1132	0.27	0.61	759	2580	2275	0.55	1762	0.09	770	0.67		0.40	0.5	0.13
DA	0.50	290	789	0.19	0.43	1132	1066	0.26	0.57	774	2580	2313	0.55	1776	0.09	787	0.66		0.50	0.4	0.10
DA	0.60	275	806	0.19	0.42	1111	1121	0.26	0.58	761	2580	2384	0.55	1767	0.09	773	0.67		0.60	0.3	0.08
		269	753	0.18	0.40	1104	1150	0.27	0.60	772	2580	2360	0.55		0.09	785	0.66				
		269	762	0.18	0.40	1107	1162	0.27	0.60	774	2580	2327	0.55		0.09	786	0.66				
distance *r*		**6.5**				**9.0**										**8.1**					

Biot/QD 4

intensity information		
% τ_i*$\alpha_{i,1}$	% τ_i*$\alpha_{i,2}$	% τ_i*$\alpha_{i,3}$
0.000	0.039	0.96
0.022	0.141	0.84
0.025	0.157	0.82
0.027	0.167	0.81
0.028	0.168	0.80
0.026	0.215	0.76
0.028	0.169	0.80
0.025	0.169	0.81
0.031	0.163	0.81
0.029	0.163	0.81
0.0	0.168	0.81
0.0	0.171	0.80

Acceptor Channel

Channel 25-3000 fixed decay background

τ_{DA}	Qdot [nM]	τ_0	A_0	α_{AD*0}	k_{FRET0}	α_{AD0}	τ_1	A_1	α_{AD*1}	k_{FRET1}	α_{AD1}	τ_2	A_2	α_{AD*2}	k_{FRET2}	α_{AD2}	$\langle\tau_{DA}\rangle$	fixed τ_3	A_3	α_{AD*3}	z(A)	$\langle\tau_{DA}\rangle$ corr	η_{FRET}	averaging	Qdot [nM]	sAv/QD	sAv/Biot
2312	0.06	71	552	0.16	0.0137	0.020	336	2035	0.59	0.00255	0.40	925	745	0.22	0.00065	0.58	671	2580	114	0.033	0.0054	671	0.71		0.06	3.3	0.83
2312	0.10	74	670	0.17	0.0132	0.024	334	2254	0.58	0.00257	0.41	898	826	0.21	0.00068	0.57	647	2580	128	0.033	0.0053	647	0.72		0.10	2.0	0.50
2312	0.15	67	681	0.17	0.0144	0.021	325	2360	0.57	0.00265	0.39	874	939	0.23	0.00071	0.58	640	2580	136	0.033	0.0053	640	0.72		0.15	1.3	0.33
2312	0.20	72	782	0.19	0.0135	0.025	342	2436	0.58	0.00249	0.42	925	834	0.20	0.00065	0.55	658	2580	132	0.032	0.0051	658	0.72		0.20	1.0	0.25
2312	0.25	58	759	0.18	0.0167	0.020	324	2432	0.57	0.00265	0.40	872	956	0.22	0.00071	0.58	637	2580	138	0.032	0.0052	637	0.72		0.25	0.8	0.20
2312	0.30	58	743	0.18	0.0167	0.020	320	2392	0.57	0.00269	0.40	862	941	0.22	0.00073	0.58	629	2580	137	0.032	0.0052	629	0.73		0.30	0.7	0.17
2312	0.40	53	833	0.19	0.0186	0.020	318	2423	0.56	0.00271	0.40	860	954	0.22	0.00073	0.58	628	2580	138	0.032	0.0051	628	0.73		0.40	0.5	0.13
2312	0.50	48	865	0.20	0.0203	0.019	311	2413	0.55	0.00279	0.39	832	997	0.23	0.00077	0.59	612	2580	145	0.033	0.0053	612	0.74		0.50	0.4	0.10
2312	0.60	42	969	0.20	0.0235	0.018	297	2520	0.52	0.00294	0.37	803	1173	0.24	0.00081	0.62	605	2580	154	0.032	0.0052	604	0.74		0.60	0.3	0.08
		60	761	0.18	0.0167	0.021	323	2363	0.57	0.00267	0.40	872	929	0.22	0.00072	0.58	637	2580	136	0.032	0.0052	636	0.72				
		59	788	0.18	0.0171	0.021	321	2404	0.56	0.00269	0.40	866	952	0.22	0.00072	0.58	632	2580	139	0.032	0.0052	632	0.73				
distance *r*		**5.0**					**6.7**					**8.4**										**7.7**					

Biot/QD 4

intensity information			
% τ_0*α_{0}	% τ_i*$\alpha_{i,1}$	% τ_i*$\alpha_{i,2}$	% τ_i*$\alpha_{i,3}$
0.023	0.40	0.40	0.17
0.026	0.40	0.40	0.18
0.023	0.39	0.41	0.18
0.028	0.42	0.39	0.17
0.022	0.39	0.41	0.18
0.022	0.39	0.41	0.18
0.022	0.39	0.41	0.18
0.021	0.38	0.42	0.19
0.019	0.35	0.44	0.19
0.023	0.39	0.41	0.18
0.023	0.39	0.41	0.18

Complete data from the TR-analysis of the Lumi4-Tb-sAv-biot-eFluorNC605 FRET system (all values are average values from three replicate measurements)

Donor Channel R_0(nm) 7.8

Channel 10-3999 fixed decay background

Biot/QD 4

D or DA	eFluor [nM]	τ_1	A_1	α_{DA*1}	α_{DA1}	τ_2	A_2	α_{DA*2}	α_{DA2}	$\langle\tau_{DA}\rangle$	fixed τ_3	A_3	α_{DA*3}	$\langle\tau_D\rangle$	z(D)	$\langle\tau_{DA}\rangle$ corr	η_{FRET}	averaging	eFluor [nM]	sAv/QD	sAv/Biot	intensity information % $\tau_1*\alpha_{1*}$	% $\tau_2*\alpha_{2*}$	% $\tau_3*\alpha_{3*}$
D	0.00					619	596	0.14			2560	3515	0.86	2279					0.00	inf.	inf.	0.000	0.039	0.96
DA	0.06	234	522	0.12	0.30	1050	1238	0.29	0.70	808	2560	2480	0.58	1833	0.10	829	0.64		0.06	3.3	0.83	0.016	0.167	0.82
DA	0.10	233	580	0.14	0.29	1094	1414	0.34	0.71	843	2560	2207	0.53	1745	0.09	865	0.62		0.10	2.0	0.50	0.018	0.211	0.77
DA	0.15	235	572	0.14	0.29	1090	1427	0.35	0.71	846	2560	2120	0.51	1728	0.09	867	0.62		0.15	1.3	0.33	0.019	0.219	0.76
DA	0.20	240	595	0.14	0.29	1111	1477	0.35	0.71	861	2560	2101	0.50	1716	0.09	883	0.61		0.20	1.0	0.25	0.020	0.229	0.75
DA	0.25	240	560	0.14	0.28	1103	1443	0.35	0.72	862	2560	2073	0.51	1725	0.09	884	0.61		0.25	0.8	0.20	0.019	0.226	0.75
DA	0.30	242	547	0.14	0.28	1107	1399	0.36	0.72	864	2560	1937	0.50	1710	0.08	886	0.61		0.30	0.7	0.17	0.020	0.233	0.75
DA	0.40	250	567	0.15	0.29	1122	1419	0.37	0.71	873	2560	1898	0.49	1697	0.08	896	0.61		0.40	0.5	0.13	0.022	0.241	0.74
DA	0.50	243	569	0.14	0.28	1123	1468	0.37	0.72	877	2560	1932	0.49	1696	0.08	901	0.60		0.50	0.4	0.10	0.021	0.245	0.73
DA	0.60	262	610	0.15	0.29	1147	1472	0.37	0.71	887	2560	1903	0.48	1686	0.08	911	0.60		0.60	0.3	0.08	0.024	0.251	0.72
		242	569	0.14	0.29	1105	1417	0.35	0.71	858	2560	2072	0.51		0.09	880	0.61					0.0	0.225	0.76
		243	575	0.14	0.29	1112	1440	0.36	0.71	864	2560	2021	0.50		0.08	887	0.61					0.0	0.232	0.75
distance *r*		**5.5**				**7.7**										**7.2**								

Acceptor Channel

Channel 25-3000 fixed decay background

Biot/QD 4

τ_{DA}	eFluor [nM]	τ_0	A_0	α_{AD*0}	k_{FRET0}	α_{AD0}	τ_1	A_1	α_{AD*1}	k_{FRET1}	α_{AD1}	τ_2	A_2	α_{AD*2}	k_{FRET2}	α_{AD2}	$\langle\tau_{DA}\rangle$	fixed τ_3	A_3	α_{AD*3}	z(A)	$\langle\tau_{DA}\rangle$ corr	η_{FRET}	averaging	eFluor [nM]	sAv/QD	sAv/Biot
2279	0.06	82	644	0.30	0.0118	0.033	348	830	0.38	0.00243	0.21	1075	614	0.28	0.00049	0.76	891	2560	85	0.039	0.0066	893	0.61		0.06	3.3	0.83
2279	0.10	74	755	0.28	0.0131	0.030	319	1011	0.38	0.00270	0.20	1009	814	0.30	0.00055	0.77	845	2560	108	0.040	0.0068	847	0.63		0.10	2.0	0.50
2279	0.15	70	776	0.28	0.0138	0.028	316	1073	0.39	0.00273	0.20	1032	817	0.29	0.00053	0.77	863	2560	104	0.038	0.0064	865	0.62		0.15	1.3	0.33
2279	0.20	60	828	0.27	0.0162	0.025	296	1177	0.39	0.00294	0.19	1003	898	0.30	0.00056	0.78	842	2560	116	0.038	0.0065	844	0.63		0.20	1.0	0.25
2279	0.25	63	874	0.30	0.0154	0.028	311	1129	0.38	0.00278	0.20	1024	838	0.28	0.00054	0.77	854	2560	110	0.037	0.0063	855	0.62		0.25	0.8	0.20
2279	0.30	57	877	0.30	0.0171	0.026	296	1127	0.38	0.00294	0.20	1009	840	0.28	0.00055	0.78	844	2560	109	0.037	0.0063	846	0.63		0.30	0.7	0.17
2279	0.40	56	963	0.31	0.0174	0.027	289	1191	0.38	0.00302	0.19	1002	879	0.28	0.00056	0.78	837	2560	114	0.036	0.0061	838	0.63		0.40	0.5	0.13
2279	0.50	54	1103	0.33	0.0181	0.030	286	1224	0.36	0.00306	0.19	982	923	0.27	0.00058	0.78	819	2560	123	0.036	0.0062	820	0.64		0.50	0.4	0.10
2279	0.60	53	1229	0.34	0.0184	0.031	288	1315	0.36	0.00303	0.20	1000	940	0.26	0.00056	0.77	829	2560	123	0.034	0.0058	830	0.64		0.60	0.3	0.08
		63	894	0.30	0.0157	0.029	305	1120	0.38	0.00285	0.20	1015	840	0.28	0.00055	0.77	847	2560	110	0.037	0.0063	849	0.63				
		61	926	0.30	0.0162	0.028	300	1156	0.38	0.00290	0.20	1008	869	0.28	0.00055	0.77	842	2560	113	0.037	0.0063	843	0.63				
distance *r*		**4.3**					**5.7**					**7.5**										**7.1**					

intensity information			
% $\tau_0*\alpha_{0*}$	% $\tau_1*\alpha_{1*}$	% $\tau_2*\alpha_{2*}$	% $\tau_3*\alpha_{3*}$
0.043	0.24	0.54	0.18
0.038	0.22	0.56	0.19
0.036	0.23	0.56	0.18
0.031	0.22	0.56	0.19
0.036	0.23	0.56	0.18
0.033	0.22	0.56	0.18
0.034	0.22	0.56	0.19
0.037	0.21	0.56	0.19
0.038	0.22	0.55	0.19
0.036	0.22	0.56	0.18
0.035	0.22	0.56	0.19

Complete data from the TR-analysis of the Lumi4-Tb-sAv-biot-TP605(A) FRET system (all values are average values from three replicate measurements)

Donor Channel R_0(nm) 7.4

Channel 10-3999 fixed decay background

Biot/QD 4

D or DA	TP(A) [nM]	τ_1	A_1	α_{DA*1}	α_{DA1}	τ_2	A_2	α_{DA*2}	α_{DA2}	$\langle\tau_{DA}\rangle$	fixed τ_3	A_3	α_{DA*3}	$\langle\tau_D\rangle$	z(D)	$\langle\tau_{DA}\rangle$ corr	η_{FRET}	averaging	TP(A) [nM]	sAv/QD	sAv/Biot	intensity information % $\tau_1*\alpha_{1}$	% $\tau_2*\alpha_{2}$	% $\tau_3*\alpha_{3}$
D	0.00					635	600	0.14			2566	3593	0.86	2289					0.00	inf.	inf.	0.000	0.040	0.96
DA	0.06	194	865	0.21	0.44	1007	1108	0.26	0.56	650	2570	2233	0.53	1669	0.09	652	0.72		0.06	3.3	0.83	0.024	0.159	0.82
DA	0.10	196	1077	0.27	0.47	1017	1211	0.30	0.53	630	2570	1726	0.43	1464	0.07	630	0.72		0.10	2.0	0.50	0.036	0.210	0.75
DA	0.15	185	1085	0.28	0.48	995	1174	0.30	0.52	606	2570	1663	0.42	1439	0.07	604	0.74		0.15	1.3	0.33	0.035	0.207	0.76
DA	0.20	187	1111	0.29	0.50	996	1095	0.28	0.50	589	2570	1644	0.43	1434	0.07	585	0.74		0.20	1.0	0.25	0.038	0.197	0.76
DA	0.25	175	1111	0.29	0.51	971	1076	0.28	0.49	567	2570	1697	0.44	1442	0.07	561	0.75		0.25	0.8	0.20	0.035	0.186	0.78
DA	0.30	161	1093	0.29	0.51	943	1046	0.27	0.49	544	2570	1666	0.44	1431	0.07	536	0.77		0.30	0.7	0.17	0.032	0.181	0.79
DA	0.40	163	1077	0.29	0.52	939	987	0.27	0.48	534	2570	1643	0.44	1436	0.07	526	0.77		0.40	0.5	0.13	0.033	0.174	0.79
DA	0.50	154	1104	0.29	0.53	911	974	0.26	0.47	509	2570	1681	0.45	1430	0.07	498	0.78		0.50	0.4	0.10	0.032	0.165	0.80
DA	0.60	149	1173	0.31	0.55	927	962	0.25	0.45	499	2570	1687	0.44	1413	0.07	489	0.79		0.60	0.3	0.08	0.032	0.165	0.80
		174	1077	0.28	0.50	967	1070	0.28	0.50	570	2570	1738	0.45		0.07	565	0.75					0.0	0.183	0.78
		171	1104	0.29	0.51	962	1066	0.28	0.49	560	2570	1676	0.44		0.07	554	0.76					0.0	0.186	0.78
distance *r*		**4.9**				**7.0**										**6.1**								

Acceptor Channel

Channel 25-3000 fixed decay background

Biot/QD 4

τ_{DA}	TP(A) [nM]	τ_0	A_0	α_{AD*0}	k_{FRET0}	α_{AD0}	τ_1	A_1	α_{AD*1}	k_{FRET1}	α_{AD1}	τ_2	A_2	α_{AD*2}	k_{FRET2}	α_{AD2}	$\langle\tau_{DA}\rangle$	fixed τ_3	A_3	α_{AD*3}	z(A)	$\langle\tau_{DA}\rangle$ corr	η_{FRET}	averaging	TP(A) [nM]	sAv/QD	sAv/Biot
2289	0.06	50	235	0.27	0.0196	0.041	199	390	0.44	0.00459	0.29	690	196	0.22	0.00101	0.67	520	2570	57	0.065	0.0108	519	0.77		0.06	3.3	0.83
2289	0.10	37	210	0.22	0.0266	0.026	160	459	0.48	0.00581	0.26	609	259	0.27	0.00121	0.71	477	2570	38	0.039	0.0066	475	0.79		0.10	2.0	0.50
2289	0.15	51	257	0.31	0.0192	0.044	211	366	0.44	0.00430	0.28	774	174	0.21	0.00086	0.67	583	2570	35	0.042	0.0070	583	0.75		0.15	1.3	0.33
2289	0.20	32	239	0.28	0.0308	0.032	174	378	0.45	0.00531	0.29	644	183	0.22	0.00112	0.68	487	2570	39	0.046	0.0078	486	0.79		0.20	1.0	0.25
2289	0.25	30	250	0.32	0.0329	0.037	158	326	0.41	0.00589	0.27	599	178	0.22	0.00123	0.70	460	2570	39	0.049	0.0082	459	0.80		0.25	0.8	0.20
2289	0.30	25	245	0.32	0.0396	0.032	158	333	0.43	0.00589	0.29	613	156	0.20	0.00119	0.68	461	2570	37	0.048	0.0080	460	0.80		0.30	0.7	0.17
2289	0.40	26	296	0.39	0.0380	0.045	151	283	0.37	0.00619	0.27	593	147	0.19	0.00125	0.69	449	2570	36	0.047	0.0079	448	0.80		0.40	0.5	0.13
2289	0.50	21	317	0.39	0.0472	0.050	131	308	0.38	0.00720	0.32	454	148	0.18	0.00177	0.63	329	2570	36	0.044	0.0074	326	0.86		0.50	0.4	0.10
2289	0.60	21	347	0.45	0.0472	0.051	123	233	0.30	0.00769	0.21	548	148	0.19	0.00139	0.74	432	2570	37	0.048	0.0081	430	0.81		0.60	0.3	0.08
		33	266	0.33	0.0334	0.040	163	342	0.41	0.00587	0.28	614	177	0.21	0.00122	0.68	466	2570	39	0.048	0.0080	465	0.80				
		30	270	0.33	0.0352	0.040	158	336	0.41	0.00604	0.27	604	174	0.21	0.00125	0.69	460	2570	37	0.046	0.0076	458	0.80				
distance *r*		**3.6**					**4.8**					**6.2**										**5.9**					

intensity information			
% $\tau_0*\alpha_{0}$	% $\tau_1*\alpha_{1}$	% $\tau_2*\alpha_{2}$	% $\tau_3*\alpha_{3}$
0.032	0.21	0.36	0.39
0.023	0.22	0.47	0.29
0.042	0.25	0.43	0.29
0.026	0.23	0.40	0.34
0.028	0.19	0.40	0.38
0.025	0.21	0.38	0.38
0.033	0.19	0.38	0.40
0.032	0.20	0.33	0.45
0.034	0.14	0.38	0.45
0.031	0.20	0.39	0.37
0.030	0.20	0.40	0.37

Complete data from the TR-analysis of the Lumi4-Tb-sAv-biot-TP605(B) FRET system (all values are average values from three replicate measurements)

Donor Channel R_0(nm) 7.4

Channel 10-3999 fixed decay background

D or DA	TP(B) [nM]	τ_1	A_1	α_{DA*1}	α_{DA1}	τ_2	A_2	α_{DA*2}	α_{DA2}	$\langle\tau_{DA}\rangle$	fixed τ_3	A_3	α_{DA*3}	$\langle\tau_D\rangle$	z(D)	$\langle\tau_{DA}\rangle$ corr	η_{FRET}	averaging	TP(B) [nM]	sAv/QD	sAv/Biot
D	0.00					560	1242	0.14			2564	7351	0.86	2274					0.00	inf.	inf.
DA	0.06	168	1441	0.16	0.43	948	1942	0.22	0.57	616	2560	5532	0.62	1822	0.10	622	0.73		0.06	3.33	3.33
DA	0.10	192	2101	0.25	0.47	1053	2397	0.28	0.53	651	2560	3982	0.47	1547	0.08	659	0.71		0.10	2.00	2.00
DA	0.15	202	2473	0.30	0.48	1059	2671	0.32	0.52	647	2560	3109	0.38	1368	0.06	653	0.71		0.15	1.33	1.33
DA	0.20	200	2841	0.36	0.50	1044	2843	0.36	0.50	622	2560	2310	0.29	1182	0.05	626	0.72		0.20	1.00	1.00
DA	0.25	202	2889	0.36	0.50	1041	2865	0.36	0.50	620	2560	2234	0.28	1162	0.05	623	0.73		0.25	0.80	0.80
DA	0.30	212	3097	0.41	0.53	1040	2764	0.37	0.47	602	2560	1694	0.22	1041	0.04	604	0.73		0.30	0.67	0.67
DA	0.40	207	3195	0.43	0.54	1024	2773	0.37	0.46	586	2560	1545	0.21	992	0.03	587	0.74		0.40	0.50	0.50
DA	0.50	204	3257	0.43	0.54	1017	2774	0.37	0.46	578	2560	1543	0.20	982	0.03	579	0.75		0.50	0.40	0.40
DA	0.60	203	3285	0.43	0.54	1014	2787	0.36	0.46	575	2560	1581	0.21	985	0.03	576	0.75		0.60	0.33	0.33
DA	0.70	201	3342	0.43	0.54	1012	2804	0.36	0.46	571	2560	1589	0.21	979	0.03	571	0.75		0.70	0.29	0.29
		199	2792	0.36	0.51	1025	2662	0.34	0.49	607	2560	2512	0.31		0.05	610	0.73				
		203	2942	0.38	0.52	1034	2742	0.35	0.48	606	2560	2176	0.27		0.05	609	0.73				
distance *r*		**5.0**				**7.2**										**6.3**					

Biot/QD 1

intensity information			
% τ_1*α_{x_1}	% τ_2*α_{x_2}	% τ_3*α_{x_3}	
0.000	0.036	0.96	
0.015	0.113	0.87	
0.031	0.192	0.78	
0.044	0.251	0.71	
0.060	0.314	0.63	
0.063	0.321	0.62	
0.084	0.365	0.55	
0.089	0.381	0.53	
0.090	0.379	0.53	
0.088	0.375	0.54	
0.089	0.374	0.54	
0.07	0.31	0.63	
0.07	0.33	0.60	

Acceptor Channel

Channel 25-3000 fixed decay background

τ_{DA}	TP(B) [nM]	τ_0	A_0	α_{AD*0}	k_{FRET0}	α_{AD0}	τ_1	A_1	α_{AD*1}	k_{FRET1}	α_{AD1}	τ_2	A_2	α_{AD*2}	k_{FRET2}	α_{AD2}	$\langle\tau_{DA}\rangle$	fixed τ_3	A_3	α_{AD*3}	z(A)	$\langle\tau_{DA}\rangle$ corr	η_{FRET}	averaging	TP(B) [nM]	sAv/QD	sAv/Biot
2274	0.06	69	277	0.29	0.0141	0.056	228	403	0.43	0.00395	0.29	799	186	0.20	0.00081	0.65	592	2560	77	0.082	0.0138	593	0.74		0.06	3.3	3.33
2274	0.10	62	397	0.28	0.0157	0.049	226	648	0.46	0.00398	0.31	773	282	0.20	0.00085	0.64	567	2560	74	0.053	0.0089	567	0.75		0.10	2.0	2.00
2274	0.15	61	507	0.29	0.0159	0.051	225	789	0.46	0.00401	0.31	746	361	0.21	0.00090	0.64	549	2560	71	0.041	0.0070	548	0.76		0.15	1.3	1.33
2274	0.20	63	615	0.30	0.0155	0.051	232	977	0.47	0.00386	0.33	770	412	0.20	0.00086	0.62	558	2560	66	0.032	0.0054	558	0.75		0.20	1.0	1.00
2274	0.25	66	622	0.31	0.0146	0.056	236	937	0.46	0.00380	0.33	771	401	0.20	0.00086	0.62	557	2560	63	0.031	0.0052	557	0.76		0.25	0.8	0.80
2274	0.30	72	722	0.34	0.0135	0.067	250	965	0.45	0.00356	0.34	792	389	0.18	0.00082	0.59	559	2560	56	0.026	0.0044	559	0.75		0.30	0.7	0.67
2274	0.40	62	706	0.32	0.0158	0.059	230	974	0.45	0.00390	0.33	718	445	0.20	0.00095	0.61	520	2560	60	0.027	0.0046	519	0.77		0.40	0.5	0.50
2274	0.50	55	622	0.29	0.0178	0.049	207	974	0.46	0.00438	0.31	673	478	0.22	0.00105	0.64	498	2560	63	0.029	0.0050	497	0.78		0.50	0.4	0.40
2274	0.60	52	661	0.29	0.0188	0.047	210	1061	0.47	0.00432	0.33	692	477	0.21	0.00101	0.63	505	2560	65	0.029	0.0048	505	0.78		0.60	0.3	0.33
2274	0.70	53	675	0.31	0.0185	0.051	219	997	0.46	0.00412	0.34	724	415	0.19	0.00094	0.61	520	2560	59	0.027	0.0046	520	0.77		1.60	0.1	0.13
		61	580	0.303	0.0160	0.054	226	872	0.46	0.00399	0.32	746	385	0.20	0.00091	0.63	542	2560	65	0.038	0.0064	542	0.76				
		61	614	0.304	0.0162	0.053	226	925	0.46	0.00399	0.32	740	407	0.20	0.00092	0.62	537	2560	64	0.033	0.0056	537	0.76				
distance *r*		**4.1**					**5.1**					**6.6**										**6.1**					

Biot/QD 1

intensity information			
% τ_0*α_{x_0}	% τ_1*α_{x_1}	% τ_2*α_{x_2}	% τ_3*α_{x_3}
0.042	0.20	0.33	0.43
0.042	0.25	0.38	0.33
0.047	0.27	0.41	0.28
0.051	0.30	0.42	0.22
0.056	0.30	0.42	0.22
0.070	0.32	0.41	0.19
0.059	0.30	0.43	0.21
0.048	0.28	0.45	0.22
0.046	0.30	0.44	0.22
0.050	0.31	0.43	0.21
0.051	0.284	0.411	0.254
0.052	0.293	0.421	0.234

6.4.2 QD-hexahistidine self-assembly

Original publication:

Three-Dimensional Solution-Phase Förster Resonance Energy Transfer Analysis of Nanomolar Quantum Dot Bioconjugates with Subnanometer Resolution.

K. D. Wegner, F. Morgner, E. Oh, R. Goswami, K. Susumu, M. H. Stewart, I. L. Medintz, and N. Hildebrandt.

Chemistry of Materials **2014**, 26 (14), 4299-4312.

CHEMISTRY OF MATERIALS

Article

pubs.acs.org/cm

Three-Dimensional Solution-Phase Förster Resonance Energy Transfer Analysis of Nanomolar Quantum Dot Bioconjugates with Subnanometer Resolution

K. David Wegner,[†] Frank Morgner,[‡] Eunkeu Oh,[§,#] Ramasis Goswami,[∥] Kimihiro Susumu,[§,#] Michael H. Stewart,[§] Igor L. Medintz,[⊥] and Niko Hildebrandt*[,†]

[†]NanoBioPhotonics, Institut d'Electronique Fondamentale, Université Paris-Sud, 15 Rue Georges Clemenceau, 91400 Orsay, France

[‡]Fraunhofer Institut für Angewandte Polymerforschung, Geiselbergstraße 69, 14476 Potsdam, Germany

[§]Optical Sciences Division, Code 5600, [∥]Multifunctional Materials, Code 6351, and [⊥]Center for Bio/Molecular Science and Engineering, Code 6900, U.S. Naval Research Laboratory, 4555 Overlook Avenue SW, Washington, DC 20375, United States

[#]Sotera Defense Solutions, Inc., Columbia, MD 21046, United States

Supporting Information

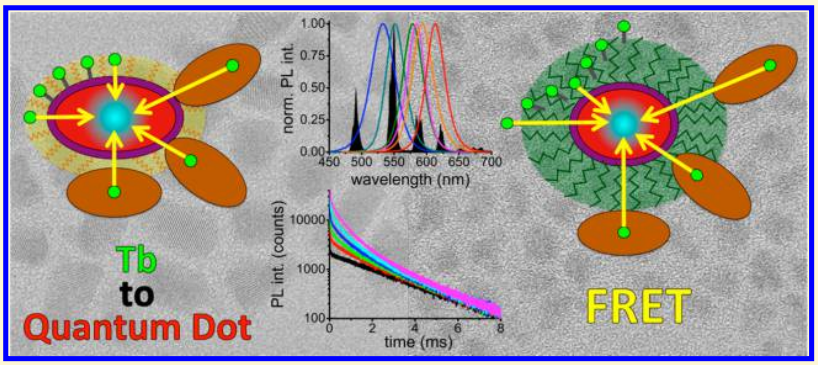

ABSTRACT: Luminescent semiconductor quantum dots (QDs) play an important role in optical biosensing and, in particular, in FRET (Förster resonance energy transfer)-based luminescent probes. The QD materials that form the basis for these probes are in actuality quite heterogeneous and consist of different types of QDs with variations in material compositions, surface coatings, and available biofunctionalization strategies. To optimize their role in active sensors that rely on FRET, extensive physicochemical characterization is required. A technique that can provide precise information about size, shape, and bioconjugation properties of different QD−biomolecule conjugates from a single sample and measurement under actual experimental biosensing conditions would therefore be highly important for advancing QDs to a next generation nanobiosensing tool. Here, we present a detailed FRET study on a large set of QD−biomolecule conjugates, which allows for a homogeneous solution-phase size, shape, and bioconjugation analysis of peptide and protein self-assembled QDs at subnanomolar concentrations and with subnanometer resolution. Direct incorporation of luminescent Tb-complexes (Tb) in the peptides or proteins leads to Tb-to-QD FRET upon assembly to the different QD surfaces. Luminescence decay times and time-gated intensities, which precisely decode the FRET interactions, provide a wealth of useful information on the underlying composite structure and even biochemical functionality. In contrast to other high-resolution techniques, which require rather sophisticated instrumentation, well-defined experimental conditions, and low sample throughput, our technique uses a commercial time-resolved fluorescence plate reader for very fast and simple data acquisition of many aqueous samples in a standard microtiter plate.

INTRODUCTION

Among the most important properties of fluorescent biosensors are brightness, photostability, and color-tunability. It is exactly because of these properties that semiconductor quantum dots (QDs) are immensely valuable tools in optical spectroscopy and microscopy.[1−10] Driven by the occurrence of many biological interactions on the nanometric distance scale, the advantageous combination of QDs with FRET (Förster resonance energy transfer) has become an important biosensing technology.[11−16] In particular, multiplexed (multiple targets), highly sensitive (low detection limits), and homogeneous (no separation steps) assay formats are feasible using QD-based FRET.[17−24]

Despite the multiple photophysical and photochemical advantages of QDs for optical biosensing, the variability of QD surface properties from one QD type to another prevents a general strategy of designing the ultimate QD-biosensor, which

Received: June 3, 2014
Revised: June 10, 2014
Published: June 11, 2014

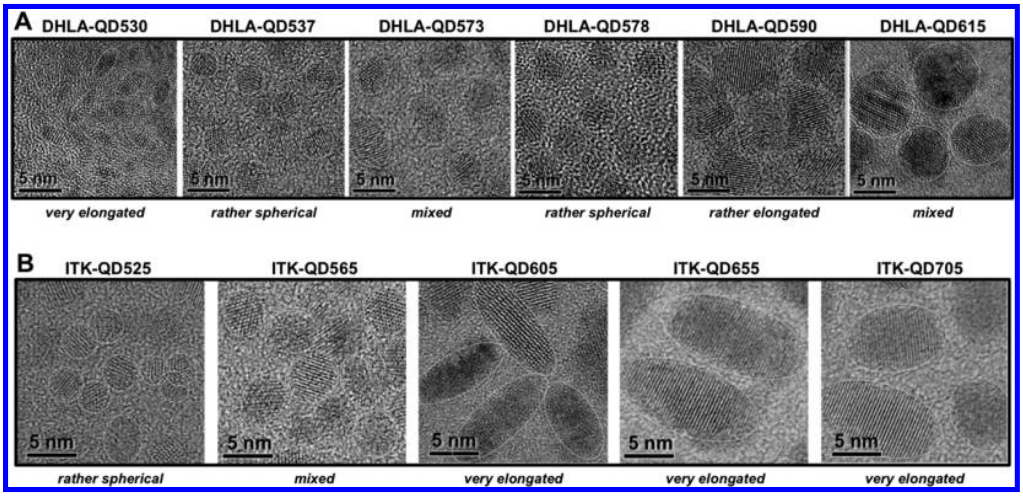

Figure 1. Transmission electron microscopy (TEM) images of the different DHLA-QDs (A) and ITK-QDs (B) used in this study. Only representative QDs are shown here (their shapes are surrounded by a thin gray line for better visualization) to illustrate the different sizes and shapes. Complete TEM images can be found in the Supporting Information.

would be applicable to many targets. Differences in materials, material combinations, surface coatings and functionalization, size, shape, and the QD-surrounding environment (e.g., solvent, pH, temperature, concentration, and interacting molecules) can be responsible for the inconsistency of QD nanosurfaces. It is therefore of paramount importance to be able to carefully analyze each individual QD-bioconjugate (different QDs and different biomolecules), ideally under experimental conditions that will be used in the actual biosensing application. Only then can the photophysical and biological functionalities of the QD-bioconjugates both be understood and fully exploited; these are the minimum necessary requirements for producing and applying efficient QD-based FRET biosensors.

Although many studies have investigated the photophysical, photochemical, and material properties of QDs,[25−29] methods for detecting several functional and structural characteristics of different biocompatible QDs in aqueous solutions at low concentrations are not available. In two recent studies, we demonstrated the use of Tb-to-QD FRET for analyzing sizes and shapes of different biocompatible QDs under physiological conditions.[30,31] One type of Tb (supramolecular terbium complex) could be used to FRET-sensitize various types of QDs (multiplexing), whose absorption spectrally overlapped with the Tb photoluminescence (PL). Other important advantages of Tb are extremely long excited-state lifetimes (up to several milliseconds), which allow a clear distinction of FRET-sensitization from directly excited QDs, and very long Förster distances (R_0, donor−acceptor distance where the FRET efficiency η_{FRET} = 50%; up to an almost unrivaled 11 nm for Tb-to-QD FRET[32]). The latter are necessary to characterize large QDs with thick polymer coatings and their further biomolecular functionalization. Although our initial proof-of-principle studies demonstrated the feasibility of the Tb-to-QD spectroscopic ruler[30] and pointed out the influence of different QD properties on the sensitivity of QD-based FRET bioassays,[31] they were based on polymer-coated and biotinylated QDs (using biotin−streptavidin interactions), which only provided limited information concerning the variability of QDs, biomolecules, and different bioconjugation strategies. A profound characterization of a much larger set of QDs with many more physical, chemical, and biological variables would therefore be highly desirable to gain a deeper understanding of such nanometric FRET biosensors and lead to a more efficient and generalized implementation of QD-based FRET in the life sciences.

Here, we present a detailed time-resolved FRET spectroscopy study using 11 QDs with different sizes, shapes, and surface coatings in combination with two prototypical biomolecules (peptide and protein), which also present significantly different sizes, shapes, orientations, and binding conditions. The Tb-to-QD spectroscopic ruler allows the determination of QD shapes and sizes at subnanomolar concentrations with subnanometer resolution as well as an evaluation of binding orientations, valences, and strengths of peptide and protein coordination to the QDs by polyhistidine-mediated self-assembly. All measurements were homogeneous (no washing and separation steps) and were carried out in aqueous solution on a commercial fluorescence plate reader system, which allowed fast measurements and high sample throughput. The exhaustive FRET analysis and the comparison with other techniques such as transmission electron microscopy (TEM), high performance liquid chromatography (HPLC), and dynamic light scattering (DLS) demonstrate the significant advantages of the Tb-to-QD FRET spectroscopic ruler for size, shape, and bioconjugation analysis within a single measurement under physiological conditions.

■ RESULTS AND DISCUSSION

Quantum Dot Bioconjugates. To provide a large set of sizes, shapes, and binding conditions, we selected two types of QDs (11 different QDs in total) and two types of biomolecules (one peptide with a molecular weight of $M \sim 1.5$ kDa and one protein with $M \sim 44$ kDa). The first type of QD (DHLA-QDs) is an in-house-synthesized dihydrolipoic acid (DHLA)-capped core/shell QD (cf. Table 1 for core/shell compositions) with PL wavelengths from ca. 530 to 615 nm (emission peaks). The six different DHLA-QDs are very challenging for precise size and shape analysis by spectroscopic methods because they present three groups of paired QDs with relatively similar sizes but rather different shapes as indicated by the TEM images (Figure 1) and in Table 1. DHLA-QD530 and DHLA-QD537 are the smallest QDs and have an elongated and rather spherical shape, respectively. DHLA-QD573 and

dx.doi.org/10.1021/cm502021m | Chem. Mater. 2014, 26, 4299−4312

Table 1. Distance, Shape, and Photophysical Information of the QD-Bioconjugates[a]

	quantum dots				Tb-PEP-QD FRET systems								Tb-MBP-QD FRET systems							
	sizes (radii or ellipse half axes) in nm				FRET-properties				sizes (D-A distances) in nm				FRET-properties				sizes (D-A distances) in nm			
name *(composition)*	TEM	TEM[b]	HPLC[b]	DLS	$\langle\tau(\mathrm{Tb})\rangle$ in ms	Φ(Tb)	R_0 in nm	estimated Tb-QD distance range in nm	$\langle r\rangle$	r_1	r_2	r_3	$\langle\tau(\mathrm{Tb})\rangle$ in ms	Φ(Tb)	R_0 in nm	estimated Tb-QD distance range in nm	$\langle r\rangle$	r_1	r_2	r_3
DHLA-QD530 (CdSe/ZnS)	2.4 ± 0.4			5.9 ± 1.0	2.8	0.81	5.8	2.3–4.1	D: 3.7	D: 3.2	A: 3.7	D: 4.5	2.18	0.63	5.5	3.2–7.2	D: 4.9	D: 3.6	A: 3.9	D: 5.7
	1.2 ± 0.2								A: 4.1	A: 3.0		A: 4.8					A: 5.0	A: 3.0		A: 5.5
DHLA-QD537 (CdSe/ZnS)	2.4 ± 0.3			5.6 ± 1.0	2.8	0.81	6.3	3.4–4.0	D: 4.3	D: 3.8	A: 4.7	D: 5.3	2.63	0.76	6.1	4.3–7.1	D: 5.2	D: 4.0	A: 4.2	D: 5.8
									A: 4.2	A: 3.7							A: 5.3	A: 3.2		A: 5.7
DHLA-QD573 (CdSe-CdZnS/ZnS)	2.7 ± 0.3			5.4 ± 1.0	2.8	0.81	7.5	3.7–4.3	D: 6.1	D: 4.5	A: 4.7	D: 7.8	2.22	0.64	7.1	4.6–7.4	D: 6.8	D: 4.9	A: 5.0	D: 7.6
									A: 5.0	A: 3.8		A: 6.5					A: 6.6	A: 3.8		A: 7.1
DHLA-QD578 (CdSe/ZnS)	2.4 ± 0.3			5.9 ± 1.0	2.8	0.81	7.7	3.4–4.0	D: 6.1	D: 4.8	A: 5.0	D: 7.2	2.68	0.78	7.5	4.3–7.1	D: 7.1	D: 5.2	A: 5.1	D: 7.8
									A: 5.4	A: 4.0		A: 6.6					A: 6.7	A: 3.8		A: 7.2
OHLA-QD590 (CdSe/ZnS)	4.0 ± 0.3			6.3 ± 1.0	2.8	0.81	7.6	3.2–5.6	D: 5.0	D: 4.2	A: 4.6	D: 6.2	2.64	0.77	7.4	4.1–7.7	D: 6.4	D: 4.9	A: 5.3	D: 7.1
	2.1 ± 0.3								A: 4.7	A: 3.7		A: 5.9					A: 6.4	A: 4.1		A: 7.1
DHLA-QD615 (CdSe CdS-CdZnS-ZnS)	4.0 ± 0.4			6.3 ± 1.0	2.8	0.81	7.8	4.9–5.7	D: 6.1	D: 4.7	A: 5.1	D: 7.6	2.11	0.61	7.3	5.8–8.8	D: 7.0	D: 5.0	A: 5.4	D: 7.7
									A: 5.2	A: 4.2		A: 6.8					A: 6.8	A: 4.2		A: 7.5
ITK-QD525 (CdSe/ZnS)	2.0 ± 0.2	1.5 to 2.0	6.0	9.4 ± 1.7	2.7	0.79	5.5	3.1–10.5	D: 4.3	D: 3.4	A: 4.0	D: 4.8	2.25	0.65	5.4	4.0–13.6	D: 4.2	D: 3.0	A: 3.5	D: 5.1
									A: 4.8	A: 2.7		A: 4.0					A: 4.3	A: 2.5		A: 5.0
ITK-QD565 (CdSe/ZnS)	2.6 ± 0.3	2.3	7.0	10.3 ± 0.5	2.7	0.79	7.7	3.6–11.2	D: 5.6	D: 4.8	A: 5.2	D: 6.8	2.24	0.65	7.4	4.5–14.3	D: 5.8	D: 4.7	A: 5.2	D: 6.7
									A: 5.3	A: 4.4		A: 5.2					A: 5.7	A: 4.0		A: 6.6
ITK-QD605 (CdSe/ZnS)	5.0 ± 0.7	4.7	8.0	13.3 ± 0.6	2.7	0.79	9.4	3.2–14.0	D: 7.3	D: 5.9	A: 6.2	D: 8.6	2.21	0.64	9.1	4.1–17.1	D: 7.1	D: 5.6	A: 6.3	D: 8.2
	2.2 ± 0.3	2.0							A: 6.6	A: 5.1		A: 6.2					A: 7.3	A: 4.7		A: 8.5
ITK-QD655 (CdSe/ZnS)	6.4 ± 0.7	6.0	9.0	14.8 ± 0.6	2.8	0.80	11.3	3.9–15.4	D: 8.2	D: 6.3	A: 7.2	D: 10.3	2.25	0.65	11.0	4.8–18.5	D: 8.8	D: 6.6	A: 7.1	D: 10.4
	2.9 ± 0.3	3.0							A: 7.2	A: 6.0		A: 7.2					A: 7.8	A: 5.6		A: 9.7
ITK-QD705 (CdSeTe/ZnS)	5.5 ± 0.8	6.0	9.3	13.5 ± 0.6	2.7	0.79	11.5	4.1–14.6	D: 8.1	D: 6.8	A: 7.5	D: 10.0	2.24	0.65	11.1	5.0–17.7	D: 8.3	D: 6.7	A: 7.4	D: 9.8
	3.2 ± 0.4	3.0							A: 7.6	A: 6.3		A: 7.5					A: 7.9	A: 5.7		A: 9.6

[a] $\langle\tau_{Tb}\rangle$ and Φ_{Tb} are the amplitude-averaged excited-state lifetime and the PL quantum yield of the Tb-ion, respectively. R_0 is the Förster distance (donor–acceptor distance of 50% FRET efficiency) for each Tb-QD-pair bioconjugate calculated as $R_0 = 0.02108\ (\kappa^2\ \Phi_{Tb}\ n^{-4}\ J)^{1/6}$ nm, with the FRET orientation factor $\kappa^2 = 2/3$, the refractive index $n = 1.35$, and the overlap integral $J = \int F_{Tb}\ \varepsilon_{QD}\ \lambda^4\ d\lambda$ (from 450 to 700 nm with the area-normalized Tb emission spectrum F_{Tb} and the QD molar absorptivity spectra ε_{QD}; cf. Figure 2). Distance values from the FRET analysis are given for the decay time fits in the Tb-donor (D) and QD-acceptor (A) channels, respectively. Estimated Tb-QD distance ranges were calculated as follows: The length of DHLA (covering the DHLA-QDs) was estimated to 3.3 nm by subtracting the TEM values (average half axis assuming one long and two short ellipsoidal axes) from the DLS values and taking the average of all calculated values. The length of polymers (covering the ITK-QDs) was estimated to 7.0 nm by subtracting the average of TEM and HPLC values from the DLS values and taking the average of all calculated values. PEP was estimated to be 1.3 nm (1.1 nm PEP + 0.1 nm Tb + 0.1 nm His_6) in its elongated form. MBP was considered to bind to the QDs in its elongated form (6.5 nm length) with Tb labeling in the first third (2.2 nm) for shortest Tb-QD distance estimation or in the last third (4.4 nm) for longest Tb-QD distance estimation. For the PEP-systems, the shortest Tb-QD distance was calculated as the lowest TEM value plus 1.3 nm (PEP length), and the longest Tb-QD distance was calculated as the highest TEM value plus 1.3 nm (PEP length) for PEP-DHLA-QDs or plus 8.3 nm (polymer length plus PEP length) for PEP-ITK-QDs. For the MBP-systems, the shortest Tb-QD distance was calculated as the lowest TEM value plus 2.2 nm (Tb in the first third of MBP), and the longest Tb-QD distance was calculated as the highest TEM value plus 4.4 nm (Tb in the last third of MBP) for MBP-DHLA-QDs or plus 11.4 nm (polymer length plus Tb in the last third of MBP) for MBP-ITK-QDs. [b] Values as provided by LifeTechnologies.

dx.doi.org/10.1021/cm502021m | Chem. Mater. 2014, 26, 4299–4312

DHLA-QD578 are slightly larger and have a mixed long and spherical shape, respectively. DHLA-QD590 and DHLA-QD615 are again slightly larger and have rather elongated and mixed shapes, respectively. The second type of QD (ITK-QD) is commercial (LifeTechnologies) core/shell QDs (cf. Table 1 for core/shell compositions), which were purchased with a coating containing carboxyl-functionalized polymers (Qdot ITK carboxyl QDs). The five different ITK-QDs increase in size and length with increasing PL wavelengths, which range from ca. 525 to 705 nm (emission peaks). Apart from the differences in sizes and shapes, the major difference of the two types of QDs can be found in their coatings, which embed the semiconductor core/shell structures. The DHLA-QDs are coated with relatively short DHLA ligands, whereas the ITK-QDs are coated with relatively long polymers. Subtracting the TEM (average of TEM and HPLC for ITK-QDs) from the DLS radii (Table 1) results in lengths of 3.3 ± 0.8 nm and 7.0 ± 1.1 nm for DHLA and polymer, respectively. Although these values do not represent the real coating thicknesses (overestimated because DLS values include the hydration thickness and solvation layer), they give at the least a good indication of the significant difference of organic shell thicknesses between the two QD types.

All QDs were conjugated with Lumi4 terbium complex (Tb)-functionalized peptides (PEP, GSGAAAGLS$(His)_6$, 1 Tb/PEP) or Tb-functionalized maltose binding proteins (MBP, 1.3 Tb/MBP) as shown in Scheme 1. Both biomolecules can bind to the QDs via hexa-histidine self-assembly to the Zn-rich surfaces of the DHLA-QDs or to the COOH-functionalized polymers of the ITK-QDs.[17,33,34] In the case of MBP, electrostatic interactions between the QD carboxyls and the protein may also play a role in MBP-QD attachment.[35] The main difference between the PEP and MBP is their size, with a length of ca. 1.2 nm for PEP and a 3.0 nm × 4.0 nm × 6.5 nm shape for MBP.[36−38] This dimensional difference leads to different binding conditions, which result in expected binding maxima of ca. 50 PEP/QD and ca. 10 MBP/QD depending on the type, size, and surface characteristics of the QD.[38] Moreover, metal affinity coordination between His_6 and Zn (for the DHLA-QDs) is expected to be stronger than coordination between His_6 and COOH (for the ITK-QDs). In the latter case, we assume that there are sufficient COOH-groups available to mimic nitrilotriacetic acids (NTAs), which are known to efficiently chelate divalent metal cations, such as Ni(II) or Zn(II), which in turn bind to His_6.[17,33,34,36−39] After verifying that binding of the His_6-modified PEP and MBP to the ITK-QDs was still possible without the addition of divalent ions, we did not use any in our FRET experiments to avoid interferences with the Tb-complexes. More importantly, one of the aims of our study was the evaluation of binding strengths, and we therefore used the differences in His_6-Zn and His_6-COOH assembly as two prototypical binding conditions. Another major difference between the PEP and MBP systems is the Tb-conjugation. The short PEP is labeled with Tb at one terminus and His_6 on the other. Thus, after attachment to the QD surface, the distance between Tb and the QD is relatively well-defined. MBP (which contains His_6 in its sequence) was labeled with Tb via amine-reactive chemistry. The approximately 30 available primary amines on MBP lead to very heterogeneous binding conditions, which means that the Tb (1.3 Tb/MBP on average) can range from very close to ca. 6.5 nm away from the QD organic surface coating (depending on Tb-labeling, on the type of QD, and on MBP-to-QD orientation; cf. Scheme 1).

Scheme 1. Illustration of the QD Bioconjugation and Distances to Tb[a]

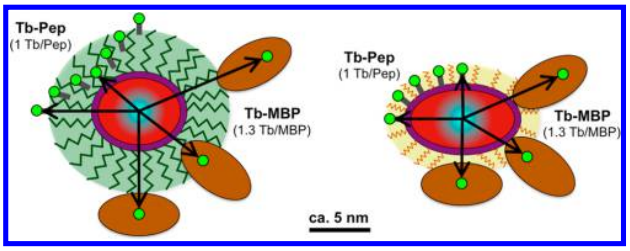

[a]The inorganic core/shell structures are shown in red/purple (for different shapes of all QDs, see Figure 1 and Table 1), whereas the organic coatings are shown in green for ITK-QDs (polymer-based coating) and yellow/orange for DHLA-QDs (DHLA ligands). The biomolecules Tb-PEP (with a length of ca. 1.3 nm) and Tb-MBP (with a size of ca. 3.0 × 4.0 × 6.5 nm and ca. 1.3 Tb/MBP) are conjugated via polyhistidine−COOH interactions to the polymers of the ITK-QDs and via polyhistidine-Zn coordination to the Zn-rich QD surface of the DHLA-QDs, respectively. Tb-to-QD distances are variable due to elongated QD shapes, nonoriented biomolecule conjugation, and heterogeneous labeling of Tb to MBP. Note: Shapes and sizes are not representative for all QDs and were chosen arbitrarily. Chemical structures of DHLA and the ITK amphiphilic polymer can be found in reference 35.

Photophysical Properties of the FRET System. Our FRET spectroscopic ruler is composed of a Tb-donor and several different QD-acceptors. The advantages of Tb-to-QD FRET for biosensing and nanometric distance measurements have been described in detail elsewhere.[19,21,22,40] Briefly, these consist of (i) access to large Förster distances originating from the excellent spectral overlap between Tb PL and QD absorption and the large molar absorptivity values of QDs; (ii) access to deep multiplexing capabilities (due to spectral overlap, Tb-QD FRET pairs consisting of the same type of Tb but different types and colors of QDs are possible); and (iii) the large difference in excited-state lifetimes of Tb (milliseconds) and QDs (nanoseconds), which allows time-delayed FRET from Tb to QD, multiple sequential FRET steps from different Tb to the same QD, and nearly background-free time-gated detection of Tb PL and FRET-sensitized QD PL. We have previously shown the efficient use of different Tb-to-QD-based FRET systems for homogeneous multiplexed diagnostics as well as spectroscopic ruler measurements using streptavidin−biotin binding.[20,30] In the present article, we extend our former size- and shape-determination studies to a large set of different QDs from both custom in-house production and commercial sources and to very distinct biomolecules (PEP and MBP) conjugated via histidine-self-assembly to the QD inorganic (for DHLA-QDs) or organic (for the ITK-QDs) surfaces.

Most of the QD absorption spectra show excellent overlap with the Tb emission spectrum, which result in R_0 values ranging from 5.4 nm to an almost unprecedented 11.5 nm (Table 1). The ITK-QDs provide larger molar absorptivities and therefore longer Förster distances compared to the DHLA-QDs (Figure 2A and D). The PL spectra show the typical Gaussian-shaped narrow emission bands spanning a spectral range from ca. 500 to 750 nm (Figure 2B and E). The native unconjugated PL decay curves of directly excited QDs manifest a multiexponential decay with components in the one to several hundred nanoseconds range (Figure 2C and F). The excited-state lifetimes of Tb depend on the environment and biomolecule they are conjugated to. The Tb-PEP has an almost single exponential PL decay with an average

dx.doi.org/10.1021/cm502021m | Chem. Mater. 2014, 26, 4299−4312

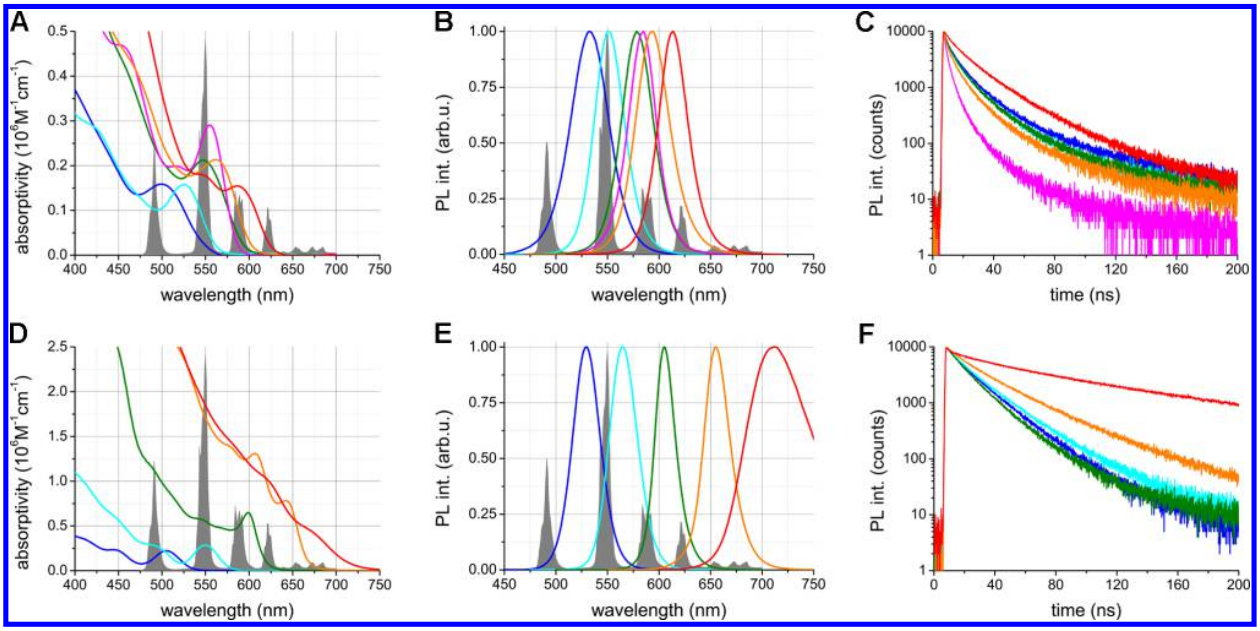

Figure 2. Left: Absorption spectra of the different QDs (A, DHLA-QDs; D, ITK-QDs). For illustration of the overlap between Tb-donor emission and QD-acceptor absorption, the Tb emission spectrum (gray in the background) is also shown. Center: PL emission spectra of Tb (gray) and the different QDs (B, DHLA-QDs; E, ITK-QDs). All spectra were normalized to the PL intensity maxima. The PL quantum yields were 0.23, 0.20, 0.08, 0.14, 0.10, and 0.24 for DHLA-QD 530, 537, 573, 578, 590, and 615, respectively, and 0.52, 0.75, 0.7, 0.64, and 0.5 for ITK-QD 525, 565, 605, 655, and 705, respectively. Right: Multiexponential PL decay curves of the different QDs (C, DHLA-QDs; F, ITK-QDs) after direct QD excitation at 405 nm showing decay times in the one to few hundred nanosecond range. A, B, and C: DHLA-QD530 = blue, DHLA-QD537 = cyan, DHLA-QD573 = green, DHLA-QD578 = magenta, DHLA-QD590 = orange, DHLA-QD615 = red. D, E, and F: ITK-QD525 = blue, ITK-QD565 = cyan, ITK-QD605 = green, ITK-QD655 = orange, ITK-QD705 = red.

lifetime of 2.75 ± 0.05 ms, whereas the Tb-MBP has a double-exponential decay with an average lifetime of 2.35 ± 0.35 ms (Table 1). These differences arise from the different environments provided by either the peptide or protein. Indeed similar differences have been noted for cyanine and other dyes when conjugated to the same protein and similar peptide sequences.[36,41] Because the donor quantum yield (necessary for the calculation of the Förster distance) is the quantum yield of the Tb-ion within the Tb-complex (and not the quantum yield of the complete Tb-complex), the excited-state lifetimes, which are proportional to the Tb-ion quantum yield, also determine the Förster distance.[22] Thus, the R_0 values were calculated for the experimental conditions of each Tb-QD donor−acceptor pair assay (Table 1).

Size and Shape Analysis. The major goal of our study was to provide information about the sizes, shapes, and binding conditions of several different QD bioconjugates at low nanomolar and subnanomolar concentrations from a single measurement (per QD bioconjugate sample) directly in solution on a commercial time-resolved fluorescence plate reader. Tb-to-QD FRET can fulfill this challenging goal, while at the same time overcoming the disadvantages of other analytical methods to determine dimensions with nanometer resolution such as DLS (no shape determination and inclusion of hydration and solvation layers) or TEM (measurement on Cu-grids, problematic for measuring organic materials, and very sophisticated equipment). Because Tb is conjugated to PEP and MBP, it can transfer its excitation energy to a QD upon self-assembly of PEP or MBP to the QD surface (cf. Scheme 1) due to the close distance between Tb and QD. The large difference between Tb and QD excited-state lifetimes allows for extraction of the FRET (and therefore distance) related PL decay times from both the FRET-quenched Tb PL and the FRET-sensitized QD PL.[19,22] We therefore performed a simultaneous time-resolved PL decay time analysis using one Tb donor and different QD acceptor detection channels (depending on the QD emission wavelengths). Because of the nonspherical shapes of most of the QDs as well as the variable orientations and heterogeneous Tb-conjugation of MBP, one can expect Tb-to-QD distance distributions. To account for such distributions, we performed multiexponential decay time fits on the PL decay curves in the Tb-donor and QD-acceptor channels. Because too many exponentials and the associated amplitudes lead to unsatisfactory fit results (where amplitudes and decay times can balance each other to achieve the mathematically most appropriate fit), we chose 4-exponential fits in the Tb and QD channels, respectively:

$$I = \mathrm{A}\cdot\exp\left(-\frac{t}{\tau_0}\right) + B\left[\alpha_1\cdot\exp\left(-\frac{t}{\tau_1}\right) + \alpha_2\cdot\exp\left(-\frac{t}{\tau_2}\right) + \alpha_3\cdot\exp\left(-\frac{t}{\tau_3}\right)\right] \quad (1)$$

Here, the first decay time τ_0 is a constant (accounting for unquenched Tb donors), and $\alpha_1 + \alpha_2 + \alpha_3 = 1$. A detailed description of this fit procedure and its applicability to Tb-to-QD FRET can be found elsewhere.[31,42] As the FRET efficiency η_{FRET} is dependent on both decay times and distances, the different FRET decay times (τ_1, τ_2, and τ_3), the average decay times of Tb in the absence of QDs ($\langle\tau_{\mathrm{Tb}}\rangle$, Table 1), and the Förster distances R_0 (Table 1) were used to calculate the distances r_1, r_2, and r_3:[42]

$$r_{\mathrm{i}} = R_0\left(\frac{\tau_{\mathrm{i}}}{\langle\tau_{\mathrm{Tb}}\rangle - \tau_{\mathrm{i}}}\right)^{1/6} \quad (2)$$

dx.doi.org/10.1021/cm502021m | Chem. Mater. 2014, 26, 4299−4312

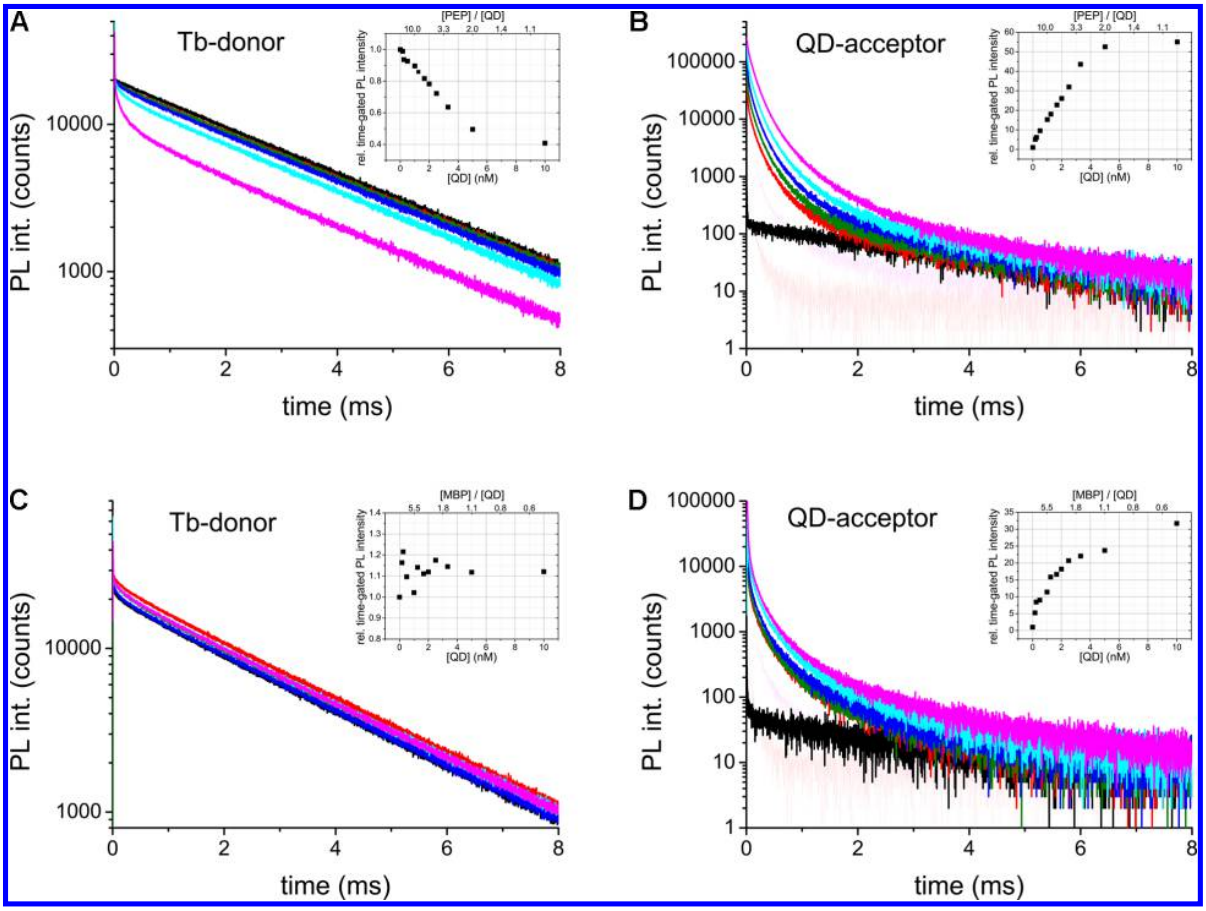

Figure 3. Representative PL decay curves measured in the Tb-donor detection channel (left) and QD-acceptor detection channel (right) for the Tb-PEP-ITK-QD705 conjugate (A and B) and the Tb-MBP-ITK-QD705 conjugate (C and D) for increasing ITK-QD705 concentrations (black, 0 nM; red, 0.25 nM; green, 0.5 nM; blue, 1.0 nM; cyan, 2.0 nM; and magenta, 5.0 nM) in solutions of constant Tb-PEP (10 nM) or Tb-MBP (5.5 nM) concentrations. The black curves in B and D (0 nM QD) are caused by spectral cross-talk from Tb PL. The thin red and magenta curves in the background are the decay curves of pure ITK-QD705 at 0.25 nM and 5.0 nM, respectively. These do not significantly contribute to the FRET-sensitized curves (logarithmic intensity scale). The insets show the time-gated intensities (integration of PL intensity decays from 0.2 ms−2 ms) measured for 12 different decay curves with QD concentrations ranging from 0 to 10 nM. Decay curves and time-gated intensities for all ITK-QD bioconjugate systems can be found in the Supporting Information.

In combination with the amplitudes α_i (α_1, α_2, α_3), which give the fractions of donor−acceptor pairs separated at distances r_i, it becomes possible to distinguish among spherical QD-bioconjugates (one major distance because spheres have only one axis), elongated ones (two shorter distances and one longer distance because elongated ellipsoids have two short and one long axes), or flat ones (two longer distances and one shorter distance because flat ellipsoids have two long and one short axes). It is also possible to calculate an average distance $\langle r \rangle$ using eq 2 and the amplitude averaged PL lifetime (instead of τ_i) by using

$$\tau = \sum \alpha_i \tau_i \tag{3}$$

To be able to study a large set of decay curves at different QD concentrations, we performed time-resolved spectroscopy experiments of various concentrations of QDs (from ca. 0.2 to 10 nM depending on the Tb-QD-bioconjugate) with constant concentrations of Tb-PEP or Tb-MBP (between ca. 5 and 10 nM depending on the type of Tb-QD-bioconjugate) in 150 μL sample volumes. By varying the ratios incrementally, we were able to collect far more useful data for subsequent analysis in contrast to a single point. Figures 3 and 4 show representative PL decay curves in the Tb-donor and the QD-acceptor channels for the ITK-QD705 and the DHLA-QD578 for the PEP and MBP conjugates, respectively (decay curves for all other QD-bioconjugate systems can be found in the Supporting Information). The PL decay curves of the Tb-ITK-QD705 bioconjugate in Figure 3 clearly show that the PEP systems (for which Tb is relatively close to the QD surface; cf. Scheme 1) provide a better accessibility of Tb for FRET to QD because the Tb-donor is significantly quenched with increasing QD concentrations (Figure 3A), whereas the MBP systems show rather constant Tb PL decay curves (Figure 3C), which fluctuate in intensity by ca. ± 10% due to slightly variable excitation and assay conditions from one sample to another. Although the Tb quenching is not visible for the MBP systems (most probably due to a large majority of Tb that does not participate at all in FRET, caused by too large a distance from the QD-acceptor), a strong sensitization can be detected in the QD-channel. It should be noted that the strong UV excitation (337 nm) and the extremely large molar absorptivities (or extinction coefficients) of the QDs at this wavelength lead to a very efficient direct excitation of QDs. Although the PL decay times are in the tens to hundreds of nanoseconds range

dx.doi.org/10.1021/cm502021m | Chem. Mater. 2014, 26, 4299−4312

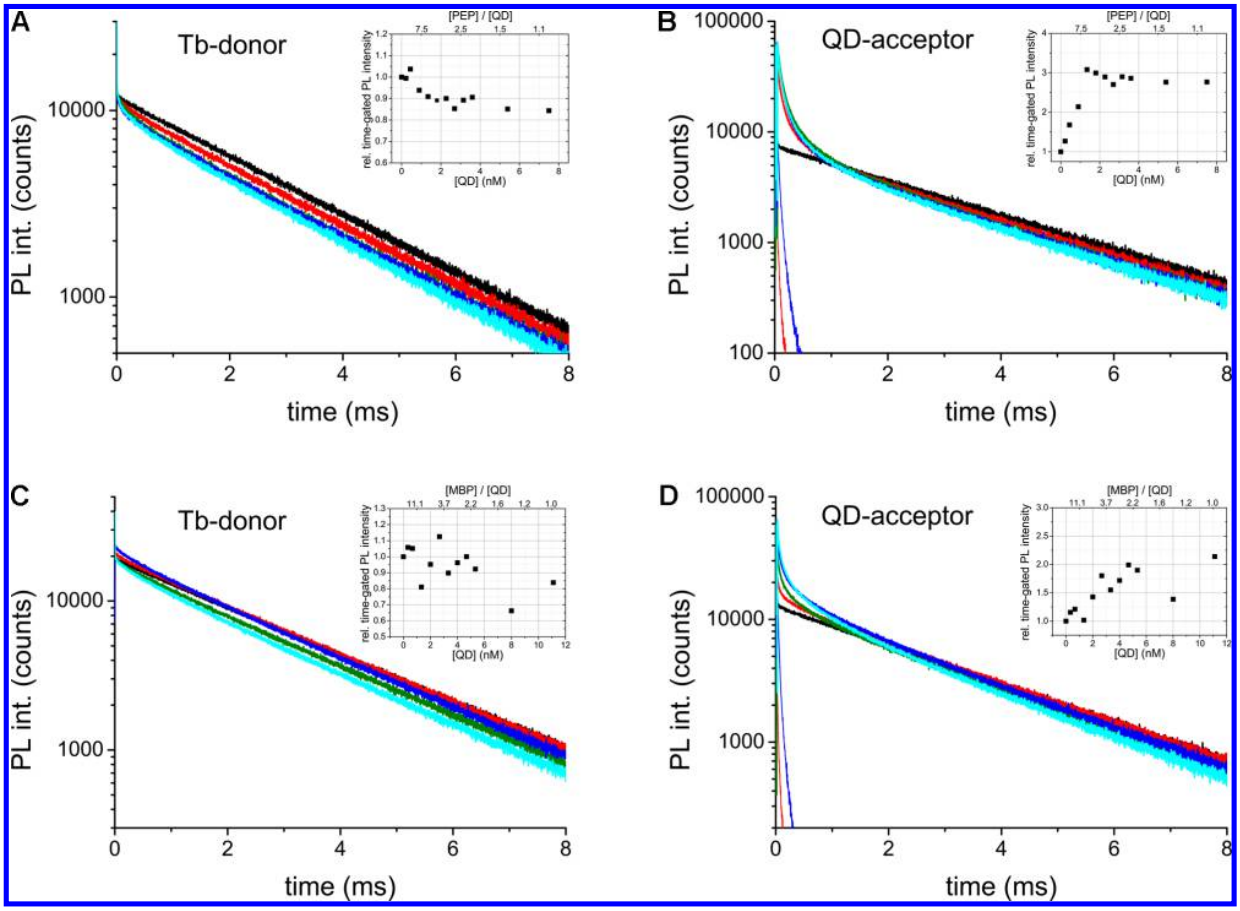

Figure 4. Representative PL decay curves measured in the Tb-donor detection channel (left) and QD-acceptor detection channel (right) for the Tb-PEP-DHLA-QD578 conjugate (A and B) and the Tb-MBP-DHLA-QD578 conjugate (C and D) for increasing DHLA-QD578 concentrations (black, 0 nM; red, 0.9 nM; green, 1.8 nM; blue, 2.7 nM; and cyan, 5.4 nM) in solutions of constant Tb-PEP (7.5 nM) or Tb-MBP (11 nM) concentrations. The black curves in B and D (0 nM QD) are caused by spectral cross-talk from Tb PL. The thin red and magenta curves (within the first 0.5 ms) are the decay curves of pure DHLA-QD578 at 0.9 nM and 5.4 nM, respectively. These do not significantly contribute to the FRET-sensitized curves (logarithmic intensity scale). The insets show the time-gated intensities (integration of PL intensity decays from 0.05 ms−0.5 ms) measured for 12 different decay curves with QD concentrations ranging from 0 to 7.5 nM (0 to 11 nM for Tb-MBP-DHLA-QD578). Decay curves and time-gated intensities for all DHLA-QD bioconjugate systems can be found in the Supporting Information.

(cf. Figure 2C and F), the very high PL intensity saturates the very sensitive detection setup, which is optimized for the measurement of long-lived PL signals. This saturation leads to a much slower decaying photon count signal of the PMT (photomultiplier tube) detectors (thin curves in Figure 3B and D). However, the FRET-sensitized PL decay curves show a significantly longer and much more intense (logarithmic intensity scale) decay than the sum of pure Tb PL (which can be detected in the QD channels due to spectral cross-talk; black curves in Figure 3B and D) and pure QD PL (thin curves) signals. Therefore, the analysis of long-lived FRET-sensitized QD PL has the clear advantage of measuring against a low background signal (weak Tb cross-talk and weak directly excited QD signals), whereas Tb-quenching is measured against a very high background (Tb at constant concentration and many unquenched Tb), which leads to large differences in relative quenching and sensitization. Integrating the PL intensities from 0.2 to 2.0 ms after the excitation pulse leads to ca. 2.5-fold quenching and ca. 50-fold sensitization for the PEP systems (insets in Figure 3A and B), and no quenching and ca. 30-fold sensitization for the MBP systems (insets in Figure 3C and D).

The Tb-donor PL decay curves of the Tb-DHLA-QD578 bioconjugate in Figure 4 show behavior similar to that of the ITK curves in Figure 3, namely, quenching for the PEP systems and fluctuation (without quenching) for the MBP conjugates with increasing QD concentrations. Again the FRET-sensitized QD curves provide more information about FRET. Although the Tb cross-talk (black curves in Figure 4B and D) is much stronger for this detection wavelength (in addition, the signals from direct QD excitation are much weaker compared to that of the pure Tb signal) and the QD quantum yield is lower, there is still efficient time-gated (integration from 0.05 to 0.5 ms) intensity sensitization (up to ca. 3-fold; inset in Figure 4B). Moreover, the FRET-sensitized long PL decay times are significantly shorter (in the first 1.5 ms of the decay curves) compared to the ones in Figure 3, which is in good agreement with the much thinner organic layer of the DHLA-QDs (cf. Scheme 1) leading to shorter donor−acceptor distances.

For obtaining detailed information about the shapes and distances of all QD-bioconjugates, their decay curves were fit using eq 1, and the Tb-QD donor−acceptor distances were calculated using eqs 2 and 3. All the extrapolated distances can be found in Table 1 and are presented graphically together with

dx.doi.org/10.1021/cm502021m | Chem. Mater. 2014, 26, 4299−4312

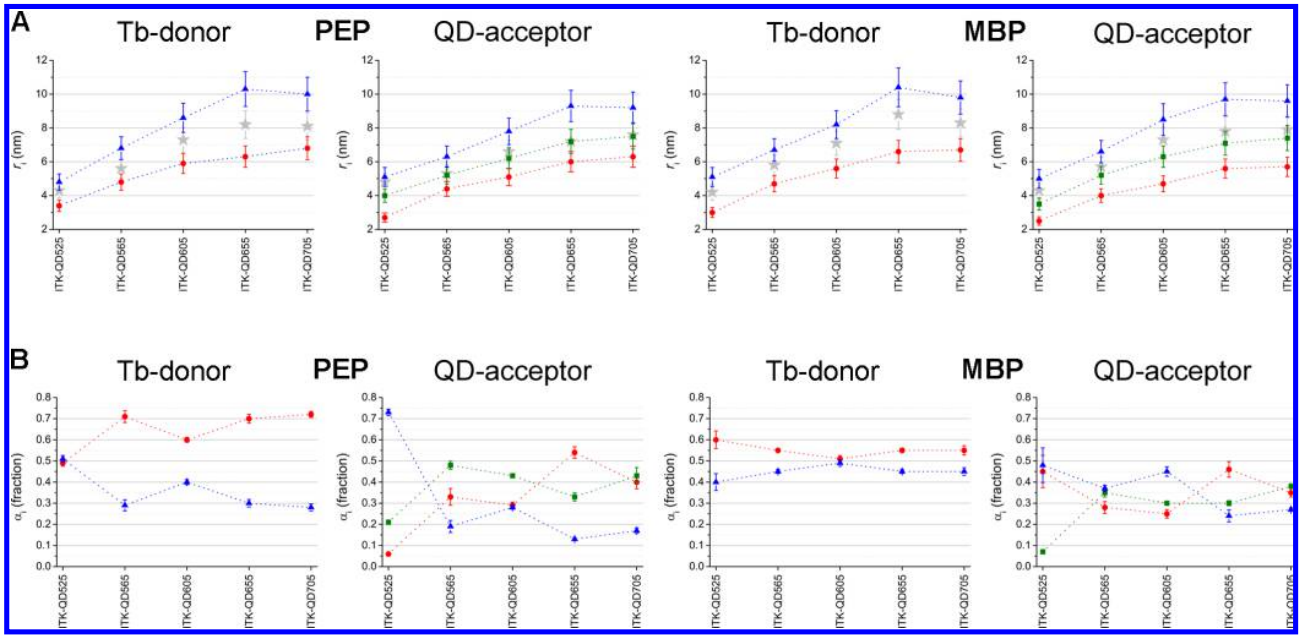

Figure 5. (A) Average distances ($\langle r \rangle$ in gray) and single distances (r_1 = red, r_2 = green, and r_3 = blue) as determined from the FRET PL decay curve fits of the ITK-QD bioconjugates and calculated by eqs 1 to 3. (B) Fractions (α_1 = red, α_2 = green, and α_3 = blue) of the single distances as calculated from eq 1.

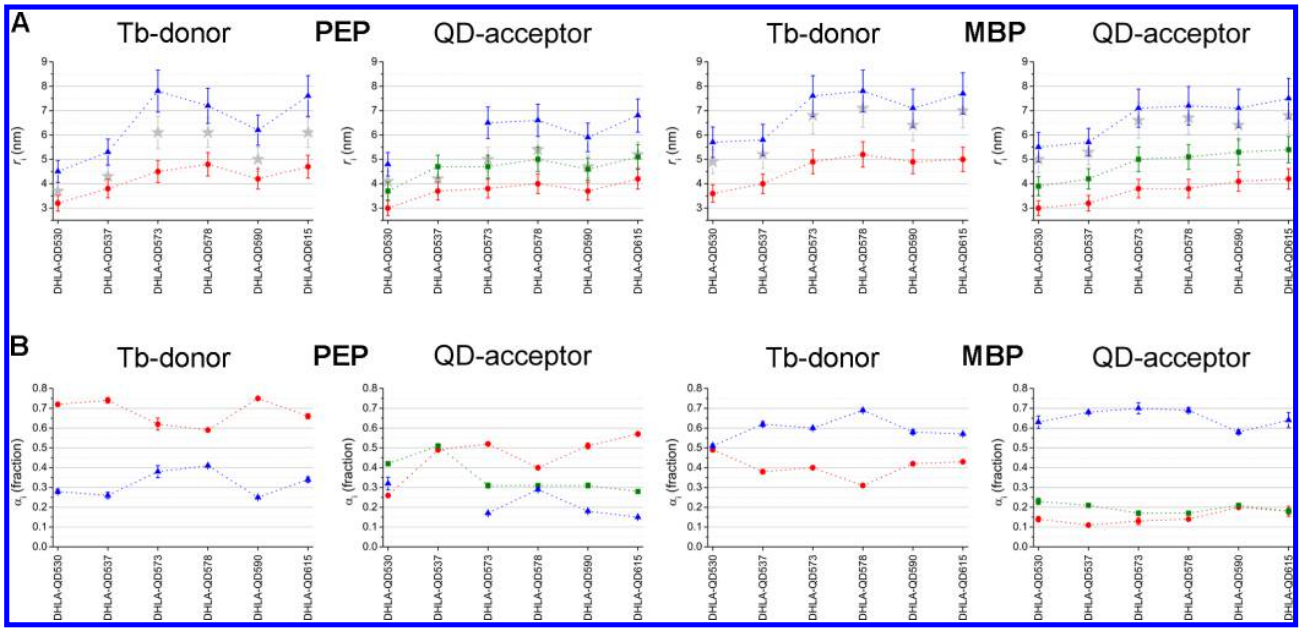

Figure 6. (A) Average distances ($\langle r \rangle$ in gray) and single distances (r_1 = red, r_2 = green, and r_3 = blue) as determined from the FRET PL decay curve fits of the DHLA-QD bioconjugates and calculated by eqs 1 to 3. (B) Fractions (α_1 = red, α_2 = green, and α_3 = blue) of the single distances as calculated from eq 1.

the fractions corresponding to each component for each single distance in Figure 5 for the ITK-QDs and in Figure 6 for the DHLA-QDs. As PL decay times are concentration independent, all decay curves (from lowest to highest concentration for all QD-bioconjugates) were used to determine the various distances. In fact for the majority of the Tb-QD-systems even the subnanomolar concentrations of QDs inside the 150 μL samples (subpicomol) gave very good fit results without large deviations from the average values of the complete set of fits. For the ITK-QDs (Figure 5) and for both biomolecules (PEP and MBP), the average size ($\langle r \rangle$) increases from ITK-525 to ITK-QD655 (ITK-QD705 shows a size similar to that of ITK-QD655) as expected from the TEM data and previous results.[30] On average, the donor fits lead to larger distance values, which is most probably caused by the long-lifetime component of the unquenched Tb. This signal can be quite strong in the Tb-donor detection channel (cf. Figures 3 and 4). Although our fit algorithm contains an efficient correction for the free Tb PL background,[31,42] this much larger background compared to that of the QD-acceptor channel still leads to slightly larger distance

dx.doi.org/10.1021/cm502021m | Chem. Mater. 2014, 26, 4299−4312

values. Another inherent advantage of the lower background PL in the QD channel is the possibility to fit with three different decay times (not possible for the donor curves, which provide only two decay times), which gives access to a third distance and therefore more information about the shape of the QDs. The average distances are lower than HPLC and DLS values (Table 1) because the FRET measurements do not require a weight standard (as with HPLC) and are not dependent on hydration and solvation effects (as with DLS). Moreover, they are larger than the TEM distances because TEM does not measure the organic coatings of the QDs. Therefore, the FRET distance values are expected to be closer to the real distances of the QD systems. Both Tb-donor and QD-acceptor curves show that (apart from the DHLA-QD578 and DHLA-QD590) the FRET-distances are within the expected distance range (from TEM, HPLC, and DLS measurements; cf. Table 1). Because of the lower background signal, QD-acceptor fits provide better agreement with the expected distance ranges. Because the Tb-PEP system causes almost no distance distribution (only one Tb terminally attached per PEP and a relatively stable distance due to the short 1.2 nm peptide length), the PEP distance values are also better suited for extracting more reliable distance and shape information.

ITK-QD Bioconjugates. Regarding the ITK-QD bioconjugates, the Tb-donor fits of the PEP systems (Figure 5A) show an increasing difference between the short (red) and the long (blue) distance with increasing size, which suggests an elongation. This effect is much less pronounced in the MBP systems. The fractions (Figure 5B) of the Tb-donor fits also provide more information for PEP compared to that for MBP. The ITK-QD525 shows two equal fractions (of distances with only ca. 1.5 nm difference) suggesting a rather spherical shape with relatively narrow distance distribution as confirmed by the TEM data. All the other ITK-QDs show two well distinguishable fractions, for which the short one is ca. 70%. This suggests a rather ellipsoidal shape (two short and one long axes). The fractions of the MBP systems are very similar for all QDs and do not allow for the extraction of significant shape information, which would be in agreement with the TEM shapes. The QD-acceptor fits lead to three distinguishable distances r_i (three-dimensional fit), and it is very important to relate these distances to their respective fractions α_i. The fractions of D-A pairs separated by r_i (Figure 5B) are very valuable for characterizing the QD shapes and show that the Tb-PEP systems contain much more information due to the narrower distance distribution compared to that of Tb-MBP. For the PEP QD-acceptor fits, the ITK-QD525 fractions show a clear preference for one distance (fraction of ca. 75%), which confirms the spherical character of this QD. For the other QDs, there is a tendency of an increasing shorter fraction (red) and simultaneously decreasing longer fractions (green and blue) with the longest distance (blue) always showing the lowest fraction, pointing again to an elongation with increasing size. Although the MBP QD-acceptor fits can also distinguish between the spherical ITK-QD525 (only two main fractions) and the other ITK-QDs, a distinction among those is not possible using the fraction information. This first set of ITK-QDs already shows the advantages of well-defined donor−acceptor distances (PEP binding) and the FRET analysis of the QD-acceptor channels (low background and strong sensitization) for size and shape analysis.

DHLA-QD Bioconjugates. The DHLA-QD bioconjugates present a very challenging system for size and shape analysis because there are three groups of paired QDs (DHLA-QD530/537, DHLA-QD573/578, and DHLA-QD590/615), which are very similar in size as shown in the average distance values of Figure 6A and in the TEM and DLS data (cf. Figure 1 and Table 1). Moreover, these QDs have less of a size range and change in aspect ratio compared to those of the ITK-QDs. We therefore discuss the fit results for the three paired systems starting with the PEP systems, which (similar to the ITK systems) provide more distance and shape information.

DHLA-QD530/537 PEP. The Tb-donor fits do not provide sufficient information to distinguish these two QDs. The fractions are very similar, and the distances ($\langle r \rangle$, r_1 and r_3) are slightly increasing. However, the TEM images show that only the shapes but not the sizes are different (cf. Figure 1). The QD-acceptor fits can clearly distinguish these two QDs. Although the average distance $\langle r \rangle$ is very similar, the single distances r_i show significant differences. DHLA-QD530 has three distinguishable distances with fractions between ca. 25 and 45%. This suggests an elongation (or a very broad size distribution). The DHLA-QD537 can only be fit for two different FRET distances both with ca. 50% of the fraction, which suggests rather spherical QDs with a relatively broad size distribution around the main distance values of 3.8 and 4.8 nm.

DHLA-QD573/578 PEP. These two QDs are also very similar in shape and size (cf. Figure 1), and the Tb-donor fits cannot distinguish between them. The QD-acceptor fits confirm the similar size (three very similar distances), and in addition, they provide shape information. The slightly longer shape of the DHLA-QD573 is visible through the more pronounced short distance (ca. 50%) and the lower amount of long distance fraction (ca. 20%). For the DHLA-QD578, the short fraction is decreased, the long fraction is increased, and the medium distance is unchanged, which can be attributed to less elongation compared to that of DHLA-QD573. For both QDs (and especially for the Tb-donor fits), the sizes from FRET-analysis are larger than the expected values from TEM and DLS (Table 1).

DHLA-QD590/615 PEP. These two QDs cannot be clearly distinguished by the time-resolved FRET analysis because they have similar sizes and are rather elongated (for QD590) and mixed (for QD615), which leads to similar FRET distances. Nevertheless, both QDs show two (for the donor) or three (for the acceptor) clearly distinguishable distances with larger fractions for the shorter distances, pointing toward elongation or distribution as mentioned above. Both the Tb-donor and the QD-acceptor fits also suggest that the DHLA-QD615 are slightly larger than the DHLA-QD590, which confirms the estimated Tb-QD distance range using TEM and DLS values (Table 1).

DHLA-QD MBP Systems. On average, the distances of the MBP systems show the same trend as the PEP systems with ca. 1 to 1.5 nm increased values. This increase of distances from PEP to MBP is stronger compared to that of the ITK-QDs, which we attribute to the thicker organic coating of the ITK-QDs. The attachment of MBP to the carboxyl-functionalized polymers places a significant amount of Tb very far away from the QD (cf. Scheme 1), so they cannot participate in FRET. In other words, only Tb which are close to the ITK-QD surface can transfer their energy to the QD, and therefore, the difference in average Tb-QD FRET distances from PEP to MBP is not very large. For the DHLA-QDs, the organic ligands are much shorter, and all Tb on the MBP (close and far from the QD surface) can participate in FRET (independent of the orientation and labeling position), which provides information about the complete MBP and therefore a larger difference in

dx.doi.org/10.1021/cm502021m | Chem. Mater. 2014, 26, 4299−4312

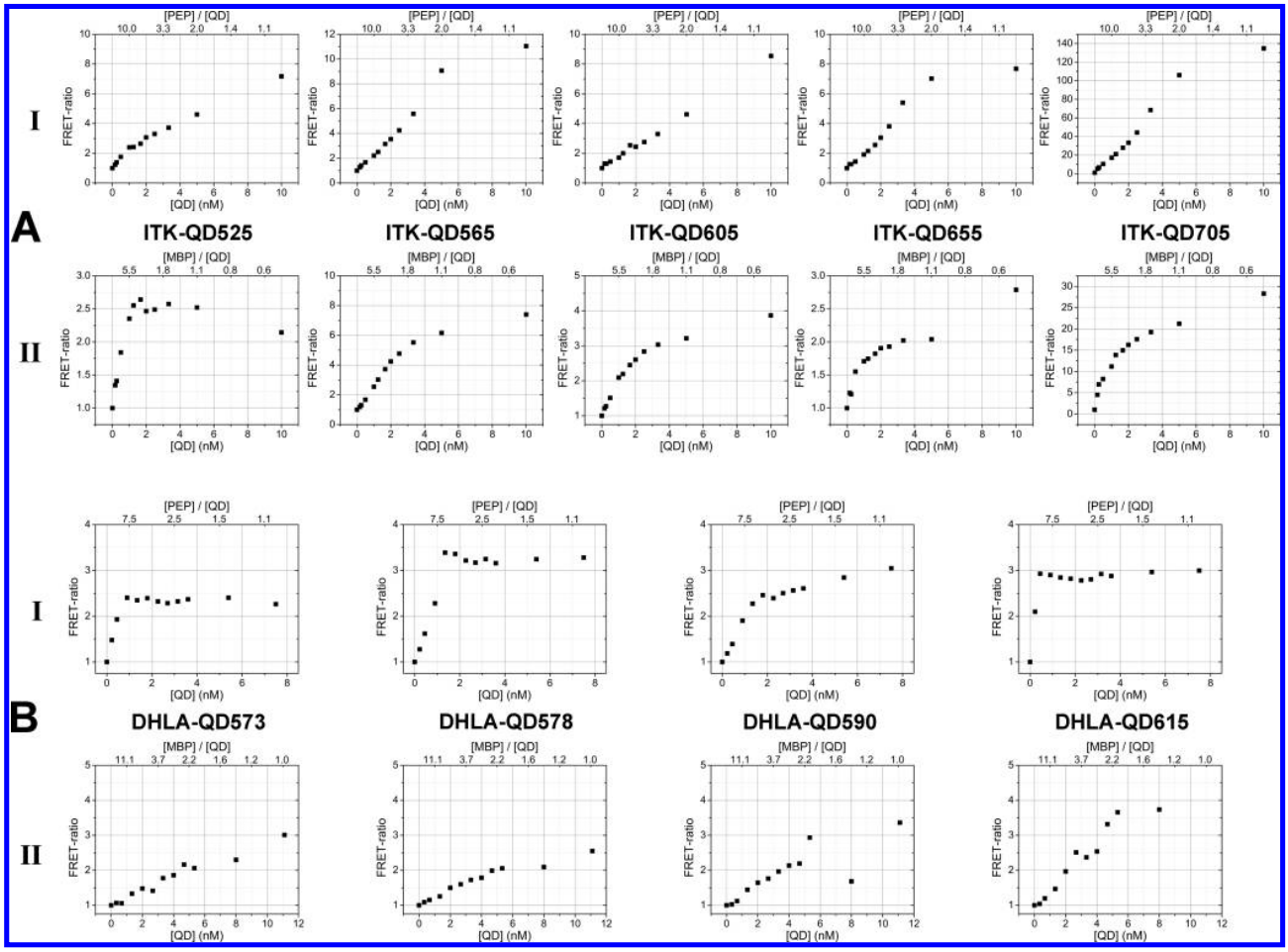

Figure 7. FRET-ratios (ratios of time-gated intensities of QD-acceptor and Tb-donor normalized to unity at concentrations of [QD] = 0) as a function of concentration (±40% error) for [Tb-PEP]-[ITK-QD] (A-I), [Tb-MBP]-[ITK-QD] (A-II), [Tb-PEP]-[DHLA-QD] (B-I), and [Tb-MBP]-[DHLA-QD] (B-II). Tb-PEP (±20% error) and Tb-MBP (±25% error) have constant concentrations of 10 nM, 5.5 nM, 11 nM, and 7.5 nM for Tb-PEP]-[ITK-QD], [Tb-MBP]-[ITK-QD], [Tb-PEP]-[DHLA-QD], and [Tb-PEP]-[DHLA-QD], respectively. Note that DHLA-QD530 and DHLA-QD537 were not included in this concentration-dependent study because of their relatively large errors in QD-concentration (more than ±100%). It should be noted that the differences of FRET-ratio values of the different QDs at a given QD concentration do not comprise any information about the amount of FRET-pairs but are caused by the differences in FRET-efficiencies for the different Tb-QD FRET-pairs and the spectral cross-talk of Tb in the QD detection channels. (For example, for ITK-QD705 the spectral cross-talk from Tb is very low, and the FRET-efficieny is very high, and therefore, the relative FRET-ratio increases from 1 to 140, whereas spectral cross-talk is higher and FRET-efficiency lower for the Tb-ITK-QD565 FRET-pair. Thus, the increase is only from 1 to 11.) Applied time-gates were 0.2 ms−2 ms for the ITK-QD-based systems and 0.05 ms−0.5 ms for the DHLA-QD-based systems.

distances between PEP and MBP compared to the ITK-QDs. In fact, the fraction of the longest distance (Figure 6, blue) is quite dominant (ca. 60 to 70%) for all DHLA-QD MBP bioconjugates, which indicates that on average less Tb are close to the QD surface. The distribution of Tb over the MBP does not allow any specific distinction between the QD shapes because the changes in fraction over the complete set of QDs are almost negligible.

Although the DHLA-QD bioconjugate FRET size and shape analysis was more challenging compared to that of the ITK-QDs, the data clearly show that quite precise distance and shape information (without the problems arising from TEM, HPLC, and DLS measurements) can be achieved at very low concentrations under physiological conditions. The shorter and more rigid PEP with a 1:1 Tb/PEP labeling can provide much more precise distance and shape information than the heterogeneously labeled and relatively large and elongated MBP. The three-dimensional character of the QD-acceptor fits provides a clear advantage over the two-dimensional Tb-donor fits for shape analysis. Nevertheless, as both Tb-donor and QD-acceptor can be measured simultaneously, the most information can be obtained by analyzing both PL decay curves and in the best case in connection with TEM, HPLC, and DLS.

Binding Analysis of Peptide and Maltose Binding Protein Quantum Dot Conjugates. Taking the time-gated intensities (integrated intensities of the PL decay curves from 0.2 to 2.0 ms for the ITK-QD systems and from 0.05 to 0.5 ms for the DHLA-QD systems) of the Tb-donor and QD-acceptor channels (insets in Figures 3 and 4) allows for calculation of FRET-ratios (ratio of time-gated QD and Tb intensities), which are much less prone to fluctuations from varying excitation or sample conditions and combine Tb-donor quenching and QD-acceptor sensitization in one graph. Within these experiments, the concentrations of Tb-PEP (Figure 7A-I and B-I) or Tb-MBP

dx.doi.org/10.1021/cm502021m | Chem. Mater. 2014, 26, 4299−4312

(Figure 7A-II and B-II) were kept constant, and the concentrations of ITK-QDs or DHLA-QDs were increased. Because the time-gated intensities are measured in a time window that mainly contains the PL decay time changes caused by FRET (Tb-donor quenching and QD-acceptor sensitization), the relative FRET-ratios as a function of QD-acceptor concentration represent the amount of Tb-QD FRET-pairs. We expected that the addition of increasing concentrations of QDs to the samples (containing constant concentrations of Tb-PEP or Tb-MBP) leads to an increasing FRET-ratio because more QDs can be FRET-sensitized by Tb (more Tb-QD FRET-pairs). The very large difference in excited-state lifetimes (milliseconds for Tb and nanoseconds for QDs) allows for sequential FRET-sensitization of the same QD by many Tb (on the surface of that QD) after only one excitation pulse.[22,24,40] In contrast to the creation of biexcitons, which would necessitate a very fast second excitation of the QD before its relaxation to the ground state, the QD acceptor receives excitation energy from a first Tb, and the generated exciton leads to almost immediate photon emission (nanosecond excited-state lifetime of QD) and relaxation of the QD. This FRET-excitation and photon-emission process can be repeated with many other Tb donors because of their extremely long excited-state lifetimes (after each QD relaxation, the probability of finding another excited Tb donor is very high). This means that one QD can be excited by several Tb donors and that there will be no significant difference in the FRET-sensitized signals between, for example, one QD with 50 Tb and 50 QDs with one Tb each. At QD concentrations that correspond to PEP/QD or MBP/QD concentration ratios of saturated PEP- or MBP-binding to the QD surface, the FRET-ratios are expected to saturate, and further addition of QDs should not lead to additional Tb-QD FRET-pairs. In the case of biexcitonic excitation of one QD-acceptor by several Tb-donors, a 1:1 Tb-per-QD ratio would be preferred to high Tb-to-QD ratios because biexciton quantum yields are significantly lower (due to Auger effects).[43] This would lead to an increasing FRET-ratio with increasing QD concentrations until a 1:1 Tb-per-QD ratio is reached. Taking into account the nanosecond excited-state lifetimes of the QD acceptors, the millisecond excited-state lifetimes of the Tb-donors, and the relatively long donor−acceptor distances (moderate FRET efficiencies), the probability of sequential FRET is much higher compared to that of simultaneous FRET. Therefore, evaluation of slopes and saturations of the increasing FRET-ratios over QD concentrations should allow comparison of valences (biomolecules per QD) and binding strengths (association/dissociation of biomolecules to/from QD) among the four different bioconjugate systems ([Tb-PEP]-[ITK-QD], [Tb-MBP]-[ITK-QD], [Tb-PEP]-[DHLA-QD], and [Tb-MBP]-[DHLA-QD]). Indeed, the experiments show an increase of the FRET-ratios with increasing QD concentrations for all bioconjugate systems (Figure 7). However, there are significant differences in the saturation concentrations.

PEP-Based Systems. For the ITK-QDs (Figure 7A-I), the FRET-ratios of the PEP systems increase until saturation becomes visible at concentrations between ca. 8 and 10 nM (ca. 1.3−1.0 PEP/QD) for some of the QDs. Regarding the large surface of the ITK-QDs, many PEP should be able to bind to one QD. It has been shown that ca. 50 ± 10 peptides can self-assemble on average via hexa-histidine to the Zn-rich surface of a single DHLA-functionalized QD.[38] However, saturation becomes only visible at concentrations of an approximate PEP/QD concentration ratio of 1 and not at much higher ratios (lower QD concentrations) as expected from a pure QD-surface-availability estimation. This "late" FRET-ratio saturation can be attributed to the polyhistidine-mediated self-assembly to the carboxyls of the organic ITK-QD coating. As expected, the polyhistidine−COOH interaction (COOH-groups mimicking NTA, vide supra) is less effective than the polyhistidine-Zn coordination (with the Zn-rich surface of the semiconductor QD), which was shown to provide a dissociation constant of ca. 2 nM.[34] In fact, the FRET-ratios for the [Tb-PEP]-[DHLA-QD] systems (Figure 7B-I) increase very steeply until saturation is reached at QD concentrations between ca. 0.5 and 3 nM (ca. 15−6 PEP/QD), which is very close to the previously found dissociation constant of 2 nM. The different valences (PEP/QD) of these two systems contain another interesting aspect. Although they were somewhat lower than expected, the results show that simultaneous QD FRET sensitization (generation of biexcitons) plays a minor role. Such a fast process should be much more efficient for higher FRET efficiencies. In contrast to this requirement, the FRET system with the significantly shorter donor−acceptor distance (higher FRET efficiency), namely, [Tb-PEP]-[DHLA-QD], shows a saturation at elevated PEP/QD ratios (6 to 15), whereas the larger [Tb-PEP]-[ITK-QD] system (lower FRET efficiency) saturates at much lower PEP/QD ratios (1.0 to 1.3). We therefore believe that the low nanomolar concentrations and the different binding strengths are the major reasons for these lower and differing valences.

MBP-Based Systems. The [Tb-MBP]-[DHLA-QD] systems (Figure 7B-II) show a much less inclined increase of the FRET-ratio, and a saturation is not obvious for any of the QDs within the applied range of concentrations. This effect can be attributed to a lower accessibility of the large polyhistidine-modified protein to the QD surface as well as a much lower valence (the 3.0 nm × 4.0 nm × 6.5 nm size of MBP results in a much lower theoretical MBP/QD surface coverage) compared to that of the smaller peptide (ca. 1.1 nm). The [Tb-MBP]-[ITK-QD] systems (Figure 7A-II) show a steeper FRET-ratio increase with saturations reached between ca. 2 and 6 nM (ca. 3 to 1 MBP/QD) for the different QDs, which we attribute to the lower Tb-MBP concentrations (5.5 nM) and the larger ITK-QDs, which provide a larger surface and therefore a larger valence of MBP/QD compared to the smaller DHLA-QDs. Moreover, charged as well as hydrophobic and hydrophilic patches on the protein can also interact with the carboxylated QD surface for an increased binding strength.

The analysis of QD-concentration-dependent FRET-ratios provides a good quantitative estimation of valences and binding strengths and a very good comparison of the different binding conditions for peptides and MBPs to the various QDs. Moreover, the same PL intensity decay curves as those for the FRET distance and shape analysis were used, which is extremely convenient as all data can be extracted from one experimental setup under conditions that are also used for the application of the nanoconjugates for biosensing.

■ CONCLUSIONS

Precise size, shape, and bioconjugation analysis of biocompatible, water-soluble QDs at low concentrations within a single homogeneous measurement is a challenging task that cannot be fulfilled by analytical methods such as TEM, DLS, and HPLC. Here, we described a 3-dimensional size and shape characterization study using 11 QDs with different organic surface coatings, which bind to two different biomolecules, namely, PEP and MBP, via polyhistidine self-assembly. Conjugating PEP and MBP with Tb allowed fast and homogeneous time-resolved detection of FRET from Tb to QD at QD concentrations ranging from 0.2 to 12 nM in 150 μL samples on a commercial

fluorescence plate reader. Analysis of the different multi-exponential PL decay curves resulted in up to three different distances and their fractions, which allowed for precise size and shape quantification, which was in good agreement with the expected size and shape ranges estimated from different TEM and DLS measurements. We found that the measurement of FRET-sensitized QD-acceptor PL is more precise than the analysis of FRET-quenched Tb-donor PL because the QD-sensitization increases against a much lower background compared to the quenching of the Tb, which has to be acquired against a high PL background of unquenched Tb. This higher precision is extremely advantageous for shape analysis, as elongated forms can be distinguished from spherical forms, which is not possible for the Tb-donor PL analysis. Another interesting aspect is the difference in the small PEP (ca. 1.3 nm including His_6 and Tb functionalization) and the rather large MBP (ca. 3.0 nm × 4.0 nm × 6.5 nm). The 1:1 Tb/PEP labeling ratio leads to a fixed Tb-to-QD distance, which allows much higher precision in shape and size determination compared to those of the randomly Tb-labeled and large MBP, which results in a large distance distribution and only few information about QD shapes. Our distance analysis also shows that both PEP and MBP can access the Zn-rich surface of the semiconductor QD for the DHLA-QD, which have a relatively short DHLA ligand on their surface. For the ITK-QDs, both PEP and MBP can bind to the carboxyl-functionalized polymers at different distances from the semiconductor QD surface but at different ratios. In general, different Tb-donor to QD-acceptor distances (as illustrated in Scheme 1) can be achieved for the polyhistidine-functionalized PEP and MBP assembly to the different QDs. Analyzing the time-gated PL intensities of FRET-quenched Tb and FRET-sensitized QDs further allows characterization of the binding conditions. Our results show that PEP self-assembly to the DHLA-QDs via His_6-Zn coordination is stronger than PEP self-assembly to the ITK-QDs via His_6-COOH interactions. They also confirmed previous findings of dissociation constants of ca. 2 nM for hexahistidine-Zn self-assembly on DHLA-QDs. From all of the investigated QD-bioconjugate systems, DHLA-QD-PEP provides strongest binding due to efficient His_6-Zn coordination, followed by ITK-QD-MBP due to combined electrostatic plus His_6-COOH interactions and large MBP/QD valences. Both ITK-QD-PEP and DHLA-QD-MBP show significantly weaker binding due to a weaker His_6−COOH interaction and a lower QD-surface accessibility of the relatively large MBP, respectively.

In summary, our time-resolved Tb-to-QD FRET analysis allows a homogeneous, fast, and simultaneous measurement of QD sizes, shapes, and bioconjugation conditions at very low (≤nanomolar) concentrations in solution with extremely high (mostly subnanometer) spatial resolution. The results confirm distances and shapes from TEM and DLS analysis and binding conditions found in previous studies. These results confirm that time-resolved Tb-to-QD FRET is a highly sensitive nanotool for quantitative concentration and distance analysis with a large potential for biosensing applications.

■ MATERIALS AND METHODS

Materials. The Lumi4 terbium complex was provided by Lumiphore, Inc. (Berkeley, CA, USA).[44] Conjugation to peptides (Tb-PEP, Tb-GSGAAAGLS$(His)_6$) obtained from Biosynthesis (Lewisville, TX USA) or maltose binding proteins (MBP) was performed using published protocols.[37,45] The preparation of the different emitting dihydrolipoic acid (DHLA) capped core/shell QDs is described elsewhere.[46] The five Qdot ITK carboxyl quantum dots (ITK-QD525, ITK-QD565, ITK-QD605, ITK-QD655, and ITK-QD705) were purchased from Life Technologies (Carlsbad, CA, USA). For all measurements, sodium-tetraborate buffer (10 mM, pH 8.5, Sigma-Aldrich) was used. For Tb and the ITK-QDs, we used the molar absorptivities provided by the suppliers: $\varepsilon^{Tb}(340\text{ nm}) = 2.6 \times 10^3\ M^{-1}cm^{-1}$, $\varepsilon^{QD525}(405\text{ nm}) = 3.6 \times 10^5\ M^{-1}cm^{-1}$, $\varepsilon^{QD565}(405\text{ nm}) = 1.1 \times 10^6\ M^{-1}cm^{-1}$, $\varepsilon^{QD605}(405\text{ nm}) = 2.8 \times 10^6\ M^{-1}cm^{-1}$, $\varepsilon^{QD655}(405\text{ nm}) = 5.7 \times 10^6\ M^{-1}cm^{-1}$, and $\varepsilon^{QD705}(405\text{ nm}) = 8.3 \times 10^6\ M^{-1}cm^{-1}$. For the DHLA-QDs, the molar absorptivities were calculated using the energy (wavelength) of the first absorption peak.[26] Taking into account conjugation to biomolecules (PEP and MBP) for Tb, the significantly different solvent conditions for QDs (absorptivity calculations are based on noncapped core-QDs in organic solvents, whereas our measurements are carried out with surface-functionalized QDs in aqueous solution) and their nonspherical shapes, and dilution errors (dilution of micromolar concentrated stock solutions to nanomolar working solutions) we estimated concentration errors of the working solutions of ±20% for Tb-PEP, ±25% for Tb-MBP, and ±40% for the QDs. The relative concentrations within one assay are very precise with estimated error of ±5%.

QD Characterization. Structural characterization of the QDs was carried out using transmission electron microscopy (TEM) and dynamic light scattering (DLS). TEM was carried out using a JEOL 2200-FX analytical high-resolution transmission electron microscope with a 200 kV accelerating voltage. Samples were prepared by spreading a drop (5−10 μL) of the filtered QD dispersion (filtered by using 0.25 μm syringe filters (Millipore)) onto the ultrathin carbon/holey support film on a 300 mesh Au grid (Ted Pella, Inc.) and letting it dry. The concentration of QDs in the deionized water used was typically ∼1 μM for ITK-QDs and ∼5 μM for DHLA-QDs. Individual particle sizes were measured using a Gatan Digital Micrograph (Pleasanton, CA); average sizes along with standard deviations were extracted from analysis of at least 50−100 nanoparticles. DLS measurements were carried out using a CGS-3 goniometer system equipped with a HeNe laser illumination at 633 nm and a single-photon counting avalanche photodiode for signal detection (Malvern Instruments, Southborough, MA, USA). The autocorrelation function was performed by an ALV-5000/EPP photon correlator (ALV, Langen, Germany) and analyzed using Dispersion Technology Software (DTS, Malvern Instruments). QDs solutions (ITK-QDs, 50−100 nM in pH 8.5 sodium borate buffer; DHLA-QDs, deionized water, adjusted to pH 9) were prefiltered through 0.25 μm syringe filters (Millipore) prior to DLS measurements to remove dust or impurities in the sample. Sample temperature was maintained at 20 °C. For each sample, the autocorrelation function was the average of three runs of 10 s each and then repeated at different scattering angles (within 80° and 120°). CONTIN analysis was then used to extract number versus hydrodynamic size profiles for the dispersions studied.[47] Absorption spectra were recorded in 1 cm quartz cells with a UV−vis-spectrometer (Lambda35, PerkinElmer). PL spectra and lifetimes were recorded in 3 mm quartz cells with a fluorescence lifetime spectrometer (FLS920, Edinburgh Instruments, UK). For steady-state measurements, samples were excited with a Xe-Lamp. For the lifetime measurements, the samples were excited with a diode-laser (405.6 nm center wavelength, 2 MHz repetition rate, and 5 mW maximum average power). PL quantum yields and Förster distances were calculated as described elsewhere.[31]

Size, Shape, and Binding Analysis. All self-assembly measurements were performed with a modified KRYPTOR fluorescence plate reader (Cezanne/Thermo Fisher Scientific, France) using 4000 detection-bins of 2 μs integration time. A pulsed nitrogen laser was used for excitation (337.1 nm, 20 Hz, 800 flashes). All measurements were performed in sodium tetraborate buffer (pH of 8.5) and in black 96-well microtiter plates with an optimal working volume of 150 μL. Optical transmission filter center/band-pass wavelengths were 497/16 nm (Semrock) for the Tb channel and 525/15 nm (Semrock) for ITK-QD525. The bandpassfilter 567/15 nm (Semrock) was used for DHLA-QD573, DHLA-QD578, and ITK-QD525. For the detection of DHLA-QD590, DHLA-QD615, and ITK-QD605, a transmission filter of 605/15 (Semrock) was used. ITK-QD655 and ITK-QD705 were detected using 655/15 (Semrock) and 740/13 (Semrock) filters,

respectively. The different samples contained increasing concentrations of QDs and constant concentrations of Tb-PEP or Tb-MBP for each QD-bioconjugate system. The solutions were incubated for 1 h before the measurements on the KRYPTOR. The PL decay data were fitted using FAST software, version 3.1 (Edinburgh Instruments, UK). Origin Pro 8.1 SR3 (OriginLab Corporation) and Microsoft Excel (Microsoft Corporation) were used for graphs and calculations.

■ ASSOCIATED CONTENT

Supporting Information

TEM images of all ITK-QDs and DHLA-QDs, and PL decay curves and time-gated intensities for all ITK-QD and DHLA-QD bioconjugate systems. This material is available free of charge via the Internet at http://pubs.acs.org.

■ AUTHOR INFORMATION

Corresponding Author

*E-mail: niko.hildebrandt@u-psud.fr.

Notes

The authors declare no competing financial interest.

■ ACKNOWLEDGMENTS

We thank Lumiphore, Inc. for the gift of Lumi4-Tb-NHS reagent and the European Commission (FP7 project NANOGNOSTICS) and the Agence National de la Recherche France (project NanoFRET) for financial support. We also acknowledge support from the Office of Naval Research (ONR), the Naval Research Laboratory (NRL), the NRL Nanosciences Institute (NSI), and the Defense Threat Reduction Agency Joint Science and Technological Office (DTRA-JSTO) Military Interdepartmental Purchase Requisition (MIPR) #B112582M.

■ REFERENCES

(1) Algar, W. R.; Susumu, K.; Delehanty, J. B.; Medintz, I. L. *Anal. Chem.* **2011**, *83*, 8826−8837.
(2) Biju, V.; Itoh, T.; Ishikawa, M. *Chem. Soc. Rev.* **2010**, *39*, 3031−3056.
(3) Hildebrandt, N. *ACS Nano* **2011**, *5*, 5286−5290.
(4) Jin, Z.; Hildebrandt, N. *Trends Biotechnol.* **2012**, *30*, 394−403.
(5) Mattoussi, H.; Palui, G.; Na, H. B. *Adv. Drug Delivery Rev.* **2012**, *64*, 138−166.
(6) Petryayeva, E.; Algar, W. R.; Medintz, I. L. *Appl. Spectrosc.* **2013**, *67*, 215−252.
(7) Zrazhevskiy, P.; Sena, M.; Gao, X. H. *Chem. Soc. Rev.* **2010**, *39*, 4326−4354.
(8) Rosenthal, S. J.; Chang, J. C.; Kovtun, O.; McBride, J. R.; Tomlinson, I. D. *Chem. Biol.* **2011**, *18*, 10−24.
(9) Grigsby, C. L.; Ho, Y.-P.; Leong, K. W. *Nanomedicine* **2012**, *7*, 565−577.
(10) Tyrakowski, C. M.; Snee, P. T. *Phys. Chem. Chem. Phys.* **2014**, *16*, 837−855.
(11) Algar, W. R.; Tavares, A. J.; Krull, U. J. *Anal. Chim. Acta* **2010**, *673*, 1−25.
(12) Freeman, R.; Willner, I. *Chem. Soc. Rev.* **2012**, *41*, 4067−4085.
(13) Hötzer, B.; Medintz, I. L.; Hildebrandt, N. *Small* **2012**, *8*, 2297−2326.
(14) Medintz, I. L.; Hildebrandt, N., Eds. *FRET - Förster Resonance Energy Transfer. From Theory to Applications*; Wiley-VCH: Weinheim, Germany, 2014.
(15) Medintz, I. L.; Mattoussi, H. *Phys. Chem. Chem. Phys.* **2009**, *11*, 17−45.
(16) Sapsford, K. E.; Wildt, B.; Mariani, A.; Yeatts, A. B.; Medintz, I. L. In *FRET - Förster Resonance Energy Transfer. From Theory to Applications*; Medintz, I. L., Hildebrandt, N., Eds.; Wiley-VCH: Weinheim, Germany, 2014; pp 165−268.
(17) Blanco-Canosa, J. B.; Wu, M.; Susumu, K.; Petryayeva, E.; Jennings, T. L.; Dawson, P. E.; Algar, W. R.; Medintz, I. L. *Coord. Chem. Rev.* **2014**, *263*−*264*, 101−137.
(18) Algar, W. R.; Wegner, D.; Huston, A. L.; Blanco-Canosa, J. B.; Stewart, M. H.; Armstrong, A.; Dawson, P. E.; Hildebrandt, N.; Medintz, I. L. *J. Am. Chem. Soc.* **2012**, *134*, 1876−1891.
(19) Charbonnière, L. J.; Hildebrandt, N. *Eur. J. Inorg. Chem.* **2008**, 3241−3251.
(20) Geißler, D.; Charbonnière, L. J.; Ziessel, R. F.; Butlin, N. G.; Löhmannsröben, H.-G.; Hildebrandt, N. *Angew. Chem. Int. Ed.* **2010**, *49*, 1396−1401.
(21) Geißler, D.; Linden, S.; Liermann, K.; Wegner, K. D.; Charbonnière, L. J.; Hildebrandt, N. *Inorg. Chem.* **2014**, *53*, 1824−1838.
(22) Hildebrandt, N.; Wegner, K. D.; Algar, W. R. *Coord. Chem. Rev.* **2014**, *273*−*274*, 125−138.
(23) Wegner, K. D.; Jin, Z.; Linden, S.; Jennings, T. L.; Hildebrandt, N. *ACS Nano* **2013**, *7*, 7411−7419.
(24) Wegner, K. D.; Linden, S.; Jin, Z. W.; Jennings, T. L.; el Khoulati, R.; van Bergen en Henegouwen, P. M. P.; Hildebrandt, N. *Small* **2014**, *10*, 734−740.
(25) Snee, P. T.; Tyrakowski, C. M.; Page, L. E.; Isovic, A.; Jawaid, A. M. *J. Phys. Chem. C* **2011**, *115*, 19578−19582.
(26) Jasieniak, J.; Smith, L.; van Embden, J.; Mulvaney, P.; Califano, M. *J. Phys. Chem. C* **2009**, *113*, 19468−19474.
(27) Pelaz, B.; Jaber, S.; de Aberasturi, D. J.; Wulf, V.; Aida, T.; de la Fuente, J. M.; Feldmann, J.; Gaub, H. E.; Josephson, L.; Kagan, C. R.; Kotov, N. A.; Liz-Marzan, L. M.; Mattoussi, H.; Mulvaney, P.; Murray, C. B.; Rogach, A. L.; Weiss, P. S.; Willner, I.; Parak, W. J. *ACS Nano* **2012**, *6*, 8468−8483.
(28) Wang, X. Y.; Ren, X. F.; Kahen, K.; Hahn, M. A.; Rajeswaran, M.; Maccagnano-Zacher, S.; Silcox, J.; Cragg, G. E.; Efros, A. L.; Krauss, T. D. *Nature* **2009**, *459*, 686−689.
(29) Shen, H.; Jawaid, A. M.; Snee, P. T. *ACS Nano* **2009**, *3*, 915−923.
(30) Morgner, F.; Geißler, D.; Stufler, S.; Butlin, N. G.; Löhmannsröben, H.-G.; Hildebrandt, N. *Angew. Chem. Int. Ed.* **2010**, *49*, 7570−7574.
(31) Wegner, K. D.; Phung Thi, L.; Jennings, T.; Oh, E.; Jain, V.; Fairclough, S. M.; Smith, J. M.; Giovanelli, E.; Lequeux, N.; Pons, T.; Hildebrandt, N. *ACS Appl. Mater. Interfaces* **2013**, *5*, 2881−2892.
(32) Byrne, A. G.; Byrne, M. M.; Coker, G., III; Boeneman-Gemmill, K.; Spillman, C.; Medintz, I. L.; Sloan, S. L.; van der Meer, B. W. In *FRET - Förster Resonance Energy Transfer. From Theory to Applications*; Medintz, I. L., Hildebrandt, N., Eds.; Wiley-VCH: Weinheim, Germany, 2014; pp 657−766.
(33) Boeneman, K.; Delehanty, J. B.; Susumu, K.; Stewart, M. H.; Medintz, I. L. *J. Am. Chem. Soc.* **2010**, *132*, 5975−5977.
(34) Sapsford, K. E.; Pons, T.; Medintz, I. L.; Higashiya, S.; Brunel, F. M.; Dawson, P. E.; Mattoussi, H. *J. Phys. Chem. C* **2007**, *111*, 11528−11538.
(35) Dennis, A. M.; Sotto, D. C.; Mei, B. C.; Medintz, I. L.; Mattoussi, H.; Bao, G. *Bioconjugate Chem.* **2010**, *21*, 1160−1170.
(36) Medintz, I. L.; Clapp, A. R.; Mattoussi, H.; Goldman, E. R.; Fisher, B.; Mauro, J. M. *Nat. Mater.* **2003**, *2*, 630−638.
(37) Medintz, I. L.; Goldman, E. R.; Lassman, M. E.; Mauro, J. M. *Bioconjugate Chem.* **2003**, *14*, 909−918.
(38) Prasuhn, D. E.; Deschamps, J. R.; Susumu, K.; Stewart, M. H.; Boeneman, K.; Blanco-Canosa, J. B.; Dawson, P. E.; Medintz, I. L. *Small* **2010**, *6*, 555−564.
(39) Sapsford, K. E.; Algar, W. R.; Berti, L.; Gemmill, K. B.; Casey, B. J.; Oh, E.; Stewart, M. H.; Medintz, I. L. *Chem. Rev.* **2013**, *113*, 1904−2074.
(40) Algar, W. R.; Kim, H.; Medintz, I. L.; Hildebrandt, N. *Coord. Chem. Rev.* **2014**, *263*−*264*, 65−85.
(41) Clapp, A. R.; Medintz, I. L.; Mauro, J. M.; Fisher, B. R.; Bawendi, M. G.; Mattoussi, H. *J. Am. Chem. Soc.* **2004**, *126*, 301−310.

(42) Hildebrandt, N. In *FRET - Förster Resonance Energy Transfer. From Theory to Applications*; Medintz, I. L., Hildebrandt, N., Eds.; Wiley-VCH: Weinheim, Germany, 2014; pp 105−164.
(43) Klimov, V. I.; Mikhailovsky, A. A.; Su, Xu; Malko, A.; Hollingsworth, J. A.; Leatherdale, C. A.; Eisler, H.-J.; Bawendi, M. G. *Science* **2000**, *290*, 314−317.
(44) Xu, J.; Corneillie, T. M.; Moore, E. G.; Law, G.-L.; Butlin, N. G.; Raymond, K. N. *J. Am. Chem. Soc.* **2011**, *133*, 19900−19910.
(45) Sapsford, K. E.; Farrell, D.; Sun, S.; Rasooly, A.; Mattoussi, H.; Medintz, I. L. *Sens. Actuators, B* **2009**, *139*, 13−21.
(46) Clapp, A. R.; Goldman, E. R.; Mattoussi, H. *Nat. Protoc.* **2006**, *1*, 1258−1266.
(47) Oh, E.; Susumu, K.; Jain, V.; Kim, M.; Huston, A. *J. Colloid Interface Sci.* **2012**, *376*, 107−111.

■ NOTE ADDED AFTER ASAP PUBLICATION

This article was published ASAP on June 27, 2014, with minor text errors and incorrect versions of Figures 5 and 6. The corrected version was published ASAP on July 2, 2014.

Three-dimensional solution-phase Förster resonance energy transfer analysis of nanomolar quantum dot bioconjugates with sub-nanometer resolution

K. David Wegner[1], Frank Morgner[2], Eunkeu Oh[3,4], Ramasis Goswami,[5] Kimihiro Susumu[3,4], Michael H. Stewart[3], Igor L. Medintz[6], and Niko Hildebrandt[1*]

[1] NanoBioPhotonics, Institut d'Electronique Fondamentale, Université Paris-Sud, Orsay, France

[2] Fraunhofer Institut für Angewandte Polymerforschung, Potsdam, Germany

[3] Optical Sciences Division, Code 5600
[5] Multifunctional Materials, Code 6351
[6] Center for Bio/Molecular Science and Engineering, Code 6900
U.S. Naval Research Laboratory, Washington, DC, USA

[4] Sotera Defense Solutions, Inc., Columbia, MD, USA

*corresponding author: niko.hildebrandt@u-psud.fr

SUPPORTING INFORMATION

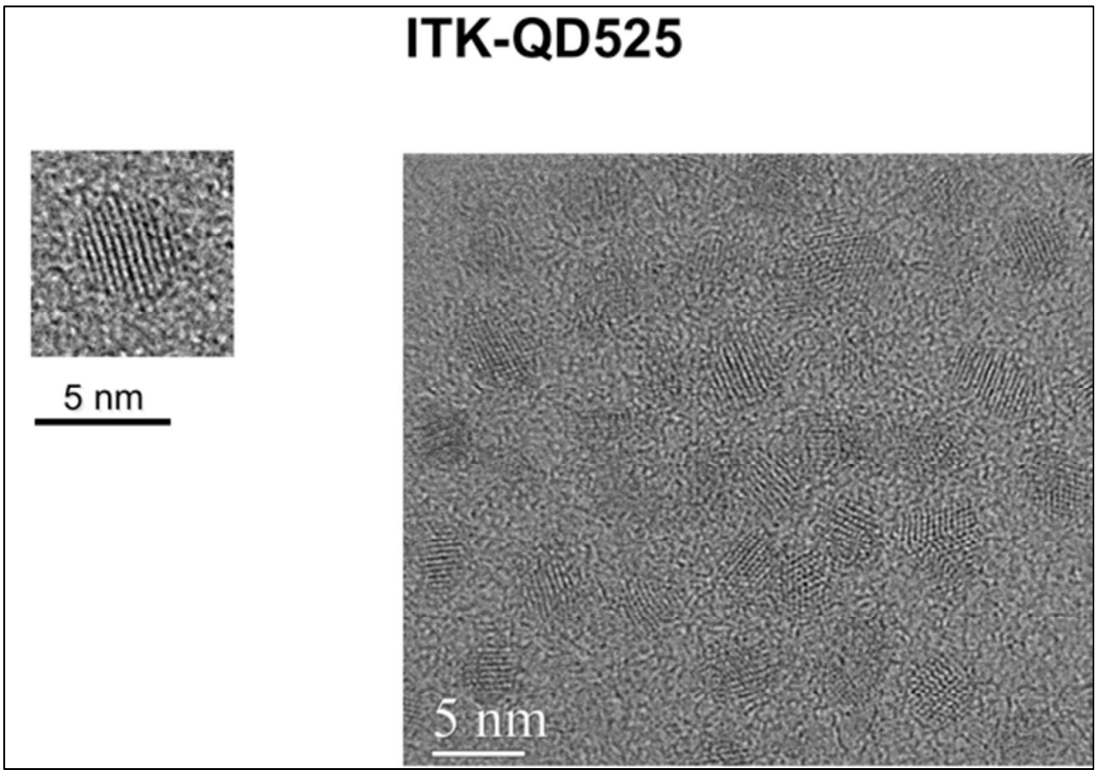
ITK-QD525
5 nm
5 nm

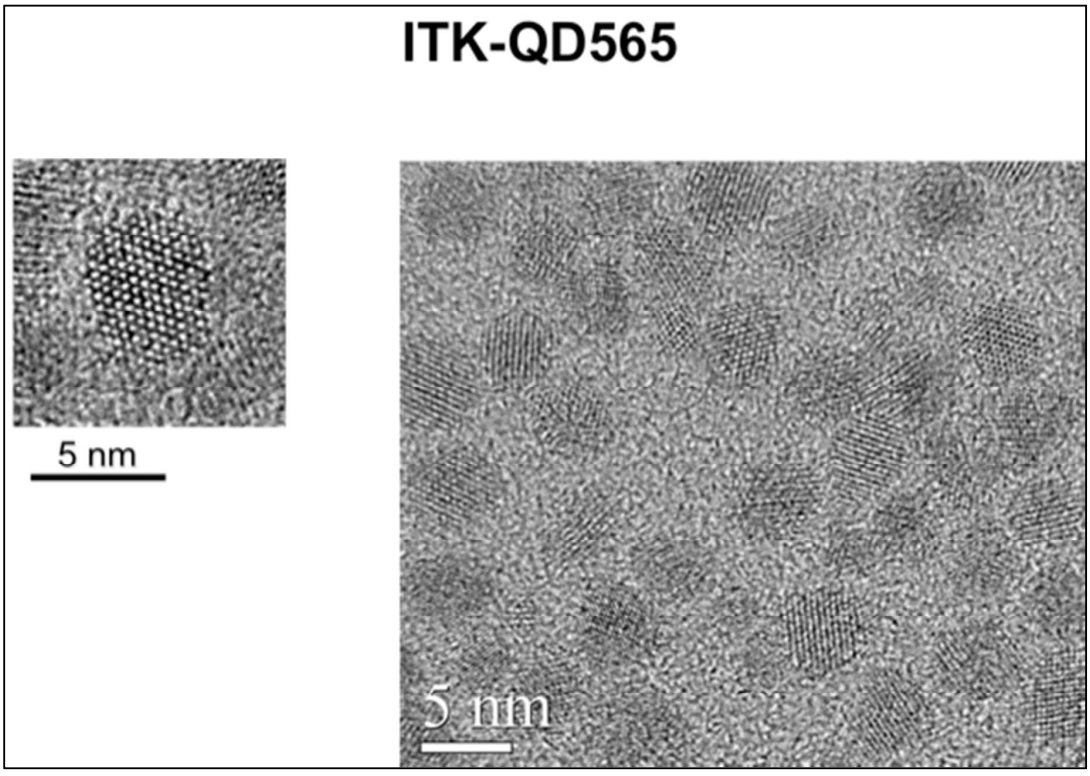
ITK-QD565
5 nm
5 nm

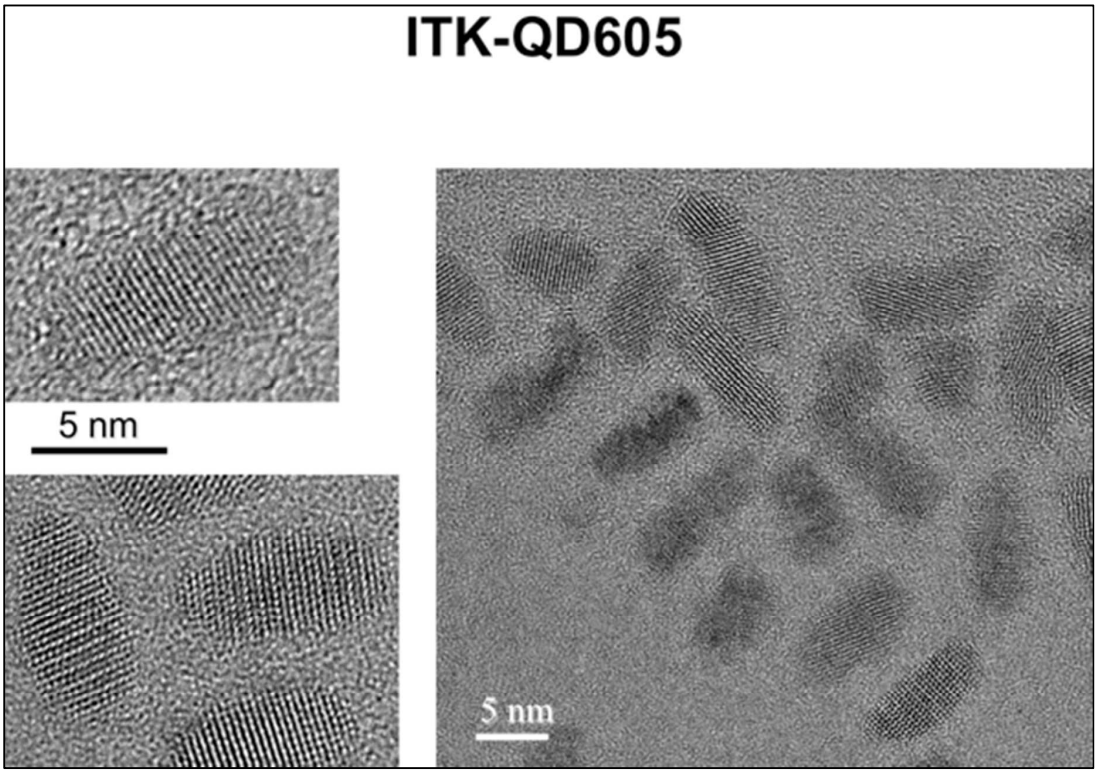
ITK-QD605
5 nm
5 nm

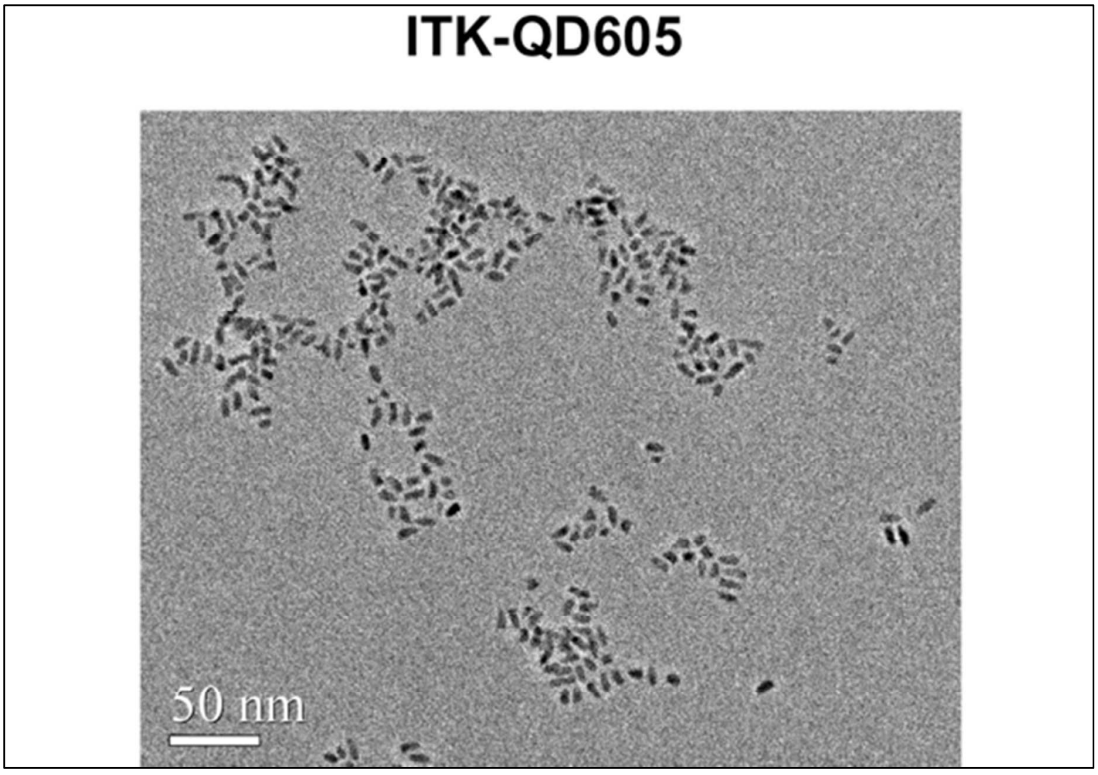
ITK-QD605
50 nm

ITK-QD655

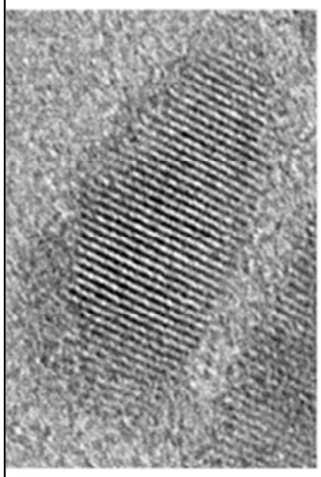

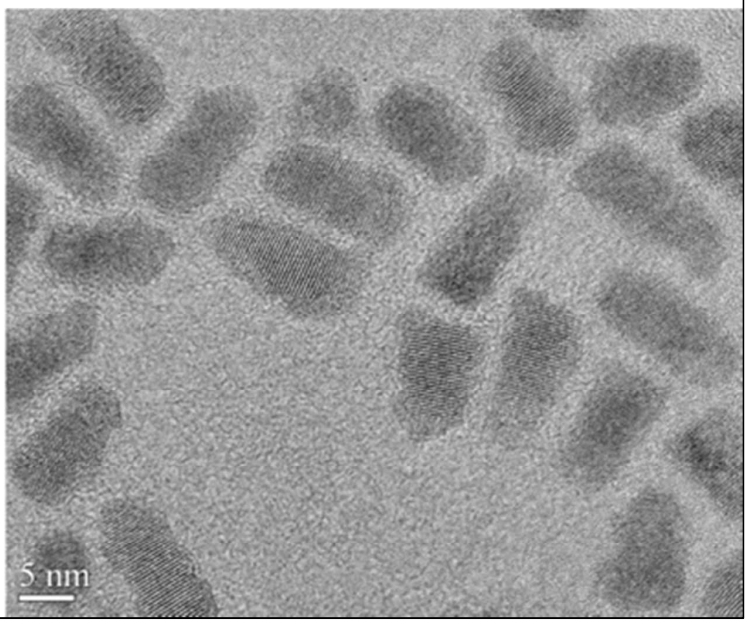

ITK-QD655

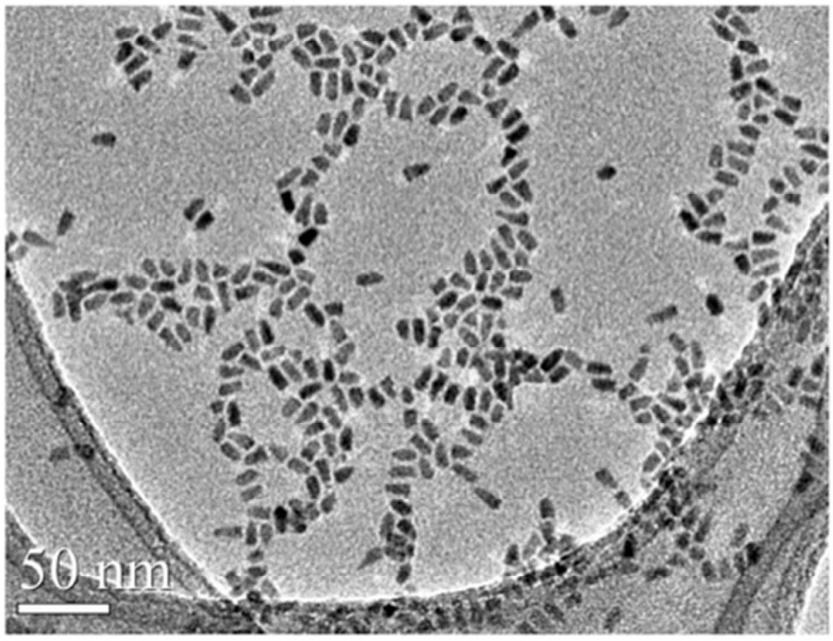

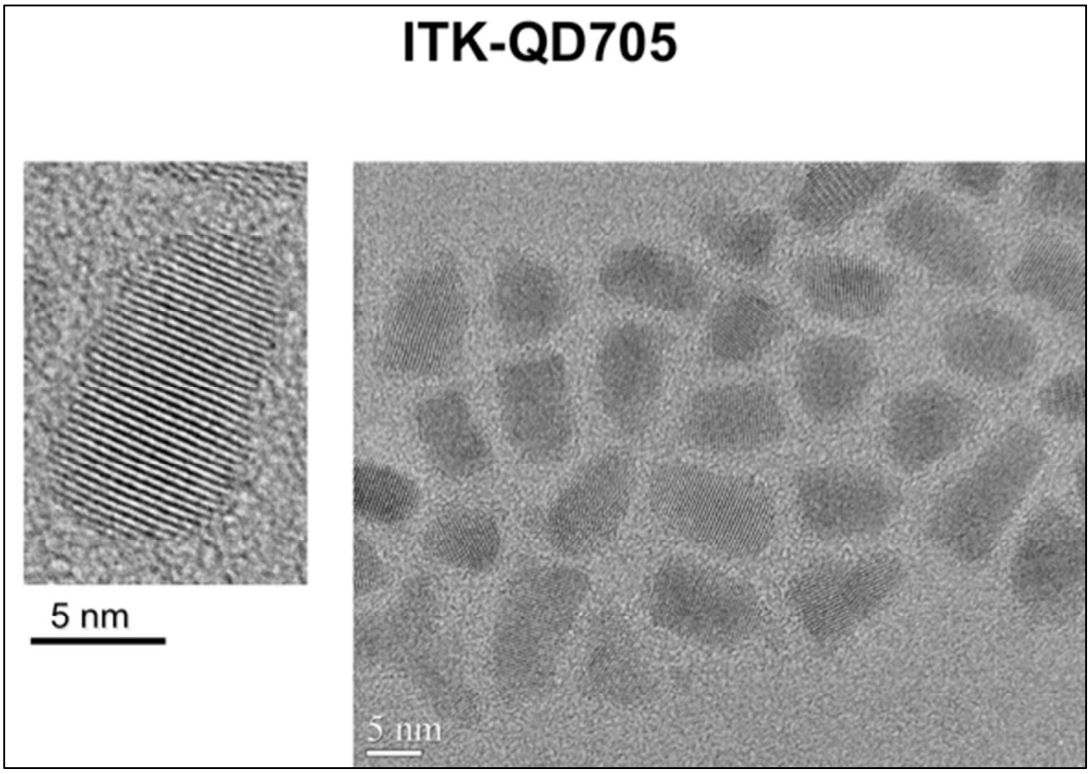
ITK-QD705
5 nm
5 nm

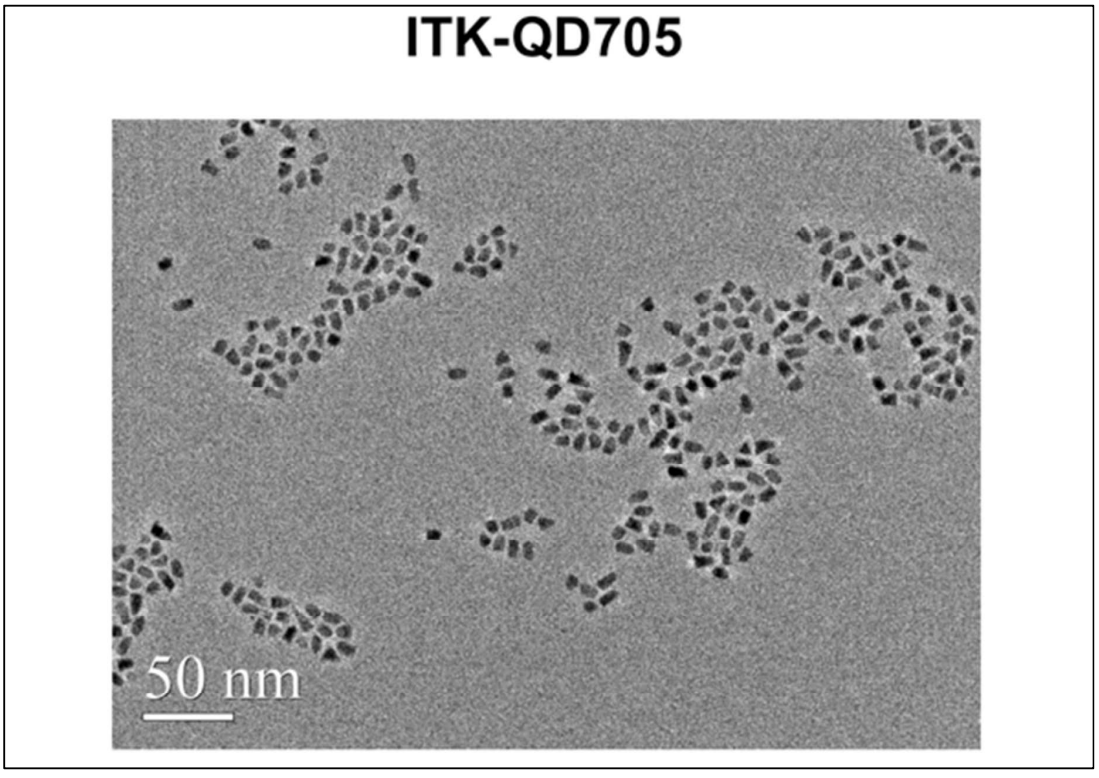
ITK-QD705
50 nm

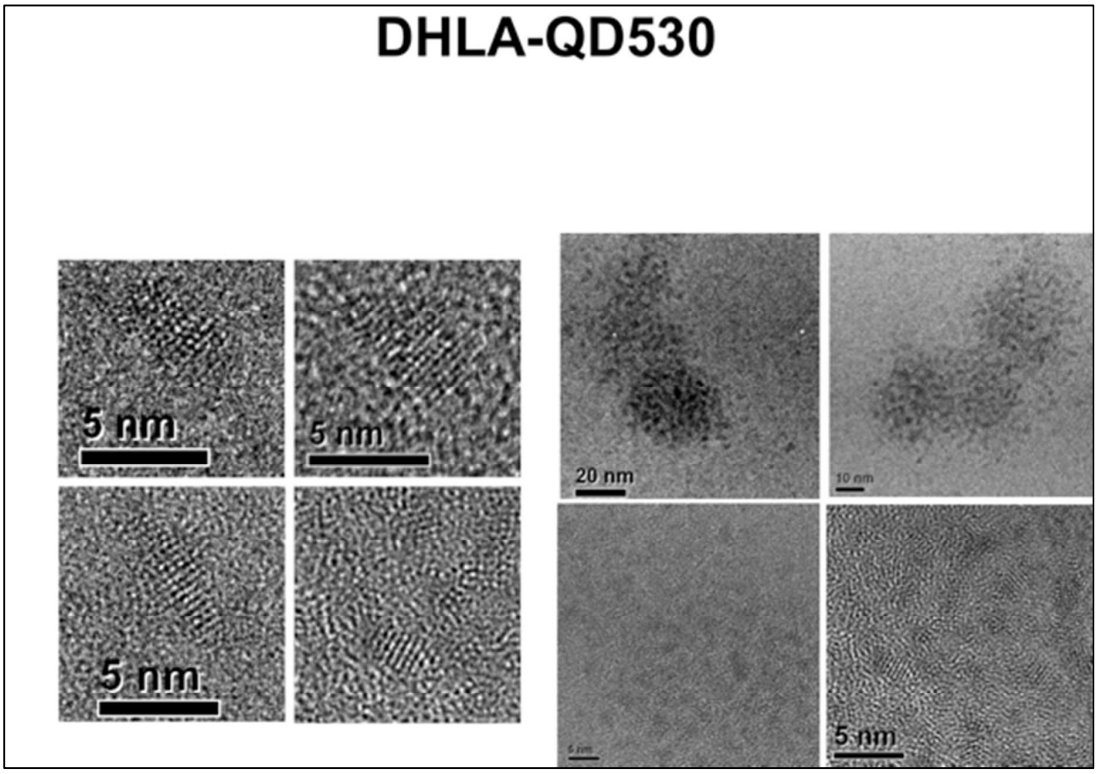
DHLA-QD530
5 nm
5 nm
5 nm
20 nm
10 nm
5 nm

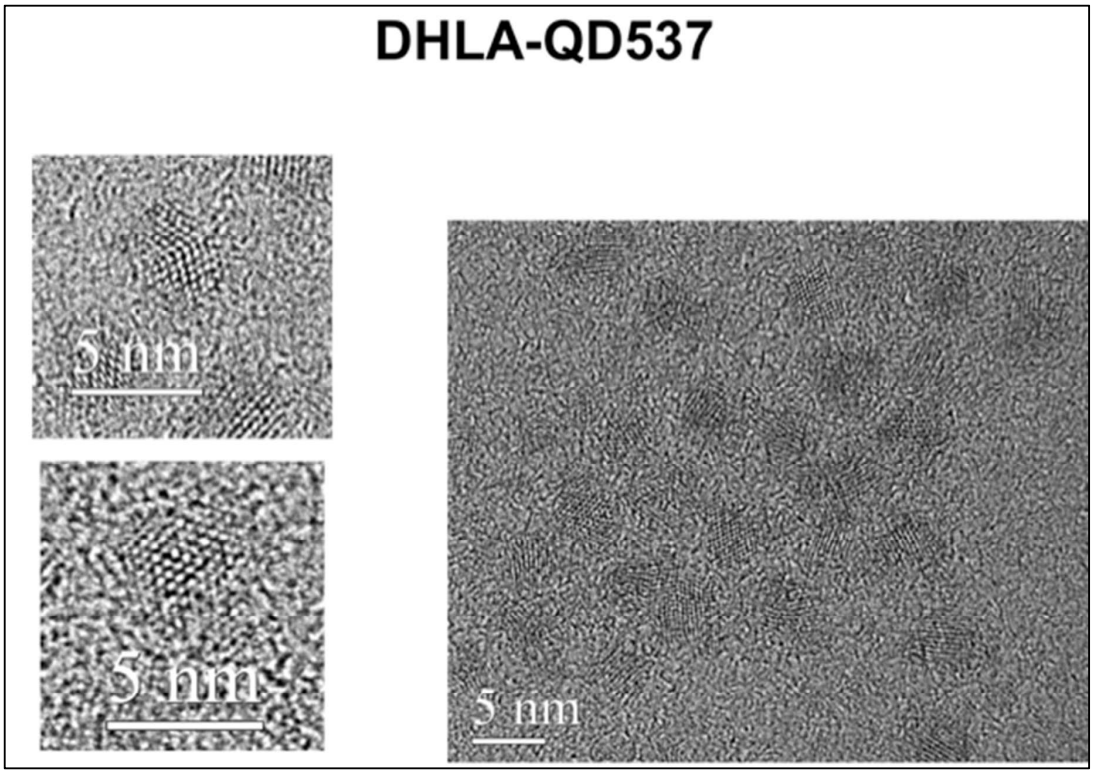
DHLA-QD537
5 nm
5 nm
5 nm

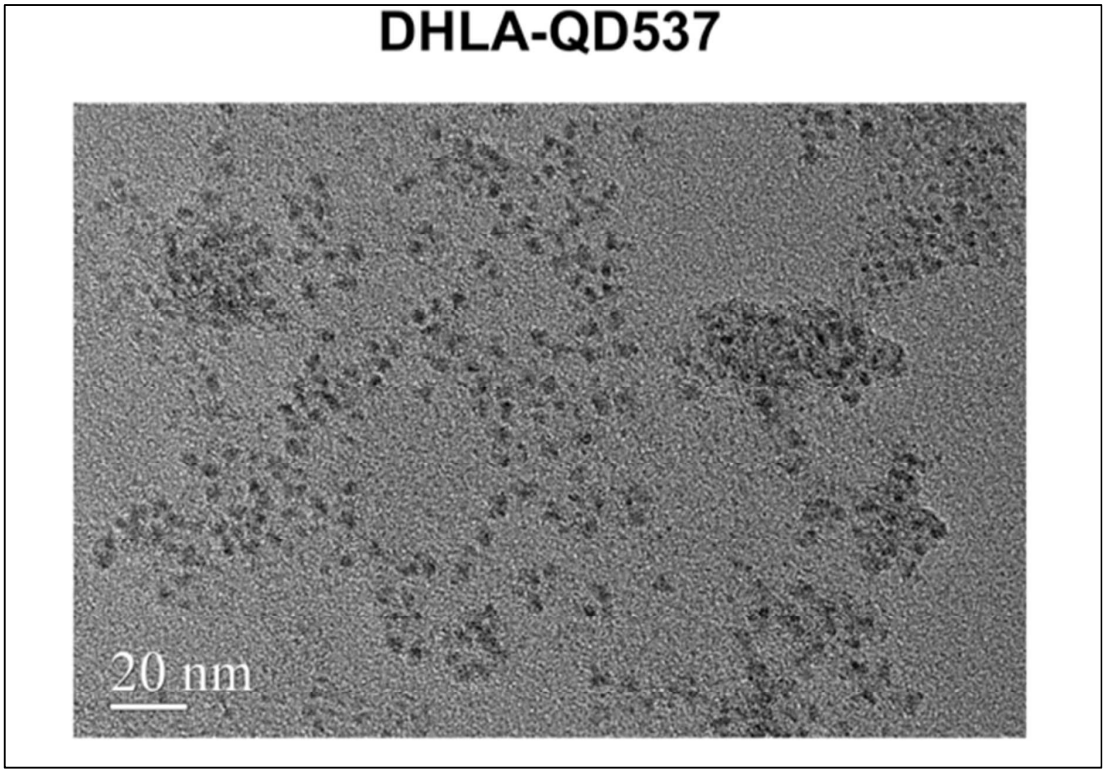
DHLA-QD537
20 nm

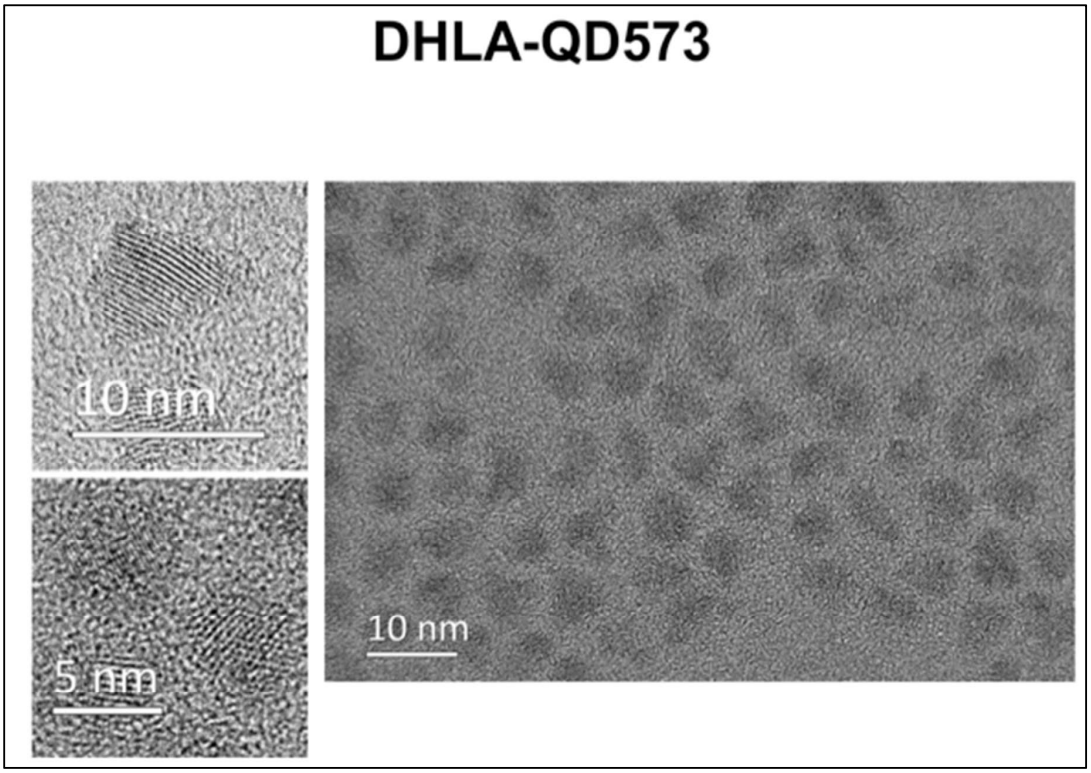
DHLA-QD573
10 nm
5 nm
10 nm

DHLA-QD573

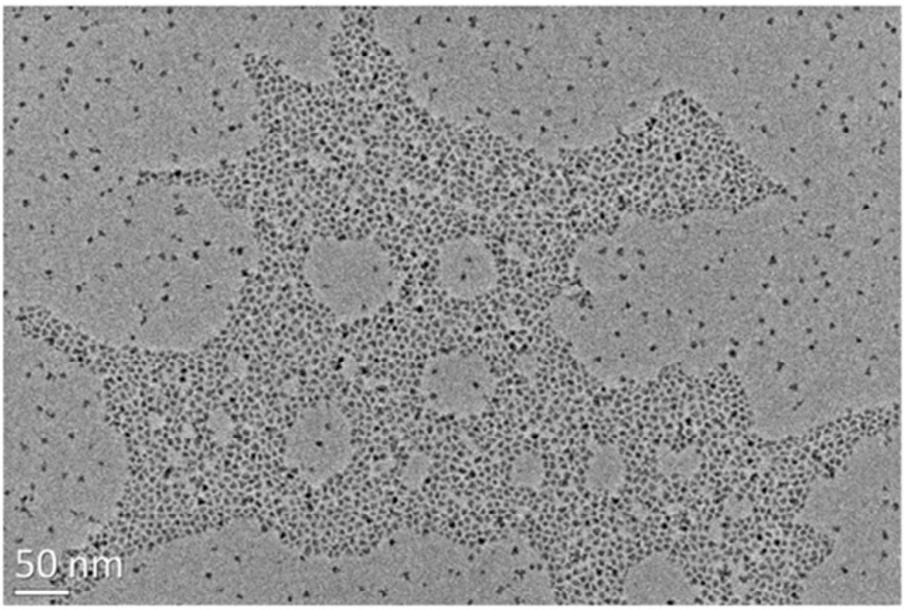

DHLA-QD578

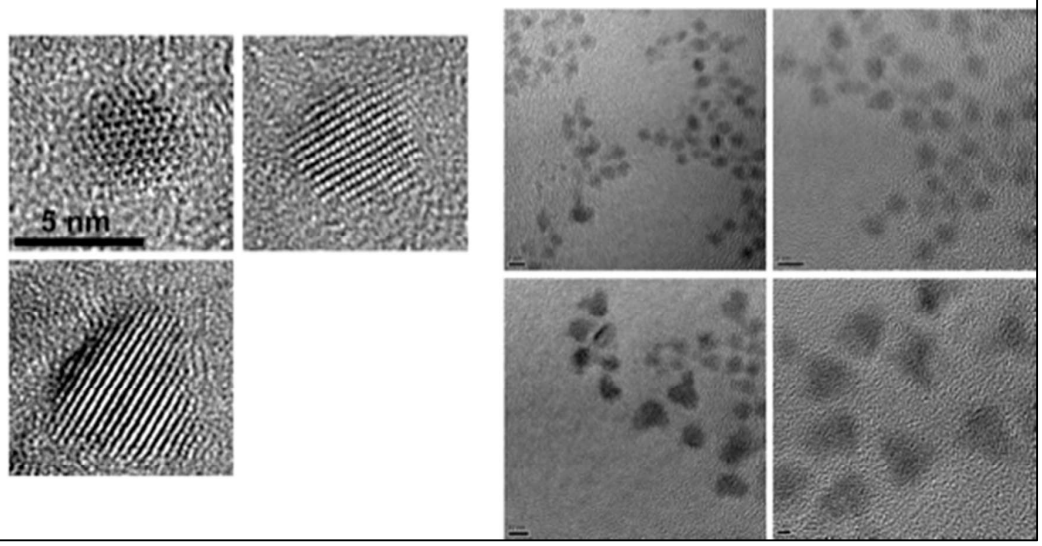

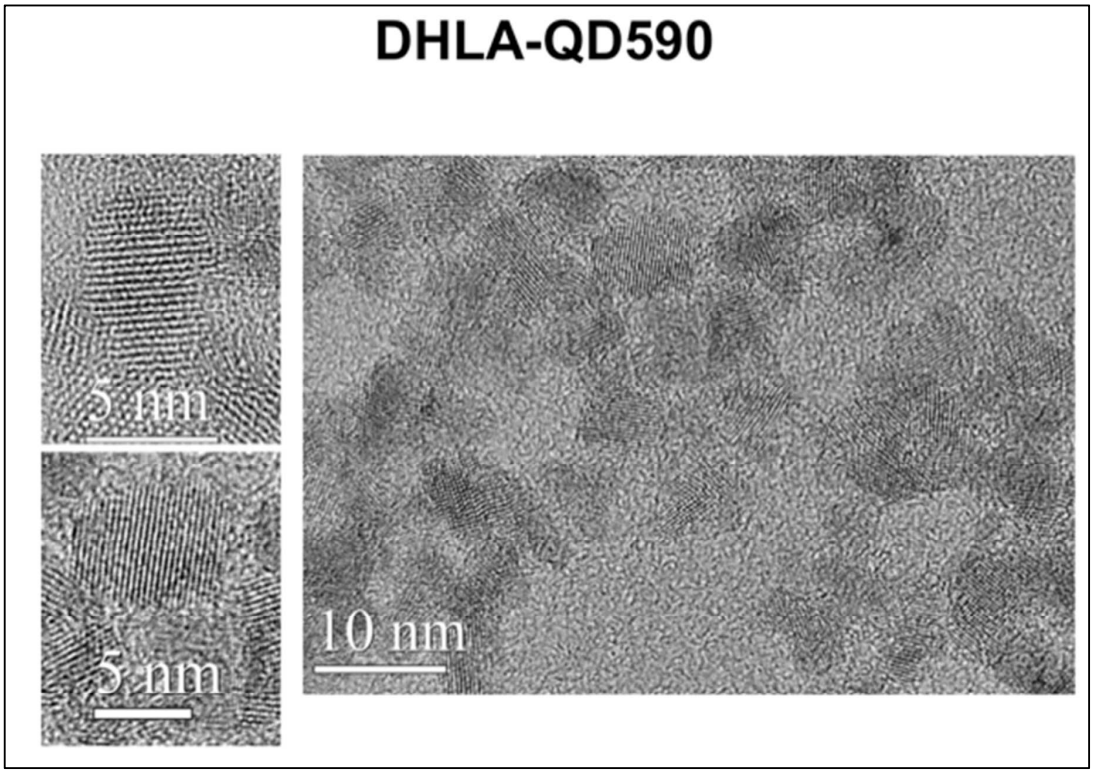
DHLA-QD590
5 nm
5 nm
10 nm

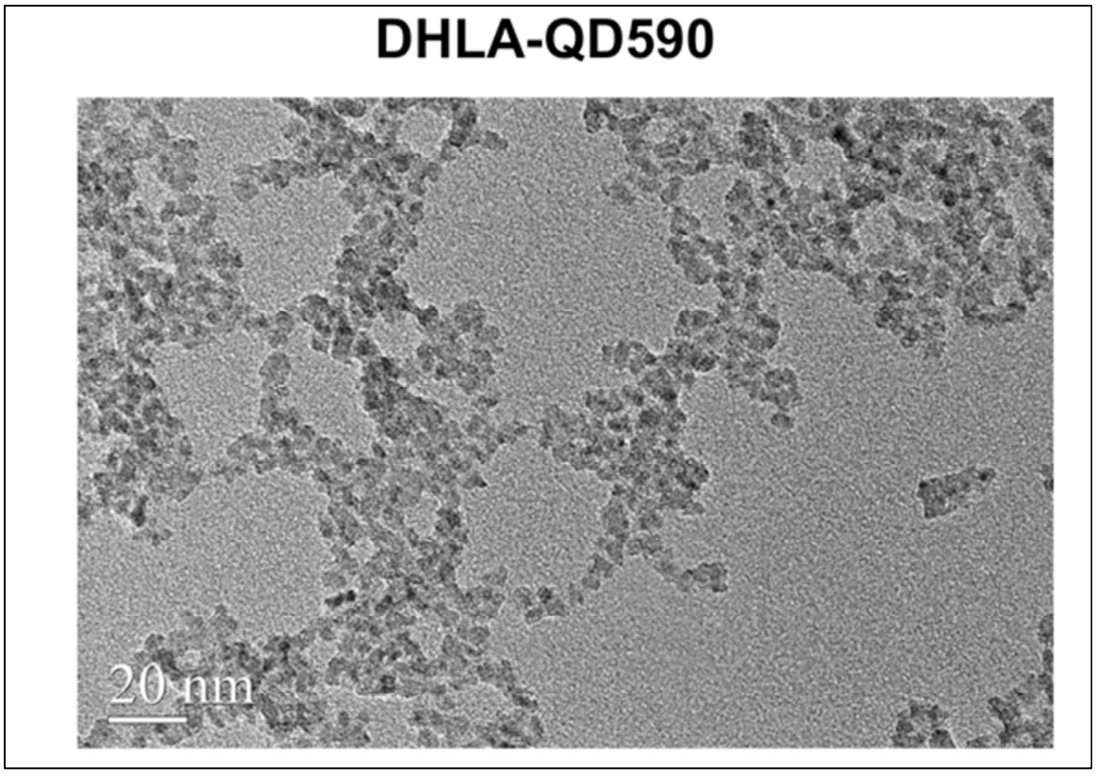
DHLA-QD590
20 nm

DHLA-QD615

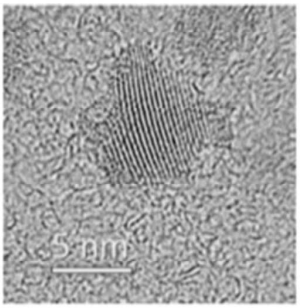

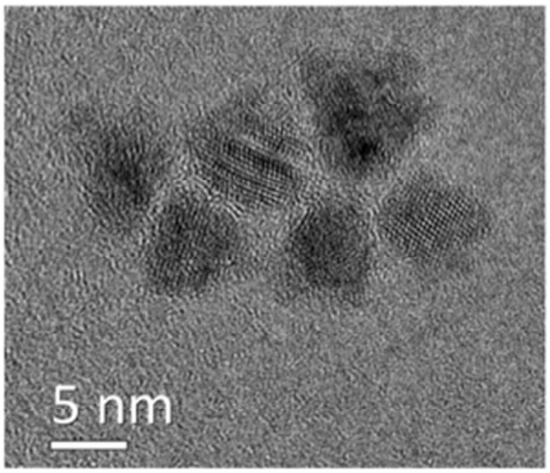

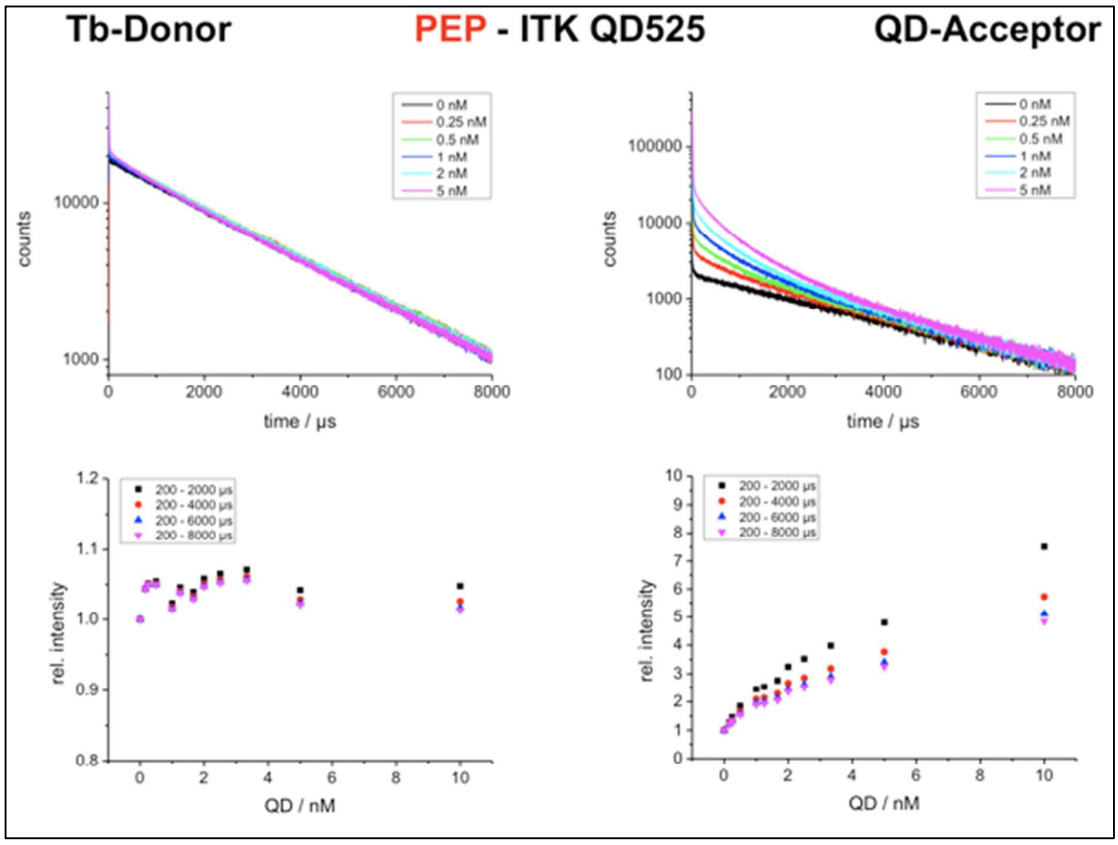
Tb-Donor
PEP - ITK QD525
QD-Acceptor
0 nM
0.25 nM
0.5 nM
1 nM
2 nM
5 nM
counts
time / µs
200 - 2000 µs
200 - 4000 µs
200 - 6000 µs
200 - 8000 µs
rel. intensity
QD / nM

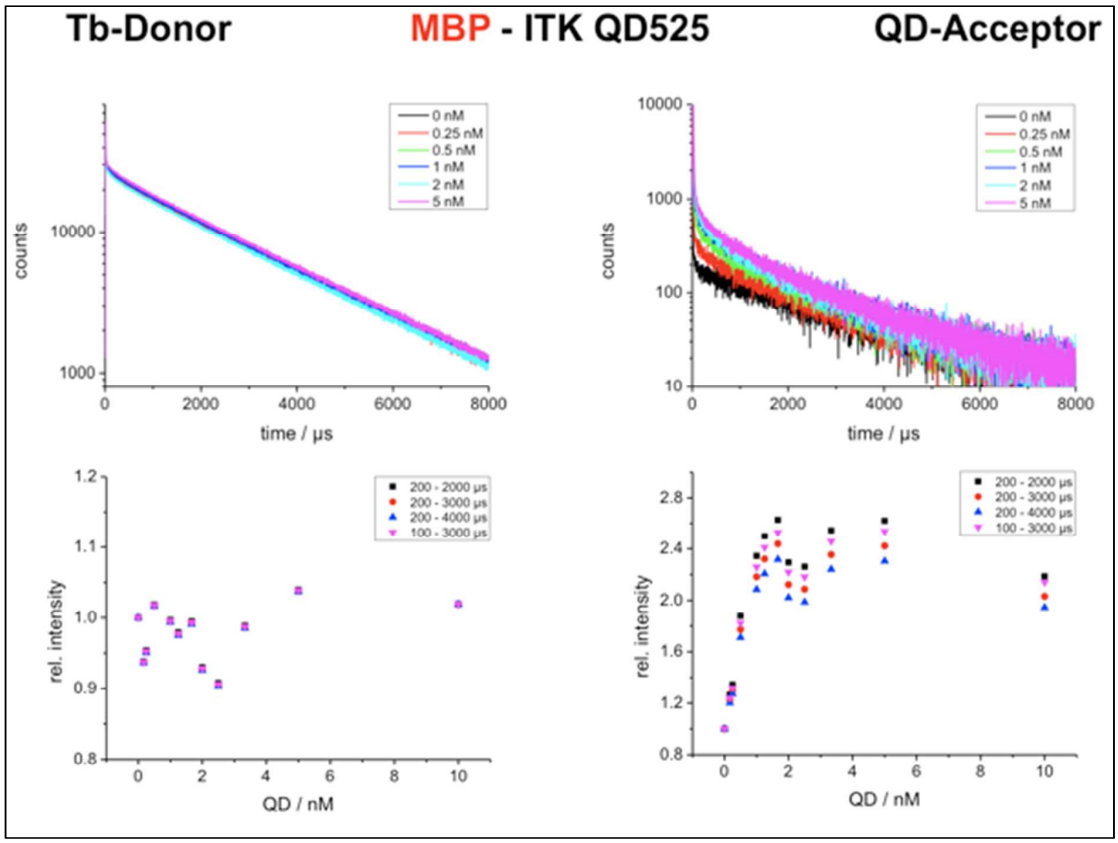
Tb-Donor
MBP - ITK QD525
QD-Acceptor
0 nM
0.25 nM
0.5 nM
1 nM
2 nM
5 nM
counts
time / µs
200 - 2000 µs
200 - 3000 µs
200 - 4000 µs
100 - 3000 µs
rel. intensity
QD / nM

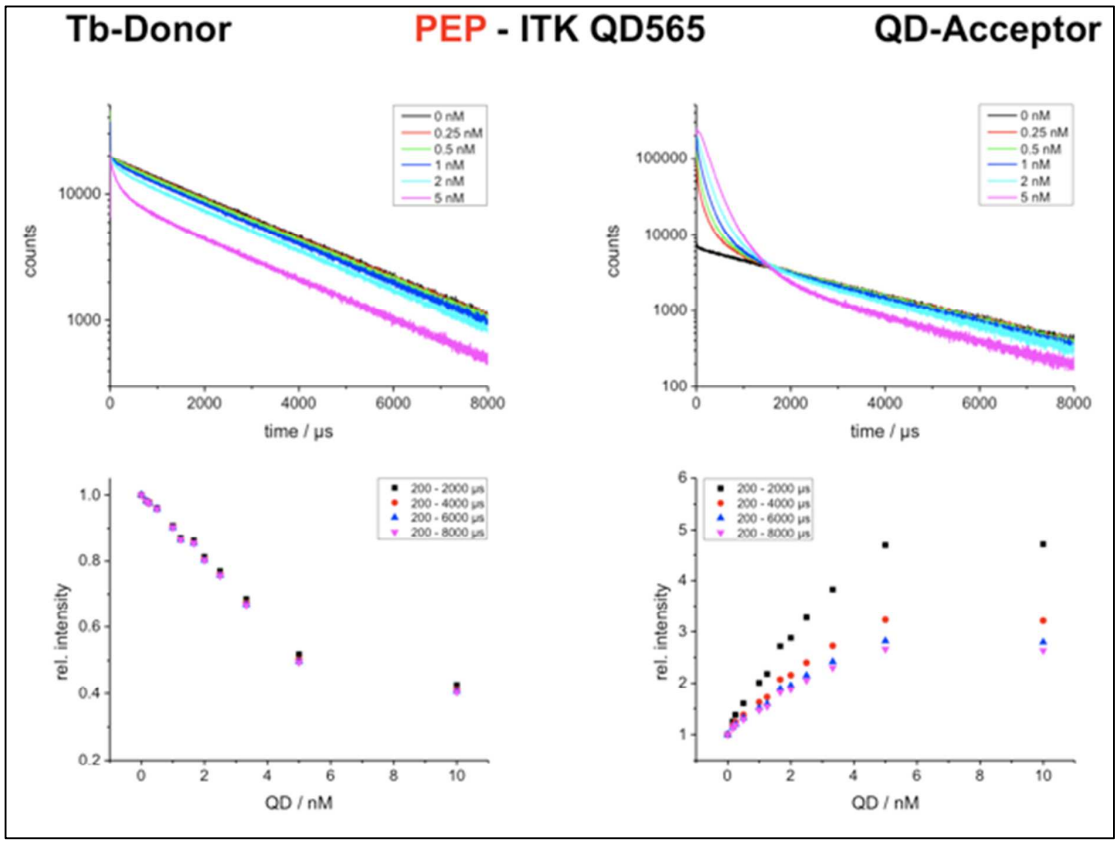
Tb-Donor
PEP - ITK QD565
QD-Acceptor
0 nM
0.25 nM
0.5 nM
1 nM
2 nM
5 nM
counts
time / µs
200 - 2000 µs
200 - 4000 µs
200 - 6000 µs
200 - 8000 µs
rel. intensity
QD / nM

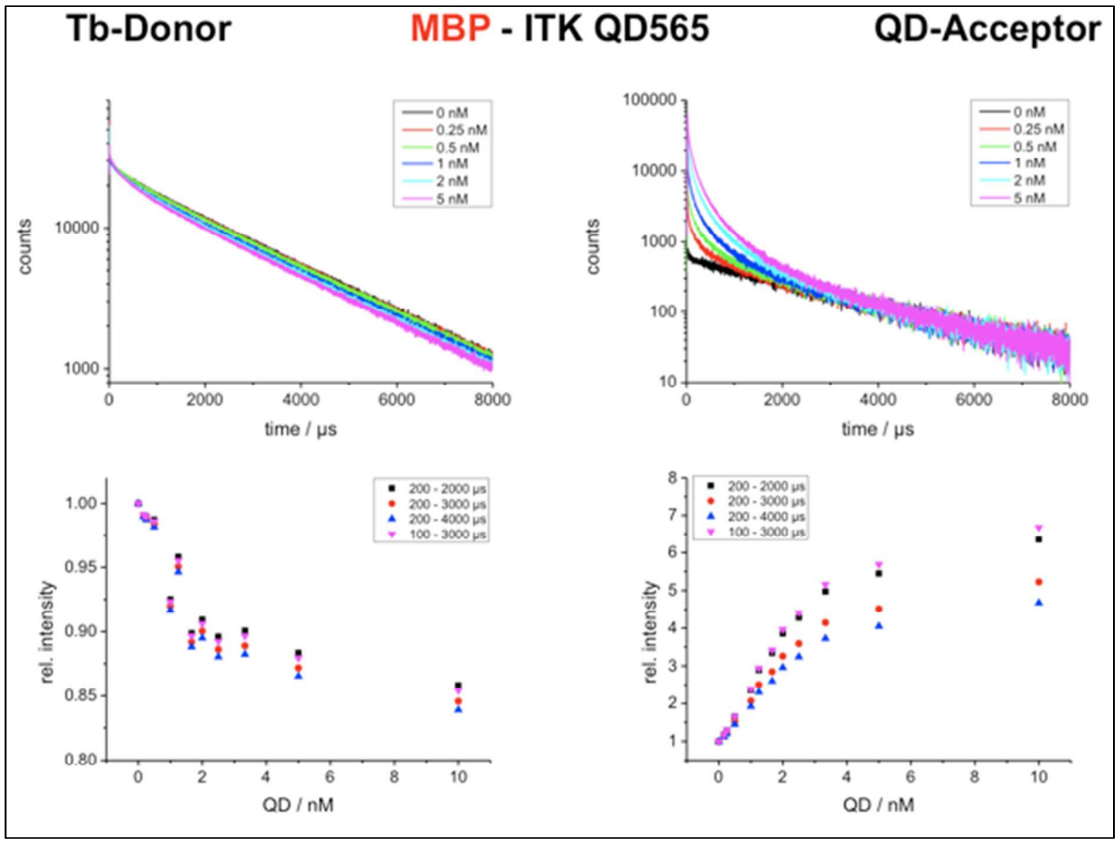
Tb-Donor
MBP - ITK QD565
QD-Acceptor
0 nM
0.25 nM
0.5 nM
1 nM
2 nM
5 nM
counts
time / µs
200 - 2000 µs
200 - 3000 µs
200 - 4000 µs
100 - 3000 µs
rel. intensity
QD / nM

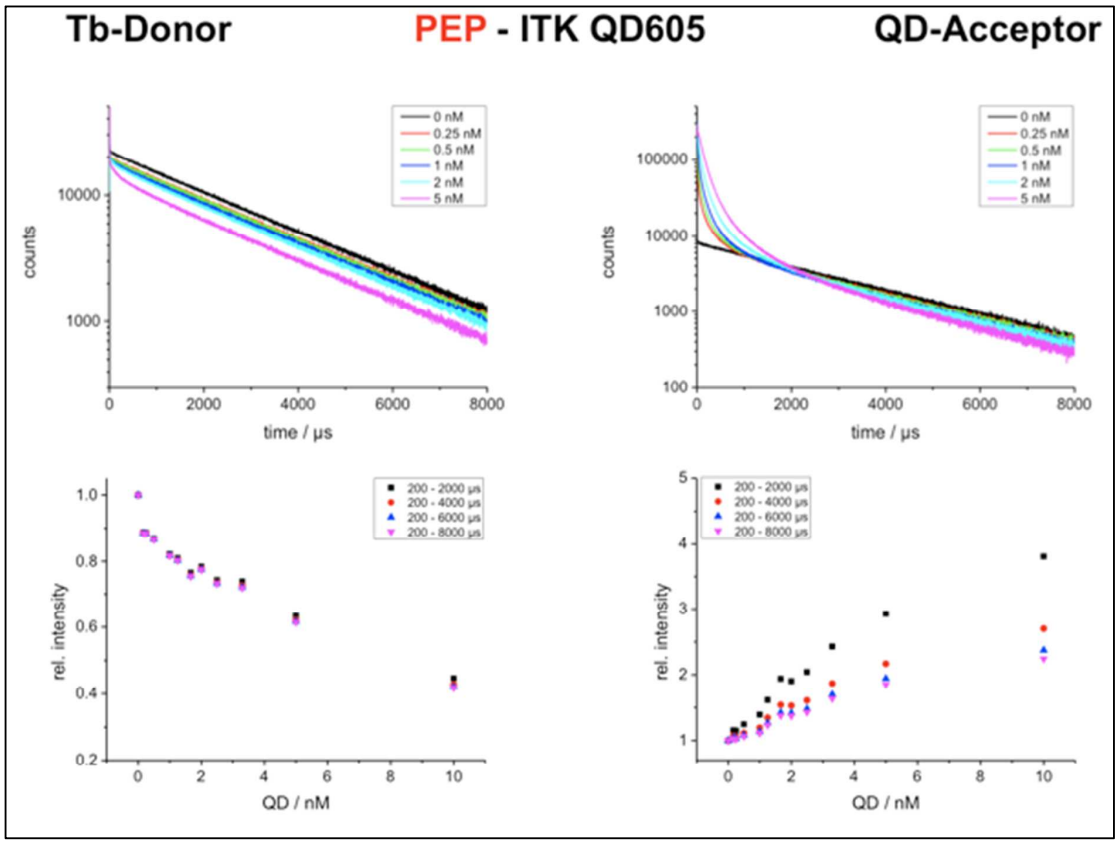
Tb-Donor
PEP - ITK QD605
QD-Acceptor
counts
time / µs
0 nM
0.25 nM
0.5 nM
1 nM
2 nM
5 nM
rel. intensity
QD / nM
200 - 2000 µs
200 - 4000 µs
200 - 6000 µs
200 - 8000 µs

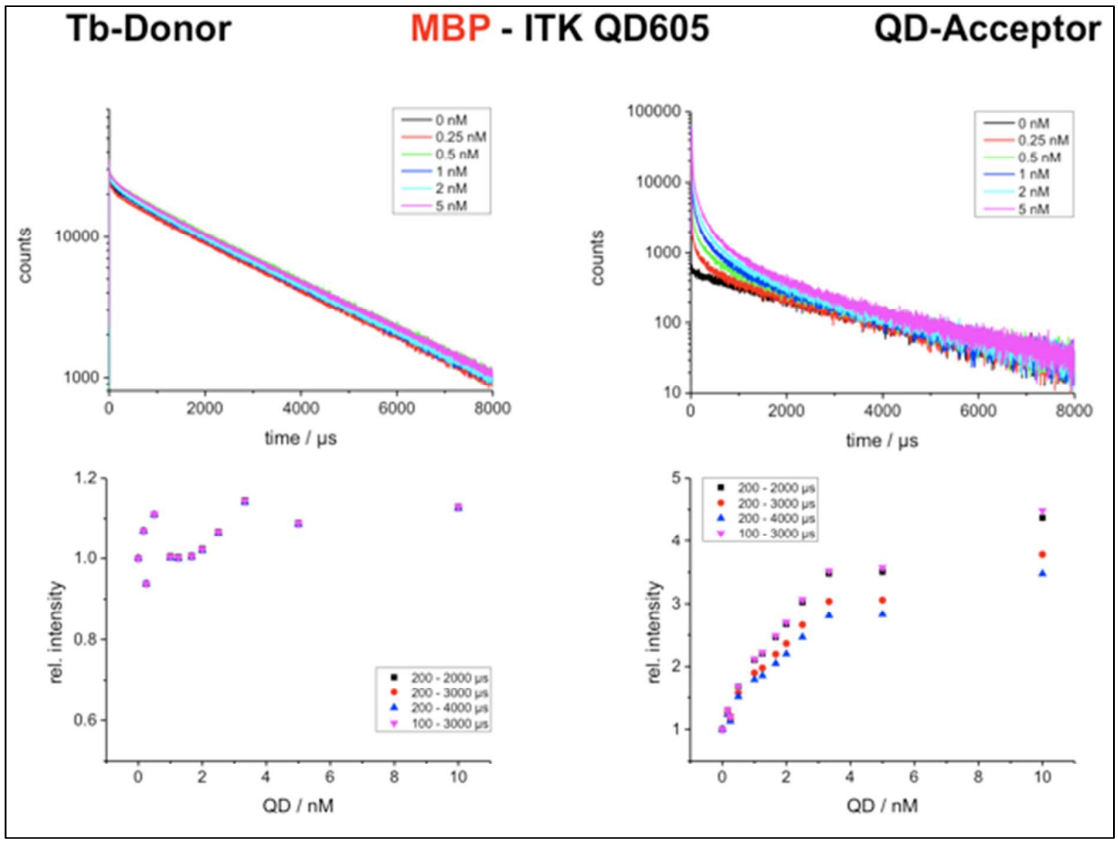
Tb-Donor
MBP - ITK QD605
QD-Acceptor
counts
time / µs
0 nM
0.25 nM
0.5 nM
1 nM
2 nM
5 nM
rel. intensity
QD / nM
200 - 2000 µs
200 - 3000 µs
200 - 4000 µs
100 - 3000 µs

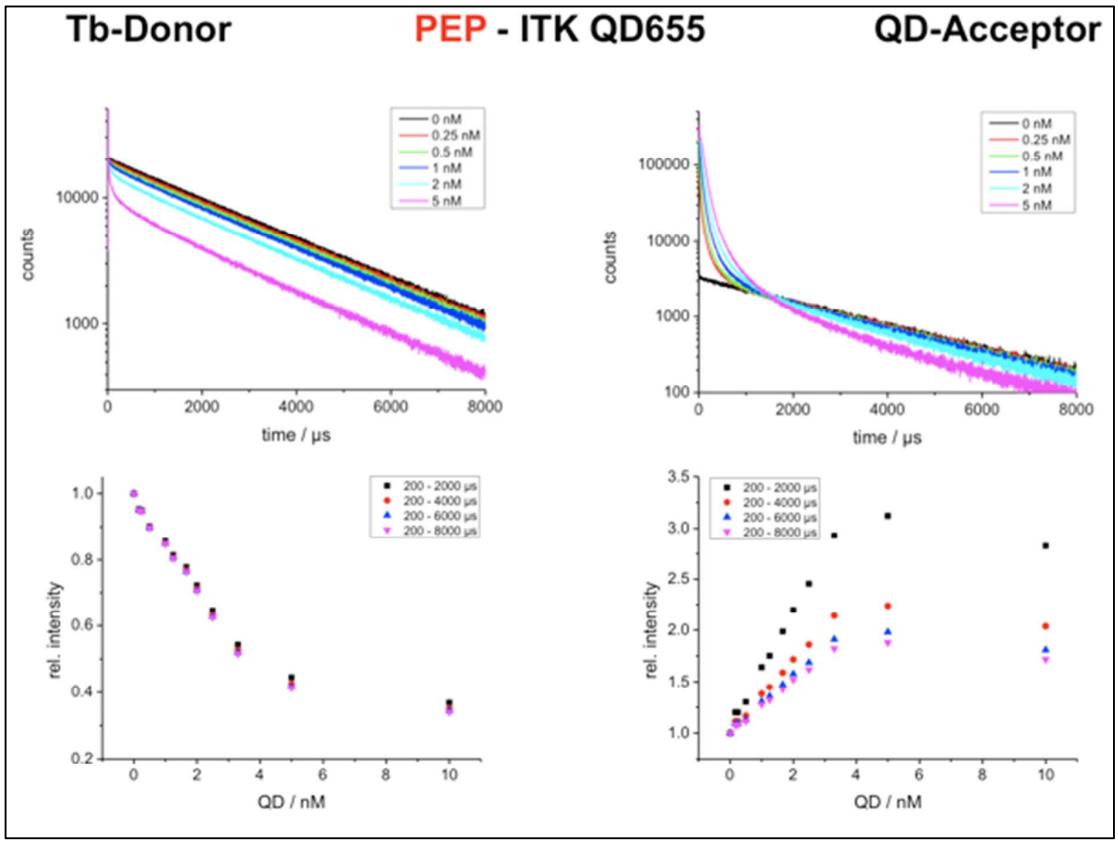
Tb-Donor
PEP - ITK QD655
QD-Acceptor
0 nM
0.25 nM
0.5 nM
1 nM
2 nM
5 nM
counts
time / µs
200 - 2000 µs
200 - 4000 µs
200 - 6000 µs
200 - 8000 µs
rel. intensity
QD / nM

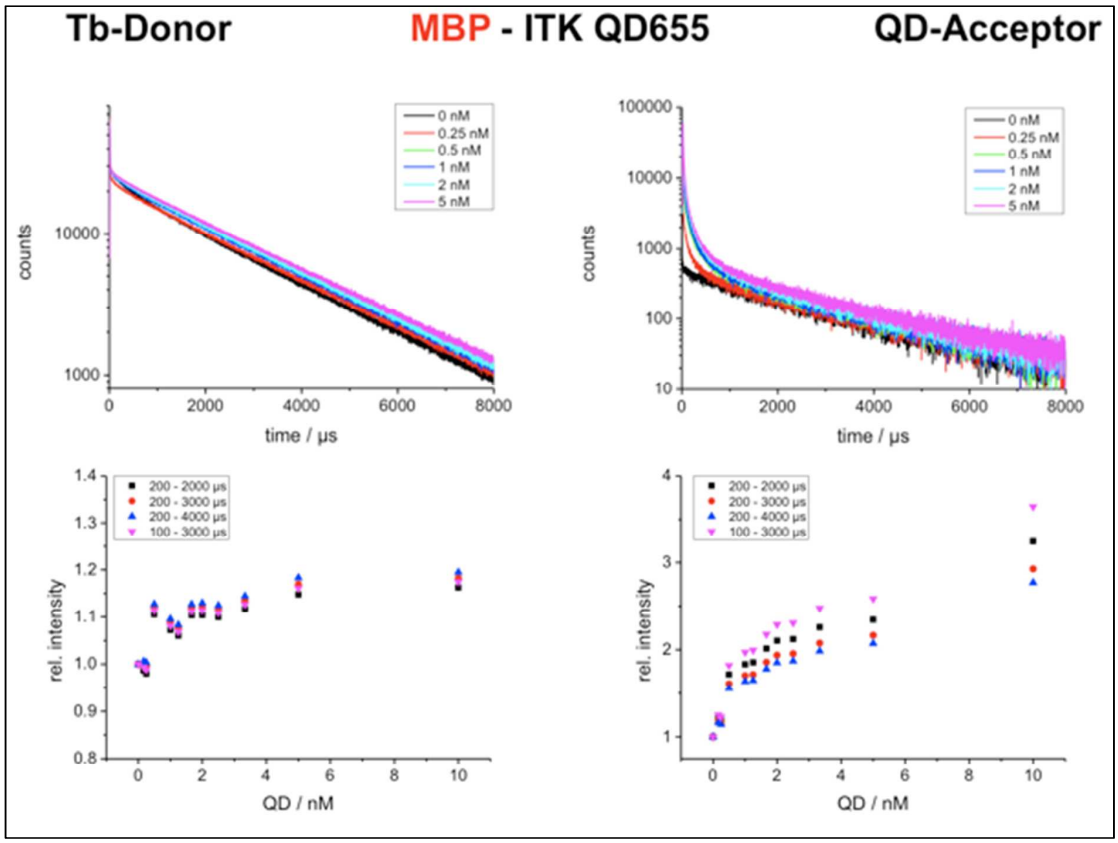
Tb-Donor
MBP - ITK QD655
QD-Acceptor
0 nM
0.25 nM
0.5 nM
1 nM
2 nM
5 nM
counts
time / µs
200 - 2000 µs
200 - 3000 µs
200 - 4000 µs
100 - 3000 µs
rel. intensity
QD / nM

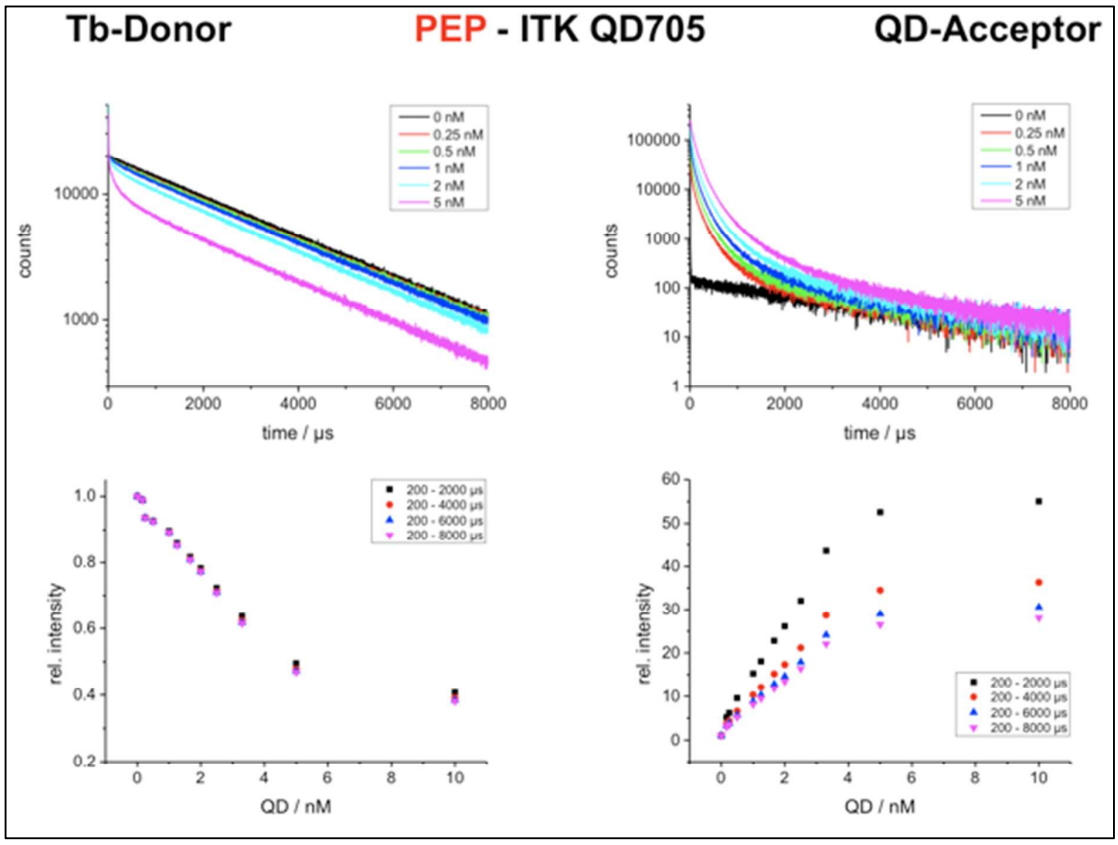
Tb-Donor
PEP - ITK QD705
QD-Acceptor
counts
time / µs
0 nM
0.25 nM
0.5 nM
1 nM
2 nM
5 nM
rel. intensity
QD / nM
200 - 2000 µs
200 - 4000 µs
200 - 6000 µs
200 - 8000 µs

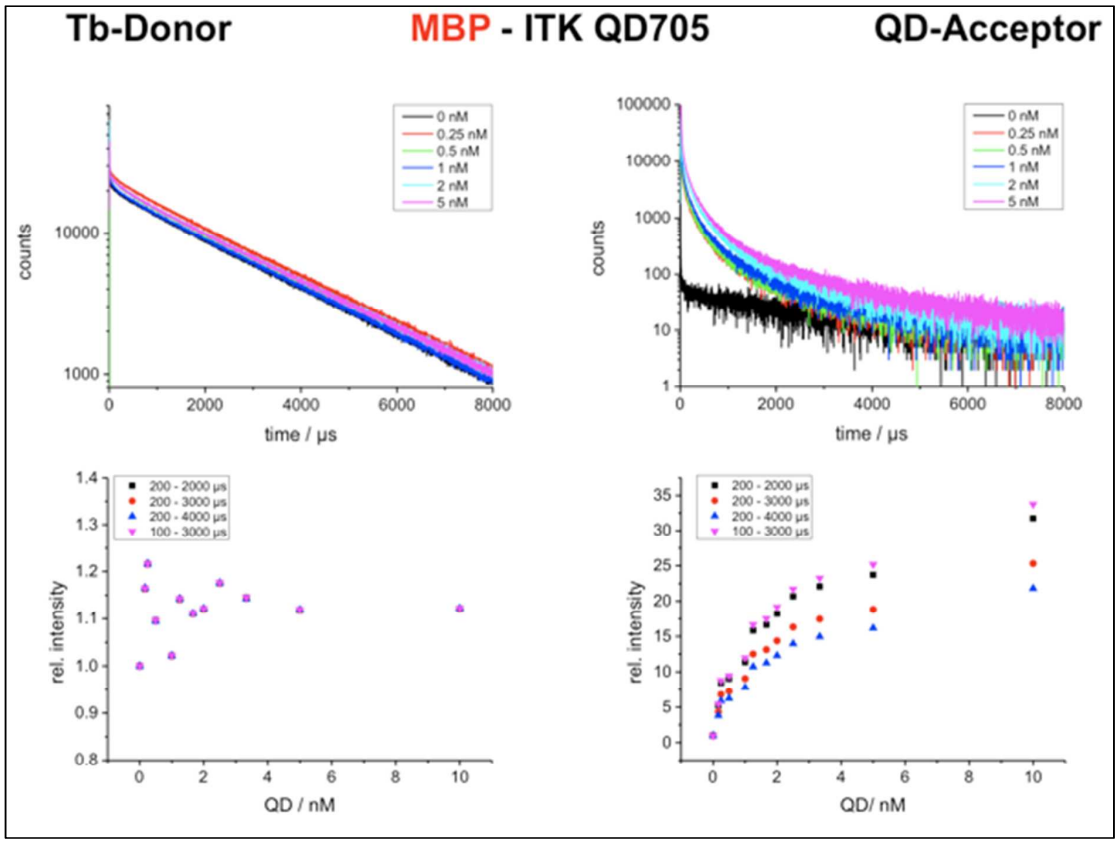
Tb-Donor
MBP - ITK QD705
QD-Acceptor
counts
time / µs
0 nM
0.25 nM
0.5 nM
1 nM
2 nM
5 nM
rel. intensity
QD / nM
QD/ nM
200 - 2000 µs
200 - 3000 µs
200 - 4000 µs
100 - 3000 µs

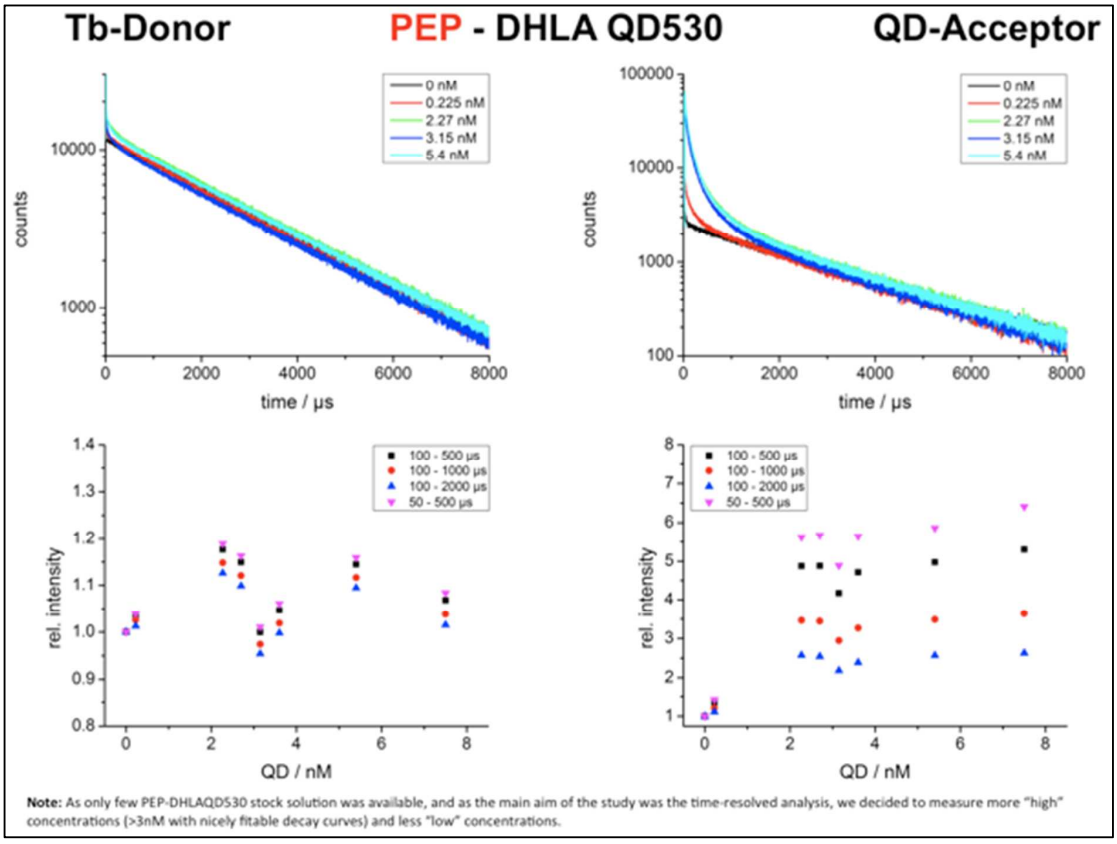

Note: As only few PEP-DHLAQD530 stock solution was available, and as the main aim of the study was the time-resolved analysis, we decided to measure more "high" concentrations (>3nM with nicely fitable decay curves) and less "low" concentrations.

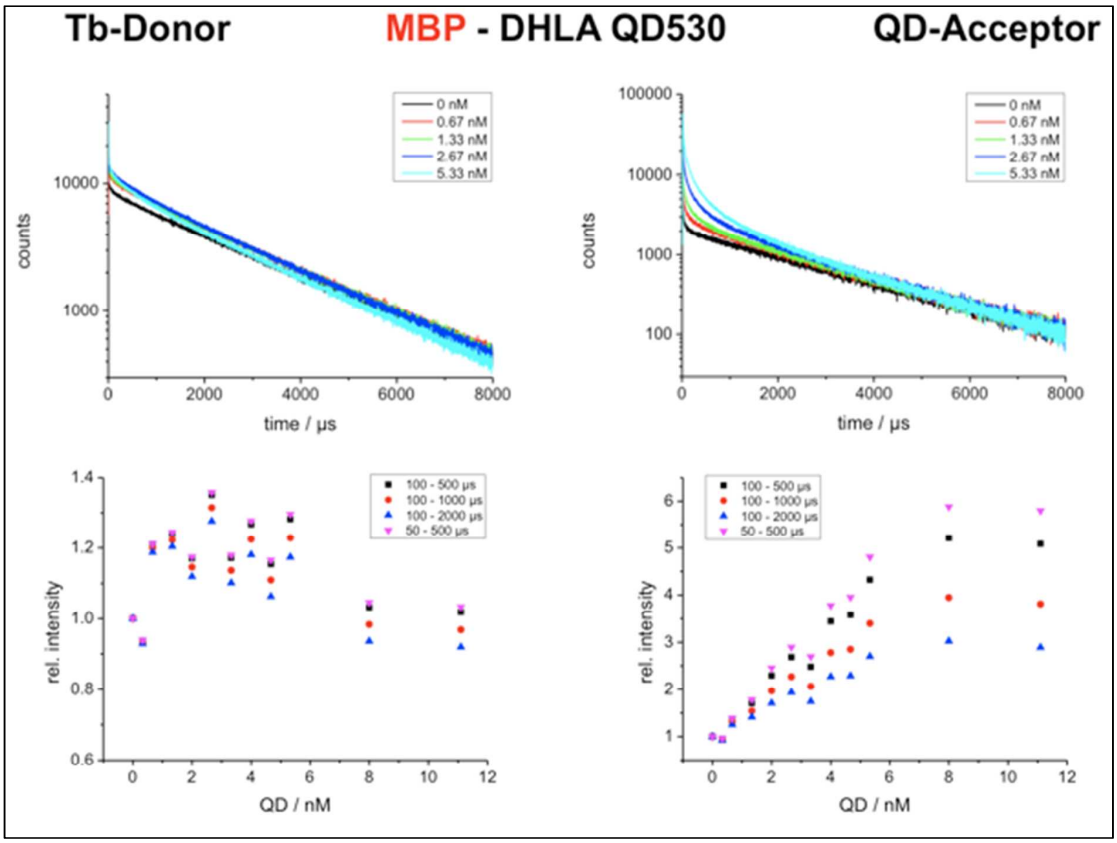

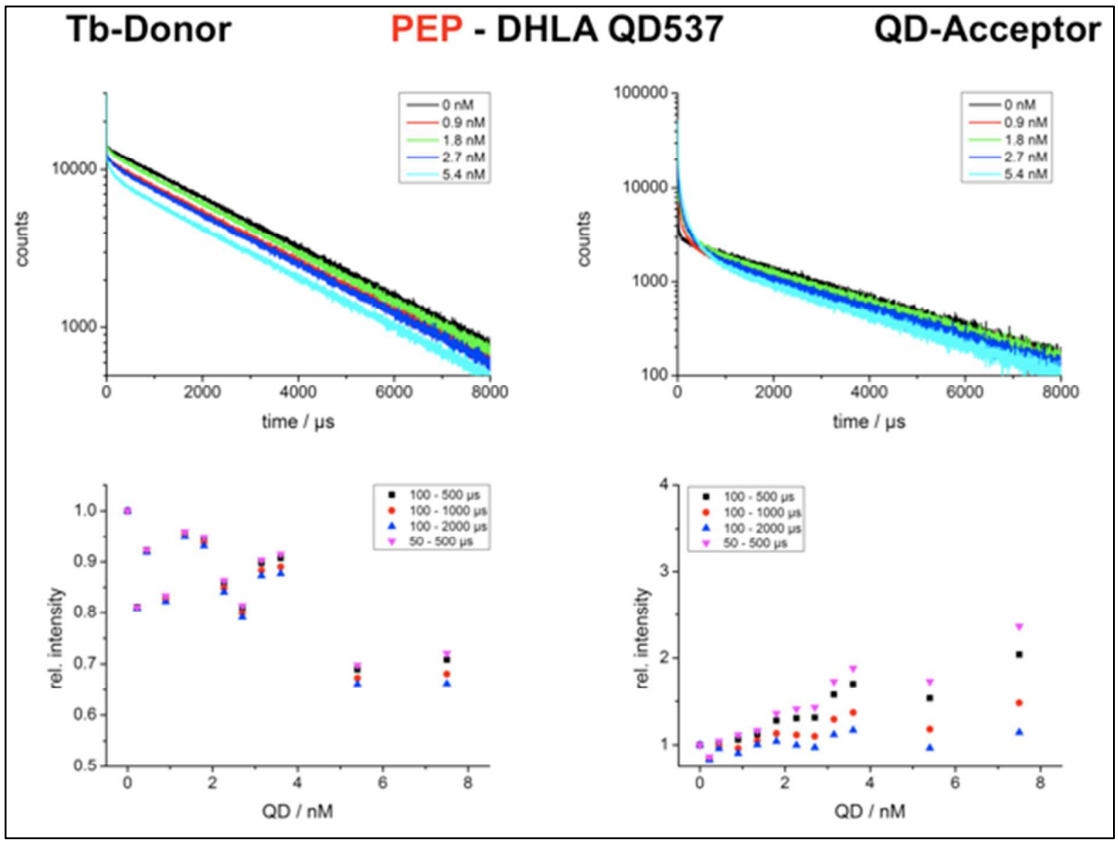
Tb-Donor
PEP - DHLA QD537
QD-Acceptor
counts
time / µs
0 nM
0.9 nM
1.8 nM
2.7 nM
5.4 nM
rel. intensity
QD / nM
100 - 500 µs
100 - 1000 µs
100 - 2000 µs
50 - 500 µs

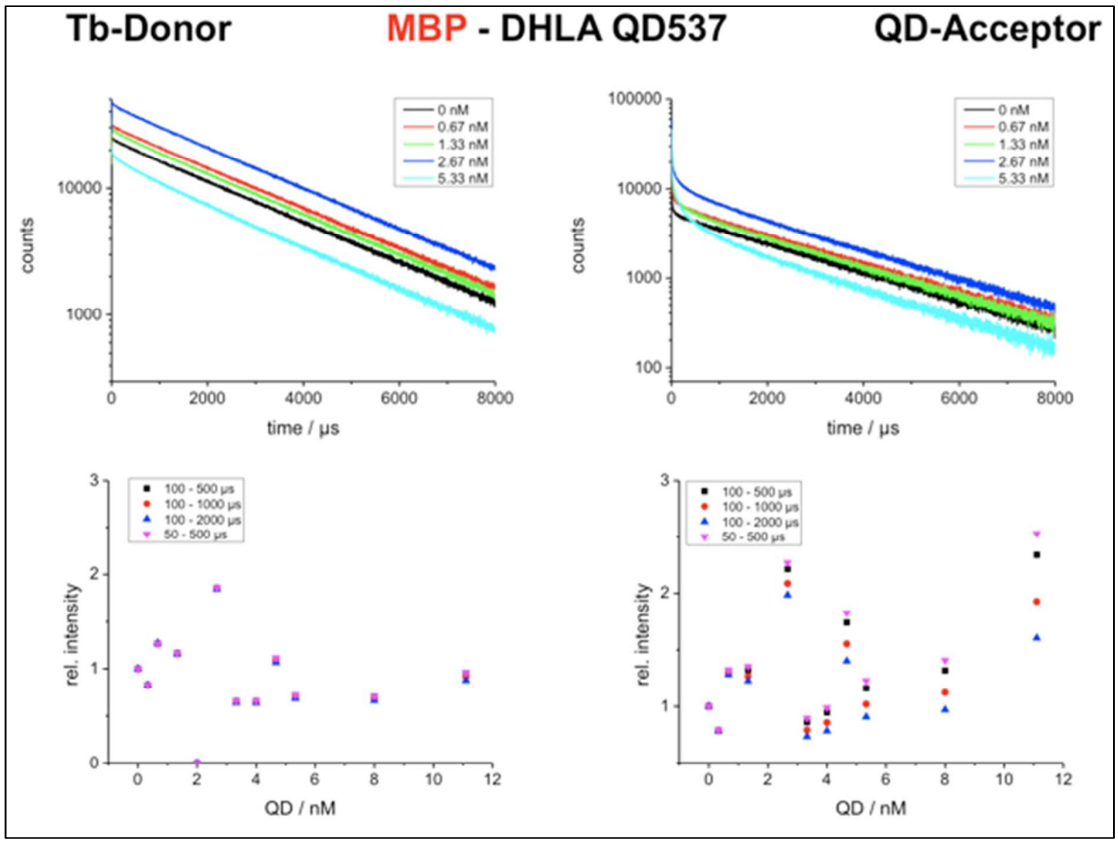
Tb-Donor
MBP - DHLA QD537
QD-Acceptor
counts
time / µs
0 nM
0.67 nM
1.33 nM
2.67 nM
5.33 nM
rel. intensity
QD / nM
100 - 500 µs
100 - 1000 µs
100 - 2000 µs
50 - 500 µs

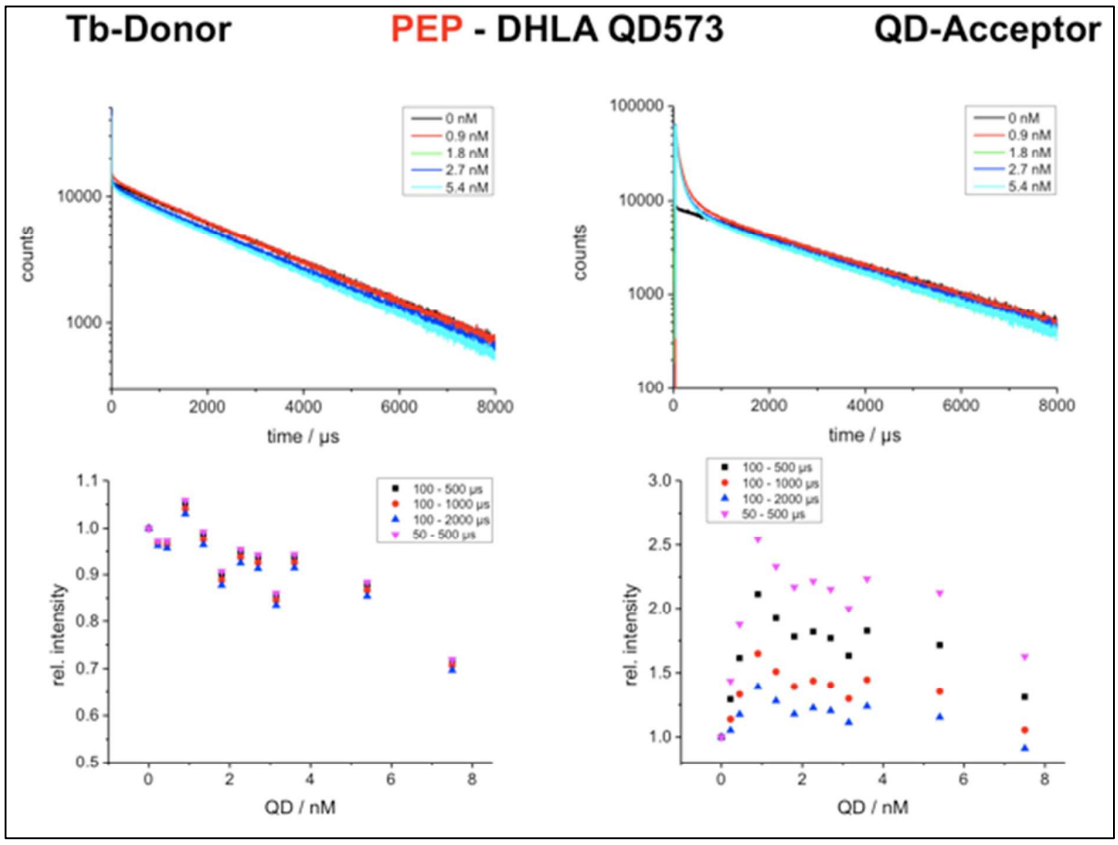
Tb-Donor
PEP - DHLA QD573
QD-Acceptor
0 nM
0.9 nM
1.8 nM
2.7 nM
5.4 nM
counts
time / µs
100 - 500 µs
100 - 1000 µs
100 - 2000 µs
50 - 500 µs
rel. intensity
QD / nM

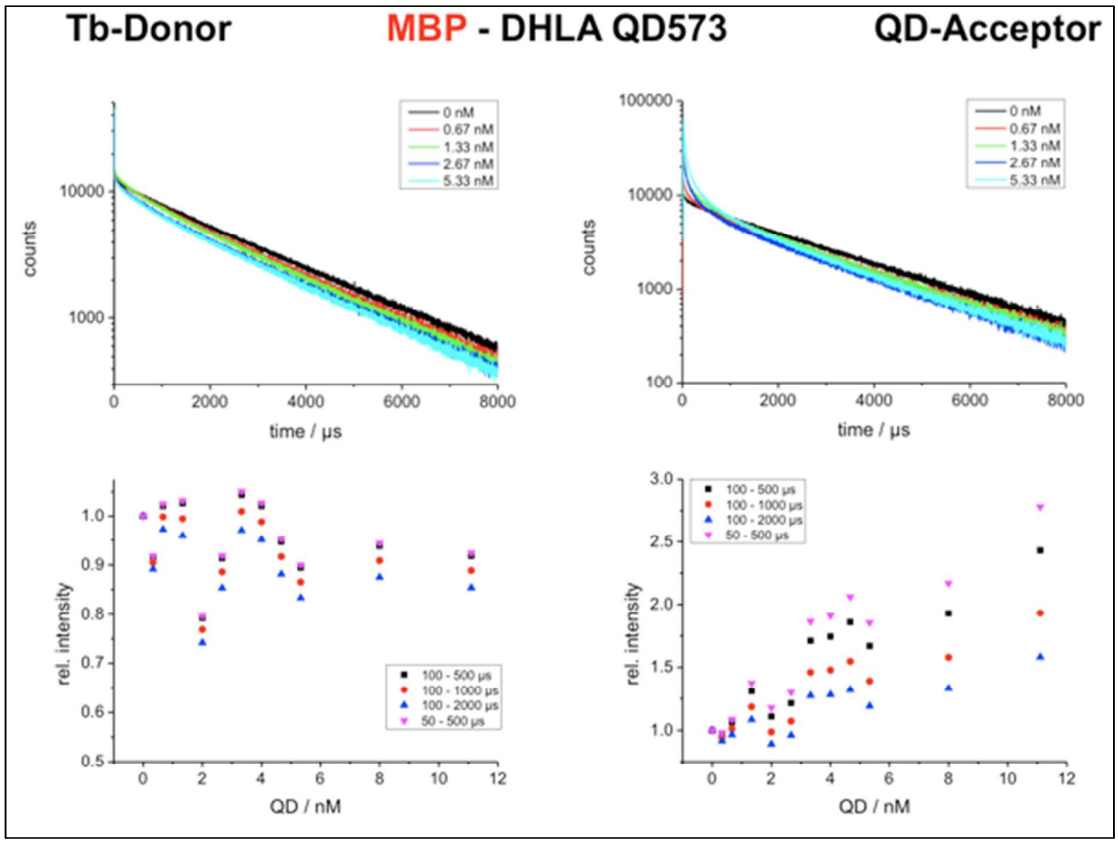
Tb-Donor
MBP - DHLA QD573
QD-Acceptor
0 nM
0.67 nM
1.33 nM
2.67 nM
5.33 nM
counts
time / µs
100 - 500 µs
100 - 1000 µs
100 - 2000 µs
50 - 500 µs
rel. intensity
QD / nM

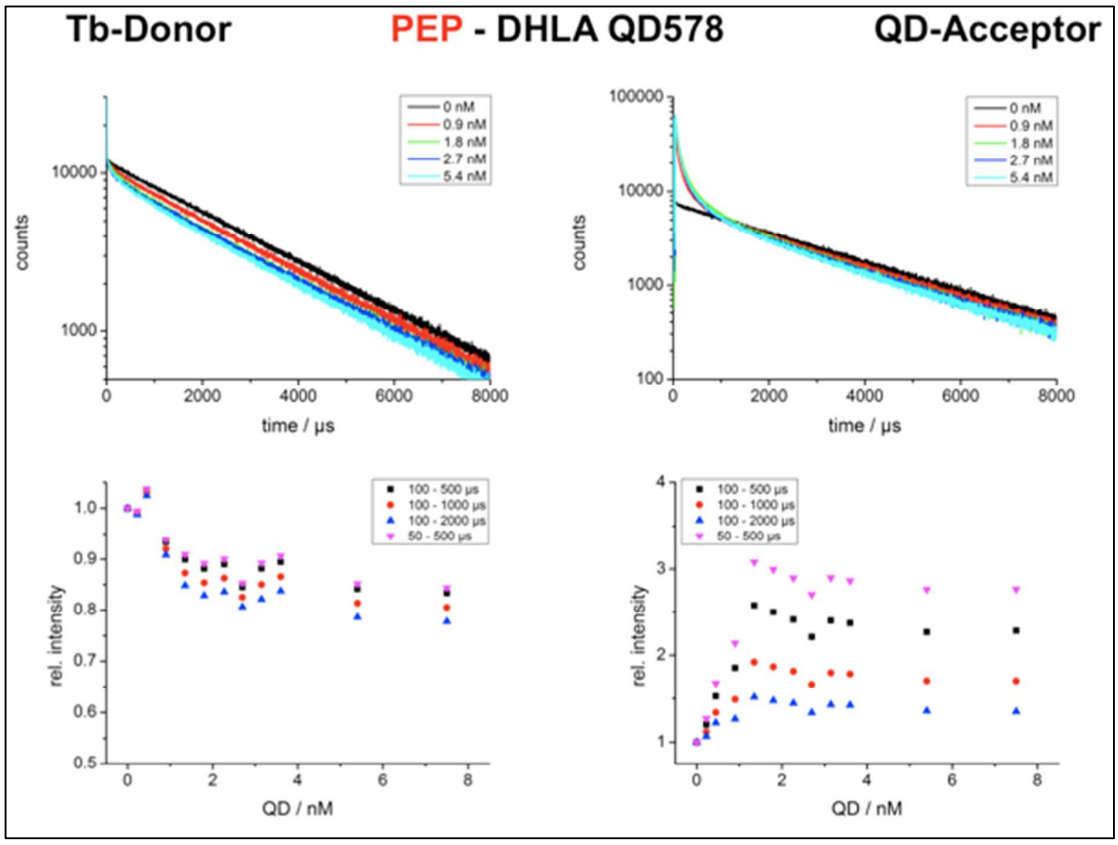
Tb-Donor
PEP - DHLA QD578
QD-Acceptor
counts
time / µs
0 nM
0.9 nM
1.8 nM
2.7 nM
5.4 nM
rel. intensity
QD / nM
100 - 500 µs
100 - 1000 µs
100 - 2000 µs
50 - 500 µs

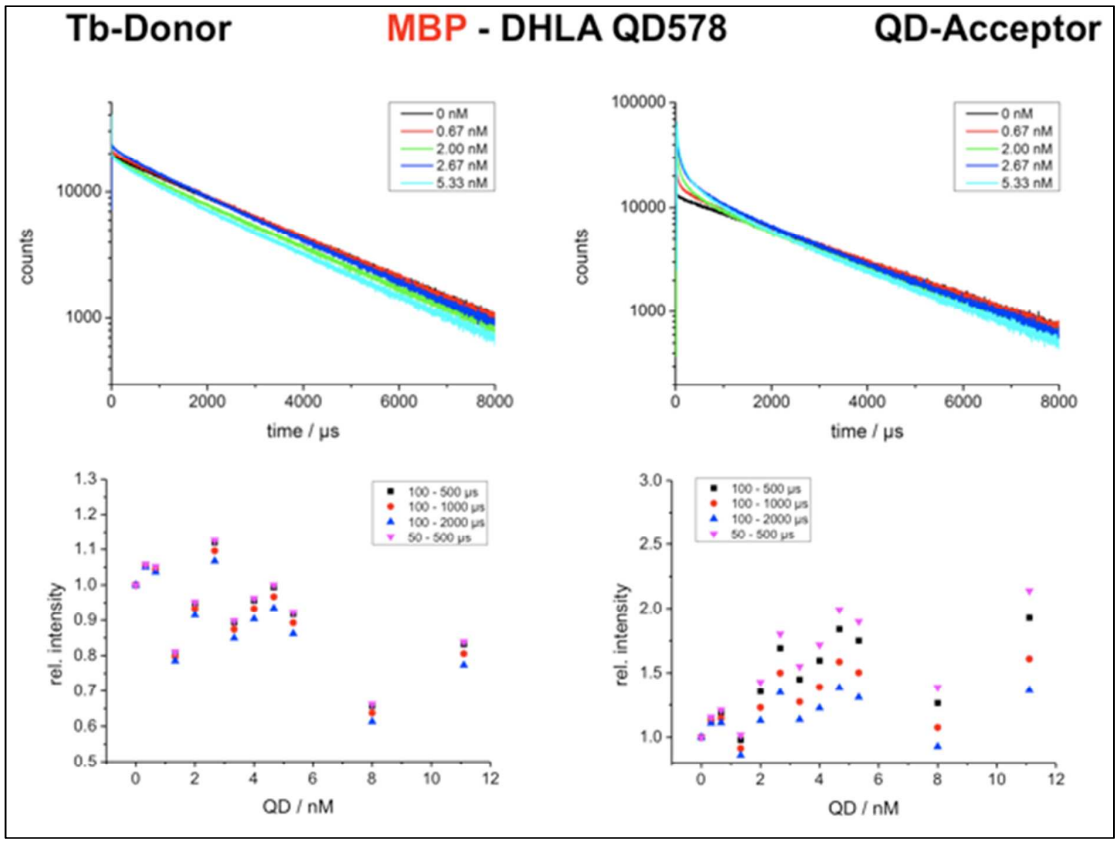
Tb-Donor
MBP - DHLA QD578
QD-Acceptor
counts
time / µs
0 nM
0.67 nM
2.00 nM
2.67 nM
5.33 nM
rel. intensity
QD / nM
100 - 500 µs
100 - 1000 µs
100 - 2000 µs
50 - 500 µs

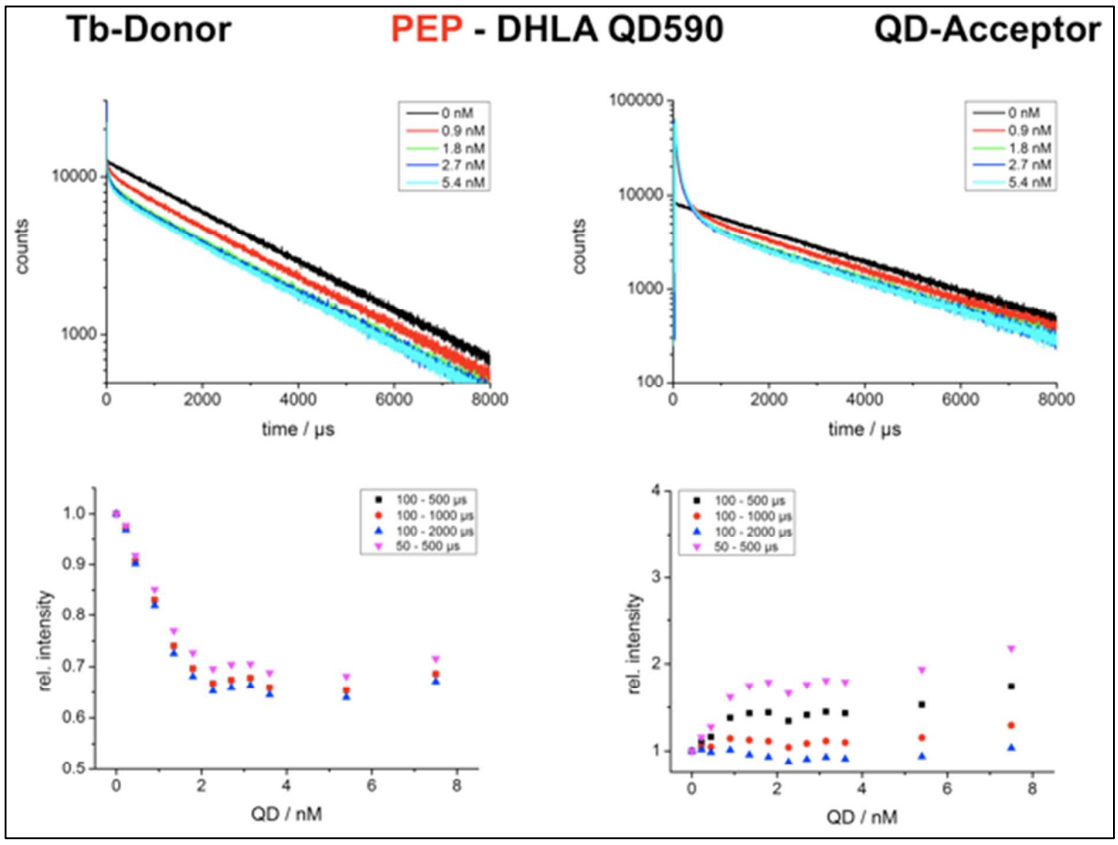
Tb-Donor
PEP - DHLA QD590
QD-Acceptor
counts
time / µs
0 nM
0.9 nM
1.8 nM
2.7 nM
5.4 nM
rel. intensity
QD / nM
100 - 500 µs
100 - 1000 µs
100 - 2000 µs
50 - 500 µs

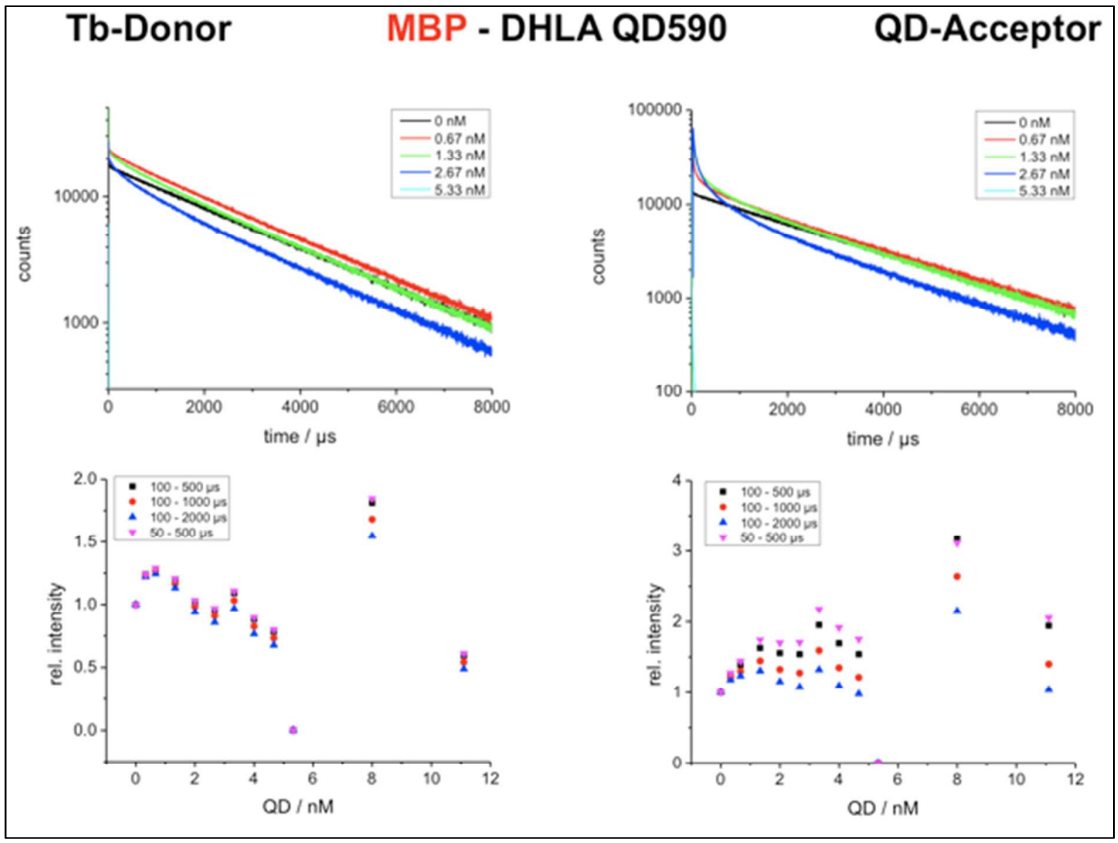
Tb-Donor
MBP - DHLA QD590
QD-Acceptor
counts
time / µs
0 nM
0.67 nM
1.33 nM
2.67 nM
5.33 nM
rel. intensity
QD / nM
100 - 500 µs
100 - 1000 µs
100 - 2000 µs
50 - 500 µs

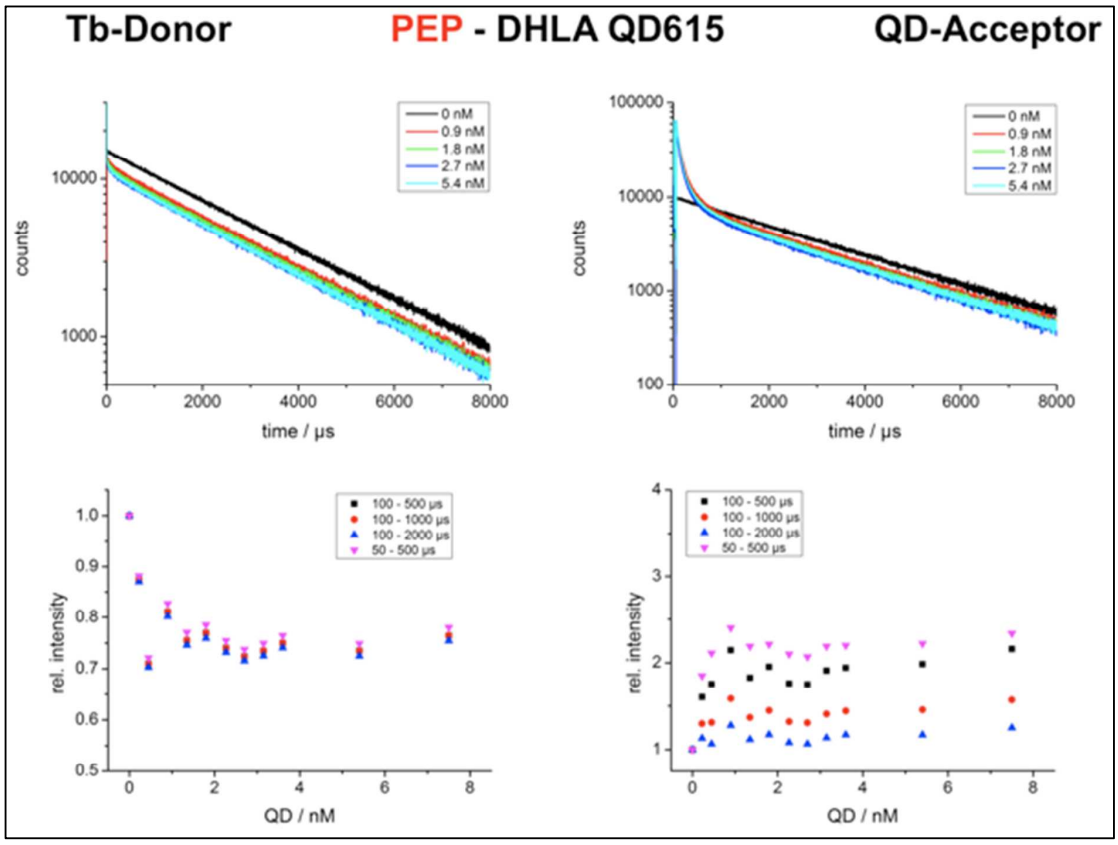
Tb-Donor
PEP - DHLA QD615
QD-Acceptor
counts
time / µs
0 nM
0.9 nM
1.8 nM
2.7 nM
5.4 nM
rel. intensity
QD / nM
100 - 500 µs
100 - 1000 µs
100 - 2000 µs
50 - 500 µs

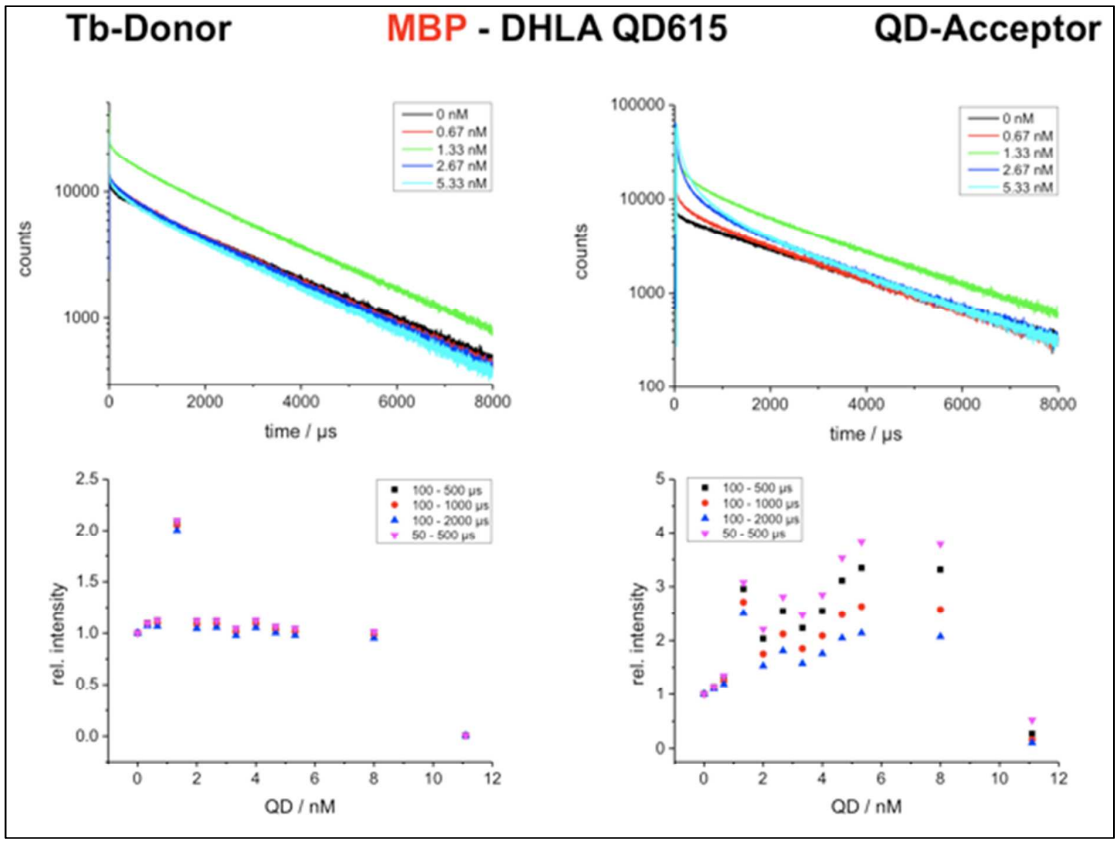
Tb-Donor
MBP - DHLA QD615
QD-Acceptor
counts
time / µs
0 nM
0.67 nM
1.33 nM
2.67 nM
5.33 nM
rel. intensity
QD / nM
100 - 500 µs
100 - 1000 µs
100 - 2000 µs
50 - 500 µs

Bibliography

[1] B. W. Van der Meer, G. Coker, and S.-Y. S. Chen. *Resonance Energy Transfer: Theory and Data*. Wiley-VCH Verlag GmbH, Weinheim, 1994.

[2] B. Valeur. *Molecular Fluorescence: Principles and Applications*. Wiley-VCH Verlag GmbH, Weinheim, 2002.

[3] J. R. Lakowicz. *Principles of fluorescence spectroscopy*. Springer, New York, 3rd edition, 2006.

[4] T. Förster. Zwischenmolekulare Energiewanderung und Fluoreszenz. *Annalen der Physik*, 2:55–75, 1948.

[5] H. Sahoo. Förster resonance energy transfer – A spectroscopic nanoruler: Principle and applications. *Journal of Photochemistry and Photobiology C: Photochemistry Reviews*, 12:20–30, 2011.

[6] F. Morgner, D. Geißler, S. Stufler, N. G. Butlin, H.-G. Löhmannsröben, and N. Hildebrandt. A Quantum-Dot-Based Molecular Ruler for Multiplexed Optical Analysis. *Angewandte Chemie International Edition*, 49:7570–7574, 2010.

[7] D. Geißler, L. J. Charbonnière, R. F. Ziessel, N. G. Butlin, H.-G. Löhmannsröben, and N. Hildebrandt. Quantum Dot Biosensors for Ultrasensitive Multiplexed Diagnostics. *Angewandte Chemie International Edition*, 49:1396–1401, 2010.

[8] N. Hildebrandt. How to Apply FRET: From Experimental Design to Data Analysis. In *FRET - Förster Resonance Energy Transfer From Theory to Applications*, pages 105–156. Wiley-VCH Verlag GmbH, Weinheim, 2014.

[9] F. S. Richardson. Terbium(III) and europium(III) ions as luminescent probes and stains for biomolecular systems. *Chemical Reviews*, 82:541–552, 1982.

[10] J.-C. G. Bünzli. Lanthanide Luminescence for Biomedical Analyses and Imaging. *Chemical Reviews*, 110:2729–2755, 2010.

[11] E. G. Moore, A. P. S. Samuel, and K. N. Raymond. From Antenna to Assay: Lessons Learned in Lanthanide Luminescence. *Accounts of Chemical Research*, 42:542–552, 2009.

[12] J.-C. G. Bünzli, A.-S. Chauvin, H. K. Kim, E. Deiters, and S. V. Eliseeva. Lanthanide luminescence efficiency in eight- and nine-coordinate complexes: Role of the radiative lifetime. *Coordination Chemistry Reviews*, 254:2623–2633, 2010.

[13] M. Starck, P. Kadjane, E. Bois, B. Darbouret, A. Incamps, R. Ziessel, and L. J. Charbonnière. Towards Libraries of Luminescent Lanthanide Complexes and Labels from Generic Synthons. *Chemistry - A European Journal*, 17:9164–9179, 2011.

[14] E. P. Diamandis. Immunoassays with time-resolved fluorescence spectroscopy: Principles and applications. *Clinical Biochemistry*, 21:139–150, 1988.

[15] A. K. Hagan and T. Zuchner. Lanthanide-based time-resolved luminescence immunoassays. *Analytical and Bioanalytical Chemistry*, 400:2847–2864, 2011.

[16] K. R. Kupcho, D. K. Stafslien, T. DeRosier, T. M. Hallis, M. S. Ozers, and K. W. Vogel. Simultaneous Monitoring of Discrete Binding Events Using Dual-Acceptor Terbium-Based LRET. *Journal of the American Chemical Society*, 129:13372–13373, 2007.

[17] T. Kokko, T. Liljenbäck, M. T. Peltola, L. Kokko, and T. Soukka. Homogeneous Dual-Parameter Assay for Prostate-Specific Antigen Based on Fluorescence Resonance Energy Transfer. *Analytical Chemistry*, 80:9763–9768, 2008.

[18] T. Kokko, L. Kokko, and T. Soukka. Terbium(III) Chelate as an Efficient Donor for Multiple-Wavelength Fluorescent Acceptors. *Journal of Fluorescence*, 19:159–164, 2009.

[19] D. Geißler, S. Stufler, H.-G. Löhmannsröben, and N. Hildebrandt. Six-Color Time-Resolved Förster Resonance Energy Transfer for Ultrasensitive Multiplexed Biosensing. *Journal of the American Chemical Society*, 135:1102–1109, 2013.

[20] U. Resch-Genger, M. Grabolle, S. Cavaliere-Jaricot, R. Nitschke, and T. Nann. Quantum dots versus organic dyes as fluorescent labels. *Nature Methods*, 5:763–775, 2008.

[21] A. P. Alivisatos. Semiconductor Clusters, Nanocrystals, and Quantum Dots. *Science*, 271:933–937, 1996.

[22] C. J. Murphy and J. L. Coffer. Quantum Dots: A Primer. *Applied Spectroscopy*, 56:16–27, 2002.

[23] W. J. Parak, D. Gerion, T. Pellegrino, D. Zanchet, C. Micheel, S. C. Williams, R. Boudreau, M. A. L. Gros, C. A. Larabell, and A. P. Alivisatos. Biological applications of colloidal nanocrystals. *Nanotechnology*, 14:R15–R27, 2003.

[24] V. Biju, T. Itoh, and M. Ishikawa. Delivering quantum dots to cells: bioconjugated quantum dots for targeted and nonspecific extracellular and intracellular imaging. *Chemical Society Reviews*, 39:3031–3056, 2010.

[25] R. A. Sperling and W. J. Parak. Surface modification, functionalization and bioconjugation of colloidal inorganic nanoparticles. *Philosophical Transactions of the Royal Society A: Mathematical, Physical and Engineering Sciences*, 368:1333–1383, 2010.

[26] P. Zrazhevskiy, M. Sena, and X. Gao. Designing multifunctional quantum dots for bioimaging, detection, and drug delivery. *Chemical Society Reviews*, 39:4326–4354, 2010.

[27] W. R. Algar, K. Susumu, J. B. Delehanty, and I. L. Medintz. Semiconductor Quantum Dots in Bioanalysis: Crossing the Valley of Death. *Analytical Chemistry*, 83:8826–8837, 2011.

[28] E. Petryayeva, W. R. Algar, and I. L. Medintz. Quantum Dots in Bioanalysis: A Review of Applications Across Various Platforms for Fluorescence Spectroscopy and Imaging. *Applied Spectroscopy*, 67:215–252, 2013.

[29] A. R. Clapp, I. L. Medintz, B. R. Fisher, G. P. Anderson, and H. Mattoussi. Can Luminescent Quantum Dots Be Efficient Energy Acceptors with Organic Dye Donors? *Journal of the American Chemical Society*, 127:1242–1250, 2005.

[30] D. Geißler, S. Lindén, K. Liermann, K. D. Wegner, L. J. Charbonnière, and N. Hildebrandt. Lanthanides and Quantum Dots as Förster Resonance Energy Transfer Agents for Diagnostics and Cellular Imaging. *Inorganic Chemistry*, 53:1824–1838, 2014.

[31] N. Hildebrandt, K. D. Wegner, and W. R. Algar. Luminescent terbium complexes: Superior Förster resonance energy transfer donors for flexible and sensitive multiplexed biosensing. *Coordination Chemistry Reviews*, 273-274:125–138, 2014.

[32] W. R. Algar, D. Wegner, A. L. Huston, J. B. Blanco-Canosa, M. H. Stewart, A. Armstrong, P. E. Dawson, N. Hildebrandt, and I. L. Medintz. Quantum Dots as Simultaneous Acceptors and Donors in Time-Gated Förster Resonance Energy Transfer Relays: Characterization and Biosensing. *Journal of the American Chemical Society*, 134:1876–1891, 2012.

[33] D. Wild. *The immunoassay handbook: theory and applications of ligand binding, ELISA, and related techniques*. Elsevier, Oxford ; Waltham, MA, 4th edition, 2013.

[34] J. Szöllosi, S. Damjanovich, and L. Mátyus. Application of fluorescence resonance energy transfer in the clinical laboratory: routine and research. *Cytometry*, 34:159–179, 1998.

[35] G. Mathis. Rare earth cryptates and homogeneous fluoroimmunoassays with human sera. *Clinical Chemistry*, 39:1953–1959, 1993.

[36] G. Mathis. Probing molecular interactions with homogeneous techniques based on rare earth cryptates and fluorescence energy transfer. *Clinical Chemistry*, 41:1391–1397, 1995.

[37] G. Mathis. HTRF(R) Technology. *Journal of Biomolecular Screening*, 4:309–313, 1999.

[38] K. Blomberg, P. Hurskainen, and I. Hemmilä. Terbium and rhodamine as labels in a homogeneous time-resolved fluorometric energy transfer assay of the beta subunit of human chorionic gonadotropin in serum. *Clinical Chemistry*, 45:855–861, 1999.

[39] G. Wang. Homogeneous time-resolved fluoroimmunoassay of bensulfuron-methyl by using terbium fluorescence energy transfer. *Talanta*, 55:1119–1125, 2001.

[40] R. C. Roovers, T. Laeremans, L. Huang, S. De Taeye, A. J. Verkleij, H. Revets, H. J. de Haard, and P. M. P. van Bergen en Henegouwen. Efficient inhibition of EGFR signalling and of tumour growth by antagonistic anti-EGFR Nanobodies. *Cancer Immunology, Immunotherapy*, 56:303–317, 2007.

[41] G. P. Anderson, R. D. Bernstein, M. D. Swain, D. Zabetakis, and E. R. Goldman. Binding Kinetics of Antiricin Single Domain Antibodies and Improved Detection Using a B Chain Specific Binder. *Analytical Chemistry*, 82:7202–7207, 2010.

[42] A. de Marco. Biotechnological applications of recombinant single-domain antibody fragments. *Microbial Cell Factories*, 10:44, 2011.

[43] A. Sukhanova, K. Even-Desrumeaux, A. Kisserli, T. Tabary, B. Reveil, J.-M. Millot, P. Chames, D. Baty, M. Artemyev, V. Oleinikov, M. Pluot, J. H.M. Cohen, and I. Nabiev. Oriented conjugates of single-domain antibodies and quantum dots: toward a new generation of ultrasmall diagnostic nanoprobes. *Nanomedicine: Nanotechnology, Biology and Medicine*, 8:516–525, 2012.

[44] L. Stryer and R. P. Haugland. Energy transfer: a spectroscopic ruler. *Proceedings of the National Academy of Sciences*, 58:719–726, 1967.

[45] L. Stryer. Fluorescence Energy Transfer as a Spectroscopic Ruler. *Annual Review of Biochemistry*, 47:819–846, 1978.

[46] B. Schuler, E. A. Lipman, P. J. Steinbach, M. Kumke, and W. A. Eaton. Polyproline and the "spectroscopic ruler" revisited with single-molecule fluorescence. *Proceedings of the National Academy of Sciences*, 102:2754–2759, 2005.

[47] B. Schuler and W. A. Eaton. Protein folding studied by single-molecule FRET. *Current Opinion in Structural Biology*, 18:16–26, 2008.

[48] B. Prevo and E. J. G. Peterman. Förster resonance energy transfer and kinesin motor proteins. *Chemical Society Reviews*, 43:1144–1155, 2014.

[49] R.A. Sperling, T. Liedl, S. Duhr, S. Kudera, M. Zanella, C.-A.J. Lin, W.H. Chang, D. Braun, and W.J. Parak. Size Determination of (Bio)conjugated Water-Soluble Colloidal Nanoparticles: A Comparison of Different Techniques. *Journal of Physical Chemistry C*, 111:11552–11559, 2007.

[50] K. D. Wegner, Z. Jin, S. Lindén, T. L. Jennings, and N. Hildebrandt. Quantum-Dot-Based Förster Resonance Energy Transfer Immunoassay for Sensitive Clinical Diagnostics of Low-Volume Serum Samples. *ACS Nano*, 7:7411–7419, 2013.

[51] K. D. Wegner, S. Lindén, Z. Jin, T. L. Jennings, R. el Khoulati, P. M. P. van Bergen en Henegouwen, and N. Hildebrandt. Nanobodies and Nanocrystals: Highly Sensitive Quantum Dot-Based Homogeneous FRET Immunoassay for Serum-Based EGFR Detection. *Small*, 10:734–740, 2014.

[52] K. D. Wegner, P. T. Lanh, T. Jennings, E. Oh, V. Jain, S. M. Fairclough, J. M. Smith, E. Giovanelli, N. Lequeux, T. Pons, and N. Hildebrandt. Influence of Luminescence Quantum Yield, Surface Coating, and Functionalization of Quantum Dots on the Sensitivity of Time-Resolved FRET Bioassays. *ACS Applied Materials & Interfaces*, 5:2881–2892, 2013.

[53] K. D. Wegner, F. Morgner, E. Oh, R. Goswami, K. Susumu, M. H. Stewart, I. L. Medintz, and N. Hildebrandt. Three-Dimensional Solution-Phase Förster Resonance Energy Transfer Analysis of Nanomolar Quantum Dot Bioconjugates with Subnanometer Resolution. *Chemistry of Materials*, 26:4299–4312, 2014.

[54] L. E. Morrison. Time-resolved detection of energy transfer: Theory and application to immunoassays. *Analytical Biochemistry*, 174:101–120, 1988.

[55] P. R. Selvin. The renaissance of fluorescence resonance energy transfer. *Nature Structural Biology*, 7:730–734, 2000.

[56] E. A. Jares-Erijman and T. M. Jovin. FRET imaging. *Nature Biotechnology*, 21:1387–1395, 2003.

[57] K. E. Sapsford, L. Berti, and I. L. Medintz. Materials for Fluorescence Resonance Energy Transfer Analysis: Beyond Traditional Donor–Acceptor Combinations. *Angewandte Chemie International Edition*, 45:4562–4589, 2006.

[58] I. L Medintz and N. Hildebrandt. *FRET - Förster resonance energy transfer from theory to applications*. Wiley-VCH Verlag GmbH, Weinheim, Germany, 2014.

[59] G. Cario. Über Entstehung wahrer Lichtabsorption und scheinbare Kopplung von Quantensprüngen. *Zeitschrift für Physik*, 10(1):185–199, 1922.

[60] G. Cario and J. Franck. Über Zerlegung von Wasserstoffmolekülen durch angeregte Quecksilberatome. *Zeitschrift für Physik*, 11:161–166, 1922.

[61] R. M. Clegg. The history of FRET. In C. D. Geddes and J. R. Lakowicz, editors, *Reviews in Fluorescence*, pages 1–45. Springer, Boston, MA, 2006.

[62] J. Franck. Einige aus der Theorie von Klein und Bosseland zu ziehende Folgerungen über Fluoreszenz, photochemische Prozesse und die Elektronenemission glühender Körper. *Zeitschrift für Physik*, 9:259–266, 1922.

[63] H. Kallmann and F. London. Über quantenmeachnische Energieübertragung zwischen atomaren Systemen. Ein Beitrag zum Problem der anomalgrossen Wirkungsquerschnitte. *Zeitschrift für physikalische Chemie*, B2:207–243, 1929.

[64] M. N. Berberan-Santos. Pioneering Contributions of Jean and Francis Perrin to Molecular Luminescence. In B. Valeur and J.-C. Brochon, editors, *New Trends in Fluorescence Spectroscopy. Application to Chemical and Life Sciences*, pages 7–33. Springer-Verlag, Berlin, 2001.

[65] T. Förster. Energiewanderung und Fluoreszenz. *Naturwissenschaften*, 33:166–175, 1946.

[66] B. W. Van der Meer. Förster theory. In I. L. Medintz and N. Hildebrandt, editors, *FRET - Förster resonance energy transfer from theory to applications*, pages 23–59. Wiley-VCH Verlag GmbH, Weinheim, Germany, 2014.

[67] B. W. Van der Meer, D. M. Van der Meer, and S. S. Vogel. Optimizing the orientation factor kappa-squared for more accurate FRET measurements. In I. L. Medintz and N. Hildebrandt, editors, *FRET - Förster resonance energy transfer from theory to applications*, pages 63–103. Wiley-VCH Verlag GmbH, Weinheim, Germany, 2014.

[68] V. Gubala, L. F. Harris, A. J. Ricco, M. X. Tan, and D. E. Williams. Point of Care Diagnostics: Status and Future. *Analytical Chemistry*, 84:487–515, 2012.

[69] S. Spindel, J. Granek, and K. E. Sapsford. In vitro FRET sensing, diagnostics, and personalized medicine. In I. L. Medintz and N. Hildebrandt, editors, *FRET - Förster resonance energy transfer from theory to applications*, pages 269–305. Wiley-VCH Verlag GmbH, Weinheim, Germany, 2014.

[70] S. Hohng, S. Lee, J. Lee, and M. H. Jo. Maximizing information content of single-molecule FRET experiments: multi-color FRET and FRET combined with force or torque. *Chemical Society Reviews*, 43:1007–1013, 2014.

[71] T. Pons. Single-molecule applications. In I. L. Medintz and N. Hildebrandt, editors, *FRET - Förster resonance energy transfer from theory to applications*, pages 323–353. Wiley-VCH Verlag GmbH, Weinheim, Germany, 2014.

[72] A. Roda, E. Guardigli, M.and Michelini, and M. Mirasoli. Nanobioanalytical luminescence: Förster-type energy transfer methods. *Analytical and Bioanalytical Chemistry*, 393:109–123, 2009.

[73] W. Zhong. Nanomaterials in fluorescence-based biosensing. *Analytical and Bioanalytical Chemistry*, 394:47–59, 2009.

[74] B. Hötzer, I. L. Medintz, and N. Hildebrandt. Fluorescence in Nanobiotechnology: Sophisticated Fluorophores for Novel Applications. *Small*, 8:2297–2326, 2012.

[75] K. E. Sapsford, B. Wildt, A. Mariani, A. B. Yeatts, and I. L. Medintz. Materials for FRET analysis: Beyond traditional dye-dye combinations. In I. L. Medintz and N. Hildebrandt, editors, *FRET - Förster resonance energy transfer from theory to applications*, pages 165–236. Wiley-VCH Verlag GmbH, Weinheim, Germany, 2014.

[76] J. M. Singer and R. M. Plotz. The latex fixation test. I. Application to the serologic diagnosis of rheumatoid arthritis. *Am. J. Med.*, 21:888–892, 1956.

[77] P. L. Masson, C. L. Cambiaso, D. Collet-Cassart, C. G. M. Magnusson, C. B. Richards, and C. J. M. Sindic. *Methods Enzymology*, 74:106–139, 1981.

[78] Gustav K. Von Schulthess, Richard J. Cohen, and George B. Benedek. Laser light scattering spectroscopic immunoassay in the agglutination-inhibition mode for human chorionic gonadotropin (hCG) and human luteinizing hormone (hLH). *Immunochemistry*, 13:963–966, 1976.

[79] J. H. Leuvering, P. J. Thal, M. van der Waart, and A. H. Schuurs. Sol particle immunoassay (SPIA). *Journal of Immunoassay*, 1:77–91, 1980.

[80] Xiong Liu, Qiu Dai, Lauren Austin, Janelle Coutts, Genevieve Knowles, Jianhua Zou, Hui Chen, and Qun Huo. A One-Step Homogeneous Immunoassay for Cancer Biomarker Detection Using Gold Nanoparticle Probes Coupled with Dynamic Light Scattering. *Journal of the American Chemical Society*, 130:2780–2782, 2008.

[81] Ji-Wei Chen, Yong Lei, Xiang-Jiang Liu, Jian-Hui Jiang, Guo-Li Shen, and Ru-Qin Yu. Immunoassay using surface-enhanced Raman scattering based on aggregation of reporter-labeled immunogold nanoparticles. *Analytical and Bioanalytical Chemistry*, 392:187–193, 2008.

[82] A. Yasuda, Y. Ishimori, and M. Umeda. Immunoassay Using Fluorescent Dye-Trapped Liposomes Liposome Immune Lysis Assay (LILA). *Nonisotopic Immunoassay*, pages 389–399, 1988.

[83] R. Leute, E. F. Ullman, and A. Goldstein. Spin immunoassay of opium narcotics in urine and saliva. *J. Am. Med. Asso.*, 221:1231–1234, 1972.

[84] H. E. Hart and E. B. Greenwald. Scintillation proximity assay (SPA)–a new method of immunoassay. Direct and inhibition mode detection with human albumin and rabbit antihuman albumin. *Molecular Immunology*, 16:265–267, 1979.

[85] G. A. Robinson, G. Martinazzo, and G. C. Forrest. A homogeneous bioelectrochemical immunoassay for thyroxine. *Journal of Immunoassay*, 7:1–15, 1986.

[86] Y. Ikariyama, H. Kunoh, and M. Aizawa. Electrochemical luminescence-based homogeneous immunoassay. *Biochemical and Biophysical Research Communications*, 128:987–992, 1985.

[87] N. Hoshino, R. Nakajima, and I. Yamazaki. The effect of polymerization of horseradish peroxidase on the peroxidase activity in the presence of excess H2o2: a background for a homogeneous enzyme immunoassay. *Journal of Biochemistry*, 102:785–791, 1987.

[88] I. Gibbons, T. M. Hanlon, C. N. Skold, M. E. Russel, and E. F. Ullman. Enzyme-enhancement immunoassay: a homogeneous assay for polyvalent ligands and antibodies. *Clinical Chemistry*, 27:1602–1608, 1981.

[89] D. J. Litman, T. M. Hanlon, and E. F. Ullman. Enzyme channeling immunoassay: a new homogeneous enzyme immunoassay technique. *Analytical Biochemistry*, 106:223–229, 1980.

[90] M. Gonnelli, E. Gabellieri, G. Montagnoli, and R. Felicioli. Complementing S-peptide as modulator in enzyme immunoassay. *Biochemical and Biophysical Research Communications*, 102:917–923, 1981.

[91] E. F. Ullman, H. Kirakossian, A. C. Switchenko, J. Ishkanian, M. Ericson, C. A. Wartchow, M. Pirio, J. Pease, B. R. Irvin, S. Singh, R. Singh, R. Patel, A. Dafforn, D. Davalian, C. Skold, N. Kurn, and D. B. Wagner. Luminescent oxygen channeling assay (LOCI): sensitive, broadly applicable homogeneous immunoassay method. *Clinical Chemistry*, 42:1518–1526, 1996.

[92] David M. Jameson and Justin A. Ross. Fluorescence polarization/anisotropy in diagnostics and imaging. *Chemical Reviews*, 110:2685–2708, 2010.

[93] Christian Eggeling, Peet Kask, Dirk Winkler, and Stefan Jäger. Rapid analysis of Förster resonance energy transfer by two-color global fluorescence correlation spectroscopy: trypsin proteinase reaction. *Biophysical Journal*, 89:605–618, 2005.

[94] K. Kuningas, H. Pakkila, T. Ukonaho, T. Rantanen, T. Lovgren, and T. Soukka. Upconversion Fluorescence Enables Homogeneous Immunoassay in Whole Blood. *Clinical Chemistry*, 53:145–146, 2006.

[95] A. Patel and A. K. Campbell. Homogeneous immunoassay based on chemiluminescence energy transfer. *Clinical Chemistry*, 29:1604–1608, 1983.

[96] M. Nič, J. Jirát, B. Košata, A. Jenkins, and A. McNaught, editors. *IUPAC Compendium of Chemical Terminology: Gold Book,http://goldbook.iupac.org.* IUPAC, Research Triagle Park, NC, 2.1.0 edition, 2009.

[97] R. Ekins and P. Edwards. On the meaning of "sensitivity". *Clinical Chemistry*, 43:1824–1831, 1997.

[98] H. L. Pardue. The inseparable triad: analytical sensitivity, measurement uncertainty, and quantitative resolution. *Clinical Chemistry*, 43:1831–1837, 1997.

[99] C. A. Spencer. Thyroid profiling for the 1990's: free T4 estimate or sensitive TSH measurement. *J. Clin. Immunoassay*, 12:82–89, 1989.

[100] R. B. Murphy. On the meaning of precision and accuracy. *Mater. Res. Stand.*, 1:264–267, 1961.

[101] D. MacDougall and W. B. Crummett. Guidelines for data acquisition and data quality evaluation in environmental chemistry. *Analytical Chemistry*, 52:2242–2249, 1980.

[102] P. C. Ray, Z. Fan, R. A. Crouch, S. S. Sinha, and A. Pramanik. Nanoscopic optical rulers beyond the FRET distance limit: fundamentals and applications. *Chemical Society Reviews*, 43:6370–6404, 2014.

[103] S. Weiss. Fluorescence Spectroscopy of Single Biomolecules. *Science*, 283:1676–1683, 1999.

[104] J. Hohlbein, T. D. Craggs, and T. Cordes. Alternating-laser excitation: single-molecule FRET and beyond. *Chemical Society Reviews*, 43:1156–1171, 2014.

[105] X. Zhuang. Single-Molecule RNA Science. *Annual Review of Biophysics and Biomolecular Structure*, 34:399–414, 2005.

[106] R. E. Stenkamp, I. Le. Trong, L. Klumb, P. S. Stayton, and S. Freitag. Structural studies of the streptavidin binding loop. *Protein Science*, 6:1157–1166, 1997.

[107] A. Pähler, W. A. Hendrickson, M. A. Kolks, C. E. Argaraña, and C. R. Cantor. Characterization and crystallization of core streptavidin. *The Journal of Biological Chemistry*, 262:13933–13937, 1987.

[108] W. A. Hendrickson, A. Pahler, J. L. Smith, Y. Satow, E. A. Merritt, and R. P. Phizackerley. Crystal structure of core streptavidin determined from multiwavelength anomalous diffraction of synchrotron radiation. *Proceedings of the National Academy of Sciences*, 86:2190–2194, 1989.

[109] P. Weber, D. Ohlendorf, J. Wendoloski, and F. Salemme. Structural origins of high-affinity biotin binding to streptavidin. *Science*, 243:85–88, 1989.

[110] A. Loosli, U. E. Rusbandi, J. Gradinaru, K. Bernauer, C. W. Schlaepfer, M. Meyer, S. Mazurek, M. Novic, and T. R. Ward. (Strept)avidin as Host for Biotinylated Coordination Complexes: Stability, Chiral Discrimination, and Cooperativity. *Inorganic Chemistry*, 45:660–668, 2006.

[111] S. Freitag, I. Le Trong, L. Klumb, P. S. Stayton, and R. E. Stenkamp. Structural studies of the streptavidin binding loop. *Protein Science: A Publication of the Protein Society*, 6:1157–1166, 1997.

[112] T. Sano and C. R. Cantor. Cooperative biotin binding by streptavidin. Electrophoretic behavior and subunit association of streptavidin in the presence of 6 M urea. *The Journal of Biological Chemistry*, 265:3369–3373, 1990.

[113] M. Lisa Jones and Gary P. Kurzban. Noncooperativity of Biotin Binding to Tetrameric Streptavidin. *Biochemistry*, 34:11750–11756, 1995.

[114] N. M. Green. Avidin and Streptavidin. *Methods Enzymology*, 184:51–67, 1990.

[115] E. A. Bayer, H. Ben-Hur, and M. Wilchek. Isolation and Properties of Streptavidin. *Methods Enzymology*, 184:80–89, 1990.

[116] M. Howarth, D. J.-F. Chinnapen, K. Gerrow, P. C. Dorrestein, M. R. Grandy, N. L. Kelleher, A. El-Husseini, and A. Y. Ting. A monovalent streptavidin with a single femtomolar biotin binding site. *Nature Methods*, 3:267–273, 2006.

[117] M. Howarth and A. Y. Ting. Imaging proteins in live mammalian cells with biotin ligase and monovalent streptavidin. *Nature Protocols*, 3:534–545, 2008.

[118] K.E. Sapsford, T. Pons, I.L. Medintz, S. Higashiya, F.M. Brunel, P.E. Dawson, and H. Mattoussi. Kinetics of Metal-Affinity Driven Self-Assembly between Proteins or Peptides and CdSe-ZnS Quantum Dots. *Journal of Physical Chemistry C*, 111:11528–11538, 2007.

[119] A. M. Dennis and G. Bao. Quantum dot-fluorescent protein pairs as novel fluorescence resonance energy transfer probes. *Nano Letters*, 8:1439–1445, 2008.

[120] D. E. Prasuhn, J. B. Blanco-Canosa, G. J. Vora, J. B. Delehanty, K. Susumu, B. C. Mei, P. E. Dawson, and I. L. Medintz. Combining Chemoselective Ligation with Polyhistidine-Driven Self-Assembly for the Modular Display of Biomolecules on Quantum Dots. *ACS Nano*, 4:267–278, 2010.

[121] A. M. Dennis, D. C. Sotto, B. C. Mei, I. L. Medintz, H. Mattoussi, and G. Bao. Surface Ligand Effects on Metal-Affinity Coordination to Quantum Dots: Implications for Nanoprobe Self-Assembly. *Bioconjugate Chemistry*, 21:1160–1170, 2010.

[122] J.-C. G. Bünzli and C. Piguet. Taking advantage of luminescent lanthanide ions. *Chemical Society Reviews*, 34:1048–1077, 2005.

[123] S. V. Eliseeva and J.-C. G. Bünzli. Lanthanide luminescence for functional materials and bio-sciences. *Chemical Society Reviews*, 39:189–227, 2010.

[124] D. A. Atwood. *The rare earth elements: fundamentals and applications*. John Wiley & Sons, Inc, Chichester, West Sussex, United Kingdom ; Hoboken, 2012.

[125] C. Janiak, T. M. Klapötke, H.-J. Meyer, and E. Riedel. *Moderne anorganische Chemie*. De Gruyter, Berlin; New York, 2nd edition, 2003.

[126] Richard Beatty. *The lanthanides*. The elements. Marshall Cavendish Benchmark, New York, 2008.

[127] F. A. Cotton. *Advanced inorganic chemistry*. Wiley, New York, 6th edition, 1999.

[128] A. F. Holleman, E. Wiberg, and N. Wiberg. *Lehrbuch der anorganischen Chemie*. de Gruyter, Berlin; New York, 2007.

[129] C. Görller-Walrand and K. Binnemans. Rationalization of Crystal-Field Parametrization. In *Handbook on the Physics and Chemistry of Rare Earths*, pages 121–283. Elsevier Science B. V., 1996.

[130] P. W. Atkins, A. Höpfner, and A. Schleitzer. *Physikalische Chemie*. Wiley-VCH, Weinheim, 2001.

[131] Niko Hildebrandt. *Lanthanides and Quantum Dots - Time-Resolved Laser Spectroscopy of Biochemical Förster Resonance Energy Transfer (FRET) Systems*. PhD thesis, University Potsdam, 2006.

[132] William T. Carnell. The absorption and fluorescence spectra of rare earth ion sin solution. In K. A. Geschneidner and L. Eyring, editors, *Handbook on the Physics and Chemistry of Rare Earth*, pages 171–208. North-Holland Publishing Company, 1979.

[133] S. I. Weissman. Intramolecular Energy Transfer The Fluorescence of Complexes of Europium. *The Journal of Chemical Physics*, 10:214–217, 1942.

[134] B. D. Schlyer, D. G. Steel, and A. Gafni. Direct Kinetic Evidence for Triplet State Energy Transfer from Escherichia coli Alkaline Phosphatase Tryptophan 109 to Bound Terbium. *Journal of Biological Chemistry*, 270:22890–22894, 1995.

[135] M. Latva, H. Takalo, V.-M. Mukkala, C. Matachescu, J. C. Rodríguez-Ubis, and J. Kankare. Correlation between the lowest triplet state energy level of the ligand and lanthanide(III) luminescence quantum yield. *Journal of Luminescence*, 75:149–169, 1997.

[136] W. DeW. Horrocks and D. R. Sudnick. Lanthanide ion probes of structure in biology. Laser-induced luminescence decay constants provide a direct measure of the number of metal-coordinated water molecules. *Journal of the American Chemical Society*, 101:334–340, 1979.

[137] Martinus H. V. Werts, Ronald T. F. Jukes, and Jan W. Verhoeven. The emission spectrum and the radiative lifetime of Eu3+ in luminescent lanthanide complexes. *Physical Chemistry Chemical Physics*, 4:1542–1548, 2002.

[138] Annina Aebischer, Frédéric Gumy, and Jean-Claude G. Bünzli. Intrinsic quantum yields and radiative lifetimes of lanthanide tris(dipicolinates). *Physical Chemistry Chemical Physics*, 11:1346, 2009.

[139] J.-C. G. Bünzli and S. V. Eliseeva. Intriguing aspects of lanthanide luminescence. *Chemical Science*, 4:1939–1949, 2013.

[140] Erkki Soini, Timo Lövgren, and Charles B. Reimer. Time-Resolved Fluorescence of Lanthanide Probes and Applications in Biotechnology. *C R C Critical Reviews in Analytical Chemistry*, 18:105–154, 1987.

[141] L. Seveus, M. Väisälä, S. Syrjänen, M. Sandberg, A. Kuusisto, R. Harju, J. Salo, I. Hemmilä, H. Kojola, and E. Soini. Time-resolved fluorescence imaging of europium chelate label in immunohistochemistry and in situ hybridization. *Cytometry*, 13:329–338, 1992.

[142] J. Yu, D. Parker, R. Pal, R. A. Poole, and M. J. Cann. A Europium Complex That Selectively Stains Nucleoli of Cells. *Journal of the American Chemical Society*, 128:2294–2299, 2006.

[143] B. Song, C. D. B. Vandevyver, A.-S. Chauvin, and J.-C. G. Bünzli. Time-resolved luminescence microscopy of bimetallic lanthanide helicates in living cells. *Organic & Biomolecular Chemistry*, 6:4125, 2008.

[144] C. P. Montgomery, B. S. Murray, E. J. New, R. Pal, and D. Parker. Cell-Penetrating Metal Complex Optical Probes: Targeted and Responsive Systems Based on Lanthanide Luminescence. *Accounts of Chemical Research*, 42:925–937, 2009.

[145] E. J. New, D. Parker, D. G. Smith, and J. W. Walton. Development of responsive lanthanide probes for cellular applications. *Current Opinion in Chemical Biology*, 14:238–246, 2010.

[146] H. Rajapakse, D. R. Reddy, S. Mohandessi, N. Butlin, and L. W. Miller. Luminescent Terbium Protein Labels for Time-Resolved Microscopy and Screening. *Angewandte Chemie International Edition*, 48:4990–4992, 2009.

[147] T. Ito, M. Inoue, K. Akamatsu, E. Kusaka, K. Tanabe, and S.-i. Nishimoto. $\alpha_v\beta_3$-Integrin-targeting lanthanide complex: Synthesis and evaluation as a tumor-homing luminescent probe. *Bioorganic & Medicinal Chemistry Letters*, 21:3515–3518, 2011.

[148] V. Fernández-Moreira, B. Song, V. Sivagnanam, A.-S. Chauvin, C. D. B. Vandevyver, M. Gijs, I. Hemmilä, H.-A. Lehr, and J.-C. G. Bünzli. Bioconjugated lanthanide luminescent helicates as multilabels for lab-on-a-chip detection of cancer biomarkers. *The Analyst*, 135:42–52, 2010.

[149] S. Lindén, M. K. Singh, K. D. Wegner, M. Regairaz, F. Dautry, F. Treussart, and N. Hildebrandt. Terbium-based time-gated Förster resonance energy transfer imaging for evaluating protein–protein interactions on cell membranes. *Dalton Transaction*, 44:4994–5003, 2015.

[150] C. Bouzigues, T. Gacoin, and A. Alexandrou. Biological Applications of Rare-Earth Based Nanoparticles. *ACS Nano*, 5:8488–8505, 2011.

[151] C. S. Bonnet, F. Buron, F. Caillé, C. M. Shade, B. Drahoš, L. Pellegatti, J. Zhang, S. Villette, L. Helm, C. Pichon, F. Suzenet, S. Petoud, and É. Tóth. Pyridine-Based Lanthanide Complexes Combining MRI and NIR Luminescence Activities. *Chemistry - A European Journal*, 18:1419–1431, 2012.

[152] F. Caillé, C. S. Bonnet, F. Buron, S. Villette, L. Helm, S. Petoud, F. Suzenet, and É. Tóth. Isoquinoline-Based Lanthanide Complexes: Bright NIR Optical Probes and Efficient MRI Agents. *Inorganic Chemistry*, 51:2522–2532, 2012.

[153] F. Auzel. Upconversion and Anti-Stokes Processes with f and d Ions in Solids. *Chemical Reviews*, 104:139–174, 2004.

[154] G. Chen, H. Qiu, P. N. Prasad, and X. Chen. Upconversion Nanoparticles: Design, Nanochemistry, and Applications in Theranostics. *Chemical Reviews*, 114:5161–5214, 2014.

[155] J. Zhou, Z. Liu, and F. Li. Upconversion nanophosphors for small-animal imaging. *Chemical Society Reviews*, 41:1323–1349, 2012.

[156] P. R. Selvin. Principles and Biophysical Applications of Lanthanoid-Based Probes. *Annual Review of Biophysics and Biomolecular Structure*, 31:275–302, 2002.

[157] L. J. Charbonnière, N. Hildebrandt, R. F. Ziessel, and H.-G. Löhmannsröben. Lanthanides to Quantum Dots Resonance Energy Transfer in Time-Resolved Fluoro-Immunoassays and Luminescence Microscopy. *Journal of the American Chemical Society*, 128:12800–12809, 2006.

[158] L. J. Charbonnière and N. Hildebrandt. Lanthanide Complexes and Quantum Dots: A Bright Wedding for Resonance Energy Transfer (Eur. J. Inorg. Chem. 21/2008). *European Journal of Inorganic Chemistry*, 2008:3231–3231, 2008.

[159] Cisbio, "HTFR Technology". *http://www.cisbio.com/usa/drug-discovery/htrf-technology*, (24.04.2015).

[160] BRAHMS, "TRACE Technology". *http://www.kryptor.net/Default.aspx?tabindex= 4&tabid=254*, (24.04.2015).

[161] Perkin elmer, "LANCE TR-FRET assays". *http://www.perkinelmer.com/catalog/category/id/lance%20reagents*, (24.04.2015).

[162] Life Technologies, "LanthaScreen TR-FRET". *http://www.lifetechnologies.com/fr/fr/home/life-science/drug-discovery/target-and-lead-identification-and-validation/kinasebiology/kinase-activity-assays/lanthascreen-tr-fret-toolbox/lanthascreen-tr-fret-technology-overview.html*, (24.04.2015).

[163] A. I. Ekimov and A. A. Onushchenko. Quantum size effect in three-dimensional microscopic semiconductor crystals. *JETP Letters*, 34:345–349, 1981.

[164] A. L. Efros and A. L. Efros. Interband Absorption of Light in a Semiconductor Sphere. *Soviet Physics-Semiconductors*, 16:772–775, 1982.

[165] R. Rosetti, J. L. Ellison, J. M. Gibson, and L. E. Brus. Size effects in the excited electronic states of small colloidal CdS crystallites. *The Journal of Chemical Physics*, 80:4464–4469, 1984.

[166] L. Brus. Electronic wave functions in semiconductor clusters: experiment and theory. *The Journal of Physical Chemistry*, 90:2555–2560, 1986.

[167] V. Biju. Chemical modifications and bioconjugate reactions of nanomaterials for sensing, imaging, drug delivery and therapy. *Chemical Society Reviews*, 43:744–764, 2014.

[168] M. Bruchez Jr., M. Moronne, P. Gin, S. Weiss, and A. P. Alivisatos. Semiconductor Nanocrystals as Fluorescent Biological Labels. *Science*, 281:2013–2016, 1998.

[169] W. C. W. Chan and S. Nie. Quantum Dot Bioconjugates for Ultrasensitive Nonisotopic Detection. *Science*, 281:2016–2018, 1998.

[170] C. B. Murray, D. J. Norris, and M. G. Bawendi. Synthesis and characterization of nearly monodisperse CdE (E = sulfur, selenium, tellurium) semiconductor nanocrystallites. *Journal of the American Chemical Society*, 115:8706–8715, 1993.

[171] M. A. Hines and P. Guyot-Sionnest. Synthesis and Characterization of Strongly Luminescing ZnS-Capped CdSe Nanocrystals. *The Journal of Physical Chemistry*, 100:468–471, 1996.

[172] B. O. Dabbousi, J. Rodriguez-Viejo, F. V. Mikulec, J. R. Heine, H. Mattoussi, R. Ober, K. F. Jensen, and M. G. Bawendi. (CdSe)ZnS Core-Shell Quantum Dots: Synthesis and Characterization of a Size Series of Highly Luminescent Nanocrystallites. *The Journal of Physical Chemistry B*, 101:9463–9475, 1997.

[173] Z. A. Peng and X. Peng. Formation of High-Quality CdTe, CdSe, and CdS Nanocrystals Using CdO as Precursor. *Journal of the American Chemical Society*, 123:183–184, 2001.

[174] A. P. Alivisatos, W. Gu, and C. Larabell. QUANTUM DOTS AS CELLULAR PROBES. *Annual Review of Biomedical Engineering*, 7:55–76, 2005.

[175] T. Pellegrino, L. Manna, S. Kudera, T. Liedl, D. Koktysh, A. L. Rogach, S. Keller, J. Rädler, G. Natile, and W. J. Parak. Hydrophobic Nanocrystals Coated with an Amphiphilic Polymer Shell: A General Route to Water Soluble Nanocrystals. *Nano Letters*, 4:703–707, 2004.

[176] D. Gerion, F. Pinaud, S. C. Williams, W. J. Parak, D. Zanchet, S. Weiss, and A. P. Alivisatos. Synthesis and Properties of Biocompatible Water-Soluble Silica-Coated CdSe/ZnS Semiconductor Quantum Dots †. *The Journal of Physical Chemistry B*, 105:8861–8871, 2001.

[177] H. Mattoussi, G. Palui, and H. B. Na. Luminescent quantum dots as platforms for probing in vitro and in vivo biological processes. *Advanced Drug Delivery Reviews*, 64:138–166, 2012.

[178] T. Pons, H. T. Uyeda, I. L. Medintz, and H. Mattoussi. Hydrodynamic Dimensions, Electrophoretic Mobility, and Stability of Hydrophilic Quantum Dots. *The Journal of Physical Chemistry B*, 110:20308–20316, 2006.

[179] P. del Pino, B. Pelaz, Q. Zhang, P. Maffre, G. U. Nienhaus, and W. J. Parak. Protein corona formation around nanoparticles – from the past to the future. *Materials Horizon*, 1:301–313, 2014.

[180] E. L. Bentzen, I. D. Tomlinson, J. Mason, P. Gresch, M. R. Warnement, D. Wright, E. Sanders-Bush, R. Blakely, and S. J. Rosenthal. Surface Modification To Reduce Nonspecific Binding of Quantum Dots in Live Cell Assays. *Bioconjugate Chemistry*, 16:1488–1494, 2005.

[181] K. Susumu, H. T. Uyeda, I. L. Medintz, T. Pons, J. B. Delehanty, and H. Mattoussi. Enhancing the Stability and Biological Functionalities of Quantum Dots via Compact Multifunctional Ligands. *Journal of the American Chemical Society*, 129:13987–13996, 2007.

[182] B. C. Mei, K. Susumu, I. L. Medintz, J. B. Delehanty, T. J. Mountziaris, and H. Mattoussi. Modular poly(ethylene glycol) ligands for biocompatible semiconductor and gold nanocrystals with extended pH and ionic stability. *Journal of Materials Chemistry*, 18:4949–4958, 2008.

[183] T. L. Jennings, S. G. Becker-Catania, R. C. Triulzi, G. Tao, B. Scott, K. E. Sapsford, S. Spindel, E. Oh, V. Jain, J. B. Delehanty, D. E. Prasuhn, K. Boeneman, W. R. Algar, and I. L. Medintz. Reactive Semiconductor Nanocrystals for Chemoselective Biolabeling and Multiplexed Analysis. *ACS Nano*, 5:5579–5593, 2011.

[184] S. Clarke, F. Pinaud, O. Beutel, C. You, J. Piehler, and M. Dahan. Covalent Monofunctionalization of Peptide-Coated Quantum Dots for Single-Molecule Assays. *Nano Letters*, 10:2147–2154, 2010.

[185] J. Farlow, D. Seo, K. E. Broaders, M. J. Taylor, Z. J. Gartner, and Y.-W. Jun. Formation of targeted monovalent quantum dots by steric exclusion. *Nature Methods*, 10:1203–1205, 2013.

[186] A. L. Rogach, L. Katsikas, A. Kornowski, D. Su, A. Eychmüller, and H. Weller. Synthesis and characterization of thiol-stabilized CdTe nanocrystals. *Ber. Bunsenges. Phys. Chem.*, 100:1772–1778, 1996.

[187] Y. Zheng, S. Gao, and J. Y. Ying. Synthesis and Cell-Imaging Applications of Glutathione-Capped CdTe Quantum Dots. *Advanced Materials*, 19:376–380, 2007.

[188] W.-C. Law, K.-T. Yong, I. Roy, H. Ding, R. Hu, W. Zhao, and P. N. Prasad. Aqueous-Phase Synthesis of Highly Luminescent CdTe/ZnTe Core/Shell Quantum Dots Optimized for Targeted Bioimaging. *Small*, 5:1302–1310, 2009.

[189] G. H. T. Au, W. Y. Shih, and W.-H. Shih. High-conjugation-efficiency aqueous CdSe quantum dots. *The Analyst*, 138:7316–7325, 2013.

[190] S. R. Stürzenbaum, M. Höckner, A. Panneerselvam, J. Levitt, J.-S. Bouillard, S. Taniguchi, L.-A. Dailey, R. Ahmad Khanbeigi, E. V. Rosca, M. Thanou, K. Suhling, A. V. Zayats, and M. Green. Biosynthesis of luminescent quantum dots in an earthworm. *Nature Nanotechnology*, 8:57–60, 2012.

[191] H. Trabelsi, I. Azzouz, M. Sakly, and H. Abdelmelek. Subacute toxicity of cadmium on hepatocytes and nephrocytes in the rat could be considered as a green biosynthesis of nanoparticles. *International Journal of Nanomedicine*, 8:1121–1128, 2013.

[192] X. Michalet. Quantum Dots for Live Cells, in Vivo Imaging, and Diagnostics. *Science*, 307:538–544, 2005.

[193] C. A. Leatherdale, W.-K. Woo, F. V. Mikulec, and M. G. Bawendi. On the Absorption Cross Section of CdSe Nanocrystal Quantum Dots. *The Journal of Physical Chemistry B*, 106:7619–7622, 2002.

[194] D. R. Larson. Water-Soluble Quantum Dots for Multiphoton Fluorescence Imaging in Vivo. *Science*, 300:1434–1436, 2003.

[195] A. R. Clapp, T. Pons, I. L. Medintz, J. B. Delehanty, J. S. Melinger, T. Tiefenbrunn, P. E. Dawson, B. R. Fisher, B. O'Rourke, and H. Mattoussi. Two-Photon Excitation of Quantum-Dot-Based Fluorescence Resonance Energy Transfer and Its Applications. *Advanced Materials*, 19:1921–1926, 2007.

[196] M. Dahan, T. Laurence, F. Pinaud, D. S. Chemla, A. P. Alivisatos, M. Sauer, and S. Weiss. Time-gated biological imaging by use of colloidal quantum dots. *Optics Letters*, 26:825–827, 2001.

[197] X. Wu, H. Liu, J. Liu, K. N. Haley, J. A. Treadway, J. P. Larson, N. Ge, F. Peale, and M. P. Bruchez. Immunofluorescent labeling of cancer marker Her2 and other cellular targets with semiconductor quantum dots. *Nature Biotechnology*, 21:41–46, 2002.

[198] H.E. Grecco, K.A. Lidke, R. Heintzmann, D.S. Lidke, C. Spagnuolo, O.E. Martinez, E.A. Jares-Erijman, and T.M. Jovin. Ensemble and single particle photophysical

properties (two-photon excitation, anisotropy, FRET, lifetime, spectral conversion) of commercial quantum dots in solution and in live cells. *Microscopy Research and Technique*, 65:169–179, 2004.

[199] Y. Choi, H. P. Kim, S. M. Hong, J. Y. Ryu, S. J. Han, and R. Song. In situ Visualization of Gene Expression Using Polymer-Coated Quantum-Dot-DNA Conjugates. *Small*, 5:2085–2091, 2009.

[200] I. L. Medintz and H. Mattoussi. Quantum dot-based resonance energy transfer and its growing application in biology. *Physical Chemistry Chemical Physics*, 11:17–45, 2009.

[201] W. R. Algar, A. J. Tavares, and U. J. Krull. Beyond labels: A review of the application of quantum dots as integrated components of assays, bioprobes, and biosensors utilizing optical transduction. *Analytica Chimica Acta*, 673:1–25, 2010.

[202] Z. Jin and N. Hildebrandt. Semiconductor quantum dots for in vitro diagnostics and cellular imaging. *Trends in Biotechnology*, 30:394–403, 2012.

[203] W. J. Parak, T. Pellegrino, and C. Plank. Labelling of cells with quantum dots. *Nanotechnology*, 16:R9–R25, 2005.

[204] Q. Li, L. Liu, J.-W. Liu, J.-H. Jiang, R.-Q. Yu, and X. Chu. Nanomaterial-based fluorescent probes for live-cell imaging. *TrAC Trends in Analytical Chemistry*, 58:130–144, 2014.

[205] M. Chen, X. He, K. Wang, D. He, X. Yang, and H. Shi. Inorganic fluorescent nanoprobes for cellular and subcellular imaging. *TrAC Trends in Analytical Chemistry*, 58:120–129, 2014.

[206] X. Gao, L. Yang, J. A. Petros, F. F. Marshall, J. W. Simons, and S. Nie. In vivo molecular and cellular imaging with quantum dots. *Current Opinion in Biotechnology*, 16:63–72, 2005.

[207] L. A. Bentolila, Y. Ebenstein, and S. Weiss. Quantum Dots for In Vivo Small-Animal Imaging. *Journal of Nuclear Medicine*, 50:493–496, 2009.

[208] M. A. Walling, J. A. Novak, and J. R. E. Shepard. Quantum Dots for Live Cell and In Vivo Imaging. *International Journal of Molecular Sciences*, 10:441–491, 2009.

[209] V. Biju, S. Mundayoor, R. V. Omkumar, A. Anas, and M. Ishikawa. Bioconjugated quantum dots for cancer research: Present status, prospects and remaining issues. *Biotechnology Advances*, 28:199–213, 2010.

[210] R. Hardman. A Toxicologic Review of Quantum Dots: Toxicity Depends on Physicochemical and Environmental Factors. *Environmental Health Perspectives*, 114:165–172, 2006.

[211] B. A. Rzigalinski and J. S. Strobl. Cadmium-containing nanoparticles: Perspectives on pharmacology and toxicology of quantum dots. *Toxicology and Applied Pharmacology*, 238:280–288, 2009.

[212] J. L. Pelley, A. S. Daar, and M. A. Saner. State of Academic Knowledge on Toxicity and Biological Fate of Quantum Dots. *Toxicological Sciences*, 112:276–296, 2009.

[213] M. Bottrill and M. Green. Some aspects of quantum dot toxicity. *Chemical Communications*, 47:7039–7050, 2011.

[214] S. J. Soenen, P. Rivera-Gil, J.-M. Montenegro, W. J. Parak, S. C. De Smedt, and K. Braeckmans. Cellular toxicity of inorganic nanoparticles: Common aspects and guidelines for improved nanotoxicity evaluation. *Nano Today*, 6:446–465, 2011.

[215] F. M. Winnik and D. Maysinger. Quantum Dot Cytotoxicity and Ways To Reduce It. *Accounts of Chemical Research*, 46:672–680, 2013.

[216] R. L. Orndorff and S. J. Rosenthal. Neurotoxin Quantum Dot Conjugates Detect Endogenous Targets Expressed in Live Cancer Cells. *Nano Letters*, 9:2589–2599, 2009.

[217] D.-H. Huang, L. Su, X.-H. Peng, H. Zhang, F. R. Khuri, D. M. Shin, and Z. Chen. Quantum dot-based quantification revealed differences in subcellular localization of EGFR and E-cadherin between EGFR-TKI sensitive and insensitive cancer cells. *Nanotechnology*, 20:225102, 2009.

[218] W. Jiang, A. Singhal, B. Kim, J. Zheng, J. Rutka, C. Wang, and W. Chan. Assessing Near-Infrared Quantum Dots for Deep Tissue, Organ, and Animal Imaging Applications. *Journal of the Association for Laboratory Automation*, 13:6–12, 2008.

[219] A. B. Rosen, D. J. Kelly, A. J. T. Schuldt, J. Lu, I. A. Potapova, S. V. Doronin, K. J. Robichaud, R. B. Robinson, M. R. Rosen, P. R. Brink, G. R. Gaudette, and I. S. Cohen. Finding Fluorescent Needles in the Cardiac Haystack: Tracking Human Mesenchymal Stem Cells Labeled with Quantum Dots for Quantitative In Vivo Three-Dimensional Fluorescence Analysis. *Stem Cells*, 25:2128–2138, 2007.

[220] K. Kikushima, S. Kita, and H. Higuchi. A non-invasive imaging for the in vivo tracking of high-speed vesicle transport in mouse neutrophils. *Scientific Reports*, 3:1913, 2013.

[221] Y. Zhao, S. L. Lo, Y. Zheng, D. H. Lam, C. Wu, M. Y. Han, and S. Wang. Quantum dot coating of baculoviral vectors enables visualization of transduced cells and tissues. *Biochemical and Biophysical Research Communications*, 434:110–116, 2013.

[222] R. Savla, O. Taratula, O. Garbuzenko, and T. Minko. Tumor targeted quantum dot-mucin 1 aptamer-doxorubicin conjugate for imaging and treatment of cancer. *Journal of Controlled Release*, 153:16–22, 2011.

[223] D. Shao, J. Li, X. Xiao, M. Zhang, Y. Pan, S. Li, Z. Wang, X. Zhang, H. Zheng, X. Zhang, and L. Chen. Real-Time Visualizing and Tracing of HSV-TK/GCV Suicide Gene Therapy by Near-Infrared Fluorescent Quantum Dots. *ACS Applied Materials & Interfaces*, 6:11082–11090, 2014.

[224] C.-J. Wen, C. T. Sung, I. A. Aljuffali, Y.-J. Huang, and J.-Y. Fang. Nanocomposite liposomes containing quantum dots and anticancer drugs for bioimaging and therapeutic delivery: a comparison of cationic, PEGylated and deformable liposomes. *Nanotechnology*, 24:325101, 2013.

[225] S. Kim, Y. T. Lim, E. G. Soltesz, A. M. De Grand, Ja. Lee, A. Nakayama, J. A. Parker, T. Mihaljevic, R. G. Laurence, D. M. Dor, L. H. Cohn, M. G. Bawendi, and J. V. Frangioni. Near-infrared fluorescent type II quantum dots for sentinel lymph node mapping. *Nature Biotechnology*, 22:93–97, 2004.

[226] E. Tanaka, H. S. Choi, H. Fujii, M. G. Bawendi, and J. V. Frangioni. Image-Guided Oncologic Surgery Using Invisible Light: Completed Pre-Clinical Development for Sentinel Lymph Node Mapping. *Annals of Surgical Oncology*, 13:1671–1681, 2006.

[227] A. Amit, R. Mariuzza, S. Phillips, and R. Poljak. Three-dimensional structure of an antigen-antibody complex at 2.8 A resolution. *Science*, 233:747–753, 1986.

[228] P.G. Wu and L. Brand. Resonance Energy Transfer: Methods and Applications. *Analytical Biochemistry*, 218:1–13, 1994.

[229] A. Sillen and Y. Engelborghs. The correct use of "average" fluorescence parameters. *Photochemistry and Photobiology*, 67:475–486, 1998.

[230] Lei Zhu, Sarath Samudrala, Nikolai Stelmakh, and Michael Vasilyev. Spontaneous decay of CdSe / ZnS core-shell quantum dots at the air-dielectric interface. *Optics Express*, 20:3144, 2012.